STRUCTURE DIRECTION IN THE FORMATION OF ZEOLITIC MATERIALS

Stewart James Warrender

A Thesis Submitted for the Degree of PhD
at the
University of St Andrews

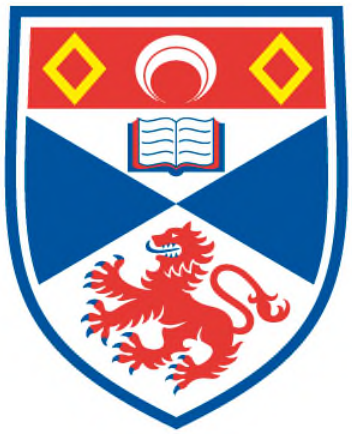

2007

Full metadata for this item is available in
St Andrews Research Repository
at:
http://research-repository.st-andrews.ac.uk/

Please use this identifier to cite or link to this item:
http://hdl.handle.net/10023/376

This item is protected by original copyright

This item is licensed under a
Creative Commons Licence

Structure Direction in the Formation of Zeolitic Materials

A thesis presented for the degree of

Doctor of Philosophy

in the Faculty of Science of the University of St. Andrews

by Stewart James Warrender BSc (Hons)

April 2007

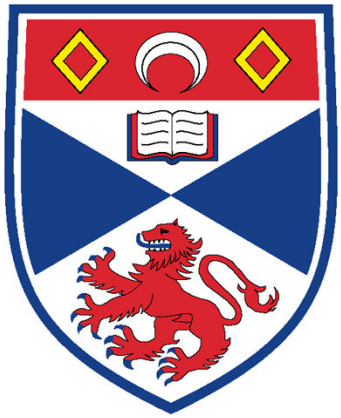

University
of
St Andrews

Declaration

1. I, Stewart J Warrender, hereby certify that this thesis, which is approximately 60,000 words in length, has been written by me, that it is the record of work carried out by me and that it has not been submitted in any previous application for a higher degree.

   date signature of candidate

2. I was admitted as a research student in September 2003 and as a candidate for the degree of PhD in September 2004; the higher study for which this is a record was carried out in the University of St Andrews between 2003 and 2007.

   date signature of candidate

3. I hereby certify that the candidate has fulfilled the conditions of the Resolution and Regulations appropriate for the degree of PhD in the University of St Andrews and that the candidate is qualified to submit this thesis in application for that degree.

   date signature of supervisor

4. In submitting this thesis to the University of St Andrews I wish access to it to be subject to the following conditions: for a period of one year from the date of submission, the thesis shall be withheld from use. I understand, however, that the title and abstract of the thesis will be published during this period of restricted access; and that after the expiry of this period the thesis will be made available for use in accordance with the regulations of the University Library for the time being in force, subject to any copyright in the work not being affected thereby, and a copy of the work may be made and supplied to any bona fide library or research worker, that my thesis will be electronically accessible for personal or research use, and that the library has the right to migrate my thesis into new electronic forms as required to ensure continued access to the thesis. I have obtained any third-party copyright permissions that may be required in order to allow such access and migration.

   date signature of candidate

Abstract

Structure direction in the formation of zeolitic materials has been investigated through the parallel approaches of structural and synthesis studies. The structures of gallosilicates TNU-6 and TNU-7 have been solved from powder X-ray diffraction. TNU-6 ($P6_3$, $a = b = 10.5078(1)$Å, $c = 8.5277(1)$Å) is found to possess a stuffed tridymite-like structure isostructural with $BaFeGaO_4$. Evidence from electron diffraction, single crystal and high-resolution powder X-ray diffraction suggests the presence of a $\sqrt{3}a$ superstructure, analogous to the related $KAlGeO_4$ phase, arising from a subtle variation in tilt of tetrahedral units. The structure of TNU-7 consists of an ordered 1:1 intergrowth of alternating sheets of mazzite and mordenite (*Pmmn*, $a = 7.5721(1)$Å, $b = 17.0739(2)$Å, $c = 25.8438(5)$Å). The crystallisation field of TNU-7 is found to lie between those of mazzite and mordenite, suggesting that this is an example of a 'boundary phase' - phase selectivity being governed strongly by the presence and quantity of Ga in the synthesis gel. The distribution of extra-framework Na^+ cations in the as-made material, and Cs^+ and Sr^{2+} in ion-exchanged samples, suggests a higher extra-framework charge per T-site associated with the mazzite region of the structure, indicating the possible existence of compositional zoning, consistent with the preference to form mazzite at high Ga gel-content. The structures and synthesis conditions for both TNU-6 and TNU-7 suggests a cooperative effect between Ga and extra-framework species in directing the formation of these phases.

The structure of the novel aluminosilicate TNU-9 has been confirmed by energy minimisation and powder neutron diffraction studies (*C2/m*, $a = 28.177(2)$Å, $b = 20.030(1)$Å, $c = 19.464(1)$Å, $\beta = 92.311(4)^o$). Monte Carlo-Simulated Annealing studies have been employed to investigate the favoured location of the 1,4-bis(N-methylpyrrolidinium)butane template molecule within the complex pore system. Remarkably, three (possibly four) different positions are assumed by the structure-directing agent, forming head-to-middle and head-to-head motifs between constituent framework aluminosilicate sheets. TNU-9 crystallises in a very narrow gel composition window suggesting a strong cooperative effect between organic and inorganic gel components.

Structure direction of phosphate-based materials (aluminophosphates, magnesium aluminophosphates and silicoaluminophosphates) has been investigated through co-templating synthesis studies. In particular, the structure-directing activity of Cu^{2+} (and to a lesser extent Ni^{2+}) complexes of the azamacrocyles cyclam and cyclen, and related derivatives, is investigated in the presence of additional amines (dipropylamine, diisopropylamine, tetraethylammonium hydroxide, diisopropylethylamine). Complexes of a selection of linear polyamines, and also cobalticinium are studied for comparison. Although added primarily as pH moderators, the additional amines are also found to influence the crystallisation and hence provide effective routes to the synthesis of transition metal-containing materials with potential catalytic application. The 'strength' of the structure-directing ability of the additional amines is found to vary depending on the identity of the primary structure-directing agent, with behaviour ranging from passive pH moderator to dominating structure-directing agent. The outcome of syntheses is also highly dependent on inorganic gel composition.

Through appropriate combination of structure-directing agent and additional amine, mixed Cu^{2+}/Ni^{2+}-containing MgAPO and SAPO STA-6 (SAS) and STA-7 (SAV) materials have been synthesised for the first time, as well as a low Si form of SAPO STA-7 (with and without Cu^{2+}). Also, the combination of cyclam, tetraethylammonium hydroxide and HF has been found to produce a SAPO analogue of STA-7 possessing silicate islands. In addition, transition metal-containing materials possessing the AEL, AFI, CHA, UT-6 and LEV topologies have also been synthesised via this approach. Elemental analysis, UV-Vis, ESR and NMR spectroscopy are employed to confirm the presence of the desired complex in selected samples, while X-ray diffraction and ESR spectroscopy are employed to investigate the environment of extra-framework transition metal species, post calcination, in MgAPO STA-6, SAPO STA-6 and STA-7, MgAPO-18, and MgAPO-5.

Publications arising from this work

1. **Complex Zeolite Structure Solved by Combining Powder Diffraction and Electron Microscopy**, F. Gramm, C. Baerlocher, L. B. McCusker, S. J. Warrender, P. A. Wright, S. B. Hong, Z. Liu, T. Ohsuna, O. Terasaki, *Nature*, 2006, **444**, 79

2. **The First Route to Large Pore Metal Phosphonates**, J. A. Groves, S. R. Miller, S. J. Warrender, C. Mellot-Draznieks, P. Lightfoot and P. A. Wright, *Chem. Comm*., 2006, **31**, 3305

3. **Structural Chemical Zoning in the Boundary Phase Zeolite TNU-7 (EON)**, B. Han, C. H. Shin, S. J. Warrender, P. Lightfoot, P. A. Wright, M. A. Camblor, S. B. Hong, *Chem. Mater*, 2006, **18**, 3023

4. **Structure of the Novel Large Pore Gallosilicate TNU-7**, S. J. Warrender, P. A. Wright, W. Zhou, P. Lightfoot, M. A. Camblor, C. H. Shin, D. J. Kim and S. B. Hong, *Stud. Surf. Sci. Catal,* 2005, **158**, Part A 89

5. **A Large-Pore Gallosilicate Zeolite Constructed of Strictly Alternating MOR and MAZ Layers**, S. J. Warrender, P. A. Wright, W. Zhou, P. Lightfoot, M. A. Camblor, C. Shin, D. J. Kim and S. B. Hong, *Chem. Mater*., 2005, **17**, 1272

Acknowledgements

I wish to take this opportunity to thank the many people who have helped during the course of these studies.

Firstly, I would like to thank my supervisor, Dr Paul A Wright, for allowing me to conduct this project and for his perpetual enthusiasm, understanding and encouragement. I would also like to thank Dr Philip Lightfoot for his supervision, and assistance and advice on diffraction and Rietveld refinements; and members of the Wright and Lightfoot groups for their friendship over the past few years.

Thanks also to Drs Ross Blackley and Calum Dickinson for assistance on the SEM; Prof. Suk Bong Hong (Korea) for providing the TNU samples; Dr Paul Cox (Portsmouth) for an enjoyable fortnight of computer simulations; Dr Nandini Devi for assistance with EXPO; and Dr Véronique Patinec (Brittany) for supplying novel ligands for experimental trials.

I would like to acknowledge Dr Philip Wormald, Mrs Silvia Williamson, Dr Wuzong Zhou, Prof. Alex Slawin and Prof. John Walton for conducting solid-state NMR, CHN/ICP analysis, electron diffraction, single crystal X-ray diffraction and ESR spectroscopy, respectively. Also Stuart Miller for conducting single crystal analyses, Dr David Richens for helpful discussions on UV-Vis spectroscopy, and the EPSRC for financial support.

Special thanks must be given to Gemma, Calum, Russell and Phil for their continual friendship, understanding and humour, and for all their help and advice.

Above all, however, I wish to thank my close family – Mum, Dad, Lorna, Colin and Isla – with deepest gratitude, for their unconditional love, support and encouragement throughout all of my studies. Thank you.

Dedication

This thesis is dedicated to '*The Grans*'
Ivy Taylor and Jessie Warrender
who, sadly, did not live to see it completed.

Contents

List of Abbreviations

a	unit cell parameter
A	hyperfine coupling constant
b	unit cell parameter
c	unit cell parameter
CHN	elemental analysis for carbon, hydrogen and nitrogen
CP	cross polarisation
DIP	diisopropylamine
D*n*R	double *n*-ring
DP	dipropylamine
DP	direct polarisation
EDX	energy dispersive X-ray analysis
ESR	electron spin resonance spectroscopy
ESRF	European Synchrotron Radiation Facility
FOM	factor of merit
FWHM	full width at half maximum
g	ESR proportionality constant (‘g factor’)
H	half height of the detector slit in an XRD diffractometer
HB	Hunig’s base (diisopropylethylamine)
GSAS	General Structure Analysis System
HRTEM	high resolution transmission electron microscopy
ICP	inductively coupled plasma (elemental analysis)
IGA	intelligent gravimetric analysis
IZA	International Zeolite Association
L	sample-detector separation in an XRD diffractometer
MAS	magic angle spinning
MAPO	metal aluminophosphate
*n*MR	*n*-membered ring
NMR	nuclear magnetic resonance
R_p	goodness of fit value
rpm	revolutions per minute
R_{wp}	goodness of fit value

S	half sample height in an XRD experiment
SAPO	silicoaluminophosphate
SDA	structure-directing agent
SEM	scanning electron microscope
SRS	Synchrotron Radiation Source
STA	St Andrews
T	atom occupying tetrahedral sites in a zeolitic material
TEA	tetraethylammonium
TEAOH	tetraethylammonium hydroxide
TGA	thermogravimetric analysis
TMA	tetramethylammonium
TMAOH	tetramethylammonium hydroxide
TMC	tetramethyl cyclam
tmtacn	tetramethyl cyclam (= TMC)
TNU	Taejon National University
TPA	tripropylamine
TPAOH	tetrapropylammonium hydroxide
U_{iso}	isotropic thermal parameter
UV-Vis	ultra violet-visible spectroscopy
XRD	X-ray diffraction

Overview

Zeolites and zeolitic materials belong to an extensive group of solids known as microporous materials. This broad, generic title encompasses a wide range of materials including amorphous carbons and silica gels as well as crystalline silicates and phosphates, all of which possess channels and/or cages with diameters in the region 2.5-20Å. Work presented in this thesis focuses specifically on zeolitic materials and investigates the manner in which particular structures are formed through studies of both structure and synthesis. By means of an introduction to these studies, Part 1 discusses the specific characteristics and applications of zeolites and zeolitic materials before presenting a brief overview of the principal characterisation techniques employed during this work. Part 2 discusses structural analyses of three silicate-based zeolitic materials (denoted TNU-6, -7 and -9) and attempts to rationalise their crystallisation through consideration of inorganic and organic structure-directing influences, while Part 3 investigates the synthesis of phosphate-based zeolitic materials, employing specific organic structure-directing agents.

PART 1: INTRODUCTION

Chapter 1: Structure, Properties and Applications of Zeolitic Materials

Chapter 2: Characterisation Techniques

Chapter 1: Structure, Properties and Applications of Zeolitic Materials

1.1: Zeolites and Zeolitic Materials[1]

Zeolites, rigorously defined as crystalline microporous aluminosilicate materials with three-dimensionally connected framework structures, were the first group of microporous materials to be discovered. Indeed, naturally occurring zeolites have been known to mineralogists since at least the eighteenth century. Their regular framework structures (often referred to as the 'topology'; see below) are composed of vertex-sharing TO_4 tetrahedra (T = Si, Al) with each oxygen being shared between two T-atoms. Since the advent of laboratory synthesis techniques (discussed more fully in Part 3), many new framework structures have been discovered in addition to those found in nature. Moreover, many other framework compositions have been achieved including alumino- zinco-, beryllo- and gallo-phosphates, gallo- and germano-silicates and many other substituted analogues. While many of these novel materials possess analogous topologies to known aluminosilicates, others exhibit entirely new topologies, which are still, nevertheless, zeolitic in nature. Materials such as these, which exhibit zeolitic topologies but possess different framework compositions, are increasingly referred to as 'zeotypes' or simply zeolitic materials.

1.2: Structural Characteristics of Zeolites and Zeolitic Materials

The mineralogist A F Cronstedt coined the term Zeolite (from the Greek words zeo (to boil) and lithos (stone)) in 1756 following his observation that certain unknown silicate minerals exhibited intumescence upon heating.[2] Almost a century later this phenomenon was also observed to be reversible, without loss of structural integrity.[3] However, it was 1896 before an open framework structure was suggested to rationalise this behaviour,[4] and a zeolite structure was not determined fully until 1930.[5]

As crystalline tectoaluminosilicates, zeolites are constructed from $[SiO_{4/2}]$ and $[AlO_{4/2}]^-$ tetrahedral units (Figure 1.1), which link together through common vertices to form ordered and often highly symmetrical frameworks. Running through these framework

structures are well-defined pore networks. These pores, or internal voids, may take the form of cages (to which access is restricted by small openings in the framework), cavities (accessed by larger openings), channels (considered as infinitely extended cavities) or a system of cavities interconnected by channels. Access to the internal voids of these solids is therefore restricted by a limiting aperture or pore size, which can vary from approximately 4Å (for example, Zeolite-A) to 14Å (for example, Cloverite) (Figure 1.2). Pores are generally circular or elliptical in character and may be connected in one, two, or all three spacial dimensions. The implication of these structural aspects on properties and applications will be discussed in section 1.5.

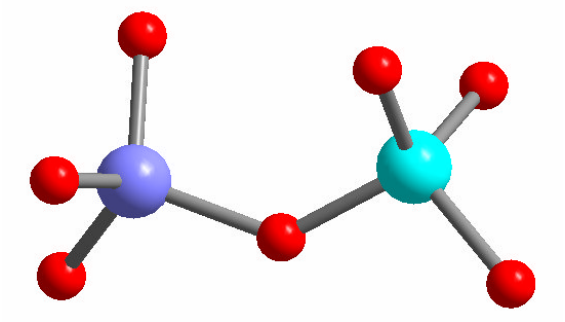

Figure 1.1: Two vertex-sharing tetrahedra – the primary building units of zeolitic materials.

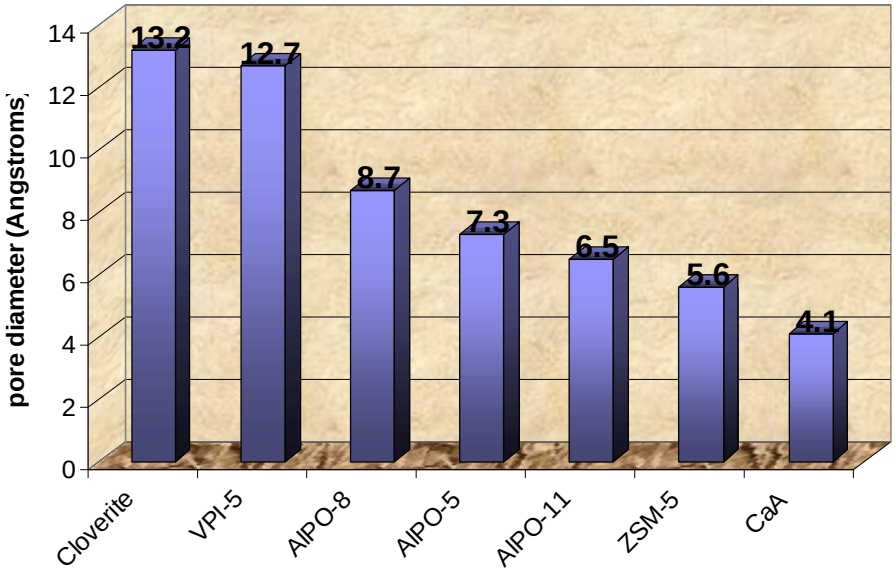

Figure 1.2: Pore diameters of some common zeolitic materials.

There are several means of describing a zeolitic structure depending on the context. While the basic tetrahedral units are generally referred to as primary building units,

Meier[6] derived the expression 'secondary building units' to describe structural units built from more than two tetrahedral groups, and from which entire structures may be considered as being built (Figure 1.3). Rings are described by the number of T-atoms they contain (for example, six-membered rings, 6MR), while pairs of rings are denoted as double n-rings (for example, double six-rings, D6R). In this manner, for example, the structure of the phosphate-based material denoted STA-6 (St Andrews-6) could be described in terms of D6R units connected to others via 4- and 6-MRs (Figure 1.4). STA-6 is discussed further in Part 3.

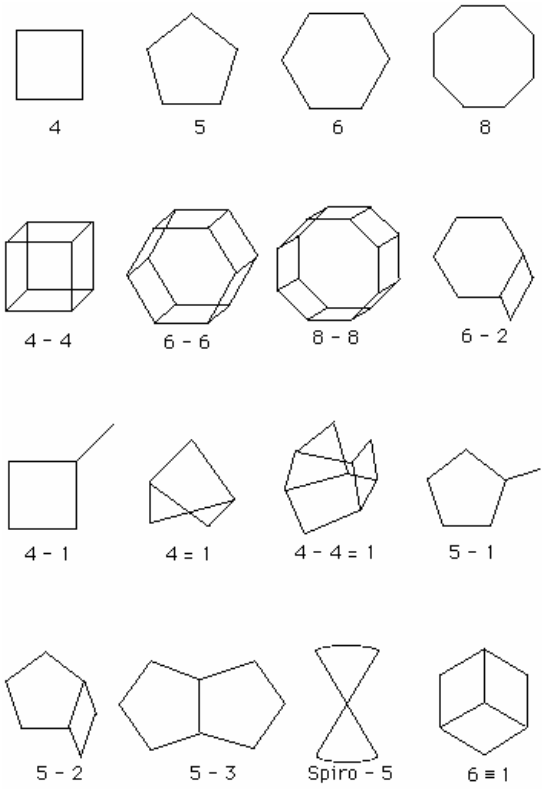

Figure 1.3: A selection of secondary building units found in zeolitic frameworks (oxygens not shown, T-atoms situated at unit apices).[7]

Alternatively, a zeolitic framework may be described in terms of the stacking of different polyhedral cage units such as those illustrated in Figure 1.5. For example, the structure of the industrially important material known as ZSM-5 (Zeolite Secony Mobil-5) may be described as being built predominantly from 5^8-cages (Figure 1.6). In this notation, n^m is employed where m gives the number of n-sided polygons defining the polyhedron, and Σm gives the number of faces possessed by the polyhedron.

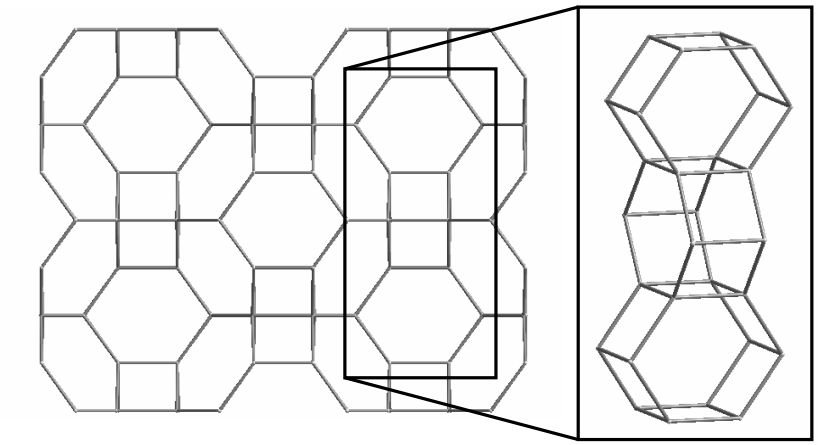

Figure 1.4: The structure of STA-6 may be considered as being constructed from chains of D6R units (inset), connected through 6MRs (oxygens removed and T-atom radii reduced for clarity).

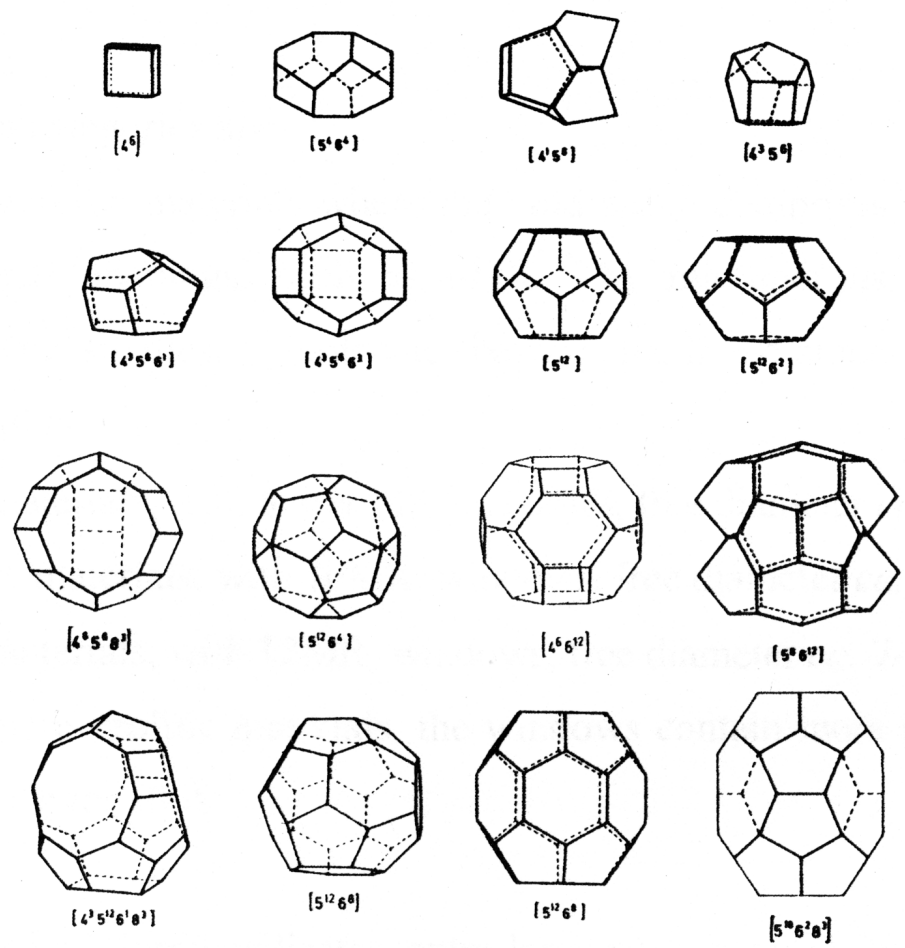

Figure 1.5: A selection of polyhedral units which form cages in zeolitic frameworks (oxygens not shown).[8]

In addition, many structures can be considered in terms of layers stacked upon each other. ZSM-5 may also be described in this manner (Figure 1.6); as can, for example, mordenite, mazzite, and indeed TNU-7 and TNU-9 (Taejon National University), each of which are discussed fully in Part 2.

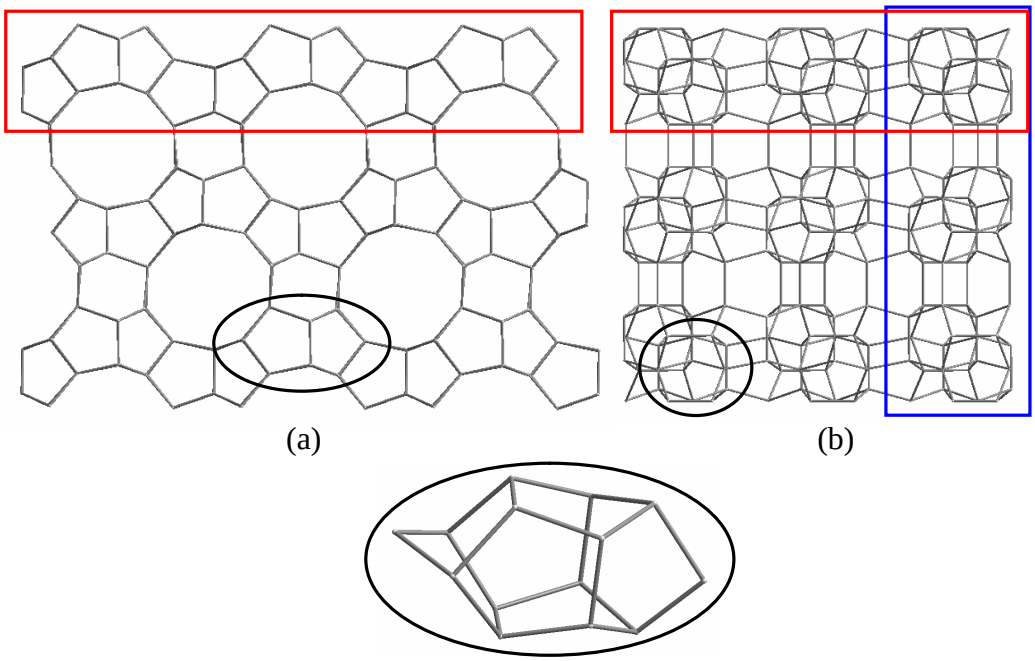

Figure 1.6: The structure of ZSM-5, viewed here along the (a) b- and (b) c-axes can be considered as being built from 5^8-cages (circled and inset) or from the stacking of horizontal or vertical framework layers (highlighted in red and blue, respectively) (oxygens removed for clarity).

Category	Description of void space	Pore diameter (Å)
Clathrasils	Cages connected by small openings (for example, 6MRs)	~2
Small pore	8, 9MRs	4
Medium pore	10MRs	5.5
Large pore	12MRs	7-7.5
Extra large pore	>12MRs	>10

Table 1.1: Classification of microporous materials based on pore size.

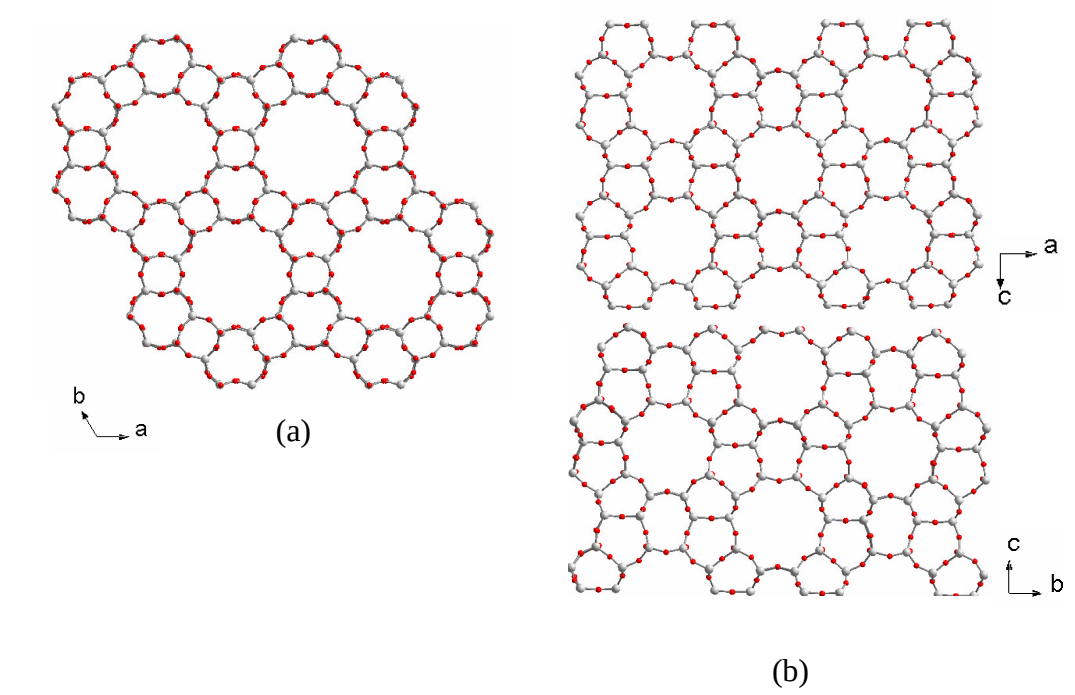

(a)

(b)

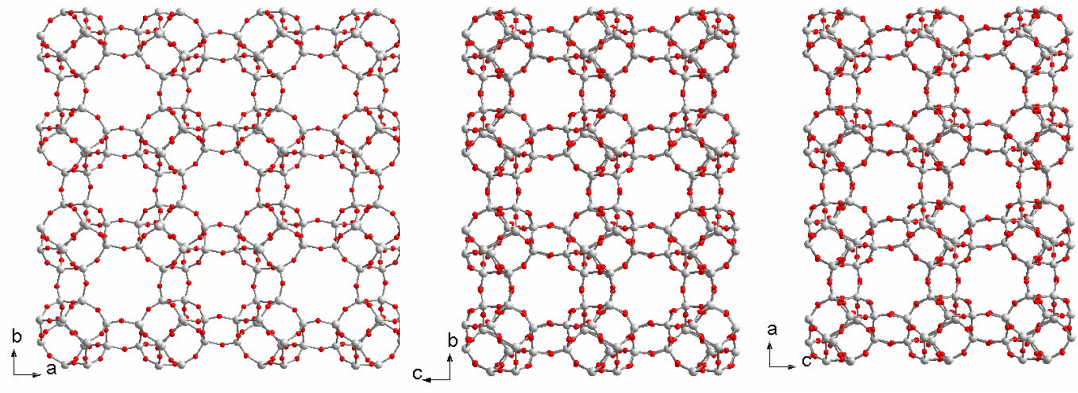

(c)

Figure 1.7: Examples of (a) one-, (b) two- and (c) three-dimensional pore systems: AlPO-5, ZSM-11 and STA-7, respectively.

Zeolitic materials may also be classified in terms of their pore dimensionality (particularly relevant in catalysis and sorption studies). A channel system may be one-dimensional (for example, AlPO-5, Figure 1.7(a)), two-dimensional (for example, ZSM-11, Figure 1.7(b)) or three-dimensional (for example, STA-7, Figure 1.7(c)). Alternatively, materials are often classified on the basis of the size of the windows that provide access to the channel system (number of T-atoms in the ring). Table 1.1 summarised the principal categories as defined on pore size.

Zeolitic topologies in the form of a tetrahedrally connected, three-dimensional net are assigned a structure code by the International Zeolite Association (IZA). This code takes the form of three capital letters and, throughout this thesis, will be given (where applicable) in parentheses after the material name. For example, STA-7 (SAV) indicates that the material known as STA-7 possesses the SAV structure type. Full listings of structure codes are published by the IZA in the Atlas of Zeolite Structure Types[9a] and on the web.[9b]

1.3: Composition

Substitution of silicon by aluminium in the formation of a traditional aluminosilicate zeolite results in the introduction of one negative charge per aluminium to the framework. This charge imbalance is commonly remedied by the presence of so-called extra-framework cations – i.e. cationic species that occupy the void areas of the material and which do not form part of the framework. Typically, these species take the form of alkali metal, alkaline earth or organic (for example R_4N^+, R = H, alkyl, aryl) cations, which are incorporated during synthesis and may perform an important role in directing the crystallisation of a particular phase. Water can also be present within the pore areas. The general compositional formula for a zeolite is therefore:

$$M^{n+}_{x/n}[Al_xSi_{1-x}O_2].yH_2O$$

where n represents the charge associated with extra-framework species M, x indicates the degree of Al substitution and y represents the number of water molecules present in the pore system. While the framework composition (i.e. Si/Al ratio) can vary, Loewenstein's rule[10] dictates that the Si/Al ratio cannot fall below one in order to avoid energetically unfavourable Al-O-Al linkages. Post-synthesis heating (calcination) is often employed to remove any organic cation and permit access to the pore system. Metallic cations are often readily exchangeable with other suitably sized cationic species.

Over the last few decades there has been growing interest in zeolitic solids that incorporate elements other than Al and Si in their frameworks (i.e. 'zeotypes'). One such group of materials is the gallosilicates, which are composed of vertex-sharing

$[SiO_{4/2}]$ and $[GaO_{4/2}]^-$ tetrahedra. Around 30 gallosilicate versions of known zeolites have been reported[11,12] such as TNU-3 and TNU-4[13], which are counterparts of the naturally occurring zeolites gonnardite and natrolite, respectively. Other gallosilicates reported to date are analogous to the aluminosilicate RHO,[14] SOD,[15] MAZ[16] and ABW[17] topologies. The gallosilicates TNU-6 and TNU-7 are discussed in Part 2.

Variation in framework composition has led to a vast array of materials, many of which have topologies not previously observed. A further such group of materials is the aluminophosphates (or AlPOs). First synthesised by Flanigen and co-workers[18] in 1982, these zeotype materials are composed of vertex-sharing $[AlO_{4/2}]^-$ and $[PO_{4/2}]^+$ tetrahedra and exhibit similar features to their aluminosilicate relatives.

AlPO materials are commonly denoted as 'AlPO-n', where n refers to the specific crystallographic structure. For example, AlPO-11 (AEL) is an aluminophosphate zeotype with structure type 11, and has been assigned the AEL structure code. As with pure silica, $AlPO_4$ frameworks bear no charge as they may be visualised as strictly alternating and mutually compensating $[AlO_{4/2}]^-$ and $[PO_{4/2}]^+$ units (known as Flanigen's rule). There is, therefore, no requirement for charge-balancing cations. A further consequence of Flanigen's rule is that the number of T atoms in a particular ring within an aluminophosphate structure must be even.[19] Hence many zeolite structures are unattainable in the AlPO form. Yet over 30 different structures have been achieved, some of which are completely novel.

A charge imbalance may be imparted to the AlPO framework, however, by substituting Al^{3+} with divalent metals such as Mg^{2+}, Co^{2+}, Be^{2+} etc. that are quite stable in tetrahedral geometry. The resulting compounds are termed metal aluminophosphates (MAPOs, where M denotes the divalent metal involved). Silicon can also be substituted into AlPO frameworks. However, while divalent metals typically replace only Al, Si can substitute for both P and Al. Figure 1.8 illustrates the four principal theoretical modes of Si incorporation into AlPO frameworks.[20] Substitution via SM1 and SM3 are not observed due to the resulting formation of P-O-Si linkages. Much more common is SM2-type substitution whereby silicon replaces only P. However, a coupled SM2-SM3-type substitution has also been observed,[21] resulting in the formation of silicate islands within the AlPO framework. As implied above, Leowenstein's (or Flanigen's) rule also

extends to substituted AlPO systems and forbids P-O-Si, M-O-Al and M-O-M linkages, as well as Al-O-Al and P-O-P. Substituted AlPO phases may therefore be represented by the general formula:

$$(Al_{1-x-y}M_xSi_y)(P_{1-z}Si_z)O_4$$

MAPO and SAPO materials are named in a similar fashion to AlPOs, For example, MgAPO-5 and SAPO-5 are the magnesium- and silico-aluminophosphate analogues of AlPO-5, respectively (AFI topology).

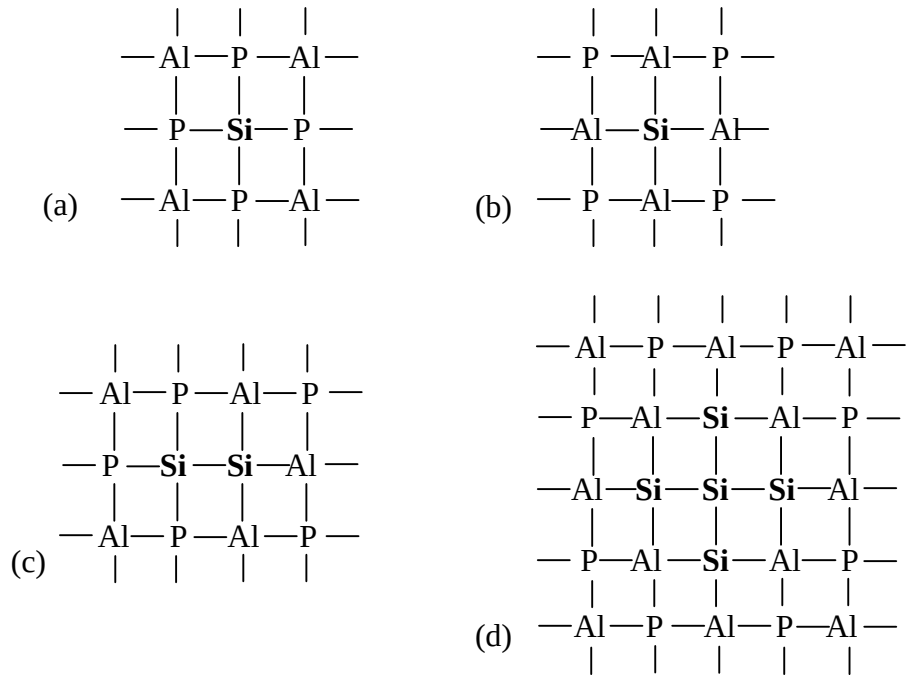

Figure 1.8: Two-dimensional representations of the different Si substitution mechanisms in AlPO materials; (a) SM1, (b) SM2, (c) SM3, (d) coupled SM2-SM3

1.4: Synthesis of Zeolitic Materials

1.4.1: The Development of Hydrothermal Synthesis

Naturally occurring zeolites such as clinoptilolite and mordenite are found in volcanic facies, often as secondary minerals occupying vesicles that were created by volcanic gases while the host rock was still fluid.[22] Their formation under geological conditions at high temperature (> 200^{o}C) and pressure (>100 bar) focussed many early attempts at

zeolite synthesis on reconstructing such conditions in the laboratory,[23] and although the first zeolite synthesis was reported in 1862,[24] this area of research did not reach fruition until the middle of the twentieth century with the advent of hydrothermal synthesis at milder conditions.

Following Barrer's ground-breaking synthesis of the first synthetic zeolite - zeolite P - in 1948[25] from the conversion of known mineral phases, Milton and co-workers[24] developed a synthetic approach using reactive alkali-metal aluminosilicate gels under relatively low temperatures (~ 100^{o}C) and autogeneous pressures, thus laying the foundations of modern zeolite synthesis method – that of hydrothermal synthesis. The potential of this new approach to zeolite synthesis was evident from the beginning with 20 different zeolites being synthesised within a few years, 14 of which had no naturally occurring counterpart.

Typically, aluminosilicate gels are prepared from alkali-metal hydroxides, reactive forms of alumina (for example, aluminium hydroxide) and silica (for example, fumed silica) and water, with a pH of generally greater than 13. In this way many aluminium-rich zeolites were synthesised including zeolites A, X, Y, L and synthetic mordenite.[26]

Until 1960 synthesis gels were entirely inorganic. However, in 1961 Barrer and Denny[27] introduced the tetramethylammonium cation (TMA) to an aluminosilicate gel system. The resulting phase (analogous to zeolite A) was found to possess a higher Si/Al ratio than previously observed. A variety of different organic species have since been employed (including, for example, tetraethylammonium, and tetrapropylammonium cations) subsequently leading to the synthesis of many high silica zeolites including zeolite β[28] (the first high silica zeolite) and the commercially important ZSM-5,[29] as well as a new class of silicate molecular sieves.[30] The organic additive is thought to exercise a certain 'templating' or 'structure directing' effect, alluded to by the observation that it cannot diffuse into or out of the cage in which it resides.[23] In other words, the cage must form around the organic additive. In general, it is observed that linear SDAs direct the formation of one-dimensional channels, while cyclic species direct cage structures and branched species favour two/three-dimensionally connected pore systems. This aspect of hydrothermal synthesis is discussed further in section 1.4.2.

From the late 20th Century to the present day there has been a rapid increase in discoveries of new topologies primarily due to the innovative exploitation of organic species as structure directing agents, but also thanks to the incorporation of different heteroatoms into framework sites affording new families of zeolitic materials, many of which exhibit entirely novel topologies due to the variation in T-atom radius and associated bond lengths and angles.

As part of such studies into frameworks of different composition, the first member of the aluminophosphate (or AlPO) family of molecular sieves was synthesised in 1982 by Flanigen[31] and co-workers. Analogous to aluminosilicate zeolites, AlPOs are synthesised from gels consisting generally of alumina, H_3PO_4, water and an organic additive, and are heated to 100-200^oC under autogeneous pressure. However, unlike aluminosilicate synthesis, no alkali-metal is necessary, crystallisation periods are generally shorter and the gel pH is required to be approximately seven. The latter is satisfied by the organic species, which performs the dual role of structure-directing agent and neutralising base. Since the early work by Flanigen, a plethora of organic species have been employed in the synthesis of AlPOs including tri-, di-, and mono-alkylamines, alkylethanolamines, diamines as well as cyclic and bicyclic amines.[26] The extensive variety of possible organic additives, coupled with the change in gel chemistry away from the aluminosilicate regime proved fruitful in producing many new topologies (such as AlPO-18[32] (AEI) and STA-6[33] (SAS)), as well as analogues of many known aluminosilicate phases (such as AlPO-34[34] (CHA) and AlPO-35[35] (LEV)).

1.4.2: A System of Interrelated Variables.

The development of hydrothermal molecular sieve synthesis was fundamental to the evolution of this field of materials research, facilitating the widespread study and application of these materials. However, associated with the technique is a formidable collection of reaction variables including time, temperature, pH, cation identity and source, organic species, gel pre-treatment and percentage filling of the autoclave - not to mention the gel composition itself. Each of these parameters will affect the pathway and kinetics of the reaction. Furthermore, many of these variables are interrelated, thus presenting a significant challenge in the investigation and optimisation of novel molecular sieve synthesis. Although a number of general trends and guidelines have

been presented, there is as yet no clear understanding of the interplay of these variables, or indeed of the mechanism by which microporous solids crystallise (see section 1.4.3). The following sections outline some of the effects of these variables.

Templating[26]

The term 'templating agent' is often bestowed on the cationic species present in a hydrothermal preparation. However, for reasons that will become apparent, the looser term of 'structure-directing agent' (SDA) may be more appropriate. These species may be introduced to the gel mixture specifically for the purpose of structure direction, however some species, which are introduced for other reasons, may also exert a structure directing influence as a secondary effect. In some way the templating or structure directing species acts to stabilise a particular structure through electronic or geometric means.

The concept of templating was first proposed to describe the influence that alkali-metal ions exert on aluminosilicate zeolite synthesis. Although present as a source of hydroxyl ions and to achieve the necessary basic conditions, it is postulated that the hydrated cation may stabilise silicate, aluminate or aluminosilicate anion species and encourage the formation of regions of micro-order.[36] Today, however, templating cannot be discussed without inclusion of the organic moiety that is so often present in molecular sieve synthesis.

The notion that the organic species not only remedies the framework charge imbalance but may direct the condensation of oxide tetrahedra to form a particular geometry arose due to the close relationship between the size and shape of the species and the geometry of the pore in which it is found. The aluminosilicate ZSM-5, for instance, is formed in the presence of TPA cations; the cation resides at the intersection of two pore systems, with the alkyl chains extending along each channel.[37]

The vast variety of organic species that can be utilised affords extensive flexibility in both geometric and electronic properties, thus encouraging the synthesis of many new topologies. In recent years the synthesis of novel structures has relied on the innovative use of organic templates[33] (typically amines or quaternary ammonium salts). Indeed,

organic species have been 'designed' specifically to target particular pore sizes and connectivities. For instance, the novel magnesium aluminophosphate (MgAPO) STA-2 (SAT)[38] was prepared using diquinuclidinium ions of the form $[(C_7H_{13}N)\text{-}(CH)_n\text{-}(NC_7H_{13})]^{2+}$ (n = 4,5). This structure is comprised of columns consisting of units of two cancrinite cages bound via D6Rs, separated by larger cages in which reside the diquinuclidinium cations. Figure 1.9 illustrates the intimate relationship between template and framework topology in STA-2

Zones *et al*[39-41] have studied the design of polycyclic quaternary ammonium species for the use as SDAs quite extensively. In this way many novel topologies have been synthesised. Furthermore, the tolerance of certain frameworks to structural alterations in the structure directing species can be probed in an analogous fashion to the probing of an active site in an enzyme by systematic alteration of a substrate.

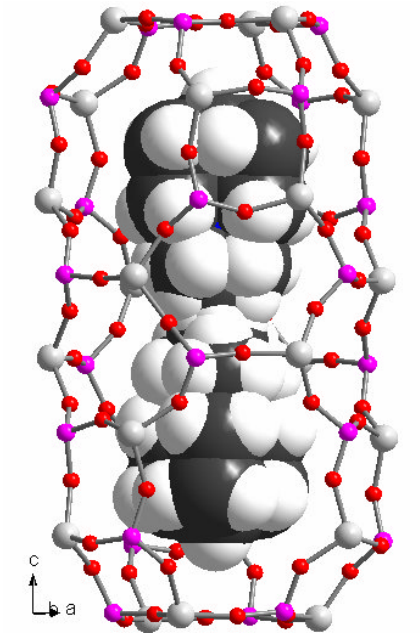

Figure 1.9: Experimentally derived position of the diquinuclidinium template (space filling model: black = C, white = H, blue = N) in the large cage of STA-2 (ball and stick model: grey = Al, purple = P, red = O) illustrating a close relationship between the shape of the structure-directing agent and the surrounding framework topology. The methylene chain is disordered about a triad axis.

Often the templating species can be removed post-synthesis via chemical or thermal decomposition leaving the framework intact – an approach that has proved most successful in the preparation of solids for adsorption and catalysis.

Table 1.2 shows a selection of templating agents and typical resulting AlPO structures. It is evident that while some frameworks such as AlPO-20 (SOD) can only be obtained from one templating agent, some structures (such as AlPO-5 (AFI)) can be synthesised from several. Furthermore, some templating agents can yield many different structures.

Organic Species	**Typical Resulting AlPO structure**
TMAOH	AlPO-20
TEAOH	AlPO-18, AlPO-5
TPAOH	AlPO-5
Me_3N	AlPO-21
Et_3N	AlPO-5
Dipropylamine	AlPO-11, AlPO-31
Diisopropylamine	AlPO-11
Dicyclohexylamine	AlPO-5
Isopropylamine	AlPO-14
Tert-$BuNH_2$	AlPO-14
Diethylethanolamine	AlPO-5
Dimethylethanolamine	AlPO-5, AlPO-21
Ethylene urea	AlPO-12
Tetraethylethylene diamine	AlPO-21
Quinuclidine	AlPO-7, AlPO-16, AlPO-17

Table 1.2: A selection of organic species commonly employed in AlPO syntheses and typical structures obtained from them.[26]

This has led to a more subtle distinction being made between true templating (a unique structure from a unique template), structure directing and simply space filling.[23] Space fillers act to exclude water from the framework pores and hence stabilise the forming structure – as observed for AlPO-5. The term templating agent applies to the organic species employed in the synthesis of a phase that could only be obtained using that

species (for example ZSM-18[42,43] requires 2,2,5,5,8,8-hexamethyl-2,3,4,5,6,7,8,9-octahydro-1H-2,5,8-triazatrindene or 'tri-quat'). The less restricting term 'structure-directing agent' would apply to species used in the synthesis of a phase that could be prepared from a few (although often related) species, but not any species.

As yet, there is no *a priori* method of establishing whether a particular species would be successful as an SDA. There has recently been much interest in computer modelling as a tool to predict potential candidates' suitability as SDAs based on template-framework interactions. For instance, Willock *et al*[44] have employed the ZEBEDDE program to 'grow', computationally, potential new template species for known structures EU-1 (EUO) and chabazite (CHA). The molecule is built sequentially within the host pore by adding fragments from a library and altering atom identities to suit. The molecular conformation is optimised and non-bonding interaction between the molecule and framework are maximised during the process. However, the usual experimental approach is still very much that of trial and error. Although the synthesis of several structures *can* now be directed with confidence (such as SSZ-26,[45] ZSM-18,[46] MeAPO-18,[47] DAF-4[48]) this is the result of systematic and extensive experimental variation rather than *a priori* methods.

Gel Chemistry and Treatment

It is apparent from the foregoing discussion of templating *vs* structure direction that the gel chemistry and treatment must also play a significant role in determining the identity of the phase produced from a given system. Moreover, the observations that ZSM-5 can be synthesised under certain gel conditions with *no* template,[49] and that the organic species (dipropylamine) used to synthesis CoAPO-H3 is excluded from the framework pores[50] raise questions about the whole aspect of structure direction.

Firstly, the cation source must be considered; zeolite Y, for instance, is much easier to prepare from amorphous silica than from sodium silicate[51] (zeolite P is favoured by the latter). Dense phase impurities are favoured by the use of crystalline (instead of amorphous) aluminium oxide hydrate in the synthesis of AlPO-5.[52] Also, changing from aluminium hydroxide to aluminium isopropoxide has been shown to favour the formation of a triclinic variant of STA-6 over chabazite.[53]

The gel composition is, of course, also very important. For example, increasing the concentration of alkali-metal cations present in the synthesis gel can reduce the Si/Al ratio in aluminosilicates.[23] As will be discussed in Chapter 6, 1,4-bis(N-methypyrrolidinium)butene (1,4-MPB) can direct the formation of aluminosilicates TNU-10, analcime, IM-5, NU-87 and TNU-9, depending on the Na/Si ratio in the synthesis gel.[54] Similarly, a progression from SSZ-24 through SSZ-23 to SSZ-13 is observed by decreasing the Si content of aluminosilicate gels in the presence of N,N,N-trimethyl adamantammonium cations.[55] The synthesis of the novel MAPO phases STA-6 and STA-7 is also influenced by the identity of framework species (Part 3).[56] Clearly the identity and quantity of substituting species has a significant influence on the crystallisation of microporous materials. Indeed, the completely inorganic structure direction of Ga-MAZ, TNU-7 and Ga-MOR discussed in Chapter 5 emphasises the powerful ability of heteroatoms to affect the crystallisation process.

An interesting contrast in behaviour is illustrated by studies of SAPO syntheses; while increasing the Si content of a SAPO gel in the presence of cyclohexylamine yields a transition from an erionite-like structure at low Si content, through SAPO-35 (LEV) to SAPO-34 (CHA) at high Si content,[57] similar treatment of a SAPO-20 (SOD) synthesis gel results in a complete compositional progression to the pure aluminosilicate with the same structure.[58]

The gel composition can also influence the crystallisation time. SAPOs, for example, generally require longer crystallisation periods (up to one week) than MAPOs and unsubstituted AlPOs (two days). Similarly, the addition of Ge to silicate syntheses has been found to increase the rate of formation; Ti-Ge-ITQ-7, for example, can be prepared in less than 12 hours compared to more than 40 days for its Ge-free analogue.[59] A further example is the crystallisation of aluminosilicate ZSM-12 which requires three days in the presence of Na^+ ions, but as long as seven days in its absence.[23]

Some authors have also reported the use of promoter ions to decrease crystallisation times. Species such as perchlorate, phosphate, nitrate, sulphate and carbonate ions are all reported to promote faster crystallisation.[60]

An important development in the synthesis of aluminosilicate zeolites in the late 1970s was the introduction of fluoride as a mineralising agent.[61] This has permitted aluminosilicate and pure silicate zeolites to be synthesised at near neutral pH and favours the formation of large, relatively defect-free crystals.[62] Fluoride ions can also be employed in AlPO synthesis whereby they become incorporated into the framework, thus introducing a negative charge that is balanced by the organic cation. $AlO_{4/2}F^-$ units have been identified through solid state NMR studies, for example.[63] The principal role of fluoride in silica-containing preparations is the solubilisation of silicate ions at neutral pH, and to catalyse the formation of Si-O-Si bonds,[64] yet it is clear that addition of fluoride also modifies the gel composition and may also, therefore, influence the identity of the crystalline phase.

Digestion time is also influential – indicative of the metastable character of these materials. Zeolite A, for example, will make way for zeolite P if left in contact with the mother liquor for three days.[51] The more kinetically favoured phase will form first and recrystallise with time to the more thermodynamically stable phase, ultimately forming more dense phases. This phenomenon is known as Ostwald's rule of successive transformation. In addition, pH, temperature, gel ageing and agitation have also all been shown to influence the outcome of molecular sieve synthesis.[26,53] High temperature, for example, favours the formation of denser phases with lower water content.[37]

Evidently, there is a complex interplay of many synthetic variables. Altering the proportion of H_3PO_4 or basic SDA in an AlPO gel, or NaOH in an aluminosilicate gel, for instance, not only modifies the gel composition but also affects the overall pH. Therefore, it is often difficult to associate any given effect with a particular variable. With such a complex set of interrelated variables, there is of course much scope for experimental variation.

1.4.3: Mechanism

It is evident from the foregoing sections that hydrothermal synthesis is a complex multicomponent system. Consequently, little is known about the exact mechanism by which zeolites and related phases crystallise. Two general mechanisms have been proposed: the solution-mediated transport mechanism whereby nucleation and growth occur in the solution phase fed by a constantly dissolving solid phase; and the solid hydrogel transformation mechanism whereby the crystalline phase forms directly from the gel.[37]

Key to the widespread utility of the hydrothermal technique is the highly effective solvating ability of water under these conditions, permitting reactant dissolution and mixing prior to nucleation and crystal growth.[37] Indeed, mobility appears to be a key element in crystal formation, relying largely on the action of the mineralising agent (OH^- or F^-) to convert reactants into mobile and reactive forms.

It is proposed (for siliceous zeotypes at least) that clathration of the structure directing cation by, for example, silicate anions may occur in the early stages, with the SDA adopting the configuration it will ultimately exhibit in the final product. Through time, these randomly connected units anneal to form an ordered arrangement through continual T-O-T bond formation and cleavage catalysed by the mineralising agent. A crystal may grow in a layer-by-layer fashion via the diffusion of these species to the surface of a growing crystallite.

In a recent comprehensive review on the subject, Cundy and Cox[65] argue that the location of crystal nucleation and growth (i.e. solution-mediated *vs*. solid hydrogel transformation) is irrelevant and simply variations on a general theme. They present a generally applicable mechanism in which initially amorphous material, in equilibrium with solution species (either in the bulk solution phase or a solvated layer on the solid gel surface), eventually gives way to a sufficiently ordered region to allow a periodic structure to establish. Through further T-O-T cleavage and re-formation equilibria, the crystal grows at the expense of amorphous material. The exact nature/geometry of the ordered region is dictated by interaction with the SDA.

1.5: Properties and Applications[66]

Zeolitic materials have found many industrially important applications encompassing the chemicals, fine chemicals, oil, pharmaceutical and catalyst industries thanks to properties that stem directly from the particular characteristics of their crystal structure. Regular and well-defined pore networks allow molecules of an appropriate size and shape to diffuse into the framework voids. As a result microporous solids are capable of selectively recognising, discriminating and adsorbing small molecules. Weigel and Steinhoff[67] first noted this property in 1925 when dehydrated chabazite was observed to selectively adsorb water, methanol, ethanol and formic acid over acetone, benzene and ether. Consequently, zeolitic materials are often referred to as 'molecular sieves' - a term coined by McBain in 1932 to describe microporous zeolites but which today encompasses both zeolites and the now much-extended zeotype families collectively. Zeolitic materials are also widely employed as drying agents due their most fundamental behaviour – reversible dehydration. Indeed, microporous aluminosilicate materials have long been utilised in such applications.

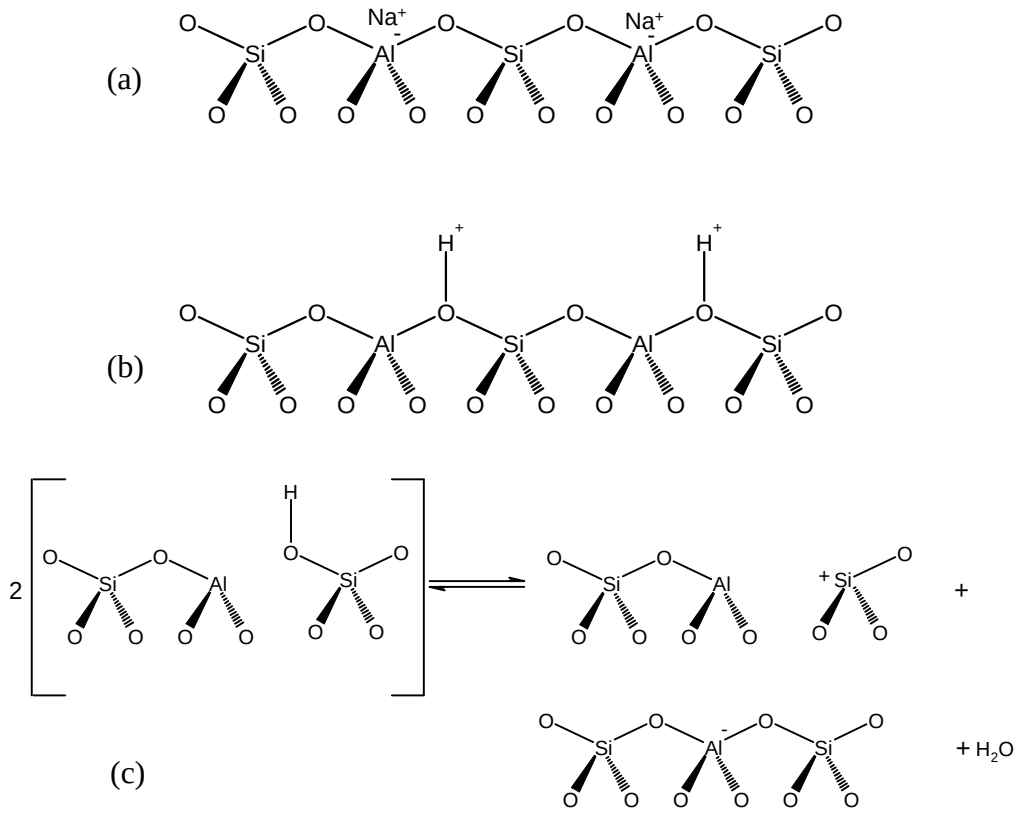

Figure 1.10: Illustration of (a) balancing of framework charge by extra-framework cations (b) Brønsted acid sites, and (c) Lewis acid sites in aluminosilicate zeolites.

The exchangeability of extra-framework cations is exploited in applications such as water softeners; Na Zeolite-A, for example, is present as a water softener in washing powder. Molecular sieves are also used to extract radioisotopes from nuclear waste and are being developed for pollution remediation such as ground water decontamination.[68] Cation exchange capacity in aluminosilicate materials depends on the Si/Al ratio (which is variable) since mono- or di-valent cations are incorporated in order to balance the negative charge associated with framework Al^{3+} sites (Figure 1.10(a)) (in reality the negative charge is in fact distributed over all of the framework oxygen sites). Protons may also balance this charge (Figure 1.10(b)), thus producing Brønsted acid sites (proton donors). Lewis acid sites (electron acceptors) may also be present. These are associated with charge-balancing cations or coordinatively unsaturated Al^{3+} ions, the latter of which may be generated by heating the protonic form to drive off water (Figure 1.10(c)).

Aluminophosphates are inherently inactive as acid catalysts since their framework bears no charge, However, by replacing some Al^{3+} by divalent metal cations such as Mg^{2+}, or by replacing P^{5+} with Si^{4+}, active sites can be created since protons or extra-framework cations are required to maintain charge neutrality (Figure 1.11).

Acid zeolites[69] are by far the most common class of solid acid catalyst applied in industry today courtesy of their relatively high acid strength, high adsorption capacities and hydrothermal stability coupled with their ability to impart shape selectivity to the process they catalyse. Clearly the pore geometry can have a direct influence on the catalytic behaviour of these materials by controlling the diffusion of reactants and products to and from the active sites, as well as exerting influence on the shape of the transition state forming within. For example, the methylation of toluene using methanol over ZSM-5 exhibits product selectivity in producing the para isomer only.[70] Para-xylene is a feedstock for the production of artificial fibres and can also be obtained from the isomerisation of less valuable ortho and meta isomers (also over ZSM-5). Here, the pore geometry restricts the transition state, as well as permitting only the desired isomer to leave.

Similarly, catalysis is the principal application of interest for MAPO and SAPO materials, which offer unique conversion capabilities for hydrocarbon reactions.

MgAPO-18, for instance, can catalyse the conversion of methanol to ethene and propene.[71]

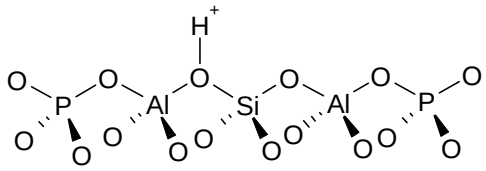

Figure 1.11: Illustration of a Brønsted acid site in a SAPO material.

By incorporating species such as Co^{2+} into framework positions it is possible to introduce redox properties to the system through oxidation to the trivalent state upon calcination of the as-synthesised material, promising a new area of redox chemistry.[72] Furthermore, introduction of transition metals to the pores of these materials offers great opportunities in catalysis and may be achieved through ion-exchange or via the use of a suitable templating agent (see Part 3). Such systems offer the possibility of combining the properties of a catalytically active metal and the functionality of a solid acid catalyst such as in the case of a zeolite-supported Pt catalyst, which catalyses the branching of hydrocarbons via dehydrogenation, isomerisation and subsequent rehydrogenation.[69] Also, Cu-containing ZSM-5 and SAPO-34 have proved particularly active towards the decomposition of NO with potential application in deNO_x processes.[73,74]

Chapter 2: Characterisation Techniques

2.1: Basic Crystallography[75,76]

As indicated in Chapter 1, zeolites and zeotypes are crystalline solids with highly ordered and regular arrangements of pores running through an oxide framework. Indeed, perhaps their most endearing characteristic is the symmetry exhibited in their framework and pore systems alike. The structure of crystalline materials, such as zeolites, can be described in terms of a repeat unit (or 'unit cell'), the symmetry associated with that unit, and additional symmetry associated with the distribution of atoms within it. In this way the location of only a (relatively) few atoms are required to generate the entire topology via application of symmetry elements (these atoms represent the 'asymmetric unit').

The unit cell is a parallel-sided, three-dimensional box and defines the smallest unit of structure that can generate the entire structure through translation alone. Although it may not be uniquely defined, it is customary to select a unit cell which reflects the overall symmetry of the structure, and which, therefore, exhibits the highest symmetry possible. Seven different cell-types or 'crystal systems' exist (Table 2.1). These are defined, formally, by their minimum symmetry requirements, and are described in terms of the resulting parallelepid dimensions (*a, b, c*) and inter-axis angles (α, β, γ). The unit cell connects eight identical points of the structure (or 'lattice points'). A cell containing one such point at each corner only is termed primitive (P), while face-centred cells contain an additional identical point in the middle of one set of opposite faces (A, B, C) or at the centre of all faces (F). A body-centred cell (I) contains an identical lattice point in the centre of the parallelepipid.

Crystal system	Unit cell	Essential symmetry requirements
Cubic	$a = b = c$	Four three-fold axes
	$\alpha = \beta = \gamma = 90^o$	
Tetragonal	$a = b \neq c$	One four-fold axis or one inverse
	$\alpha = \beta = \gamma = 90^o$	four-fold axis
Hexagonal	$a = b \neq c$	One six-fold axis or one inverse
	$\alpha = \beta = 90^o, \gamma = 120^o$	six-fold axis
Trigonal	$a = b = c$	One three-fold axis
	$\alpha = \beta = \gamma \neq 90^o$	
Orthorhombic	$a \neq b \neq c$	Three orthogonal two-fold axes or
	$\alpha = \beta = \gamma = 90^o$	planes
Monoclinic	$a \neq b \neq c$	One two-fold axis and/or one
	$\alpha = \gamma = 90^o, \beta \neq 90^o$	symmetry plane
Triclinic	$a \neq b \neq c$	None
	$\alpha \neq \beta \neq \gamma \neq 90^o$	

Table 2.1: The seven crystal systems.

By combining lattice type (i.e. P, C, I etc.) with point symmetry elements (i.e. symmetry around a point; inversion centre, rotation axes, mirror planes), and space symmetry elements (i.e. movement from point to point through space; screw axes, glide planes), 230 ‘space groups’ are generated. Viewed differently, there are 230 ways of arranging objects in space. Table 2.2 lists space group symmetry elements and their symbols. Space group symbols, therefore, contain information on the lattice type and the relationship of symmetry elements with the principal axes of the cell. For example, *Pmmn* is an orthorhombic space group describing a primitive unit cell with mirror planes perpendicular to the *a*- and *b*-axes, and an n glide plane perpendicular to the *c*-axis.

Symmetry element	Symbol
Centre of inversion	-1
Mirror plane	m (≡ -2)
Glide planes	a, b, c, d, n
Rotation axis	2, 3, 4, 6
Screw axis	2_1, 3_1, 3_2, 4_1, 4_2, 4_3, 6_1, 6_2, 6_3, 6_4, 6_5
Inversion axis	-3, -4, -6

Table 2.2: Space group symmetry elements and their symbols (note, the minus sign in inversion operators is usually written above the number).

Miller Indices

Miller indices, named after the British mineralogist William H Miller, are employed to define sets of planes within a crystal and are quoted as three numbers in parentheses (*hkl*), where *a/h, b/k, c/l* defines the intercept of the plane with the three unit cell edges *a, b, c* within the unit cell. For example, the (002) plane will be parallel to the *a*- and *b*-axes and intercept the *c*-axis at ½ its unit cell length. (002), therefore represents a set of parallel planes separated by ½*c* and parallel to *a* and *b*. Indices quoted in square brackets define a 'zone axis'. A zone is a collection of planes whose intersections are all parallel. The zone axis is parallel to the intersection of the planes, or, viewed differently, is perpendicular to the plane defined by the three indices within the square brackets – i.e. the [001] zone axis is equivalent to the *c*-axis.

2.2: Investigating Long-Range Order

2.2.1: X-Ray Diffraction[76,77]

X-ray diffraction (XRD) is perhaps the most widely employed technique for the characterisation of microporous materials, providing information on long-range order. Employed routinely for both everyday phase identification and in-depth structure analysis and solution, XRD is a powerful technique in the analysis of crystalline structures. The process of (any) diffraction is dependent upon the relationship between

the wavelength of the radiation involved and the separation of potential diffracting objects; diffraction will occur if the radiation wavelength is of the same magnitude as the object separation. X-radiation (a form of electromagnetic radiation lying between ultra violet and gamma rays) is particularly well suited, therefore, to the investigation of atomic arrangements within materials due to the similarity between its wavelength (typically in the order of 1Å ($1x10^{-10}$m)) and inter-atomic distances.

The resulting diffraction pattern (usually given as a plot of intensity *vs* angle (2θ) for powder samples) is a product of the interference (constructive and destructive) of the diffracted waves and can be regarded as an indirect 'image' of the atomic arrangement within the structure. The collection of good quality XRD data and its analysis is therefore key to successful structure analysis. The following sections introduce the key principles of the technique – from X-ray generation to data collection and analysis – with particular focus on the powder technique (i.e. analysis of polycrystalline materials).

X-Ray Sources

In a standard laboratory X-ray diffractometer, X-rays are produced in an 'X-ray tube' (Figure 2.1). In this device, electrons are emitted from an electrically heated tungsten cathode and accelerated towards a target anode, which can be made of several metals but is most commonly Cu (other common examples are Fe, Mo, Co, Cr). The impact of the electron with the target metal results in sudden and unpredictable deceleration, and the emission of 'white radiation'. White radiation, which possesses a continuous envelope of wavelengths, is undesirable in common X-ray diffraction experiments and is therefore removed by monochromators (discussed later).

In addition to this phenomenon, the impacting electron may eject an electron from the 1s (K) shell, thus creating a vacancy into which a 2p (L) or 3p (M) electron may drop (governed by the selection rule $\Delta l = \pm 1$, e.g. $p \rightarrow s$). In doing so, X-rays of energy equivalent to ΔE (inter-shell energy) are emitted. Since the exact wavelength of these X-rays is dependent upon the energy gap between electron shells, which in turn is dependent upon the identity of the metal element involved, X-rays generated in this manner possess wavelengths characteristic of the metal target (Table 2.3). Figure 2.2 illustrates the generation of an X-ray photon via the ejection of a K-shell electron and its

replacement by an L-shell electron. X-rays generated from a transition from L → K are denoted K_α, while M → K transitions are denoted K_β. These are further subdivided according to the total angular momentum quantum number j. For example, $2p_{3/2}$ (L) → $1s_{1/2}$ (K) = $K_{\alpha1}$ and $2p_{1/2}$ (L) → $1s_{1/2}$ (K) = $K_{\alpha2}$. $K_{\alpha1}$ and $K_{\alpha2}$ wavelengths are often sufficiently different to allow selection of one or the other by use of monochromators. However, K_β lines tend to overlap and are therefore less easily separated. K_α and K_β X-rays form sharp peaks at well-defined wavelengths superimposed on the broad background 'hump' of white radiation in the X-ray emission spectrum of the target metal (Figure 2.2).

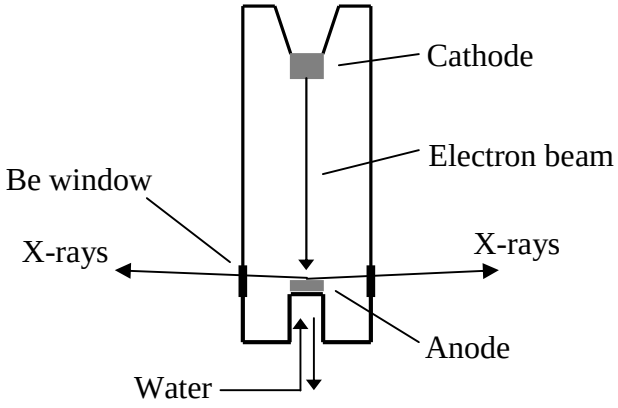

Figure 2.1: Schematic illustration of a laboratory X-ray tube.

	Wavelength (Å)		
Metal	**$K_{\alpha1}$**	**$K_{\alpha2}$**	**K_β**
Cr	2.28975(3)	2.293652(2)	2.08491(3)
Fe	1.93608(1)	1.94002(1)	1.75664(3)
Co	1.78900(1)	1.79289(1)	1.62082(3)
Cu	1.5405929(5)	1.54441(2)	1.39225(1)
Mo	0.7093171(4)	0.71361(1)	0.63230(1)

Table 2.3: Typical X-ray wavelengths generated from common anode materials.

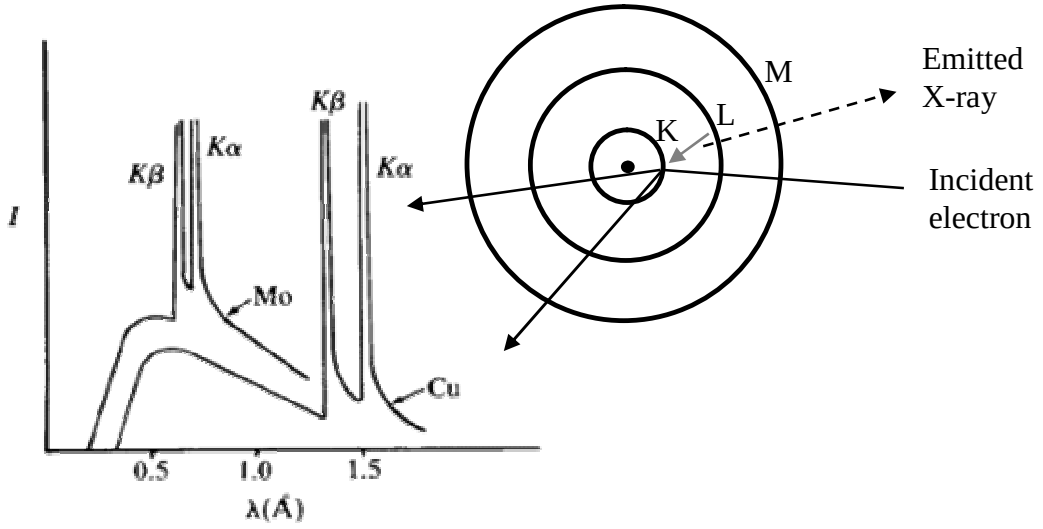

Figure 2.2: Schematic illustration of the generation of K_α X-radiation, and typical X-ray emission spectra for Mo and Cu.

A second source of X-rays is the synchrotron radiation source.[78] Acceleration of an electron beam in a 'storage ring' (tens of metres in diameter) results in the emission of radiation as cones tangential to the circumference of the beam path. The desired wavelength is selected using monochromators and directed to the various stations situated round the ring (Figure 2.3). Station 9.1 at the Synchrotron Radiation Source (SRS), Daresbury Laboratory and the materials beam line ID31 at the ESRF, Grenoble were used for powder diffraction for some samples in this work. Synchrotron X-rays are more intense than laboratory sources and offer a wide range of tunable wavelengths. Furthermore, there is the opportunity of using much lower wavelengths (Table 2.4), which have lower absorption coefficients, for example.

Station	**Typical operating wavelength (Å)**
SRS 9.1	0.4-4.5
ESRF ID31	0.3-0.9

Table 2.4: Typical operating wavelengths of stations used in this work.

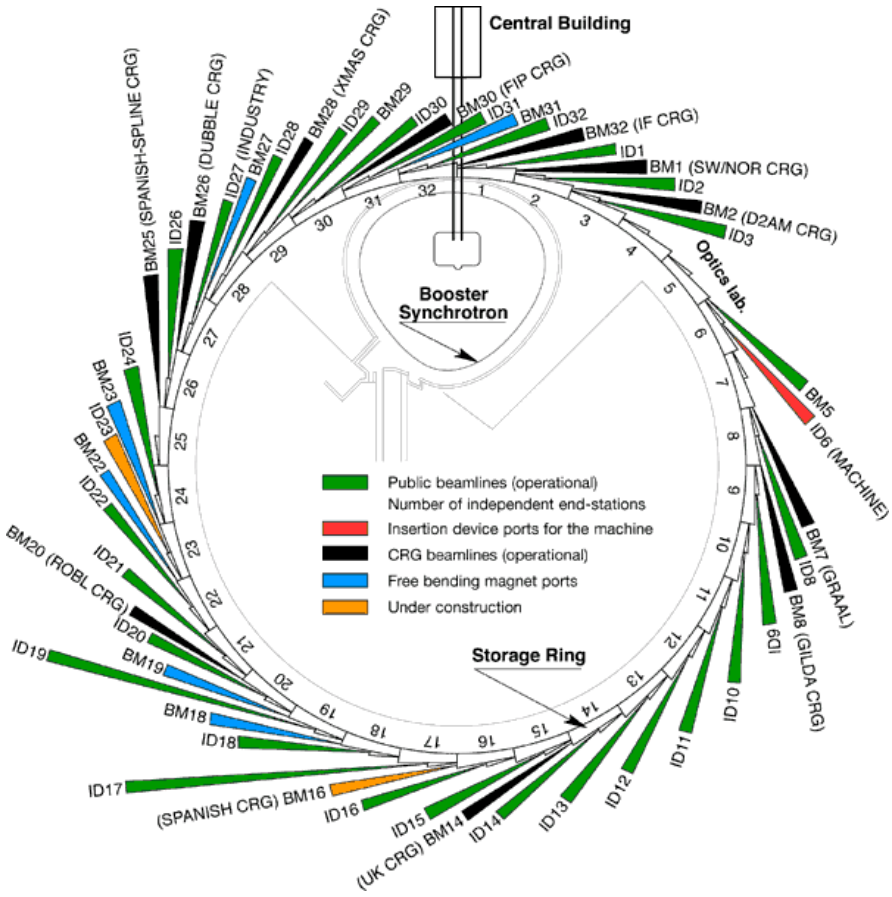

Figure 2.3: Diagrammatic representation of the ESRF synchrotron facility.[79]

Beam Conditioning

Prior to striking the sample the as-emitted X-ray beam must be conditioned in two principal ways. To permit ready analysis of the diffraction data the beam must be monochromatic – i.e. of single wavelength. This is achieved by a monochromator, often a crystal of Si or Ge. Following Bragg's law (see later), different wavelengths diffract at particular angles from a given set of planes within a crystal allowing selection of the desired wavelength by appropriate manipulation of the angle at which the crystal is set to the incident beam (Figure 2.4). In this way only the desired wavelength (usually $K_{\alpha 1}$ in the case of work discussed in this thesis from laboratory diffractometers) is permitted to exit the monochromator.

In addition, the beam that exits from the source is often wedge-shaped – i.e. it possesses an axial divergence. This phenomenon results in broad and asymmetric (see later) diffraction peaks and therefore should be overcome as far as possible. The process

whereby X-rays with parallel (or nearly parallel) propagation vectors are selected is called collimation and is achieved by a series of slits (Figure 2.5). The monochromatic and collimated beam is now directed to the sample.

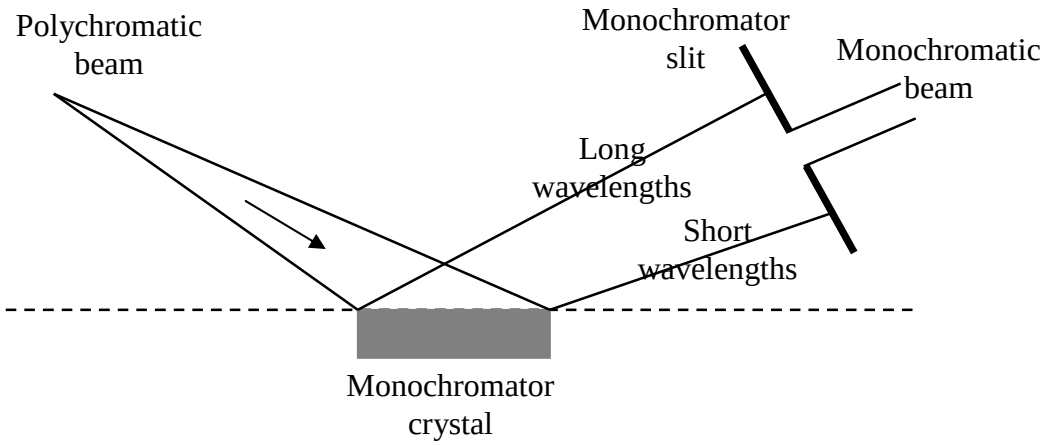

Figure 2.4: Schematic illustration of a crystal monochromator. Adapted from ref. 77.

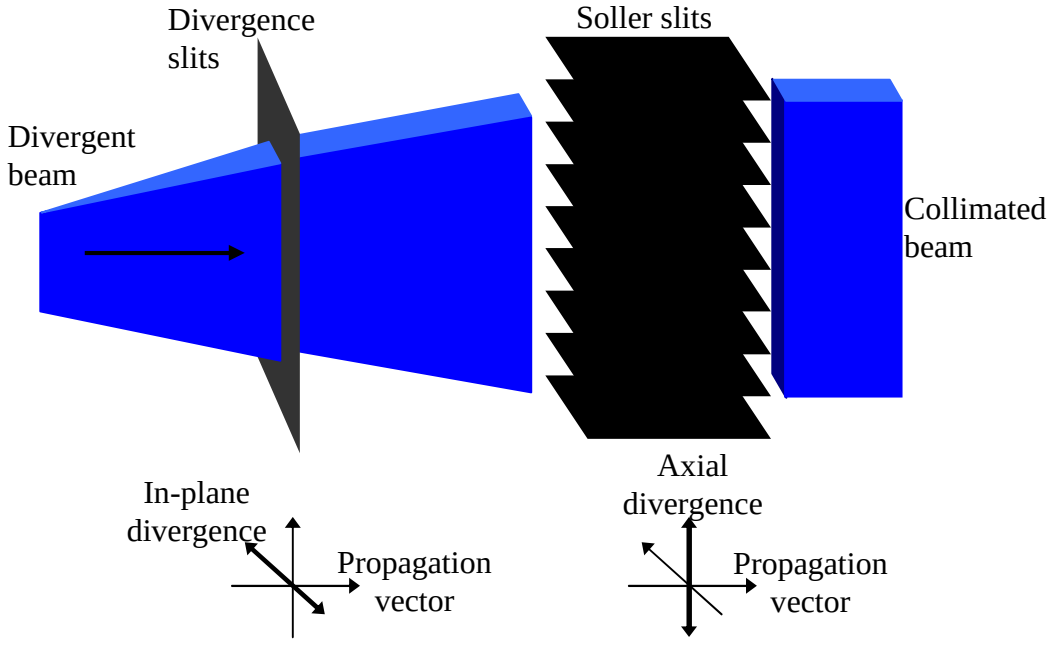

Figure 2.5: Schematic illustration of beam collimation achieved via a series of slits. The coordinate systems illustrate the type of divergence corrected at each step. Adapted from ref. 77.

Diffraction of X-rays: Bragg's Law and the Ewald Sphere

W L Bragg derived a law of diffraction describing the process, mathematically, as 'reflection' from atomic planes within the crystal, which can be defined by their Miller indices. The resulting equation and its derivation are illustrated in Figure 2.6. The path difference for two waves both before and after reflection is indicated in Figure 2.6 as distance AB; AB = dsinθ. The total path difference is therefore

$$2AB = 2d\sin\theta \qquad \text{eqn. 2.1}$$

and constructive interference occurs when 2AB = nλ, where n is an integer and λ is the wavelength of the diffracting beam.

Therefore, at fixed wavelength the angular position of a diffraction maximum yields information on the lattice plane *d*-spacing; and conversely, different wavelengths will 'reflect' at different angles from any given set of planes (the basis of a crystal monochromator discussed previously). Miller indices are employed to index the diffraction peaks resulting from a particular set of planes.

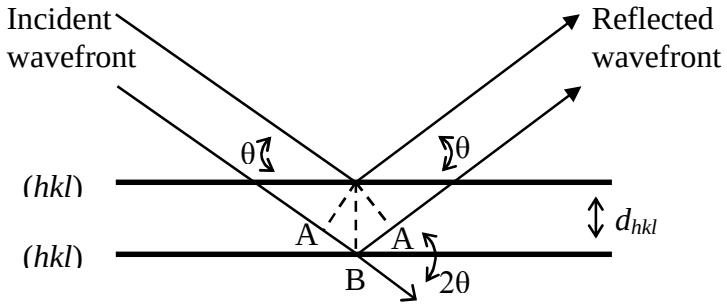

AB = *d*sinθ

Total path difference = 2AB = 2*d*sinθ

For constructive interference 2AB = nλ = 2*d*sinθ

Figure 2.6: Derivation of Bragg's Law from consideration of two parallel reflecting beams.

A geometrical consideration of Bragg's Law is given by the Ewald sphere. The Ewald sphere is an imaginary sphere of radius 1/λ, centred on the diffracting sample (Figure

2.7). If the origin of the *reciprocal* lattice is centred where the incident (or 'direct') beam exits the sphere, only those planes (*hkl*) whose reciprocal lattice point sits on the sphere surface (remembering this is a three dimensional model) will satisfy Bragg's Law and produce a diffraction spot/peak.

Single Crystal Analysis

Single crystal XRD is by far the most preferred method for structural analysis. However, single (i.e. non-twinned etc.) crystals of sufficient size are only occasionally encountered in zeolitic materials research, thus necessitating the use of powder diffraction. Nevertheless, the experimental set-up for single crystal analysis provides a bases for the understanding of powder diffraction and is therefore briefly summarised here.

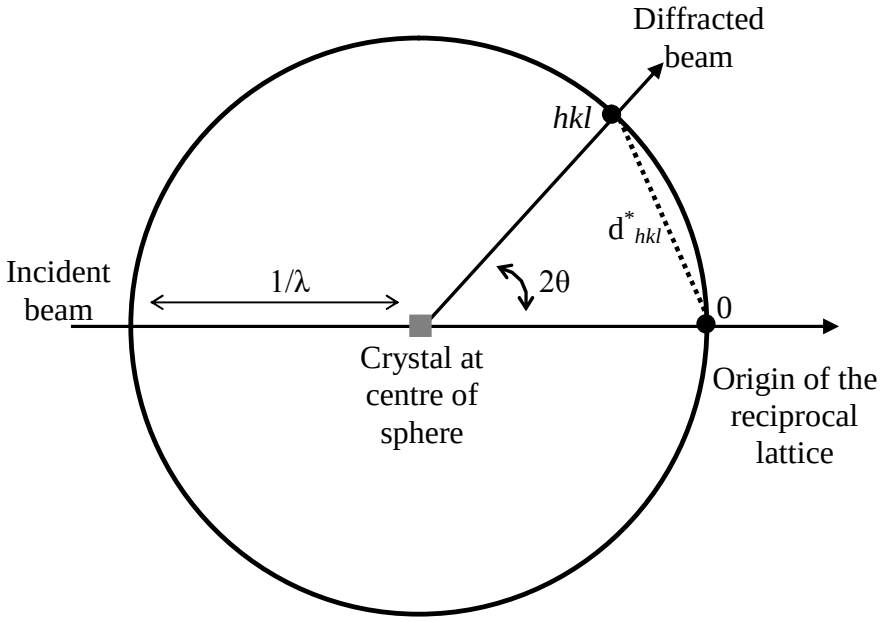

Figure 2.7: A two-dimensional representation of the equatorial plane of the Ewald sphere (equivalent to a plan view of Figure 2.8).

A crystal is selected and mounted on a fine glass capillary and fixed at a particular orientation to the X-ray beam. Data collection is conducted and measures those 'reflections' that satisfy the Bragg equation, or which sit on the Ewald sphere as described above. Whether a particular reciprocal lattice point sits on the Ewald sphere surface depends greatly on the angle at which the crystal is oriented towards the beam.

Therefore, the crystal is re-oriented after each data acquisition step to bring different reflections into contact with the Ewald sphere. Ultimately this permits the construction of a three-dimensional electron density map (see later) – i.e. three-dimensionality is maintained from structure to diffraction pattern, and structure solution is therefore (relatively) straightforward.

Powder Diffraction

Most samples to be analysed in work discussed in this thesis are polycrystalline – i.e. of many tiny crystallites, too small to be analysed by single crystal analysis (or exhibiting twinning/intergrowth). A small sample of powder, placed in the X-ray beam, therefore contains many crystallites at random orientation to the beam. The consequence of this is that for any set of (*hkl*) planes a diffraction beam exits the sample in all possible directions. Since the angle (2θ) between the direct and 'reflected' beam must be constant for a given set of planes, a cone is produced around the direct beam, the surface of which is formed by the accumulation of all diffracted beams from this set of planes.

Consequently, rather than discrete spots on the Ewald sphere, diffraction maxima are smeared into concentric rings about the direct beam (Figure 2.8). In a typical powder diffractometer, the diffracted X-ray beams are recorded by a detector, which scans through an arc from $2\theta = 1\text{-}3^{o}$ to up to 90^{o}, following the equatorial line of the Ewald sphere. In doing so, the ring base of each cone is traversed once and indicated in the powder diffractogram as a peak, the height of which (intensity) reflects the intensity (brightness) of the ring observed had a photographic film been employed for data collection. As a result powder diffractograms represent three-dimensional information on a two-dimensional scale, and information is therefore lost due to peak overlap and the summing of intensities.

Samples analysed during studies discussed in later chapters were either mounted in the sample holder as thin films (between plastic discs), or in capillaries (Figure 2.9). In both cases the sample is rotated to help ensure random sample orientation.

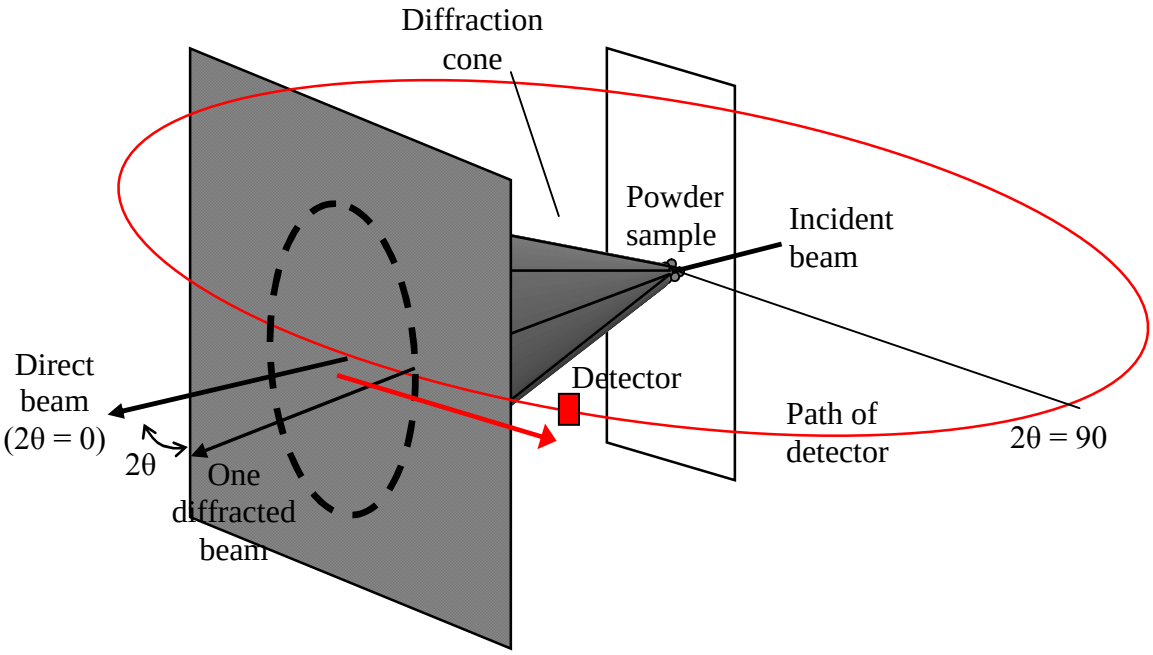

Figure 2.8: Schematic illustration of the diffraction of an X-ray beam from one set of planes in a powdered sample.

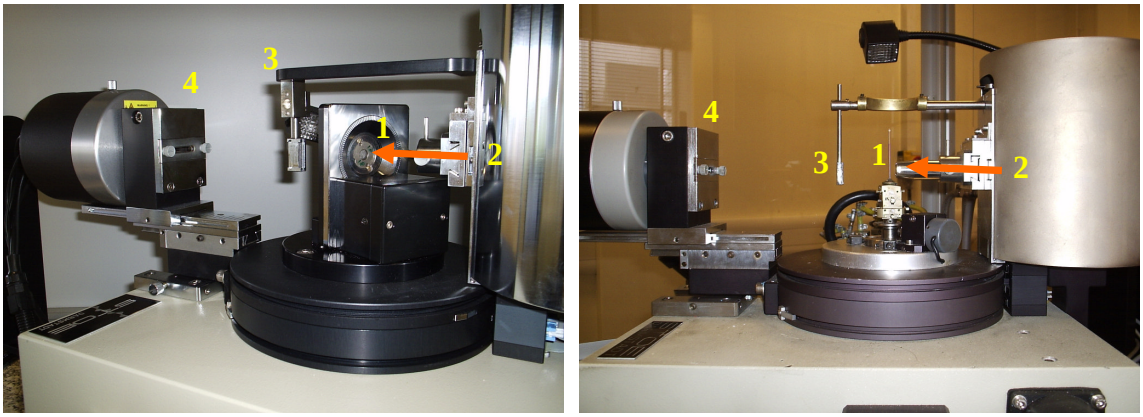

(a) (b)

Figure 2.9: Two X-ray diffractometers employed in this work: (a) for thin film samples and (b) for capillaries. (1 – sample holder, 2 – X-ray 'source', 3 – beam stop, 4 – detector, arrow indicates direction of incident X-ray beam).

Analysis of Powder Diffraction Patterns

As mentioned above, a diffraction peak represents the constructive interference of diffracted beams from a set of crystal planes. The position (in 2θ) of the diffraction peak is characteristic of the plane separation (*d*-spacing) and this can be related to the unit

cell parameters for the material studied and the Miller indices of the planes involved. For example, in an orthorhombic system:

$$1/d_{hkl}^2 = h^2/a^2 + k^2/b^2 + l^2/c^2 \qquad \text{eqn. 2.2}$$

This equation can be readily simplified for tetragonal ($a = b$) and cubic ($a = b = c$) systems. More complex equations exist for the other systems. Therefore, through analysis of peak position, peaks (or the pattern) are 'indexed' and the unit cell may be established. This process is conducted by algorithms accommodated in computer software, which generate a list of possibilities. A factor of merit (FOM) is given with each to aid interpretation by the user. Pattern indexing, although automated, is by no means trivial, however, and depends on accurate peak position picking and therefore data quality and resolution, and the absence of impurity peaks.

Higher resolution can be achieved from synchrotron radiation as a result of the collimated nature of synchrotron beams.[78,79] The tangentially emitted radiation possesses a vertical divergence (θ_v) given by:

$$\theta_v \approx mc^2/E \approx 5x10^{-4}/E \qquad \text{eqn. 2.3}$$

where m = electron mass, c = speed of light, E = energy of the ring (GeV)

At the SRS Daresbury Laboratory, which has an operating energy of 2GeV, the vertical divergence is approximately 0.25milliradians. This gives a vertical beam thickness of approximately 0.6cm at a 25m working distance (Table 2.5).

Source	Operating E (GeV)	θ_v (mrad)	Beam thickness at 25m (cm)
SRS	2.00	0.250	0.6
ESRF	6.03	0.083	0.2

Table 2.5: Vertical beam divergence and thickness of synchrotron sources.

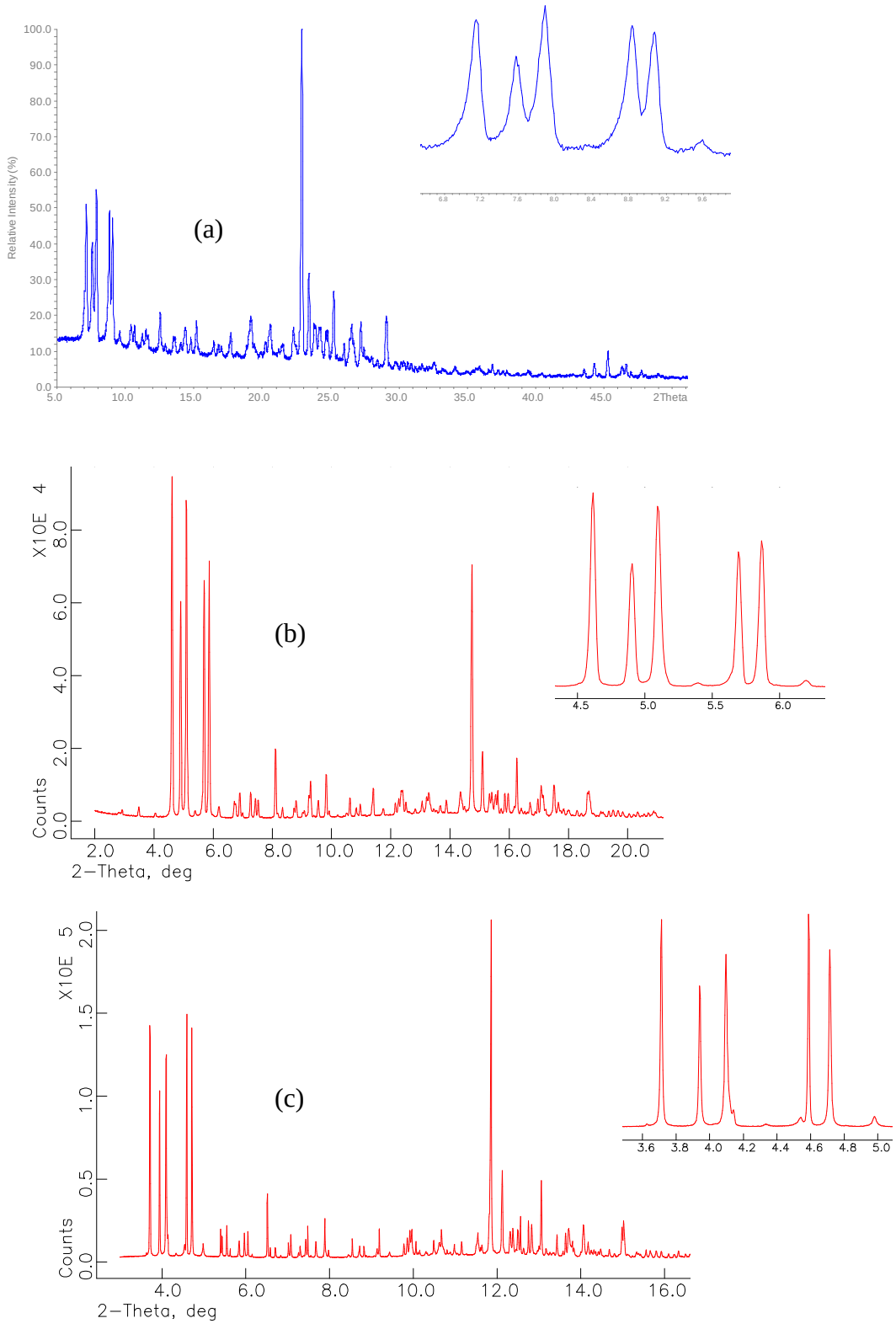

Figure 2.10: Powder XRD patterns of aluminosilicate TNU-9 recorded on (a) STOE STADI/P diffractometer (1.54056Å), (b) Station 9.1 SRS Daresbury (0.995559Å) and (c) Station ID31 ESRF (0.80124Å).

The improvement in resolution is clearly illustrated in Figure 2.10: note, for instance, the improved base-line separation of the five principal peaks at low angle (insets) in the synchrotron data, as well as a better signal-to-noise ratio.

The resolution of a diffractometer is often expressed in one of three ways[80]:

- Angular Full Width at Half Maximum (FWHM) as a function of 2θ
- FWHM as ΔQ ($\sin\theta_1$-$\sin\theta_2/\lambda$) as a function of Q ($\sin\theta/\lambda$)
- $\Delta d/d$ as a function of d.

Figures 2.11 and 2.12 illustrate the differences in resolution of the three instruments employed in this work. In this case, angular Full Width at Half Maximum (FWHM) as a function of 2θ would not be appropriate as the data were recorded at three different wavelengths. Therefore, plots of ΔQ *vs* Q and $\Delta d/d$ *vs* d are used. Clearly, synchrotron data is of superior resolution, particularly at low angle.

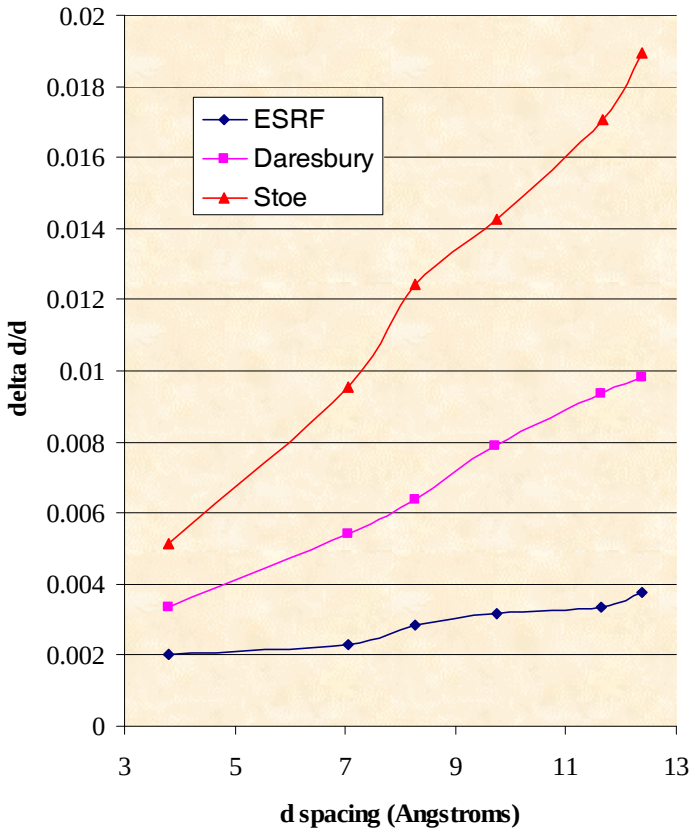

Figure 2.11: Plot of Δd/d vs d

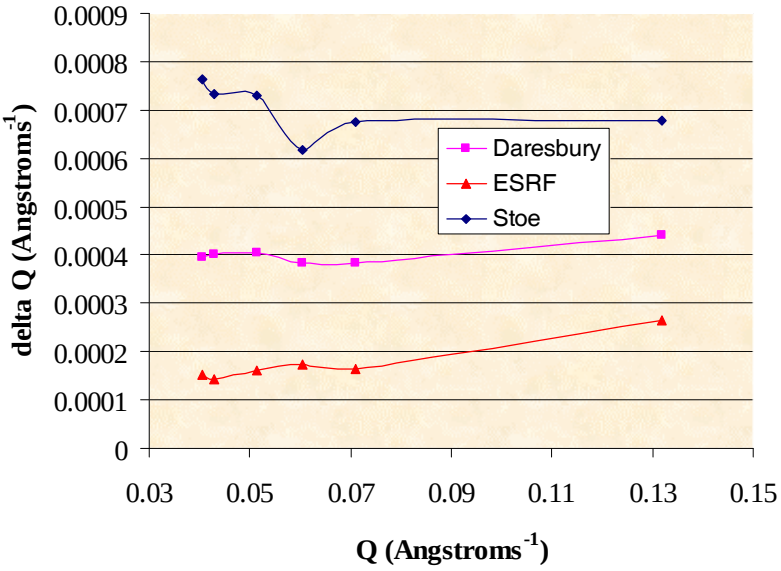

Figure 2.12: Plot of ΔQ vs Q

The absence of certain reflections in the diffraction pattern (known as systematic absences) arises from lattice centring and symmetry elements present in the structure being analysed. For example, a body centred cubic crystal will exhibit diffraction maxima only from planes with Miller indices (*hkl*) where $h+k+l$ = even. Consequently, an analysis of systematic absences can yield the space group of the structure.

While the peak positions and absences yield information on the unit cell parameters and symmetry, it is their intensities that contain information on the atomic arrangement within the unit cell. In solving an unknown structure from XRD data, the electron density (ρ) at different positions (*xyz*) in the unit cell must be established. As indicated in equation 2.4, ρ is dependent upon the structure factor F_{hkl}.

$$\rho(xyz) = (1/V)\Sigma_h\Sigma_k\Sigma_l F_{hkl}\exp[2\pi i(hx+ky+lz)] \qquad \text{eqn. 2.4}$$

$$F_{hkl} = \Sigma f_n \exp[2\pi i(hx_n+ky_n+lz_n)] \qquad \text{eqn. 2.5}$$

The structure factor represents the scattering ability of the unit cell and must therefore take into account the scattering ability (or 'scattering factor', f) of each individual atom within the unit cell (equation 2.5). The ability to scatter X-rays varies from atom to atom and depends on the number of electrons present (larger atoms therefore exhibit larger

scattering factors and are more easily 'seen' or located by XRD). The atomic scattering factor is also dependent on scattering angle and decreases as illustrated in Figure 2.13 (hence the drop-off in peak intensity with 2θ in diffraction patterns).

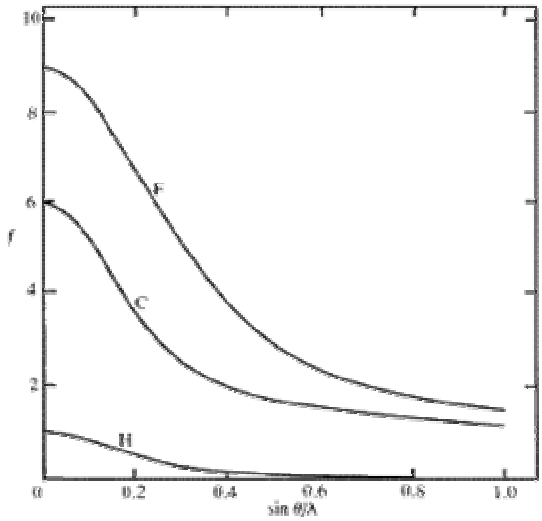

Figure 2.13: The atomic scattering factor decreases with angle.[81]

The square of the structure factor F_{hkl} is directly proportional to the integrated intensity of the diffraction peak, I_{hkl}, as indicated in equation 2.6. The constant of proportionality (K) is comprised of the product of a number of geometric specimen and instrumental parameters. Therefore, while the absolute value of F_{hkl} may readily be established, its sign (or 'phase angle') has been lost and cannot be found directly from either powder or single crystal diffraction.

$$I_{hkl} = KF^2_{hkl} \qquad \text{eqn. 2.6}$$

The technique known as Direct Methods attempts to solve the 'phase problem' by applying mathematical relationships between indices and intensities of reflections. Two assumptions apply: firstly that the electron density must not be negative, and secondly that the structure is composed of discrete atoms.

The computer program EXPO[82] is a Direct Methods package combining the existing program SIRPOW[83] with a specially designed program EXTRA.[84] EXTRA calculates integrated intensities that are input to SIRPOW, which was designed specifically for structure solution from powder data. That is, EXTRA produces a set of F_{hkl}s, which are input to SIRPOW.

The program requires such information as unit cell dimensions and space group, as obtained from peak indexing, along with the expected unit cell content (Figure 2.14) before performing the structure factor amplitude extraction. It is possible to adjust the data range that is to be included in the extraction and it is also possible to intervene at the extraction stage, for example to adjusts the background fit. The final suggested solution could also be altered to yield a more realistic model; atom types and location as well as bonds can all be edited. The amended structure can then be employed in an in-built refinement process.

FOCUS[85] is a further structure solution program, developed by Lynne McCusker and co-workers. Developed specifically with zeolites in mind, information such as bond lengths, angles and coordination (i.e. tetrahedral units) is also input to the program.

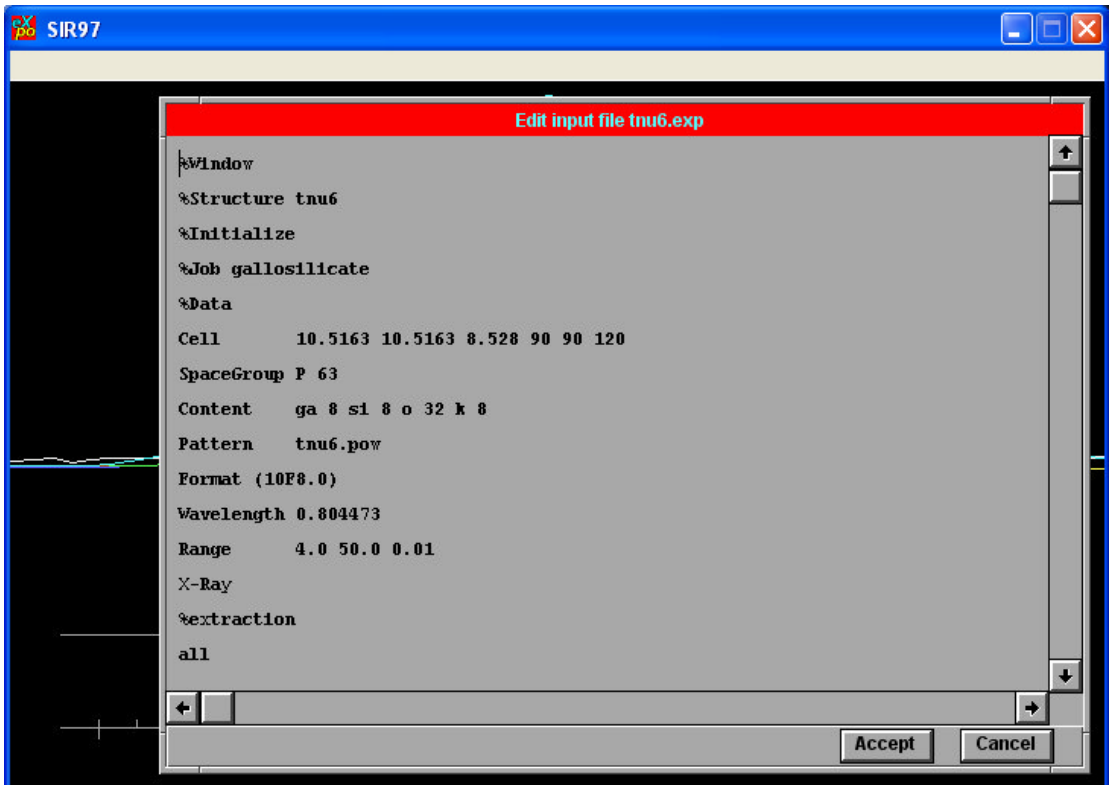

Figure 2.14: Input file for EXPO prior to intensity extraction.

2.2.2: Powder Pattern Refinement: The Rietveld Method[77,86,87]

As mentioned above, structure solution from powder XRD data is not straightforward. However, once a starting model (complete or partial) has been established the theoretical model XRD pattern can be readily compared to experimental data, and refinement of the model can commence. Even if the topology is known, much information can be gained from a refinement against powder data including unit cell parameters, atomic coordinates and bond lengths and angles. Refinement is conducted via the Rietveld method (executed in the GSAS[88] software package) in which the intensity y_{io} at the i^{th} step is compared with the corresponding intensity y_{ic} from the model. The model is refined by minimizing, via a least-squares process, the residual:

$$S = \Sigma w_i \left| y_{io} - y_{ic} \right|^2 \qquad \text{eqn. 2.7}$$

where w_i is a suitable weight based on the uncertainty of each reflection and is given by:

$$(w_i)^{-1} = \sigma_{ip}^2 + \sigma_{ib}^2 \qquad \text{eqn. 2.8}$$

(σ_{ip} is the standard deviation associated with the peaks and σ_{ib} is that associated with the background)

The agreement between experimental data and the model is given by the goodness of fit parameters R_p and R_{wp} (weighted profile):

$$R_p = \Sigma \left| y_{io} - y_{ic} \right| / \Sigma y_{io} \qquad \text{eqn. 2.9}$$

$$R_{wp} = [\Sigma w_i (y_{io} - y_{ic})^2 / \Sigma w_i y_{io}^2]^{1/2} \qquad \text{eqn. 2.10}$$

For powder data, an R_{wp} value of around 10% or less is desirable.

The sum of contributions from neighbouring Bragg reflections (y_{ic}) depends on scale, Lorentz-polarization and structure functions, as well as the peak profile and background functions. There are, therefore, two models contributing to the refinement: a structural model based on approximate atomic coordinates, and a profile model which accounts

for individual line profiles and background variations resulting from instrumental and sample effects. Indeed, a large proportion of the R_p and R_{wp} values in a least squares refinement is often due to poor profile matching. It is therefore essential to refine instrumental/profile parameters such as background, peak shape and asymmetry as well as structural parameters including unit cell and atom positions, fractional occupancies and thermal parameters to achieve the most satisfactory data fit. These parameters can be dampened to allow them to vary in a controlled manner. Their adjustment is continued to achieve as low a value as possible for R_p and R_{wp}. The following sections discuss some of the most important parameters that are variable during Rietveld refinement.

Background

Along with the zero point and scale factor, background is one of the first parameters to be refined during a structural refinement. Background is a result of several factors including, for example, scattering from air and the sample holder, incomplete monochromation, detector noise etc. In Rietveld analysis of an XRD pattern, background can be approximated via the use of various functions. In refinements discussed in this thesis a cosine Fourier series is employed whereby background (b_i) is modelled as a sum of cosines (summed over all data points):

$$b_i = B_1 + \Sigma B_m \cos(2\theta_{m-1}) \qquad \text{eqn. 2.11}$$

where i varies from 1 to n (n = total number of data points measured in the whole of the region of interest), and B_m represents background parameters that can be refined (typically $2 \leq m \leq 36$).

Peak Shape

The observed peak shape in a powder diffraction pattern results from the convolution of three terms or functions relating to specimen (f(x)), instrument (G) and wavelength (W) factors:

$$h(x) = (W*G)*f(x) + \text{background} \qquad \text{eqn. 2.12}$$

Over-and-above the intrinsic peak width (i.e. reciprocal lattice points sitting on the Ewald sphere surface have finite size), the specimen function, f(x), includes contributions from grain size and microstrain as defined in equations 2.13 and 2.14, respectively.

$$\beta = \lambda/\tau\cos\theta \qquad \text{eqn. 2.13}$$

$$\beta = k\varepsilon\tan\theta \quad (k \text{ is a constant}) \qquad \text{eqn. 2.14}$$

As crystal size (τ) decreases, or microstrain (ε) increases, the additional width (β) added to the intrinsic width of a peak increases. The instrumental function includes geometrical effects from location of the source, monochromator(s) and specimen, while the wavelength dispersion function accounts for the distribution of wavelengths present in the beam (dependent on monochromatisation).

These effects are generally symmetrical and can be closely modelled by employing Lorentzian and/or Gaussian profiles. Commonly a pseudo-Voigtian function is employed in studies discussed in later chapters. This function represents a combination of both Lorentzian and Gaussian components in which the calculated intensity $I(\Delta 2\theta)$ at a displacement $\Delta 2\theta$ from the Bragg angle is expressed as:

$$I(\Delta 2\theta) = Ip \left[\frac{2\eta}{\pi\Gamma[1+4(\Delta 2\theta/\Gamma)^2]} + \frac{2(1-\eta)(\ln 2/\pi)^{1/2}\exp[-4\ln 2(\Delta 2\theta/\Gamma)^2]}{\Gamma} \right]$$

eqn. 2.15

Where Ip = integrated intensity for the peak

Γ = FWHM

Blue term represents the Lorentzian contribution

Red term represents the Gaussian contribution

And η = a mixing constant ($0<\eta<1$)

The pseudo-Voigt function is found to model symmetric and slightly asymmetric peak profiles more effectively than the individual functions. The FWHM of the Gaussian and Lorentzian components (Γ_G and Γ_L, respectively) vary with scattering angle given by:

$$\Gamma_G = (U\tan^2\theta + V\tan\theta + W)^{1/2} \qquad \text{eqn. 2.16}$$

$$\Gamma_L = X\tan\theta + Y/\cos\theta \qquad \text{eqn. 2.17}$$

Here, U, V and W are half width parameters accommodating Gaussian strain/disorder broadening and the minimum peak width for the machine and sample. X and Y account for Lorentzian strain/disorder and particle size broadening. U, V, W, X and Y are therefore all variable during the refinement process.

In reality, however, it is observed that peak profiles possess a significant asymmetry. This may be due to instrumental factors such as axial divergence of the beam, or to the non-zero curvature of the cone base-ring intersected by the detector (particularly at low 2θ values). These factors are usually manifested by broadening of the peak on its low angle side – an effect particularly evident on low 2θ reflections.

For certain materials discussed in later chapters (but particularly TNU-7) low angle reflections in laboratory data possessed quite pronounced asymmetries, which could not be satisfactorily modelled from the pseudo-Voigt parameters alone. To better model such deviation from isometry the asymmetry correction function developed by Finger, Cox and Jephcoat was employed.[89] Developing a formulism that was devised by van Laar and Yelon,[90] Finger, Cox and Jephcoat derive two parameters, S/L and H/L, which are variable during the refinement (2S = sample height, 2H = detector height, L = sample-detector separation). This formulism results from a geometric consideration of the diffractometer. In particular it arises from consideration of the relationship between the detector slit and the profile of the diffraction cone edge (an ellipse on the surface of the cylinder on which the detector moves) that it intercepts. Since the detector slit has finite height its upper and lower ends will intersect the curved diffraction ring first as it approaches the Bragg angle (2θ) for that particular reflection from angles below 2θ (i.e. the concave side of the ring). As the detector sweeps along its path the detected intensity will increase in an exponential-like profile until the full intensity is detected at 2θ, after which point intensity will drop off more abruptly as the detector exits the diffraction

ring on its convex side. Figure 2.15 illustrates the improvement in fit achieved by introducing this asymmetry correction function to the peak shape modelling in a refinement of TNU-7 (Chapter 5).

Since asymmetry also affects the lattice parameters, S/L and H/L are refined with all other variables switched off (they are also refined individually since they are correlated with each other). Then lattice parameters, zero point and pseudo-Voigt peak shape parameters are refined individually (and in that order), before being switched off and asymmetry parameters refined again. This cyclical procedure is repeated until no further improvement is gained. Although S, L and H are physically meaningful, the refined values for S/L and H/L may not necessarily reflect those expected. This is most probably because other factors such as beam divergence and sample effects may also be contributing to the peak shape profile and will be 'soaked up' by the S/L and H/L refinement. Nevertheless, regardless of the contributing sources of peak asymmetry, this technique has proved very useful.

Refinement of the Structural Model

Following initial refinement of background, peak shape, zero point, scale factor and unit cell, atomic coordinates may be permitted to refine. It is common to employ restraints to help maintain a chemically sensible model. For example, bond distances and angles can be restrained to within a given range. Constraints may be employed to permit groups of coordinates, fractional occupancies or thermal parameters to vary with each other.

Since, at any temperature above absolute zero, atoms exhibit a degree of oscillation about their equilibrium position, a so-called thermal parameter may be refined for each. This parameter is more properly termed 'atomic displacement parameter' since displacement observed in X-ray analysis may be due to a combination of different sample and instrumental effects, as well as thermal motion.

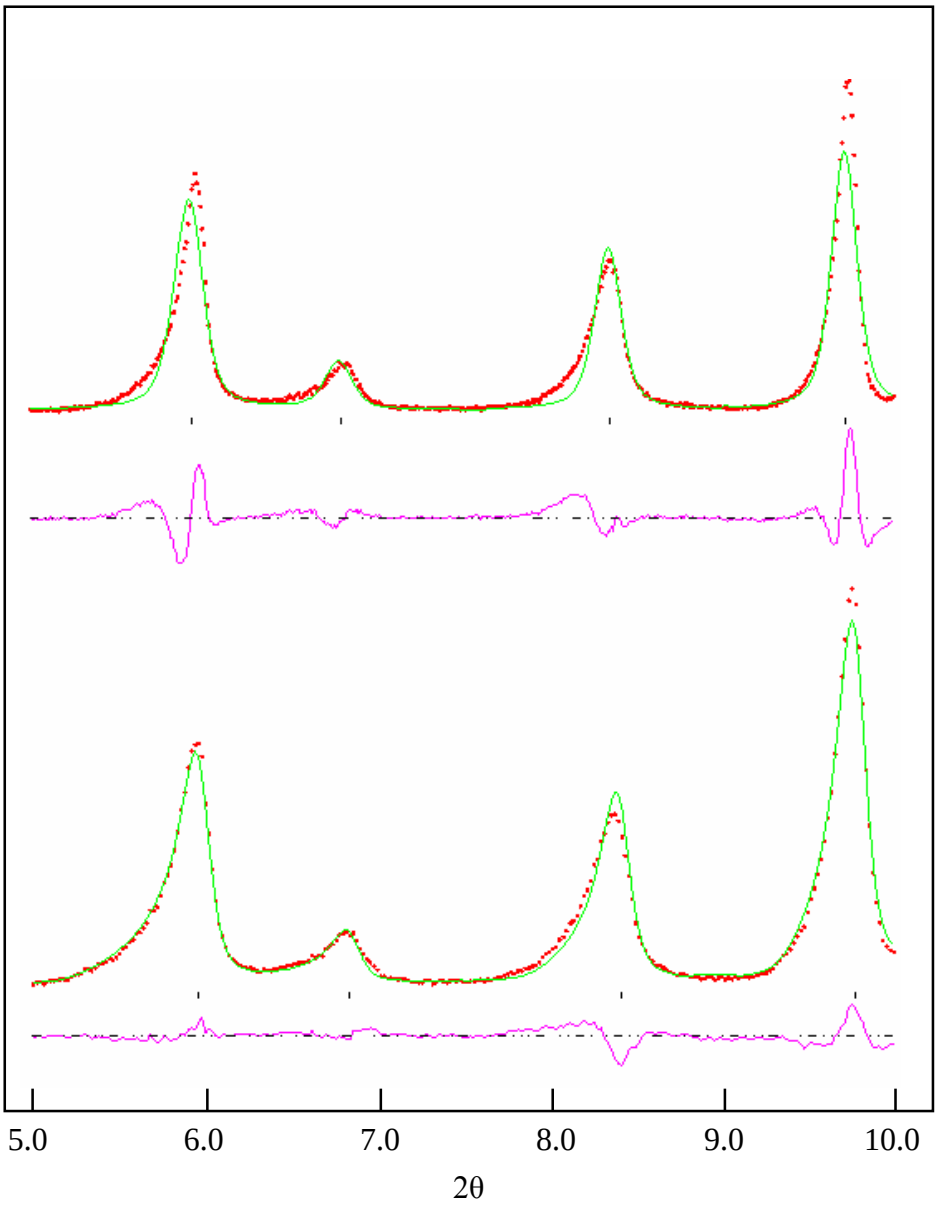

Figure 2.15: Low 2θ range of the XRD pattern of TNU-7 illustrating pronounced peak asymmetry. The lower plot illustrates the improvement achieved in peak shape modelling from the inclusion of S/L and H/L parameters (red plots = experimental data, green = model, purple = difference plot (see later)).

In all refinements discussed in later chapters, atomic thermal parameters (U) are refined isotropically – i.e. considering the atoms as diffuse spheres. U is the root mean square deviation of the j^{th} atom from its equilibrium position and defines the displacement parameter B_j of the j^{th} atom via:

$$B_j = 8\pi^2 U \qquad \text{eqn. 2.18}$$

B^j is related to the temperature factor of the j^{th} atom (t) by:

$$t_j = \exp[-B_j \sin^2\theta/\lambda^2] \qquad \text{eqn. 2.19}$$

Higher B-values result in a more dramatic decrease in F_{hkl} with 2θ and thermal parameters are therefore highly correlated to the background. Since thermal parameters absorb other unaccounted factors (or factors that are incorrectly accounted for), they are often not entirely meaningful and should be analysed with care.

Fourier Difference Maps[75]

The success of a particular structure refinement relies on the availability of a reasonable starting model. Occasionally, however, this starting model may not be entirely complete and the location of 'missing' atoms may be elucidated via Difference Fourier Maps.

In this method, which is accommodated in the GSAS suite, the electron density distribution encompassed by the calculated model ($\rho_c(xyz)$) is compared to that of the observed data ($\rho_o(xyz)$) via:

$$\Delta\rho(xyz) = \rho_o(xyz) - \rho_c(xyz) = 1/V\Sigma(F_{ohkl} - F_{chkl})\exp[-2\pi i(hx+ky+lz)] \qquad \text{eqn. 2.20}$$

Where an atom is missing from the model at a particular location, $\rho_c(xyz)$ will be zero while $\rho_o(xyz)$ will show a peak. The resulting difference map will also, therefore, exhibit a peak. Due to the overlapping of reflections, the difference Fourier method is hindered by uncertainty in the magnitude of particular I_{hkl} values. However, by refining the model as far as possible prior to F_{ohkl} extraction, these problems may be alleviated, and the phase is assumed to be equal to that of the model.

The Rietveld Plot

Figure 2.16 illustrates a Rietveld refinement plot for the refinement of MgAPO STA-7 (from Chapter 9). Red crosses represent the experimental data while the refined model data is illustrated in green. A purple 'difference' plot is included below the main

histogram and gives a visual indication of the goodness of fit. Black tick lines indicate the expected peak positions from the refined unit cell.

Summary

In summary, XRD offers a powerful means of investigating the structures of materials. Due to the similarity between X-ray wavelengths and inter-atomic distances, diffraction is possible and yields information on cell parameters, symmetry and atomic coordinates. Although certain information is lost in powder diffraction experiments, the resulting X-ray diffractogram is invaluable in phase identification. Structure solution and general structure analysis are made possible through computer software such as EXPO, FOCUS and GSAS.

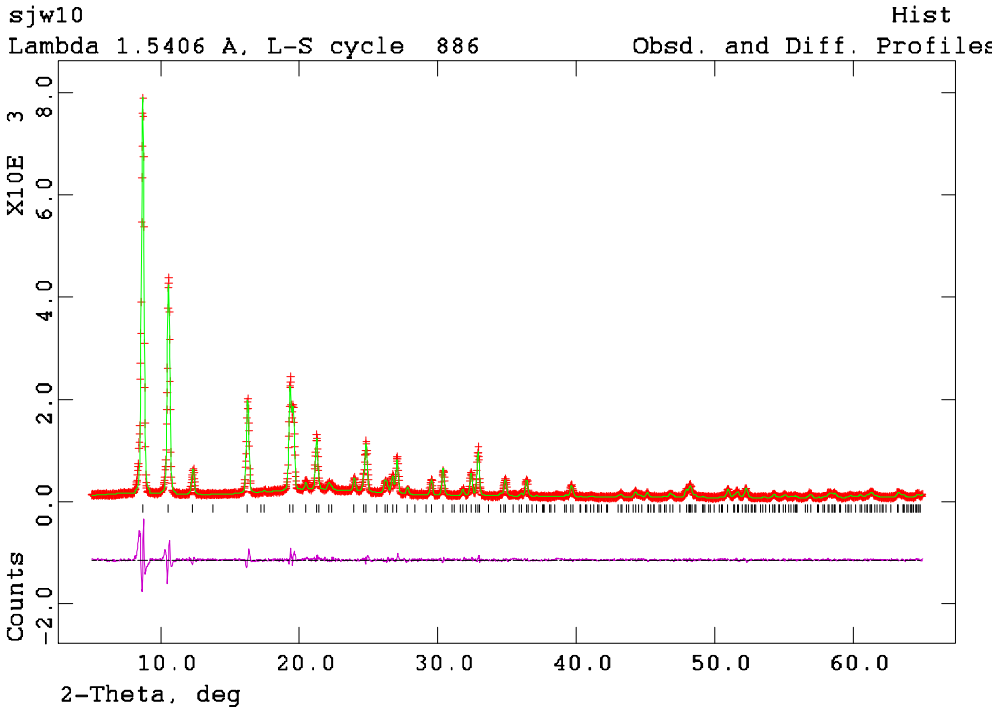

Figure 2.16: A typical Rietveld refinement plot illustrating the experimental data (red), the refining model (green) and the difference between the two (purple).

2.2.3: Powder Neutron Diffraction

To confirm the structures of TNU-7 and TNU-9 (Chapters 5 and 6, respectively), neutron powder diffraction was conducted in addition to XRD analysis. While the principles of neutron diffraction are similar to those of XRD, there are a few important

differences. Most importantly neutrons are scattered by atomic nuclei rather than electrons and atomic scattering factors vary erratically from species to species. As a result, atoms such as hydrogen and oxygen can be located more accurately from neutron data. Also, since the cross section of an atomic nucleus is very small, neutron scattering amplitudes do not decrease rapidly with angle.

Neutron diffraction was conducted at the ISIS Rutherford Laboratory where neutrons are generated from the proton bombardment of a tungsten target. Neutrons are emitted from the excited nuclei with wavelengths in the range of 1-2Å. A Time of Flight (TOF) experimental set-up was employed. In this technique the beam is polychromatic and different wavelengths are discriminated by their time of arrival at fixed detectors (Figure 2.17). The detected wavelength is related to *d*-spacing via Bragg's Law.

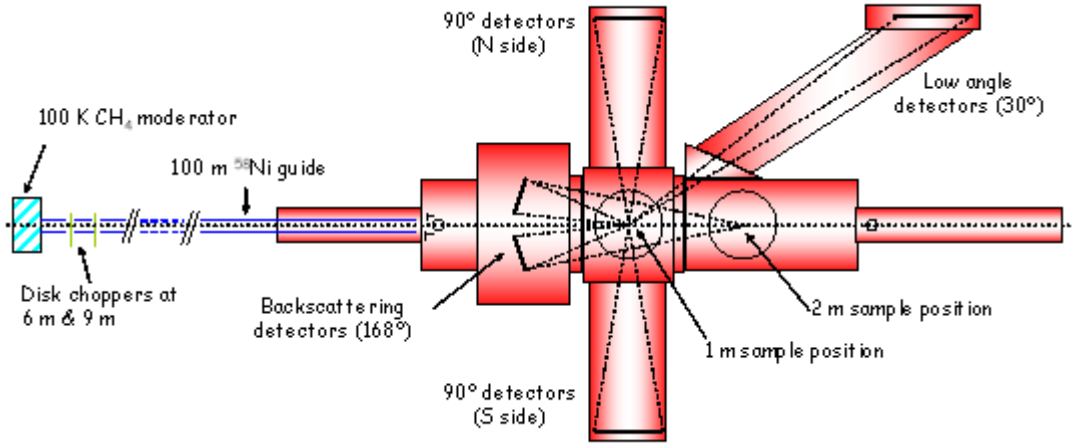

Figure 2.17: Schematic illustration of the HRPD station at the neutron source at ISIS Rutherford laboratory.[91]

2.3: Investigating Short-Range Order

While X-ray and neutron diffraction provide powerful means of determining long-range order within zeolitic materials, information on the local, short-range environment of particular species is also desirable. Two element selective techniques employed for this purpose are Electron Spin Resonance and Nuclear Magnetic Resonance spectroscopy, the underlying principles of which are discussed in the following sections.

2.3.1: Electron Spin Resonance Spectroscopy (ESR)[92,93]

ESR spectroscopy (also known as Electron Paramagnetic Resonance (EPR) spectroscopy) is employed in the characterisation of Cu complex-containing phosphate-based materials in Part 3. The technique detects species with unpaired electrons (i.e. species that are paramagnetic), and is therefore sensitive to the presence of Cu^{2+} cations (d^9). Parameters measured from the resulting spectra characterise the geometry of the paramagnetic cation and can act as a probe to the local environment around the species through comparison with related materials.

By applying a magnetic field (B) across a paramagnetic species the degeneracy of the $m_s = \pm ½$ states for the unpaired electron is lost since they align with or against the applied field (Figure 2.18). The energy of the split levels is given by equation 2.21, in which μ_B is the Bohr magneton (= $9.2741010 \times 10^{-24} JT^{-1}$), m_s is the spin quantum number (= ± ½), B is the applied magnetic field (G or T; 1G = 10^{-4}T) and g is known as the g factor.

$$E = g\mu_B m_s B \qquad \text{eqn. 2.21}$$

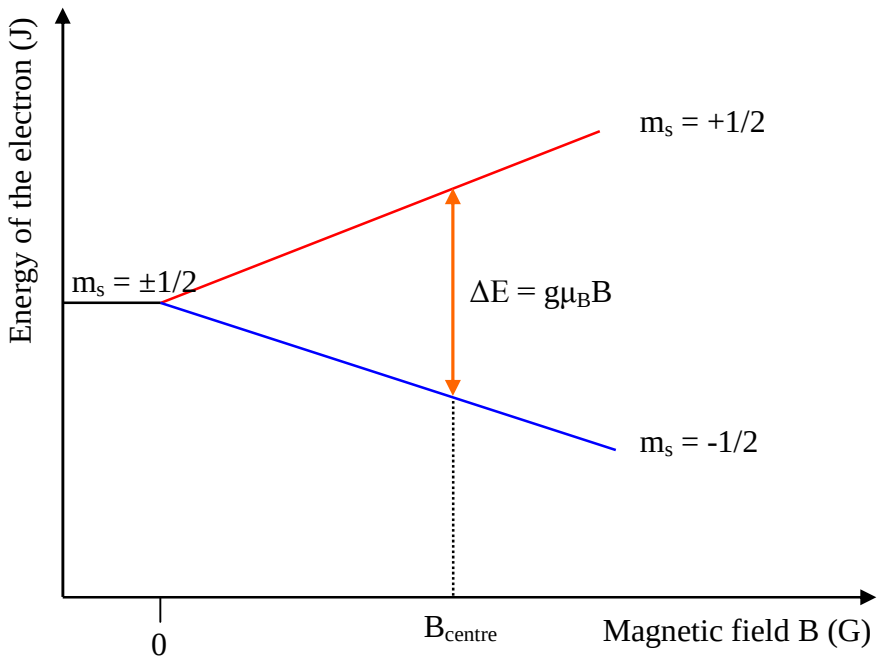

Figure 2.18: Splitting of the m_s = ± ½ states in an applied magnetic field B.

During the ESR experiment, the applied field (B) is swept through a range of values and resonance occurs when the splitting of the energy levels (ΔE) is equal to the energy of

an applied microwave pulse, thus inducing promotion from the lower to upper energy levels. In work conducted in this thesis the magnetic field is swept from 2000-6000G and microwaves of X-band (9.5-9.53 GHz) are employed. Resonance therefore occurs when:

$$\Delta E = h\nu_{microwaves} = \tfrac{1}{2}g\mu_B B + \tfrac{1}{2}g\mu_B B = \mathbf{g\mu_B B} \qquad \text{eqn. 2.22}$$

The proportionality constant g (the g factor, no units) defines the rate of divergence of the $m_s = \pm \frac{1}{2}$ levels in the magnetic field (Figure 2.19). The value of g for a free electron is 2.0023. However, the g value depends upon the environment around the unpaired electron and may range from zero to four for d-metal complexes. Its value can therefore serve to characterise a particular species.

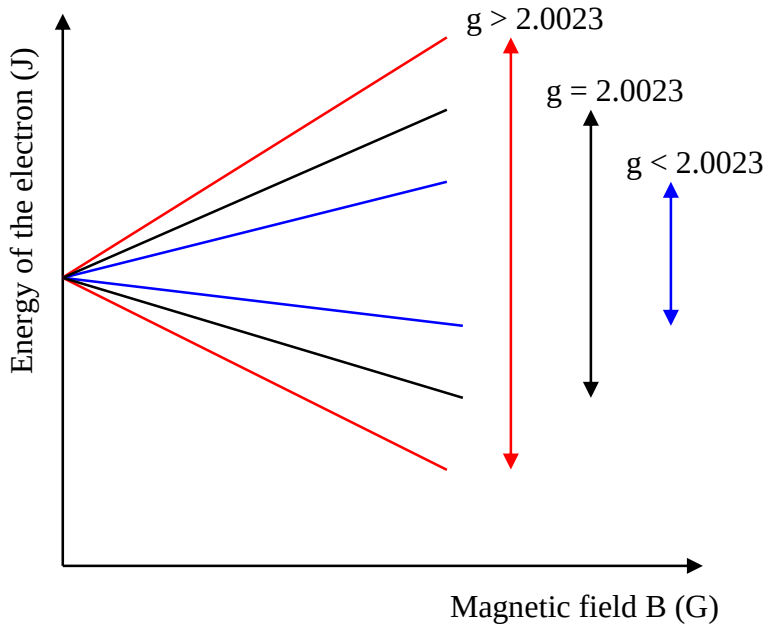

Figure 2.19: The value of g defines the rate of divergence of the $m_s = \pm \frac{1}{2}$ energy levels.

The ESR spectrum is often given as the first derivative of the signal profile (Figure 2.21). Frequently more than one peak is observed – a phenomenon known as the hyperfine structure. Hyperfine structure is a consequence of the interactions between the magnetic moments of an electron and nearby nuclei. Interaction of the unpaired electron with a nucleus of spin quantum number I results in (2I+1) lines in the ESR spectrum (i.e. 2I+1 energy levels) since the quantum number M_I, which defines the now split

energy levels, can take values I, I-1, I-2….0….-I. The magnetic field associated with the nuclear magnetic moment can either add to or subtract from the applied field B, and therefore the effective field (B_{eff}) actually experienced by the electron may be represented as equation 2.23:

$$B_{eff} = B + AM_I \qquad \text{eqn. 2.23}$$

where A is the hyperfine coupling constant (G), and hence:

$$\Delta E = g\mu_B(B+AM_I) \qquad \text{eqn. 2.24}$$

Figure 2.20 illustrates the situation for Cu^{2+}, I = 3/2. The $m_s = \pm 1/2$ levels are split into (2I+1) = 4 levels defined by M_I = -3/2, -1/2, 1/2, 3/2 (dashed and dotted black lines represent the energy levels and ΔE, respectively, in the absence of any hyperfine splitting). Since ΔE, g, μ_B and A (equation 2.24) are all constant, four different values of B exist at which resonance occurs and four peaks are observed, separated by a distance A. The g factor value is calculated from equation 2.25, where B_{centre} (G) is the mid-point of the quartet of peaks.

$$h\nu = g\mu_B B_{centre} \qquad \text{eqn. 2.25}$$

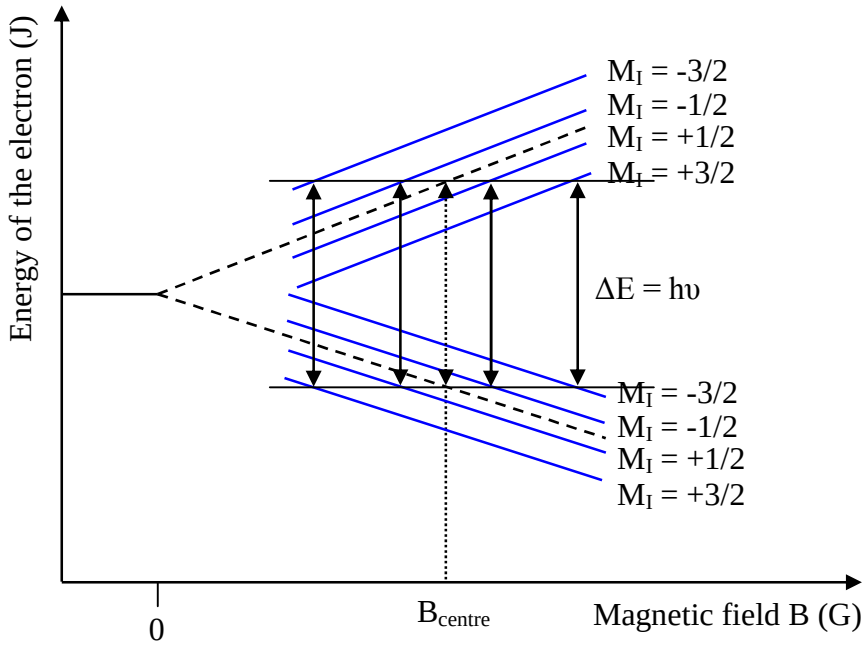

Figure 2.20: Diagrammatic illustration of the origin of hyperfine structure for Cu^{2+}.

For anisotropic species the signals do not appear as one averaged g value. For an axially distorted species (such as Cu^{2+} in Jahn-Teller distortion) different g values are observed parallel and perpendicular to the magnetic field – i.e. $g_{\|}$ (= g_{xx} = g_{yy}) ≠ $g_{\perp}$ (= g_{zz}). Figure 2.21 illustrates a typical Cu^{2+} spectrum and indicates the 'parallel' and 'perpendicular' regions. Unfortunately, at X-band, these regions partially overlap and typically only two hyperfine resonances are observed in the parallel region while the other two are lost in the perpendicular region, where a characteristic 'overshoot' peak is often observed. (Note, hyperfine splitting is not resolved well in the perpendicular region and $A_{\perp}$ is seldom quoted).

The most useful parameters extracted from an ESR spectrum are therefore $g_{\|}$ and $A_{\|}$, which can be compared to related samples and thus yield information on the species' environment.

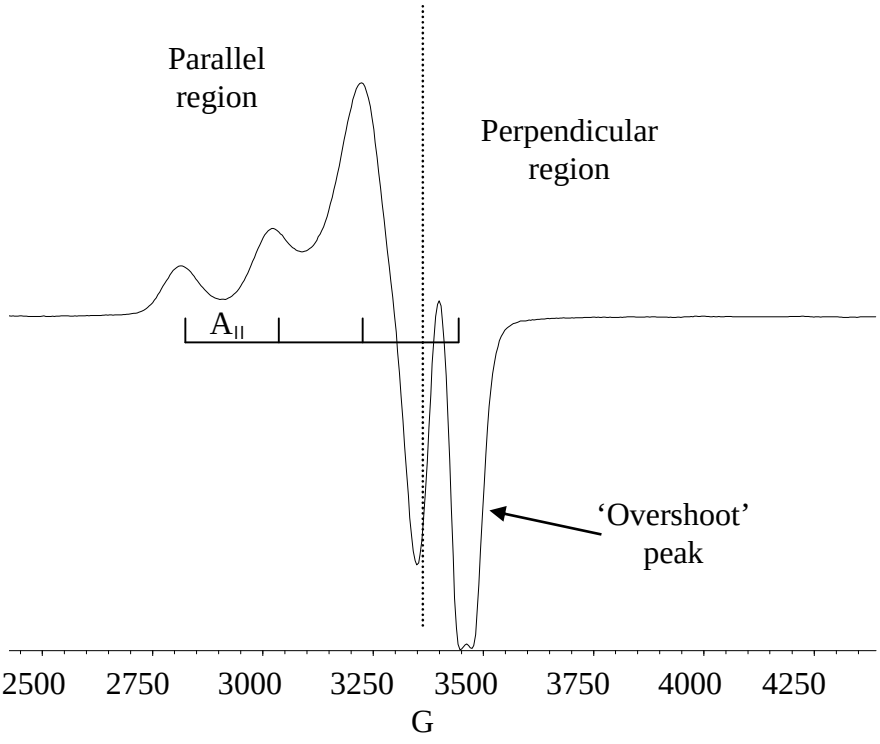

Figure 2.21: ESR spectrum of Cu^{2+} complexed to the azamacrocycle cyclam within MgAPO STA-7 (see Chapter 9).

2.3.2: Solid State Nuclear Magnetic Resonance (NMR)[92-94]

NMR may be regarded as the nuclear equivalent to ESR spectroscopy and is based on similar principles. A nucleus with spin quantum number $I \neq 0$ will possess a magnetic moment, and adopt $(2I + 1)$ energy levels defined by the quantum number m (= I, I-1, I-2…0…-I). In the absence of a magnetic field these energy levels are degenerate. However, when placed in an external magnetic field (B), splitting of the energy levels permits resonance to occur (selection rule: $\Delta m = \pm 1$) when ΔE corresponds to the energy of an applied electromagnetic radiation pulse (radio frequencies are employed in NMR). The exact frequency at which a given nucleus resonates is dependent upon its environment and therefore provides an excellent means with which to probe the local environment of NMR-active nuclei.

The processes occurring during an NMR experiment are conveniently visualised in a vector model. The magnetic moment vectors of all the nuclei are arranged on the surface of a cone around an arbitrary axis (say, the *z*-axis). Application of an external field B along *z* causes precession of these vectors around this axis at the Larmor frequency (equivalent to the resonance frequency of that nucleus) with more α-spins than β-spins (Figure 2.22). The bulk magnetisation (M), however, is parallel to and lies along the *z*-axis. Application of a radio frequency (rf) pulse of frequency equal to the Larmor frequency along, say, the *x*-axis causes the magnetic moment vectors of each nucleus to come into phase with each other and tilts the bulk magnetisation vector (M) into the *xy* plane. A coil placed along the *y*-axis detects the change and produces a signal. The duration of the rf pulse defines the angle through which M is tilted.

Restoration of the equilibrium condition (i.e. relaxation) proceeds through two mechanisms – spin-lattice and spin-spin relaxation. Spin-lattice relaxation is the distribution of energy to the rest of the sample as heat (note, since the energies involved are so small the change in total sample temperature is negligible). This is represented by the growth of the bulk magnetisation vector in the *z*-axis. Spin-spin relaxation involves the re-distribution of energy between spins; magnetic moment vectors of the nuclei become out of phase with one another. This may be visualised as the spreading out of individual vectors over the cone surface.

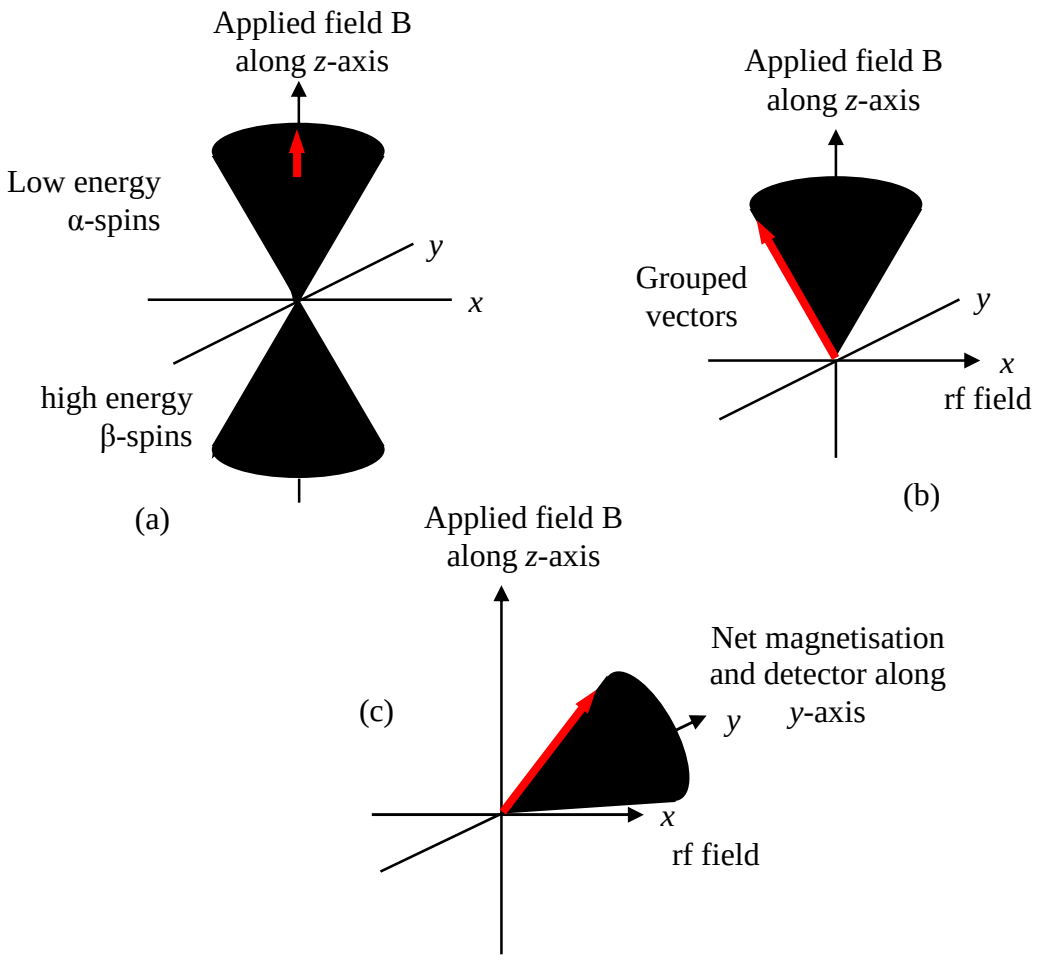

Figure 2.22: The vector model for NMR spectroscopy: (a) magnetic moment vectors precess around the applied field with bulk magnetic moment shown as red arrow; (b) magnetic moments in phase (grouped) on application of an rf pulse; (c) bulk magnetisation vector is tilted towards the xy plane (here a 90^o pulse causes the bulk magnetisation vector to precess around the y-axis).

Since the effective magnetic field experienced by a nucleus is conditioned by the additional magnetic field generated by surrounding electrons, the exact resonance frequency (or rather the position in ppm of the resonance peak relative to that of a standard on the NMR spectrum, known as 'chemical shift') is dependent on the environment around the nucleus in question. Therefore, several signals can be observed for the same nuclear species – one for each different environment. Table 2.6 lists typical chemical shifts (ppm) for framework species analysed in this work.

Adjacent I > 0 nuclei can cause splitting of the observed resonance peak ('coupling'), and therefore analysis of peak splitting can yield information on neighbouring non-

equivalent species. However, coupling may also complicate the analysis of NMR spectra and it is often desirable to remove these effects via de-coupling procedures, resulting in one signal per environment (for non quadrupolar species at least).

While solution state NMR enjoys narrow peak shapes due to rapid motion, peak shapes in solid-state spectra can be very wide and irregular. Principal contributors to these phenomena are dipole-dipole interactions, chemical shift anisotropy and quadrupolar effects ($I > ½$). However, since dipole-dipole interactions and chemical shift anisotropy factors have a strong angular dependence ($3\cos^2\theta-1$), these effects can be alleviated by spinning the sample about an axis set at an angle of 54.75^o (the 'magic angle') to the applied field. At this angle $3\cos^2\theta-1$ becomes zero and line-broadening factors are removed. This technique is known as Magic Angle Spinning NMR (MAS-NMR). Quadrupolar effects arise from the interaction of the nuclear electric quadrupole moment with local electric field gradients. In powder spectra, which consist of a superposition of signals from differently oriented crystals, low symmetry environments can result in complex peak shapes, which should not be analysed to any great depth.

Nucleus	**Environment**		**Typical chemical shift (ppm)**
^{31}P	Tetrahedral	P(4Me)	-19
		P(1Al, 3Me)	↓
		P(2Al, 2Me)	
		P(3Al, 1Me)	
		P(4Al)	-30
^{29}Si	Tetrahedral	Si(4Al)	-83 - -87
		Si(3Al,1Si)	-88 - -94
		Si(2Al,2Si)	-93 - -99
		Si(1Al,3Si)	-97 - -107
		Si(4Si)	-103 - -114
^{27}Al	Tetrahedral		30 - 50
	Octahedral/5-coordinate		0 - 22

Table 2.6: Typical chemical shifts for common framework species.

2.4: Other Techniques

2.4.1: Solid-State UV-Visible (UV-Vis) Spectroscopy[92]

Many of the phosphate-based materials synthesised in Part 3 are templated by complexes of Cu(II) (and to a lesser extent Ni(II) and Co(III)). These materials, therefore, exhibit vivid colours due to the encapsulation of the metallocomplex within their cages and channels. Since the visually observed colour may be misleading (for example due to particle size), UV-Vis spectroscopy is employed to characterise these colours and help confirm the presence of the desired complex.

The variety of colours characteristic of transition metal chemistry is due to electronic transitions predominantly between d-orbitals (dd-transitions). The energy associated with such transitions is similar to that of visible light (~ 400-700nm wavelengths) – the observed colour being complementary to that absorbed by the electron excitation process. Therefore, by recording absorbance (or, in the case of studies presented in Part 3, reflectance) as a function of wavelength over the range from near UV to near IR, the colour of the complex can be properly characterised. Since dd-transitions are formally forbidden, colours should be expected to be of low intensity. However, selection rules may be overcome, for example, by deviation away from exact octahedral symmetry, resulting in the vivid colours observed.

For Cu(II), d^9, in an octahedral environment, only one transition would be expected. However, due to Jahn-Teller distortion, which lifts the degeneracy of the two e_g orbitals and, to an extent, one of the three t_{2g} orbitals, three transitions may be observed. Unfortunately, however, due to molecular vibration, dd bands tend to be rather broad and different absorption bands often merge together to form one large (although often asymmetric) band. (For Ni(II) d^8 in non-distorted octahedral geometry, however, three bands may often be distinguished). Consequently, UV-Vis spectra are not employed in these studies for any in-depth analysis of, for example, Δ_o values, but serve merely to 'fingerprint' the complex present.

2.4.2: Scanning Electron Microscope (SEM)[95]

The SEM is employed frequently throughout the studies discussed in this thesis to identify the morphology of crystalline products and to determine their approximate inorganic compositions. By scanning a fine beam of electrons across the surface of a sample, an image is created via the analysis of secondary and backscattered electrons. The electron beam may also stimulate the emission of X-radiation via the process described in section 2.1.1. By analysing the spectrum of emitted X-rays the composition of the sample may be established since the X-ray photon energy is element dependent. This technique is known as Energy Dispersive X-ray analysis (EDX).

2.4.3: Thermogravimetric Analysis (TGA)[96]

TGA may be employed to analyse the loss of organic SDA upon calcination (heating), and to calculate unit cell compositions. In this method the weight of a sample of material is monitored as temperature is increased. The profile of the resulting thermogram can often reflect the porosity of the material and the ease with which access to the internal void space can be gained.

2.4.4: Organic Elemental Analysis

Microanalysis is employed to identify the organic species present within product materials. The technique provides percentages of carbon, hydrogen and nitrogen and can therefore indicate the presence (or otherwise) of the intended organic SDA(s). In the case of mixed template systems the relative proportions of each molecule may also be estimated.

References

1. A. K. Cheetham and P Day, *Solid State Chemistry*, Clarendon Press, 1992
2. A. F. Cronstedt, *Koongl. Vetenskaps Acad. Handl Stockholm*,1765, **17**, 120
3. A. Damour, *Ann. Mines*, 1840, **17**, 191
4. G. Friedel, *Bull. Soc. France. Mineral. Crystallogr.*, 1896, **19**, 94
5. W. H. Taylor, *Z. Kristallog.*, 1930, **74**, 1
6. W. M. Meier, *Molecular Sieves*, Society of Chemical Industry, London, 1968
7. www.iza-online.org
8. F. Liebau, H. Gies, R. P Gunawardane and B. Marler, *Zeolites*, 1986, **6**, 373
9. (a) W. M. Meier, D. H. Olson and Ch Bearlocher, *Atlas of Zeolitic Structure Types*, 5th Ed., Elsevier, 2001 (b) www.iza-structure.org/databases
10. W. Loewenstein, *Am. Mineral.*, 1950, **39**, 92
11. J. S. Yu, J. W. Ryoo, S. J. Kim, S. B. Hong and L. Kevan, *J. Phys. Chem.*, 1996, **100**, 12624
12. M. L. Occelli, H. Eckert, A. Wolker and A. Auroux, *Microporous Mesoporous Mater.*, 1999, **30**, 219
13. H. H. Cho, S. H. Kim, Y. G. Kim, Y. C. Kim, H. Koller, M. A. Camblor and S. B. Hong, *Chem. Mater.*, 2000, **12**, 2292
14. J. M. Newsam, *J. Phys. Chem.-US 92*, 1988, **2**, 445
15. J. M. Newsam and J. D. Jorgensen, *Zeolites*, 1987, **7,** 569
16. J. M. Newsam, R. H. Jarman and A. J. Jacobson, *Mat. Res. Bull*, 1985, **20**, 125
17. J. M. Newsam, *J. Chem. Soc., Chem. Commun.*, 1986, **16**, 1295
18. S. T. Wilson, B. M. Lok, C. A. Messina, T. R. Cannan and E. M. Flanigen, *J. Am. Chem. Soc.*, 1982, **104**, 1146
19. M. E. Davis and R. F. Lobo, *Chem. Mater.*, 1992, **4**, 756
20. D. Barthomeuf, E. G. Derouane and W. Holderich, *Guidelines for Mastering the Properties of Molecular Sieves*, NATO ASI Series B: Physics Vol. 221, Plenum Press, 1990
21. J. S. Chen, P. A. Wright, J. M. Thomas, S. Natarajan, L. Marchese, S. M. Bradley, G. Sankar, C. R. A. Catlow, P. L. Gaiboyes. R. P. Townsens and C. M. Lok, *J. Phys. Chem.*, 1994, **98**, 10216
22. C. Gillen, *Geology and Landscapes of Scotland*, Terra Publishing, 2003

23. M. E. Davis and R. F. Lobo, *Chem. Mater.,* 1992, **4**, 756
24. R. M. Milton, US Patent 2 882 243, 1956
25. R. M. Barrer, *J. Chem Soc.,* 1948, 127
26. B. M. Lok, T. R. Cannan and C. A. Messina, *Zeolites,* 1993, **3**, 282
27. R. M. Barrer and P. J. Denny, *J. Chem. Soc.*, 1961, 971
28. R. L. Wadlinger, G. T. Kerr and E. J. Rosinski, US Patent 3 308 069, 1967
29. R. J. Argauer and G. R. Landolt, US Patent 3 702 886, 1972
30. R. W. Grose and E. M. Flanigen, US Patent 4 061 724, 1977
31. S. T. Wilson, B. M. Lok, C. A. Messina, T. R. Cannan and E. M. Flanigen, *J. Am. Chem. Soc.,* 1982, **104**, 1146
32. A. Simmen, L. B. McCusker, Ch. Baerlocher and W. M. Meier, *Zeolites*, 1991, **11**, 654
33. V. Patinec, P. A. Wright, P. Lightfoot, R. A. Aitken and P. A. Cox., *J. Chem. Soc., Dalton Trans.,* 1999, 3909
34. M. M. Harding and B. M. Kariuki, *Acta Crystallogr.,* 1994, **C50**, 269
35. G. S. Zhu, F. S. Ziao, S. L. Quin, P. C. Hun, R. R. Xu, S. J. Ma and O. Terasaki, *Microporous Mater.,* 1997, **11**, 269
36. E. M. Flanigen, *Adv. Chem. Ser.,* 1973, **121,** 114
37. R. J. Francis and D. O'Hare, *J. Chem. Soc., Dalton Trans.,* 1998, 3133
38. G. W. Noble, P. A. Wright and A. Kvick, *J. Chem. Soc., Dalton Trans.,* 1997, 4485
39. P. Wagner, Y. Nakagawa, G. S. Lee, M. E. Davis, S. Elomari, R. C. Medrud and S. I. Zones, *J. Am. Chem. Soc.,* 2000, **122**, 163
40. S. I. Zones, Y. Nakagawa. L. T. Yuen and T. V. Harris, *J. Am. Chem. Soc.*,1996, **118**, 7558
41. S. I. Zones, M. M. Olmstead and D. S. Santilli, *J. Am. Chem. Soc.,* 1992, **114**, 4195
42. J. Cicir, US Patent 3950496, 1976
43. S. L. Lawton and W. J. Rohrbaugh, *Science,* 1990, **247**, 1319
44. D. J. Willock, D. W. Lewis, C. R. A. Catlow, G. J. Hutchings and J. M. Thomas, *J. Molec. Catal. A,* 1997, **119**, 415
45. S. I. Zones, L. T. Yuen, S. Nakagawa, R. A. van Nordstrand and S. D. Toto, *9th International Zeolites Conference,* Butterworth-Heinemann, Montreal, 1992
46. K. D. Schmitt and G. J. Kennedy, *Zeolites*, 1994, **14**, 635

47. J. Chen and J. M. Thomas, *J. Chem. Soc., Chem. Commun.*, 1994, 603
48. P. A. Barratt, R. H. Jones, J. M. Thomas, I. J. Shannon and C. R. A. Catlow, *J. Chem. Soc., Chem. Commun.*, 1996, 2001
49. F. Y. Dai, M. Suzuki, H. Takahashi and Y. Saito, *Stud. Surf. Sci. Catal.*, 1986, **28**, 223
50. L. Canesson, I. Arcon, S. Caldarelli and A. Tuel, *Microporous Mesoporous Mater.*, 1998, **26**, 117
51. D. W. Breck, *Zeolite Molecular Sieves*, John Wiley and Sons, N. Y., 1974
52. X. Ren, S. Komarneni and D. M. Roy, *Zeolites*, 1991, **11**, 142
53. P. S. Wheatley and R. E. Morris, *J. Solid State Chem.*, 2002, **167**, 267
54. S. B. Hong, E. G. Lear, P. A. Wright, W. Zhou, P. A. Cox, C. H. Shin, J. H. Park and I. S. Nam, *J. Am. Chem. Soc.*, 2004, **126**, 5817
55. S. I. Zones, R. A. van Nordstrand, D. S. Santilli, D. M. Wilson, L. T. Yuen and L. D. Scampavia, *Zeolites: Facts, Figures, Future*, P. A. Jacobs, R. van Santen Eds., Elsivier, Amsterdam, 1990, 299
56. P. A. Wright, M. J. Maple, A. M. Z. Slawin, V. Patinec, R. A. Aitken, A. Welch and P. A. Cox, *J. Chem. Soc., Dalton Trans.*, 2000, 1243
57. U. Lohse, B. Parlitz, B. Altichter, K. Jancke, E. Loffler, E. Schreier and F. Vogt, *J. Chem. Soc., Faraday Trans.*, 1995, **91**, 1155
58. D. Hasha, L. S. de Saldarriaga, C. Saldarriaga, P. E. Hathaway, D. F. Cox and M. E. Davis, *J. Am. Chem. Soc.*, 1988, **110**, 2127
59. A. Corma, M. J. Diaz-Cabanas, M. E. Domine and F. Rey, *J. Chem. Soc., Chem. Commun.*, 2000, 1725
60. R. Kumar, A. Bhaumik, R. K. Ahedi and S. Ganapathy, *Nature*, 1996, **381**, 298
61. E. M. Flanigen and R. L. Patton, US Patent 4 073 865, 1978
62. M. A. Camblor, L. A. Villaescusa and M. J. Diaz-Cabanas, *Top. Catal.*, 1993, **365**, 239
63. H. Koller, A. Wolker, L. A. Villaescusa, M. J. Diaz-Cabanas, S. Valencia and M. A. Camblor, *J. Am. Chem. Soc.*, 1999, **121**, 3368
64. P. A. Barrett, M. A. Camblor A Corma, T. H. Jones and L. A. Villaescusa, *J. Phys. Chem. B*, 1998, **102**, 4147
65. C. S. Cundy and P. A. Cox, *Microporous Mesoporous Mater.*, 2005, **82**, 1
66. L. Smart and E. Moore, *Solid State Chemistry: an Introduction*, Chapman and Hall, 1992

67. O. Weigel and E. Steinhoff, *Z. Kristallog.*, 1925, **61**, 125
68. R. S. Bowman, *Microporous Mesoporous Mater.*, 2003, **61**, 43
69. P. A. Wright, *Solid Acids*, in 'Encyclopedia of Materials: Science and Technology', Eds-in-Chief K. H. Jurgen Buschow, R. W. Cahn, M. C. Flemings, B, Ilschner, E. J. Kramer and S. Mahajan, Elsevier, 2001. 1-6
70. N. Y. Chen, *J. Catal.*, 1988, **114**, 17
71. J. M. Thomas, *Angew. Chem., Int. Ed. Engl.*, 1994, **33**, 913
72. U. Lohse, R Bertram, K, Jancke, I. Kurzawski, B. Parlitz, E. Loofler and E. Schreier, *J. Chem. Soc. Faraday Trans.*, 1995, **91**, 1163
73. A. Frache, B. I. Palella, M. Cadoni, R. Pirone, P. Ciambelli, H. O. Pastore and L. Marchese, *Catal. Today.*, 2002, **75**, 359
74. A. Frache, B. I. Palella, M. Cadoni, R. Pirone, H. O. Pastore and L. Marchese, *Topics in Catal.*, 2003, **22,** 53
75. C. Gaicovazzo, H. L. Monacco, D. Viterbo, F. Scordari, G. Gilli, G. Zanotti and M. Catti, *Fundamentals of Crystallography*, Oxford University Press, 1992
76. C. Hammond, *The Basics of Crystallography and Diffraction*, 2nd Ed., Oxford University Press, 2006
77. V. K. Pecharsky and P. Y. Zavalij, *Fundamentals of Powder Diffraction and Structural Characterisation of Materials*, Springer, 2005
78. L. W. Finger, *Reviews in Mineralogy*, 1989, **20**, 309
79. www.esrf.eu
80. J. B. Hastings, W, Thomlinson and D. E. Cox, *J. Appl. Cryst.*, 1984, **17**, 85
81. www.iucr.org
82. A. Altomare, M. C. Butla, M. Camalli, B. Carrozzini, G. L. Cascarano, C. Giacovazzo, A. Guagliardi, A. G. G. Moliterni, G. Polidori and R. Rizzi, *J. Appl. Cryst.*, 1999, **32**, 339
83. A. Altomare, G. Cascarano, C. Giacovazzo and A. Guagliardi, *J. Appl. Cryst.*, 1993, **23**, 343
84. A. Altomare, M. C. Burla, G. L. Cascarano, C. Giacovazzo, A. Guagliardi, G. Moliterni and G. Polidori, *J. Appl. Cryst.*, 1995, **28**, 842
85. L. B. McCusker, Ch. Baerlocher, R. Grosse-Kunstleve, S. Brenner and T. Wessels, *Chimia*, 2001, **55**, 497
86. R. A. Young, *The Rietveld Method*, Oxford University Press, 1996

87. L. B. McCusker, R. B. Von Dreele, D. E. Cox, D. Louer and P. Scardi, *J. Appl. Cryst.*, 1999, **32**, 36
88. A. C. Larson and R. B. von Dreele, Generalized Crystal Structure Analysis System, Los Almos National Laboratory, USA, 1988
89. (a) L. W. Finger, D. E. Cox and A. P. Jephcoat, *J. Appl. Cryst*, 1994, **27**, 892 (b) M. A. G. Aranda, E. R. Losilla, A. Cabeza and S. Bruque, *J. Appl. Cryst*, 1998, **31**, 16
90. B. Van Laar and W. B. Yelon, *J. Appl. Cryst.*, 1984, **17**, 47
91. www.isis.rl.ac.uk
92. A. K. Brisdon, *Inorganic Spectroscopic Methods*, Oxford Chemistry Primer 62, Oxford University Press, 2005
93. K. J. Laidler and J. H. Meiser, *Physical Chemistry*, 3rd Ed., Houghton Mifflin Company, 1999
94. P. J. Hore, *Nuclear Magnetic Resonance*, Oxford Chemistry Primer 32, Oxford University Press, 2004
95. P. J. Goodhew and F. J. Humphreys, *Electron Microscopy and Analysis*, 2nd Ed., Taylor and Francis, 1988
96. F. W. Fifield and D. Kealey, *Principles and Practice of Analytical Chemistry*, 3rd Ed., Blackie Academic and Professional, 1990

PART 2: STRUCTURE DIRECTION IN FRAMEWORK SILICATES

Chapter 3: Introduction to Part 2

Chapter 4: Structural Analysis of the Potassium Gallosilicate TNU-6

Chapter 5: Structural Analysis of the Sodium Gallosilicate TNU-7

Chapter 6: Structural Studies of the Aluminosilicate TNU-9

Chapter 3: Introduction to Part 2

3.1: Background to Materials TNU-6, TNU-7 and TNU-9

As part of a programme to synthesise new topologies, a series of materials denoted TNU-*N* (TNU = Taejon National University, *N* represents a number currently between 1 and 12) have been synthesised via hydrothermal synthesis by Prof. Suk Bong Hong and co-workers at Hanbat University (formally Taejon National University), South Korea. While the structures of many of these materials have been solved in the past (for example TNU-1 (CGS), -2 (GIS), -3 (NAT) and -4 (NAT))[1], several have remained elusive (including TNU-6, -7 and -9). Our interest in structure solution led to the current collaboration between our two research groups with the aim of solving these structures and gaining insight to their mode of formation.

One avenue of research adopted by Hong is the investigation of the structure-directing ability of Ga. As mentioned in Chapter 1 and discussed in more detail in Part 3, the identity of T-atom species can have a strong influence on the outcome of hydrothermal synthesis. Indeed, several novel topologies have been synthesised by substitution of T-species including, for example, the zincosilicate VPI-8, which only nucleates in the presence of Zn.[2]

In contrast, Ga was thought to possess very little structure directing ability and has been employed extensively (often in combination with organic SDAs) to produce topologies analogous to known aluminosilicate zeolites.

However, the synthesis of TNU-1 (CGS) (Figure 3.1) – a gallosilicate for which no aluminosilicate counterpart exists (replacing Ga with Al under the same conditions resulted in the crystallisation of the MER topology), encouraged further studies in this field.[3] The later synthesis of the novel 18-ring gallosilicate ECR-34 (ETR) was also significant.[4] An additional requirement in the synthesis of these novel materials, however, is the identity of extra-framework species present. TNU-1, for example, can only be synthesised in the presence of K or at high K/Na ratios (no organic necessary); low K/Na ratios resulted in gallosilicate NAT. Similarly, ECR-34 requires the presence

of both K and Na, in conjunction with tetramethylammonium ions, for successful crystallisation. There would therefore appear to be a cooperative effect between the species present in these synthesis gels, and structure direction may not necessarily be due solely to Ga. Indeed, until the 1960s, zeolitic materials were synthesised solely from inorganic gels, employing the structure directing influence of hydrated alkali-metal ions such as Na^+ and K^+, and their potential influence should not, therefore, be overlooked.

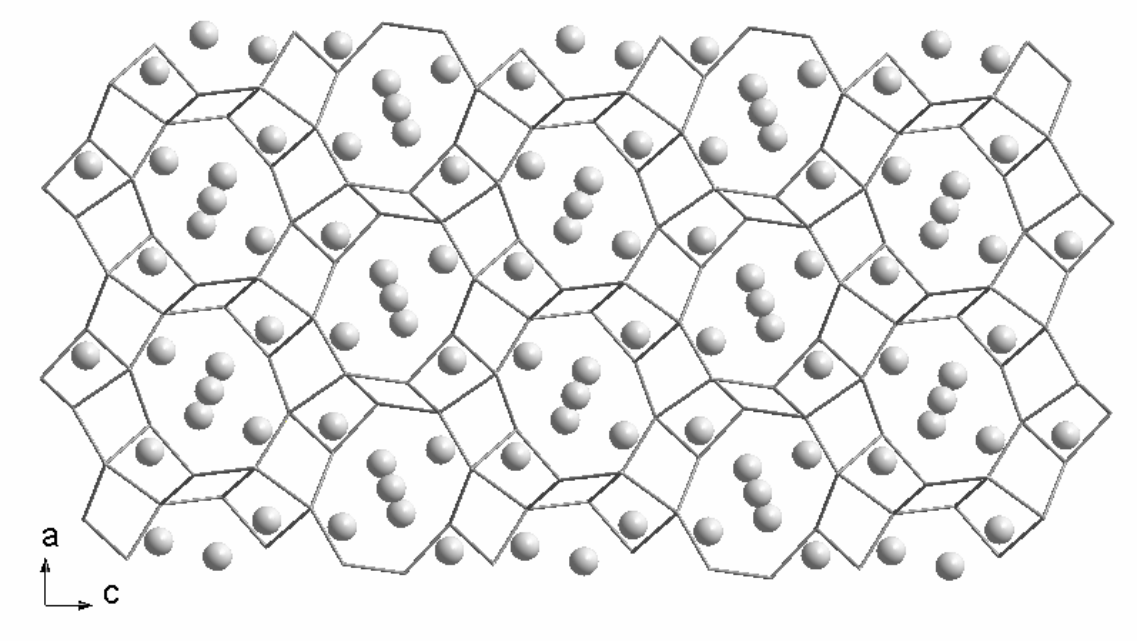

Figure 3.1: Structure of TNU-1 (CGS)[1,3] viewed along the b-axis (oxygens removed for clarity, grey spheres = K). The structure possesses an intersecting 10MR-8MR-8MR channel system resulting in a rather open structure. K ions are arranged in zigzag chains along the centre of these channels and in recesses in the channel walls.

During the course of these studies, Hong has prepared gallosilicate analogues of the aluminosilicate zeolites gismondine (GIS) (TNU-2), gannardite (NAT) (TNU-3) and natrolite (NAT) (TNU-4), while TNU-1 remains the only entirely unique topology. In addition to these materials, two further gallosilicate phases have also been synthesised from completely inorganic alkali metal-containing gels under similar conditions – TNU-6 and TNU-7 (Table 3.1). While TNU-6 is synthesised from gallosilicate gels containing K, TNU-7 is obtained in the presence of Na. Nonetheless, as will be discussed in Chapters 4 and 5, the successful synthesis of both TNU-6 and TNU-7 also depends

critically on the presence of Ga in synthesis gels, adding credence to the notion that Ga can exert a unique structure directing influence on zeotype crystallisation. The structural analysis of TNU-6 and TNU-7 is discussed in Chapters 4 and 5, respectively.

Na_2O	K_2O	Ga_2O_3	SiO_2	H_2O	T (^oC)	Time (days)	Product
0	8.0	1.0	10.0	150	100	14	TNU-6
	6.0				150	7	TNU-1 (CGS)
					100	21	TNU-1 (CGS) + TNU-2 (GIS)
					100	5	TNU-2 (GIS)
0	2.0	1.0	10.0	150	150	3	TNU-7 (EON)*
6.0	0	1.0	10.0	150	150	10	TNU-4 (NAT)
					100		TNU-3 (NAT)

*Table 3.1: Gel compositions and reaction conditions for the synthesis of selected gallosilicate TNU samples,[1,31] reagent quantities given as molar ratios. * synthesis conducted under rotation (60rpm), structure code assigned following structural studies presented in Chapter 5.*

In parallel with studies into the structure directing ability of Ga, Hong *et. al.* have also examined the use of 1,4-bis(N-methylpyrrolidinium)butane (1,4-MPB, Figure 3.2) as an SDA in the synthesis of aluminosilicate materials.[5] Table 3.2 lists the variety of topologies synthesised from this organic and illustrates the influence gel composition can have on the outcome of hydrothermal synthesis. Amongst the many topologies listed in Table 3.2, those of IM-5 and TNU-9 were unknown and of considerable interest. Chapter 6 will discuss studies conducted in relation to the structure solution of TNU-9 and energy minimisation experiments conducted to investigate the distribution of template molecules within its complex pore system.

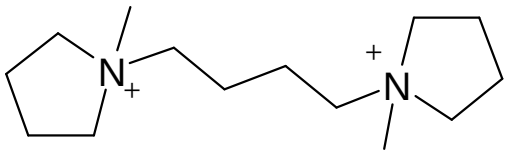

Figure 3.2: 1,4-MPB, employed as an SDA in the synthesis of aluminosilicate TNU-9.

$NaOH/SiO_2$	**SiO_2/Al_2O_3**	**Time (days)**	**Product**
1.13	60	14	Analcime (ANA)
1.00	240	14	Analcime (ANA) + TNU-10 (STI)
	120	14	TNU-10 (STI)
	60	14	TNU-10 (STI)
	30	7	TNU-10 (STI)
	15	14	Analcime (ANA)
0.87	60	14	IM-5 + TNU-9
0.73	∞	7	MCM-47 (a layered phase)
	60	14	TNU-9
	40	7	MCM-22 (MWW)
0.60	60	7	Quartz + ZSM-12 (MTW)
0.47	∞	7	MCM-47 (a layered phase)
	60	7	ZSM-12 (MTW)
0.33	60	7	ZSM-12 (MTW)

Table 3.2: Summary of products obtained from 1,4-MPB-containing aluminosilicate gels.[5] Gel compositions were 4.5(1,4-MPB):xNa_2O:yAl_2O_3:30SiO_2:1200H_2O. All syntheses conducted under rotation (100rpm), at 160^oC.

3.2: Experimental

Crystal size necessitated the use of powder X-ray diffraction (XRD) (except for in the case of TNU-6 where single crystal analysis was possible to investigate the presence of a superstructure). Preliminary powder XRD analysis of TNU-6, -7 and -9 was conducted on a Stoe STADI P diffractometer operating in transmission mode with primary monochromation and Cu $K_{\alpha 1}$ X-radiation (λ = 1.54056Å). As-received samples were mounted between two mylar (polythene) films and data were collected at room temperature with a step size of 0.01^o for a scan time of 6s per step over the range $5^o \leq 2\theta \leq 80^o$.

For initial structural refinements of TNU-7, a sample was loaded in a 0.7mm glass quartz capillary and dehydrated under a vacuum of $4x10^{-4}$ Torr at 300^oC for 6 hours. The capillary was sealed and data were collected as above.

For further detailed structural analysis of TNU-7 and to aid structure elucidation of TNU-9, data for dehydrated samples of these materials (prepared as above) were collected on station ID-31 at the ESRF (Grenoble, France) using monochromated synchrotron X-radiation (λ = 0.63248Å). Data were collected at room temperature with a step size of 0.01^o for a scan time of 7s per step over the range $3^o \leq 2\theta \leq 35^o$ (TNU-7) and $5^o \leq 2\theta \leq 50^o$ (TNU-9).

Samples of as-made Na-TNU-7 and calcined TNU-9 were also prepared for neutron diffraction by dehydration in 10mm diameter thin-walled quartz-glass tubes (procedure as above). Powder neutron diffraction data were collected at room temperature using the high-resolution time-of-flight powder diffractometer at the pulsed neutron source of the ISIS facility (Oxford, UK) on detector banks at low angle, 89.6^o and 168.3^o using a time-of-flight window of 30-200ms. Data were normalised using programs available at ISIS (by Drs Philip Lightfoot and Richard Ibberson) and the data were summed to give one histogram.

Data for structural analysis of TNU-6 were recorded on station 9.1 at the SRS (Daresbury, England) using monochromated synchrotron X-radiation (λ = 0.804473Å). The sample was dehydrated and sealed in a quartz glass capillary as described above.

Data were collected at room temperature with a step size of 0.01^{o} for a scan time of 4s per step over the range $4^{o} \leq 2\theta \leq 53^{o}$.

Single crystal analysis of TNU-6 was conducted by Stuart Miller from the University of St Andrews. Data were collected on Station 9.8 at the SRS, Daresbury, using a Bruker AXS SMART 1K CCD area detector diffractometer with X-ray wavelength set to 0.6911Å.

Powder diffraction data for TNU-6 and TNU-7 were indexed using algorithms accommodated in the Stoe software package[6] and the refinement of all structures was conducted using the GSAS suite of programs. Details of refinements are given in the respective chapters.

^{29}Si MAS NMR was performed on a sample of as-made TNU-6 at St Andrews by Dr Philip Wormald on a Varian UNITYplus spectrometer, operating at 500 MHz for ^{1}H, with a 7.5mm Doty XC5 ^{1}H/^{19}F probe. The frequency was 99.36MHz and a recycle time of 300s, and a spin rate of 4.00kHz were employed. The shift reference was ^{29}Si tetrakis(trimethylsilyl)silane (-9.9 and -135.2ppm).

To investigate the probable locations of the 1,4-MPB template molecule in as-prepared TNU-9, energy minimisation calculations were conducted in collaboration with Dr Paul Cox at the University of Portsmouth. These were carried out via a Monte Carlo–simulated annealing (MC-SA) approach[7] performed on a Silicon Graphics R10000 machine using the program Discover. The framework was held fixed during the calculations and was modelled using a fully siliceous model. Short-range forces were calculated using the CVFF forcefield, with partial charges included only on the template molecules. Initially, one template molecule was docked into a single unit cell of the TNU-9 framework. This simulation box was repeated using periodic boundary conditions in order to represent an infinite 3-D structure. Simulated annealing for 2000 time steps of 1×10^{-15}s at temperatures of 750K, 500K, 300K and 200K were performed prior to a final energy minimisation using a combination of conjugate gradient and va09a algorithms until the maximum derivative was less than 0.02kcal/Å. Further template molecules were added one at a time to the calculation until no further improvement in the binding energy per template was obtained.

Chapter 4: Structural Analysis of the Potassium Gallosilicate TNU-6

4.1: Structure Solution

As discussed in Chapter 3, TNU-6 was obtained from K-containing gallosilicate gels under hydrothermal conditions. It was therefore of interest to establish the identity of this phase, and a small quantity of the material was made available to us by Prof. Suk Bong Hong for these purposes.

Solid-state ^{29}Si and ^{71}Ga MAS NMR spectra recorded by Hong contain signals consistent with Si and Ga in tetrahedral framework materials (Figure 4.1). Elemental analysis suggests a Si/Ga ratio of 1.09 and a small signal at δ 86.5ppm in the ^{29}Si MAS NMR spectrum is thought to be due to this slight excess of Si.

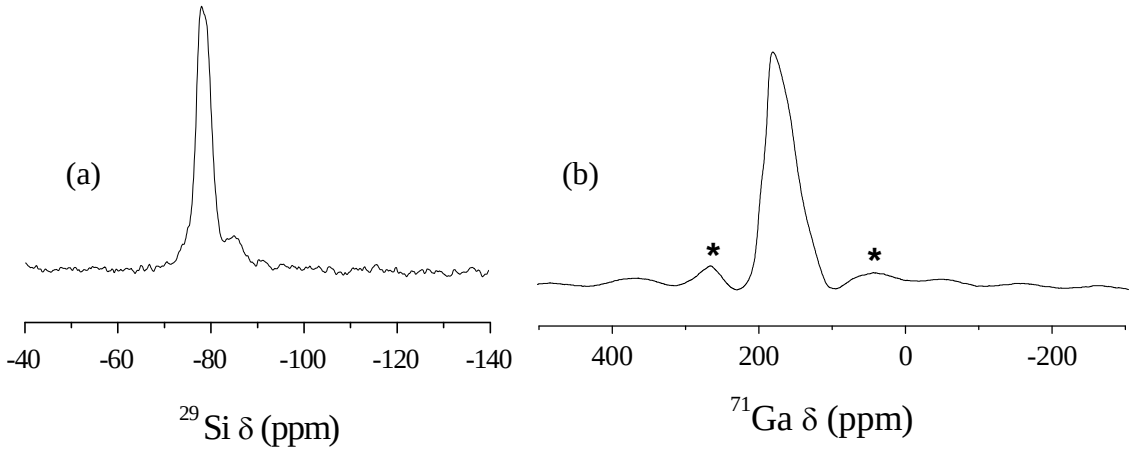

*Figure 4.1: (a) ^{29}Si and (b) ^{71}Ga MAS NMR spectra of as-made TNU-6 (courtesy of Prof Suk Bong Hong). * = spinning side bands.*

Initial attempts to solve the structure of TNU-6 had been made by Dr Miguel Camblor of the Institute de Ciencia de Materiales de Madrid. Adopting a model-building approach, based on fragments obtained from Direct Methods, an orthorhombic structure was proposed with unit cell parameters a = 8.530Å, b = 9.106Å, c = 5.252Å. Space group $P22_12_1$ was proposed. Figure 4.2 illustrates a projection of this model revealing an 8MR pore. While the theoretical XRD pattern for this hypothetical phase bears some

resemblance to that of TNU-6, there are a number of discrepancies (Figure 4.3). Indeed, refinement of this model against X-ray data was unsuccessful.

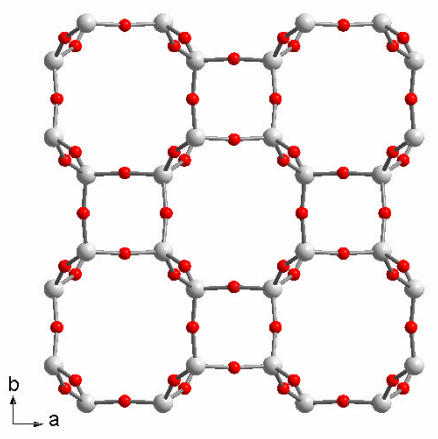

Figure 4.2: Orthorhombic structure model proposed by Dr M Camblor for TNU-6 viewed along the c-axis.

Attempts to index our own diffraction data (recorded both in-house on a Stoe STADI P diffractometer and at the SRS, Daresbury) also revealed a similar orthorhombic cell (Table 4.1) with systematic absences consistent also with $P22_12_1$ space group. However, attempts to solve the structure via Direct Methods as outlined in Chapter 2 in the EXPO program in this symmetry failed to provide any satisfactory results, despite the quality of the synchrotron data. Searches for this unit cell conducted in crystallographic databases also failed to identify any plausible starting models.

Scanning electron microscopy images of the sample, made available to us by Suk Bong Hong, revealed hexagonal morphology (Figure 4.4(a)) and drew our attention to a hexagonal cell encountered during indexing trials (Table 4.1). While clearly related, it is impossible to discriminate between these two cells on grounds of 'goodness of fit' alone (indicated by the factor of merit entries in Table 4.1). The hexagonal cell was therefore input to EXPO. Using space group $P6_3$, a plausible partial structure (Figure 4.4(b)) was obtained after only a few cycles.

Symmetry	***a* (Å)**	***b* (Å)**	***c* (Å)**	**FOM**
Orthorhombic	9.106	8.535	5.289	189
Hexagonal	10.525	10.525	8.538	151

Table 4.1: Most plausible results from indexing of powder X-ray data for TNU-6.

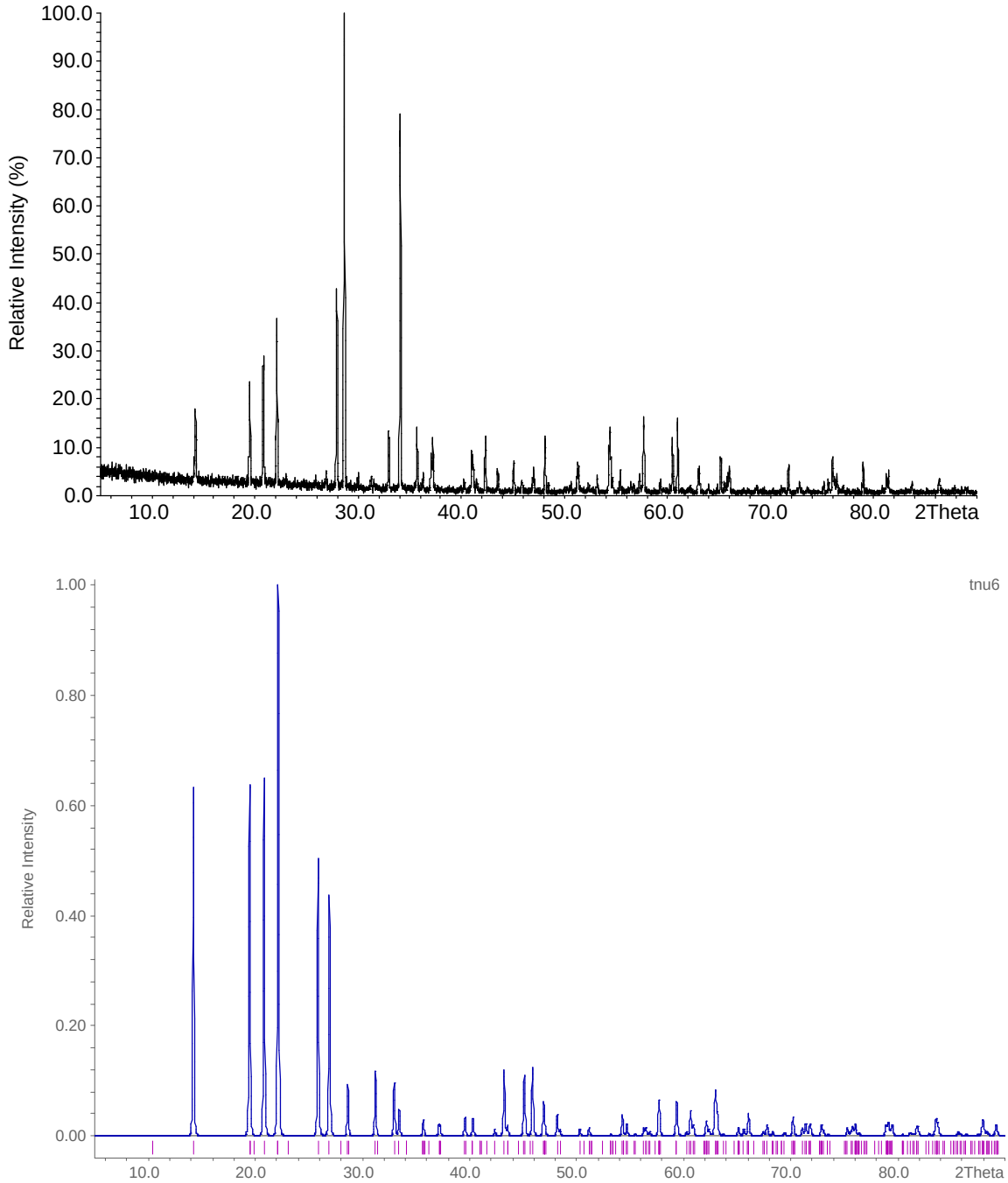

Figure 4.3: Comparison of the theoretical XRD pattern of the orthorhombic model (bottom) with experimental data for TNU-6 (top).

(a) 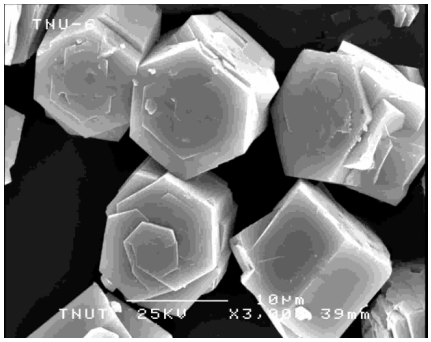 (b) 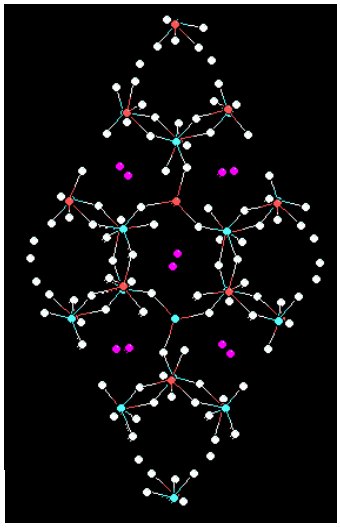

Figure 4.4: (a) SEM image of hexagonal TNU-6 crystals (courtesy of Prof. Suk Bong Hong); (b) partial structure obtained from EXPO analysis of powder data employing hexagonal cell.

By introducing the powder data along with the results from EXPO into GSAS, a Fourier difference calculation was conducted to locate extra electron density positions. The atomic identities of these positions were elucidated through structure modelling using the Diamond graphics program. A complete structural model was thus established and refined via the Rietveld method, during which Si-O, Ga-O and O-O distances were constrained to 1.7Å (σ = 0.02Å), 1.8Å (σ = 0.02Å), and 2.71Å (σ = 0.02Å), respectively. Peak shape was fitted using pseudo-Voigtian peak-shape parameters, and background was fitted using a cosine Fourier series background function fitting nine parameters. Isotropic thermal parameters of all Si atoms were constrained to be equal, as were those of all Ga atoms and O atoms, prior to their refinement. Si and Ga atoms were positioned in strict alternation with their occupancies fixed at 1. The fractional occupancy of K2 had to be capped at 1 since its refinement converged to a value of 1.02(2). Final R_{wp} and R_p values of 7.52% and 7.22%, respectively, were achieved (Figure 4.5). Final atomic coordinates, selected bond distances and selected angles are listed in Tables 4.2, 4.3 and 4.4, respectively. The final refined unit cell parameters are $a = b = 10.5078(1)$, $c = 8.5277(1)$, $\gamma = 120^{o}$.

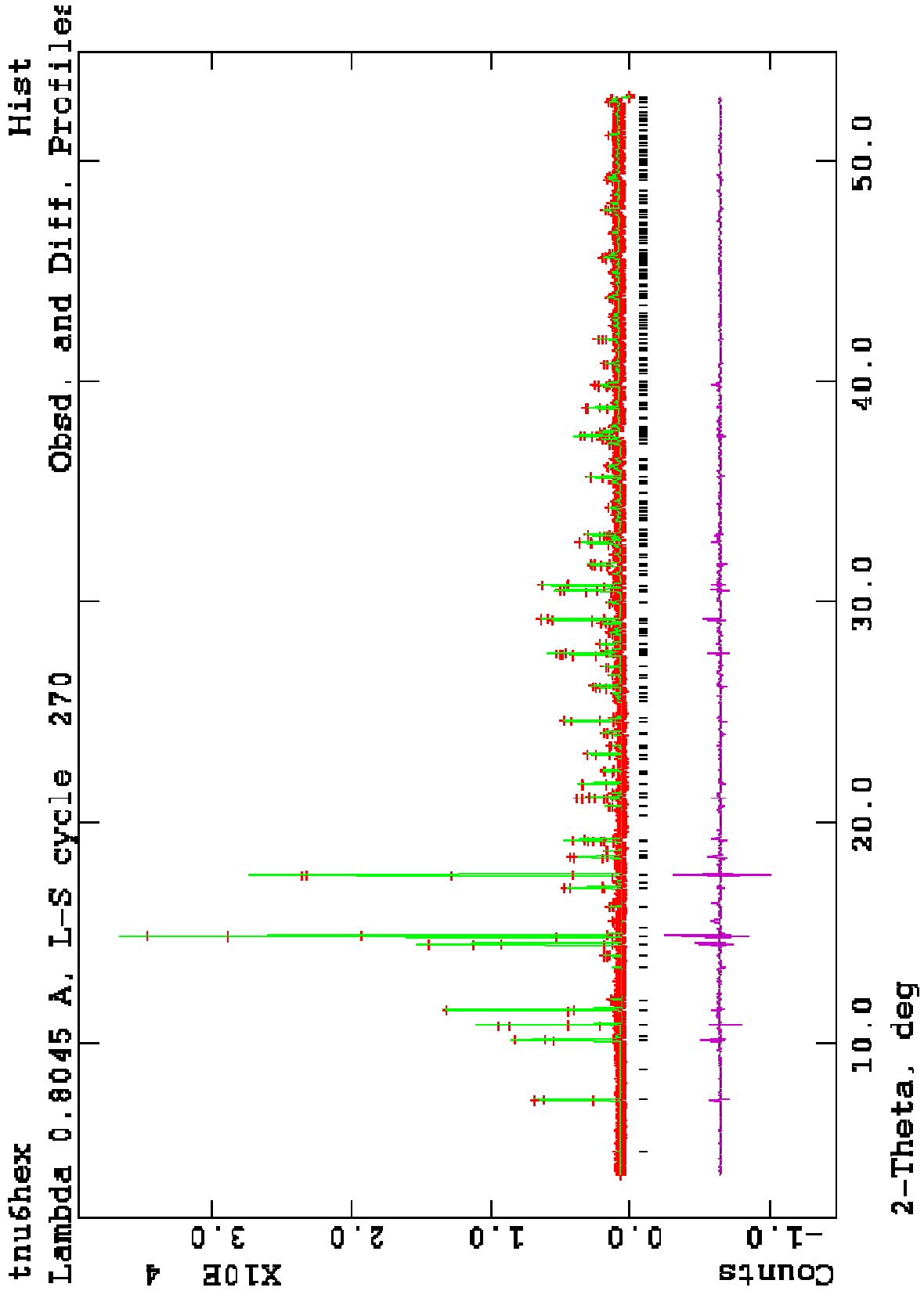

Figure 4.5: Refined powder pattern of TNU-6 (red = experimental data, green = model, purple = difference profile).

Atom	***x***	***y***	***z***	**Occupancy**	**Uiso (x10)**
Si(1)	0.183(1)	0.327(1)	0.398(1)	1	0.004(9)
Si(2)	2/3	1/3	0.503(1)	1	0.004(9)
Ga(1)	0.3285(4)	0.1622(5)	0.5156(8)	1	0.089(4)
Ga(2)	2/3	1/3	0.896(1)	1	0.089(4)
O(1)	0.328(2)	0.102(2)	0.707(2)	1	0.35(2)
O(2)	0.706(2)	0.509(2)	0.967(2)	1	0.35(2)
O(3)	0.014(2)	0.305(2)	0.424(2)	1	0.35(2)
O(4)	0.791(2)	0.498(2)	0.433(2)	1	0.35(2)
O(5)	0.193(2)	0.199(2)	0.477(2)	1	0.35(2)
O(6)	2/3	1/3	0.696(2)	1	0.35(2)
K(1)	0.531(1)	0.481(1)	1.207(1)	0.94(1)	0.18(1)
K(2)	0.000	0.000	0.213(1)	1 (capped)	0.18(1)

Table 4.2: Refined atomic coordinates of TNU-6.

Bond length (Å)					
Si(1)-O(1)	1.69(2)	Ga(2)-O(2)	1.79(2)	K(1)-O(1)	2.77(2)
Si(1)-O(2)	1.63(2)	Ga(2)-O(6)	1.71(2)	K(1)-O(2)	2.67(2)
Si(1)-O(3)	1.68(2)			K(1)-O(2)	3.46(2)
Si(1)-O(5)	1.55(2)	Si(2)-O(4)	1.68(2)	K(1)-O(2)	3.38(2)
		Si(2)-O(6)	1.65(2)	K(1)-O(3)	2.83(2)
Ga(1)-O(1)	1.76(2)			K(1)-O(3)	3.27(2)
Ga(1)-O(3)	1.89(2)	K(2)-O(1)	3.06(2)	K(1)-O(4)	3.28(2)
Ga(1)-O(4)	1.79(2)	K(2)-O(3)	3.61(2)	K(1)-O(4)	2.67(2)
Ga(1)-O(5)	1.69(2)	K(2)-O(5)	3.04(2)	K(1)-O(4)	3.47(2)
		K(2)-O(5)	2.88(2)	K(1)-O(6)	3.489(3)

Table 4.3: Selected bond lengths for the refined structure of TNU-6 as solved from powder data.

O-T-O bond angles (°)					
O(1)-Si(1)-O(2)	110(1)	O(4)-Si(2)-O(4)	108(1)	O(1)-Ga(1)-O(3)	95(1)
O(1)-Si(1)-O(3)	113(1)	O(4)-Si(2)-O(6)	110(1)	O(1)-Ga(1)-O(4)	117(1)
O(1)-Si(1)-O(5)	107(1)			O(1)-Ga(1)-O(5)	115(1)
O(2)-Si(1)-O(3)	104(1)	O(2)-Ga(2)-O(2)	109(2)	O(3)-Ga(1)-O(4)	103(1)
O(2)-Si(1)-O(5)	116(1)	O(2)-Ga(2)-O(6)	110(2)	O(3)-Ga(1)-O(5)	111(1)
O(3)-Si(1)-O(5)	110(1)			O(4)-Ga(1)-O(5)	113(1)

Table 4.4: Selected bond angles for the refined structure of TNU-6 as solved from powder data.

The refined structure (Figure 4.6) may be considered as a derivative of the mineral kalsilite[8] – a stuffed tridymite[9] with the formula $KAlSiO_4$ (Figure 4.12(a)). TNU-6 consists of GaO_4 and SiO_4 tetrahedra (instead of AlO_4 and SiO_4 tetrahedra) arranged in characteristic ditrigonally distorted rings, within which resides the potassium. The key difference between the refined structure and that of kalsilite is in the directedness of the tetrahedra. In kalsilite the directedness of the tetrahedra in all 6-membered rings is UDUDUD (U = up, D = down) However, two different types of arrangement exist within a single layer of TNU-6: one quarter of the rings have UDUDUD topology, while that of the remaining rings is UUUDDD. This alteration in topology results in a doubling of the *a* parameter relative to kalsilite and produces two different K sites.

The layers are stacked in an ABAB fashion where B corresponds to a laterally translated *and* inverted A layer such that the rings on adjacent layers are distorted with opposite rotation.[9] The basal O atoms within the more symmetrical UDUDUD tunnels form a tricapped trigonal antiprism around the K, while the K in the UUUDDD channels is probably more irregularly coordinated by eight O atoms.[10]

This structure belongs to a large group of stuffed frameworks related to the nepheline-kalsilite $(Na,K)AlSiO_4$ series[10-14] with general formula AB_2O_4, where B occupies framework sites while A is a charge balancing cation within the 6MR channel. The particular arrangement of tetrahedral units observed in the refined structure above has been reported in $BaFeGaO_4$.[10]

Close inspection of the structure reveals an interlayer Si-O-Ga bond angle of 180° between Ga(2) and Si(2) due to the oxygen being positioned on a three-fold axis. This is also observed in other related phases[15,16] and was rationalised by Perotta and Smith[8] by the O being disordered between three positions around this axis.

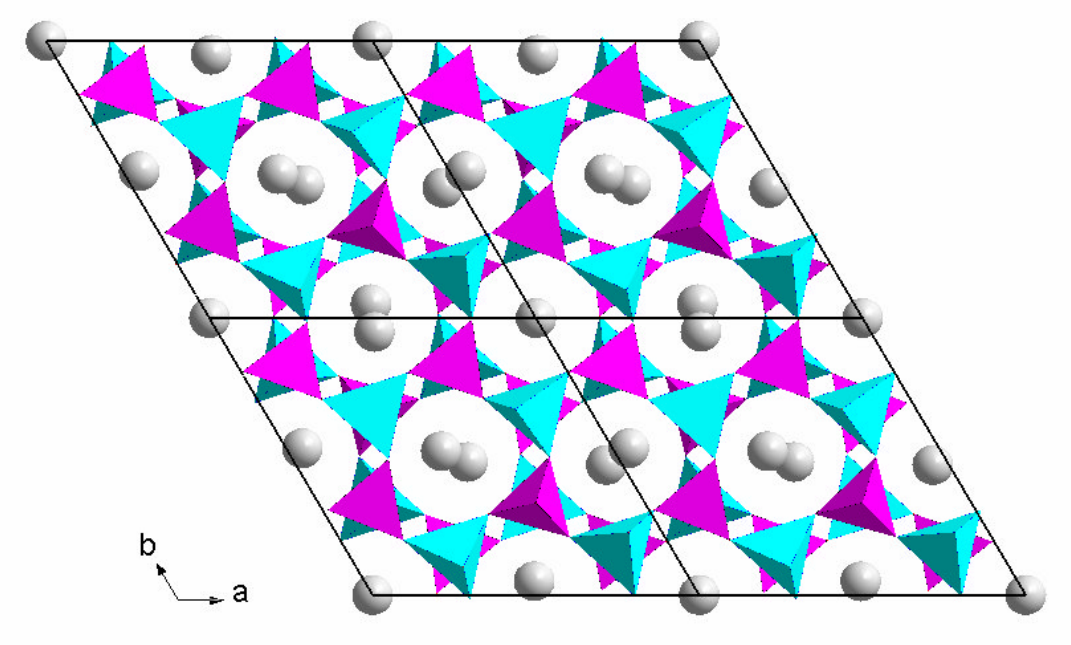

Figure 4.6: Refined structural model for TNU-6 viewed along the c-axis (grey = K, purple = SiO_4 tetrahedra, cyan = GaO_4 tetrahedra).

Selected Area Electron Diffraction (SAED) studies conducted by Dr Wuzong Zhou at St Andrews confirm a hexagonal 10x10x8Å cell. However, weaker reflections indicate the existence of a $\sqrt{3}a$ superstructure – i.e. a hexagonal cell of approximate dimensions 18x18x8Å (Figure 4.7(a)). Such a cell had indeed been encountered during X-ray data indexing trials and close inspection of high-resolution synchrotron powder XRD data suggests that additional reflections due to this larger cell may indeed be present (Figure 4.7(b)), although of very low intensity.

(a)

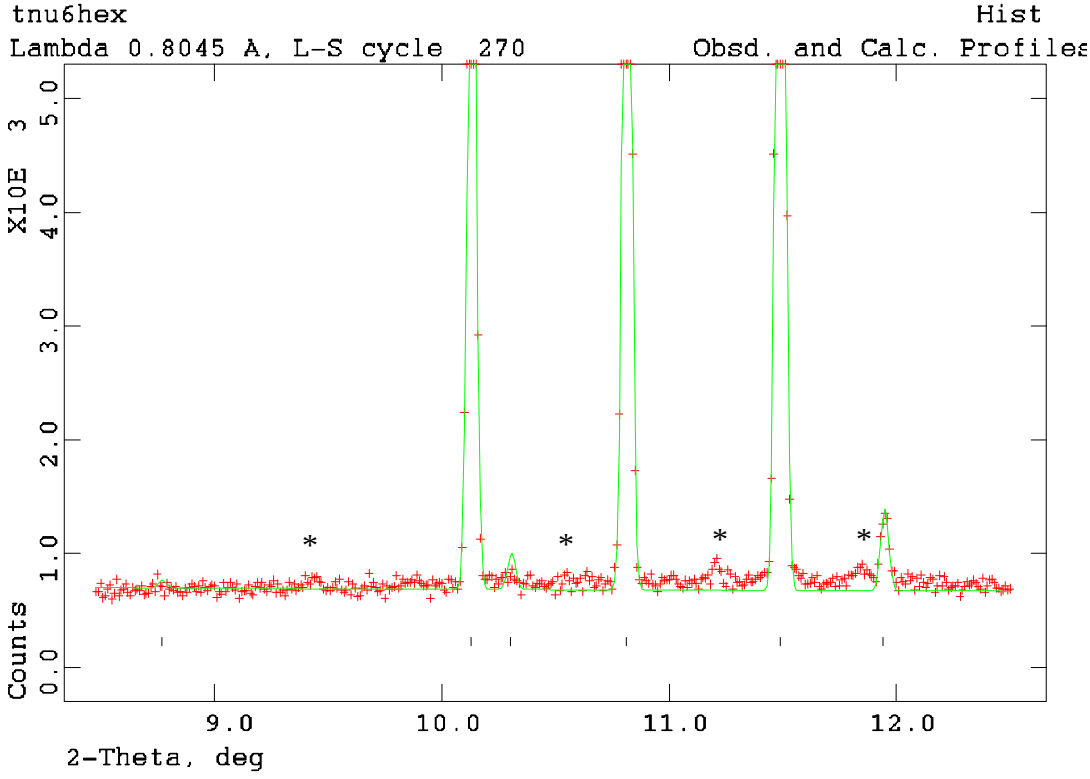

(b)

*Figure 4.7: (a) SAED pattern of TNU-6 viewed along [001] revealing a √3a superstructure; (b) enlarged section of synchrotron powder diffraction data revealing presence of weak superstructure reflections (marked as *), original cell marked as tick lines below histogram, experimental data shown in red, refined model shown in green.*

A search through extensive literature on related phases revealed the potassium aluminogerminate ($KAlGeO_4$) analogue as possessing both the observed supercell and the $BaFeGaO_4$ arrangement of tetrahedral units.[17,18] Barbier *et al.* implied that the tridymite-like phase $KGaSiO_4$ (now known to be equivalent to TNU-6) is indeed isostructural with its AlGe counterpart.[12] However, the structure of this analogue has not been explicitly solved or reported in the literature. This is also the first time, to our

knowledge, this phase has been synthesised under relatively mild hydrothermal conditions.

Figure 4.8 illustrates the $KAlGeO_4$ structure. While it is observed to possess the same arrangement of tetrahedral units as found in $BaFeGaO_4$ (i.e. UUUDDD, UDUDUD), a larger unit cell is created by a subtle variation in the direction of tilt of tetrahedral units within the UDUDUD rings; instead of tilting slightly clockwise (as observed in $BaFeGaO_4$, Figure 4.6), one half of these rings tilt in an anticlockwise direction.

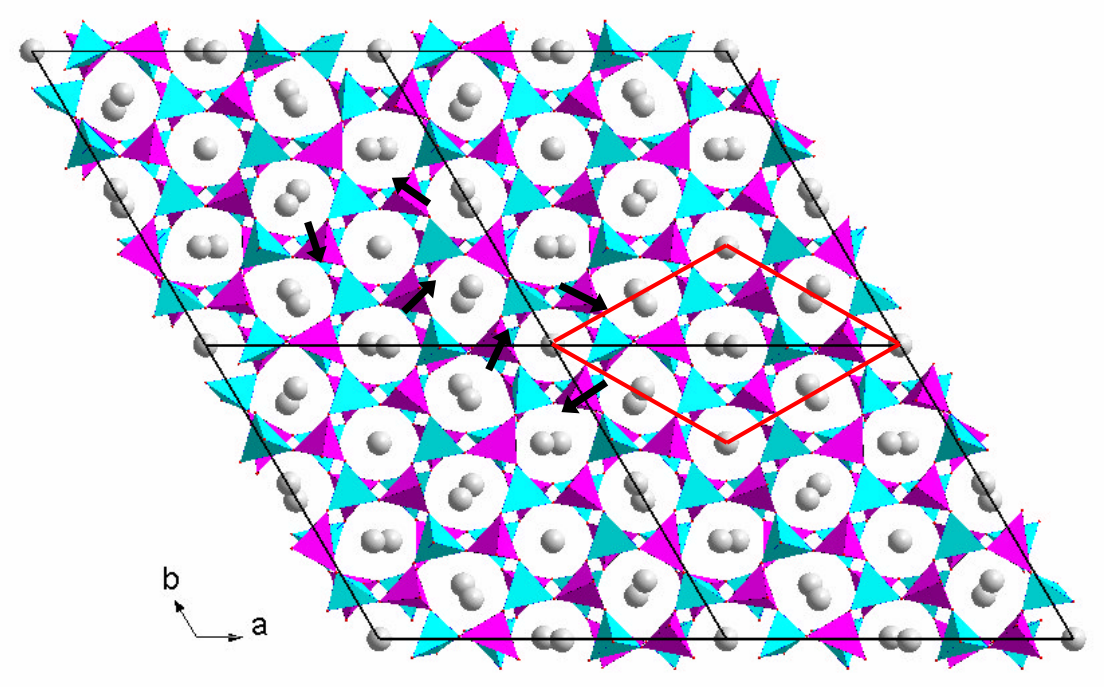

Figure 4.8: Structure of $KAlGeO_4$ viewed along the c-axis with $BaFeGaO_4$-type cell overlain in red. The variation in tilting of tetrahedral units is indicated by black arrows.

Unfortunately, since the additional reflections in the powder XRD data are so weak, refinement cycles of the $KAlGeO_4$ structure against data for TNU-6 (altering the composition to suit) were highly unstable and failed to converge satisfactorily. Permitting the isotropic thermal parameters of all O atoms in the original refinement to vary independently resulted in elevated values (compared to those of other oxygens) for O1, O3, O6, and O4 (Table 4.5). R_{wp} and R_p values were only marginally improved to values of 7.48% and 7.19%, respectively. The variation in thermal parameters is illustrated schematically in Figure 4.9. Elevated values for O1 are suggestive of

displacement of this atom in the formation of anticlockwise and clockwise motifs of the Ga1(O1O3O4O5) tetrahedron. A similar value for O3 and O4 suggests that, in doing so, O1 displaces O3 and O4 to a greater extent than O5. It is possible, therefore that the tilting of this tetrahedron occurs predominantly through rotation about the Ga1-O5 bond. An elevated value for O6 is consistent with its movement about the three-fold axis as discussed above. The movement of O6 in this manner will also affect O4.

Oxygen	**Uiso (x10)**
1	0.6(1)
2	0.1(1)
3	0.5(1)
4	0.4(1)
5	0.1(1)
6	0.6(1)

Table 4.5: Refined isotropic thermal parameters for oxygen atoms in TNU-6.

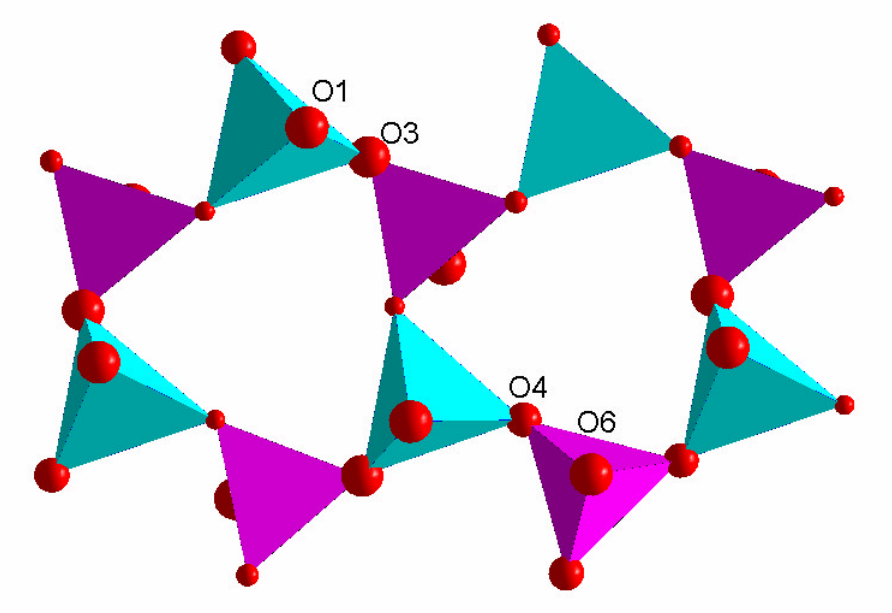

Figure 4.9: Section of the refined structure of TNU-6. The radii of oxygen atoms (red) are representative of their independently refined isotropic thermal parameters.

Single crystal analysis was conducted to investigate the existence of the $KAlGeO_4$-like superstructure. The structure was solved in $P6_3$ symmetry with unit cell $a = b =$ 18.1723(3), c = 8.5127(6), γ = 120° in agreement with the previously observed superstructure (single crystal data given in Appendix A). The principal arrangement of tetrahedral units in the UDUDUD rings is indeed observed to be that of the $KAlGeO_4$ structure (Figure 4.10). However, relatively large (3 or 4 electrons) residual electron density peaks are observed close to the apical oxygen atoms suggesting possible twinning in the structure with a second domain possessing the opposite arrangement of tetrahedral tilting. While no attempts have been made to refine the structure as twinned, twinning is indeed prevalent in related phases and would appear to be the most likely explanation.

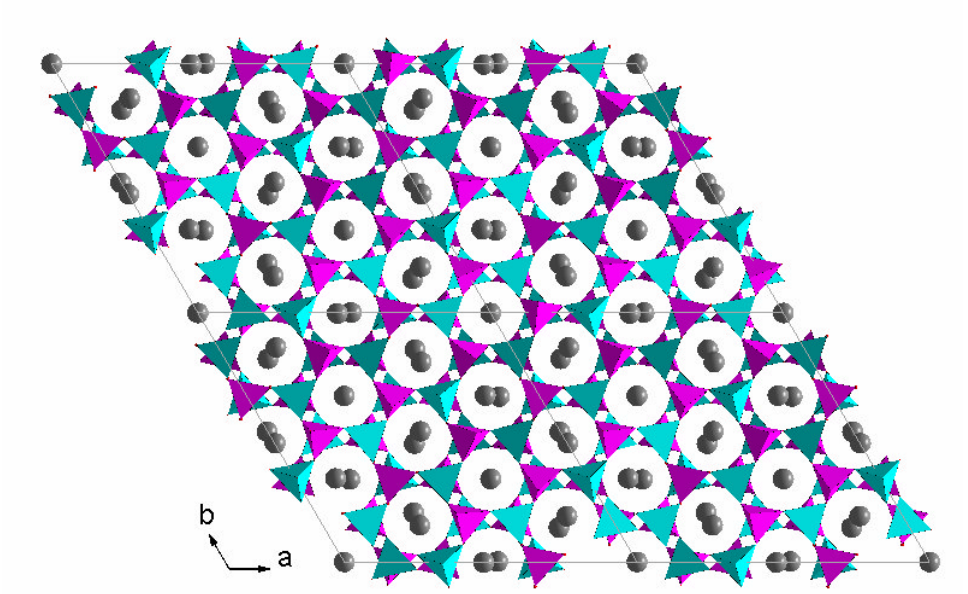

Figure 4.10: Structure of TNU-6 as solved from single crystal analysis.

Higher resolution ^{29}Si MAS NMR analysis conducted at St Andrews revealed a splitting of the signal at δ -79ppm into two components (Figure 4.11). While the smaller signal at lower field may be attributed to excess Si, signals at δ -78.3 and -79.1ppm suggest two crystallographically distinct Si sites in a ratio of 1:1. Two sites would indeed be expected for the $BaFeGaO_4$ structure, but in a ratio of 1:3. However, by imposing the $KAlGeO_4$ structure and thus doubling the number of Si sites from two to four (all with equal multiplicity), the observed ratio may be achieved by pairing these sites as 1+1:1+1.

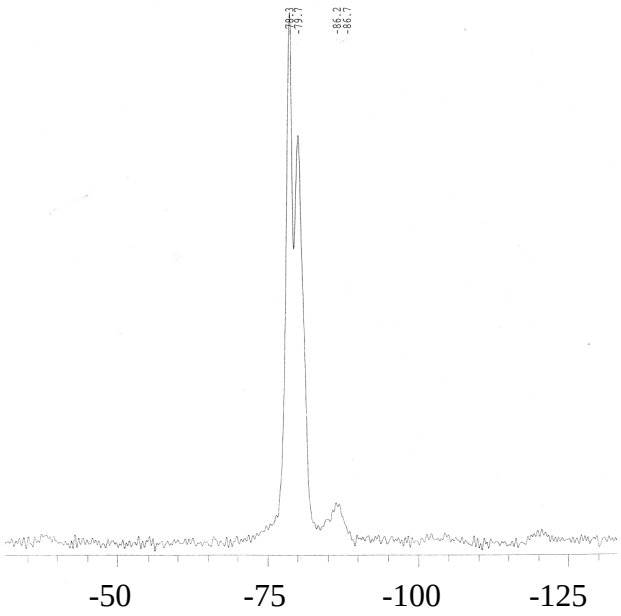

Figure 4.11: Solid-state ^{29}Si MAS NMR spectrum of TNU-6 recorded at St Andrews.

4.2: Comparison with related phases

As mentioned above, $KGaSiO_4$ (equivalent to TNU-6) belongs to an extensive group of kalsilite-like phases. The following section aims to place this material in context and discuss the structural variations existent between related phases.

The naturally occurring silicate mineral tridymite may be regarded as the parent phase. Its structure may be described in terms of layers composed from vertex-sharing SiO_4 tetrahedra which link to form regular hexagonal rings. Within each ring, tetrahedra point up and down in strict alternation (i.e. UDUDUD) (Figure 4.12(g)). Layers are stacked in an ABAB sequence in which B represents an inverted and translated A layer, and are connected through tetrahedral apices.

By replacing half of the Si sites with Al, a charge imbalance is created and necessitates the incorporation of interstitial cations. In nature, two such 'stuffed tridymites' predominate: kalsilite[8] (where K^+ cations occupy interstitial sites), and nepheline[11] (containing both Na^+ and K^+ cations in a 3:1 ratio – a purely Na-containing analogue is not known). Intercalation of these charge-balancing species results in ring distortion away from regular hexagonal geometry creating two further ring-shapes: while K^+ cations force ditrigonal distortion (characteristic of the kalsilite structure, Figure

4.12(a)), intercalation of Na^+ cations results in oval distortion (as observed in nepheline, Figure 4.12(b)). Distortion to oval geometry in nepheline is also accompanied by a change to AAAA-type stacking of aluminosilicate layers (stacking present in kalsilite is analogous to that in tridymite).

Another related Na-containing phase is the sodium beryllophosphate beryllonite[19] ($NaBePO_4$). However, in this case, the change in framework composition results in an alteration in the arrangement of tetrahedral units with both UDUDUD and UUDDUD present (Figure 4.12(c)). Perhaps as a result, the rings within this Na-containing phase are ditrigonally distorted rather than oval.

Barbier and co-workers have studied related stuffed tridymite phases extensively. In particular they have prepared synthetic analogues in the composition fields $Na_{1-x}K_xAlGeO_4$[20] and $Na_{1-x}K_xGaSiO_4$[13] ($0 \leq x \leq 1$) by heating pelletised reactants at 900°C, then at 1000°C for two days. Four different structure types were identified in the AlGe system, namely beryllonite, nepheline, kalsilite and the novel topology denoted $KAlGeO_4$ (Figure 4.12(f)) (similar to that of $BaFeGaO_4$ (Figure 4.12(e)) but with clockwise and anticlockwise tilting of tetrahedral units as discussed previously) as the K/Na ratio in synthesis mixtures is increased. Similarly, beryllonite-, kalsilite, and $KAlGeO_4$-like structures were also observed in the GaSi system as the K/Na ratio is increased, although no nepheline-like phase was observed. Interestingly, the kalsilite-like phases here possess a $\sqrt{3}a_{kal}$ (where a_{kal} refers to the *a* parameter for kalsilite) superstructure (Figure 4.12(d)), which is discussed in more detail below.

Although it is not possible to compare the structure of a solely Na-containing aluminosilicate analogue with those of $NaAlGeO_4$ and $NaGaSiO_4$, the occurrence of the nepheline structure at low K-loading in the AlGe system suggests that substitution of Si by Ge has little effect on the topology formed. However, substitution of Al by Ga appears to preclude formation of this topology. As expected, increasing K-loading in both systems results in the formation of kalsilite-like phases ($0.5 \leq x \leq 0.9$ for AlGe, and $0.1 \leq x \leq 0.5$ for the GaSi system). However, under K-rich conditions, the new '$KAlGeO_4$' structure is obtained suggesting that Ge and Ga substitution into kalsilite (i.e. K-only) results in the formation of this new structure. It is evident, however, that the charge balancing cations also contribute greatly to the identity of the phase obtained.

Indeed, $NaGaGeO_4$ is also found to possess the beryllonite structure.[12] Interestingly, however, the $KGaGeO_4$ analogue is thought to possess a kalsilite-like structure (isostructural with $BaAl_2O_4$) rather than the $KAlGeO_4$ structure.♦

The $KAlGeO_4$ structure has also been reported in two phosphate materials – α-$KZnPO_4$ and α-$KCoPO_4$.[21,22]

In their studies of the $(NaK)GaSiO_4$ system, Barbier *et. al.* attempt to rationalise the structural differences observed between kalsilite ($KAlSiO_4$), the kalsilite-like $(Na_{0.7}K_{0.3})GaSiO_4$ (with $\sqrt{3}a_{kal}$ superstructure) and $KGaSiO_4$ ($KAlGeO_4$ structure with $2\sqrt{3}a_{kal}$ superstructure) in terms of bond lengths. It is proposed that a reduction in symmetry associated with the formation of the $\sqrt{3}a_{kal}$ superstructure results in a greater degree of structural flexibility, allowing it to accommodate a range of K/Na ratios. The effect is two-fold. From only one interstitial site in kalsilite, three crystallographically unique sites are produced in the $\sqrt{3}a_{kal}$ superstructure allowing significant ordering of Na^+ and K^+ cations. Secondly, apical oxygen atoms are released from special positions permitting the framework to 'collapse' via tilting of its tetrahedral units to create suitable coordination environments for both Na and K – thus creating the clockwise and anticlockwise motifs observed in these materials (Figure 4.12(d)).

In this manner, one of the three interstitial sites in the $\sqrt{3}a$-kalsilite-like structure of $(Na_{0.7}K_{0.3})GaSiO_4$ possesses slightly shorter M-O distances to those found for the other two. Consequently, this position is preferentially occupied by Na^+ cations. Ordering of Na^+ and K^+ cations between the three sites in this fashion becomes more marked as K-loading is increased. Eventually this kalsilite-like framework can no longer accommodate the high levels of K-loading (most probably a result of T-atom substitution) and changes to the $KAlGeO_4$ ($2\sqrt{3}a_{kal}$ superstructure) structure with a further reduction in symmetry and increase in the number of crystallographically distinct cavity sites, accompanied by an alteration in the arrangement of tetrahedral units.

♦ implied but not explicitly proved.

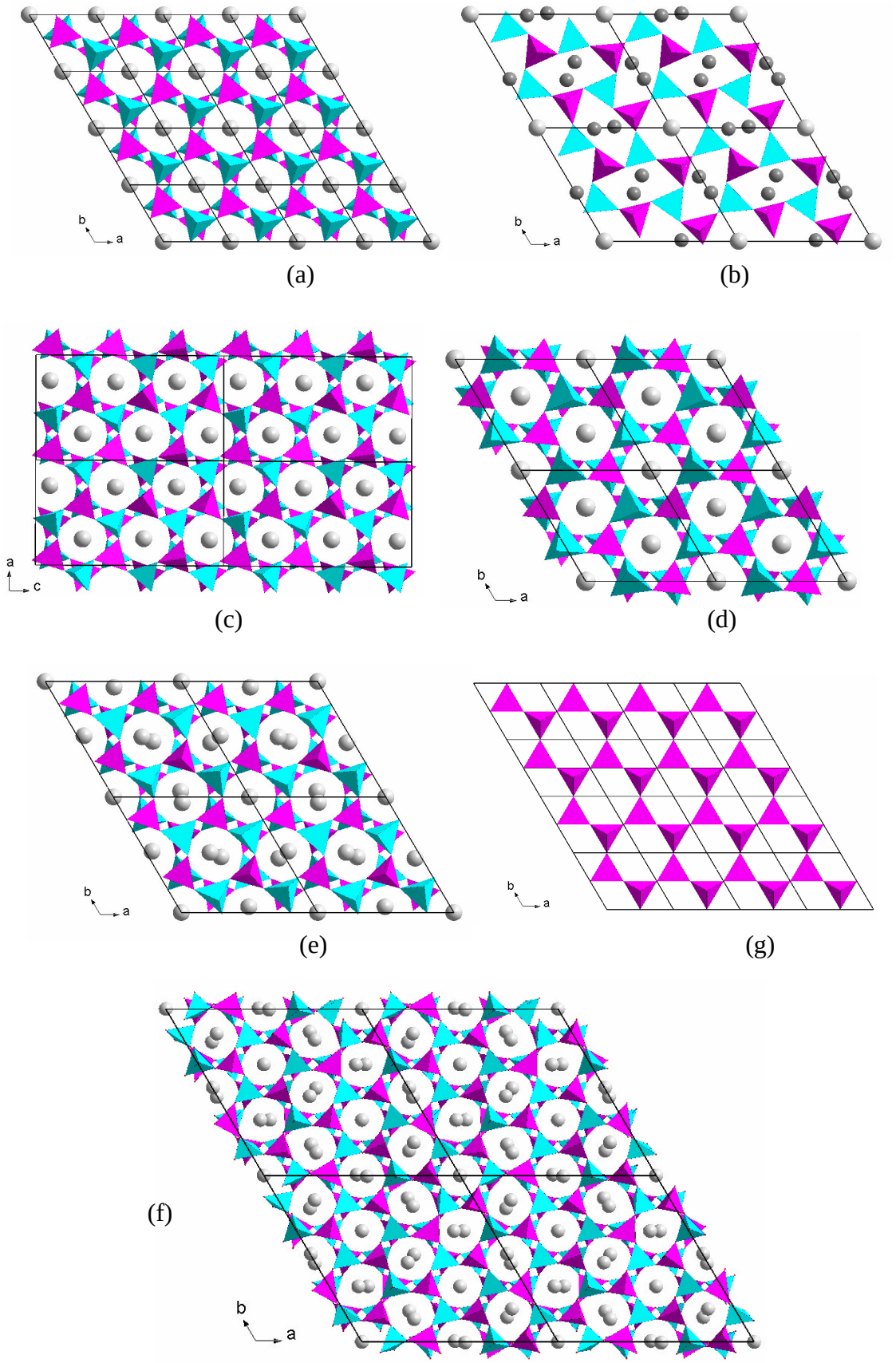

Figure 4.12: Structures of (a) kalsilite, (b) nepheline, (c) beryllonite, (d) kalsilite-like √3a superstructure (e) $BaFeGaO_4$, (f) $KAlGeO_4$ and (g) a layer of tridymite for comparison.

Barbier *et. al.* point to a correlation between T-O/M-O bond length ratios and whether the kalsilite structure or the $\sqrt{3}a_{kal}$ superstructure will be obtained (where T-O and M-O represent average tetrahedral and interstitial cavity bond lengths, respectively). Table 4.6 lists a number of hexagonal stuffed tridymite phases and illustrates that as T-O/M-O increases, the kalsilite structure (5.16x5.16x8.71Å, UDUDUD, no tilting) gives way to the $\sqrt{3}a_{kal}$ superstructure (unit cell entries in Table 4.6 are given relative to that of kalsilite).

A similar survey of $BaFeGaO_4$/$KAlGeO_4$-type materials, however, suggests that *compositional* factors may be more influential in the formation of these topologies since T-O/M-O ratios are observed to cover a broad range from 0.59 to 0.63 (i.e. covering values expected for 2A, C and $\sqrt{3}$A, C kalsilite-type structures). It is, unfortunately, impossible to draw any relationship between T-O/M-O ratios and the formation of the $KAlGeO_4$ superstructure from the $BaFeGaO_4$-type substructure since $BaFeGaO_4$ remains the sole example of this non-tilting topology (although $BaGa_2O_4$ was originally thought to possess the same topology as $BaFeGaO_4$, subsequent studies revealed the presence of the $KAlGeO_4$-type superstructure).[23] It is noted, however, that no $KAlGeO_4$-type materials posses a T-O/M-O ratio less than 0.59 and it is possible that this represents the upper limit tolerable in the kalsilite (A, C) structure. Beyond this value the framework must change in some manner to more favourably accommodate the intercalated cation(s). This can be achieved by following the 2A, C/$\sqrt{3}$A, C route and maintaining the original ring topology, or by altering the ring topology and forming the $KAlGeO_4$, $BaFeGaO_4$, $BaFe_{1.5}Al_{0.5}O_4$ or $BaFe_2O_4$-II topologies. In general, the presence of Fe appears to favour alteration in ring topology, while K is particularly prevalent in phases possessing the $KAlGeO_4$ structure.

It is therefore suggested that structure direction in these materials is a result of subtle effects arising from the geometric requirements of both the T- and interstitial-atoms. In substituting Ga for Al in kalsilite to form $KGaSiO_4$ (i.e. TNU-6), Ga clearly directs crystallisation towards the $KAlGeO_4$ structure. However, this topology may not have been obtained had Na substituted K.

Material	Cell type	T-O	M-O	T-O/ M-O	Ring type present	Tetrahedral tilt*	Ref.
$KAlSiO_4$ (kalsilite)	A, C	1.68	2.90	0.58	UDUDUD	none	8
$KLiSO_4$	A, C	1.72	2.96	0.58	UDUDUD	none	24
$KLiBeF_4$	A, C	1.69	2.87	0.59	UDUDUD	none	25
$BaAl_2O_4$-II	2A, C	1.76	2.93	0.60	UDUDUD	a	26
$BaFe_{1.5}Al_{0.5}O_4$	2A, C	1.79	2.92	0.61	UDUDUD	none	27
					UUUDDD	none	
					DDDUDU	none	
					UUUDUD	none	
$BaMgSiO_4$	√3A, C	1.77	2.86	0.62	UDUDUD	c, a	28
$BaZnSiO_4$	√3A, C	1.77	2.85	0.62	UDUDUD	c, a	28
$Sr_{0.7}Ca_{0.3}BeSiO_4$	√3A, C	1.62	2.59	0.62	UDUDUD	c, a	13
$Na_{0.7}K_{0.3}GaSiO_4$	√3A, C	1.71	2.72	0.63	UDUDUD	c, a	13
$BaCoSiO_4$	√3A, C	1.79	2.84	0.63	UDUDUD	c, a	29
$BaFe_2O_4$-II	2√3A, C	1.86	2.86	0.65	UUUUUD	negligible	30
					DDDDDU		
$KAlGeO_4$	2√3A, C	1.74	2.97	0.59	UDUDUD	c, a	17
					UUUDDD	in, out	
$KGaSiO_4$ (TNU-6)	2√3A, C	1.72	2.86	0.60	UDUDUD	c, a	
					UUUDDD	in, out	
α-$KZnPO_4$	2√3A, C	1.74	2.83	0.61	UDUDUD	c, a	21
					UUUDDD	in, out	
α-$KCoPO_4$	2√3A, C	1.74	2.81	0.62	UDUDUD	c, a	22
					UUUDDD	in, out	

Continued on next page

$BaFeGaO_4$	√3A, C	1.84	2.93	0.63	UDUDUD UUUDDD	a c	10
$BaGa_2O_4$	2√3A, C	1.84	2.92	0.63	UDUDUD UUUDDD	c, a in, out	23

Table 4.6: Comparison of T-O/M-O ratios and associated structure types for a selection of hexagonal stuffed tridymites with structures related to kalsilite. * *c = clockwise, a = anticlockwise, in = tilting towards the centre of the ring, out = tilting away from the centre of the ring.*

4.3: Summary

The potassium gallosilicate material denoted TNU-6, which was synthesised during studies into the structure direction of gallosilicate zeolitic materials, has been found to possess a stuffed tridymite-like structure. This non-zeolitic material belongs to a large group of related phases and is characterised by two different 6MR topologies: UDUDUD and UUUDDD, analogous to the $BaFeGaO_4$ structure. Evidence has been found through electron and synchrotron powder X-ray diffraction and single crystal analysis to suggest the existence of a √3*a* superstructure analogous to that observed in $KAlGeO_4$. This superstructure is the result of a variation in tilt of tetrahedral units within the UDUDUD ring. However, precise atomic detail of the superstructure has proved difficult to obtain, even by single crystal diffraction, due to the probable presence of twinning within the structure. Nevertheless, a $KAlGeO_4$-like model is consistent with suggestions in the literature. Evidence has been found to suggest that this structure crystallises as a direct consequence of the presence of both Ga and K and that structure direction in these materials is a result of subtle alterations in the framework to create more favourable coordination environments for the interstitial cations.

Chapter 5: Structural Analysis of the Sodium Gallosilicate TNU-7

5.1: Structure Solution

The sodium gallosilicate material denoted TNU-7 was synthesised by Prof Suk Bong Hong from an entirely inorganic gel of composition $2.0Na_2O:Ga_2O_3:10SiO_2:150H_2O$.[31] Crystallisation was performed hydrothermally under rotation at 60rpm, at 150°C over 7 days. Solid-state ^{29}Si and ^{71}Ga MAS NMR spectra recorded at Hanbat University exhibit resonances at shifts characteristic of tetrahedral geometry in zeolitic materials (Figure 5.1(a) and (b)). Examination of the sample by SEM (Figure 5.1(c)) revealed needle-like crystals measuring approximately 0.8μm in length by 0.1μm in diameter.

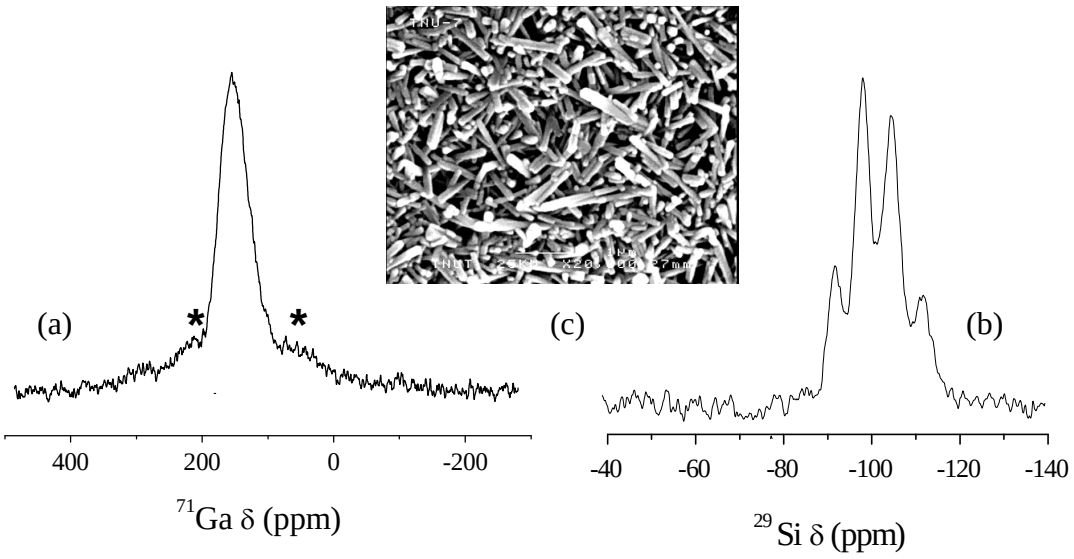

Figure 5.1: Solid-state ^{71}Ga (a) and ^{29}Si (b) MAS NMR spectra and SEM image (c) of as-prepared TNU-7 (courtesy of Prof Suk Bong Hong) (= spinning side bands).*

Identification of the Framework Structure

The powder XRD pattern (Figure 5.2) of the as-made sample (recorded in-house on a Stoe STADI P diffractometer, Cu $K_{\alpha 1}$ X-radiation) was indexed as orthorhombic with *a* = 7.59Å, *b* = 18.01Å, *c* = 26.08Å and shows systematic absences consistent with space

group *Pmmn*. Later SAED studies (conducted by Dr Wuzong Zhou at St Andrews) also revealed a similar cell.

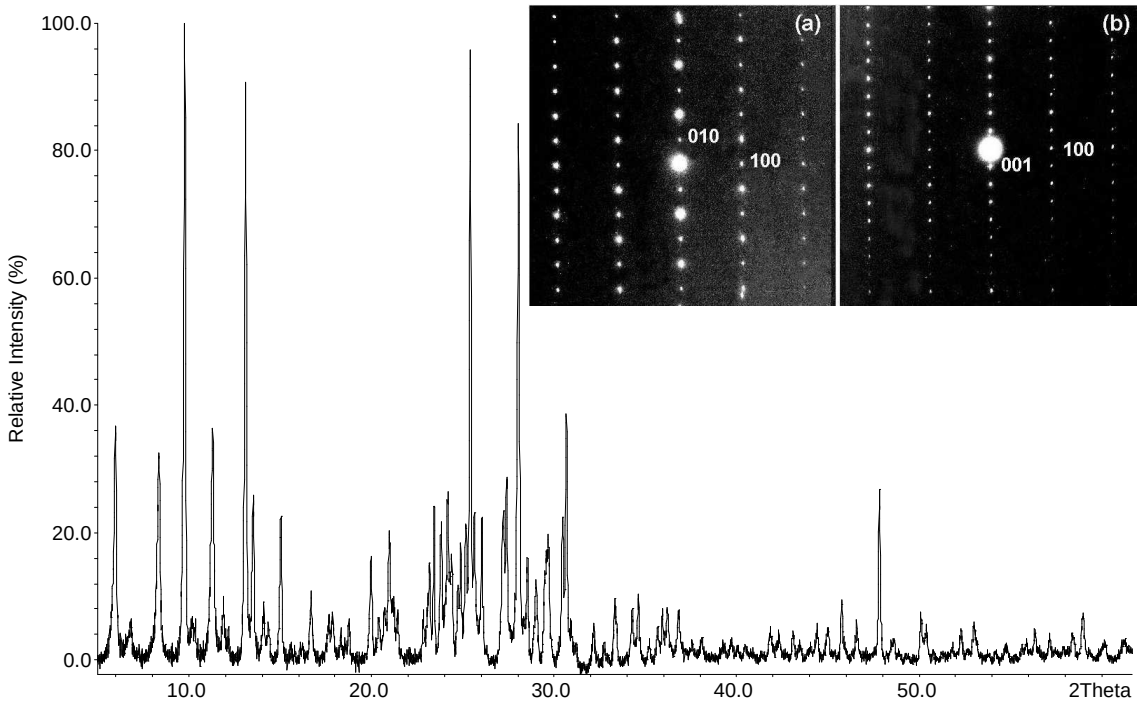

Figure 5.2: XRD and SAED patterns of as-made TNU-7. SAED pattern (a) viewed along the [001] zone axis, (b) viewed along the [010] zone axis (courtesy of Dr Wuzong Zhou).

The cell parameters, space group and indeed XRD pattern compare favourably with those of the ordered Mazzite (MAZ)/Mordenite (MOR) intergrowth structure proposed for aluminosilicate ECR-1.[32] This material was first synthesised by Leonowicz and Vaughan from hydrothermal treatment (150^{o}C) of a sodium aluminosilicate gel (Si/Al = 3.6) in the presence of bis-(2-hydroxyethyl)-dimethyl-ammonium cations. Two models, denoted ECR-1A and ECR-1B, differing in the connectivity of their alternating MAZ and MOR layers, were proposed for the structure of ECR-1 by Leonowicz and Vaughan and investigated further by Chen *et al.*.[33] While chains of 5MRs connect the layers within model ECR-1A, chains of alternating 4 and 6MRs connect those of model ECR-1B. However, explicit proof of the correct structure was not obtained since no structural refinement was conducted for ECR-1 due to the poor quality of XRD data.

By comparing the observed data with calculated patterns for both models, it became apparent at an early stage that model ECR-1A was more favourable for the gallosilicate TNU-7, as suggested by Chen *et al.*[33] for the aluminosilicate. The simulated X-ray data for model ECR-1B exhibits a number of discrepancies, notably a strong (110) peak at 2θ = 12.63° and a weak (111) peak at 2θ = 13.08°. This is in direct contrast with the observed data and simulated data of model ECR-1A where the (111) peak is particularly strong and the (110) peak intensity is negligible. Figure 5.3 illustrates the ECR-1A structure model viewed along the *a*-axis.

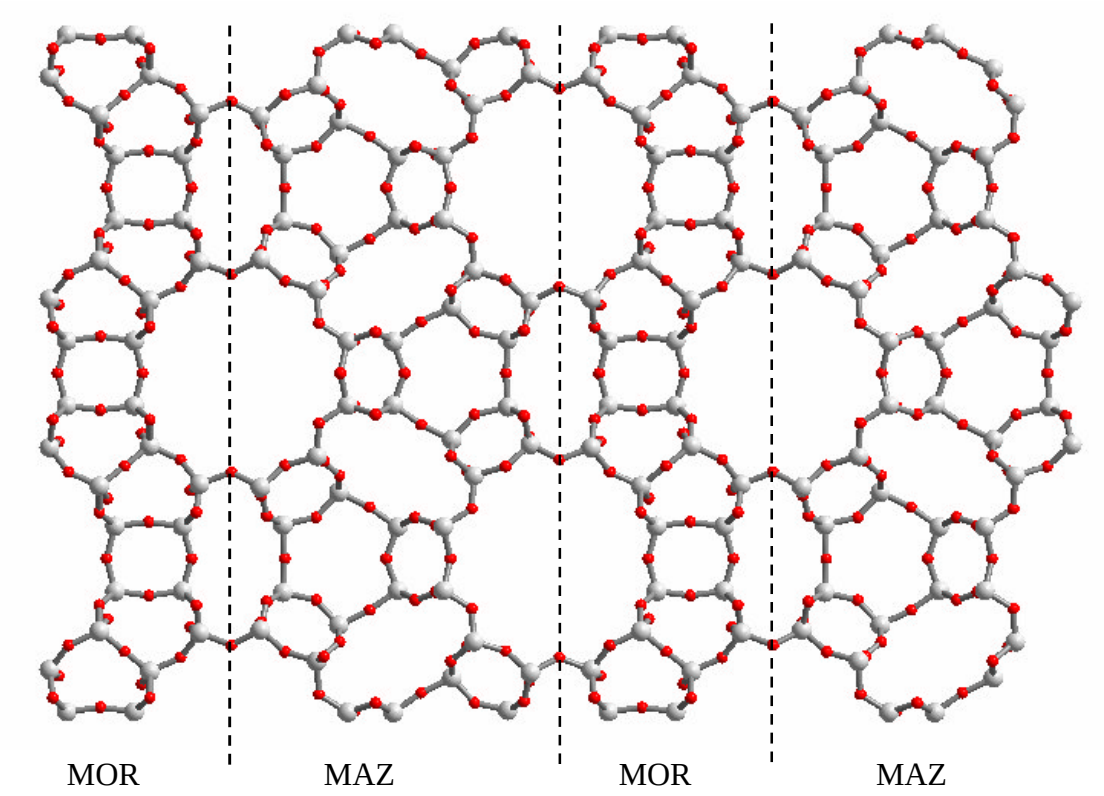

Figure 5.3: Structure model ECR-1A (red = O, grey = Si/Al). The layer structure types are indicated below with layer interfaces marked by the dashed lines.

To confirm this, refinement of the ordered ECR-1A and ECR-1B models against the X-ray profile of dehydrated TNU-7 was performed by the Rietveld method within the program GSAS. The peak shape was fitted using pseudo-Voigt profile function, and the background was fitted using a cosine Fourier series background function, fitting 36 parameters. Si and Ga atoms in TNU-7 were positioned on each T-site with estimated fractional occupancies of 0.794 and 0.206, respectively, according to its bulk Si/Ga ratio of 3.85. T-O bond lengths and O-O distances within GaO_4/SiO_4 tetrahedra were

constrained to weighted averages of 1.65Å (σ = 0.01Å) and 2.71Å (σ = 0.02Å), respectively, and these constraints were maintained throughout. R_{wp} values obtained by including only the framework atoms of the respective models into the GSAS program were 25.4% for ECR-1A and 35.7% for ECR-1B: only model ECR-1A was examined further.

As mentioned above, structural refinement of the aluminosilicate ECR-1 was not possible (and no three-letter code assigned) due to the broad nature of peaks in the powder XRD data. This was thought, most probably, to be due to stacking disorder. However, absence of streaking along the [010] axis in the SAED pattern of TNU-7 (Figure 5.2) confirms that the layers are stacked in a strictly alternating fashion in this gallosilicate analogue.

Investigation of Extra-Framework Na^+ Cation Positions

The positions of extra-framework Na^+ ions in TNU-7 were located via the parallel approaches of Fourier difference maps and cation site modelling. Fourier peaks at reasonable distances from the framework were investigated as Na^+ ions. Modelled positions were based on literature reports of the locations of Na^+ ions in the respective phases of gallosilicate mazzite[34] (hereafter denoted Ga-MAZ) and aluminosilicate mordenite[35] (hereafter denoted MOR) and converted to their equivalent positions in the ECR-1A structure.

Figure 5.4 illustrates the seven most probable sites located from Fourier difference maps (labelled F1-F7), the inclusion and refinement of each of which significantly improved the data fit. The fractional coordinates and a brief description of each of these sites are given in Table 5.1. Figure 5.5 illustrates modelled positions, labelled M1-M9 (Table 5.2). Positions M1 and M5 correspond to positions 1 and 3, respectively, as assigned by Newsam *et al.* in synthetic Ga-MAZ.[34] Position M1 is located at the centre of the narrow channels running parallel to the *a*-axis, while position M5 resides closer to the 8MR window which leads through the MAZ strip. Modelled positions M2, M3 and M4 collectively represent Newsam's position 2 in Ga-MAZ and reside near pockets within the main channel wall. Positions M6, M7, and M8 were modelled within the inter-sheet channel of ECR-1A based on analogous locations observed in both mazzite and

mordenite materials – specifically positions 1 and 3 of Newsam *et al.* in Ga-MAZ and position 1 as assigned by Meier in Na-containing MOR.[35a] A further position M9 was modelled within the large channel based on position VI as assigned by Maurin *et al.* in Na-MOR.[35b]

The modelled positions were included in an independent refinement to assess whether these sites are in fact possible Na^+ ion locations. Positions M1, M5 and M8 may be regarded as equivalent to sites F1, F3 and F6, respectively, and refined to similar locations. Positions M3 and M4 refined to a single position equivalent to F2, and sites M6 and M7 refined as F4 and F5, respectively. Modelled sites M2 and M9, however, do not appear to be occupied as no improvement in R_{wp} was achieved by their inclusion in the refinement. Furthermore, no equivalent sites were located by the Fourier Difference maps. An additional site to those modelled (F7) was found by the Fourier Difference maps to be located within the 8MR of the main channel wall.

Site	***x***	***y***	***z***	**Description**
F1	0	0	0	At the centre of small channels within the mazzite layer, between staggered chains of 8MRs running parallel to *a*
F2	0.25	0.060	0.743	Within the main channel, close to a pocket within the mazzite layer
F3	0.25	0.083	0.025	At the centre of the 8MR window which leads through and along the mazzite layer
F4	0.25	0.25	0.262	In the small inter-sheet channel, close to the centre of the 8MR window leading to the mazzite layer
F5	0.25	0.25	0.631	In the small inter-sheet channel, close to the centre of the 8MR window leading to the mordenite layer
F6	0.025	0.25	0.303	At the centre of the small inter-sheet channel, between staggered 8MR windows of the mazzite and mordenite layers
F7	0.25	0.75	0.402	Within the main channel, close to the 8MR window leading through the mordenite layer

Table 5.1: Extra-framework cation positions located by Fourier difference maps.

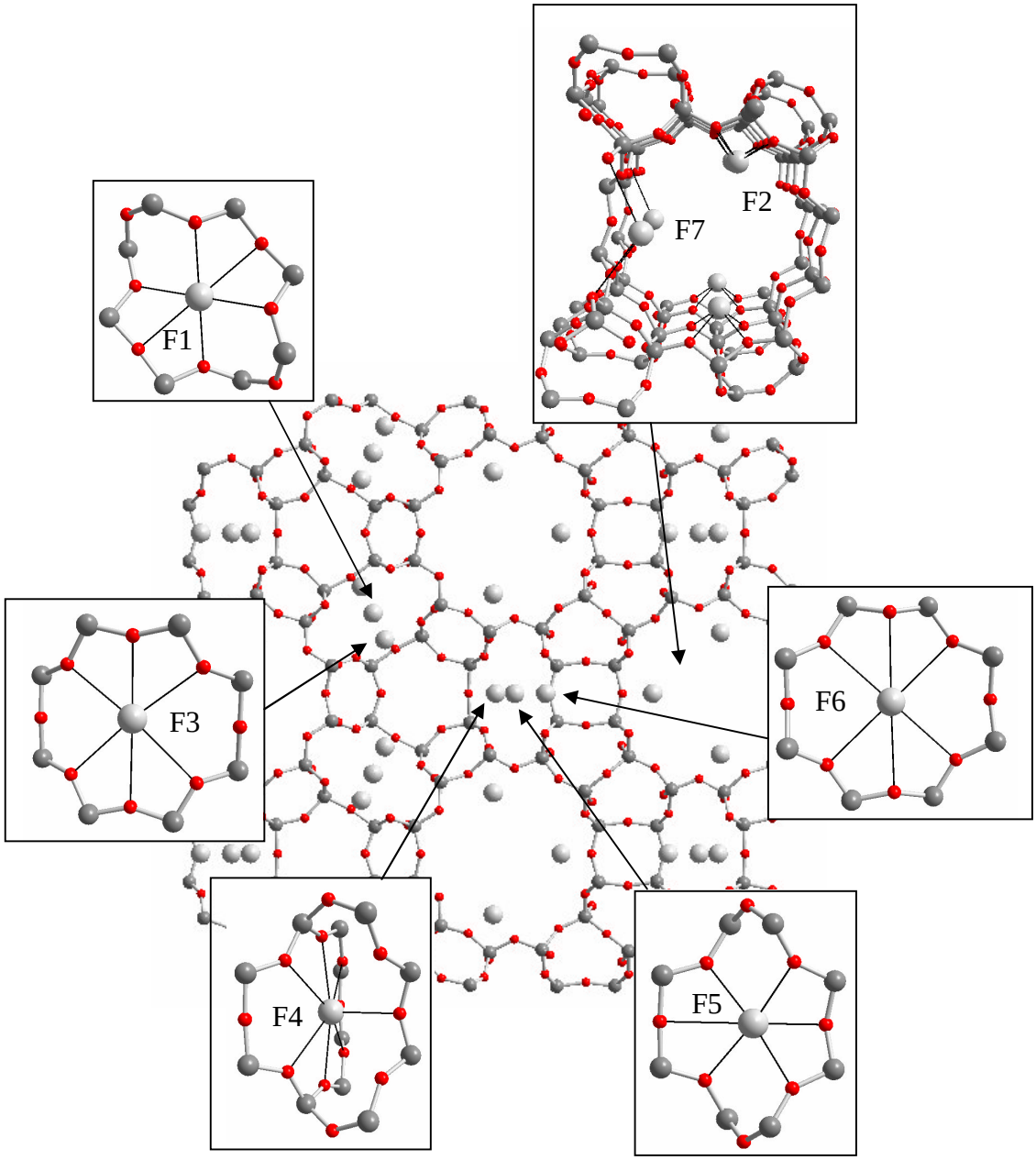

Figure 5.4: Extra-framework sodium positions F1-F7 as located by Fourier difference maps. Possible Na-O interactions are indicated in the insets (red = O, dark grey = Si/Ga, light grey = Na).

Site	*x*	*y*	*z*	Site	*x*	*y*	*z*
M1	0	0	0	M5	0.251	0.069	0.027
M2	0.25	0.700	0.157	M6	0.75	0.75	0.752
M3	0.75	0.585	0.200	M7	0.25	0.75	0.645
M4	0.75	0.540	0.261	M8	0.489	0.75	0.698
M5	0.251	0.069	0.027	M9	0.75	0.559	0.338

Table 5.2: Fractional coordinates of modelled extra-framework sodium sites.

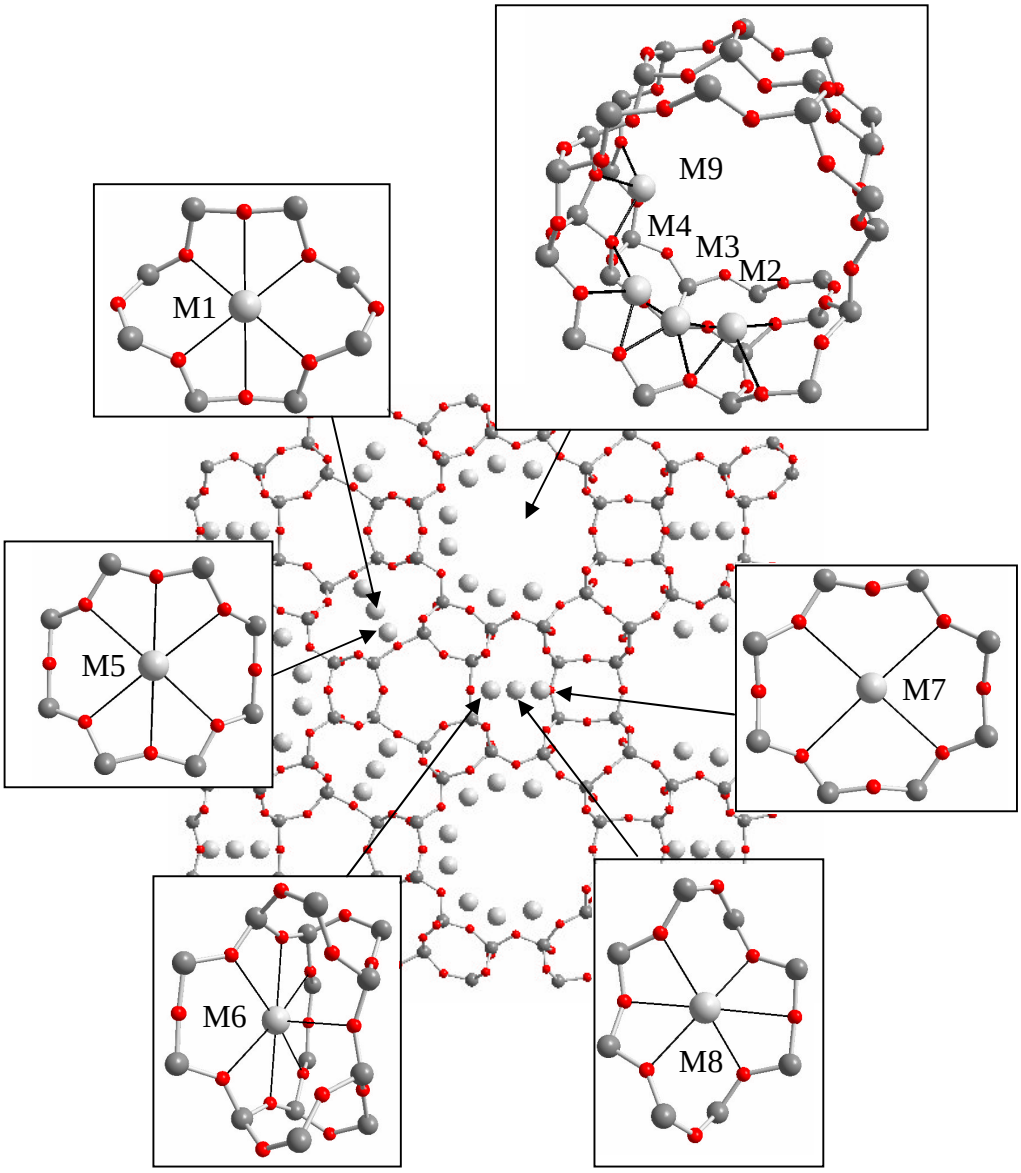

Figure 5.5: Modelled extra-framework sodium positions M1-M9 with possible Na-O interactions indicated in the insets (red = O, dark grey = Si/Ga, light grey = Na).

Full Structural Refinement

A complete refinement of the lattice parameters, framework and Na^+ ion positions as well as instrumental parameters was performed. As in preliminary refinements of the framework model, the background was fitted using a cosine fourier series function, fitting 36 parameters. Peak shape was fitted using pseudo-Voigt profile function, with asymmetry correction of Finger, Cox and Jephcoat (Chapter 2). The asymmetry parameters S/L and H/L were fixed at 0.01 during the initial stages of framework and instrumental parameter refinement before being permitted to vary independently. As both parameters are correlated with lattice parameters and zero point, a further refinement of these parameters was conducted with every new set of S/L and H/L values, followed by refinement of the peak-shape parameters. This refinement cycle was repeated until convergence was achieved.

Thermal parameters of all T-atoms were constrained to be equal, as were those of all oxygen atoms and sodium atoms prior to their refinement. The atomic coordinates of co-located T-atoms were constrained to move together and T-O and O-O distances were constrained as before. Final R_{wp} and R_p values of 7.92% and 6.30% were achieved (Figure 5.6) with a = 7.5789(4)Å, b = 18.089(1)Å, c = 25.853(2)Å. Refined atomic parameters are listed in Table 5.3, while selected bond lengths and angles are given in Tables 5.4 and 5.5, respectively. The average T-O bond length (1.642Å) and average O-T-O and T-O-T angles (109.3^o and 144.5^o, respectively) were found to be in good agreement with those expected for zeolitic materials.

In general, observed Na-Na and Na-O(framework) distances are plausible. For some cation sites (Na4, Na5 and Na6), adjacent Na-Na distances are short and indicate partial occupancies. However, in the final refinement no two sites with the sum of occupancies > 1 are closer than 3.2 Å. Na4, Na5 and Na6 form a chain running along the smaller inter-strip channels of the structure parallel to the *a*-axis. It is possible that some of these are residual water molecules. Indeed, the fractional occupancy of Na5 is significantly higher in the same sample dehydrated at the lower temperature of 250^{o}C under vacuum, and it is likely that this location is occupied by water. The final refinement located seven Na^+ locations Na(1)-Na(7), which account for approximately 10 of the estimated 12.4 Na^+ per unit cell.

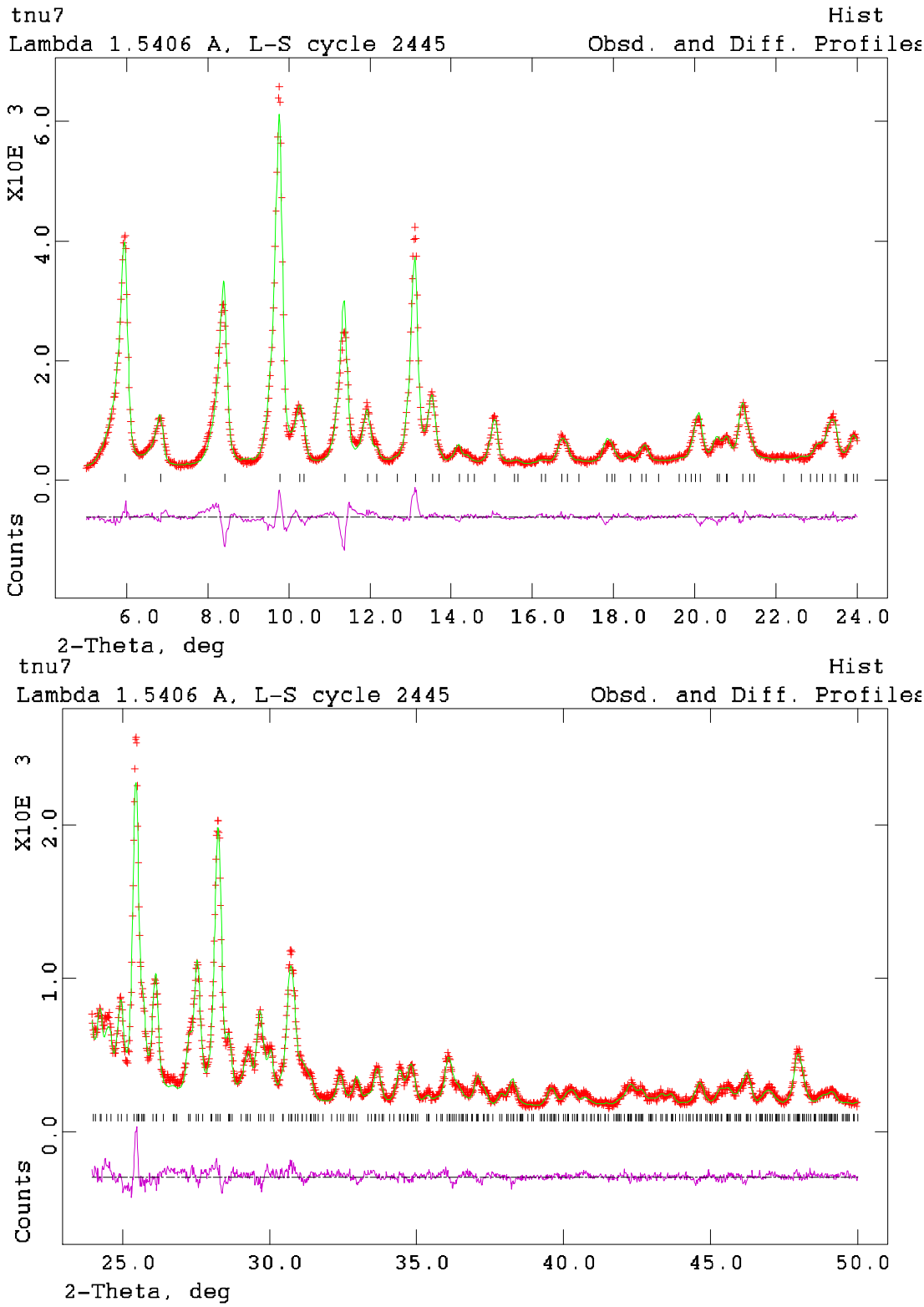

Figure 5.6: Rietveld plots for the structural refinement of TNU-7 over data range $5 \leq 2\theta \geq 50^{o}$ *. (red = experimental data, green = model, purple = difference plot).*

Atom	***x***	***y***	***z***	U_{iso} **(x100)**
T(1)	-0.2500	0.167(1)	-0.002(1)	2.0(1)
T(2)	-0.2500	0.077(1)	0.106(1)	2.0(1)
T(3)	-0.2500	0.1585(4)	0.209(1)	2.0(1)
T(4)	0.034(1)	0.1631(5)	-0.0884(4)	2.0(1)
T(5)	0.040(1)	-0.022(1)	0.1452(5)	2.0(1)
T(6)	0.041(1)	0.0569(5)	0.2510(5)	2.0(1)
T(7)	0.2500	0.162(1)	0.393(1)	2.0(1)
T(8)	0.2500	0.163(1)	0.5168(5)	2.0(1)
T(9)	-0.046(1)	0.051(1)	0.3603(5)	2.0(1)
T(10)	0.051(1)	-0.0550(5)	0.4527(4)	2.0(1)
O(1)	-0.2500	0.2500	0.022(1)	3.3(3)
O(2)	-0.2500	0.110(1)	0.047(1)	3.3(3)
O(3)	-0.2500	0.147(1)	0.146(1)	3.3(3)
O(4)	-0.2500	0.2500	0.210(2)	3.3(3)
O(5)	-0.078(2)	0.141(1)	-0.036(1)	3.3(3)
O(6)	-0.065(2)	0.031(1)	0.105(1)	3.3(3)
O(7)	-0.074(2)	0.132(1)	0.242(1)	3.3(3)
O(8)	-0.019(4)	0.2500	-0.103(1)	3.3(3)
O(9)	-0.017(3)	0.0004(1)	0.2044(5)	3.3(3)
O(10)	0.2500	0.156(2)	-0.078(1)	3.3(3)
O(11)	0.2500	-0.009(2)	0.131(1)	3.3(3)
O(12)	0.2500	0.081(2)	0.253(1)	3.3(3)
O(13)	-0.011(3)	0.112(1)	-0.140(1)	3.3(3)
O(14)	-0.020(3)	0.012(1)	0.3033(5)	3.3(3)
O(15)	0.2500	0.2500	0.381(2)	3.3(3)
O(16)	0.2500	0.2500	0.532(1)	3.3(3)
O(17)	0.2500	0.149(2)	0.4554(5)	3.3(3)
O(18)	0.072(2)	0.127(1)	0.367(1)	3.3(3)
O(19)	0.077(2)	0.129(1)	0.546(1)	3.3(3)
O(20)	0.039(3)	-0.013(1)	0.397(1)	3.3(3)
O(21)	0.0000	0.0000	0.5000	3.3(3)

Continued on next page

O(22)	-0.2500	0.071(2)	0.376(1)	3.3(3)
O(23)	-0.2500	0.088(1)	0.532(1)	3.3(3)
Na(1)	0.0000	0.0000	0.0000	3.2(1)
Na(2)	0.2500	0.068(3)	0.755(2)	3.2(1)
Na(3)	0.2500	0.07(1)	0.040(5)	3.2(1)
Na(4)	0.2500	0.2500	0.28(1)	3.2(1)
Na(5)	0.2500	0.7500	0.71(1)	3.2(1)
Na(6)	0.04(1)	0.2500	0.306(2)	3.2(1)
Na(7)	0.2500	0.7500	0.467(2)	3.2(1)

Table 5.3: Refined atomic coordinates for TNU-7 as obtained from refinement against laboratory X-ray data.

Bond length (Å)							
T(1)-O(1)	1.63(1)	T(5)-O(6)	1.63(1)	T(9)-O(14)	1.65(1)	Na(4)-O(12)	3.1(1)
T(1)-O(2)	1.63(1)	T(5)-O(9)	1.64(1)	T(9)-O(18)	1.64(1)	Na(4)-O(15)	2.4(2)
T(1)-O(3)	1.64(1)	T(5)-O(11)	1.65(1)	T(9)-O(20)	1.63(1)	Na(5)-O(4)	2.17(4)
		T(5)-O(13)	1.65(1)	T(9)-O(22)	1.64(1)	Na(5)-O(7)	2.85(2)
T(2)-O(2)	1.64(1)					Na(6)-O(7)	2.83(4)
T(2)-O(3)	1.63(1)	T(6)-O(7)	1.64(1)	T(10)-O(19)	1.65(1)	Na(6)-O(15)	2.52(5)
T(2)-O(6)	1.64(1)	T(6)-O(9)	1.64(1)	T(10)-O(20)	1.64(1)	Na(6)-O(18)	2.75(3)
		T(6)-O(12)	1.64(1)	T(10)-O(21)	1.62(1)	Na(7)-O(23)	2.93(3)
T(3)-O(3)	1.64(1)	T(6)-O(14)	1.65(1)	T(10)-O(23)	1.67(1)		
T(3)-O(4)	1.66(1)					Na(1)-Na(1)	3.789(2)
T(3)-O(7)	1.64(1)	T(7)-O(15)	1.63(1)	Na(1)-O(2)	3.01(2)	Na(1)-Na(3)	2.5(1)
		T(7)-O(17)	1.61(1)	Na(1)-O(5)	2.78(2)	Na(5)-Na(6)	2.19(5)
T(4)-O(5)	1.66(1)	T(7)-O(18)	1.64(1)	Na(1)-O(6)	2.81(2)	Na(5)-Na(4)	3.80(1)
T(4)-O(8)	1.67(1)			Na(2)-O(9)	2.40(4)	Na(6)-Na(6)	3.2(1)
T(4)-O(10)	1.67(1)	T(8)-O(16)	1.61(1)	Na(2)-O(14)	2.71(4)	Na(6)-Na(4)	1.7(1)
T(4)-O(13)	1.66(1)	T(8)-O(17)	1.61(1)	Na(3)-O(6)	3.1(1)		
		T(8)-O(19)	1.64(1)	Na(3)-O(11)	2.9(2)		

Table 5.4: Selected bond lengths for TNU-7 as obtained from refinement against laboratory X-ray data.

O-T-O bond angles (°)					
O(1)-T(1)-O(2)	107(1)	O(6)-T(5)-O(9)	109(1)	O(16)-T(8)-O(17)	113(1)
O(1)-T(1)-O(5)	118(1)	O(6)-T(5)-O(11)	104(1)	O(16)-T(8)-O(19)	105(1)
O(2)-T(1)-O(5)	104(1)	O(6)-T(5)-O(13)	117(1)	O(17)-T(8)-O(19)	114(1)
O(5)-T(1)-O(5)	105(2)	O(9)-T(5)-O(11)	115(2)	O(19)-T(8)-O(19)	106(2)
O(2)-T(2)-O(3)	108(1)	O(9)-T(5)-O(13)	107(1)	O(14)-T(9)-O(18)	113(1)
O(2)-T(2)-O(6)	100(1)	O(11)-T(5)-O(13)	105(1)	O(14)-T(9)-O(20)	99(1)
O(3)-T(2)-O(6)	114(1)	O(7)-T(6)-O(12)	106(1)	O(14)-T(9)-O(22)	115(2)
O(6)-T(2)-O(6)	118(2)	O(7)-T(6)-O(10)	107(1)	O(18)-T(9)-O(20)	109(1)
O(3)-T(3)-O(4)	98(1)	O(7)-T(6)-O(12)	113(1)	O(18)-T(9)-O(22)	108(1)
O(3)-T(3)-O(7)	118(1)	O(9)-T(6)-O(16)	117(2)	O(20)-T(9)-O(22)	113(2)
O(4)-T(3)-O(7)	107(1)	O(9)-T(6)-O(9)	102(1)	O(19)-T(10)-O(20)	111(1)
O(7)-T(3)-O(7)	109(2)	O(12)-T(6)-O(13)	112(1)	O(19)-T(10)-O(21)	110(1)
O(5)-T(4)-O(8)	107(1)	O(15)-T(7)-O(17)	110(1)	O(19)-T(10)-O(23)	104(1)
O(5)-T(4)-O(10)	110(1)	O(15)-T(7)-O(18)	107(1)	O(20)-T(10)-O(21)	112(1)
O(5)-T(4)-O(13)	115(1)	O(17)-T(7)-O(18)	111(1)	O(20)-T(10)-O(23)	115(1)
O(8)-T(4)-O(10)	111(1)	O(18)-T(7)-O(18)	110(2)	O(21)-T(10)-O(23)	105(1)
O(8)-T(4)-O(13)	107(1)				
O(10)-T(4)-O(13)	107(1)				

Table 5.5: Selected bond angles for TNU-7 as obtained from refinement against laboratory X-ray data.

Description of the TNU-7 Structure

The framework structure of TNU-7 consists of regularly alternating layers of the well known zeolites mazzite and mordenite (Figure 5.7). In the following sections, the terms MAZ and MOR are employed to denote the topological phases mazzite and mordenite, respectively, while maz and mor denote the layers from which these phases are constructed. Many zeolite structures are composed of a single type of complex silicate layer, joined to adjacent layers by T-O-T bonds that are approximately perpendicular to the plane of the layers. MAZ and MOR are two familiar examples of such frameworks (Figures 5.14 and 5.15). In addition, the MAZ and MOR structures are related so that

not only do they share two common axes (the axes defining the plane of the structural layer) but their layers are connected in a similar fashion via chains of 5-MRs.

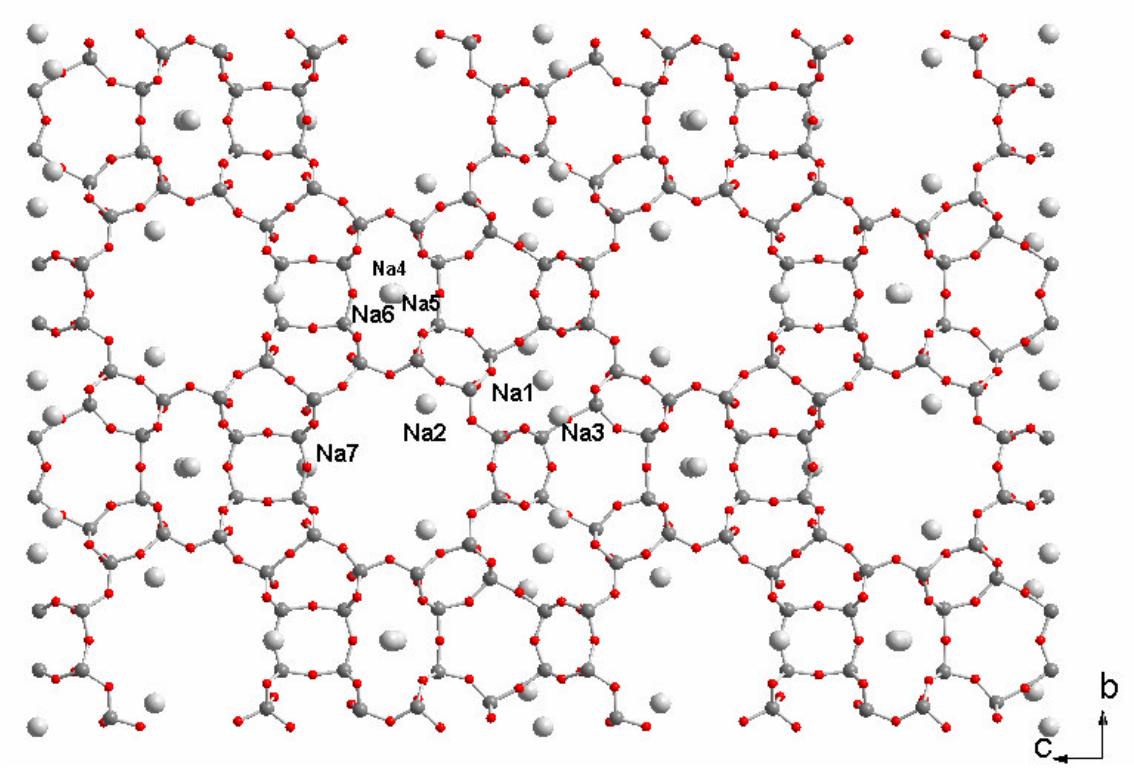

Figure 5.7: Refined structure of TNU-7 as obtained from laboratory X-ray data. (red = O, dark grey = Si/Ga, light grey = Na).

As a consequence, the formation of a MAZ-MOR intergrowth structure is highly feasible. Previously, there were doubts concerning the means by which these layers would be connected in such an intergrowth, and indeed whether such an arrangement could exist in an ordered manner. The data presented here indicate that for the gallosilicate TNU-7, maz and mor layers are connected via chains of 5MRs (model ECR-1A), as suggested by Chen *et al.* for ECR-1. Furthermore, it is evident from SAED studies that these layers are stacked in a completely ordered fashion.

The result is an interrupted three-dimensional pore system in which elements of the pore connectivity of both topologies are present. Large and remarkably asymmetric channels of free diameter 6.6x7.4Å run parallel to the *a*-axis (Figure 5.8), lined on the 'mordenite' side by slightly distorted 8MRs of free diameter 4.9x3.2Å.

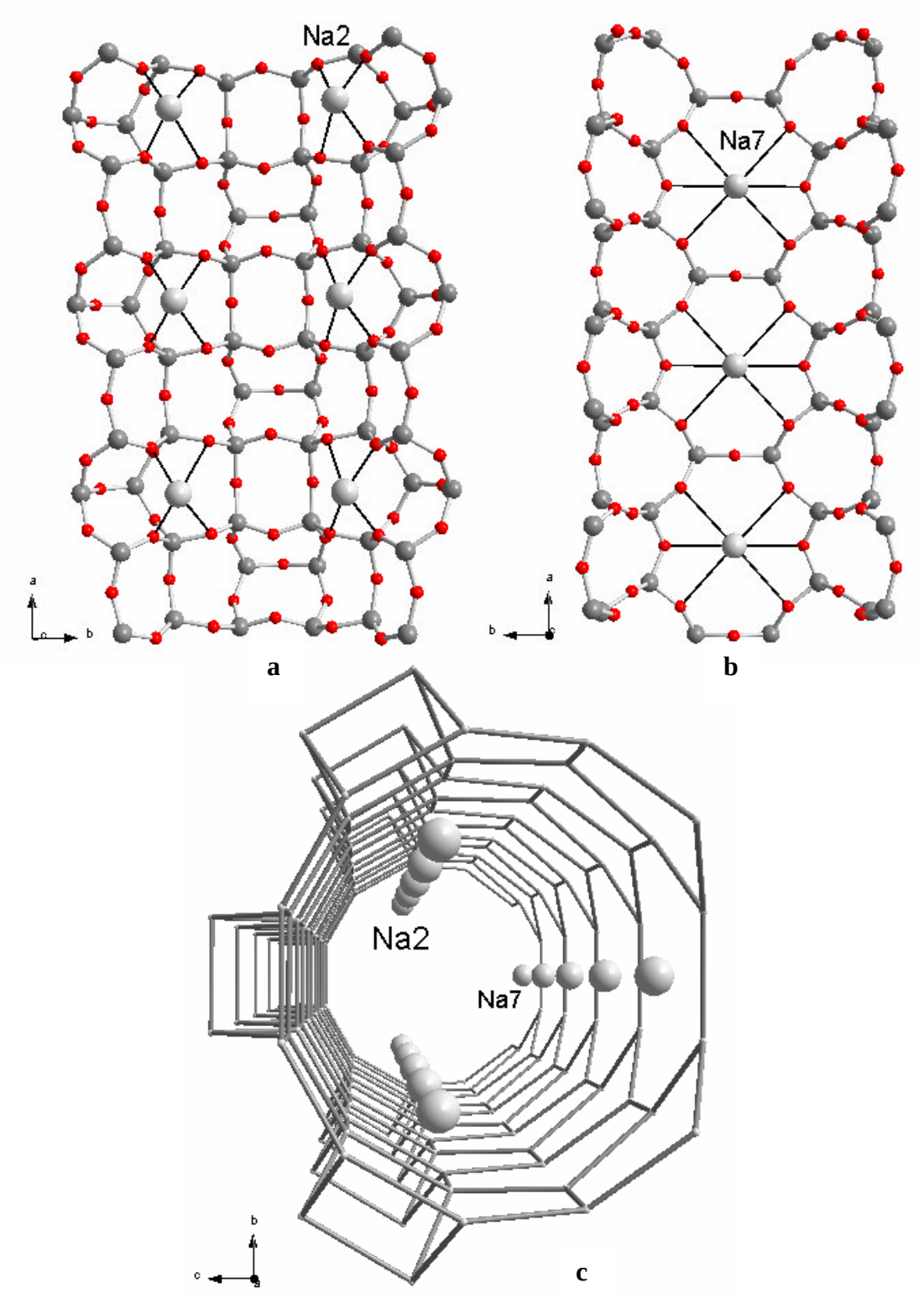

Figure 5.8: Cut-away diagrams of the main channel viewed (a) along +c and (b) along –c; (c) main channel viewed along a (oxygen atoms removed for clarity).

These provide restricted access through the mor layer (along the *c*-axis) to the narrow inter-sheet channel. From here access is gained to the maz layer through two diagonally positioned 8MRs. Movement parallel to the *b*-axis is restricted to the 8MR channel running parallel to the *b*-axis through the maz layer. In this manner, as illustrated in Figure 5.9, only certain large channels are accessible from any one maz layer. The distribution of extra-framework Na^+ cations is reflective of this unique pore system.

Refined positions Na1, Na2 and Na3 can be regarded as being analogous to sites previously identified in pure Ga-MAZ, while Na7 is associated with the mor layers. Positions Na4, Na5 and Na6, however, can be regarded as having different environments from those observed in the parent phases arising from the intergrowth arrangement.

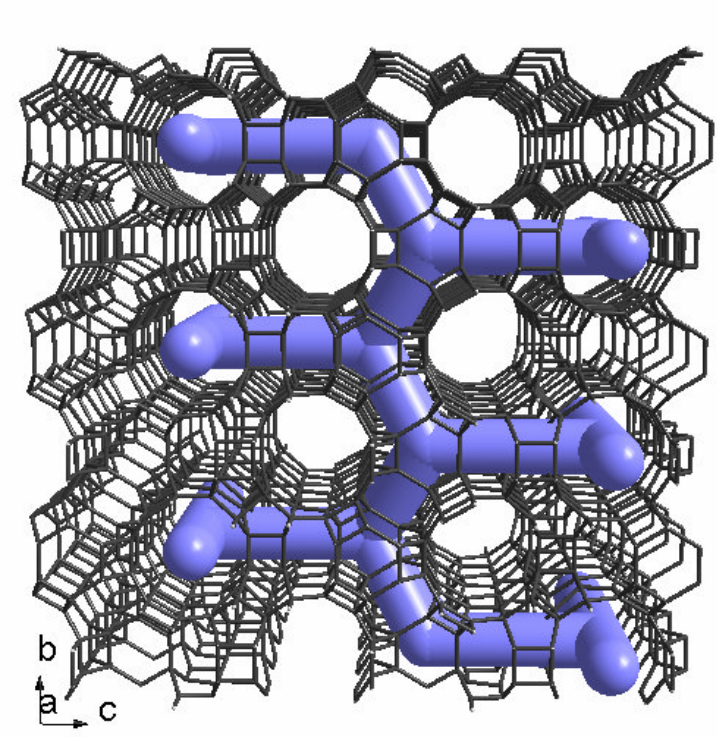

Figure 5.9: Possible pathways through the TNU-7 structure (oxygen atoms removed for clarity).

5.2: Structure Direction in the Formation of TNU-7

To investigate the structure-directing effect of Ga in the synthesis of TNU-7, Hong and co-workers conducted a series of syntheses with varying gel Ga-contents.[31,36] In addition, syntheses were also conducted in which Al replaced Ga (all other conditions

equal). The results of these studies (Table 5.6) revealed an interesting Ga-dependent phase progression from Ga-analcime (ANA) at low Si/Ga ratios through Ga-MAZ to TNU-7 and finally Ga-mordenite (Ga-MOR) at high Si/Ga ratios. In the absence of Ga (i.e. when Me = Al), aluminosilicate MOR was the only crystalline product obtained. The synthesis results suggest, therefore, that the phase selectivity of the crystallisation is strongly affected not only by the presence of Ga in the synthesis gel, but also by its concentration.

	Product[a,b]			
SiO_2/Me_2O_3 ratio	M = Na		M = K	
in the gel	Me = Ga	Me = Al	Me = Ga	Me = Al
5	Ga-ANA	amorphous	Ga-MER[c]	amorphous
6	Ga-ANA + Ga-MAZ	amorphous		
8	Ga-MAZ + TNU-7			
9	TNU-7			
10	TNU-7	Al-MOR	feldspar	Al-MER
12	Ga-MOR			
15	Ga-MOR			
20	Ga-MOR	Al-MOR	feldspar	amorphous
40	Ga-MOR + (kenyaite)	Al-MOR	feldspar	Al-FER
80	Ga-MOR + kenyaite		feldspar	Al-FER + (L)
∞	kenyaite		quartz	

Table 5.6: Summary of results of syntheses conducted with varying Si/Ga ratios and in the presence of Al and K. Gel Composition $2.0M_2O{\cdot}xMe_2O_3{\cdot}10SiO_2{\cdot}150H_2O$.
[a] The phase appearing first is the major phase, and the product obtained in a trace amount is given in parentheses. [b] ANA, analcime; MAZ, mazzite; MOR, mordenite; MER, merlinoite; FER, ferrierite; L, unknown but probably layered phase. [c] The material obtained after 4 days of heating at 150 °C.

However, dependence also exists on the identity and concentration of the extra-framework cation present. Replacing Na with K yielded feldspar in the presence of Ga, and aluminosilicate merlinoite (MER) when Ga was replaced with Al (regardless of gel

composition). Furthermore, it is noted that an increase in Na/Si ratio from 0.2 to 0.4 resulted in the formation of a gallosilicate natrolite (NAT) zeolite from synthesis mixtures with Si/Ga ratios ranging from 5 to 20. In analogy with the $(Na,K)GaSiO_4$ system discussed in Chapter 4, it appears that the presence of both Na and Ga in the synthesis mixture at well defined levels of concentration is necessary for directing the crystallisation of TNU-7, as well as Ga-ANA, Ga-MAZ and Ga-MOR.

It is also noted that gels optimised for formation of TNU-7 failed to crystallise under static conditions, even after two weeks - as did syntheses performed at 100^{o}C. In addition, syntheses at 200^{o}C resulted in the formation of quartz and an unknown phase, illustrating the importance also of gel treatment.

The synthesis of TNU-7 in association with what can be viewed as its component structural elements (i.e. Ga-MAZ and Ga-MOR), suggests that this gallosilicate material is an example of what is termed a 'boundary phase'. This phrase was coined by Vaughan to describe novel intergrowth topologies whose crystallisation fields are surrounded by those of their component phases.[32,37]

To gain further insight into the structure-directing role of Ga in the crystallisation of this boundary phase, Hong and co-workers added a small amount (2% wt of the silica gel) of previously prepared Ga-ANA, Ga-MAZ, TNU-7 and Ga-MOR as seeds to gallosilicate gels with optimised compositions for the formation of the latter three phases (Table 5.7). After only three days, gels containing seed materials had already crystallised (compared to those with no seed, which required seven days). While Ga-ANA only seeded the crystallisation of Ga-ANA (with amorphous material), Ga-MAZ, TNU-7 and Ga-MOR appear to be capable of seeding the growth of any of these three phases, with the actual phase identity depending on the Si/Ga ratio and not the seed type. Therefore, the product selectivity from Ga-MAZ, TNU-7 and Ga-MOR seeding is independent of the structure type of the seed crystal employed. This implies that mor layers can be grown from maz layers and *vice versa*, as inferred from the similarities in layer connectivity identified in the respective phases. This aspect is discussed further in later sections.

SiO_2/Ga_2O_3 ratio in the gel	**Seed crystals used**	**Product[a]**
6	none	amorphous
	Ga-ANA	amorphous + Ga-ANA
	Ga-MAZ	Ga-MAZ
	TNU-7	Ga-ANA + Ga-MAZ
	Ga-MOR	Ga-MAZ + Ga-ANA
10	none	amorphous
	Ga-ANA	amorphous + Ga-ANA
	Ga-MAZ	TNU-7
	TNU-7	TNU-7
	Ga-MOR	TNU-7
20	none	amorphous
	Ga-ANA	amorphous + Ga-ANA
	Ga-MAZ	Ga-MOR
	TNU-7	Ga-MOR
	Ga-MOR	Ga-MOR

Table 5.7: Results of seeding experiments.

[a] The phase appearing first is the major phase.

5.3: Investigation of Chemical Zoning

Elemental analysis of Ga-MAZ, TNU-7 and Ga-MOR synthesised in the studies discussed above suggest Si/Ga ratios of 3.03, 3.85 and 5.89, respectively. The trend in these values is reflective of that observed in their synthesis gel Si/Ga ratios and suggests that Ga-MAZ favours higher Ga-loading than Ga-MOR. These data raised the question of whether TNU-7 could be comprised of alternating Ga-rich (maz) and Ga-poor (mor) layers and thus possess unique compositional zoning. Working at the limit of our in-house data, fractional occupancies of Si and Ga atoms were permitted to vary, under the constraint that occupancies of co-located atoms must sum to one. However, no

discernable difference in Si/Ga ratio was observed between the two structural layers, and it is thought that the data is not sensitive enough to variation in T-site occupancy to reveal such chemical zoning. Calculation of average T-O bond lengths in each layer type was also inconclusive.

A further possible means to probe the existence of chemical zoning is to examine the distribution of extra-framework cations and to calculate the extra-framework cation charge per T-site in each layer. A higher value would be expected for areas with elevated Ga content and therefore higher framework charge.

Synchrotron Powder XRD Studies of TNU-7 and Related Phases

To obtain a more accurate and reliable model for the distribution of Na^+ cations throughout the pore system of TNU-7, data were collected for a dehydrated sample at the ESRF, Grenoble. For comparison, data were also collected for dehydrated Ga-MAZ, Ga-MOR and samples of TNU-7 exchanged with a large univalent cation (Cs^+) and also a divalent cation (Sr^{2+}). The Ga-MAZ and Ga-MOR samples were synthesised by Hong in the synthesis series discussed above, while ion-exchanged samples of TNU-7 were prepared at St Andrews by stirring as-made Na-TNU-7 in 0.1 molar aqueous solutions of the nitrate salts of the desired cations at 70^{o}C for 4hr. The solutions were refreshed after the first hour. EDX analysis revealed that, while exchange by Cs^+ had progressed to 100% completion, exchange by Sr^{2+} had stopped at 90% giving approximate unit cell compositions of $Cs_{12.4}Ga_{12.4}Si_{47.6}O_{120}$ and $Sr_{5.58}Na_{1.24}Ga_{12.4}Si_{47.6}O_{120}$.

Structures were refined via the Rietveld method using the GSAS suite in a similar fashion to that described previously. Starting models for Ga-MAZ and Ga-MOR were taken from literature atomic coordinates for gallosilicate MAZ[34] and aluminosilicate MOR,[35] respectively. Background was fitted using the cosine Fourier series with 36 parameters. Peak shape was modelled using the pseudo-Voigt profile function. Si and Ga atoms were positioned on each T-site with fractional occupancies estimated from the bulk Si/Ga ratio, assuming that the Ga atoms were disordered over all T-sites. For mazzite, Si/Ga = 3.03, the Si occupancy was 0.752; for TNU-7 the values were 3.85 and 0.794 (as before); for mordenite, 5.89 and 0.85. T-O and O-O distances were constrained at values taken as weighted averages of Ga-O and Si-O tetrahedral bond

lengths in order to keep sensible framework geometries – these constraints were maintained throughout refinement of framework positions. Extra-framework cations were located via Fourier difference maps. Difference Fourier peaks located at reasonable distances from the framework were investigated as possible sites by refinement of occupancy and position. Extra-framework cations were refined with a single thermal parameter, as were all T-sites and oxygen atoms. The Ga-MAZ sample was found to contain small quantities of Na-TNU-7 impurity. This dataset was therefore analysed by a two-phase refinement.

Refined lattice parameters and associated Rietveld R_{wp} and R_p values for the refinements are shown in Table 5.8. Refined framework atomic parameters and selected bond lengths and angles for Na-, Cs- and Sr-TNU-7, Ga-MAZ and Ga-MOR are listed in Appendix B. Rietveld plots are illustrated in Figures 5.10 and 5.11.

	Space	**Unit cell parameters**			**Agreement factors**	
Material	**group**	*a* (Å)	*b* (Å)	*c* (Å)	R_{wp} (%)	R_p (%)
Na-Ga-MAZ	*P6$_3$/mmc*	18.1314(2)	18.1314(2)	7.6854(1)	9.36	7.40
Na-TNU-7		7.5721(1)	18.0739(2)	25.8438(5)	6.47	4.74
Cs-TNU-7	*Pmmn*	7.5692(1)	18.3157(3)	26.081(1)	6.67	5.61
Sr-TNU-7		7.5784(1)	18.0998(2)	25.926(1)	5.79	4.81
Na-Ga-MOR	*Cmcm*	18.0176(1)	20.2835(2)	7.49243(2)	7.05	5.62

Table 5.8: Refined lattice parameters and associated R_{wp} and R_p values as obtained from refinement of synchrotron data.

(a)

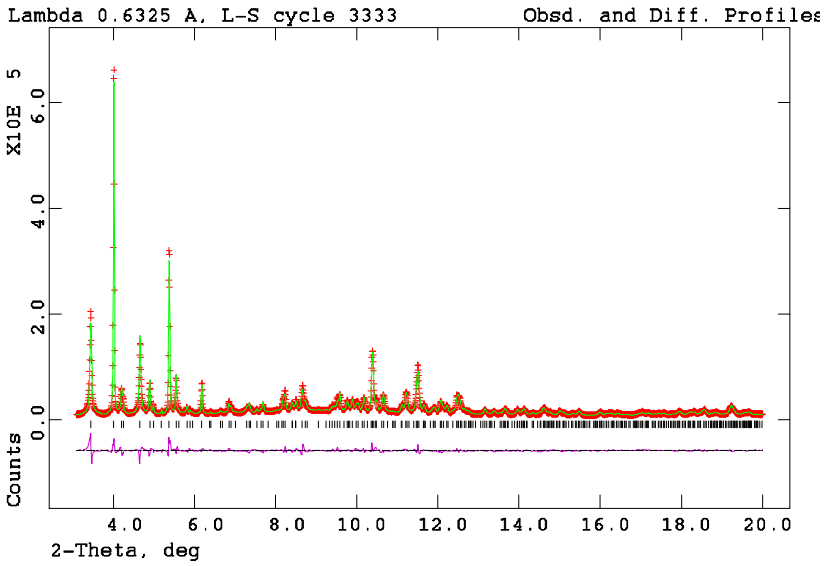

(b)

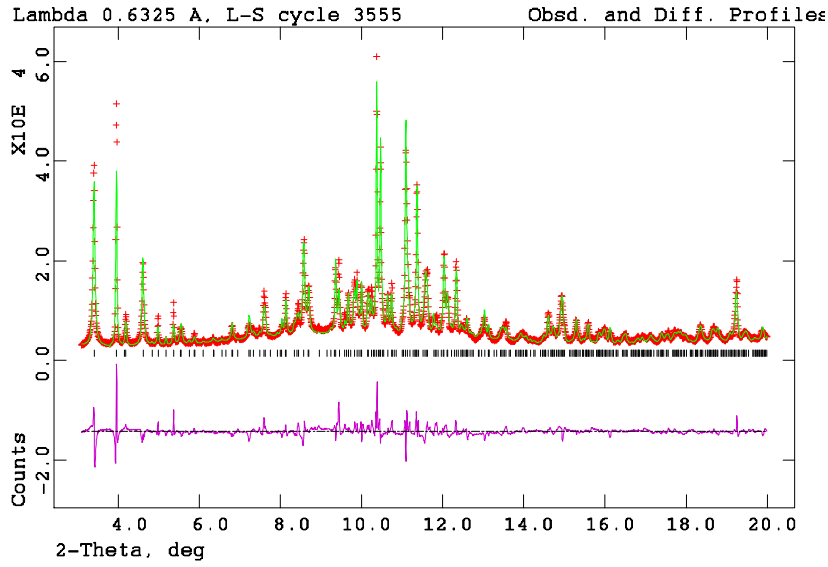

(c)

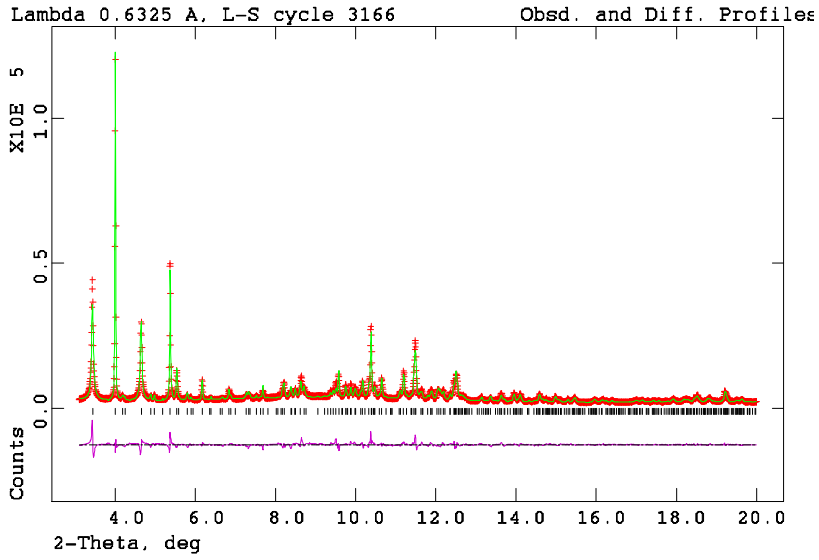

Figure 5.10: Rietveld plot from the refinement of (a) Na- (b) Cs- and (c) Sr-TNU-7 against synchrotron data. (red = experimental data, green = model, purple = difference).

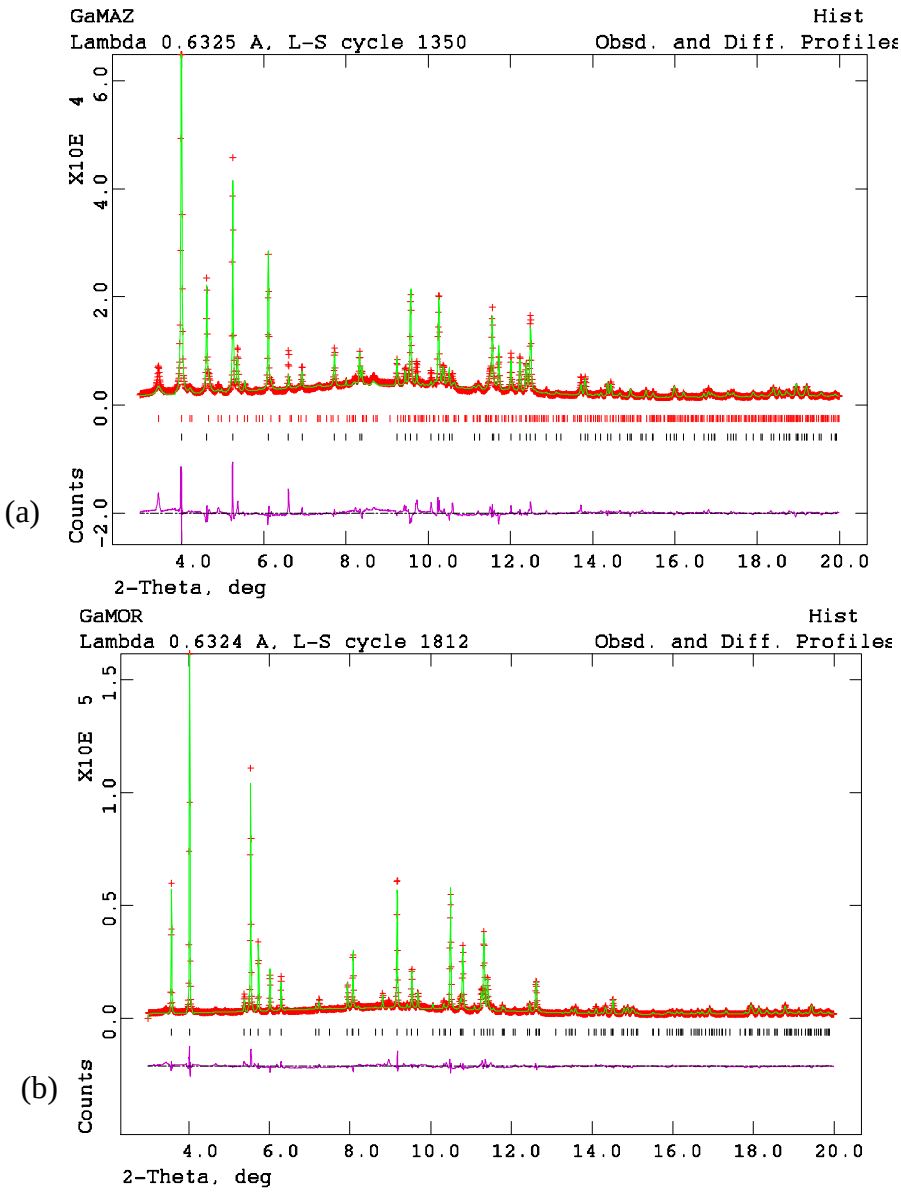

Figure 5.11: Reitveld plots for the refinement of (a) Ga-MAZ and (b) Ga-MOR against synchrotron data. (red = experimental data, green = model, purple = difference, red ticks mark reflection positions for TNU-7 impurity).

The refined positions and occupancies of Na^+ cations in TNU-7 are listed in Table 5.12 and illustrated in Figure 5.12. Six different Na^+ positions have been derived from Fourier difference maps and are labelled as A-F. In total, 11.7 ions out of the estimated 12.4 Na^+ ions required for charge balancing are located by the refinement. The locations of Na^+ cations in Ga-MAZ and Ga-MOR materials determined by Rietveld refinement of synchrotron XRD data are given in Figure 5.13. Since Ga-MAZ and Ga-MOR zeolites are closely related to the two components of the TNU-7 structure, as described above, it is of particular interest to consider the distribution of Na^+ in TNU-7 in terms of

competition between the structural environments present in the two layers. To our knowledge, no structural data on the gallosilicate analogues of MAZ and MOR zeolites prepared without recourse to organic SDAs have yet been reported in the literature.

Figure 5.12 shows that sites A and B (equivalent to Na1 and Na5, respectively, in previous refinements) are situated in the puckered 8-ring within the maz layer and smaller inter-strip channel, respectively. Site C (equivalent to Na7) is within the 8MR window entering the mor layer, while sites D (Na2) and E (not observed in refinements of laboratory data) are in the large channel associated with the maz strip. A further, previously unobserved position (site F) is in the 6-ring of the distorted gmelinite cage of the maz layer.

As expected, studies of extra-framework cation positions in Ga-MAZ and Ga-MOR reveal many similarities. In Ga-MAZ, where 7.3 ions of the estimated 8.9 Na^+ cations have been located, cations are found to occupy sites A and D. As illustrated in Figure 5.13, sites equivalent to B, C, and D are observed in Ga-MOR, where 6.4 ions of the estimated 7.0 Na^+ ions have been located. These locations compare well with literature reports of Na^+ cation positions in these phases, although a third position ('position 3') in the calcined, Na^+-exchanged form of Ga-MAZ material prepared with TMA as an organic SDA[34] is not observed in our Ga-MAZ. Fractional occupancies of sites B and C within the mor region of Na-TNU-7 are comparable to those in Ga-MOR, while this is not the case for site D. It is also noted that there are more cations in the large channel of Ga-MAZ compared with similar sites in the maz region of TNU-7. Indeed, site A in the maz layer is particularly favoured in Na-TNU-7 compared to the other sites. Of particular interest with respect to compositional zoning is the observation that the extra-framework cation charge per T-site in the distinct layers within Na-TNU-7 was calculated to be similar to those for the individual Ga-MAZ and Ga-MOR materials (Table 5.9). This indicates a higher framework charge per framework unit associated with the maz region of TNU-7 than with the mor region and therefore a larger Ga content within the maz layer, as is expected from simple stacking of maz and mor layers. This strongly suggests the presence of 'structural chemical zoning' in the TNU-7 framework, as defined above, although attempts to refine the Na-TNU-7 structure with Ga-rich and Ga-poor layers did not improve the fit.

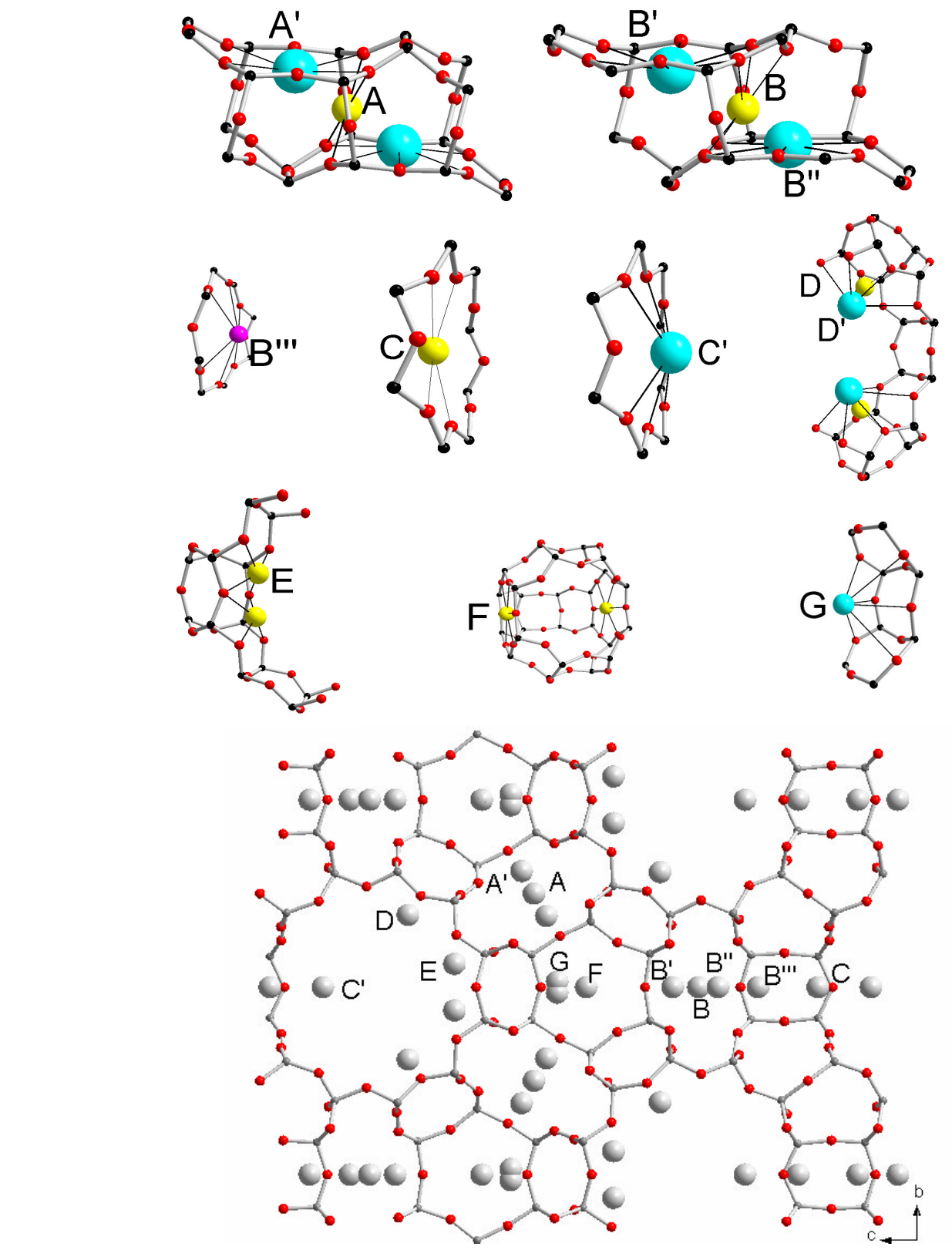

Figure 5.12: Refined extra-framework cation positions in TNU-7 located from refinement of synchrotron data.

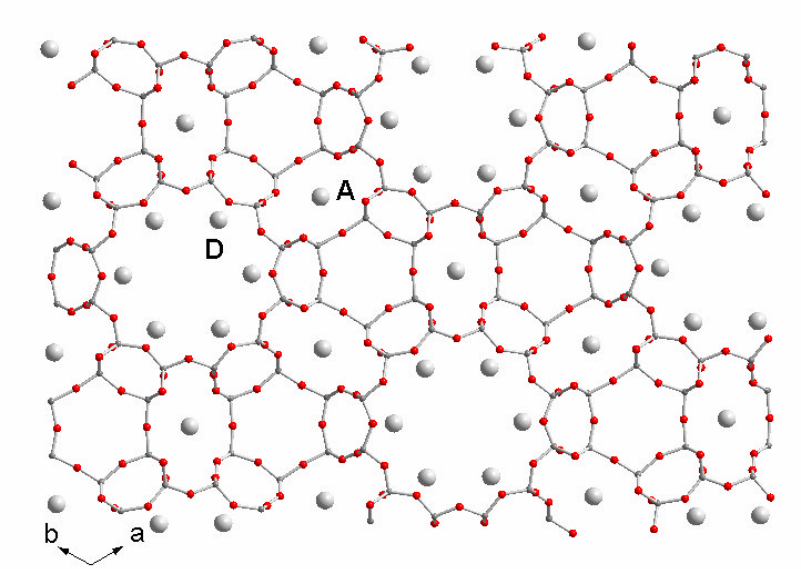

Site	*x*	*y*	*z*	Occupancy	Multiplicity
A	0.5	0	0	0.37(1)	6
D	0.239(1)	0.1196(4)	0.25	0.84(1)	6

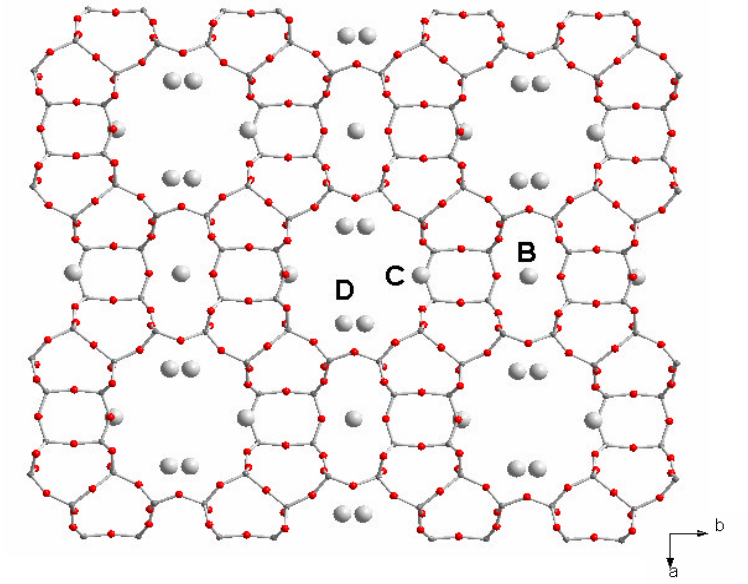

Site	*x*	*y*	*z*	Occupancy	Multiplicity
B_{mor}	0	0	0	0.55(1)	4
C	0	0.810(2)	0.112(3)	0.24(1)	8
D	0.169(1)	0.969(1)	0.25	0.29(1)	8

Figure 5.13: Refined extra-framework Na^+ positions in (top) Na-Ga-MAZ and (bottom) Na-Ga-MOR (from synchrotron data). (red = O, dark grey = Si/Ga, light grey = Na).

Material	Extra-framework cation charge per T-site	
	maz layer	mor layer
Na-Ga-MAZ	0.202	-
Na-TNU-7	0.267	0.090
Cs-TNU-7	0.225	0.090
Sr-TNU-7	0.208	0.145
Na-Ga-MOR	-	0.134

Table 5.9: Extra-framework cation charge per T-site in materials studied in this work.

Associated changes in cation distributions in TNU-7 caused by Cs^+ or Sr^{2+} ion exchange should be related to the charge and ionic radii of the different cations (ionic radii: Na^+, 1.02 Å; Cs^+, 1.67 Å; Sr^{2+}, 1.18 Å).[38] The refined locations of Cs^+ and Sr^{2+} in TNU-7 are listed in Tables 5.10 and 5.11, respectively. For Cs-TNU-7, 10.4 of the estimated 12.4 Cs^+ cations have been located: these occupy six different positions, which are denoted as A', B', B'', C', D', and G in Figure 5.12. Notably, sites A and B that were occupied by Na^+ are 'split' into two sites associated with the movement of the larger Cs^+ ion away from the puckered 8MR and into the adjacent, more planar 8MR, as illustrated in Figure 5.12. Similarly, positions C' and D' within the large channels are at longer distances from framework oxygens due to the larger ionic radius of the Cs^+ cation. While no evidence was found to suggest that sites E and F observed for the Na^+ ion are occupied, an additional site G was found close to 4MRs of the gmelinite cage. The increased cation size therefore has a strong influence on the cation distribution. Yet it is noticeable that the framework charge per T-site associated with the maz layers remains higher than that for the mor layers, again supporting the presence of chemical zoning within the TNU-7 structure.

Site	*x*	*y*	*z*	Occupancy	Multiplicity
A’	0.25	0.0597(2)	0.0225(2)	0.87(1)	4
B’	0.25	0.25	0.2532(3)	0.97(1)	2
B’’	0.75	0.25	0.349(4)	0.85(1)	2
C’	0.25	0.75	0.425(1)	0.28(1)	2
D’	0.75	0.6171(3)	0.2606(2)	0.625(5)	4
G	0.25	0.24(1)	0.0422(2)	0.047(4)	4

Table 5.10: Refined extra-framework Cs^+ positions in Cs-TNU-7 (positions illustrated in Figure 5.12).

Site	*x*	*y*	*z*	Occupancy	Multiplicity
A	0	0	0	0.56(1)	4
B	0.049(2)	0.25	0.2994(1)	0.485(5)	4
B’’	0.25	0.75	0.664(3)	0.11(1)	2
B’’’	0.37(1)	0.75	0.593(3)	0.071(5)	4
C’	0.19(1)	0.75	0.385(1)	0.065(4)	4
D	0.25	0.072(2)	0.758(2)	0.129(5)	4

Table 5.11: Refined extra-framework Sr^{2+} positions in Sr-TNU-7 (positions illustrated in Figure 5.12).

A similar result was obtained for Sr^{2+}-exchanged TNU-7. By refining all plausible extra-framework scattering as Sr^{2+} (rather than as residual Na^+), 5.5 ions of the expected 6.2 cations have been located and found to occupy sites A, B, C and D and would also appear to occupy sites B" and B"'. Partial occupancies of several close sites suggest that energies of Sr^{2+} are very similar in these different environments. As seen in Table 5.9, the charge per T-site in Sr-TNU-7 was found to be still higher in the maz layers than in the mor layers, although the difference is reduced.

Evidence from the distribution of extra-framework cations points, therefore, to there being greater charge associated with the maz regions of the TNU-7 structure, suggesting that there may indeed be greater Ga concentrations within these areas.

Powder Neutron Diffraction Studies of Na-TNU-7

Although extraframework cation charge per T-site may imply the existence of elevated Ga concentrations within the maz region of TNU-7, synchrotron data were also insensitive to subtle variations in T-site occupancies and average T-O bond lengths within the different layers. In an attempt to gain additional evidence for chemical zoning, and to further confirm the structure of TNU-7 as correct, powder neutron diffraction was conducted on a dehydrated Na-TNU-7 sample. Since neutron diffraction is more sensitive to oxygen atoms it was hoped that variations in T-O bond lengths might be more apparent from these data.

Refinement of the structure was conducted in the GSAS suite in an analogous fashion to that described above. Figure 5.14 illustrates the observed and calculated powder neutron diffraction patterns, refined in space group *Pmmn*. Final refined atomic coordinates, selected bond lengths and bond angles are listed in Appendix B. The refined unit cell parameters are a = 7.5838(4)Å, b = 18.088(1)Å, c = 25.841(1)Å, which are in close agreement with those determined from synchrotron data. A satisfactory R_{wp} of 3.04% (R_p = 4.04%) was achieved, confirming the correctness of the framework model.

The refined positions and occupancies of Na^+ cations in Na-TNU-7, where 11.9 ions out of the estimated 12.4 have been located, are compared to those located from synchrotron data in Table 5.12. While the same Na^+ positions are observed, there are a few discrepancies with the results from synchrotron XRD data. Notably, the occupancy of site B is almost doubled, which may be explained by the presence of residual water around this position. Indeed, the character of the background of the histograms reveals the presence of hydrogen, scattering neutrons incoherently. During refinement of neutron diffraction data the Na^+ ion in site F moved markedly and had to be fixed (Table 5.12). In addition, the occupancy of this site refined much lower than that obtained from synchrotron data, raising doubts as to whether this is indeed a true Na^+ site.

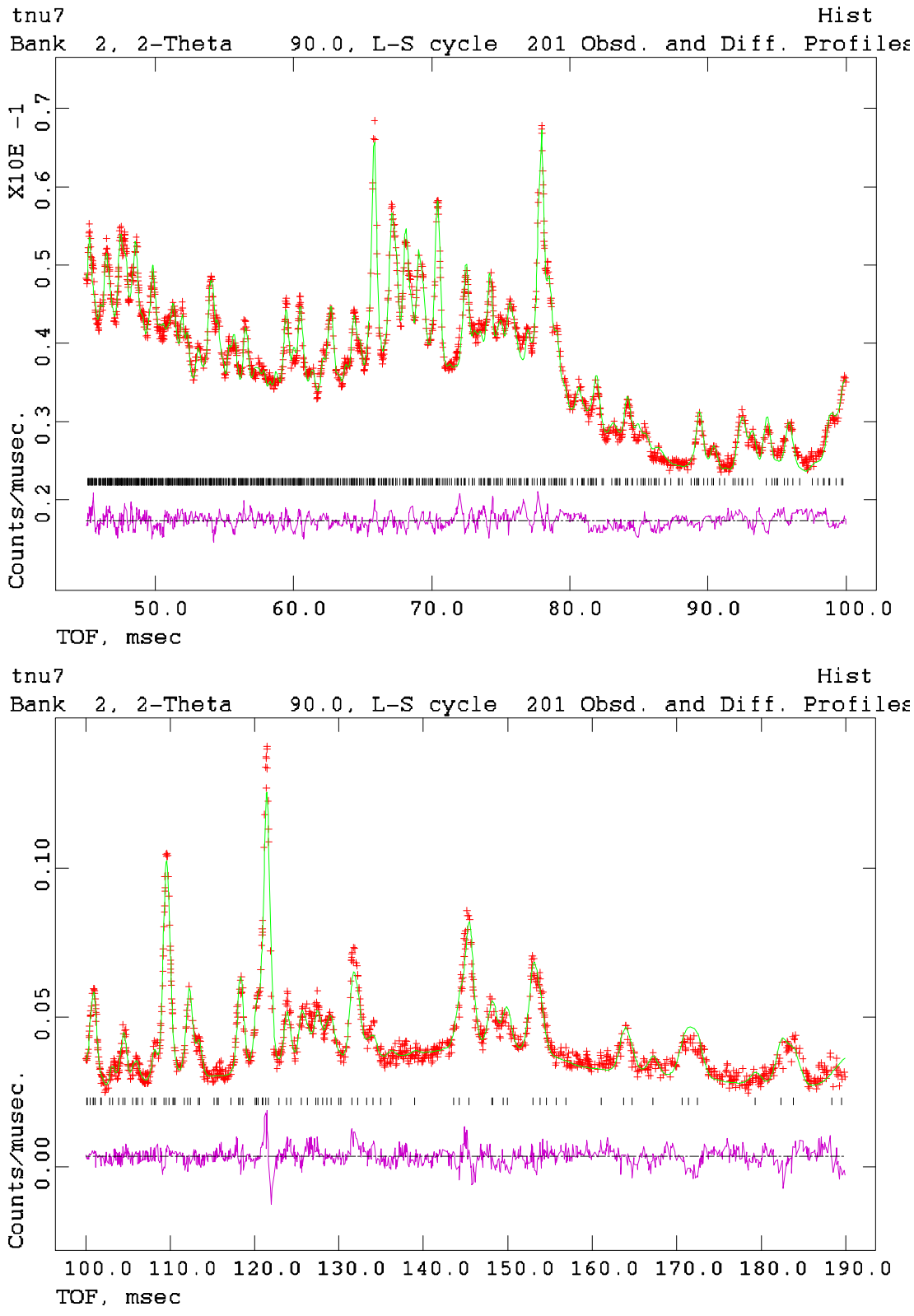

Figure 5.14: Reitveld plots from the refinement of TNU-7 against neutron diffraction data (red = experimental data, green = model, purple = difference plot).

Site	*x*	*y*	*z*	Occupancy
A	0 [0]	0 [0]	0 [0]	0.89(1) [0.64(3)]
B	0.059(3) [0.023(3)]	0.25 [0.25]	0.299(1) [0.286(1)]	0.59(1) [1 capped]
C	0.17(1) [0.28(2)]	0.75 [0.75]	0.482(2) [0.477(2)]	0.23(1) [0.28(3)]
D	0.75 [0.75]	0.557(1) [0.551(2)]	0.230(1) [0.274(2)]	0.67(1) [0.45(4)]
E	0.25 [0.25]	0.688(2) [0.728(2)]	0.145(2) [0.136(1)]	0.32(2) [0.56(3)]
F	0.25 [0.25]	0.75 [0.75]	0.905(2) [0.905]	0.45(2) [0.09(4)]

Table 5.12: Refined extra-framework Na^+ locations in Na-TNU-7 obtained from synchrotron and neutron (in square brackets) powder diffraction data.

Unfortunately, as with X-ray data, permitting individual T-site occupancies to vary did not reveal evidence of compositional zoning. Indeed, by manually fixing the compositions of the maz and mor layers to those of their respective phases, no discernable change in R values was observed, and it was therefore concluded that these data are not sufficiently sensitive to the variation in Si/Ga envisioned to be present. Similarly, calculation of average T-O bond lengths in the different regions of the TNU-7 structure (Table 5.13) was inconclusive. While a slightly larger value was observed for the maz region (as would be expected from it having a higher Ga content), the difference in values calculated for the separate layers is very small and hardly conclusive. Therefore, although neutron data have confirmed the structure model is correct, they are not as sensitive to variations in T-site occupancies and T-O bond lengths as was hoped to provide any firm evidence of chemical zoning. Nevertheless, it is noted that the extra-framework cation charge per T-site in the maz and mor layers within TNU-7 observed from neutron diffraction data are in reasonable agreement with values calculated from synchrotron XRD data. However, this remains our only evidence to suggest the presence of chemical zoning within this structure.

5.4: A Proposal for the Formation of Structural Chemical Zoning

As described above, TNU-7 is constructed by strict alternation of maz and mor layers. Such a perfect matching between both types of layers implies that maz layers may be built on mor layers, and *vice versa*. As a consequence, maz and mor layers may serve as

nucleation sites for each other, as revealed from seeding experiments. The nature of the growing layer, and hence the phase selectivity of the crystallization, however, is mainly governed by the SiO_2/Ga_2O_3 ratio of the synthesis mixtures, favouring Ga-MAZ and Ga-MOR at low and high ratios, respectively. At intermediate SiO_2/Ga_2O_3 ratios, the crystallization of TNU-7, with possible chemical zoning paralleling the alternation of maz and mor layers, is observed. It is therefore speculated that, at these intermediate gel compositions, the crystallization of Ga-rich maz layers may locally increase the SiO_2/Ga_2O_3 ratio in the mother liquor. If such is the case, this would then favour the next layer to be a Ga-poor mor layer, which, upon crystallizing, would locally decrease the SiO_2/Ga_2O_3 ratio in solution, thus favouring the next layer to be again a Ga-rich maz layer, and so on. Although a means by which to demonstrate this hypothesis has not been found, it would explain both the seeded synthesis results and the chemical zoning in TNU-7.

Framework region	Average T-O distance (Å)
mor	1.62
maz	1.63

Table 5.13: Average T-O bond lengths in the maz and mor regions of TNU-7 calculated from refined neutron diffraction data.

5.5: The EON Structure Code and ECR-1

Although the ECR-1A structure model had been proposed for aluminosilicate ECR-1, no structural refinement had been conducted on this material and no structure code was assigned. However, our refinement of the analogous and ordered TNU-7 structure has prompted the IZA Structure Commission to assign the EON structure code to this topology. The reporting of TNU-7, together with the assignment of the EON structure code, has encouraged the re-investigation of ECR-1, with results reported recently by Gualtieri *et al.*.[39] By employing the tetramethylammonium cation as an organic structure directing agent (SDA), and slightly different synthesis conditions to those reported by Leonowicz and Vaughan,[32] a sample of aluminosilicate ECR-1 was synthesised devoid of stacking faults permitting refinement of the intergrowth structure. Results of these

refinements are consistent with the structure reported for TNU-7 above. It is interesting to note that Na sites equivalent to sites A, B'' and E in TNU-7 were also observed in ECR-1, while two additional sites in the large channel (close to the mor layer) were also observed, perhaps reflective of variations in framework charge distribution between these two isotypes (although it should be noted that the refinement of ECR-1 was conducted on a hydrated sample and the assignment of sites to Na or water is difficult). Input of the three additional sites located by Gualtieri *et al.* to a refinement of TNU-7 against synchrotron data did not improve the data fit, and their occupancies refined to zero.

5.6: Summary

The novel sodium gallosilicate TNU-7 has been shown to possess a fully ordered intergrowth structure comprised of alternating layers of the well known phases MAZ and MOR. TNU-7 may, therefore, be regarded as the gallosilicate analogue of the aluminosilicate ECR-1. However, this is the first time that this highly unique topology has been refined and analysed in detail. TNU-7 may be regarded as a boundary phase whose crystallisation field is bounded by those of Ga-MAZ and Ga-MOR, and defined by the presence and concentration of both Ga and Na. As in the case of the stuffed tridymite series $(Na,K)GaSiO_4$ discussed in Chapter 4, there would appear to be a cooperative structure directing effect between Ga and Na to create a phase progression from Ga-ANA to Ga-MAZ, TNU-7 and Ga-MOR as the Si/Ga ratio in the synthesis gel is increased. The distribution of extra-framework cations in this novel topology has been examined extensively through laboratory X-ray, synchrotron and neutron powder diffraction techniques and suggests a higher charge associated with MAZ layers. This may be indicative of elevated Ga levels within these areas of the TNU-7 structure and points to the possible existence of a unique structural chemical zoning phenomenon.

Chapter 6: Structural Studies of the Aluminosilicate TNU-9

6.1: Determining the Unit Cell

As mentioned in the introduction to Part 2, the aluminosilicate material denoted TNU-9 is one of several materials synthesised hydrothermally in the presence of 1,4-bis(N-methylpyrrolidinium)butane (1,4-MPB). Powder X-ray diffraction data for a calcined and dehydrated sample recorded both in-house (λ = 1.540560Å) and at synchrotron sources at Daresbury (λ = 0.995559Å) and Grenoble (λ = 0.801240Å) proved difficult to index despite excellent resolution (Figure 2.10) and exhaustive attempts. However, electron diffraction studies, conducted by the group of Osamu Terasaki (Stockholm), suggested a triclinic cell of a = 17.34Å, b = 20.03Å, c = 19.62Å, α = 90.2^o, β = 90.2^o, γ = 125^o. Refinement of these parameters against synchrotron powder X-ray diffraction data yielded a cell of a = 17.3053(2)Å, b = 20.0094(1)Å, c = 19.4899(2)Å, α = 89.939(1)^o, β = 91.930(1)^o, γ = 125.389(1)^o (Figure 6.1(a)). This unit cell was subsequently rearranged to monoclinic a = 28.2219Å, b = 20.0123Å, c = 19.4926Å, β = 92.33^o (Figure 6.1(b)) in space group *C2/m*. Nevertheless, the presence of unindexed lines maintained doubts as to whether the indexing was indeed correct. However, subsequent syntheses have proved these additional reflections to be due to an impurity phase – thought to be NU-87.

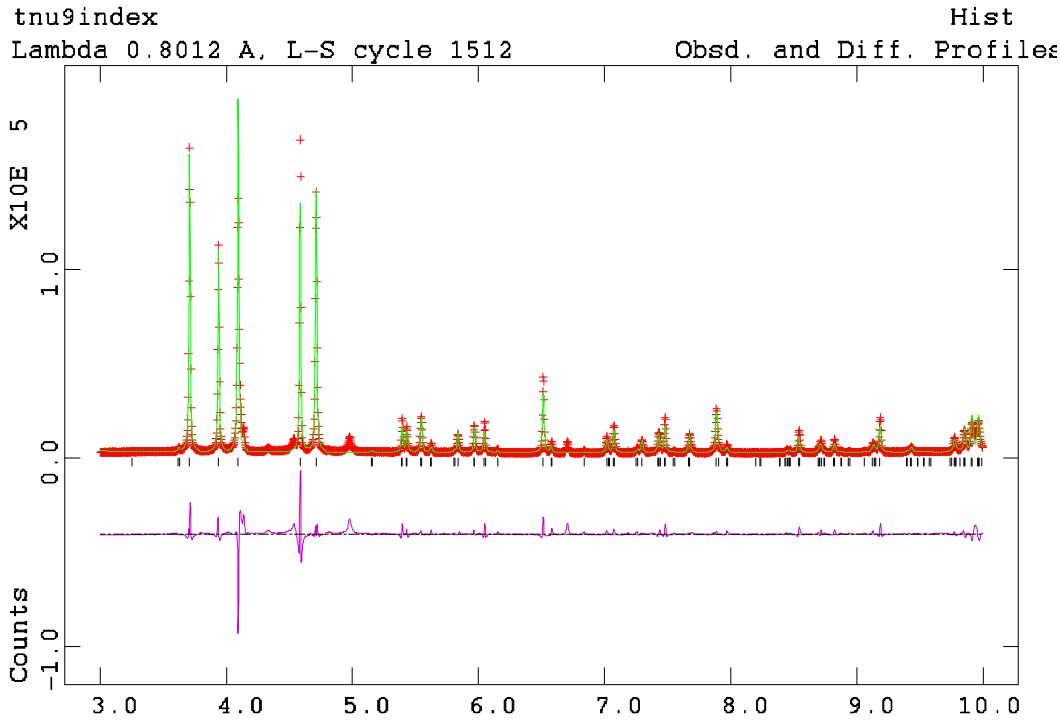

(a)

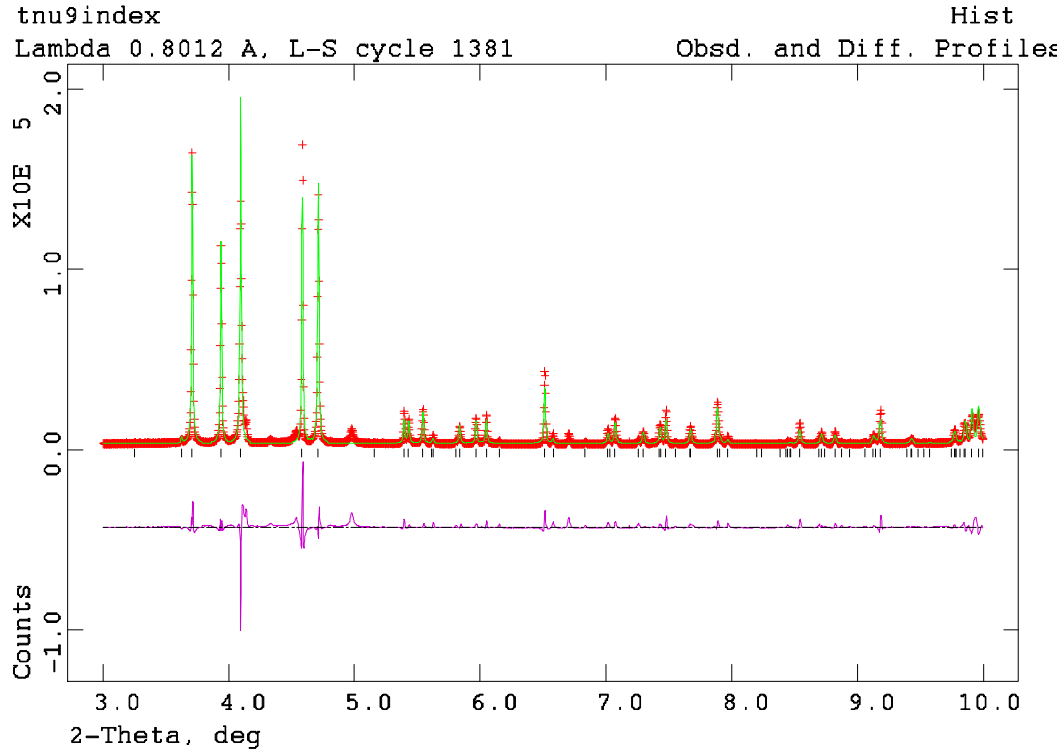

(b)

Figure 6.1: Comparison of (a) refined electron diffraction unit cell and (b) rearranged monoclinic unit cell with synchrotron powder X-ray diffraction data (3-10^{o} 2θ). Theoretical peak positions indicated by black tick lines.

6.2: Model Building Studies

Following the establishment of a plausible unit cell, it was estimated that TNU-9 would contain 24 crystallographically unique T-sites. The solution of a structure of this complexity from powder diffraction data alone appeared to be beyond the limits of current structure solution methods.

High quality HRTEM (High Resolution Transmission Electron Microscopy) images of TNU-9 were recorded at Stockholm. The projection down [010] (Figure 6.2(a)) is tantalisingly similar to that of ZSM-5 (MFI) (although the other projections are clearly different, Figures 6.2(b) and 6.2(c)). The near atomic resolution of these HRTEM images and the similarity between unit cell dimensions of TNU-9 and MFI (a = 20.1Å, b = 19.7Å, c = 13.1Å) encouraged attempts to solve the structure by simple model building based on the MFI topology. It was hoped that, by studying and slightly altering the MFI framework, a plausible model could be obtained that maintains an MFI-like projection and possesses a doubling of the c-axis. Appendix C discusses the construction of the MFI topology as well as its relative MEL and also how several theoretical topologies can be built by altering the arrangement of the 5^8-cage building units. It became evident at an early stage that many such theoretical structures can be built by systematic variation of, for example, building unit connectivity and the relative orientations of adjacent chains and layers. However, none of these theoretical structures were found to possess the desired unit cell dimensions while maintaining the correct projection.

(a)

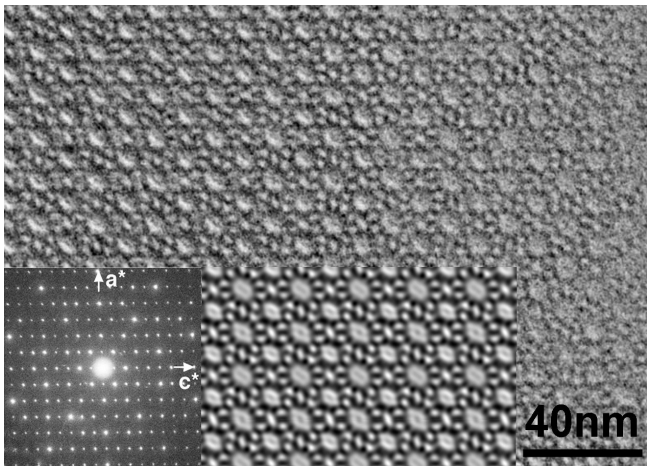

(b)

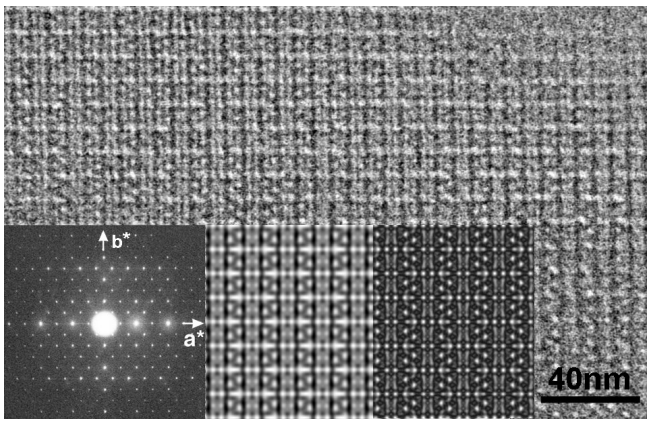

(c)

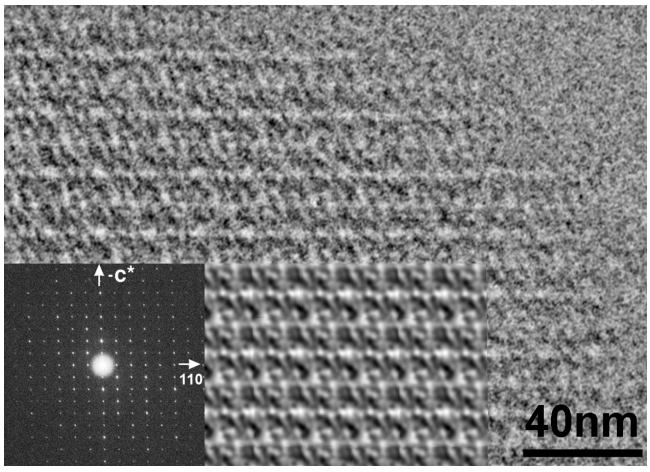

Figure 6.2: HRTEM images of the (a) [010], (b) [001] and (c) [110] zones of TNU-9.[40] *Corresponding SAED patterns and computer simulated images from the structural data are inset.*

6.3: Structure Solution

In parallel with model building studies, our synchrotron powder X-ray diffraction data were made available to Dr Lynne McCusker and her research group in Zurich, who were keen to test the data in their structure solution software FOCUS.

As discussed in Chapter 2, FOCUS partly compensates for the loss of information caused by the collapse of the three-dimensional single-crystal diffraction data onto the single axis of a powder diffractogram by including such chemical information as typical T-O bond distances, and O-T-O and T-O-T bond angles. For zeolitic materials, it is also known that each T-atom is four-connected to adjacent T-atoms via oxygen bridges giving a fully three-dimensional structure. In addition to these general constraints, Lynne McCusker and co-workers were able to glean phase information from electron diffraction and generate a nodal surface to represent the locations of pores as observed in HRTEM images. Thus by incorporating information from both X-ray and electron diffraction and HRTEM imaging into the FOCUS algorithm, the positions of all 24 T-atoms were established. The model was completed by insertion of bridging oxygen atoms and refined against synchrotron data for the calcined and dehydrated sample (R_{wp} = 15.6%). Details of the procedure are discussed in the subsequent paper published in Nature.[40] To our knowledge, this is the first time that powder data and HRTEM data have been employed simultaneously in the determination of an unknown structure. Moreover, with 24 crystallographically distinct T-atoms, the framework structure of TNU-9 represents the most complex zeolite framework known to date.

The structure of TNU-9 is remarkable in that two distinct 10MR channels, running parallel to the *b*-axis, are connected perpendicularly by short channels, which are also bounded at their narrowest by 10MRs. Figure 6.3(a) illustrates the projection of the framework down the *b*-axis and indicates the arrangement of the two main 10MR channels (denoted A and B) which lie between silicate layers: the internal surface of each of these channels is also illustrated (Figure 6.3(b)), indicating the difference in their internal dimensions. The shorter bridging channels are found to connect either between two of the narrower (B) channels or between a narrow (B) and a wider (A) channel, as illustrated in Figure 6.3(c).

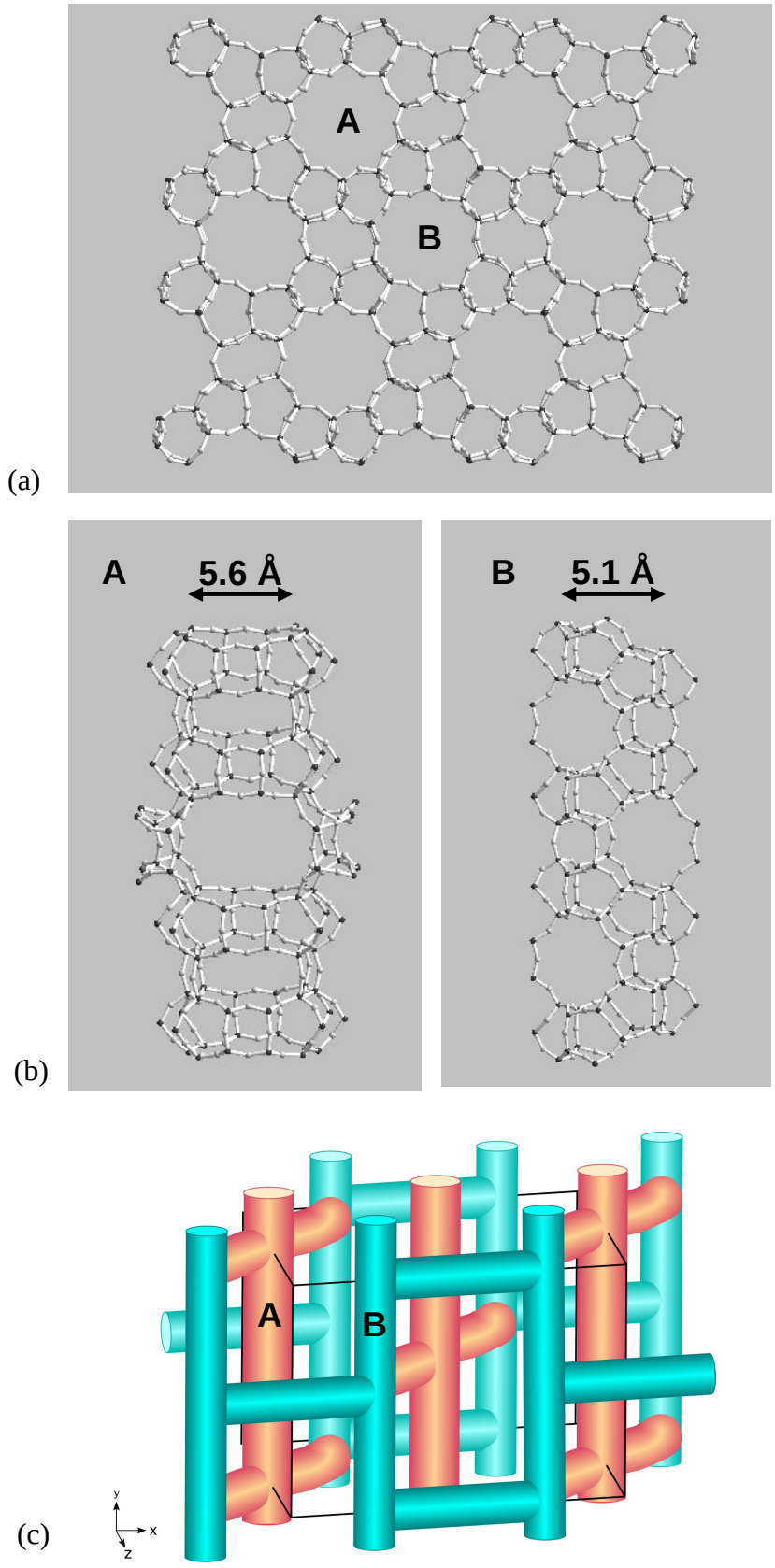

Figure 6.3: (a) Refined framework structure of TNU-9, (b) The two types of 10MR channels running parallel to the b-axis. (c) Illustration of the interconnecting pore network of the TNU-9 topology.

The framework of TNU-9 is crystallographically very complex and contains 24 symmetrically different tetrahedral sites. However, it may be regarded as being built from only one single type of chain composed of 4-, 5- and 6MRs (Figure 6.4). These chains extend along the *a*-axis and are linked into sheets in the *ab* plane via T-O-T linkages across mirror planes that are perpendicular to the *b*-axis (Figure 6.5). These sheets, which are asymmetric in that their two faces are different, contain 10MR openings that are ultimately responsible for the perpendicular connectivity between channels of type A and B. The sheets link along the *c*-axis to form the complete structure: each sheet is related to its neighbour by inversion (and 2-fold axes running down the centre of the A and B channels). Although each sheet is identical, due to their asymmetry there are two types of inter-sheet region and therefore two different channels. Also, as a consequence of their asymmetry, identical sides of two sheets cannot straightforwardly be linked.

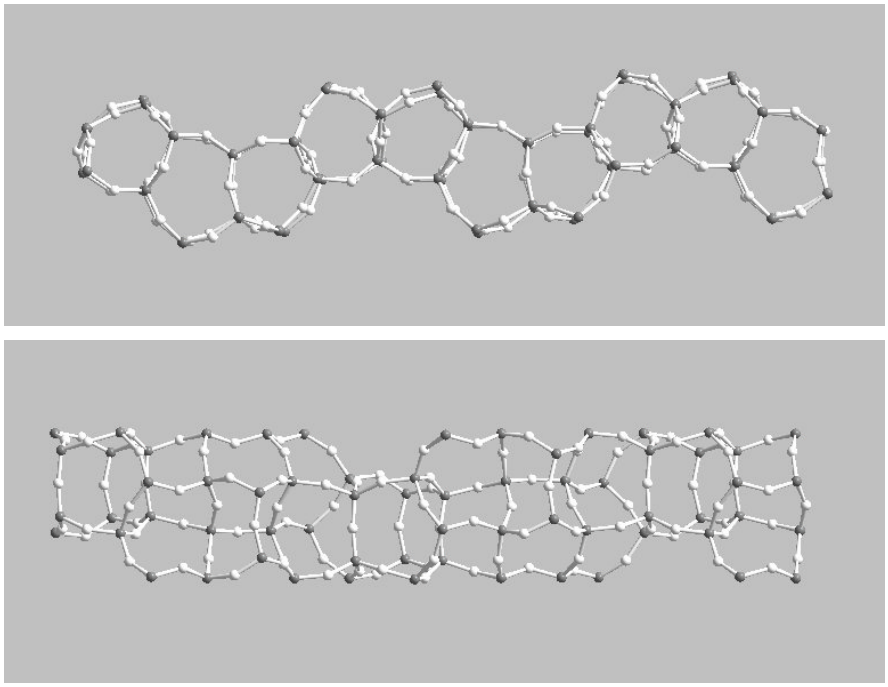

Figure 6.4: Detail of the chain unit from which the TNU-9 structure is built, viewed along the b-axis (top) and c-axis (bottom).

As observed in HRTEM imaging, the projection of the TNU-9 structure along the *b*-axis resembles very much that of the MFI topology. However, this has proved to be entirely coincidental and clearly thwarted model building approaches, which had assumed the structure to be composed entirely of 5^8-cages.

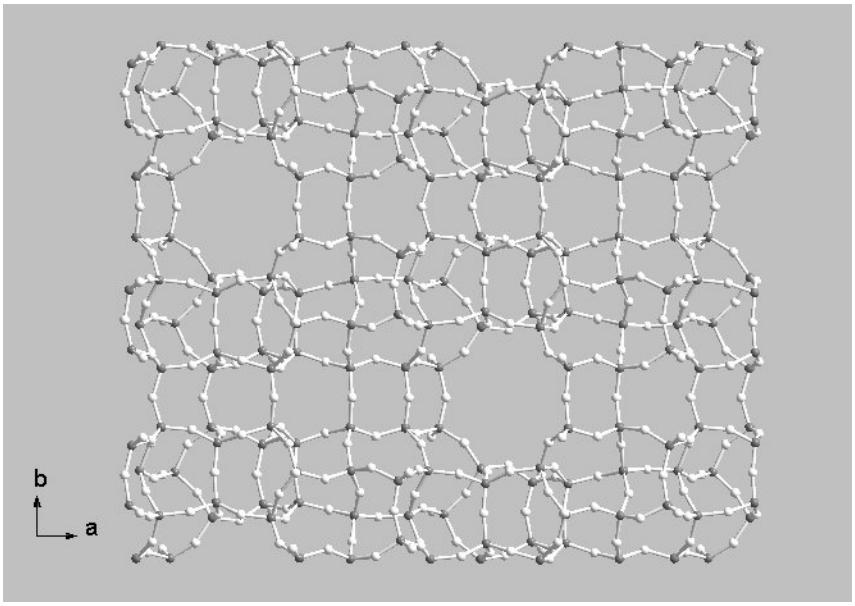

Figure 6.5: Detail of the silicate sheet found in TNU-9.

From elemental analysis, the unit cell composition was found to be $Na_{1.5}$(1,4-MPB)$_{3.9}$[1,4-MPB(OH)$_2$]$_{2.8}$Al$_{9.3}$Si$_{182.7}$O$_{384}$28.3H$_2$O, where OH has been introduced to compensate for the imbalance between framework and extra-framework charges. The TNU-9 topology has recently been assigned the TUN structure code by the International Zeolite Association.

The theoretical powder neutron diffraction pattern for the refined framework model was compared to data recorded for calcined and dehydrated TNU-9 at the pulsed neutron source of the ISIS facility (as outlined in the introduction to Part 2). Background was fitted by linear interpolation while a pseudo-Voigtian peak profile was utilised to model peak shape. The framework was modelled as completely siliceous. The unit cell refined to a = 28.177(2)Å, b = 20.030(1)Å, c = 19.464(1)Å, β = 92.344(4)^o, while isotropic thermal parameters for oxygen and silicon atoms (constrained together in their respective groups) refined to 0.03(2) and 0.07(3), respectively. Unfortunately these data were not of sufficient quality to support full structural refinement (cycles in which all framework atoms were permitted to move became unstable). Nevertheless, a reasonable enough fit was obtained (R_{wp} = 3.63%, R_p = 4.34%; Figure 6.6) from the as-solved model to suggest that the structure is correct.

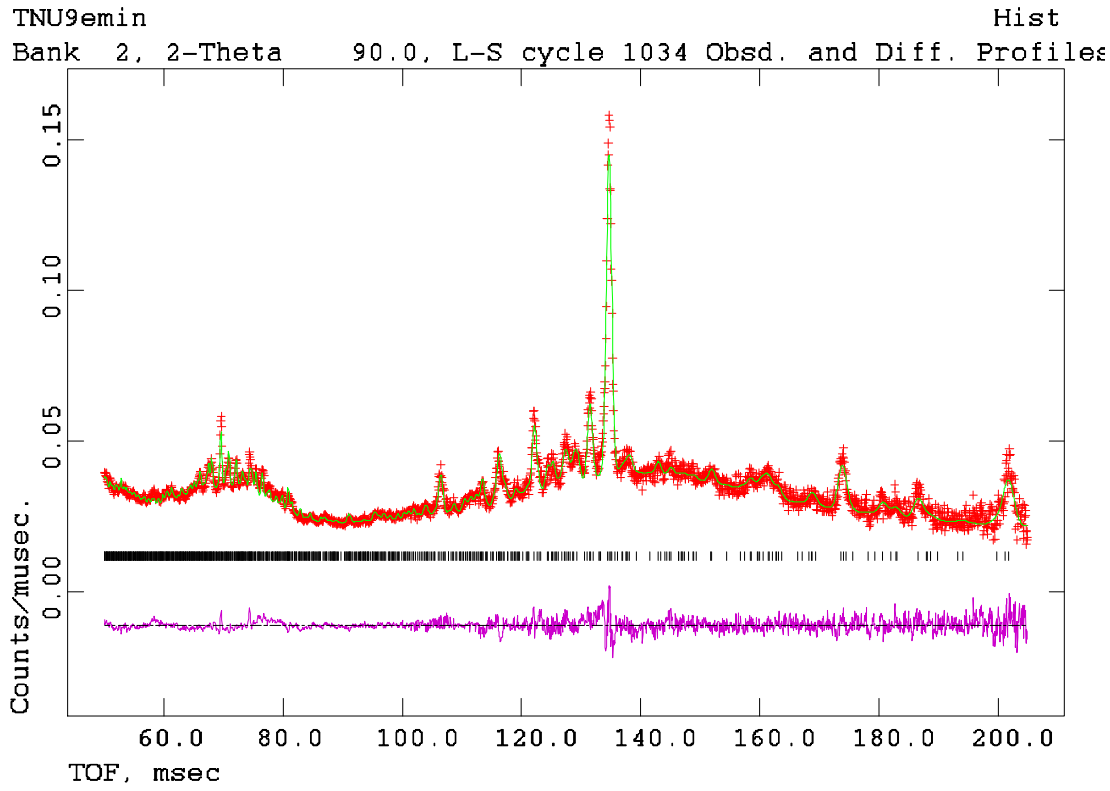

Figure 6.6: Rietveld plot from the refinement of TNU-9 against neutron powder data.

In collaboration with Dr Paul Cox at the University of Portsmouth, the as-refined framework was introduced to the energy minimisation program GULP to test whether the energy minimisation algorithm would generate the same structure. At first, the structure was modelled in *P1* symmetry to investigate whether the correct symmetry would be simulated. Unfortunately, due to the size of the unit cell and large number of framework atoms, this calculation proved beyond the scope of computing capabilities and therefore the correct symmetry (*C2/m*) was imposed on the model. Calculations were conducted under constant volume (i.e. fixed unit cell) and constant pressure (varying unit cell) conditions. Final total energies of -12.34keV were obtained from both calculations. The final unit cell obtained from the constant pressure calculation was a = 28.1598Å, b = 19.8708Å, c = 19.4405Å, β = 92.2270^{o} (to 4d.p.), in agreement with experimental results. Figures 6.7 and 6.9 compare the original structural model (blue) with those obtained from energy minimisation calculations (yellow) and illustrate the close similarity between experimental and simulation results.

The simulated powder X-ray diffractogram for the energy minimised structure (constant pressure run) is compared to experimental data collected for calcined and dehydrated

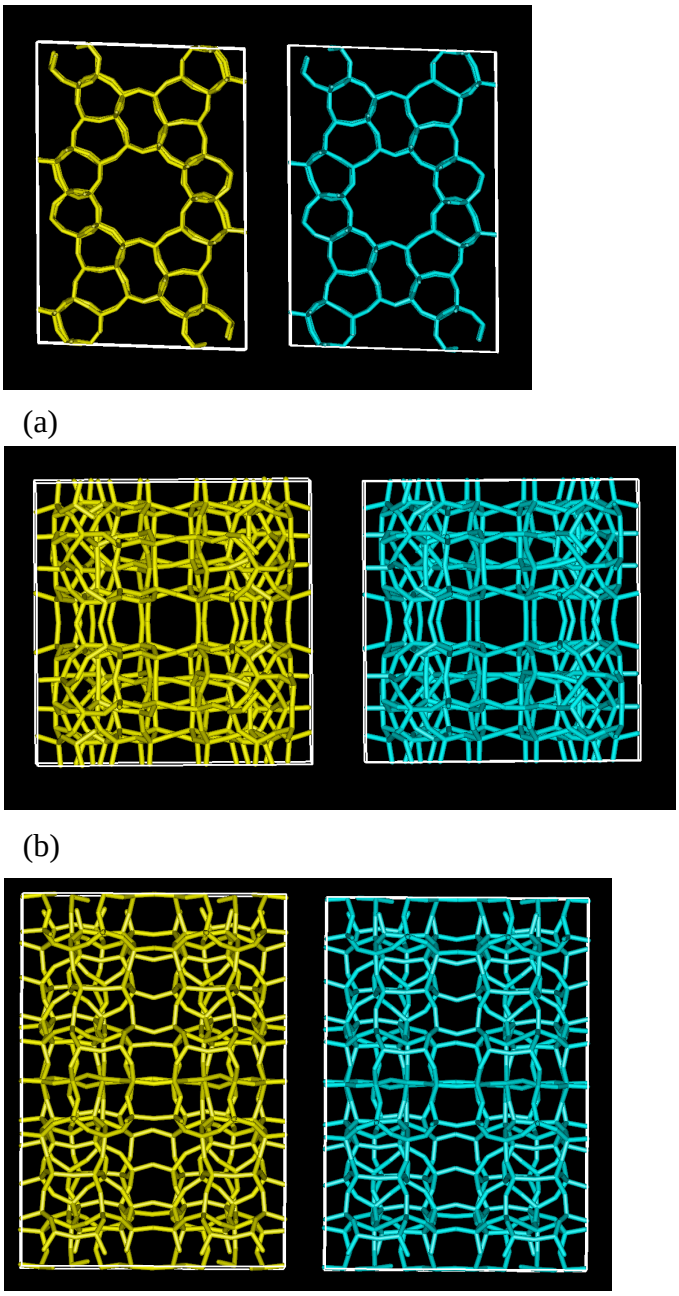

(a)

(b)

(c)

Figure 6.7: Comparison of experimental (blue) and energy minimised (constant pressure) (yellow) framework models of TNU-9, viewed along the b-axis (a), a-axis (b) and c-axis (c).

TNU-9 at the ESRF in Figure 6.8. Here, atomic coordinates were fixed at their energy minimised values while the unit cell and thermal parameters were permitted to vary (background and peak shape were modelled as before). The unit cell refined to a = 28.186(1)Å, b = 20.0324(5)Å, c = 19.469(1)Å, β = 92.321(3)^{o}, while Si and O isotropic thermal parameters refined to 0.02(2) and 0.04(2), respectively. Convergence was

achieved with respectable R_{wp} and R_p values of 10.89% and 9.55%, respectively, reflecting the close match between simulated and experimental models.

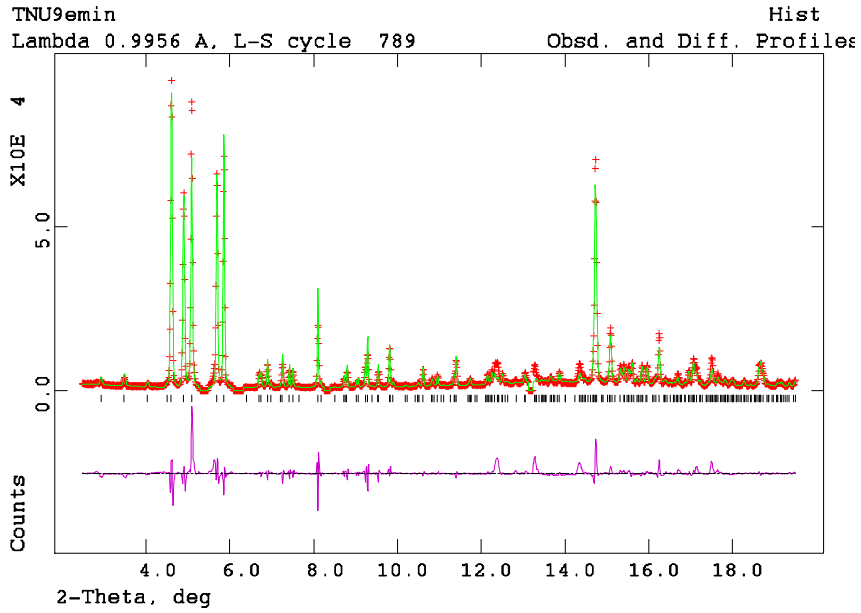

Figure 6.8: Comparison of simulated powder X-ray diffraction data for the constant pressure energy minimised model (green) with experimental data (red).

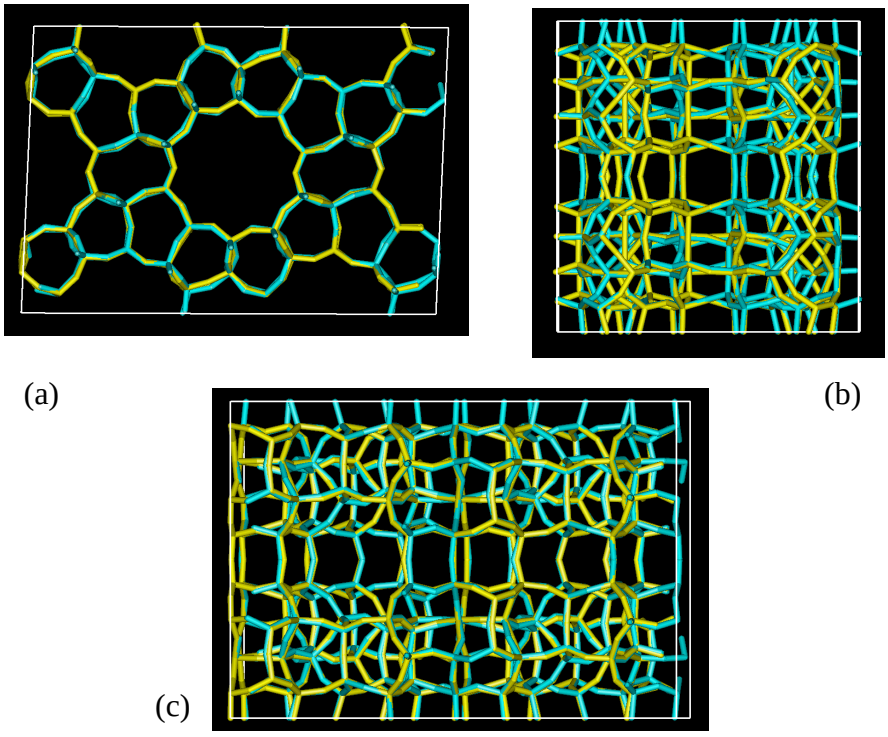

Figure 6.9: Comparison of experimental (blue) and energy minimised (constant volume) (yellow) framework models of TNU-9, viewed along the b-axis (a), a-axis (b) and c-axis (c).

6.4: Investigation of Template Locations in As-made TNU-9

In collaboration with Dr Paul Cox, modelling studies were performed to assess the role of the diquaternary cation as a structure-directing agent. The most energetically favoured locations of the molecule throughout the pore network were investigated in the program INSIGHT as outlined in the experimental section (page 63).

While chemical analysis indicates approximately seven templates per unit cell, a total of eight could be included per unit cell in the simulation. Four different template positions were determined from the modelling procedure, with a further four sites related to these by unit cell displacements of (0.5, 0.5, 0). Removal of any one of the modelled positions resulted in an increase in the total energy of the system by an amount equivalent to that associated with the removed template molecule, The non-bonding energies for each of the four unique positions, calculated for situations where the isolated molecule in each of the sites were simulated, are listed in Table 6.1. While all values are negative, it is notable that values for molecules 1, 2 and 4 are similar, while that for molecule 3 is higher.

Template number	Non-bonding energy (kcal)
1	-29.36
2	-33.50
3	-7.60
4	-26.60

Table 6.1: Binding energies for each template modelled within the TNU-9 pore network.

The four distinct template positions can best be considered in terms of their location within the inter-sheet regions of the framework, as viewed down the *b*-axis in Figure 6.10. The two different inter-sheet regions are denoted 1 and 2, and contain the larger A-channels and smaller B-channels, respectively. Two different positions were determined in each of the two inter-sheet regions.

In inter-sheet region 1, the diquaternary cations are arrayed head-to-middle-to-head, going along the A-channels (Figure 6.11). There are two clearly defined sites for template molecules within this area of the structure; one along the A-channel (labelled 1), and the second (labelled 2) within 'cages' where the main A-channels are intersected by the shorter bridging channels. Operation of the symmetry of the framework has little effect on the position of these template molecules since they are located about 2-fold axes and on mirror planes.

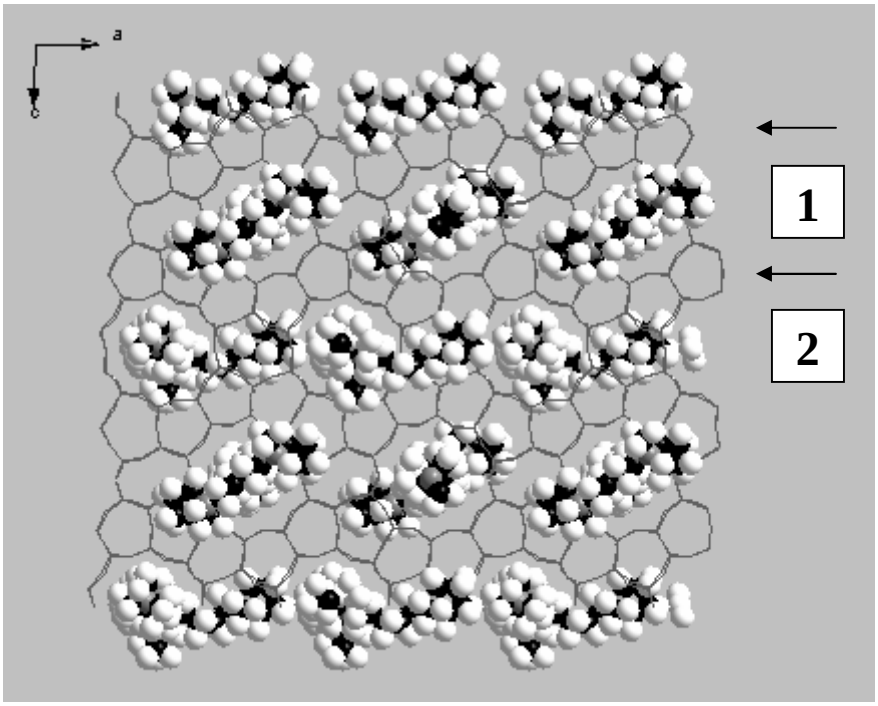

Figure 6.10: TNU-9 framework (oxygens not shown) with energy minimised template locations as viewed along the b-axis, illustrating the arrangement of template molecules between silicate sheets (indicated by arrows).

In inter-sheet region 2, it is found that pore space is again filled to a high degree by the template molecules in two positions (labelled 3 and 4). While position 4 lies along the B-channel, position 3 is in the bridging channel section between B channels. There does not seem to be enough space for molecule 3 to be fully extended and indeed this site has a less favourable non-bonding energy. If the symmetry operations of the framework are applied to these template positions, it is found that those running along the B-channels could be at several heights in the unit cell and that those in the short bridging channel sections can be displaced closer to either of the connected B channels, depending on the position of the templates in the B-channel. In this second inter-sheet region, template

molecules show both head-to-head and head-to-middle arrangements. The one shown in Figure 6.12 is one of a symmetry related set of such arrangements that all show this general motif.

(a)

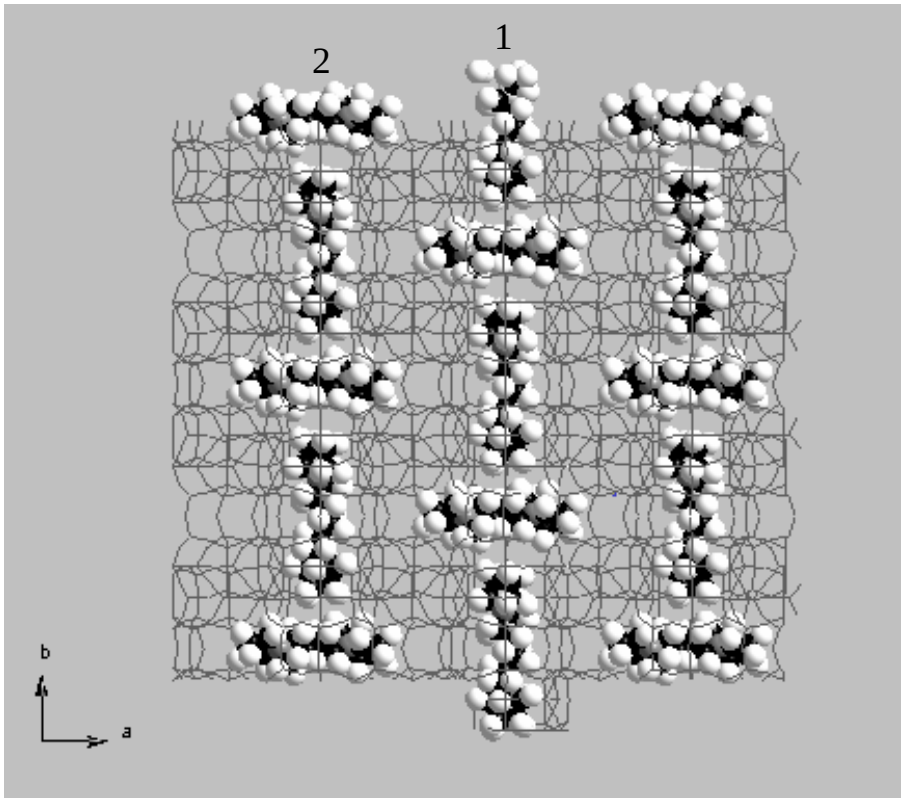

(b)

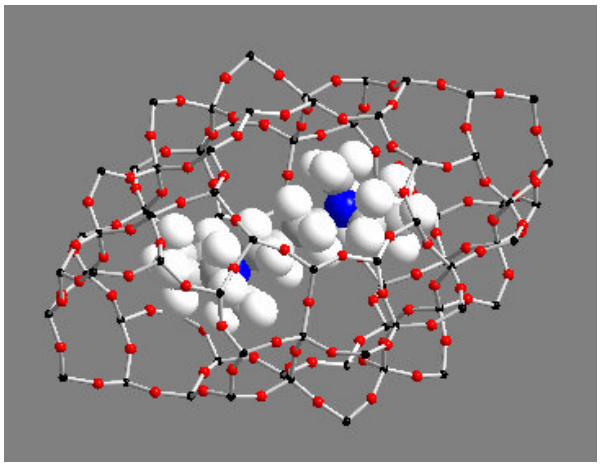

Figure 6.11: (a) Arrangement of energy minimised template locations found in inter-sheet area 1, and (b) detail of the cage located at the channel intersections, occupied by template number 2.

It is noted that the void space of the TNU-9 topology is almost completely filled by template molecules, and that the unique three-dimensionally connected channel system contains template molecules running along each of the channels. It is remarkable that

four different positions are assumed by the 1,4-MPB molecule under the reaction conditions (see below) employed resulting in the complex pore arrangement observed.

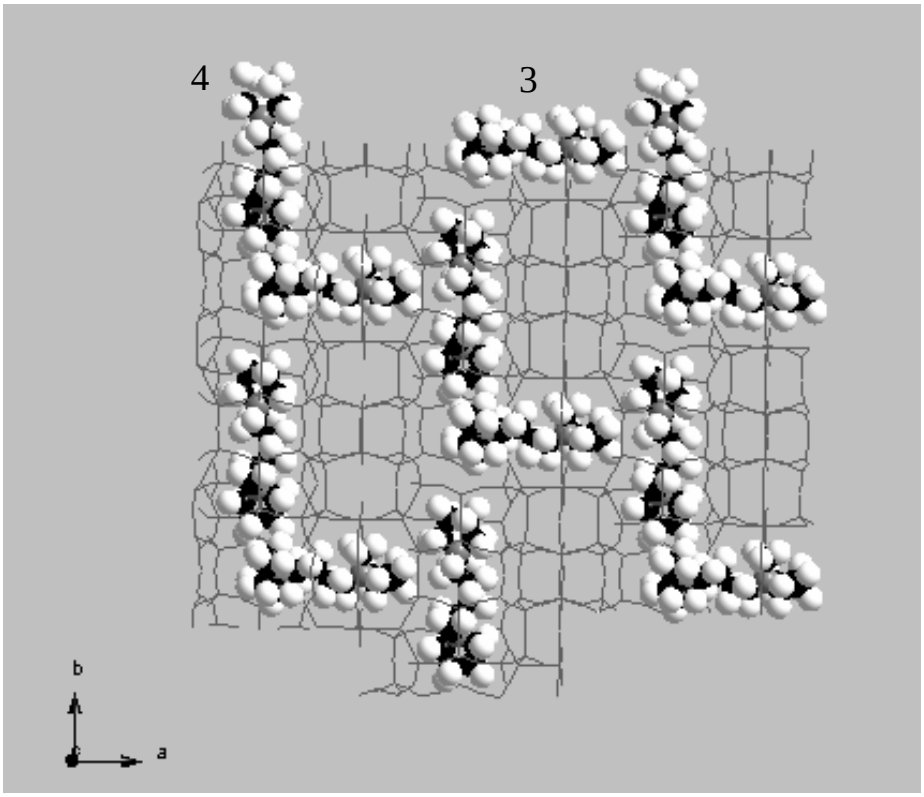

Figure 6.12: One possible arrangement of energy minimised template locations found in inter-sheet area 2.

High resolution synchrotron powder XRD data had been recorded for as-made TNU-9 on the Swiss Norwegian Beamline at the ESRF by the research group of Lynne McCusker, over the range 1-28^{o} 2θ (λ = 0.50007Å). It was therefore possible, and of interest, to compare the energy minimised model with experimental data. In a refinement conducted in the GSAS program, previously refined framework coordinates of the calcined material, along with energy minimised positions of template molecules were employed as a starting model (the framework was modelled as completely siliceous). Fractional occupancies of each template position (multiplicity of eight) were fixed at 0.25 to generate eight molecules per cell in approximate agreement with elemental analysis for the as-made material. Following refinement of instrumental parameters (peak shape fitted by pseudo-Voigt function, background fitted by linear interpolation), framework atom coordinates were permitted to refine. Si-O bond lengths

were constrained to be 1.61Å (σ = 0.005Å) and O-O distances within the same tetrahedra were constrained to be 2.63Å (σ = 0.01Å). These constraints were maintained throughout the course of the refinement. Template positions were fixed at their energy minimised locations. Isotropic thermal parameters of all Si atoms were constrained to be equal, as were those of all O atoms and those of all template atoms. Fourier difference maps revealed two areas of residual electron density within pore regions not occupied by the organic molecules. These may represent adsorbed water molecules and were introduced to the refinement as O atoms. While their occupancies refined greater than one (and were therefore capped at one), their inclusion improved the R values by approximately 1.5%, No further meaningful electron density peaks were identified. The final lattice parameters were a = 28.2377(4)Å, b = 20.0782(3)Å, c = 19.4531(4)Å, β = 92.593(1)^o, and final R_{wp} and R_p values of 13.47% and 9.55% were achieved, respectively. Appendix D1 lists refined atomic parameters and bond lengths and angles. Si-O bond lengths refined to values between 1.576(8) and 1.627(8)Å (Figure 6.13), while O-Si-O and Si-O-Si angles are found to lie in the ranges 102.0(9)-113.2(9)^o and 136(1)-179(2)^o, respectively, which are consistent with such values in zeolitic materials. Figure 6.14 illustrates the fit between observed and calculated data.

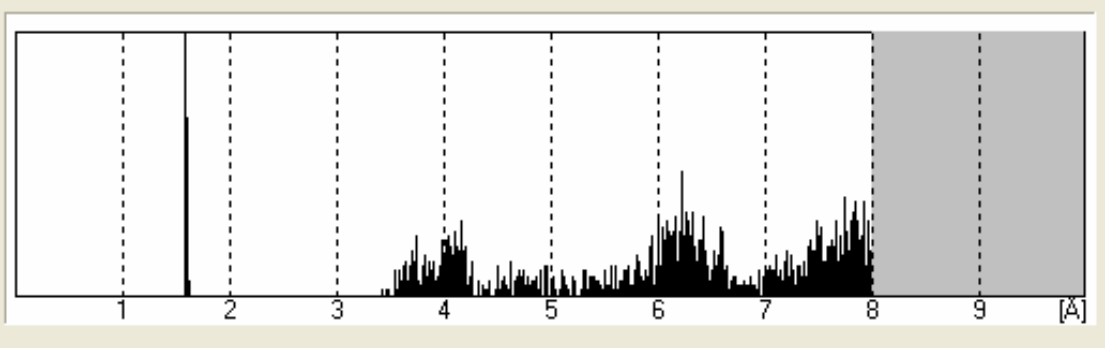

Figure 6.13: Distribution of Si-O distances in refined as-made TNU-9.

To probe the plausibility of the modelled template positions, their fractional occupancies were set to zero and allowed to refine (with all atomic fractional occupancies constrained to be equal). After only a few cycles, fractional occupancies had refined to 0.258(1). Attempts to allow the fractional occupancy of each template molecule to refine independently resulted in values of 0.263(2), 0.273(2), 0.266(2) and 0.227(3) for molecules 1, 2, 3 and 4, respectively. Consequently, fractional occupancies for

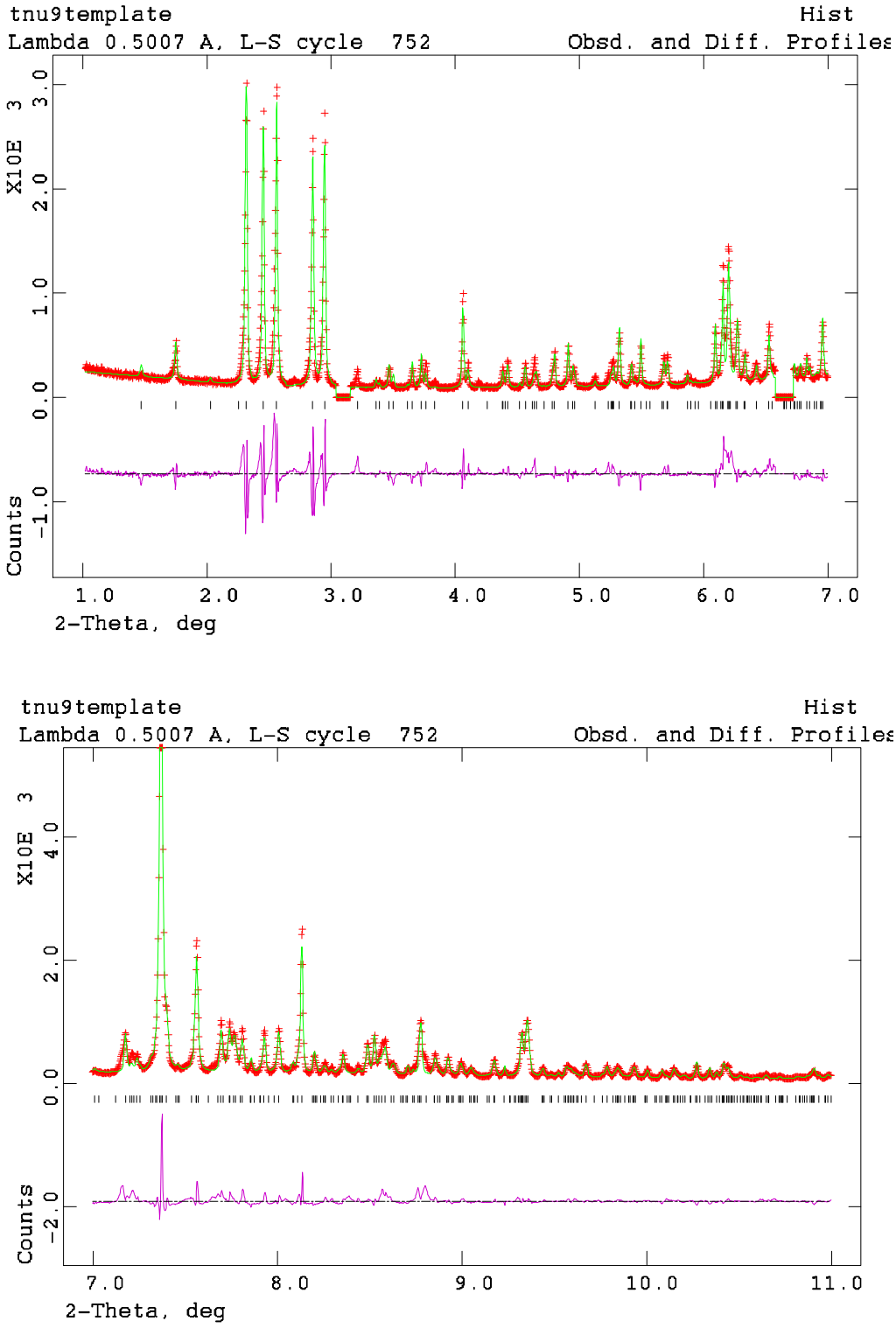

Figure 6.14: Rietveld refinement plots for as-made TNU-9 with template molecules fixed at energy minimised locations (red = experimental data, green = model, purple = difference plot). Peaks due to NU-87 impurity are excluded; lower plot is cropped at half the intensity of the most intense peak to afford improved detail.

molecules 1, 2 and 3 were capped at 0.25, while the occupancy of molecule 4 was permitted to refine. A final occupancy of 0.230(3) was obtained for this molecule, with a global isotropic thermal parameter of 0.009(9) for all molecules. R_{wp} and R_p values obtained were 13.35% and 9.50%, respectively. Refinement of template molecule occupancies after the inclusion of all H atoms to the refinement yielded values of 0.246(2), 0.232(2), 0.256(3) and 0.170(3) for molecules 1, 2, 3 and 4, respectively. The occupancy of molecule 3 was therefore capped at 0.25 and, with a globally refined thermal parameter of 0.04(1) for all template molecule atoms, final R_{wp} and R_p values of 13.13% and 9.30%, respectively, were achieved. Omission of all template molecules from the refinement resulted in final R_{wp} and R_p values of 28.12% and 20.93%, respectively.

In an additional refinement, freedom of movement was given to each molecule as a rigid unit (with H atoms included) – i.e. by constraining each atom in a given molecule to move by the same degree. (In doing so, however, flexing of the molecule is forbidden and therefore, in attempting to compensate, any observed movement may be artificial). The refinement was conducted as before with all framework, template and 'water' coordinates permitted to vary under the constraints discussed above. Isotropic thermal parameters for all framework, template and 'water' atoms were also refined. An improvement of approximately 0.5% was observed in the final R values (Figure 6.15). Template molecule occupancies were once again capped at 0.25 since their refinement at these new locations exceeded this maximum possible value.

Table 6.2 lists the observed shift for the four different template molecules. Movement of the molecules is, in general, not large (up to approximately 0.5Å), and greatest where molecule 4 has freedom to move along the main channel. However, this may not be an entirely real effect since this channel possesses a continuous cylinder of scattering generated by operation of the symmetry elements. Unfortunately the movement of molecule 4 resulted in overlap with molecule 3, and it is now not possible to select a symmetry related set of molecules in this inter-sheet region that avoids this overlap. It is possible that the position of molecule 3, being least favoured energetically, is only half occupied with the remaining space being filled by water, sodium ions and/or additional organic fragments (MAS NMR studies suggest that as well as the starting organic there could be fragments of other molecules present). This situation would overcome the

difficulties described above and would reduce the number of template molecules to seven, in closer agreement with elemental analysis.

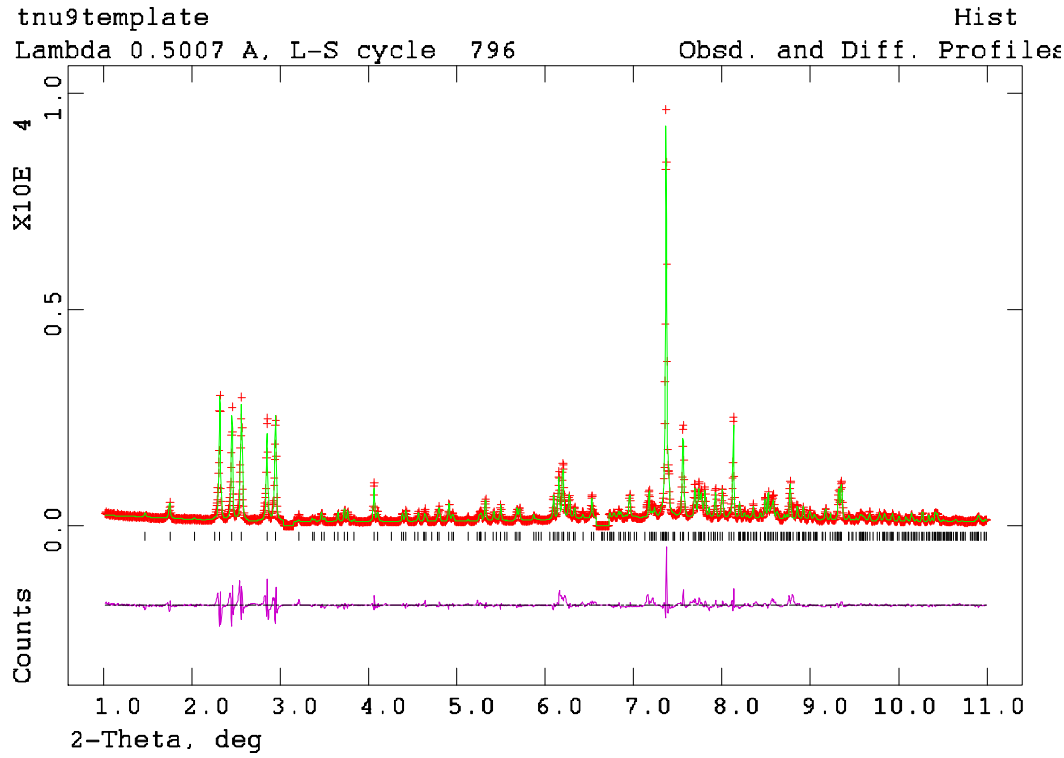

Figure 6.15: Rietveld plot for as-made TNU-9 after permitting template molecules to move as rigid units; R_{wp} = 12.49%, R_p = 8.91%.

Template number	Observed shift (Å)		
	x	*y*	*z*
1	-0.28	+0.39	-0.28
2	+0.05	-0.49	-1.15
3	+0.23	-0.56	-0.24
4	-0.06	+2.12	-1.15

Table 6.2: Movement (in Angstroms) observed in each 1,4-MPB molecule when allowed to refine as a rigid unit.

Starting from their energy-minimised positions, all template molecule atom coordinates were permitted to refine in a separate refinement (no H atoms included). In order to maintain a sensible model, C-C and N-C bond distances were constrained to 1.54Å (σ =

0.01Å) and 1.47Å (σ = 0.01Å), respectively, while tetrahedral geometry was maintained by constraining non-bonding $(C\text{-}C)_N$, $(C\text{-}C)_C$ and $(C\text{-}N)_C$ distances to 2.40Å (σ = 0.02Å), 2.51Å (σ = 0.02Å) and 2.46Å (σ = 0.02Å), respectively. Once again the occupancies of all template molecules were capped at 0.25. Template molecule thermal parameters were also fixed at their previously refined value of 0.0147 since they refined negative in this latest refinement. 'Water' molecule 2 was removed since it was found to encroach upon template molecule 2, and the occupancy and thermal parameter of 'water' molecule 1 were fixed at 1 and 0.025, respectively.

As before, molecules 3 and 4 were observed to overlap. The occupancy of molecule 3 was therefore reduced to 0.125 and Fourier difference maps were employed in an attempt to locate possible water molecules/sodium ions in the unoccupied space. Only one plausible position was identified within this region and was introduced to the refinement as an oxygen atom, improving the R_{wp} value by 1%. However, refinement of the complete model proved difficult with molecules 3 and 4 becoming distorted. The positions of molecules 3 and 4 were subsequently reset to and fixed at those obtained from energy minimisation calculations, with occupancies of 0.25.

During the refinement 'water' molecule 1 became too close to template molecule 2. Removal of this oxygen atom resulted in an increase in R_{wp} of 2%. The problem can be alleviated if the occupancy of this position is 0.5, thus permitting only those symmetry equivalent positions farthest (approximately 3Å) from molecule 2 to be occupied. The penalty paid in the goodness of fit upon halving this occupancy is partly offset by changing the atomic identity to Na and therefore increasing the scattering at this site (Figure 6.16). With template molecules 3 and 4 fixed at their energy minimised positions, framework coordinates and thermal parameters refining and atomic coordinates of template molecules 1 and 2 and 'Na' refining, final R_{wp} and R_p values of 13.66% and 9.63% were achieved, respectively (Figure 6.17 and Appendix D2). Figure 6.18 illustrates the refined positions of template molecules 1 and 2. Comparison with Figure 6.11(a) reveals that these molecules have refined to positions that are very similar to those found from energy minimisation calculations.

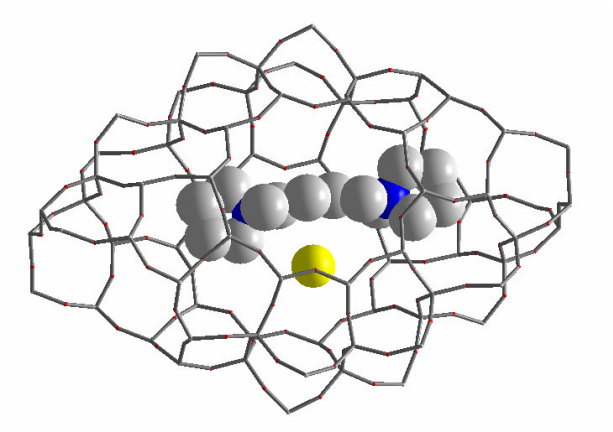

Figure 6.16: Relationship between template molecule 2 and possible Na position (yellow) within the cage located in inter-sheet area 1.

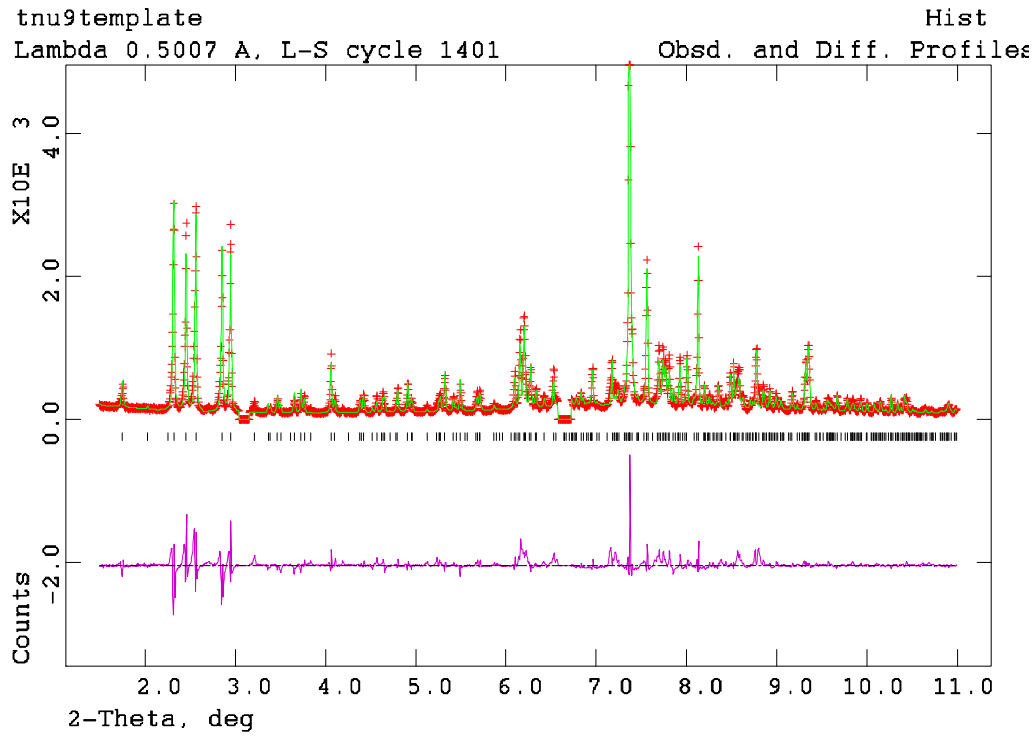

Figure 6.17: Rietveld plot for as-made TNU-9 after permitting atomic coordinates of template molecules 1 and 2 to refine individually.

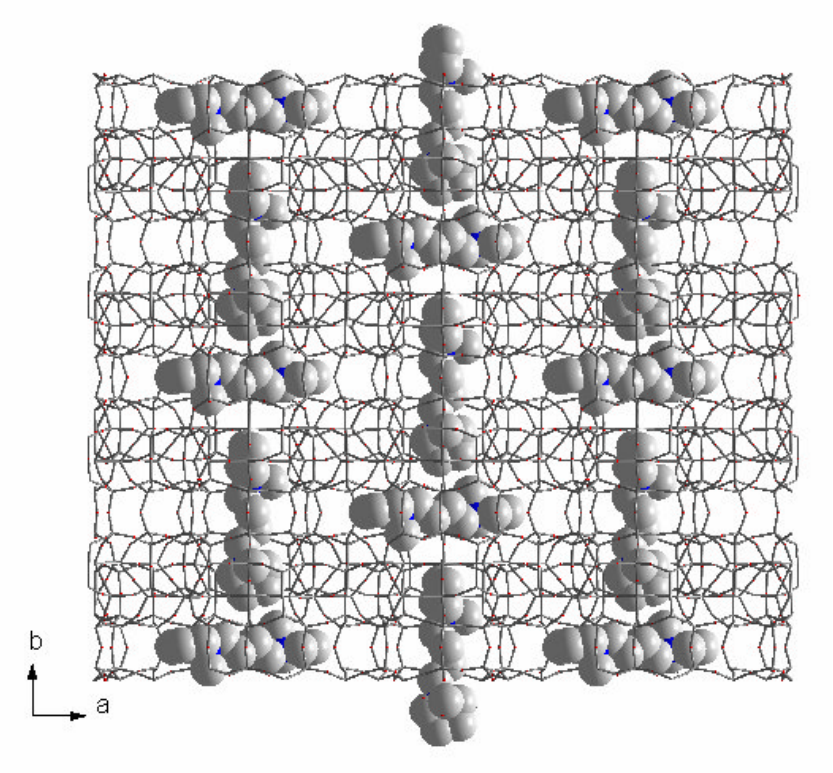

Figure 6.18: Refined locations of template molecules 1 and 2 within inter-sheet area 1.

The elemental analysis of the as-made TNU-9 suggests that there are, at maximum, seven template molecules per unit cell, and MAS NMR studies suggest that as well as the starting organic there could be fragments of other molecules present. Therefore, from the modelling studies, it is proposed that, while three of the four suggested sites are likely to be full of the initial template molecule (sites 1, 2 and 4), site 3 could contain other organic species and water molecules. This would not be expected to give a strongly different diffraction pattern.

6.5 Structure Direction in the Formation of TNU-9

As mentioned earlier, the 1,4-MPB molecule has been found to direct the formation of a number of different zeolitic materials from gels of composition 4.5(1,4-MPB) : xNa_2O : yAl_2O_3 : $30SiO_2$: $1200H_2O$ ($5 \leq x \leq 17$, $0 \leq y \leq 2$). Prof. Suk Bong Hong and co-workers have found that TNU-9, itself, crystallises within a very narrow range of SiO_2/Al_2O_3 and $NaOH/SiO_2$ ratios.[41] In general, crystallisation of phase-pure TNU-9 requires SiO_2/Al_2O_3 and $NaOH/SiO_2$ ratios of 60 and 73, respectively. Fixing any one of these ratios and varying the other was found to result in the formation of analcime

(ANA), mordenite (MOR), MCM-47, ZSM-12 (MTW), IM-5 and TNU-10 (STI) (Table 6.3). Furthermore, replacing NaOH with the equivalent amount of LiOH or KOH under conditions optimised for the formation of TNU-9 resulted in the formation of dense and amorphous phases. These results suggest that the selectivity of the 1,4-MPB molecule towards the structure-direction of different zeolitic materials is influenced strongly by the type and quantity of the alkali metal present. The structure-directing ability of 1,4-MPB would not appear to be robust enough to dominate over the effect of alterations made to the gel chemistry. However, it is emphasised that the presence of this structure directing agent in the synthesis gel is prerequisite for the successful crystallisation of TNU-9, even at otherwise optimised conditions.

It is interesting to note that syntheses conducted in the presence of a 1:2 mixture of 1,4-DBB (1,4-dibromobutane) and 1-MP (1-methylpyrrolidine) (precursors for the synthesis of 1,4-MPB) under conditions optimised for synthesis of TNU-9 were successful in yielding this phase – although it is thought that 1,4-MPB is formed in situ prior to crystallisation. However, TNU-9 was also obtained from gels containing a 1:3 mixture of these precursor materials after a crystallisation period of only six days. It is perhaps possible that 1-MP may act as an effective ‘co-template’ with 1,4-MPB in the synthesis of TNU-9. This aspect of structure direction – i.e. employing more than one type of organic additive – is discussed further in Part 3.

It is noted that, since none of the template molecules run through the framework sheets, connectivity between inter-sheet regions is not pre-programmed by the position of template molecules and would appear, in that sense, to be fortuitous. The model for the positioning of organic template molecules within the pore network of TNU-9 discussed above indicates that the same molecule is a close fit for each of the four positions it occupies, with one of the sites less favoured. Viewed differently, TNU-9 is a complex structure with four different template sites, all of which can be stabilised by the same molecule. There must be many possible structures in which there are sites that are sufficiently different that they would better be filled by two or more different structure directing agents. There is therefore a strong case for the use of co-templating strategies. For TNU-9, for example, it might be possible to find an alternative for the least favoured position (perhaps the reason for accelerated crystallisation reported in the presence of smaller additives).[42]

run no.	gel composition		Product[a]
	SiO_2/Al_2O_3	$NaOH/SiO_2$	
1	60	0.73	TNU-9
2[b]	60	0.73	Amorphous
3	15	0.73	analcime + (TNU-9)
4	30	0.73	mordenite + TNU-9
5	40	0.73	TNU-9
6	120	0.73	quartz + (TNU-9)
7	∞	0.73	MCM-47
8[c]	∞	0.73	MCM-47
9	60	1.00	TNU-10
10	60	0.87	TNU-9 + IM-5
11	60	0.60	ZSM-12
12	60	0.47	ZSM-12
13	60	0.73[d]	D + (ZSM-12)
14	60	0.73[e]	amorphous
15[f]	60	0.73	TNU-9
16[g]	60	0.73	TNU-9

Table 6.3: Summary of products obtained from 1,4-MPB by varying gel SiO_2/Al_2O_3 and $NaOH/SiO_2$ ratios. Crystallization was performed under rotation (100 rpm) at 160 °C for 14 days, unless otherwise stated. [a] The product appearing first is the major phase, and the product obtained in a trace amount is given in parentheses. D is an unknown but probably dense phase. [b] Run performed under static conditions. [c] Run performed after adding a small amount (2 wt% of the silica in the gel) of previously prepared TNU-9 as seeds to the gel. [d] LiOH/SiO_2 ratio. [e] KOH/SiO_2 ratio. [f] Run performed using a gel with the composition $4.5(1,4\text{-DBB})\cdot 9.0(1\text{-MP})\cdot 11Na_2O\cdot 0.5Al_2O_3\cdot 30SiO_2\cdot 1200H_2O$ at 160 °C for 10 days,. [g] Run performed using a gel with the composition $4.5(1,4\text{-DBB})\cdot 13.5(1\text{-MP})\cdot 11Na_2O\cdot 0.5Al_2O_3\cdot 30SiO_2\cdot 1200H_2O$ at 160 °C for 6 days.

Unlike the crystallisation of TNU-7, mixing of the synthesis gel by rotation during the crystallisation period has not been found to be a critical factor governing the synthesis of TNU-9, although static conditions required crystallisation periods of up to four weeks.

It is therefore evident that a well-defined level of Na^+ cations in the synthesis mixture, together with a reasonable level of lattice charge and the presence of 1,4-MPB are all necessary for the successful crystallisation of TNU-9. Since the conformation of a flexible organic structure directing species such as 1,4-MPB is likely to be influenced by the nature and extent of interactions between organic and inorganic components of the synthesis gel, it is possible that variation in the gel oxide composition result in sufficient conformational alteration to effect selection between the observed phases. At gel compositions specific for the synthesis of TNU-9, the 1,4-MPB molecule apparently adopts conformations suitable for the stabilisation of at least three, and possibly four, different pore environments.

6.6: Summary

The newly solved structure of aluminosilicate TNU-9 has been confirmed by refinement against neutron powder diffraction data, and energy minimisation studies. Investigation of the possible template molecule locations through energy minimisation techniques has revealed four unique locations within the unit cell. These are found to occupy pore regions between the structural sheets of the TNU-9 topology, filling most of the internal void volume. Comparisons with X-ray diffraction data for the as-made material suggest that the modelled positions are indeed plausible. It is noted that one modelled template position is particularly less favourable than the other three and it is possible that this channel region is, in fact, occupied by water and/or other organic fragments. It is remarkable that one molecule can stabilise at least three different environments in the crystallising framework – a phenomenon that only exists over a very narrow range of gel composition. There would appear, therefore, to be a co-operative structure-directing effect between the organic structure directing agent and inorganic gel components, perhaps via alteration of the 1,4-MPB molecular conformation.

References

1. H. H. Cho, S. H. Kim, Y. G. Kim, Y. C. Kim, H. Koller, M. A. Camblor and S. B. Hong, *Chem. Mater.*, 2000, **12**, 2292
2. M. A. Camblor, M. Yoshikow, S. I. Zones and M. E. Davis, *J. Am. Chem. Soc., Div. Petrol. Chem.,* 1995, **40**, 294
3. S. B. Hong, S. H. Kim, Y. G. Kim, Y. C. Kim, P. A. Barrett and M. A. Camblor, *J. Mater. Chem.*, 1999, **9**, 2287
4. K. G. Strohmaier and D. E. W. Vaughan, *J. Am. Chem. Soc.*, 2003, **125**, 16035
5. S. B. Hong, E. G. Lear, P. A. Wright, W. Zhou, P. A. Cox, C. H. Shin, J. H. Park and I. S. Nam, *J. Am. Chem. Soc.*, 2004, **126**, 5817
6. STOE Win XPOW (version 1.04), STOE & Cie GmbH, Hilpertstrasse, D-64296, Darmstadt, 1999
7. A. P. Stevens, A. M. Gorman, C. M. Freeman and P. A. Cox, *J. Chem. Soc., Faraday Trans.,* 1996, **92**, 2065
8. A. J. Perotta and J. V. Smith, *Mineral. Mag.,* 1965, **35**, 588
9. A. Putnis, *Introduction to Mineral Sciences*, Cambridge University Press, 1992
10. V. Kahlenberg, J. B. Parise, Y. Lee, and A. Tripathi, *Z. Kristallogr.,* 2002, **217**, 249
11. M. J. Buerger, G. E. Klein and G. Donnay, *Am. Mineral.,* 1954, **39**, 805
12. J. Barbier and M. E. Fleet, *J. Solid State Chem.,* 1987, **71**, 361
13. J. Barbier, B. Liu and J. Weber, *Eur. J. Mineral.,* 1993, **5**, 297
14. W. A. Dollase and W. P. Freeborn, *Am. Mineral.*, 1977, **62**, 336
15. H. Xu and D. R. Veblen, *Am. Mineral.,* 1996, **81**, 1360
16. M. A. Carpenter and D. Cellai, *Am. Mineral.,* 1996, **81**, 561
17. G. Lampert and R. Bohme, *Z. Krystallogr.*, 1986, **176**, 29
18. P. A. Sandomirskii, S. S. Mashalkin, I. V. Rozhdestvenskaya, L. N. Dem'yanets and T. G. Uvarova, *Sov. Phys. Crystallogr.,* 1986, **31**, 522
19. S. I. Zones, M. M. Olmstead and D. S. Santilli, *J. Am. Chem. Soc.,* 1992, **114**, 4195
20. (a) J. Barbier and M. E. Fleet, *Phys. Chem. Minerals,* 1988, **16**, 276, (b) R. P. Hammond and J. Barbier, *Acta. Cryst.*, 1998, **B54**, 211

21. M. Andreatschke, K. Range, H. Haase and U. Klement, *Z. Naturforsch. B*, 1992, **47**, 1249
22. M. Lujan, F. Kubel and H. Schmid, *Z. Naturforsch. B*, 1994, **49**, 1256
23. V. Kahlenberg, R. X. Fischer and J. B. Parise, *J. Solid State Chem.*, 2000, **154**, 612
24. H. Schulz, U. Zucker and R. Frech, *Acta. Cryst.*, 1985, **B41**, 21
25. J. Le Roy and S. Aleonard, *Acta. Cryst.*, 1993, **B28**, 1383
26. W. Horkner and Hk. Muller-Buschbaum., *Z. Anorg. Allg. Chem.*, 1979, **451**, 40
27. V. M. Harder and Hk. Muller-Buschbaum., *Z. Anorg. Allg. Chem.*, 1979, **448**, 135
28. B. Lui and J. Barbier, *J. Solid State Chem.*, 1993, **102**, 115
29. Barbier, B. Liu and J. Weber, *Eur. J. Mineral.*, 1993, **5**, 297
30. W. Leib and Hk. Muller-Buschbaum., *Z. Anorg. Allg. Chem.*, 1986, **538**, 71
31. S. J. Warrender, P. A. Wright, W. Zhou, P. Lightfoot, M. A. Camblor, C. H. Kim, D. J. Kim and S. B. Hong, *Chem. Mater.*, 2005, **17**, 1272
32. M. E. Leonowicz and D. E. W. Vaughan, *Nature*, 1987, **329**, 819
33. C. S. Hsia Chen, J. L. Schlenker and S. E. Wentzek, *Zeolites*, 1996, **17**, 393
34. J. M. Newsam, R. H. Jarman and A. J. Jacobson, *Mat. Res. Bull*, 1985, **20**, 125
35. (a) W. M. Meier, *Z. Kristallogr*., 1961, **115**, 439, (b) G. Maurin, R. G. Bell, S. Devautour, F. Henn and J. C. Giuntini, *Phys. Chem. Chem. Phys.*, 2004, **6**, 182
36. B. Han, C. H. Shin, S. J. Warrender, P. Lightfoot, P. A. Wright, M. A. Camblor and S. B. Hong, *Chem. Mater.*, 2006, **18**, 3023
37. (a) K. G. Strohmaier and D. E. W. Vaughan, *J. Am. Chem. Soc.*, 2003, **125**, 16035, (b) D. E. W. Vaughan and K. G. Strohmaier, *Microporous Mesoporous Mater.*, 1999, **28**, 233
38. R. D. Shannon, *Acta. Cryst.*, 1976, **A32**, 751
39. A. F. Gualtieri, S. Ferrari, E. Galli, F. D. Renzo and W. van Beek, *Chem. Mater.*, 2006, **18**, 76
40. F. Gramm, C. Baerlocher, L. B. McCusker, S. J. Warrender, P. A. Wright, B. Han, S. B. Hong, Z. Liu, T Ohsuna and O. Terasaki, *Nature*, 2006, **444**, 79
41. S. B. Hong, I. Nam, H. Min, C. H. Shin, S. J. Warrender, P. A. Wright, P. A. Cox, F. Gramm, C. Baerlocher, L. B. McCusker, Z. Liu, T. Ohsuna and O. Terasaki, *in press*, 2007

42. S. B. Hong, I. S. Nam, H. K. Min, C. H. Shin, S. J. Warrender, P. A. Wright, P. A. Cox, F. Gramm, Ch. Baerlocher, L. B. McCusker, Z. Liu, T. Ohsuna and O. Terasaki, paper accepted: *Proc. 15th IZC*, 2007

PART 3: STRUCTURE DIRECTION IN THE SYNTHESIS OF ALUMINOPHOSPHATE-BASED ZEOLITIC MATERIALS

Chapter 7: Introduction to Part 3

Chapter 8: Experimental

Chapter 9: Metallated Cyclam as a Structure Directing Agent

Chapter 10: Non-metallated Cyclam in co-Templating Studies of Silicoaluminophosphate and silicate synthesis

Chapter 11: Further Studies into the Synthesis of AlPO-related Phases Employing Metallocomplexes and co-Bases as Structure Directing Agents

Chapter 12: General Summary and Conclusions

Chapter 7: Introduction to Part 3

7.1: Complexes and co-bases in the Synthesis of Microporous Materials

Synthetic studies presented in Chapters 8-11 aim to investigate transition metal complexes as SDAs, as a potential route to incorporating transition metals into the pores of AlPO, MgAPO and SAPO materials. The azamacrocycles cyclam and cyclen and related derivatives in combination with additional amines (acting as 'co-bases') receive particular attention since they permit Cu and (to an extent) Ni to be introduced to the pores of targeted topologies. To set this work in context, the following sections discuss previous studies of metallocomplexes as SDAs and introduce the concept and role of co-bases and co-templating.

7.1.1: Encapsulating Metallocomplexes in Microporous Materials

Early interest in the incorporation of metallocomplexes into the pores of framework solids stemmed from aspirations of combining the properties of the host framework with those of the encapsulated complex, not least in the search for potential industrially relevant catalysts. With this aim, a number of strategies have been adopted and can be grouped into two broad categories: (1) post-synthesis incorporation and (2) incorporation during synthesis. The second category may be further sub-divided into processes whereby the complex is formed *in situ* during crystallisation of the framework, and syntheses in which the complex is introduced to the gel preformed and is incorporated either through fortuitous encapsulation or via a true templating process.

Post synthesis procedures may involve simple adsorption of the species of interest into the host's internal cavities. In this way, for example, cobalticinium has been introduced to the AlPO VPI-5,[1] ferrocene to AlPO-5[2] and Cu(II) purine derivatives to zeolite Y.[3]

Alternatively, the complex may be assembled within the micropores via a flexible ligand method or so-called 'ship-in-bottle' approach. In this method the ligand is adsorbed into the micropores where it complexes a previously exchanged metal ion. The formed complex becomes too large and rigid to exit from the cage in which it formed.

Mn salen complexes, for example, have been encapsulated in zeolite Y by this method,[4] and more recently Jin *et al.*[5] and Salama *et al.*[6] reported the formation of transition metal complexes with salicylidene-p-aminobenzoic acid and salen-related ligands, respectively, also in zeolite Y.

Salavati-Niasari recently reported the synthesis of the large tetra [14] annulene Cu(II) complex in the nanopores of zeolite Y by a one-pot reaction of substituted-1,2-phenylenediamine with 2,4-pentanedione in the presence of pre exchanged Cu(II) ions.[7] The resulting composite material proved active as a catalyst for the oxidation of benzyl alcohol with an increased lifespan thought to be due to the dispersed nature of the complex throughout the porous network, preventing complex dimerisation.

This area of research offers some interesting chemistry not least because of the apparent ability of host materials to capture unstable species. Kervinen *et al.*, for instance, recently reported the stabilisation of a novel 1:1 complex of Cu(II) with an MIm_2Pr ligand (Figure 7.1) in studies into the mimicking of a particular group of oxidising enzymes.[8] To mimic the coordination environment observed in the enzyme, a mononuclear complex is required with one coordinating MIm_2Pr ligand (coordinating through both nitrogens and the carboxylate oxygen) and three other weekly coordinated ligands (water in the case of the enzyme). While attempts to isolate such a complex in a homogeneous system were unsuccessful due to the formation of dinuclear species, a mononuclear complex was stabilised within zeolite Y. The reason for this is thought to be two-fold; firstly, geometric constraints imposed by the 13Å pore of zeolite Y prevent dimerisation and, secondly, oxygens from the zeolite framework occupy the free coordination sites around the copper. The composite material showed improved activity for the oxidation of benzyl alcohol at room temperature over the non-encapsulated $Cu(MIm_2Pr)_2$ relative.

A particular drawback, however, of this approach is the possible formation of unwanted by-products or presence of unreacted ligand. A far more efficient means of encapsulating metallocomplexes is to entrap them during the crystallisation process – a so-called 'build-bottle-round-ship' approach. A particular strategy in this approach involves the addition of a complex to a preparation that is known to yield a particular microporous material in the hope that it will become trapped within the forming

framework. Aluminosilicates such as zeolites X and Y are particularly conducive to such studies due to their large pore size and the absence of other organic species in their synthesis.

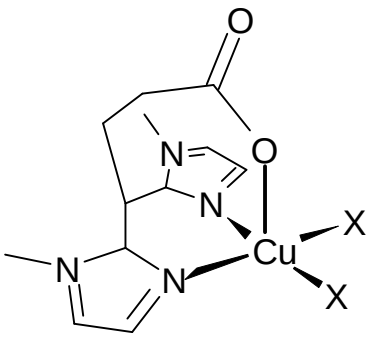

Figure 7.1: Schematic illustration of the 1:1 Cu(II)(MIm$_2$Pr) complex stabilised inside zeolite Y. (X = zeolite framework oxygens).

In studies into the encapsulation of metalloporphyrins in zeolite Y, Zhan and Li[9] proposed that loading levels are influenced by electrostatic interactions between the anionic aluminosilicate species and substituents on the porphyrin macrocycle. Crucially, anionic substituents on the periphery of the porphyrin macrocycle prevented inclusion while cationic substituents favoured loadings of up to 5 mass%. Similarly, substituents on Mn(III) salen complexes have been shown to influence their encapsulation in zeolite X.[10] These observations imply that favourable electrostatic interaction between the anionic framework and cationic complex are necessary for incorporation of metallocomplexes to be successful. Other materials with negative framework charges can also, therefore, be targeted. However, since many zeolitic materials are synthesised in the presence of a structure-directing organic species, it seems unlikely that there would be any impetus for the inclusion of an added complex in preference to the SDA, thus limiting this technique to materials synthesised in inorganic media.

A second approach to the incorporation of metallocomplexes during synthesis is to form the complex *in situ* during the crystallisation process. For example, a cobalt-substituted AlPO with the CHA topology has been synthesised with $[Co(deta)_2]^{3+}$ (deta = diethylamine triamine) occluded in the larger pore[11] (Figure 7.2). In this case the Co(II) and amine were added separately to the synthesis gel and the complex formed *in situ*

during the crystallisation of the host. Remarkably, cobalt is present in two oxidation states: Co(III) in the complex and Co(II) in the framework.

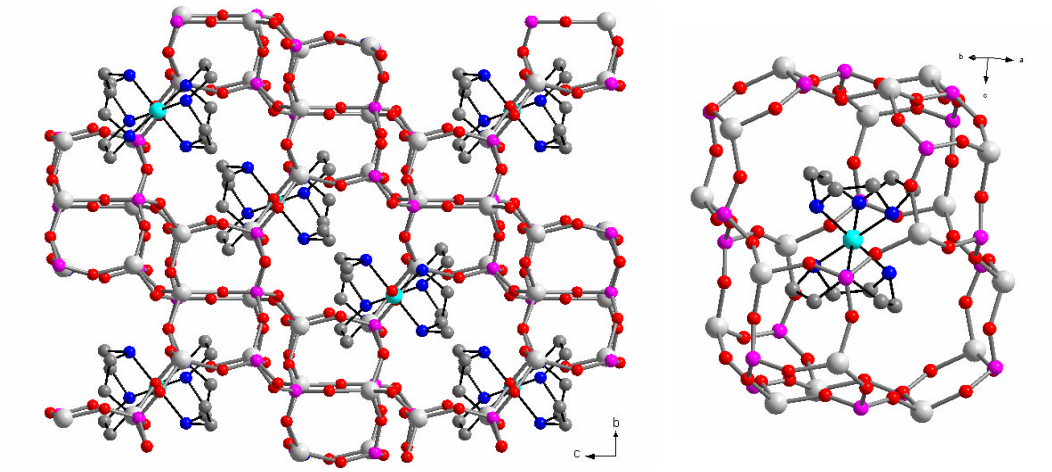

(a) (b)

Figure 7.2: (a) $[Co(deta)_2]^{3+}$-containing chabazite-like CoAPO. Single crystal analysis located Co and N positions, however C atoms of the ligand were found to be disordered, occupying four out of six positions at random. (b) detail of the complex-containing pore. (purple = P, red = O, light grey = Al/Co(II), blue = N, dark grey = C and cyan = Co(III), hydrogens not shown).

Some unusual complexes have also been introduced to the pores of zeolitic materials through this technique. The complex formed between Cu(II) and pyridine is commonly tetrahedral (1:4), however, Attfield *et al.*[12] have prepared the linear binary $[Cu(pyr)_2]^{2+}$ complex in ferrierite by exploiting a particular approach to the synthesis of pure silica ferrierite. The synthesis employs propylamine as the SDA, HF as a mobilising agent and aqueous pyridine as a solvent, thus facilitating the *in situ* formation of Cu pyridine complexes simply via the addition of Cu to the synthesis gel. The $[Cu(pyr)_2]^{2+}$ complex is occluded in the pore system of the as-made material with its charge balanced by F^- and defects in the framework. Figure 7.3 illustrates the location of the complex within the pores of ferrierite.

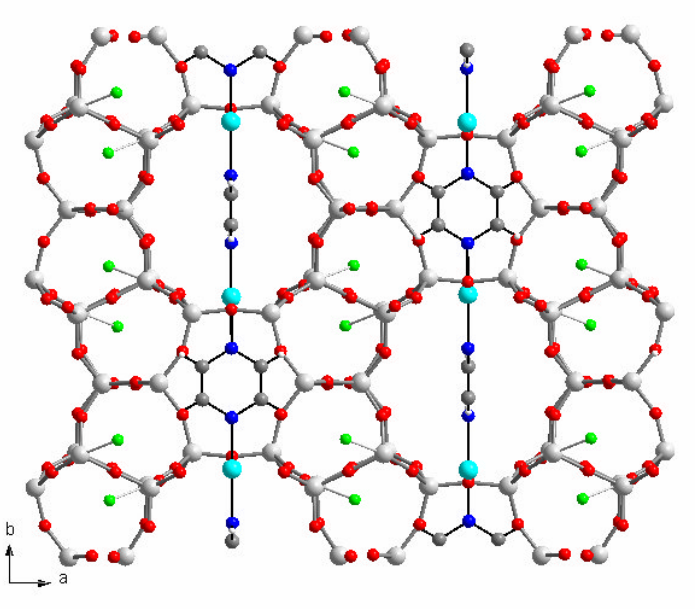

Figure 7.3: $[Cu(pyr)_2]^{2+}$-containing ferrierite. Cu^{2+} is located at the centre of the 8MR window with one pyridine residing in the 8-ring channel and one occupying the main 10-ring channel. The planes of the two pyridine rings are orthogonal to each other (light grey = Si, red = O, dark grey = C, blue = N, cyan = Cu, green = F, small light grey = H).

In a similar approach the Cu(I) complex $[Cu(NH_3)_2]^{2+}$ has been synthesised *in situ* in ferrierite by employing ammonium solution instead of pyridine.[13] The linear complexes are isolated from each other in rows extending along the 10-ring channel, with disordered propylamine occupying the 8-ring channel. It is thought that propylamine reduces Cu(II) to Cu(I), which is then stabilised by ammonium complexation.

The third approach to incorporating metallocomplexes during synthesis (and most relevant to the work in this thesis) is the addition of the *pre-formed* complex to the synthesis gel in the hope that it will itself act as an SDA. Although, traditionally, SDAs employed in the synthesis of microporous materials are predominantly linear, branched and cyclic amines or alkylammonium species, metal complexes and organometallic compounds have also received attention as possible candidates. A limiting factor in their widespread application as SDAs, however, is their stability under hydrothermal conditions; they must be sufficiently stable to withstand the temperature and pH of the synthesis conditions. Nevertheless, suitable candidates are available and have yielded interesting and often new materials.

Complexes of linear polyamines have received most attention in this role, and particularly those of Co. $[Co(en)_3]^{3+}$ (en = ethylene diamine) has been employed in a number of studies and has directed the formation of both layered and framework materials. Morgan *et al.*[14] prepared a novel AlPO consisting of layers constructed from chiral [3,3,3] propellane-like units (three folded and fused 4MRs, Figure 7.4(b)). The layers are intercalated with a layer of $[Co(en)_3]^{3+}$ cations and water molecules with H-bonding holding the layers together. This material was synthesised in the presence of a racemic mixture of $[Co(en)_3]^{3+}$ and, although the complex is found to reside in a chiral cavity formed by adjacent AlPO sheets, there are equal numbers of pockets of opposite handedness and so the structure is achiral. The same structure can also be prepared in the presence of $[Ir(en)_3]^{3+}$.[15]

A similar situation is also found in a layered gallophosphate (Figure 7.4(a)) in which layers, constructed of GaO_6 octahedra and PO_4 tetrahedra (and containing a [3,3,3] propellane-like unit as in the case above), are separated by the complex.[16] A novel borophosphate has also been prepared from this complex.[17]

As implied above, the use of such chiral complexes opens the possibility of introducing chiral features to the product. Indeed, by employing optically pure d-$[Co(en)_3]^{3+}$ a truly chiral, layered AlPO has been synthesised,[18] as well as more recently a chiral layered zincophosphate.[19a] In these structures, chirality is introduced to the layers by the same [3,3,3] propellane-like unit as above. The zincophosphate structure is particularly interesting in that the layers are connected via symmetrical P-O--H--O-P groups where one hydrogen atom is shared through hydrogen bonding between two phosphate tetrahedra. The result is a pseudo three-dimensionally connected framework with 12MR channels running along *a* and *b*. The complex resides in the pseudo-12MR window with extensive H-bonding to the framework. The analogous material with opposite handedness can also be prepared from l-$[Co(en)_3]^{3+}$.

A chiral framework has been synthesised by Stalder and Wilkinson,[19b] also employing d-$[Co(en)_3]^{3+}$. In this gallophosphate (Figure 7.5) GaO_4 tetrahedra are linked to four phosphate tetrahedra, with each phosphate tetrahedral bridging two Ga. The framework, however, is not *fully* tetrahedrally connected and possesses terminal P=O groups. The complex, occluded within the pores of the material, interacts with the framework

electrostatically and through H-bonding between NH groups on the ligand and both terminal P=O groups and bridging oxygens.

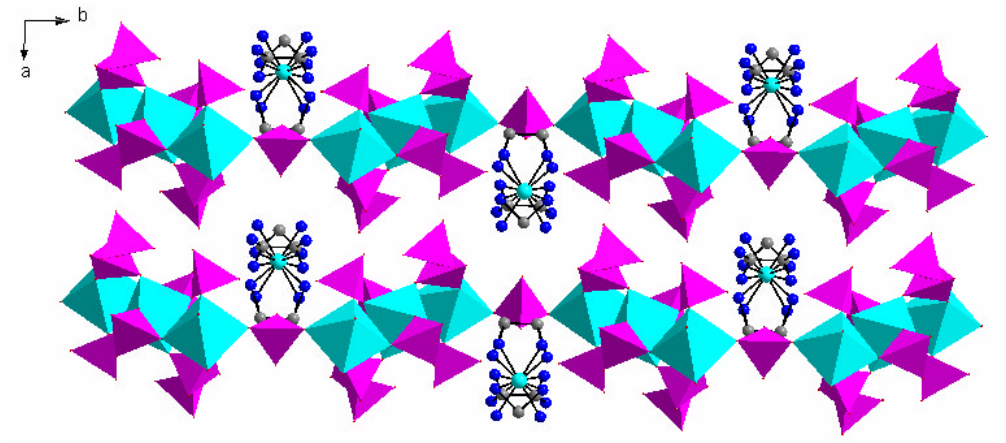

(a)

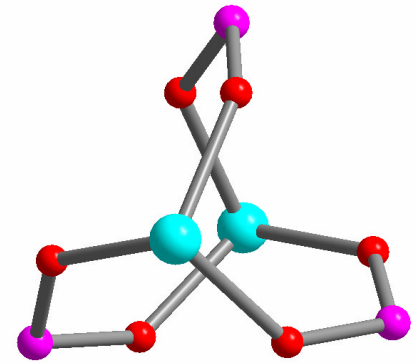

(b)

Figure 7.4: (a) Layered gallophosphate templated by $[Co(en)_3]^{3+}$ with disordered complex residing between layers (cyan = GaO_6 octahedra, purple = PO_4 tetrahedra, grey = C, blue = N, cyan sphere = Co). (b) detail of the [3,3,3] propellane-like chiral motif. In this, and related structures, two such units link through a common Ga (cyan), forming a pair of enantiomers.

Other Co complexes have also found success in this application including the $[Co(NH_3)_6]^{3+}$ complex, which directs the formation of a layered AlPO,[20] and $[Co(tn)_3]^{3+}$ (tn = 1,3-diaminopropane) and trans-$[Co(dien)_2]^{3+}$ (dien = diethylamine triamine), both of which direct the formation of chiral layered AlPOs.[21,22] In the latter case the complex was introduced to the gel as a racemic mixture but only one enantiomer was taken into the product. The AlPO layers are stacked in a helical manner with the $[Co(dien)_2]^{3+}$ complex in between.

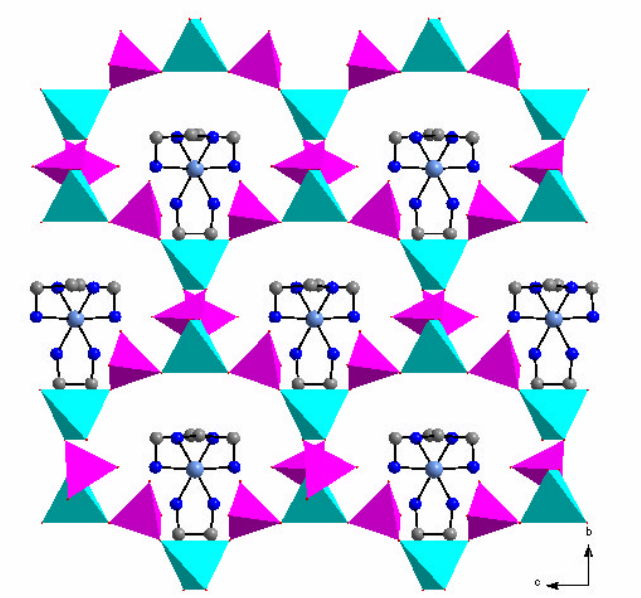

Figure 7.5: Chiral gallophosphate prepared in the presence of d-$[Co(en)_3]^{3+}$. Chirality is a consequence of the phosphate groups' orientation and an associated buckling of the framework (cyan = GaO_4 tetrahedra, purple = PO_4 tetrahedra, light blue = Co, dark blue = N, grey = C).

Linear polyamines of other metals have also been studied but to a much lesser extent. Rajic *et al.*[23] have synthesised a variant of AlPO-34 (CHA) in the presence of $[Ni(en)_3]^{2+}$. The complex is found to undergo a ligand replacement reaction under hydrothermal conditions to yield $Ni(en)_2(OH)_2$ and become covalently bound to the framework through P-O-Ni-O-P linkages. Associated with this complex-framework relationship is the cleavage of P-O-Al bonds and the formation of double Al-O-Al bridges and five-coordinate Al, resulting in a significantly distorted framework (Figure 7.6). Full tetrahedral connectivity is restored upon decomposition of the complex via calcination.

Garcia[24] has shown that $[Ni(deta)_2]^{2+}$ can direct the crystallisation of AlPO UT-6 (a varient of AlPO-34) and an orthorhombic variant of AlPO-5 in the presence of fluoride, and AlPO-5 (AFI), MgAPO-34 (CHA) and SAPO-34 in the absence of fluoride. However, under the same conditions $[Ni(tren)_2]^{2+}$ and $[Ni(trien)_2]^{2+}$ were ineffective as SDAs (tren = triethylaminetriamine, trien = (2-aminoethyl)amine). Calcination of Ni complex-containing samples yielded extra-framework Ni^{2+} cations in the pores of

charged frameworks, or nanoparticulate NiO uniformly distributed throughout the pores of AlPO materials. In the same studies, $[Cu(deta)_2]^{2+}$ yielded blue crystals of MgAPO-5.

Copper complexes have also been employed in the synthesis of various vanadium oxides[25,26] such as $Cu(en)[V_2O_6]$, which consists of one-dimensional chains of vertex-sharing VO_4 tetrahedra, linked through V-O-Cu-O-V groups.

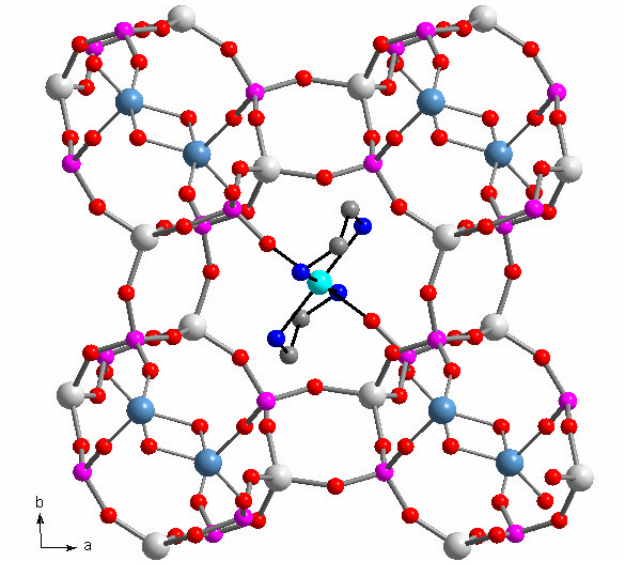

Figure 7.6: Distorted AlPO-34 framework prepared in the presence of $[Ni(en)_3]^{2+}$. One of the original en ligands has been replaced by two P-OH groups of the framework. Five-coordinated Al is illustrated as light blue for clarity (light grey/light blue = Al, purple = P, red = O, dark blue = N, dark grey = C, cyan = Ni).

A further group of metallocomplexes receiving interest as SDAs is the organometallics. Cobalticinium, for example, has proved successful and can direct the formation of AlPO-16 (AST),[27,28] as well as several silicate frameworks including nonasil (NON),[29] octadecasil (AST), dodecasil (DOH) and ZSM-48.[30] The progression from NON, through AST to DOH topologies is noteworthy in that it is achieved simply by increasing the synthesis temperature, working between 140 and 190°C. Benzene cyclopentadienyl iron is also successful in directing the formation of the DOH topology.[30]

The gallophosphate Mu-1 was synthesised in the presence of cobalticinium.[31] Structurally related to the gallophosphate Dab-4, this material consists of a network of

F^--hosting D4Rs connected via H-bonding. Cobalticinium cations act as counter ions and reside in the interstices of the network. Due to the absence of a fully three-dimensional, covalently connected framework, however, this material exhibits poor thermal stability.

Although their widespread employment is limited due to their stability under hydrothermal conditions, interest in organometallic species as templating agents is fuelled by the synthesis of the first extra-large pore, high silica aluminosilicate UTD-1, which was synthesised in the presence of permethylcobalticinium.[32-34] UTD-1 is, as yet, the only new topology to be obtained from organometallic SDAs. However, it is the first framework to contain pores bound by 14-membered rings, enlarging the pore size accessible to siliceous materials. Catalytic studies on UTD-1[35] suggest that, although overall activity is inferior to conventional materials such as zeolite Beta, the ellipsoidal 14MR channel permits the cracking of large flat molecules such as triisopropylbenzene. Such molecules are too large to enter channels of, for example, a 12MR zeolite, or indeed another 14MR zeolite CIT-5, which possesses much more puckered 14MR windows. UTD-1 has also been prepared in its Ti-substituted form from permethylcobalticinium.[36]

Many of the synthetic studies presented later in this chapter employ azamacrocyles (in both their metallated and non-metallated forms) as SDAs. As an introduction to this work, the following section discusses previous studies of these, and similar species in such roles.

7.1.2: Macrocyclic Structure-Directing Agents

Traditional organic SDAs, as discussed previously, consist typically of primary, secondary and tertiary alkyl amines or quaternary ammonium salts. However, cyclic species such as, for example, cationic porphyrins also offer great potential as SDAs due to their unique shape and increased conformational rigidity. Indeed, porphyrin-based species have proved effective in directing the formation of aluminosilicate zeolites X and Y as well as the aluminophosphate material denoted VPI-5.[37] Figure 7.8 illustrates some further macrocyclic species previously employed as possible SDAs.

The crown ether 18-crown-6 has proved fruitful in directing the synthesis of zeolites with the KFI[38] and RHO[39] topologies as well as a clathrate-like high-silica phase MCM-61[40] (MSO). In the presence of Na^+ ions, 18-crown-6 has also directed the formation of a hexagonal variant of faujasite[41] (EMT), while cubic faujasite is achieved using 15-crown-5.[42]

Diaza-polyoxa-macrocyclic species offer the advantage of possessing one or two positive charges per molecule if the nitrogen atoms are protonated, increasing the potential for favourable framework-template interactions. Kryptofix 22 (K22), for instance, can successfully direct the synthesis of an AlPO analogue of MCM-61, denoted Mu-13.[43] Figure 7.8 illustrates the framework of Mu-13 with the disordered location of K22, as indicated by a residual electron density envelope in Fourier difference calculations. Each large cavity is occupied by a diprotonated K22 and two hydroxide ions, while water molecules occupy the smaller cages. Like K222, K22 can also direct the formation of AlPOs of LTA structure type, while K21 will only direct LTA-type AlPO synthesis in the presence of tetramethylammonium.[44] This 'co-templating' approach will be discussed in the following section. K222 has also been employed in MAPO syntheses; when M = Mg, Mn, Fe or Co mixtures of MAPO-5 and MAPO-42 were obtained, while phase pure MAPO-42 was achieved in the presence of Zn. In this material the macrocycle was also found to be disordered and unmetallated within the α-cage; the Zn exclusively occupies framework positions.[45]

Analogous behaviour is observed with the azamacrocycles tmtact (or tetramethylcyclam – TMC), and hmhaco, which have proved successful in templating the two novel divalent metal-substituted MAPOs STA-6 and STA-7.[45] The identity of the product is influenced by the identity of the substituting metal. These two materials are central to studies presented later in Part 3 and are discussed in more detail in section 7.2. In similar studies, tmtacn was found to direct the formation of MAPO-18(AEI) when M = Mg or Co.

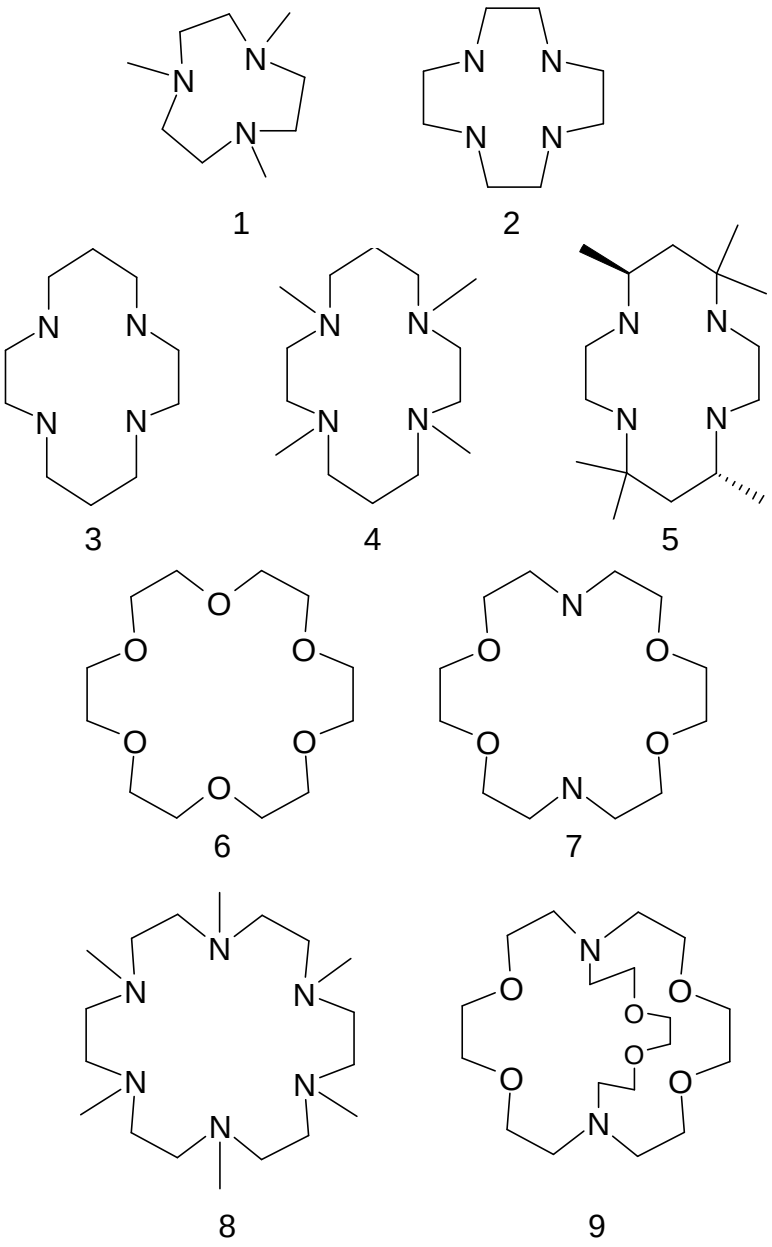

Figure 7.7: Macrocyclic species employed as SDAs: (1) tmtacn, (2) cyclen, (3) cyclam, (4) tetramethyl cyclam (TMC), (5) Tet-A, (6) 18-crown-6, (7) Kryptofix 22 (K22), (8) hmhaco (9) Krypyofix 222 (K222)

Such macrocyclic species are also able, of course, to complex metal cations and this has led to the synthesis of a family of materials in the presence of cyclam. In these materials inorganic layers or chains are linked through X-O-M-O-X bridges, where X denotes a framework species and M denotes the metal coordinated by cyclam. For example, when employed in a gallophosphate synthesis, cyclam directs the formation of a structure

consisting of layers composed of D4Rs of GaO_4 and PO_4 tetrahedra.[46] These D4Rs are connected to four others to create 10MR windows. Layers are connected via six-coordinate Ga units in which the Ga is coordinated by two oxygens from framework PO_4 tetrahedra and the four nitrogens of cyclam (Figure 7.9). Cu, Mn and Co can replace Ga in this material.[47] Similarly, when introduced to CoAPO and NiAPO syntheses, cyclam coordinates the divalent metal and the resulting complex bridges aluminophosphate chains.[45]

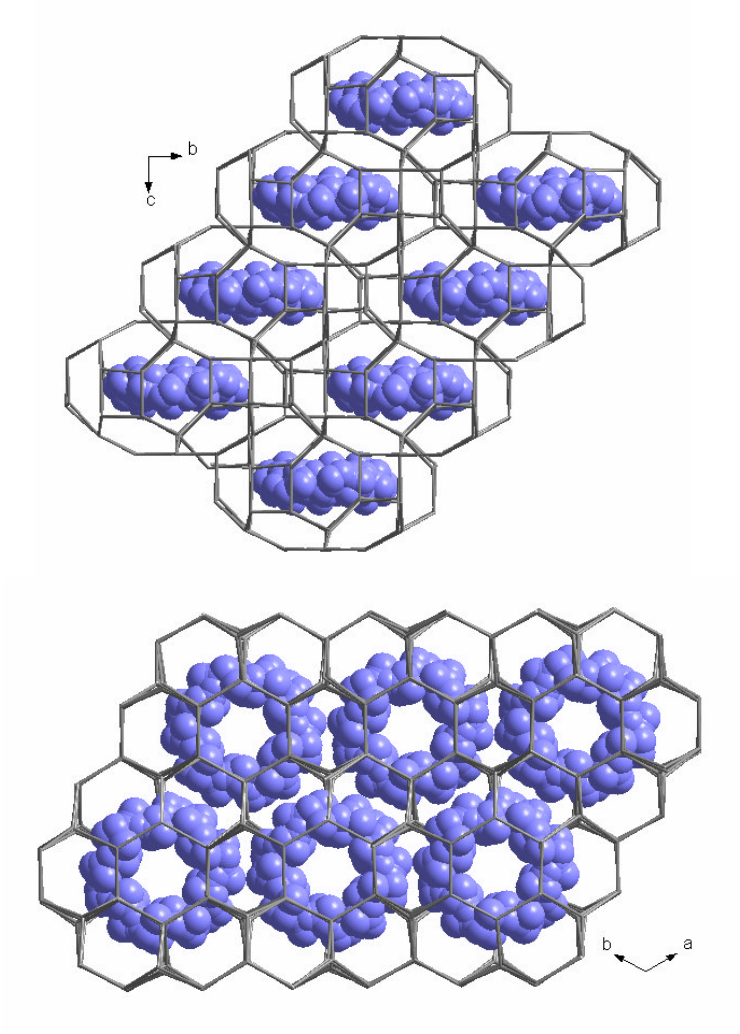

Figure 7.8: Structure of the aluminophosphate Mu-13 (oxygens removed for clarity) with residual electron density (blue) representing the disordered location of the K22 template within the cage system.

The closely related Tet-A macrocycle produces a similar CoAPO material[48] where chains of double four-membered AlPO rings are linked by the complex formed between

Tet-A and Co. However, in this material the un-metallated macrocycle is also present between the layers.

(a)

(b)

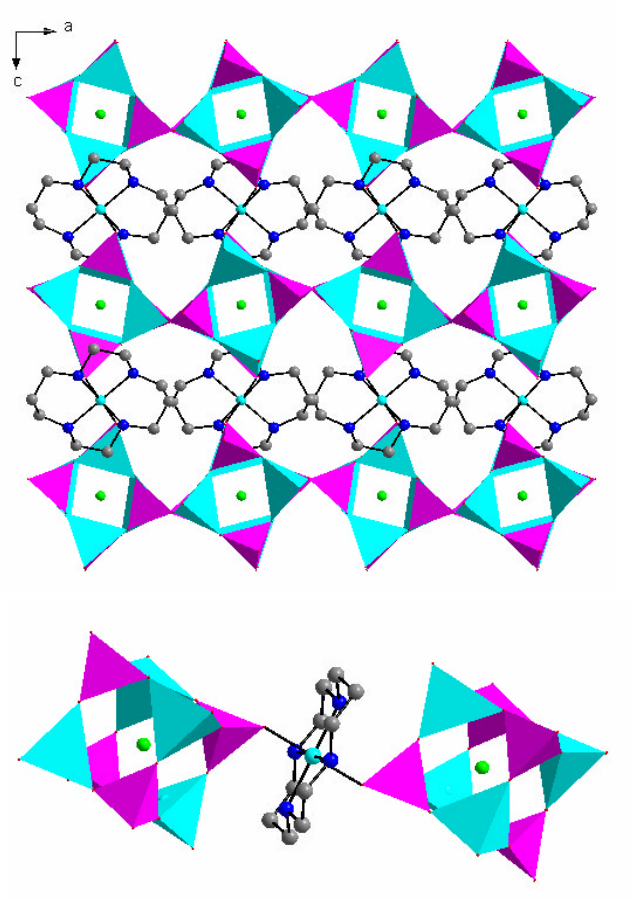

Figure 7.9: (a) Cyclam-containing gallophosphate exhibiting layers of fluoride-hosting D4R units connected via metal-cyclam bridges. (b) detail of the cyclam-coordinated metal bridge. (cyan = GaO_4 tetrahedra, purple = PO_4 tetrahedra, grey = C, blue = N, green = F, cyan sphere = Ga/Cu/Mn/Co)

In contrast to the framework structures mentioned above, these hybrid materials, in which the macrocycle is incorporated into the framework, are unstable to calcination with collapse of the structure upon removal of the organic species.

Macrocycle-metal complexes can, however, also reside unbound within the pores of as-made materials. A Cu-cyclam complex, formed *in situ* during an AlPO synthesis in fluoride medium, directed the formation of the CHA topology as well as a distorted STA-6 structure denoted [F, Cu-cyclam]-AlPO-SAS.[49] Also, a pre-formed Ni-cyclen complex has been shown to direct CoAPO gels towards the AEI topology (CoAPO-

18).[50] Ni and Cu complexes of TMC and cyclam have also been studied as SDAs for STA-6 and -7[51] and are discussed later.

7.1.3: co-Templating and co-Bases in the Synthesis of Microporous Materials

Historically, zeolite and zeotype syntheses involving structure direction by an organic additive would, generally, contain only one organic structure-directing species such as a linear, branched or cyclic amine or alkylammonium cation. Often, the selected organic species is basic and performs the dual role of SDA and pH moderator achieving the necessary pH conditions for crystallisation to occur.

An associated limitation of this approach is the constraint imposed on the quantity of (often expensive) SDA required to achieve the desired target pH. Furthermore, it is observed that, in general, only 10-50% of the organic content of a synthesis gel is occluded in the final product.[52] Consequently, several authors have exploited the properties of a 'co-base'. A co-base is a relatively small, cheap and basic organic compound such as trimethylamine (TMA) or tripropylamine (TPA), which can be introduced to the synthesis gel to (a) adjust the synthesis pH and (b) reduce the quantity of SDA required.

In this manner, the layered gallophosphate Mu-5 was synthesised in the presence of cyclam with TPA acting to adjust the synthesis pH to 4.5.[53] TPA has also been employed as a co-base with the macrocycle Tet-A (to yield the layered phase [F,Tet-A]-AlPO-1[48]), as well as with cobalticinium in the synthesis of AlPO-16[27] and the gallophosphate Mu-1.[31] Indeed, the co-base approach has proved useful in studies of metallocomplexes as SDAs. Garcia *et al.*, for example, employed dipropylamine (DP) and TPA as co-bases with the $Ni(deta)_2$ complex in synthesising MgAPO-34 and AlPO-5,[24] while employing DP with Ni-cyclen and Ni-cyclam-para-xylyl-quinuclidinium complexes yielded CoAPO-18 and MgPO-5, respectively.[49] Ethylenediamine (en) has also been employed as a co-base with Ni-cyclam in the preparation of MgAPO STA-6.[49]

In all of the above examples the co-base species is not observed in the pores of the final product and acts solely as a pH moderator, permitting structure direction to proceed through the influence of the metallocomplex/macrocycle only. However, in certain

situations the additional amine can also become involved in the structure directing process either to mimic the 'true' SDA and help stabilise the same structure, or to co-template a different structure to that observed in its absence. This latter situation often results in topologies with more than one type of cage/pore, with each cage type stabilised by a particular co-template. This is most clearly demonstrated by the Ni-cyclam MgAPO system; simply by replacing ethylenediamine with tetraethylammonium hydroxide (TEAOH), a phase change from MgAPO STA-6 to MgAPO STA-7 is effected thanks to the ability of TEA^+ cations to stabilise the secondary (or β) cage of this structure[49] (this example is discussed further in the following section).

Zones[52] has reduced the quantity of an expensive adamantyl SDA required to template the aluminosilicate SSZ-25 by replacing up to approximately 90% of the SDA with an additional amine such as cyclopentylamine and isobutylamine, which are chosen due to their resemblance to the original SDA. These additional compounds are found occluded within the pore structure and appear to act as co-templates in the stabilisation of this phase, mimicking the 'true' SDA. Surprisingly, this reduction in SDA concentration is accompanied by an increase in the rate of crystallisation. Crucially, however, a minimum quantity of adamantyl SDA is still necessary for the successful formation of the desired phase. This technique has also been extended to other systems including the synthesis of EU-1, SSZ-35, -32 and -28, and ZSM-11 and -12.

Materials with the LTA-type topology have also received much attention in studies of co-templating. Historically, aluminosilicate LTA-type zeolites (such as ZK-4) were synthesised in the presence of Na^+ and tetramethylammonium (TMA^+) cations. The TMA^+ cations were found to template the smaller β-cage of this structure. A gallophosphate analogue was first synthesised by Merrouche *et al.*[54] in the presence of fluoride and DP. In this case, it was observed that while DP resides within the larger α-cage, fluoride ions occupy the D4R units (F^- ions are often associated with D4R units in microporous materials and in such cases can also be regarded as a co-template).

The AlPO version of the LTA topology, however, remained elusive and was not achieved until 1994 by Sierra *et al.*[55] in the presence of three structuring agents – F^-, TMA^+ and diethanolamine (DEA). In this way both the α- and β-cages are stabilised by

DEA and TMA, respectively, while fluoride ions reside in the D4R units. SAPO and MAPO (M = Co, Zn) analogues were also achieved in this way.

Three years later the diaza-polyoxa-macrocycles K222 and K22 were also found to stabilise the α-cage in a gallophosphate system yielding an LTA-type $GaPO_4$ under fluoride conditions.[56] Application of K222 to an AlPO system also resulted in the formation of AlPO-LTA in both the presence and absence of fluoride (although crystallisation was faster with fluoride present). However, K22 templated a new AlPO phase denoted K22-$AlPO_4$ in the absence of fluoride and a mixture of this phase and AlPO-LTA in the presence of fluoride.[57] Only by introducing TMA^+ to the system was phase-pure AlPO-LTA achieved and it is suggested that, by stabilising the β-cage so effectively, TMA^+ helps to compensate for the weaker ability of the macrocycle to stabilise the α-cage. Similarly, the smaller macrocycle K21 failed to direct crystallisation of AlPO gels by itself but produced AlPO-LTA when combined with fluoride and TMA^+. Interestingly, while typical cubic AlPO-LTA is obtained from K222 in both the presence and absence of fluoride, a slight distortion to a rhombohedral variant is observed when TMA^+ ions are introduced (Figure 7.10). The organic co-templates were found to be highly disordered within the α and β cages.[44] Figure 7.10 illustrates one possible interpretation of the electron density envelope corresponding to these disordered species as located by Fourier difference mapping. In all these examples the macrocycle occupies the larger α cage while TMA^+ cations stabilise the smaller β-cage, and fluoride ions reside within the D4Rs, representing a trio of co-templating species.

The co-templating strategy has also proved successful in the synthesis of a thermally stable analogue of zeolite Q (denoted UZM-4).[58] This aluminosilicate material – which is stable up to 600^oC – was obtained from gels containing both TMA^+ and TEA^+ cations. Both organic species are occluded in the pores of this BPH-type framework. By altering the gel chemistry, a new phase (UZM-5) with structure code UFI was also obtained from this pair of co-templates. While both species are present in a 1:1 ratio in the product, their exact location and role in directing the formation of this phase is unclear. Nevertheless, the co-templating approach would appear to be a further viable means of synthesising new topologies. Furthermore, it offers a number of advantages to

industrial production including reduced SDA and waste stream clean-up costs, reduced reaction times and increased reagent flexibility.

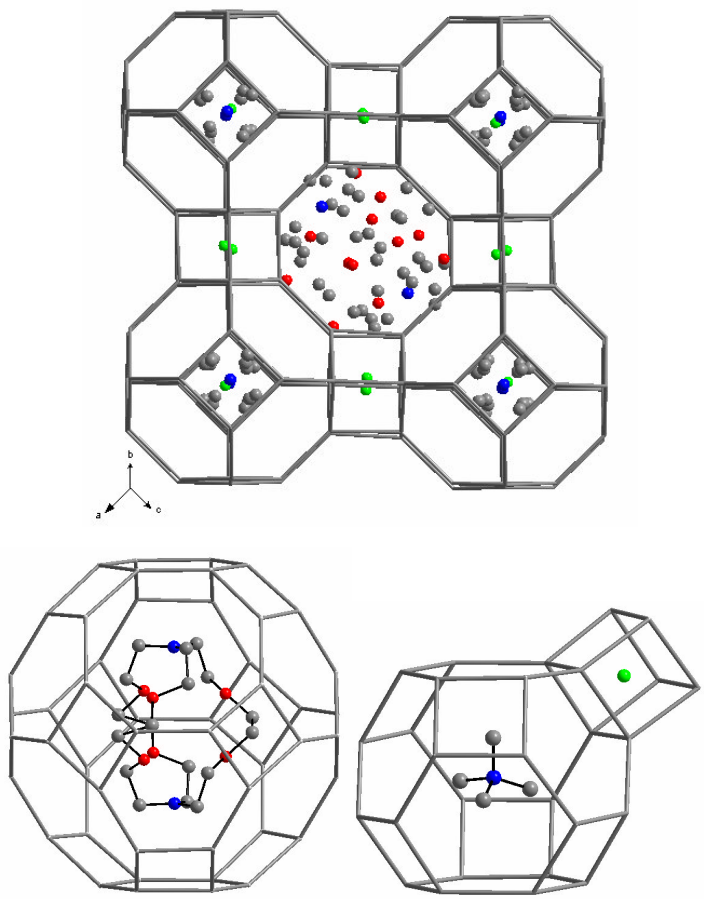

Figure 7.10: Top: experimentally observed structure of the rhomboherdally distorted AlPO-LTA templated by K222, TMA^+ and fluoride. Residual electron density representing disordered templates is illustrated within the cages. Bottom: possible interpretations of residual electron density within the α (left) and β (right) cages. (grey = C, red = O, blue = N, green = F, framework oxygens omitted for clarity).

7.2: Synthetic Studies of STA-6 and STA-7

Much of the inspiration for synthetic work conducted for this thesis came from earlier work in our research group following the first syntheses of STA-6 and STA-7. It is therefore appropriate to pull aspects of the foregoing discussions on templating with complexes, macrocycles and co-bases together into a case study of these two novel materials and outline recent results which have led to the research presented in Chapters 9-12.

The novel structure STA-6 (SAS) was first reported by Wright *et al.* in 1999 and was the first tetrahedrally-connected framework templated by an azamacrocycle.[59] It was synthesised by adding TMC to a MgAPO gel (Table 7.1), heated at 190^{o}C for two days. The resulting small pore framework material is remarkably simple. It is most conveniently described as being constructed from chains of face-sharing D6Rs in which each D6R is rotated 90^{o} around the long axis of the chain with respect to its neighbour. These chains, which parallel the *c*-axis, are connected to four others through Al-O-P bonds to produce cages as illustrated in Figure 7.11. These pores are connected through 8MR windows parallel to the *c*-axis, and 6MRs in the *a* and *b* directions resulting in a unidimensional pore system parallel to *c*.

$Mg(OAc)_2$	$Al(OH)_3$	H_3PO_4	TMC	H_2O
0-0.2	1.0-0.8	1.0	0.4	400

Table 7.1: Typical gel composition for the synthesis of MgAPO STA-6

Although the template could not be located from X-ray data, energy minimisation studies illustrated the neat fit of the macrocycle within the larger cages.

The observation that under the same conditions AlPO-21 (AWO) forms in the absence of Mg suggested a unique structure-directing role performed by the substituting cation. This was developed in studies into the products obtained from TMC in the presence of different heteroatoms. These results are summarised in Table 7.2. While TMC directed the formation of STA-6 in the presence of Mg, Mn or Fe, substitution by Co and Zn created another new phase – STA-7 (SAV).[60]

This new structure, also a fully tetrahedrally connected framework, contains two different cage systems linked in three dimensions. The larger α-cages are connected along *c* via planar 8MR windows. Elliptical 8MRs give access along *a* and *b* to the smaller β-cages which are themselves connected parallel to *c* via planar 8MRs giving a three-dimensional pore system. The framework can be described as consisting of chains of D6Rs linked along *c* by 4MRs and linked to adjacent chains by Al-O-P bonds (Figure 7.12). Indeed, in this way the STA-7 structure can be considered a relative of AlPO-34

(CHA) and AlPO-18 (AEI) topologies; all three being constructed of D6Rs connected in different ways through 4MRs.

(a)

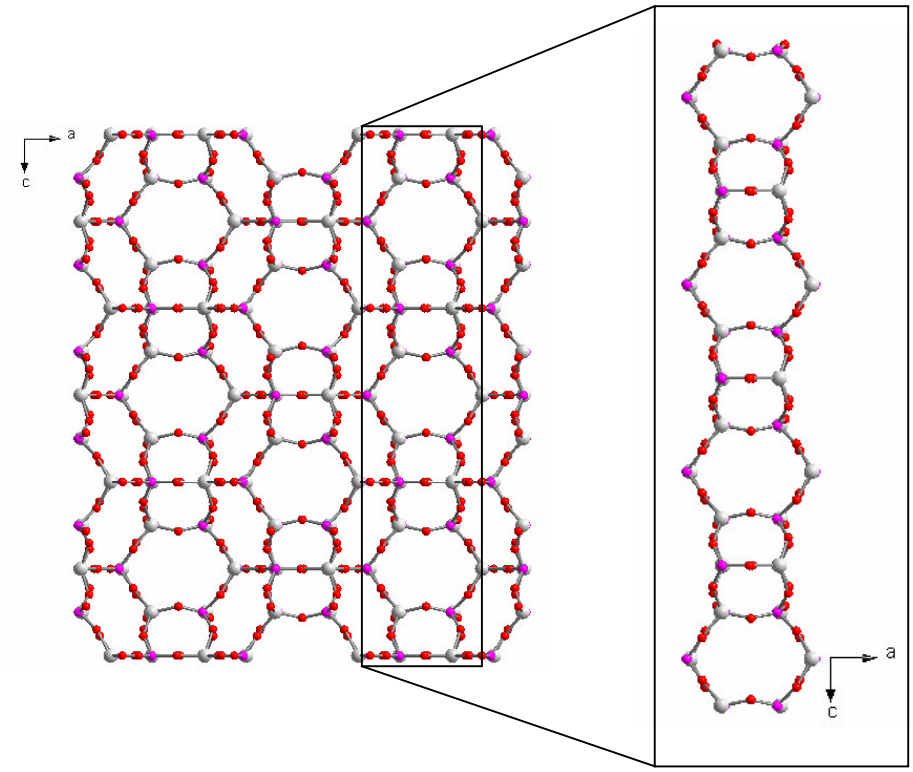

(b)

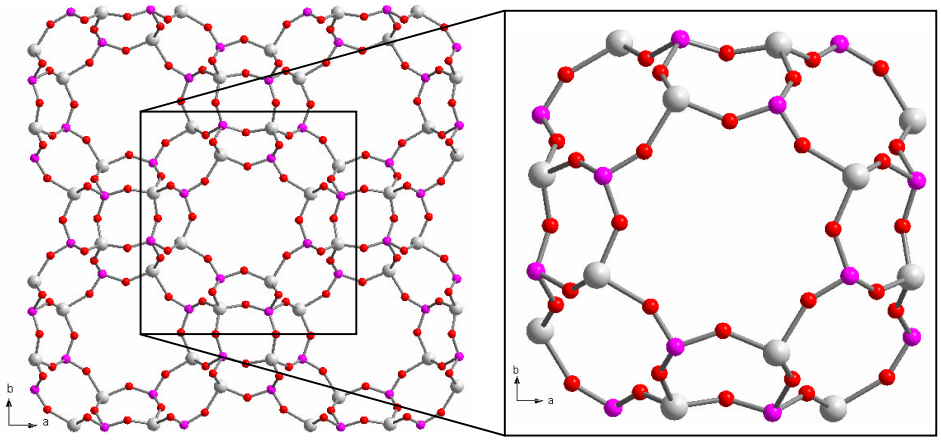

Figure 7.11: Experimentally derived SAPO STA-6 framework. (a) viewed along the b axis showing detail of the D6R chains. (b) viewed along the c axis and one-dimensional channel system with detail of the large cage (grey = Al, purple = P/Si, red = oxygen).

Cation ratio in Synthesis Gel	Product
1.0 Al:1.0 P	AlPO-21
0.2 Mg:0.8 Al:1.0 P	MgAPO STA-6
0.2 Mn:0.8 Al:1.0 P	MnAPO STA-6
0.2 Fe:0.8 Al:1.0 P	FeAPO STA-6
0.2 Co:0.8 Al:1.0 P	CoAPO STA-7
0.2 Zn:0.8 Al:1.0 P	ZnAPO STA-7

Table 7.2: Cation ratios of MAPO synthesis gels and associated products in the presence of TMC, illustrating the dependence of the product phase on the identity of the substituting species.

Once again it was not possible to unambiguously locate the template molecule from X-ray data, however energy minimization studies suggested that the macrocycle would favour location in the larger cage. It was thought that the β-cages are occupied by fragments of organic and/or water molecules.

TMC forms a strong complex with Ni^{2+} ions and the effect of complexation on the above system has been studied extensively.[50] By adding Ni acetate to a typical MAPO synthesis gel containing an excess of macrocycle, the Ni-TMC complex is formed *in situ* in the gel while the excess amine adjusts the synthesis pH to approximately seven. The presence of the Ni complex, as apposed to the unmetallated macrocycle, favoured the formation of STA-6 over STA-7 regardless of the framework compositions, thus permitting CoAPO and ZnAPO STA-6 analogues to be prepared for the first time.[61] The 2+ charge associated with the complex is balanced by a negative framework charge. SAPO STA-6 was also achieved in this way. The structures observed in all of these syntheses, however, were orthorhombically distorted. Tetragonal symmetry is restored upon calcination and the accompanying decomposition of the complex, implying that it is the Ni complex that causes this distortion.

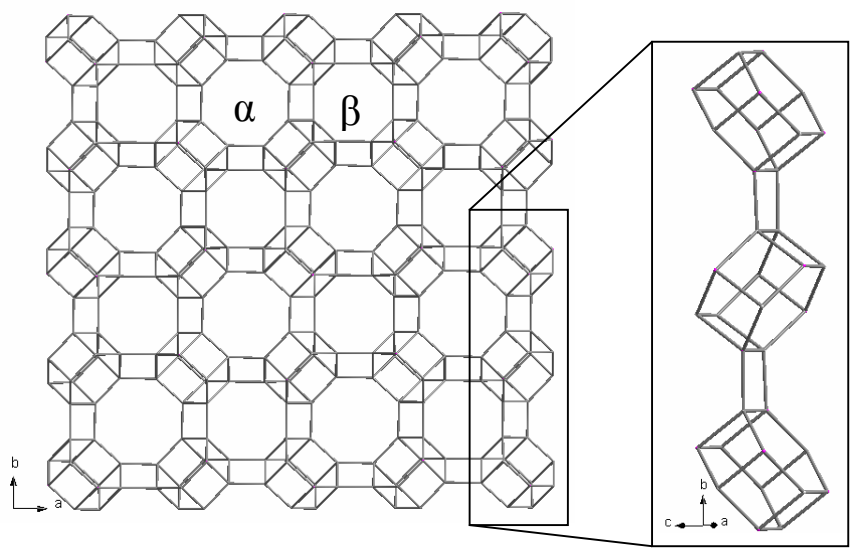

(a)

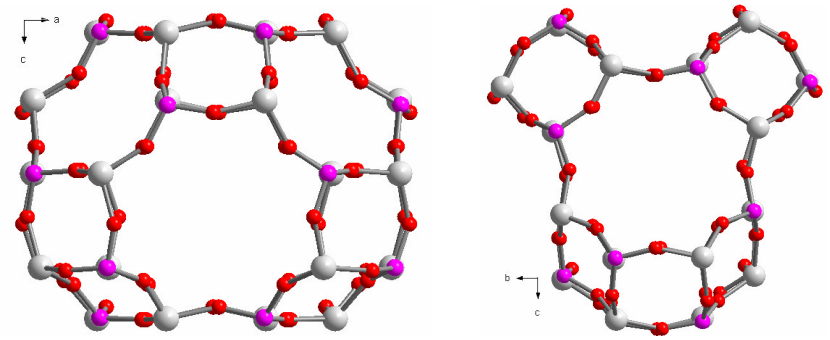

(b)

Figure 7.12: Structure of STA-7 as obtained from a CoAPO synthesis . (a) framework viewed along the c axis with α and β cages labelled, and expanded view of D6R chain showing the alternating tilt of adjacent units (oxygens have been removed for clarity). (b) detail of the α (left) and β (right) cages.

Non-distorted SAPO STA-6 was obtained by employing the closely related Ni cyclam complex.[50] However, attempts to synthesise tetragonal Mg-, Co-, and Zn-APO STA-6 in the presence of this complex resulted in a MgAPO-5/-18 mixture, a layered phase and no product, respectively. It appeared, therefore, that the structure-directing ability of Ni cyclam and TMC complexes is limited by the gel composition and to the formation of STA-6 only.

However, the addition of co-bases to these syntheses has been found to have a considerable effect. In syntheses involving co-bases, Ni and the macrocycle are present

in a 1:1 ratio and the pH is adjusted to approximately seven by the addition of a second amine. Ethylene diamine (en) and tetraethylammonium hydroxide (TEAOH) have been studied as co-bases in the presence of Ni cyclam and TMC complexes. The addition of en to a Ni-cyclam-containing MgAPO synthesis provides a dramatic example; the result is the direction of crystallisation away from the previously observed MgAPO-5/-18 mixture to non-distorted MgAPO STA-6. Its addition to Ni TMC-containing syntheses, however, had no effect on the product obtained – the distorting influence of the TMC complex would appear unavoidable. It should be noted that the co-base is not occluded in the pore system of the product.

Having structure-directing ability in its own right, TEAOH is a very interesting co-base candidate, offering the opportunity to co-template structures. Its inclusion to AlPO-related syntheses in the presence of Ni cyclam and TMC complexes has revealed a remarkable ability to stabilise the β-cage of the STA-7 structure. In this way, phase pure MgAPO and SAPO STA-7 were prepared for the first time in the presence of TEAOH and non-metallated TMC. In contrast to the above synthesis involving Ni cyclam and en, MgAPO as well as ZnAPO and CoAPO gels are directed to the STA-7 structure in the presence of Ni cyclam with TEAOH as the co-base. Ni complex-containing SAPO STA-7, however, remains elusive due to the formation of STA-6 in this regime, although *Cu* cyclam has proved successful in templating this material in the presence of TEAOH.[61]

Figure 7.13 illustrates the energy minimised location of TEA^+ cations within the β-cage of STA-7 and two possible configurations of the complex within the α-cage obtained from a combined Monte Carlo-Simulated Annealing approach similar to that discussed in Chapter 6. Single crystal studies of as made Ni TMC-STA-7 (Figure 7.14) revealed a square-planar NiN_4 unit at the centre of the α-cage, and the nitrogen of the co-base in the centre of the β-cage. Carbon atoms of both organics appeared disordered, and in the case of the macrocyclic ligand, may be interpreted as either of the two energy minimised configurations suggesting the possible presence of both.

These materials have proved stable to calcination, producing a dispersal of extraframework Ni^{2+} cations throughout the structures. The utilisation of azamacrocycle complexes in this way, therefore, provides a convenient route to the introduction of

transition metals to the pores of these materials. Cation inclusion is achieved in a two-step process rather than a three-step sequence of synthesis, calcination and subsequent ion exchange, which itself may not be entirely efficient, or result in structural degradation. The resulting materials may prove active in catalytic applications.

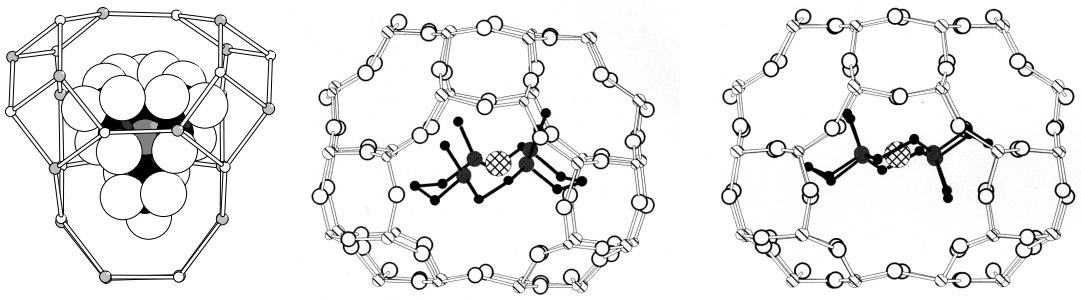

(a) (b) (c)

Figure 7.13: Energy minimised locations of the TEA^+ cation within the β-cage of STA-7 and (a) two possible configurations of the Ni-TMC complex in the α-cage: trans-I (b), and trans-III (c) (courtacy of Dr Paul Cox, Portsmouth).

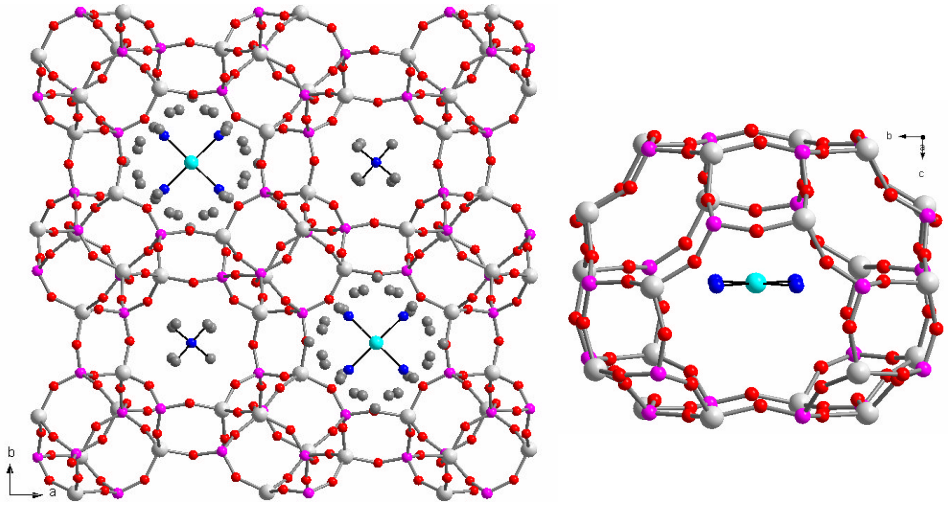

(a) (b)

Figure 7.14: Single crystal structure of CoAPO STA-7 templated by Ni-TMC and TEAOH (light grey = Al/Co, purple = P, red = O, cyan = Ni, blue = N, dark grey = C). (a) Structure viewed along the c axis showing location of Ni and nitrogens of TMC and TEAOH. C atoms (where found) are disordered. (b) square planar NiN_4 unit within the α-cage.

7.3: Aim of Synthesis Studies

Building on these studies and preliminary results for Cu cyclam in MgAPO and SAPO syntheses, the aim of work presented in the following sections was to explore this method of transition metal introduction to AlPO-related systems. Studies focus predominantly on complexes of Cu with cyclam, cyclen and derivatives thereof in the presence of a selection of co-bases to potentially broaden the range of materials achievable in this way, and obtain Cu-containing materials for potential deNO_x application. Mixtures of Cu and Ni complexes of these ligands are also employed in the hope of achieving mixed cation or metal oxide species within the pores of AlPO-related phases. Also, with this aim, the structure-directing ability of a number of linear polyamine Cu and Ni complexes, as well as cobalticinium-related species, is investigated in the presence of co-bases.

Chapter 8: Experimental

A description of the synthetic strategies adopted during the course of this work is given in this Chapter. Initially, AlPO-related phases were targeted through the use of macrocyclic SDAs such as cyclam and cyclen (in both their metallated and non-metallated form), in the presence of a selection of co-bases. Figure 8.1 illustrates the co-bases utilised in these studies. These amines were selected primarily due to their resemblance to TEAOH, and offer a variety of different shapes and geometries to probe any potential structure directing effects arising from their presence. In later studies, Cu and Ni complexes of a selection of polyamines were employed as potential SDAs for comparison, also in the presence of co-bases. The addition of cobalticinium and permethylcobalticinium was also investigated as a possible means of introducing extra-framework Co to the pores of AlPO materials.

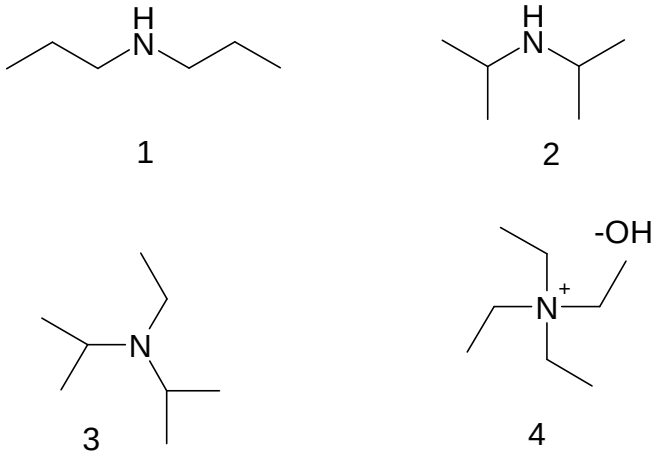

Figure 8.1: Co-bases employed in synthetic studies presented in this work.

Mg was selected as the heteroatom of choice in MAPO syntheses due to the success of using this metal in previous studies. MgAPO gels crystallise in up to two days and therefore provide relatively swift means of probing the activity of a given set of SDA and co-base. Mg itself will favour tetrahedral geometry within the framework of product materials and is unlikely to become coordinated by cyclam or cyclen. Conversely, transition metals such as Cu and Ni are likely to favour complexation and therefore be excluded from framework positions. In this way, competition between framework T-

sites and coordinated positions is minimised, and a route to the incorporation of extra-framework Cu and/or Ni in MgAPO materials becomes available.

The substitution of Al^{3+} by Mg^{2+} results in a negative framework charge. This is balanced in as-made materials by the protonated macrocycle (in the absence of transition metals) or by the 2+ charge of Cu/Ni-cyclam/cyclen complexes. Calcination of the product will result in the distribution of Cu^{2+} and/or Ni^{2+} cations within the pores of the framework, maintaining charge neutrality.

In the case of non-substituted AlPO materials, fluoride is introduced to the synthesis gel. Association of F^- anions with the product framework introduces a negative charge to the otherwise charge-neutral structure, and therefore permits the incorporation of positively charged SDAs. Calcination of transition metal-containing AlPO phases results in the loss of both the organic SDA and fluoride. The concomitant restoration of framework-charge neutrality is thought to result in the formation of nanoparticulate metal oxide within the pore system.

The third principal class of materials studied in this work is the sillicoaluminophosphates (SAPOs). The incorporation of Si into AlPO materials is known to improve the stability of the framework and therefore yield materials with greater catalytic potential. SAPO gels require up to one week to crystallise and were generally targeted after initial explorations were conducted on MgAPO regimes, with the aim of synthesising more stable analogues of the MgAPO products. Like MgAPOs, SAPO frameworks possess a negative charge associated with the substitution of P^{5+} with Si^{4+}. Therefore, calcined transition metal-containing materials are likely to host divalent metal cations rather than metal oxide particles within their pores.

8.1 Synthesis and Product Recovery

Synthesis of all AlPO, MgAPO and SAPO materials was conducted using hydrothermal techniques by combining sources of the metal framework species with distilled water, the desired organic/complex and co-base. Details of the cation sources and reagent suppliers and purity are giving in Table 8.1.

Reagent	Purity (%)	Supplier
Magnesium(II) acetate tetrahydrate	99	Fluka
Aluminium hydroxide hydrate	-	Aldrich
Aqueous orthophosphoric acid	85	Prolabo
Silica (fumed)	97	Fluka
Germanium oxide	99.99	Aldrich
Copper(II) acetate	98	Hopkin and Williams Ltd
Nickel(II) acetate tetrahydrate	98	Aldrich
HF	48	Aldrich
Cyclam	98	Aldrich
Cyclen Sulfate	98	Aldrich
TEAOH	34	Alfa Aesar
Dipropylamine	99	Aldrich
Diisopropylamine	99	Aldrich
Hunig’s base	99	Aldrich
N-(2-aminoethyl)-1,3-propanediamine	98	Aldrich
Dipropyltriamine	98	Aldrich
Tris(2-aminoethyl)amine	96	Aldrich
Triethylenetetramine	94	Aldrich
N,N’-bis(3-aminopropyl)ethylenediamine	94	Aldrich
Cobalticinium	98	Aldrich
Permethylcobalticinium	98	Aldrich

Table 8.1: Reagents used in this work. Materials were employed without further purification.

In a typical MgAPO preparation, gels of composition 0.2Mg : 0.8Al : P : 40H_2O : 0.125template : *x*co-base were prepared by adding $Al(OH)_3$ to H_3PO_4 (85%) in water prior to the addition of $Mg(OAc)_2$. The co-base was added dropwise at this stage to adjust the gel pH to approximately seven (generally 6-7.5 was achieved), prior to the addition of the desired complex. In cases where no transition metal was present, the basic ligand was added first, and any necessary adjustment of pH was achieved by final addition of the co-base.

AlPO gels were prepared by mixing $Al(OH)_3$ with H_3PO_4 (85%) in water, followed by the addition of HF (48%), the appropriate co-base and template. Gels were typically of composition Al : P : 40H_2O : 0.2HF : 0.125template : *x*co-base.

Similarly, in SAPO preparations fumed silica was introduced as the source of Si to produce gels typically of composition Al : 0.8P : 0.2Si : 40H_2O : 0.125template : *x*co-base.

In syntheses where transition metal complexes of cyclam, cyclen, their derivatives and polyamines were employed, the complex was pre-prepared by adding the ligand to aqueous solutions of the metal acetate salt (a portion of the total gel water content was set aside for this purpose). The solutions were then introduced to the gel.

All gels were stirred continuously at room temperature during the preparation procedure until homogenous, prior to being loaded in Teflon-lined stainless steel autoclaves (Figure 8.2) and heated in the oven at 190^oC for either two days (AlPOs and MAPOs) or seven days (SAPOs).

After removing the autoclave from the oven and allowing it to cool, a sample of the reaction mixture was removed and examined under the optical microscope. This provides a general impression of the success of the synthesis and the crystallinity of the product.

Reaction mixtures were suspended in water to examine the purity of the product. If necessary, the suspensions were sonicated to force separation of the desired product from amorphous material, which was decanted off. Thereafter the product may be

filtered from the reaction mixture, washed with distilled water and ethanol, and allowed to dry in air at room temperature.

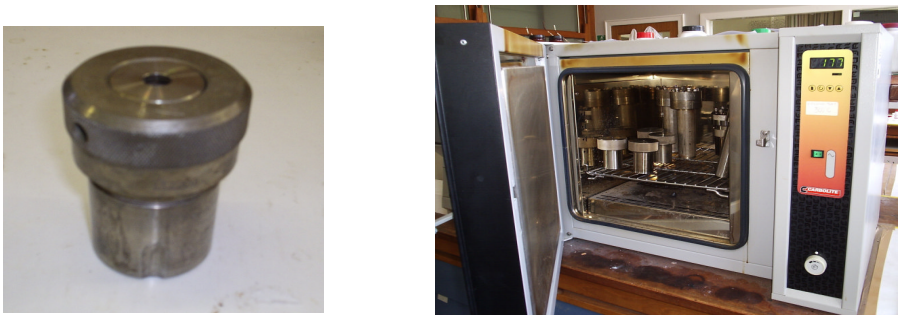

Figure 8.2: Stainless steel, teflon-lined autoclave (left) and oven (right) employed in hydrothermal synthesis.

8.2: Calcination

Calcination removes organic species from the pores of as-made materials resulting in high porosity and internal void volume and, in the case of transition metal-containing SDAs, the formation of extra-framework metal cations or metal oxide species. Selected phase pure, as-prepared samples were calcined overnight in a tube furnace at the desired temperature (often 550^{o}C) in a stream of dry oxygen or nitrogen. The temperature was increased from room temperature to the desired maximum in increments of 5^{o}Cmin^{-1}, or slower for less robust materials. The temperature maximum was maintained for 10 hours before the sample was allowed to return to room temperature.

8.3: Characterisation

Crystallography

Phase identification was conducted on all crystalline products by X-ray powder diffraction on a Stoe STADI P diffractometer operating in transmission mode with primary monochromation and Cu $K_{\alpha 1}$ X-radiation. Samples were mounted between two Mylar (polythene) discs supported on petroleum jelly. Diffraction patterns were recorded over the range 5-50^{o} 2θ for 1.5-2 hours for identification, and indexed using the Stoe software suite.[62]

For structural analysis of calcined powder samples, samples were loaded in a 0.7 or 0.5mm quartz-glass capillary and dehydrated at 250^{o}C under a vacuum of 10^{-3} mbar for several hours before being sealed and mounted on the diffractometer. Data were recorded over the range 5-90^{o} 2θ for 12 hours. Structural refinement was conducted via the Rietveld method accommodated in the GSAS program suite.[63]

Where available, single crystals were examined by single crystal diffractometry. Data for as-made MgAPO STA-6 were collected at 173K using a Rigaku MM007 High brilliance RA generator (Cu Kα radiation, confocal optics) and Rapid Image plate system. Data for as-made and calcined germanosilicate MFI were collected at 93K using a Rigaku MM007 High brilliance RA generator (Mo Kα radiation, confocal optics) and Mercury CCD system. At least a full hemisphere of data was collected using ω scans. Intensities were corrected for Lorentz-polarisation and for absorption. The structures were solved by direct methods and refined using the program SHELXTL.[64] Data collection and structural refinement were performed by Prof. A M Z Slawin at St Andrews University.

Elemental Analysis

Carbon, Hydrogen, Nitrogen (CHN) analysis was performed on pure as-prepared samples using a CE Instruments EA 1110 CHNS Analyser.

Inorganic framework compositions were estimated, and the presence of transition metals was confirmed by Energy Dispersive X-ray analysis (EDX),[65] performed on a Joel JSM-5600 SEM with an Oxford INCA Energy 200 EDX system.

ICP analysis was conducted on a series of SAPO samples in order to obtain a more accurate inorganic composition. This was performed on an Agilent 7500 Series ICP-MS instrument working on a New Wave Research Merchantek Products UP 213 lazer.

All CHN and ICP analyses were performed by Mrs Sylvia Williamson at St Andrews University.

Thermogravimetric Analysis (TGA)

For selected, pure, as-prepared materials, TGA was conducted on a TA Instruments SDT 2960 thermogravimetric analyser. Approximately 10mg of sample were loaded in an alumina crucible and data were collected from room temperature to 900^{o}C at 10^{o}Cmin^{-1} in a flow of air. Calcined alumina was used as a reference.

Scanning Electron Microscope (SEM)

Crystal morphology and sample purity were analysed on a Joel JSM-5600 SEM at St Andrews University.

Solid-State UV-Vis Spectroscopy

To characterise the colour of as-made and calcined transition metal-containing materials and confirm the presence of the desired metallocomplex, solid state UV-Vis spectroscopy was conducted on selected samples using a Perkin Elmer Lambda 35 UV-Vis Spectrometer. Samples were mixed with $BaSO_4$ (also employed as the 'blank') to (a) tone down vividly coloured samples or (b) bulk up samples available only in small quantity. Samples were loaded in 2mm path length quartz far cuvettes prior to being mounted in the beam line. Data, collected as %-reflectance over the wavelength range 300-1000nm, were handled on the accompanying Lambda 35 UVWinlab software package.

Electron Spin Resonance (ESR)

ESR spectra of selected Cu-containing materials were collected at room temperature before and after calcination on a Bruker EMX spectrometer operating at 9.52GHz. Powdered as-made and calcined samples were loaded in 4mm o. d. quartz tubes. Spectra of calcined samples were also recorded after dehydration at 250^{o}C under a vacuum of 10^{-3}mbar. In order to avoid saturation of the resonance line, low microwave power was employed (typically between 0.4 and 4.0mW). Hyperfine constants were measured using WinEPR software and g values were calculated as outlined in Chapter 2.

Nitrogen Adsorption

Nitrogen adsorption was conducted on low-silicon (no transition metal) and Cu-containing SAPO STA-7 samples on a Hiden IGA (Intelligent Gravimetric Analysis) instrument at St Andrews.

Solid State NMR

To confirm the presence of template molecules in selected samples and to characterise the template species present in SAPO STA-7, ^{13}C CP MAS NMR was performed at St Andrews by Dr Philip Wormald on a Varian UNITYplus spectrometer, operating at 500 MHz for ^{1}H, with a 7.5mm Doty XC5 $^{1}H/^{19}F$ probe. The frequency was 125.77MHz and a recycle time of 5.0s, CP contact time of 1.00ms, an 8.00μs 90^{o} pulse and a spin rate of 4.20kHz were employed. The shift reference was ^{13}C adamantane (38.5ppm). Data were also recorded for as-made SAPO STA-6 and a low silicon form of SAPO STA-7 (denoted (S)APO STA-7) at the EPSRC solid state NMR Facility in Durham by Dr David Apperley. Here, a Varian UNITY *Inova* spectrometer, operating at 300MHz for ^{1}H was employed. The frequency was 75.40MHz and a recycle time of 1.0s and a CP contact time of 1.00ms were employed. Spin rates of 5.01kHz and 10.0kHz were used for SAPO STA-6 and (S)APO STA-7, respectively. The shift reference was $(CH_3)_4Si$. Decoupling was conducted on all spectra and acquisition times varied between 8 and 30ms.

The coordination of Al, Si and P within the framework of SAPO STA-6 and STA-7 was also examined by solid state NMR at the EPSRC solid state NMR Facility in Durham, while ^{27}Al DP MAS NMR was conducted on a sample of AlPO UT-6 at St Andrews. Details of experimental parameters for these analyses are listed in Table 8.2. The shift reference samples for Al, P and Si were ^{27}Al aluminium nitrate (0.0ppm), ^{31}P calcium hydrogenphosphate (-1.2ppm) and ^{29}Si tetrakis(trimethylsilyl)silane (-9.9 and -135.2ppm) respectively. Decoupling was employed on all P and Si analyses.

Sample	Freq (MHz)	Acq^{n} time (ms)	Recycle time (s)	Polaris^{n}	Contact time (ms)	Pulse angle	Spin rate (kHz)
^{27}Al							
SAPO STA-6	78.12	10.0	0.2	DP	-	19.6^{o}	12.00
SAPO STA-7		30.0	0.5	DP	-	18.8^{o}	13.87
(S)APO STA-7		20.0	1.0	DP	-	21.4^{o}	10.00
AlPO UT-6	130.33	10.2	0.4	DP	-	1.5μs	12.00
^{31}P							
SAPO STA-6	121.37	20.0	60.0	DP	-	90.0^{o}	8.00
SAPO STA-7		20.2	60.0	DP	-	90.0^{o}	11.30
(S)APO STA-7		20.2	60.0	DP	-	90.0^{o}	11.30
^{29}Si							
SAPO STA-6	59.56	30.0	30.0	CP	1.00	-	5.00
SAPO STA-7		20.0	120	DP	-	90.0^{o}	5.00

Table 8.2: Experimental parameters for ^{27}Al, ^{31}P and ^{29}Si MAS NMR analyses conducted on selected samples from this work.

Chapter 9: Metallated Cyclam as a Structure Directing Agent

Building on preliminary results for Cu-cyclam in MgAPO and SAPO syntheses, work presented in this chapter aimed to investigate more fully the behaviour of this complex as an SDA in the synthesis of aluminophosphate-based materials. In particular, this work aimed to investigate and expand the range of materials into which transition metal cations or oxide particles can be introduced by this method. Syntheses were conducted in the presence of a selection of co-bases to investigate any influence these may exert via co-templating. These studies were focused on three material types: magnesium-substituted aluminophosphates (MgAPOs), non-substituted aluminophosphates (AlPOs) and silicon-substituted aluminophosphates (SAPOs). Results for each of these groups are discussed in the following sections.

9.1: Studies in MgAPO Synthesis

Complexed metal	Co-base	Product (by XRD)
Cu	TEAOH	STA-7
	DIP	STA-7
	DP	STA-6
	HB	STA-6
Ni	DIP	STA-7 + MgAPO-5
Cu + Ni	TEAOH	STA-7
	DIP	STA-7 + minor impurity
	DP	STA-6

Table 9.1: Summary of MgAPO products obtained from Cu- and/or Ni-cyclam in the presence of a selection of co-bases (TEAOH, tetraethylammonium hydroxide; DIP, diisopropylamine; DP, dipropylamine; HB, Hunig's base).

Table 9.1 summarises a selection of syntheses from this work that are discussed in this section. Cu-cyclam complex was prepared as a bright purple solution prior to addition to the synthesis gel as discussed previously. Persistence of this vivid colour in the gel and in the resulting phases indicated that the complex is both stable under hydrothermal

conditions and, more importantly, incorporated into the product phase (Figure 9.1). Likewise, brown Ni-cyclam yielded a yellow-coloured product, while mixed Cu/Ni-cyclam systems resulted in rusty maroon-coloured crystals.

As expected, the deployment of TEAOH as a co-base in the presence of Cu-cyclam resulted in the formation of pseudo-cubic crystals of MgAPO STA-7 (Figure 9.2), confirming that previous studies involving Ni-cyclam and TEAOH can be readily transferred to Cu. The presence of Cu, as implied by the strong purple colour of the as-made material, was confirmed by EDX analysis (Table 9.2). CHN analysis suggests that both cyclam and TEA cations are present in a 1:1 ratio as expected from the co-templating effect discussed in Chapter 7.

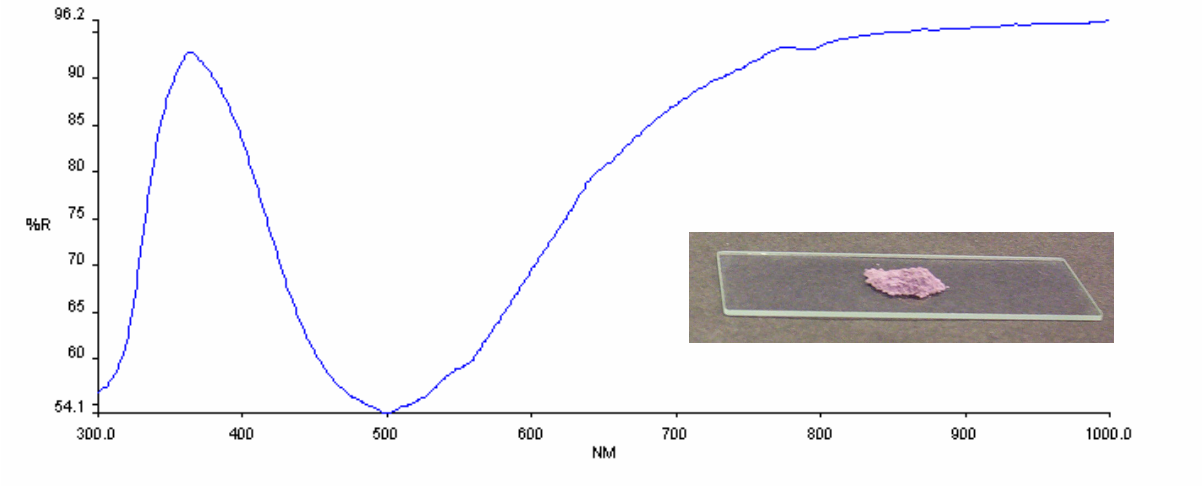

Figure 9.1: A typical solid-state UV-Vis spectrum (% reflectance) of an as-made Cu-cyclam-containing material (here, MgAPO STA-7) showing an absorption maximum (λ_{max}) at approximately 500nm, characteristic of this complex (literature reported λ_{max} = 508nm[66]); inset: photograph of as-made Cu-cyclam-containing MgAPO STA-7.

By combining previous results for Ni-cyclam with these results for Cu-cyclam it was possible to synthesise MgAPO STA-7 for the first time in the presence of both Cu- *and* Ni-cyclam with TEAOH. Once again, CHN analysis of the as-made sample confirmed that cyclam and TEA cations are present in a 1:1 ratio, and inorganic elemental analysis by EDX confirmed the presence of both Cu and Ni in this new material (Table 9.2 and Figure 9.3).

(a)

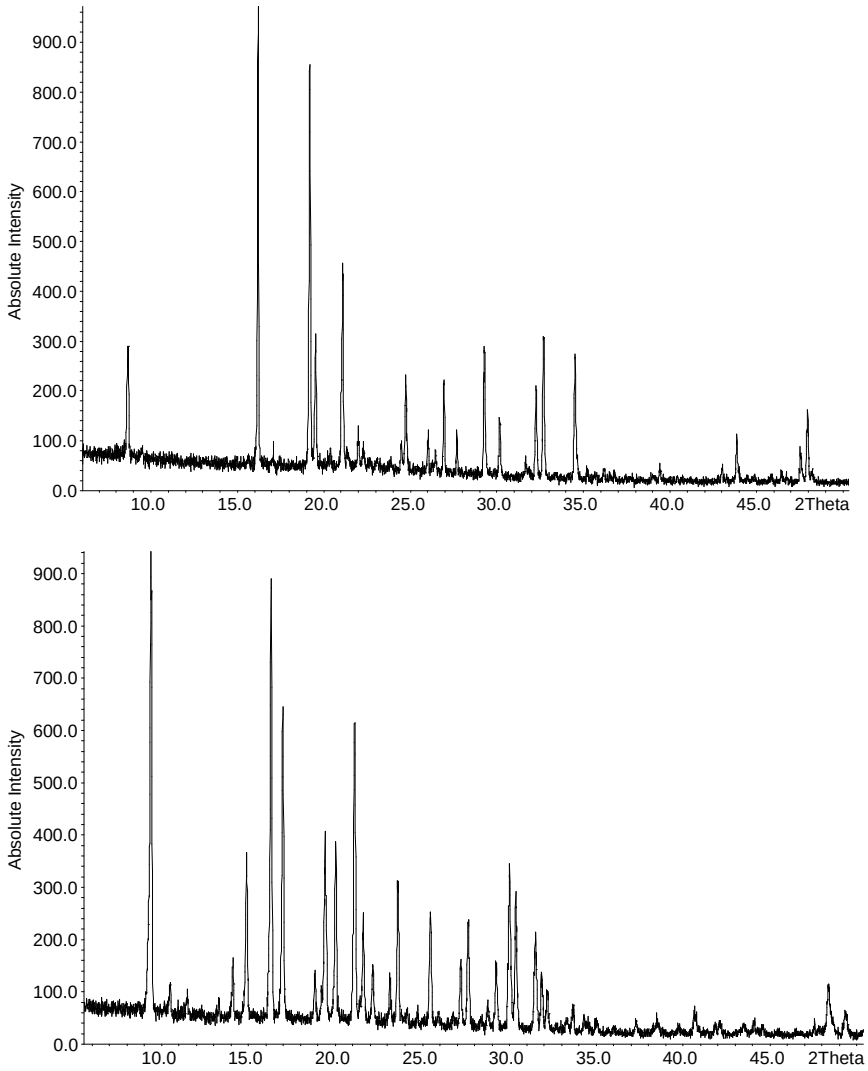

(b)

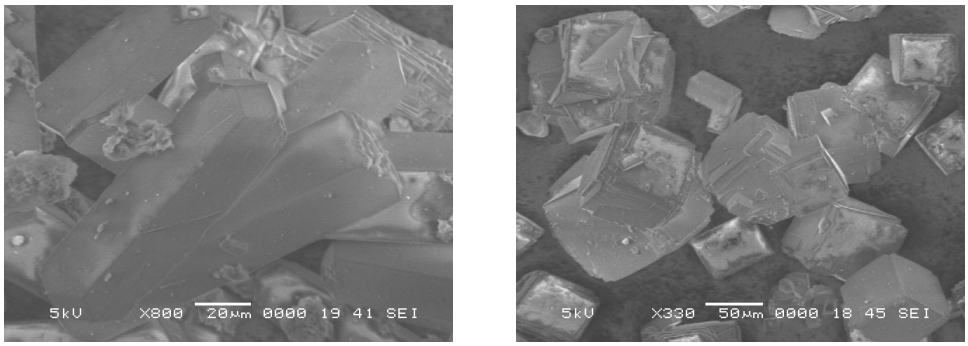

Figure 9.2: (a) Typical powder XRD patterns of as-made MgAPO STA-6 (top) and STA-7 (bottom); (b) SEM images of MgAPO STA-6 (left) and STA-7 (right).

Replacing TEAOH with DIP in a Cu-cyclam-containing preparation also yielded MgAPO STA-7 and, as in the case with TEAOH, CHN analysis revealed that both cyclam and DIP are present within the pore system in a 1:1 ratio. This implies that DIP can also stabilise the β-cage of the STA-7 structure. However, in the presence of Ni-cyclam, the large-pore material MgAPO-5 and other impurities are observed along with STA-7 suggesting that TEAOH is still the most efficient stabilising agent for this structure, able to function in the presence of both Cu and Ni-cyclam.

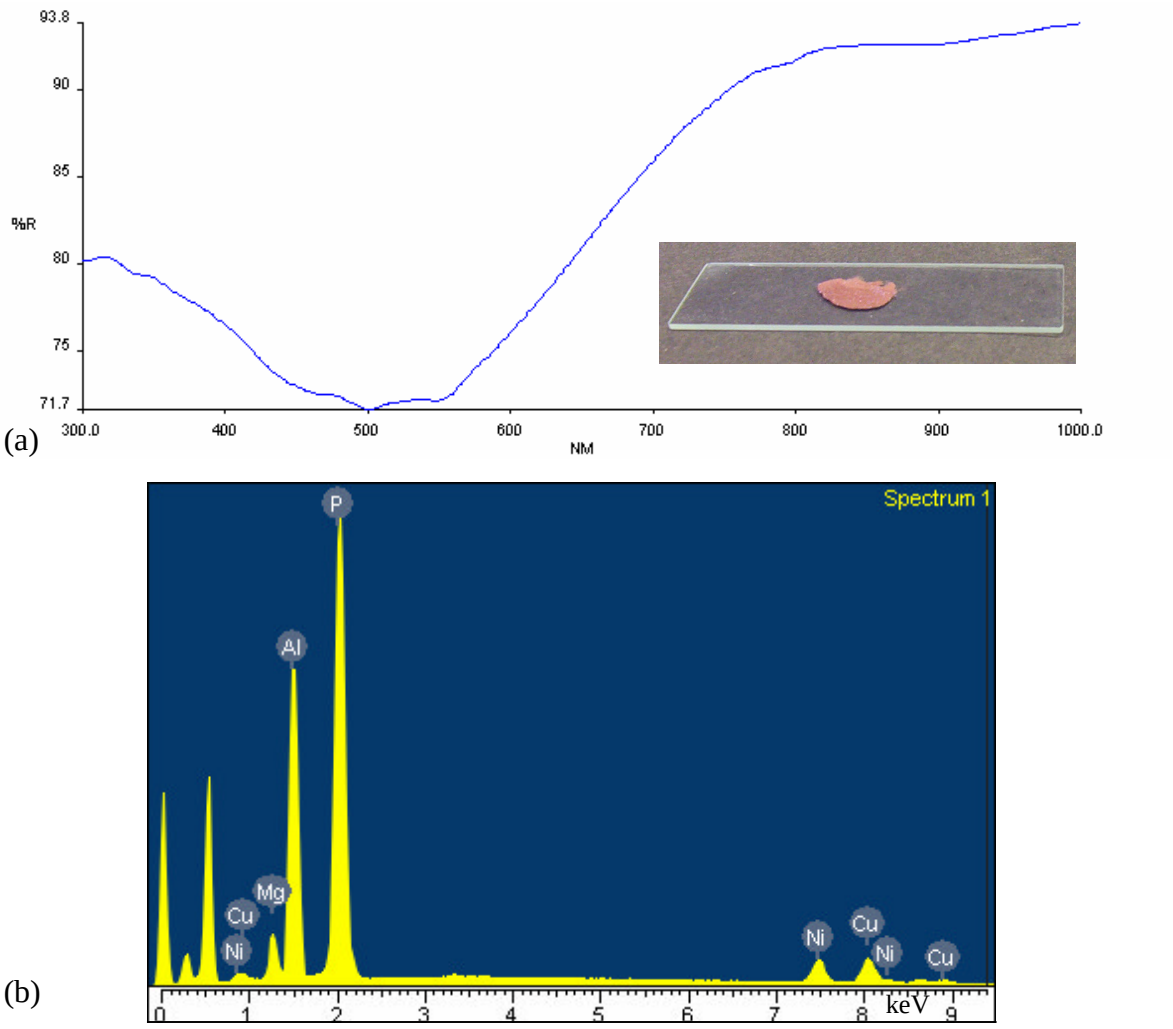

Figure 9.3: (a) Photograph and solid-state UV-Vis spectrum of Cu/Ni-cyclam-containing MgAPO STA-7. A broadening of the absorption band relative to the Cu-cyclam sample above is attributed to the presence of Ni-cyclam, which exhibits a band at approximately 430nm[66] (Figure 9.13); (b) EDX spectrum of as-made Cu/Ni-cyclam-containing MgAPO STA-7.

In contrast, the deployment of DP as the co-base favours the formation of MgAPO STA-6 (Figure 9.2) and can therefore be considered as possessing analogous structure-directing abilities to ethylene diamine (en) (section 7.4) under these conditions. Indeed, DP offers a very convenient and efficient means of achieving the STA-6 structure and can be utilised in the presence of both Cu- and/or Ni-cyclam, and has thus provided a route to a new mixed Cu/Ni-containing MgAPO STA-6 material. Inorganic elemental analysis by EDX revealed the presence of Ni and/or Cu in these samples (Table 9.2) and confirmed that a mixed Ni/Cu-containing material had indeed been synthesised. Solid-state UV-Vis analysis of this material (Figure 9.4) revealed a similar band broadening to that observed above in STA-7. This apparent shift to higher energy is consistent with literature reports[67] of λ_{max} = 488nm for a 1:1 mixture of Cu- and Ni-cyclam. CHN analysis suggests that only the complex is present in these materials; DP acts to adjust the synthesis pH and does not become incorporated in the crystallising product. Indeed, the existence of only one type of cage in STA-6 precludes the incorporation of this amine. Although on its own DP can exert some structure-directing ability, it is thought that due to its relatively small, linear shape, this effect is weak and 'overshadowed' by the stronger templating ability of the cyclam complex in these situations.

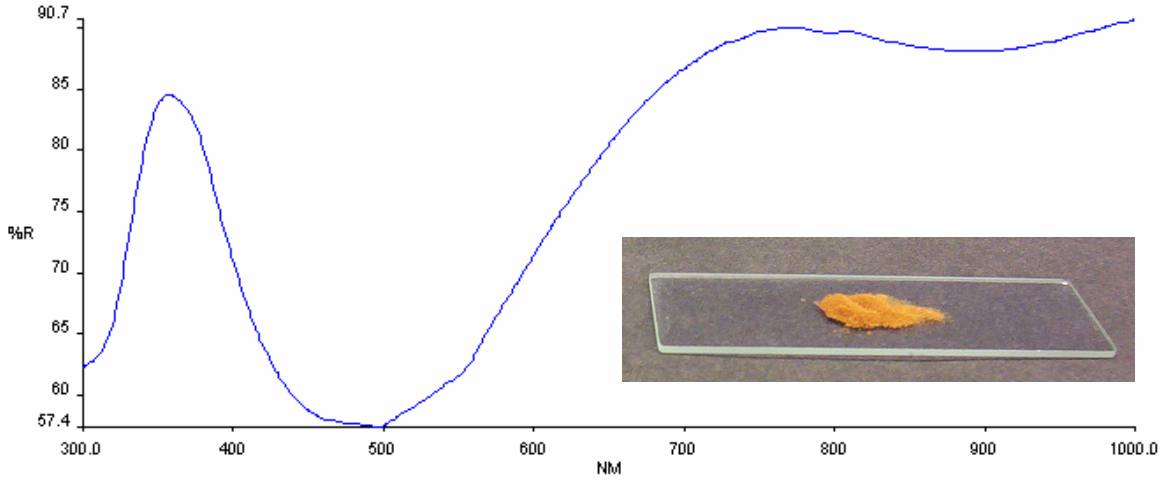

Figure 9.4: Solid-state UV-Vis spectrum and photograph of as-made Cu/Ni-cyclam-containing MgAPO STA-6

A sufficiently large crystal of as-made Cu-containing MgAPO STA-6 was examined by single crystal analysis. Although heavy twinning prevented the satisfactory solution of the structure (data suggested I-4 symmetry), Cu^{2+} was located at the centre of the large pore confirming that Cu-cyclam resides in this cage (Figure 9.5).

Disappointingly, HB also exhibited no structure-directing ability under these conditions despite possessing a geometrically interesting shape. It would appear that the addition of the $–CH_2CH_3$ substituent to DIP prevents its occlusion into the β-cage of STA-7 and structure direction proceeds through the influence of Cu-cyclam only to the STA-6 structure.

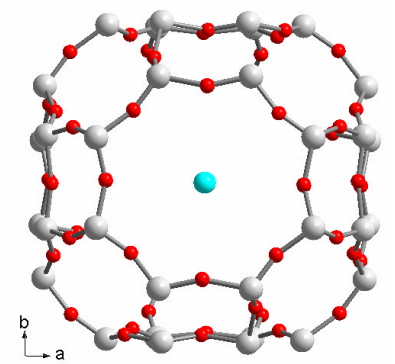

Figure 9.5: View of the main cage of as-made MgAPO STA-6 as solved from single crystal analysis. Due to twinning, data suggested I-4 symmetry and therefore all T-atoms are illustrated as the same. Cycan = Cu

ESR spectra of as-made Cu-cyclam-containing MgAPO STA-7 and STA-6 are illustrated in Figure 9.6. Due to overlap of the parallel and perpendicular regions, the spectra only show two absorptions in the parallel region and a characteristic 'overshoot' peak in the perpendicular region. Nevertheless, it is possible to measure A_{II} and to calculate g_{II} (Figure 9.6) as outlined in Chapter 2. Similarity in the ESR parameter values for these samples indicates that (as expected) Cu^{2+} ions occupy sites of similar symmetry in both materials – most probably within the macrocycle. The values of g_{II} and A_{II} compare favourably with other square-planar copper (II) systems[66] and are typical of axially symmetric copper (II) complexes with the unpaired electron in the d_{x2-y2} orbital.

By combining CHN, EDX and TGA (Figure 9.7 and Table 9.2) data, unit cell compositions were estimated for MgAPO STA-6 and STA-7 samples. These are given in Table 9.2. Framework compositions are normalised to 48 and 32 T-atoms for STA-7 and STA-6, respectively.

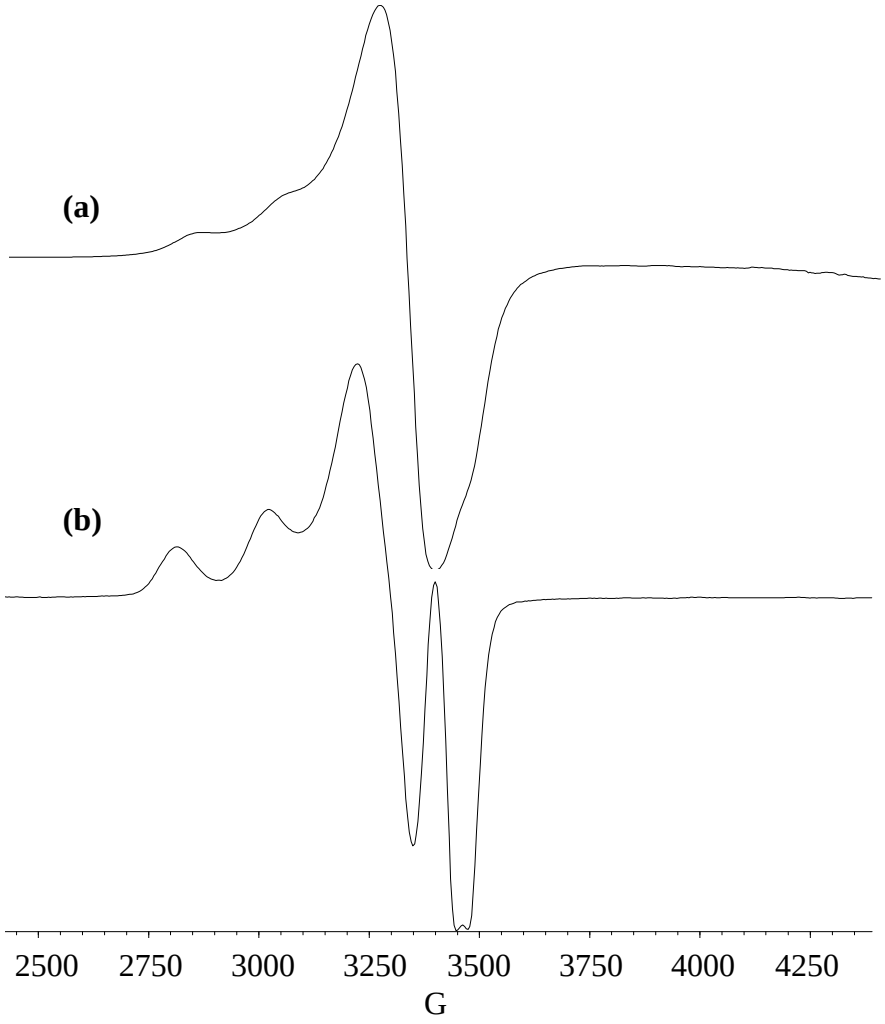

	A_{II} (G)	g_{II}
MgAPO STA-6	206	2.16
MgAPO STA-7	208	2.18
[Cu-cyclam]$(H_2O)_2$[68]	206	2.19
[Cu-cyclam]$(NO_3)_2$[66]	200	2.17
*[Cu-cyclam']$(ClO_4)_2$[69]	203	2.18

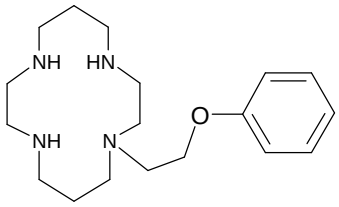

*cyclam'

Figure 9.6: ESR spectra of as-made Cu-cyclam-containing MgAPO STA-6 (a) and STA-7 (b) and table of associated parameters with comparison to similar complexes.

Sample	**C/N (CHN)**	**Cation ratio (EDX) Ni:Cu:Mg:Al:P**	**Organic content (wt%) (TGA)**	**Approximate unit cell composition**
Cu-L-MgAPO STA-7	3.6	0:2.07:11.8:12.8	16	$(CuL)_{1.8}(NC_8H_{20})_{1.8}(Mg_{3.73}Al_{21.29})P_{23.1}O_{96}$
Cu,Ni-L-MgAPO STA-7	3.3	1:1.40:3.33:26.2:30.9	17	$(NiL)_{0.78}(CuL)_{1.12}(NC_8H_{20})_{1.9}(Mg_{2.6}Al_{20.4})P_{24}O_{96}$
Cu-L-MgAPO STA-6	2.5	0:1:1.55:5.50:9.87	13	$(CuL)_{1.60}(Mg_{2.49}Al_{13.7})P_{15.8}O_{64}$
Cu,Ni-L-MgAPO STA-6	2.6	1:1.42:3.22:17.3:21.1	14	$(NiL)_{0.77}(CuL)_{1.10}(Mg_{2.48}Al_{13.3})P_{16.2}O_{96}$

Table 9.2: Elemental and TGA analysis of MgAPO samples and estimated unit cell compositions (L = cyclam).

Figure 9.7 shows typical TGA thermograms of STA-6 and STA-7. The thermogram profile would appear to be influenced by the sample's structure rather than the species present therein. For example, STA-6 exhibits a protracted weight loss in which fragments of organic material are lost gradually. In contrast, STA-7 shows a much sharper weight loss with all organic species being removed in a single, sharp event, despite there being two different organic species present. This is most probably due to the three-dimensionally connected pore system of STA-7, which will allow organic material to escape more easily than from the one-dimensionally connected pore system of STA-6. By analogy, STA-7 might be more interesting catalytically since its three-dimensionally connected pore system will permit improved diffusion and access to the internal void areas and catalytic sites.

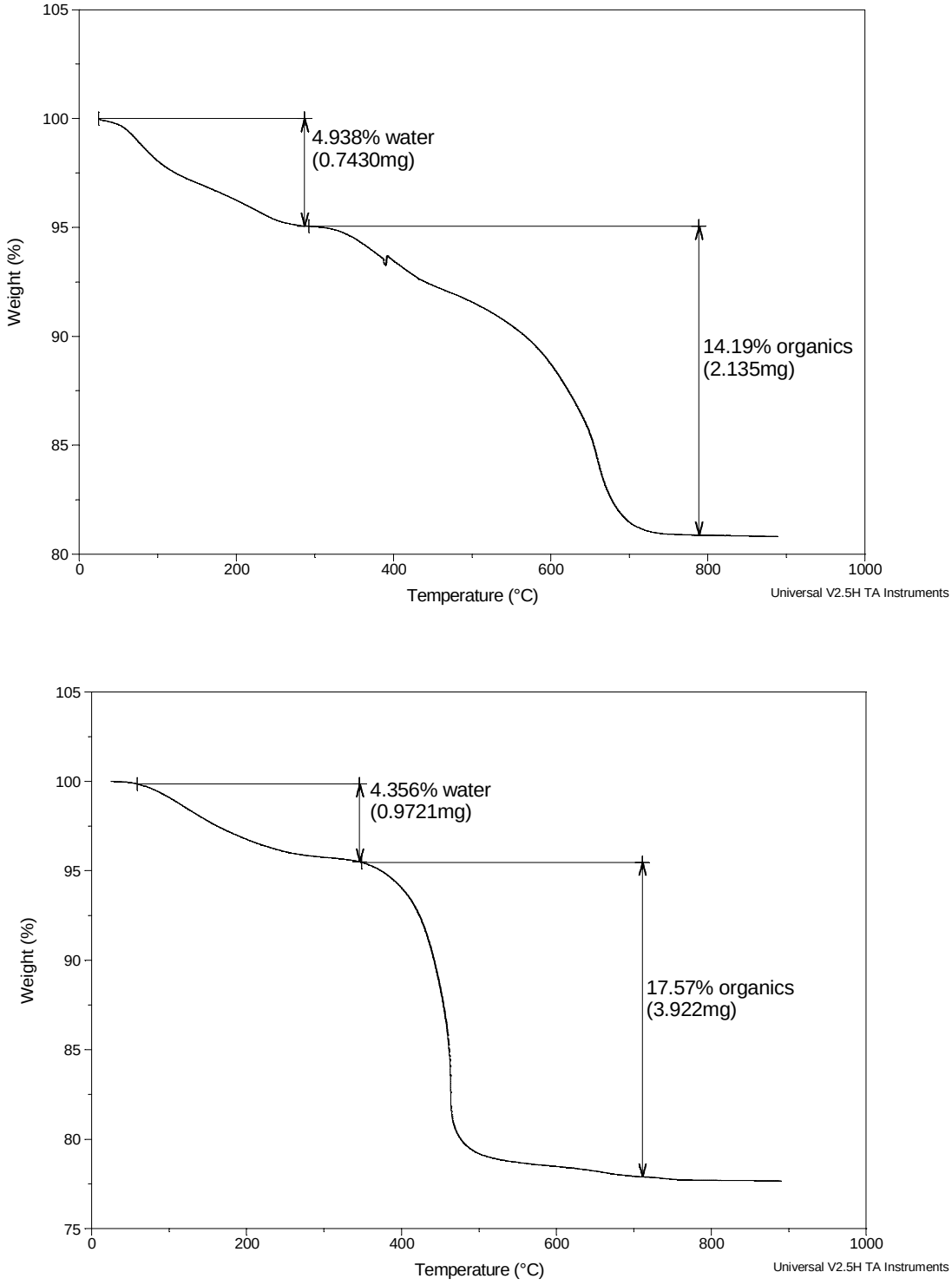

Figure 9.7: Typical TGA thermograms of MgAPO STA-6 (top) and STA-7 (bottom).

Calcination

TGA analysis indicates that while STA-7 samples are fully calcined by heating to 550°C, due to the nature of its structure STA-6 requires further heating to 750°C. Samples of MgAPO STA-6 and STA-7 containing Cu-cyclam and mixtures of Cu- and Ni-cyclam were calcined in oxygen. The resulting materials were turquoise in colour indicating, at least, the presence of Cu^{2+}. Figure 9.8 illustrates solid-state UV-Vis spectra for calcined Cu/Ni-containing MgAPO samples.

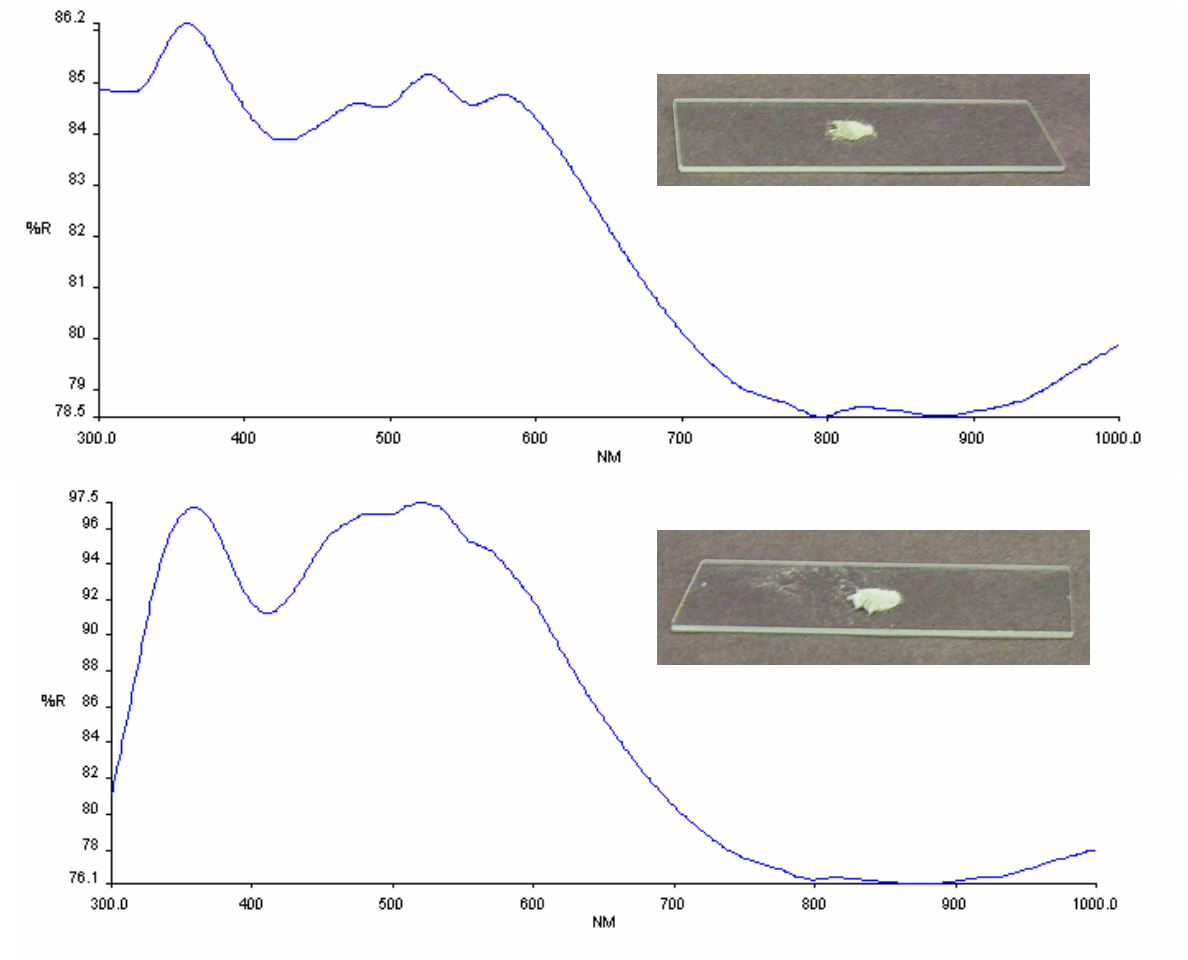

Figure 9.8: Solid-state UV-Vis spectra and photographs of calcined Cu/Ni-MgAPO STA-6 (top) and STA-7 (bottom).

A broad band at between 800 and 900nm is characteristic of Cu coordinated by oxygen (cf. aqua-copper λ_{max} = 780nm[70]). Similarly, a band at approximately 410nm (absent from the spectrum of calcined Cu-SAPO STA-7, Figure 9.19(b)) compares favourably with that of hexaaquanickel (II) (λ_{max} = 400nm[70]) and suggests that both Cu^{2+} and Ni^{2+} are indeed present and coordinated by framework and/or water oxygens. XRD analysis

of calcined samples revealed that while MgAPO STA-6 maintained its structural integrity, samples of MgAPO STA-7 partly decomposed (Figure 9.9).

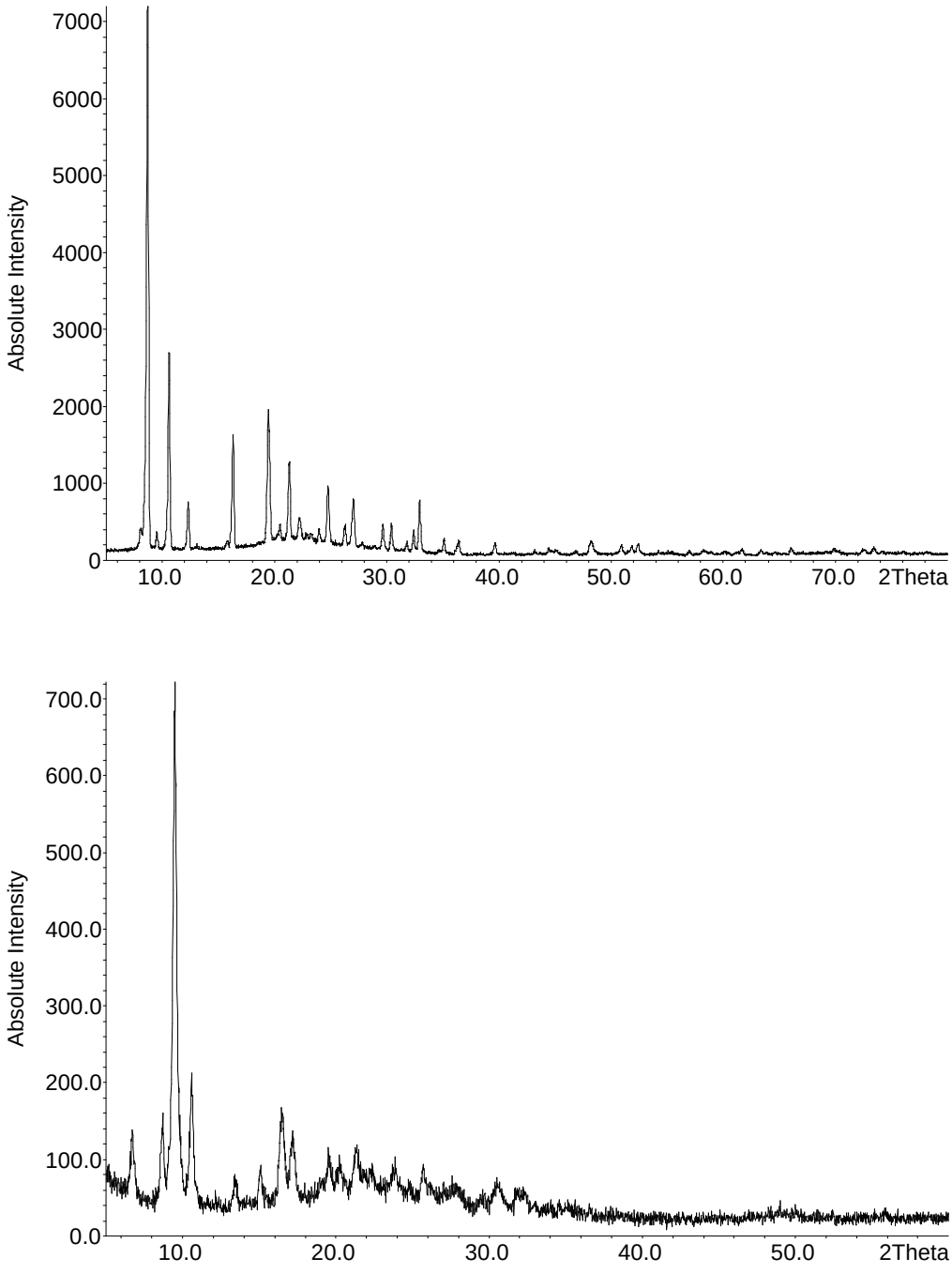

Figure 9.9: XRD patterns of calcined MgAPO STA-6 (top) and STA-7 (bottom).

Rietveld refinement of literature values for the atomic coordinates of STA-6 against XRD data for the calcined and dehydrated Cu-containing sample was conducted in an attempt to investigate the preferred location of Cu^{2+} cations within the pore system of

this structure. Following refinement of instrumental parameters, background (cosine function; 26 parameters) and peak shape (pseudo-Voigt funcion), atomic parameters were refined with Al/Mg-O, P-O, $(O\text{-}O)_P$ and $(O\text{-}O)_{Al/Mg}$ distances constrained as 1.75 Å (σ = 0.01Å), 1.53Å (σ = 0.01Å), 2.48Å (σ = 0.02Å) and 2.84Å (σ = 0.02Å), respectively, in order to maintain a sensible framework geometry (refined parameters are listed in Appendix E(1)). However, due to the general instability of MgAPO materials on calcination and the appearance of impurity peaks in the XRD pattern for this sample (excluded from the refinement, phase identity not known), data quality was not ideal for detailed structural analysis. Consequently, although still reasonable, the framework geometry exhibits more variability than observed in other similar phases (see later refinements), and attempts at locating Cu^{2+} cations via Fourier difference maps were unsuccessful. Nevertheless, a final R_{wp} of 13.1% and R_p of 9.48% were achieved and the structure was confirmed as correct (Figure 9.10).

Summary

These initial exploratory studies of Cu- and Ni-cyclam in combination with a selection of co-bases confirm that both complexes can direct the formation of either STA-6 or STA-7 depending on the co-base present. Consequently, both phases have been synthesised with a mixture of Cu- and Ni-cyclam within their pores for the first time. It would appear that under these conditions, Cu- and Ni-cyclam complexes will direct the formation of MgAPO STA-6 unless in the presence of a co-base that can stabilise the β-cage of STA-7 and thus favour the formation of this phase. It should be noted that in the presence of Mg, STA-6 is, historically, the favoured phase and therefore should be expected from syntheses involving co-bases with little or no structure-directing ability. While DP and HB permit the formation of STA-6, TEAOH and DIP stabilise STA-7. Through careful choice of co-base, therefore, it is possible to discriminate between the formation of STA-6 and STA-7. This targeting strategy was expanded to other framework types, which are discussed in the following sections.

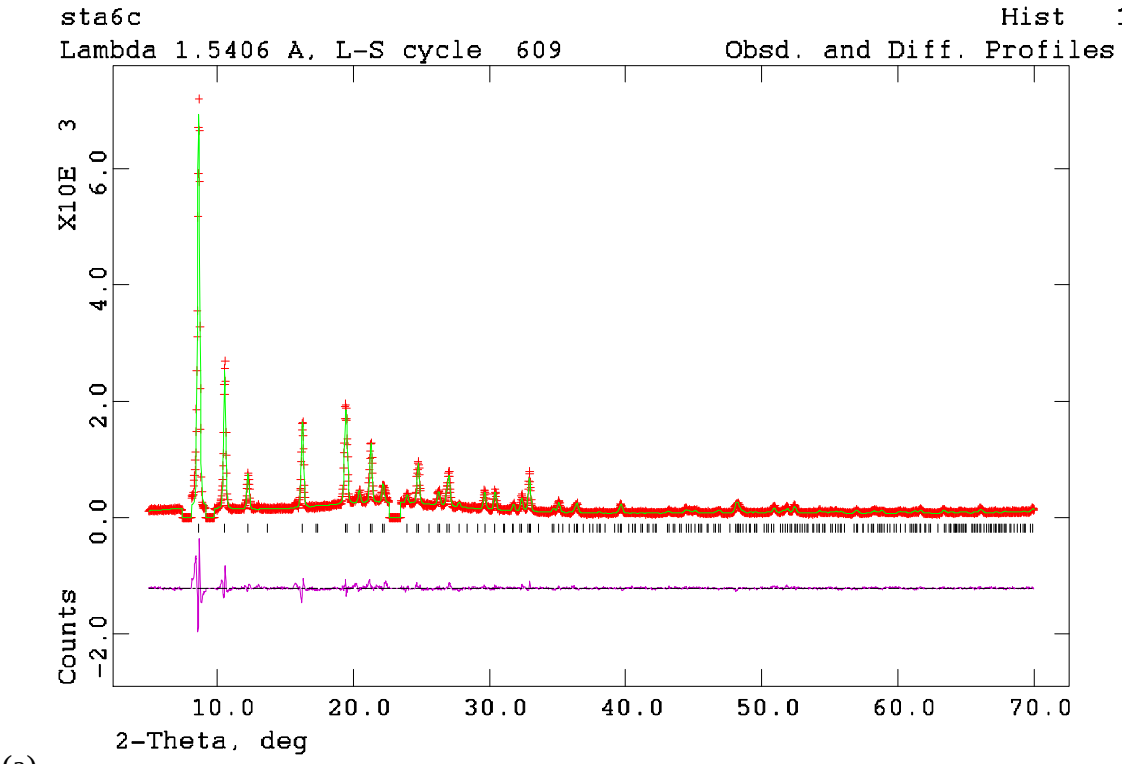

(a)

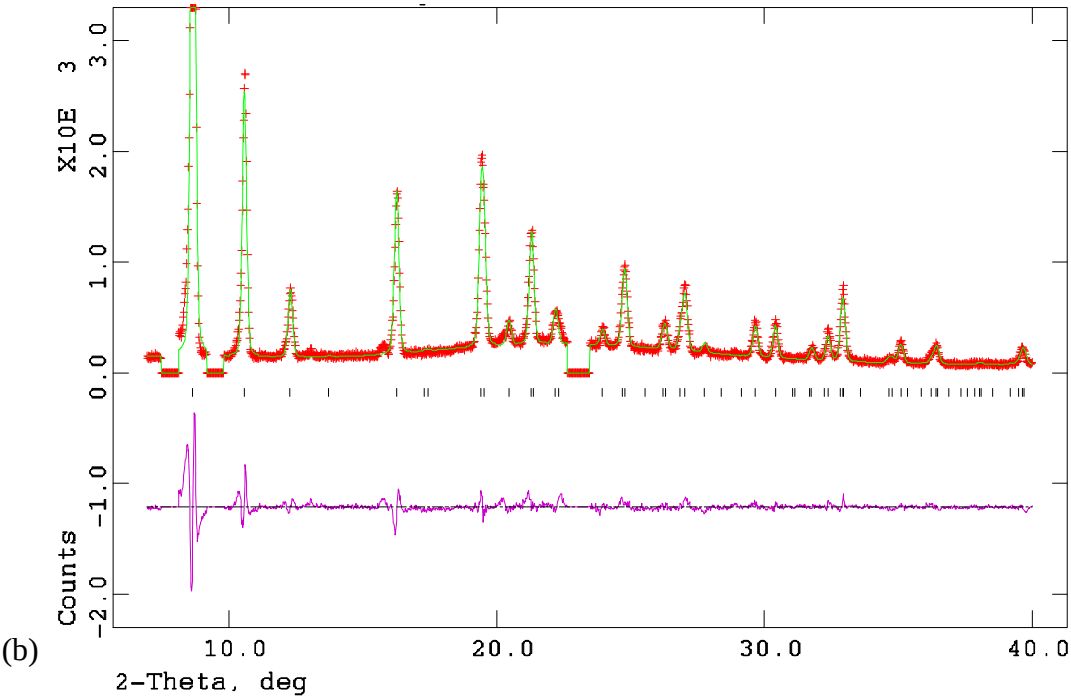

(b)

Figure 9.10: (a)Rietveld plot from the structural refinement of MgAPO STA-6. (red: experimental data, green: model, purple: difference), (b) expanded low angle region. Impurity peaks are excluded at 8, 10 and 23^{o} 2θ.

9.2: Extension to AlPO Synthesis

The metallated cyclam route to structure direction offers a convenient means of introducing metals such as Cu and Ni into the pores of target materials. Upon calcination of MgAPO (and SAPO) species, divalent cations are distributed through the pore system. A non-substituted AlPO framework, however, has no charge. The incorporation of cationic structure-directing species may be facilitated by the addition of fluoride, which will associate with framework T-sites and thus introduce a balancing negative charge. Calcination of such materials, however, will result in the loss of fluoride and organic species and the formation, therefore, of nanoparticulate metal oxide within the pores. With the aim of synthesising Cu and/or Ni oxide nanoparticle-containing STA-6 and STA-7, the above structure directing approaches were applied to fluoride-containing AlPO gels.

Complexed metal	Co-base	Product (by XRD)
No metal	TEAOH	STA-7 (with trace Si)
		Berlinite and/or AlPO-5
	DP	[F,cyclam]-AlPO-CHA (UT-6)
Cu	TEAOH	STA-7 (with trace Si)
		AlPO-5 + trace STA-7
		Layered Phase
	DP	[F, Cu-cyclam]-AlPO-SAS
	DIP	[F, Cu-cyclam]-AlPO-SAS
Ni	TEAOH	Layered phase + AlPO-11
	DP	Layered phase + AlPO-11
	DIP	Layered phase + AlPO-11
Cu + Ni	TEAOH	AlPO-5
	DP	Layered phase + AlPO-11

Table 9.3: Summary of AlPO syntheses with cyclam and typical products.

As test cases, AlPO gels containing non-metallated cyclam were prepared with DP and TEAOH co-bases (Table 9.3). Gels containing DP and cyclam crystallised as spherulitic

assemblages of plate-like crystals with the [F, cyclam]-AlPO-CHA structure (Figure 9.11) denoted UT-6.[71] This structure was synthesised previously by Morris *et al.* in the presence of cyclam only,[49] and therefore DP would not appear to influence this system. The structure may be considered as a triclinic variant of the mineral Chabazite (CHA) and contains both tetrahedral AlO_4 and octahedral AlO_4F_2 units, as confirmed by ^{27}Al MAS NMR (Figure 9.11). The structure of UT-6 is discussed further in section 11.3.

Introduction of Cu (as Cu-cyclam) to this synthesis resulted in the formation of [F, Cu-cyclam]-AlPO-SAS. This phase was also observed by Morris *et al.* in the absence of co-bases as a minor impurity in a fluoride-AlPO synthesis involving Cu-cyclam.[49] However, until now, it has not been synthesised as a phase-pure powder sample. The structure of this material (as solved by Morris *et al.* from single crystal data) is a monoclinic variant of STA-6, with the distortion caused primarily by the association of fluoride with Al T-sites within D6R units. The same material is also obtained in the presence of DIP co-base. Figure 9.12 illustrates the behaviour of this material upon calcination under various treatments. TGA analysis (Figure 9.12) suggests calcination temperatures of 390^{o}C and above would be sufficient.

Typical calcination treatment (550^{o}C, 5^{o}C/min, under O_2) resulted in partial loss of crystallinity and a change of phase. The same poorly crystalline phase is also observed at lower temperatures and slower heating rates. However, heating to 390^{o}C at 1^{o}C/min under O_2 resulted in a transformation to tetragonal AlPO STA-6. Restoration of tetragonal symmetry is also observed on calcination at 450^{o}C, 5^{o}C/min under a N_2 atmosphere. Combining EDX and TGA data suggests an approximate unit cell composition of $Cu_{1.8}(C_{10}N_4)_{1.8}F_{0.64}Al_{16.2}P_{15.8}O_{64}$ (based on tetragonal STA-6) for the as-made material, and therefore approximately two Cu per unit cell of the calcined material.

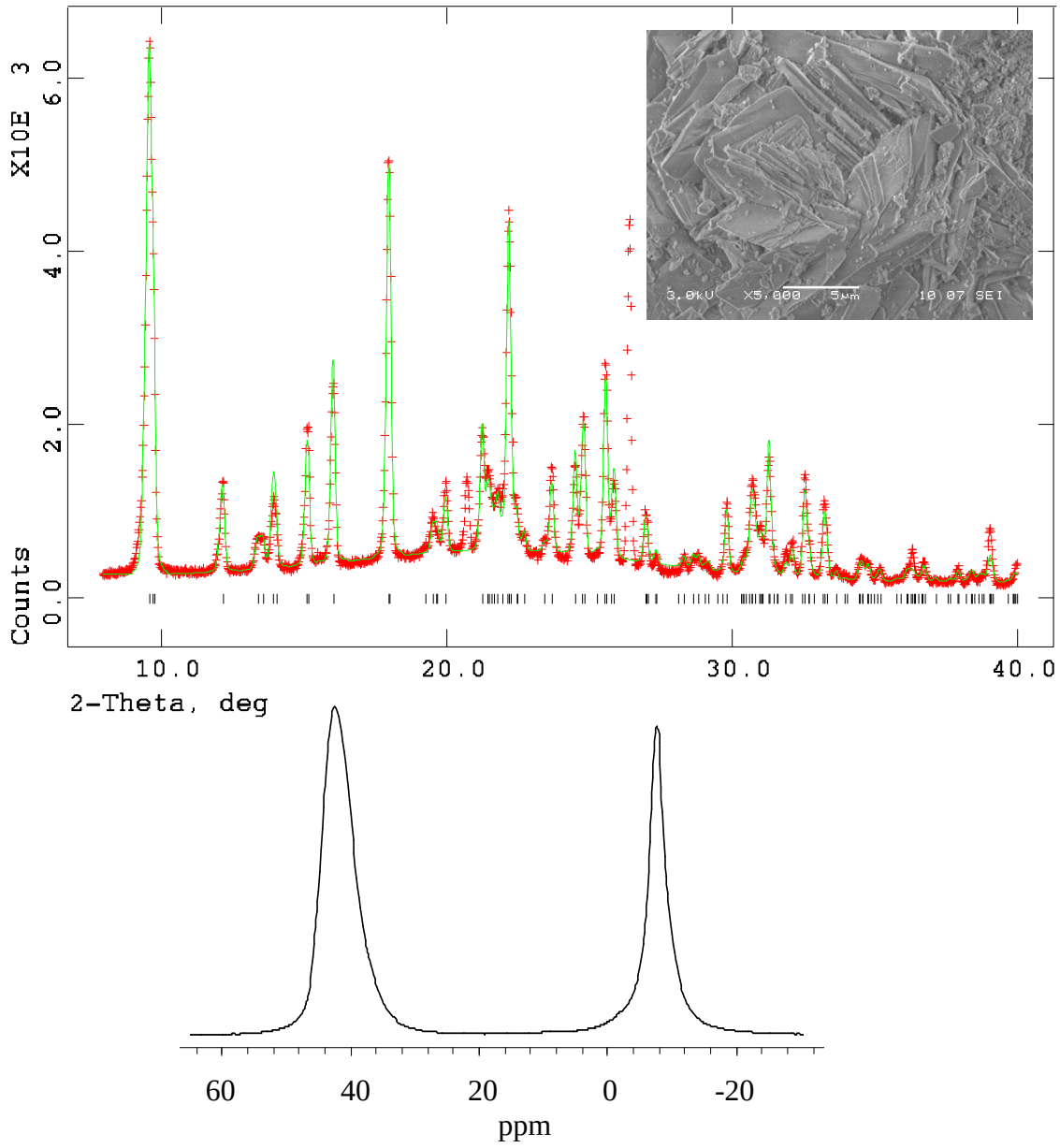

Figure 9.11: (top) Comparison of experimental (red) and theoretical (green) XRD patterns for as-made [F, cyclam]-AlPO-CHA (UT-6) (unmatched peaks are berlinite impurity), inset: SEM images of plate-like crystals, (bottom) ^{27}Al MAS NMR spectrum of the as-made material (δ –6.6ppm octahedral Al (AlO_4F_2), 40.7ppm tetrahedral Al (AlO_4)).

(a)

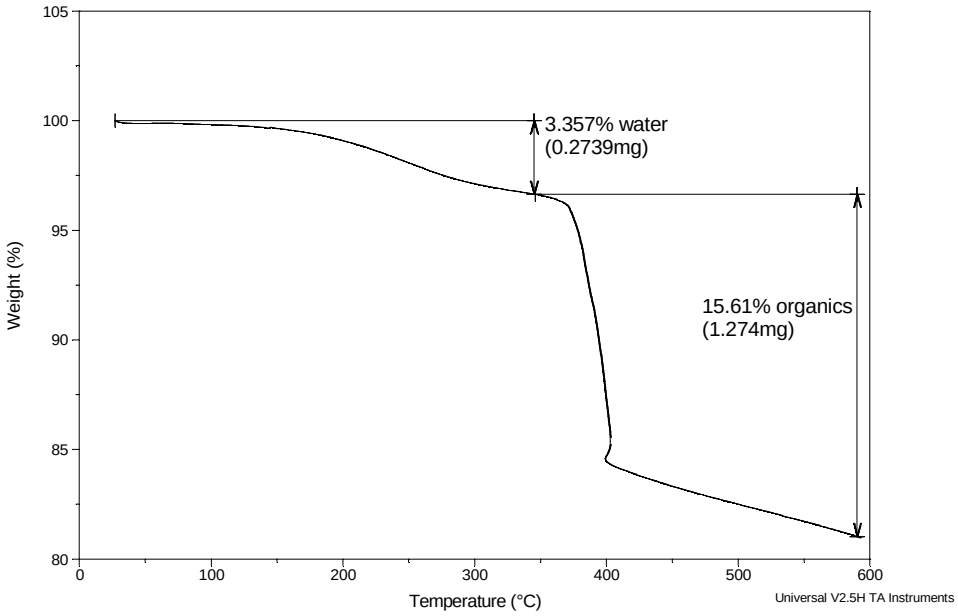

(b)

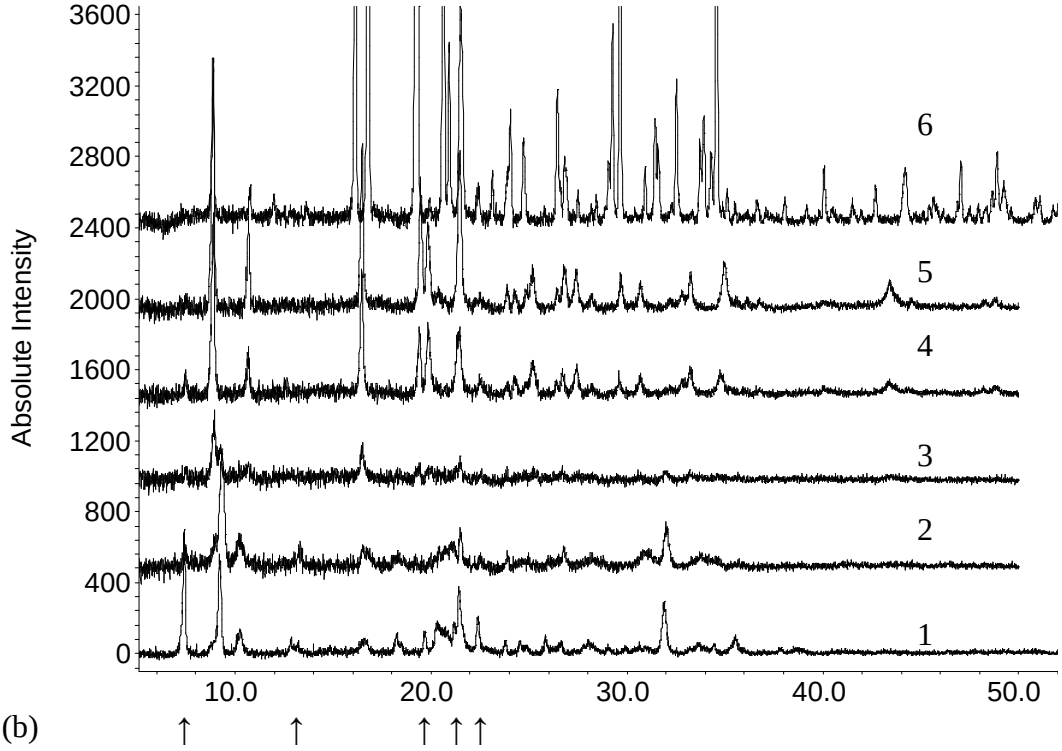

Figure 9.12: (a) TGA thermogram of as-made [F, Cu-cyclam]-AlPO-SAS, and (b) XRD patterns of [F, Cu-cyclam]-AlPO-SAS calcined under different conditions: (1) 550^{o}C, 5^{o}C/min, under O_2, (2) 550^{o}C, 1^{o}C/min, under O_2, (3) 450^{o}C, 1^{o}C/ min, under O_2, (4) 390^{o}C, 1^{o}C/ min, under O_2; restoration of tetragonal symmetry, (5) 450^{o}C, 5^{o}/min under N_2; restoration of tetragonal symmetry, (6) as-made monoclinic material for comparison. (principal AlPO-5 impurity peaks marked by ↑)

AlPO-5 is present to a certain extent in all calcined samples (but especially those conducted under O_2 at 5°C/min). This is regarded as a stable intermediate between [F, Cu-cyclam]-AlPO-SAS and the dense phase AlPO berlinite. It is thought that any loss of crystallinity on calcination under O_2 is due to the formation of acidic species (HF + H_2O) under these conditions, which dissolve the AlPO framework.

In contrast, replacing Cu-cyclam with Ni-cyclam in the presence of DP resulted in the formation of a purple, layered phase analogous to CoAlPO-cyclam-1[45] mixed with yellow crystals of AlPO-11 (AEL). By reducing the quantity of Ni-cyclam present in the gel, the formation of the layered phase can be discouraged and AlPO-11 becomes the major phase (Table 9.4). CHN analysis suggests a C/N ratio of 2.96. This is slightly higher than what is expected from only cyclam being present (2.5) and may indicate the presence of a small amount of DP.

Al	**P**	**H_2O**	**HF**	**Ni-cyclam**	**DP**	**Major phase**
1	1	50	0.5	0.125	1.4	LP
				0.063	1.2	LP + AlPO-11
				0.031	1.1	LP + AlPO-11
				0.016	1.0	AlPO-11

Table 9.4: Optimising synthesis conditions to favour Ni-cyclam-containing AlPO-11

DP can, itself, direct the formation of AlPO-11.[72] It is possible that the complexation of Ni by cyclam reduces cyclam's ability to direct the formation of, for example, STA-6 in the AlPO regime. As a result, the influence of DP overrides and directs the growth of AlPO-11, which fortuitously encapsulates the Ni-cyclam complex. Any residual complex may then become incorporated in a layered phase. EDX and TGA analysis suggests an approximate unit cell composition of $(\text{Ni-cyclam})_{0.5}F_{1.03}Al_{20}P_{20}O_{80}$. Figure 9.13 illustrates the solid-state UV-Vis spectrum of as-made Ni-cyclam-containing AlPO-11, exhibiting a band at approximately 430nm characteristic of the yellow, square-planar Ni-cyclam complex.[66] XRD analysis suggests that the AEL structure is retained upon calcination at 370°C, 5°C/min under O_2. The calcined material is black in colour, suggestive of the formation of nickel oxide.

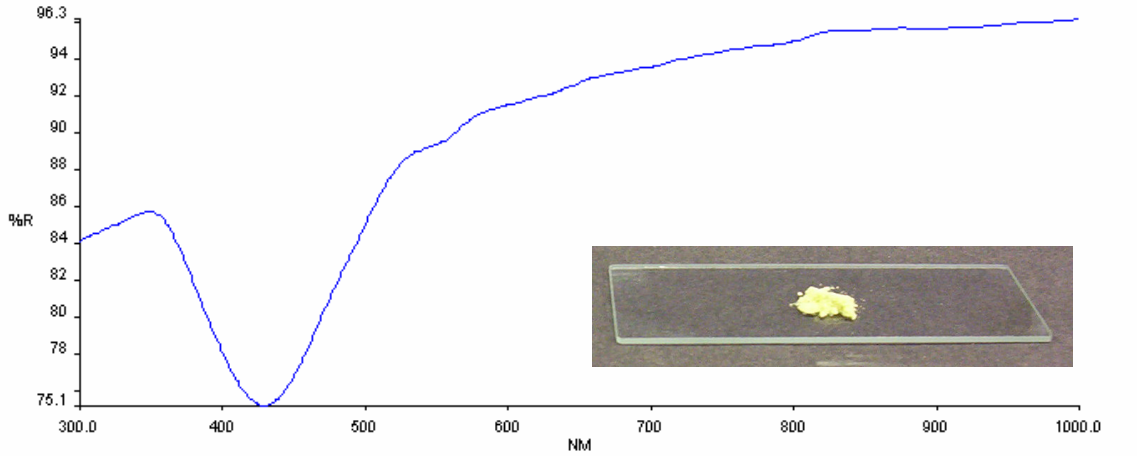

Figure 9.13: Solid-state UV-Vis spectrum and photograph of as-made Ni-cyclam-containing AlPO-11.

To date, the pure AlPO analogue of STA-7 has not been synthesised. It was therefore hoped that by employing the cyclam/TEAOH co-templating approach, this material could be synthesised. Indeed, initial attempts employing either non-metallated cyclam or the Cu-cyclam complex with TEAOH produced highly crystalline samples of STA-7. However, calcination of the Cu-cyclam-containing sample resulted in a colour change to *turquoise*. This was highly unexpected since black CuO was anticipated to form within the pores. Subsequent elemental analysis by EDX revealed that both samples contain adventitious Si impurity (Table 9.5 and Figure 9.14). Nevertheless, at 4% of total T-sites in both samples, this represents the lowest observed Si loading in the SAPO form of this phase. Both samples are stable to calcination at 550^{o}C, 5^{o}C/min under O_2.

Nitrogen adsorption was conducted gravimetrically on a calcined sample of the Cu-free (S)APO STA-7 at -175^{o}C. The resulting isotherm (Figure 9.15) exhibits a typical type 1 profile, characteristic of microporous materials with fast initial uptake followed by a levelling off as the pore network fills. A maximum uptake of approximately 19.5% by mass is observed, suggesting an internal pore volume of approximately 0.24cm^3/g.

(a)

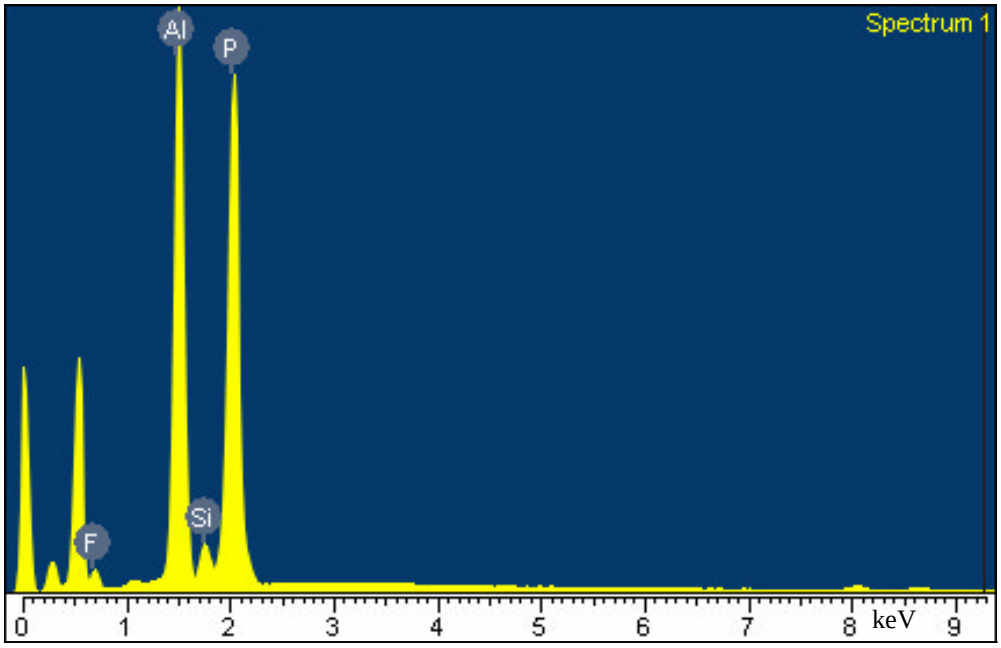

(b)

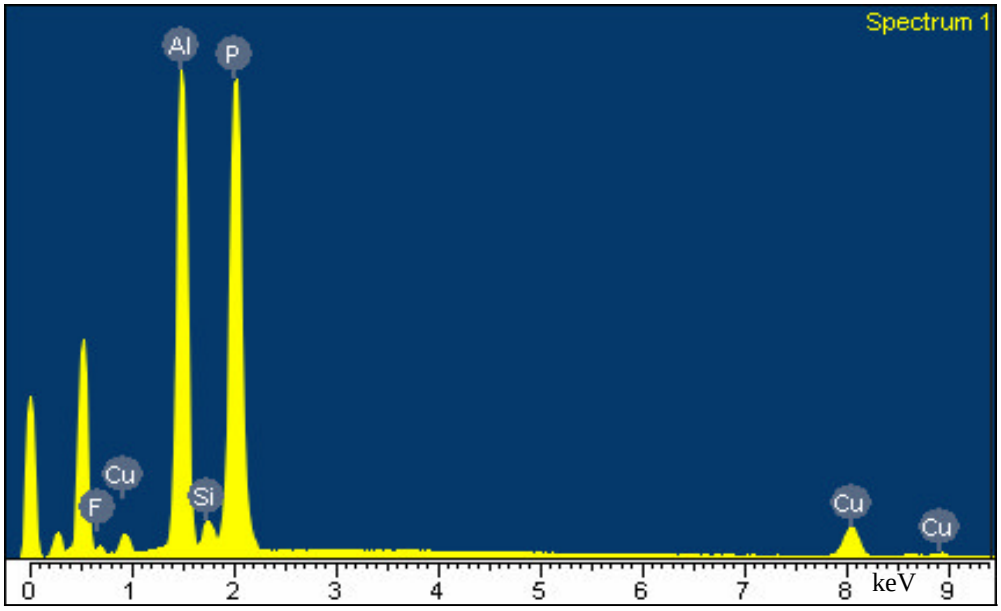

Figure 9.14: EDX spectra of (a) 'AlPO' STA-7 and (b) Cu-cyclam-containing 'AlPO' STA-7 showing Si impurity peak at approximately 1.75keV.

Sample	Approximate unit cell composition
(Si)AlPO STA-7	$(cyclam)_{1.96}(NC_8H_{20})_{1.96}F_{1.96}Al_{23.8}(Si_{1.90}P_{22.3})O_{96}$
Cu-cyclam-(Si)AlPO STA-7	$(Cu\text{-}cyclam)_{1.9}(NC_8H_{20})_{1.9}F_{2.44}Al_{23.9}(Si_{1.87}P_{22.2})O_{96}$

Table 9.5: Approximate unit cell compositions of (Si)AlPO and Cu-(Si)AlPO STA-7 from EDX, CHN and TGA analysis.

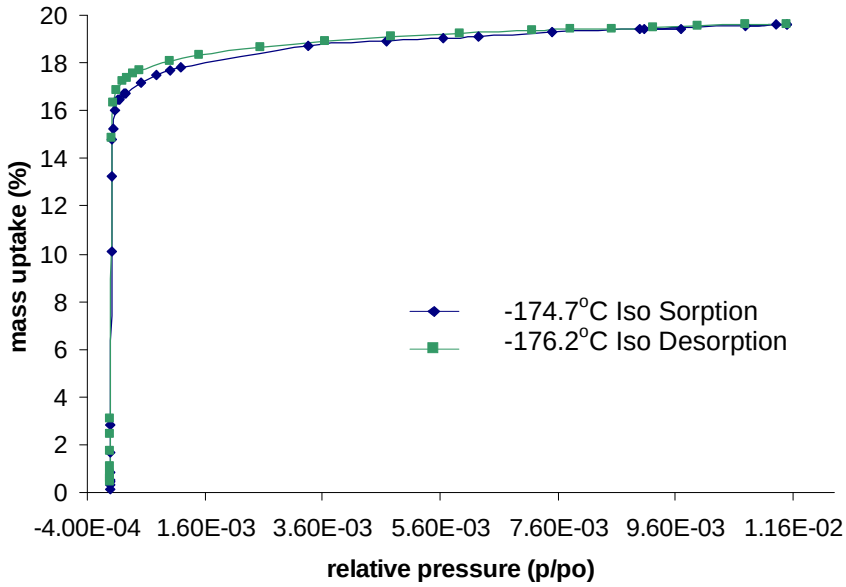

Figure 9.15: Nitrogen adsorption/desorption isotherm for (S)APO STA-7.

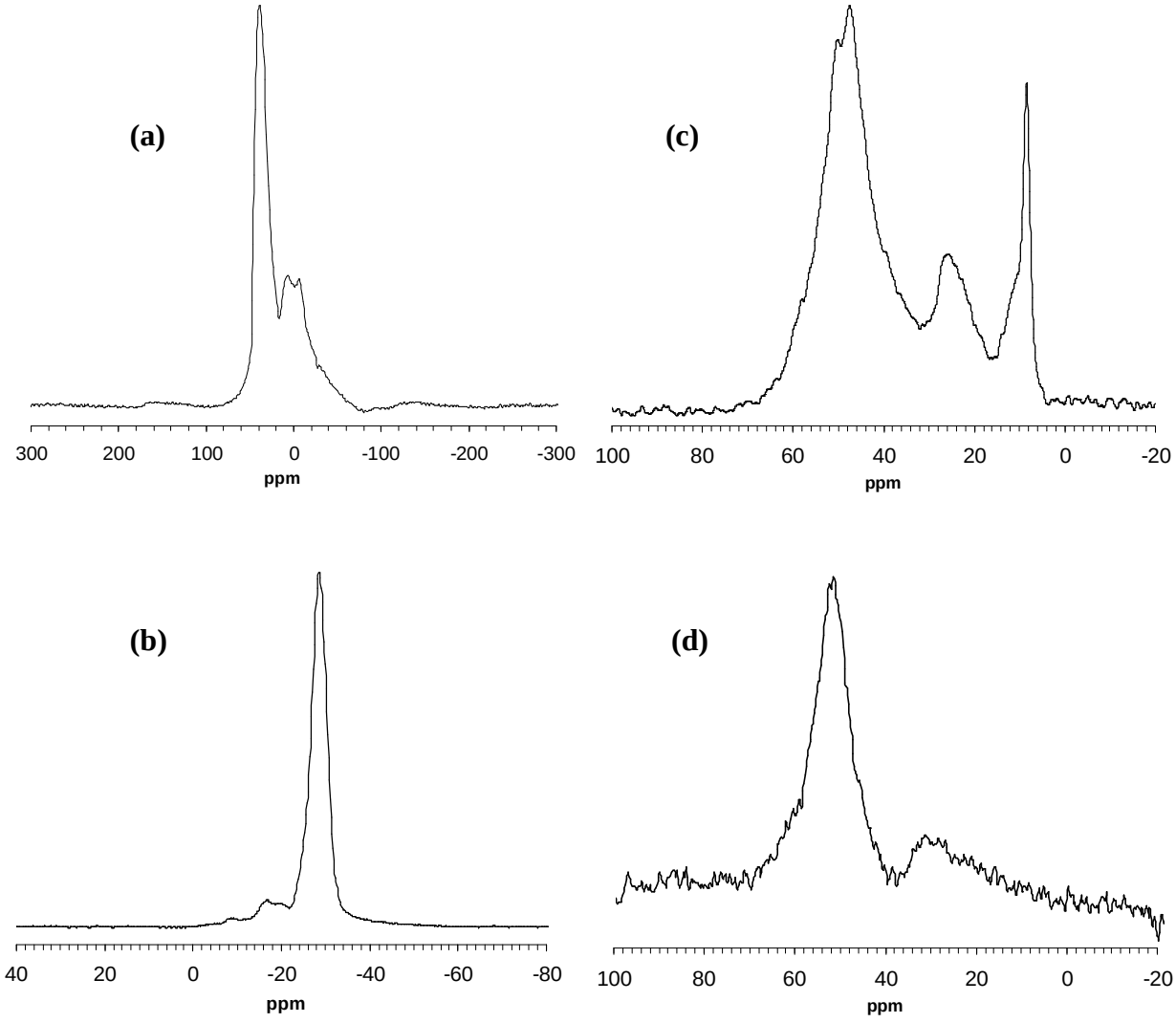

Figure 9.16: (a) ^{27}Al (b) ^{31}P and (c) ^{13}C MAS NMR spectra of as-made (S)APO STA-7; (d) ^{13}C spectrum of cyclam starting material for comparison.

The ^{27}Al MAS NMR spectrum (Figure 9.16(a)) of this sample exhibits at least one signal at δ 37.6ppm, and probably a second at δ 6.88ppm. While a chemical shift of around 38ppm is characteristic of tetrahedral Al,[73] the signal at lower ppm is suggestive of five and/or six coordinate Al and implies association of extraframework fluoride, hydroxyl and/or water species with certain framework aluminium sites. A strong signal at δ 28.7ppm in the ^{31}P MAS NMR spectrum (Figure 9.16(b)) is consistent with tetrahedral P.[73] However, the source of a weaker signal at δ 16.9ppm is unclear. The ^{13}C MAS NMR spectrum (Figure 9.16(c)) exhibits several overlapping signals due to the macrocycle and co-base as expected. By comparing this spectrum with that of the cyclam starting material (Figure 9.16(d)), in conjunction with that of TEAOH-containing MgAPO-34 (Figure 11.14(a)), it is possible to assign signals at δ 8.34 and 50.1ppm to the CH_3 and CH_2 groups, respectively, of TEAOH. Signals at δ 25.6 and 47.5ppm are assigned to the central carbon of the $CH_2CH_2CH_2$ moiety and the carbon attached directly to nitrogen in cyclam, respectively. Comparison with the ^{13}C MAS NMR spectrum of as-made SAPO STA-6 (Figure 10.1(d)) (containing only cyclam) reveals that a shoulder at δ 11ppm is due to cyclam and it would appear that signals from the central carbon of the propyl chain, which overlap in the spectrum of the starting material, are being resolved in these materials, and it is likely that the macrocycle is adopting several different conformations within the α-cages of this structure.

Subsequent attempts at synthesising pure AlPO STA-7 in the presence of non-metallated cyclam resulted invariably in the formation of either the dense phase berlinite or AlPO-5.

Table 9.6 summarises various strategies adopted to achieve Cu-cyclam-containing AlPO STA-7. Unfortunately, the principal phase obtained in most syntheses was AlPO-5 with, in certain preparations, a small amount of STA-7, and phase-pure Cu-containing AlPO STA-7 remained elusive. EDX analysis of the STA-7-containing AlPO-5 samples suggested that Cu is predominantly located in STA-7 (with approximately 2 Cu per cell as expected). However, higher than background levels of Cu were also detected in the bulk AlPO-5 phase (although at much lower levels and approximately 0.5 Cu per unit cell) and it is therefore likely that some Cu-cyclam has been entrained into the large

channels of this phase. Figure 9.17 illustrates the XRD pattern, EDX and solid-state UV-Vis spectra and an SEM image of this sample.

Al	P	H_2O	HF	TEAOH	Cu-Cyclam	Product
1	1	40	0.24	0.6	0.13	amorphous
			0.50			amorphous
		70	0.50			amorphous
		40	0.24		0.25	LP + AlPO-5
			0.10			
			0.24		0.38	
	0.85	80	0.50	0.6	0.25	amorphous
			0.24	0.5	0.25	LP
			0.24	0.4	0.13	AlPO-5 + STA-7
			0.20*			
			0.14			
			0.07			
		40	0.24			
		28				

Table 9.6: Summary of gel compositions explored in the search for phase pure Cu-cyclam-containing AlPO STA-7. All syntheses conducted at pH 7 and 190^oC. Ageing of gels prior to addition to autoclave for between 1 and 20 hours at RT and 80^oC, with and without stirring, had no effect on the outcome of these syntheses.

** synthesis also conducted in the presence of seed SAPO STA-7crystals.*

LP = unknown, probably layered phase.

By increasing the quantity of Cu-cyclam in the preparations an, as yet, unidentified phase was obtained. XRD and SEM analysis revealed a small quantity of AlPO-5 impurity (Figure 9.18). The bulk phase exhibits random shard-like assemblages of needle-shaped crystals, and a cationic ratio of 1.2Al : 1P : 0.22 Cu (from EDX). CHN analysis suggests a C/N ratio of 2.5, which is consistent with only cyclam being present. This deep purple-coloured material, however, is not stable to calcination (even with gentle heating under N_2) and is thought to be a layered phase.

(a)

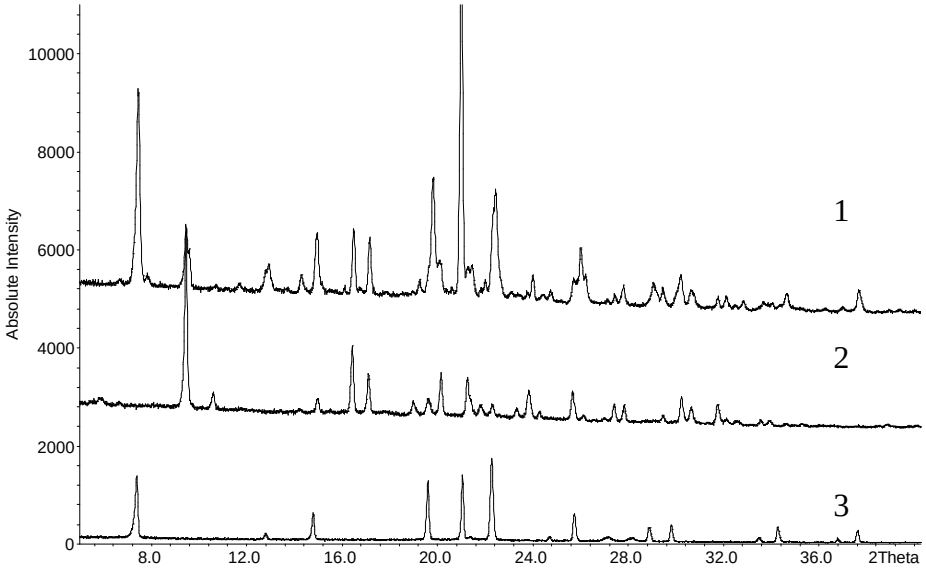

(b)

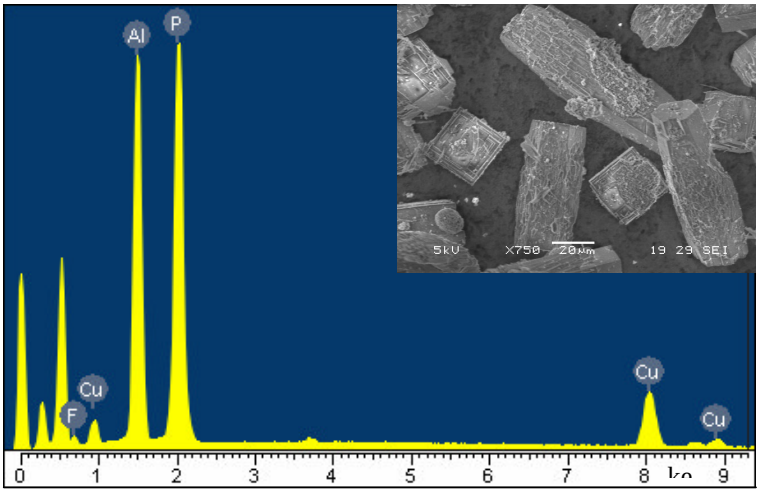

(c)

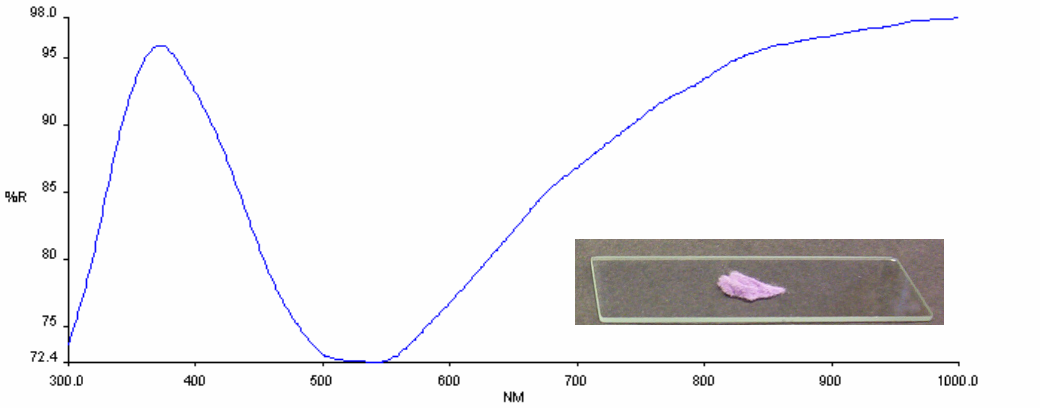

Figure 9.17: (a) XRD pattern of as-made Cu-cyclam-containing AlPO-5 + STA-7 (1) with typical XRD patterns of SAPO STA-7 (2) and AlPO-5 (3) for comparison, (b) EDX spectrum revealing no Si impurity and presence of Cu and (inset) SEM image showing pseudo-cubic STA-7 crystals amongst poorly formed hexagonal AlPO-5 crystals, (c) solid-state UV-Vis spectrum and photograph of the as-made material consistent with Cu-cyclam.

As is the case with DP, replacing Cu-cyclam with Ni-cyclam in the presence of TEAOH resulted in a mixture of a purple, layered phase and yellow AlPO-11. A similar result was also obtained with DIP as the co-base.

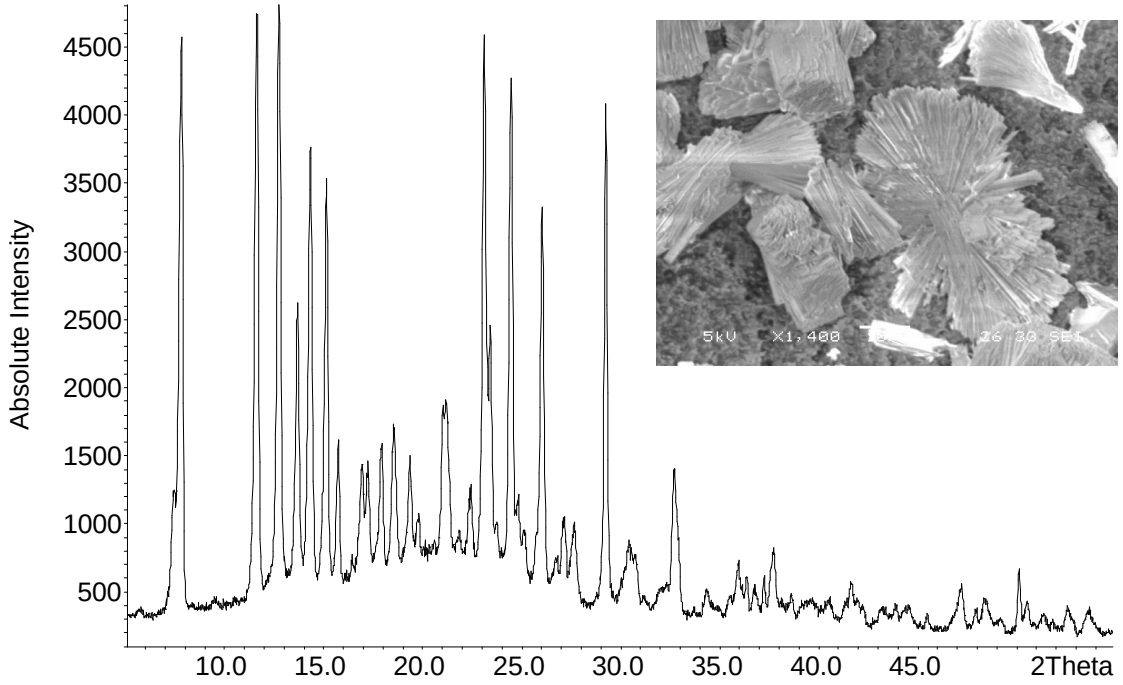

Figure 9.18: XRD pattern and SEM images of unknown Cu-cyclam-containing AlPO phase.

Summary

The structure directing strategies developed in the MgAPO regime would not appear to transfer easily to unsubstituted AlPO systems. While Cu-containing STA-6 was achieved (post calcination), AlPO STA-7 proved difficult to synthesise. At best, mixtures of AlPO-5 and trace STA-7 were achieved in the presence of Cu-cyclam. By increasing the quantity of Cu-cyclam present an unknown and probably layered phase is obtained. Similarly, Ni-cyclam would appear to favour the formation of a layered phase, although it can also be encapsulated in AlPO-11. It is likely, however, that the latter is templated by the co-base and traps Ni-cyclam within its pores as it forms, resulting in low Ni-loading.

9.3: Extension to SAPO Synthesis

Since SAPO materials are generally more stable than their MAPO and AlPO counterparts and therefore more attractive as potential catalysts, the strategies developed in the MgAPO regime discussed above were extended to SAPO synthesis gels in order to target SAPO STA-6 and STA-7 with Cu and/or Ni in the pore system.

Complexed metal	Co-base	Product (by XRD)
Cu	TEAOH	STA-7
	DIP	STA-7 + STA-6
	DP	STA-6
Cu + Ni	TEAOH	STA-7
	DP	STA-6
No metal	TEAOH	STA-7
	DIP	STA-6 + trace STA-7
	DP	STA-6

Table 9.7: Summary of templating species employed in SAPO syntheses and typical products obtained.

As illustrated in Table 9.7, the structure directing strategies developed for MgAPO synthesis transfer much more readily to the synthesis of SAPO materials than to AlPO materials. In this way, SAPO STA-6 was successfully synthesised in the presence of Cu-cyclam and, for the first time, Cu-/Ni-cyclam mixtures when DP was acting as co-base. SAPO STA-7 could be obtained with TEAOH as co-base. Deployment of DIP in a SAPO regime, however, resulted in a mixture of both STA-6 and STA-7, and therefore TEAOH was elected as the co-base of choice in later attempts at targeting STA-7. As in the case of MgAPO samples, EDX analysis confirmed the presence of Ni and/or Cu and CHN analysis indicated the presence of both complex and co-base in STA-7 samples, while only the complex is present in STA-6. Solid-state UV-Vis spectra (Figures 9.19(a), 9.20(a) and 9.21(a)) of as made samples are, once again, consistent with the presence of the desired complex(s), while ESR spectra (Figure 9.22) and parameters of as-made Cu-cyclam-containing materials are in agreement with those of MgAPO

analogues and confirm the presence of the Cu-cyclam complex. Table 9.8 summarises elemental analysis of these materials and lists suggested unit cell compositions.

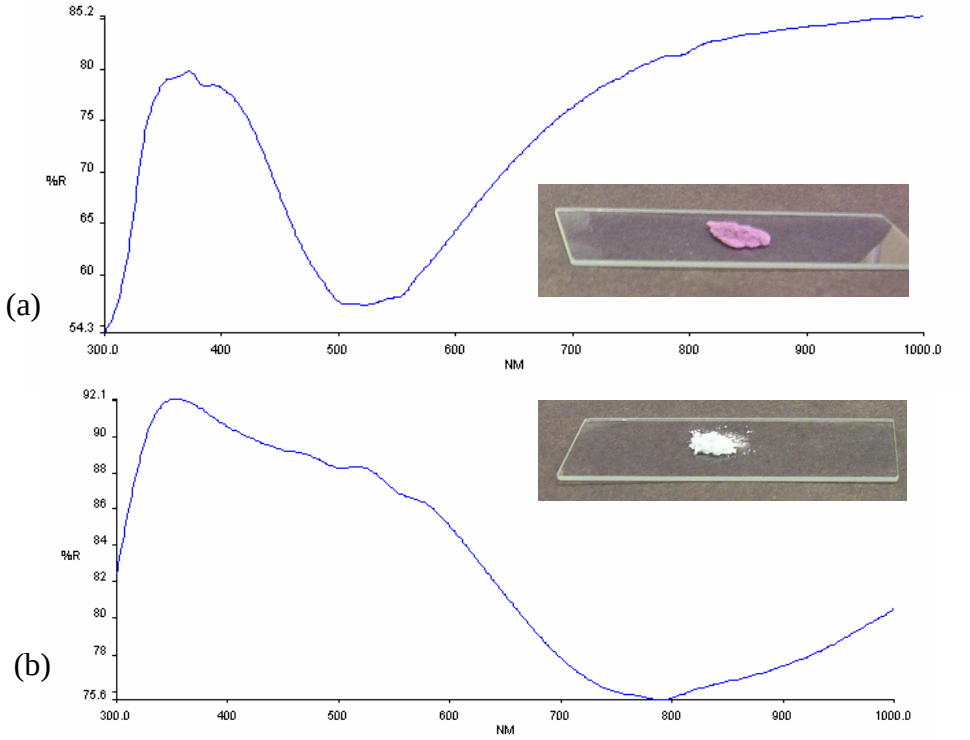

Figure 9.19: Solid-state UV-Vis spectra and photographs of as-made (a) and calcined (b) Cu-cyclam-containing SAPO STA-7.

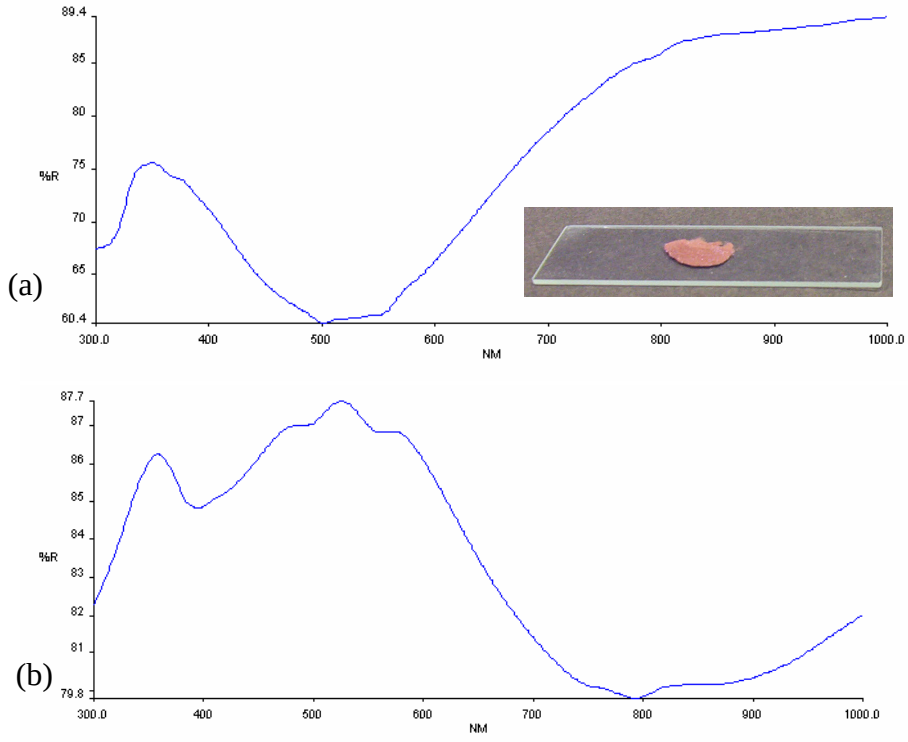

Figure 9.20: Solid-state UV-Vis spectra and photograph of as-made (a) and calcined (b) Cu/Ni-cyclam-cotaining SAPO STA-7.

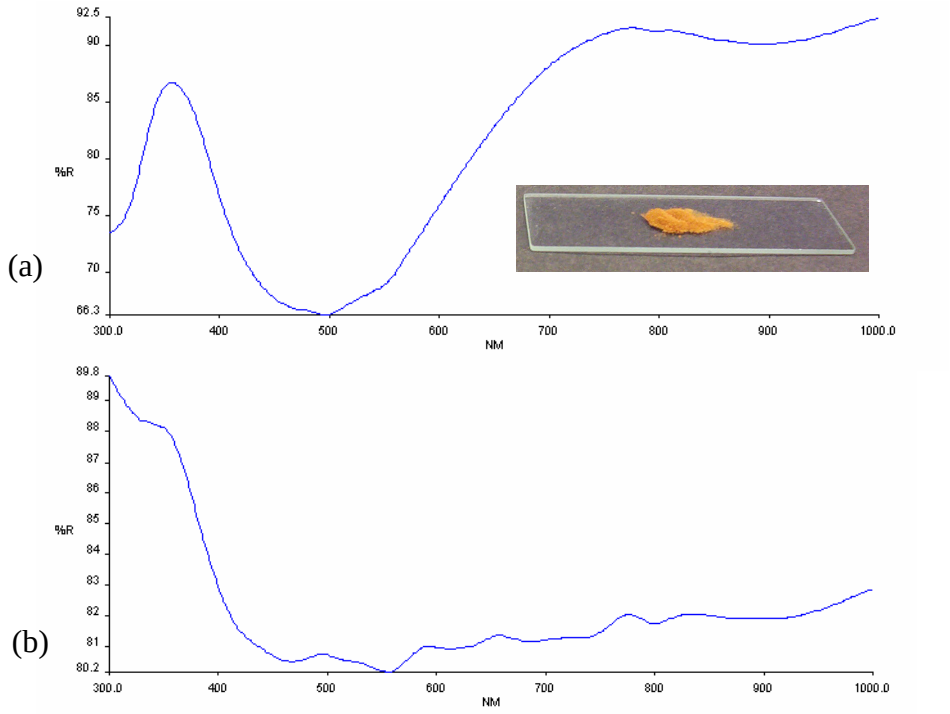

Figure 9.21: Solid-state UV-Vis spectra and photograph of as-made (a) and calcined (b) Cu/Ni-cyclam-containing SAPO STA-6.

Sample	**C/N (CHN)**	**Cation ratio (EDX) Ni:Cu:Al:Si:P**	**Organic content (wt%) (TGA)**	**Approximate unit cell composition**
Cu-L-SAPO STA-7	3.6	0:1:11.48:3.13:9.39	17	$(CuL)_{2.09}(NC_8H_{20})_{2.09}Al_{22.9}(Si_{6.26}P_{18.78})O_{96}$
Cu,Ni-L-SAPO STA-7	3.6	1:1.29:26.3:8.99:22.0	16	$(NiL)_{0.84}(CuL)_{1.09}(NC_8H_{20})_{1.93}Al_{22.1}(Si_{7.38}P_{18.5})O_{96}$
Cu-L-SAPO STA-6	2.6	0:1:11.5:2.91:9.62	13	$(CuL)_{1.3}Al_{15}(Si_{3.79}P_{12.5})O_{94}$
Cu,Ni-L-SAPO STA-6	2.2	1:1.07:17.4:4.28:14.7	14	$(NiL)_{0.88}(CuL)_{0.94}Al_{15.3}(Si_{3.77}P_{12.96})O_{94}$

Table 9.8: Elemental analysis of phase-pure SAPO materials and approximate unit cell compositions (L = cyclam).

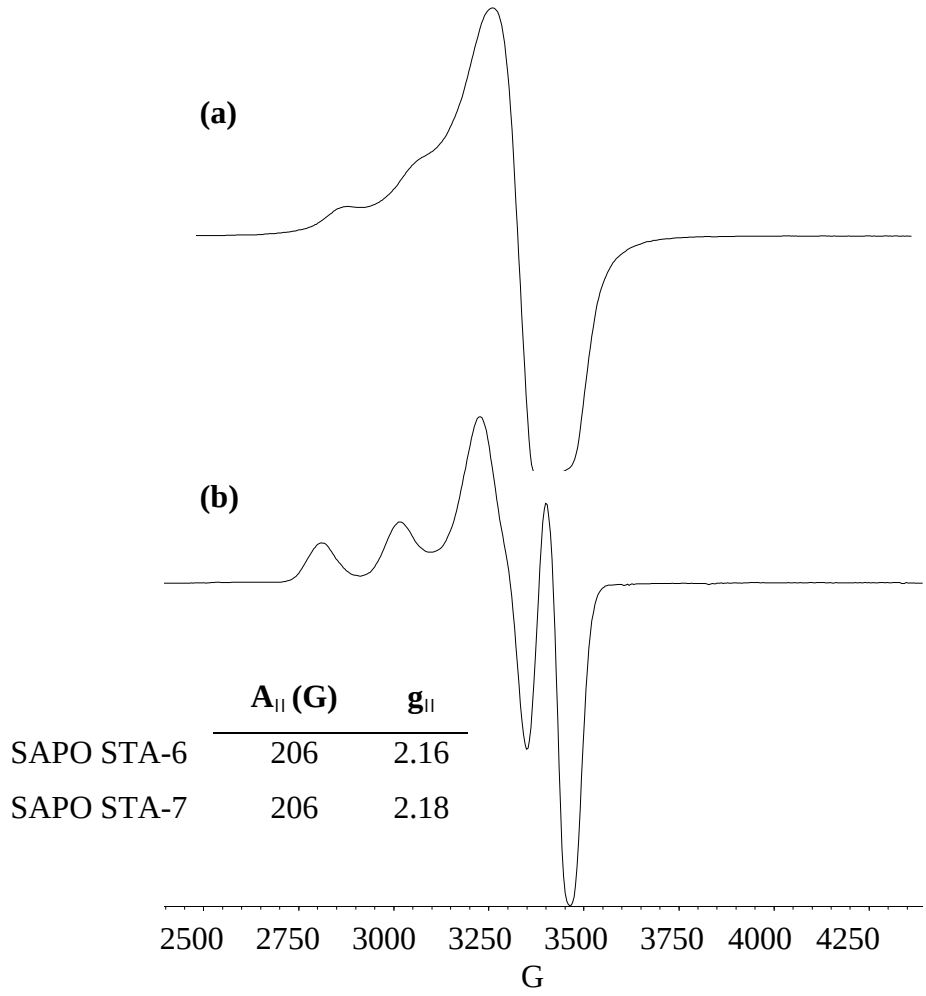

	A_{II} (G)	g_{II}
SAPO STA-6	206	2.16
SAPO STA-7	206	2.18

Figure 9.22: ESR spectra of as-made Cu-cyclam-containing SAPO STA-6 (a) and STA-7 (b) and table of associated parameters.

Examination of SAPO samples by SEM (Figure 9.23) revealed a variety of crystal morphologies for SAPO STA-7. STA-6 is more consistent and exhibits fan-like assemblages of rod-shaped crystals, which occasionally develop to completely spherical assemblages.

Calcination of as-made, phase-pure samples as before confirmed the superior stability of these materials, as illustrated by powder XRD (Figure 9.24). Like their MgAPO analogues, Cu- and Cu/Ni-containing samples became turquoise in colour upon calcination (Figures 9.19(b) and 9.20(b)), except Cu/Ni-SAPO STA-6, which became brown (Figure 9.21(b)). CHN analysis of this calcined sample suggests that residual carbon is the most likely reason for this. It was hoped that the improved X-ray data over equivalent MgAPO samples would aid the refinement of calcined and dehydrated Cu-

containing SAPO STA-6 and STA-7 samples, with the aim of locating extra-framework Cu^{2+} locations.

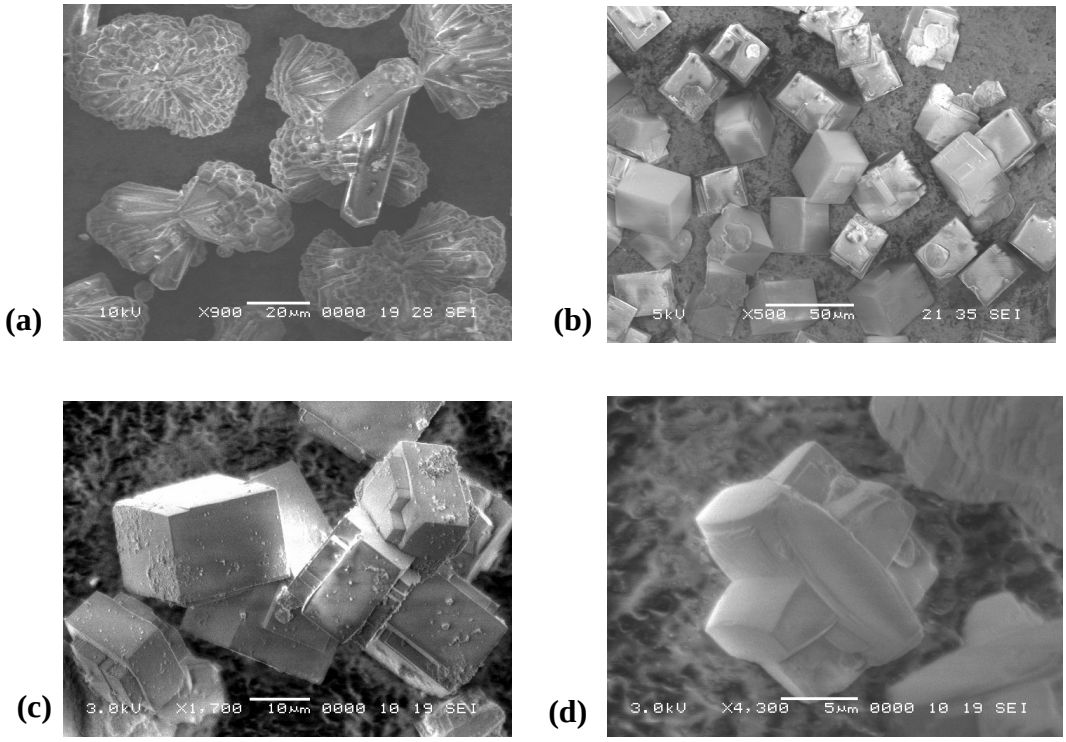

Figure 9.23: SEM images of (a) Typical fan-like and spherical assemblages of rod-shaped SAPO STA-6 crystals; (b)-(d) A selection of different morphologies observed for SAPO STA-7 synthesised from non-metallated cyclam (Chapter 10) (b) and Cu-containing cyclam (c) and (d)

Literature values of atomic coordinates of SAPO STA-6 and STA-7 in *P4/mnc* and *P4/nmm* symmetry, respectively, were taken as starting models for the refinements. Si/P-O, Al-O, $(O\text{-}O)_{Si/P}$ and $(O\text{-}O)_{Al}$ distances were constrained to 1.53Å (σ = 0.01Å), 1.73Å (σ = 0.01Å), 2.48Å (σ = 0.02Å)and 2.84Å (σ = 0.02Å), respectively. In the refinement of SAPO STA-6, instrument parameters, background (cosine function; 26 parameters) and peak shape (pseudo-Voigt function) were refined prior to atomic parameters. Possible Cu^{2+} locations were investigated through a modelling approach, based on Cu^{2+} locations in other zeolitic phases. Hence, five positions were modelled (Figure 9.25) and input to the refinement, where the occupancy and location of each were allowed to refine. Initially, only one of these positions (position 4) refined satisfactorily and converged to a position within the 8MR window of the large cage. Resulting Cu-O distances of 2.41(7)Å and 2.36(8)Å are plausible. Following further

refinement of the background, peak shape and framework parameters, Fourier difference maps revealed a second position equivalent to modelled site 3. Its re-introduction at this stage of the refinement was successful with the refined position generally 2.3Å from nearest oxygens. Figure 9.26(a) illustrates the refined structure and Cu^{2+} locations, while refined parameters are listed in Appendix E(2). A final R_{wp} of 11.27% and R_p of 8.05% (Figure 9.26(b)) were achieved. Combining refined Cu occupancies (Cu4 0.047(2), Cu3 0.037(5)) with their site multiplicities suggests 1.04 Cu^{2+} cations per unit cell. This is in agreement with elemental analysis and consistent with there being 0.5 Cu per large cage in the STA-6 structure – suggesting 50% occupancy of the STA-6 cage by Cu-cyclam in the as-made material.

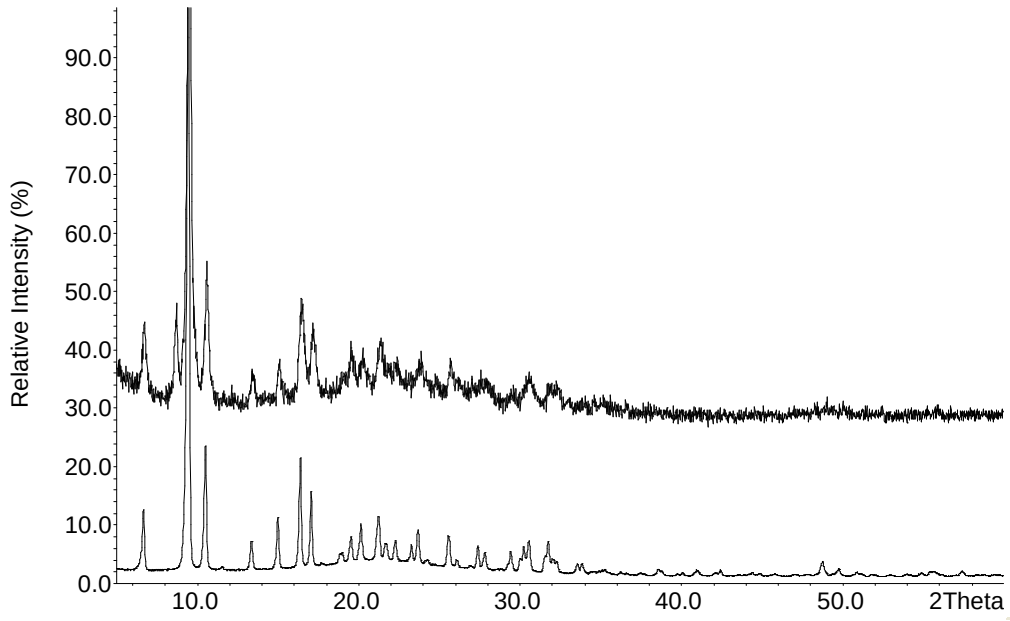

Figure 9.24: XRD patterns of calcined SAPO STA-7 (bottom) and calcined MgAPO STA-7 (top) for comparison.

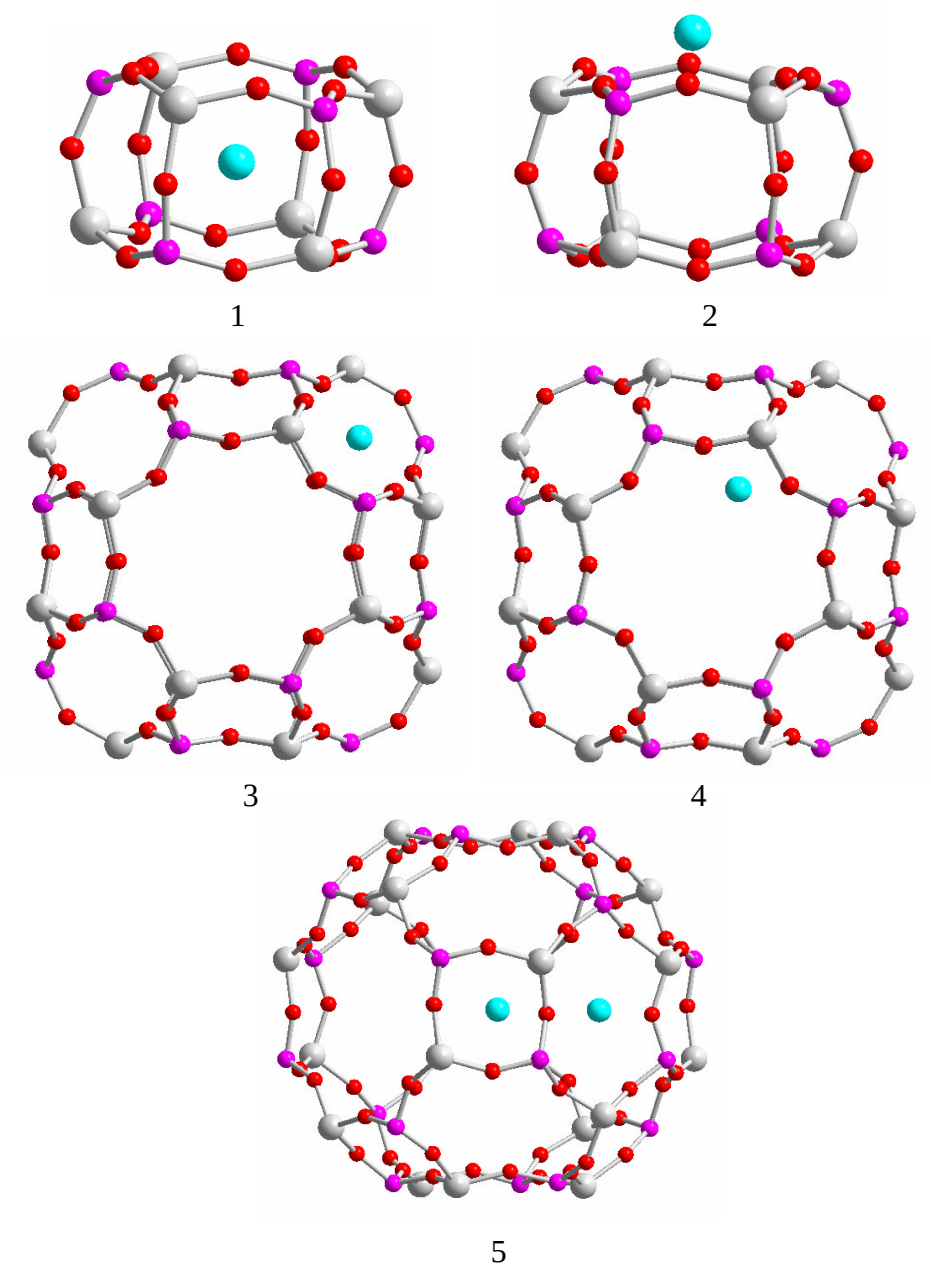

Figure 9.25: Modelled Cu-locations in SAPO STA-6: (1) inside the D6R, (2) just outside the D6R, (3) inside the 6MR of the cage wall, (4) inside the 8MR of the cage wall and (5) two-coordinate near the 4MR of the cage wall.

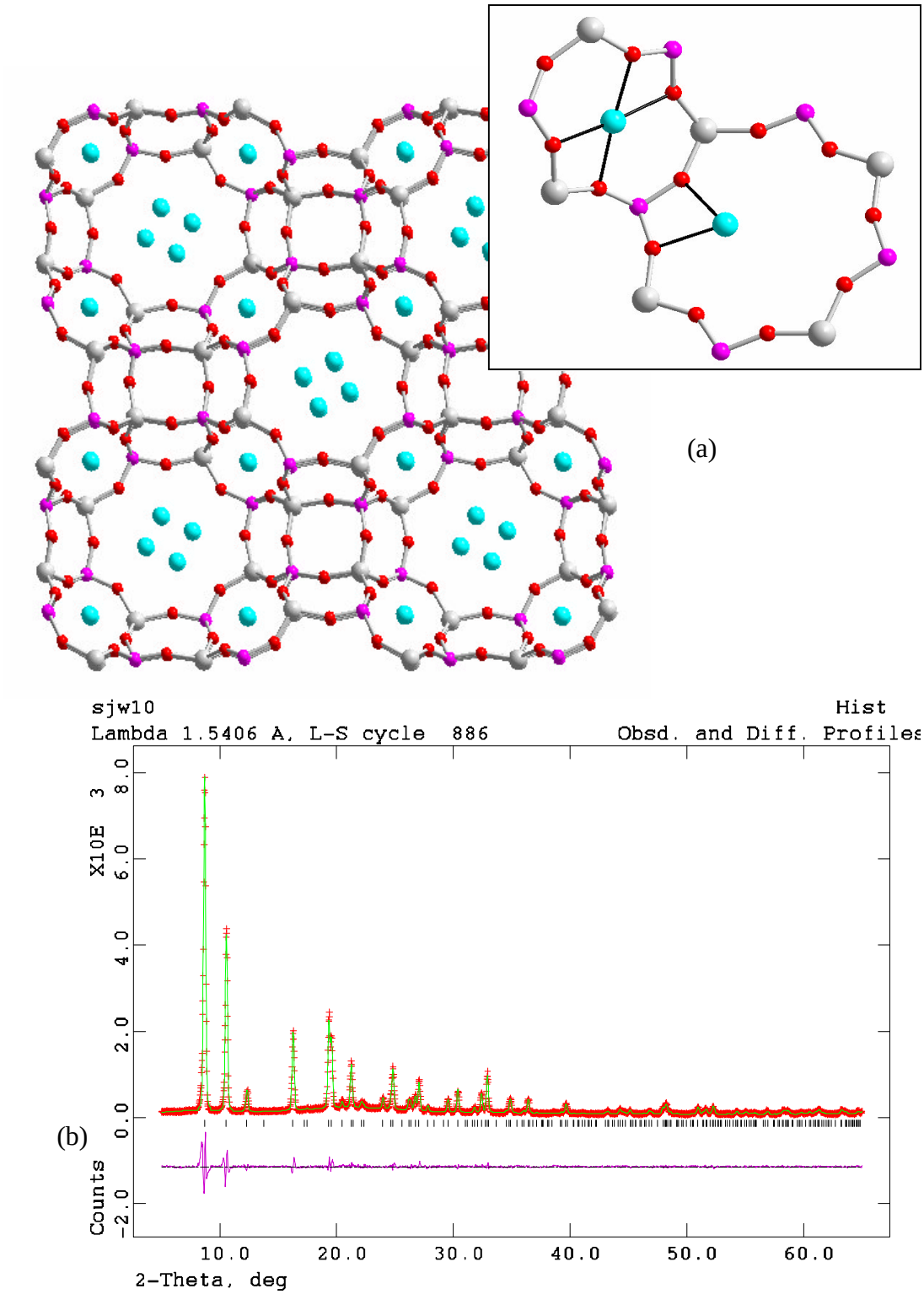

Figure 9.26: (a) Refined structure of Cu-SAPO STA-6 (purple = P/Si, grey = Al, red = O, cyan = Cu), Inset: detail of the Cu environments, (b) Rietveld refinement plot (red = experimental data, green = model, purple = difference plot).

The structure refinement of SAPO STA-7 proceeded in a similar fashion with instrument parameters, background (cosine function; 33 parameters) and peak shape (pseudo-Voigt function) being refined prior to atomic parameters (with constraints as before). Possible Cu^{2+} locations were probed directly by Fourier difference maps in this instance. Peaks at plausible distances from framework oxygens were input as Cu to the refinement and their occupancies and positions were allowed to vary. Several such locations were identified but only four refined satisfactorily. These are illustrated in Figure 9.27(a). Cu1 and its similar position Cu2 are located in the 8MR window of the β- and α-cage, respectively, and may be regarded as being equivalent to the position observed above in SAPO STA-6. A third position (Cu3) close to the 4MR of the main cage wall is also plausible. Cu-O distances refined to between 2.1 and 2.3Å (full listings of refined parameters appear in Appendix E(3)). A fourth position was also found just outside the D6R unit. However, this position refined with very low occupancy and continuously oscillated around the original location. Such a location has been observed in other zeolitic phases and it is possible that a small amount of Cu^{2+} occupies this position but, due to the low occupancy, it is not possible to fix its location definitely from the data. Each position has a multiplicity of eight which, when combined with their refined occupancies (Cu1 0.092(7), Cu2 0.06(1), Cu3 0.026(7)), gives 1.6 Cu^{2+} per unit cell (including Cu4 increases this value to 1.9). This is in agreement with elemental analysis, which implies 100% occupancy of the cages in as-made STA-7 and therefore two Cu^{2+} cations per unit cell. A final R_{wp} of 7.46% and R_p of 5.26% were achieved (Figure 9.27(b)).

The ESR spectrum of calcined and hydrated Cu-SAPO STA-7 (Figure 9.28) suggests the presence of one copper environment, again with axial symmetry. The hyperfine splitting constant and g_{II} value for the parallel region are comparable to those reported for other hydrated Cu-containing zeolites (Table 9.9). The equivalent spectrum for calcined and hydrated Cu-SAPO STA-6, however, appears more complex with additional features appearing in the perpendicular region at higher field.

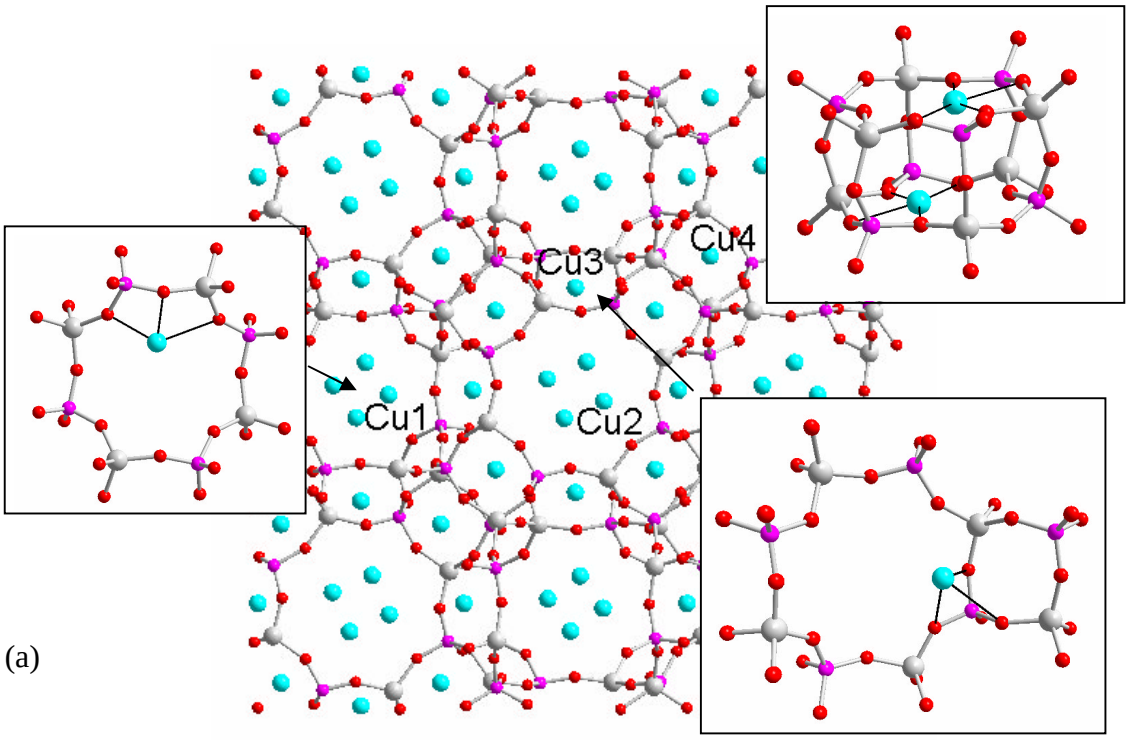

(a)

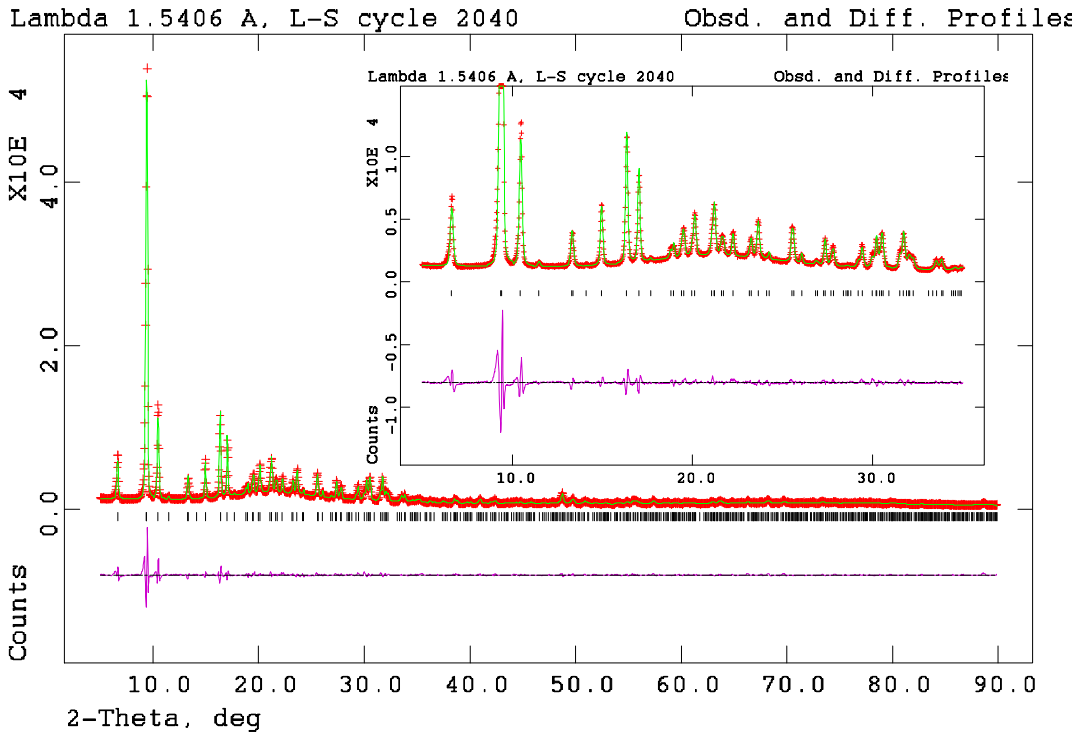

(b)

Figure 9.27: (a) Refined structure of Cu-SAPO STA-7(purple = P/Si, grey = Al, red = O, cyan = Cu) insets illustrate detail of Cu environments, (b) Rietveld refinement plot, inset: expanded view of 5-35^{o} 2θ region (red = experimental data, green = model, purple = difference plot).

Material	**A_{II} (G)**	**g_{II}**	**Material**	**A_{II} (G)**	**g_{II}**
Cu-Erionite h[74]	132	2.37	Cu-ZSM-5 h[75]	130	2.39
Cu-Erionite d[74]	156	2.33	Cu-ZSM-5 d[75]	145	2.33
Cu-Mordenite d[74]	154	2.33		165	2.27
	161	2.33	Cu-Zeolite A h[76]	100	2.50
			$Cu(H_2O)_6$[76]	140	2.39

Table 9.9: ESR parameters of selected Cu-containing materials. h = hydrated, d = dehydrated.

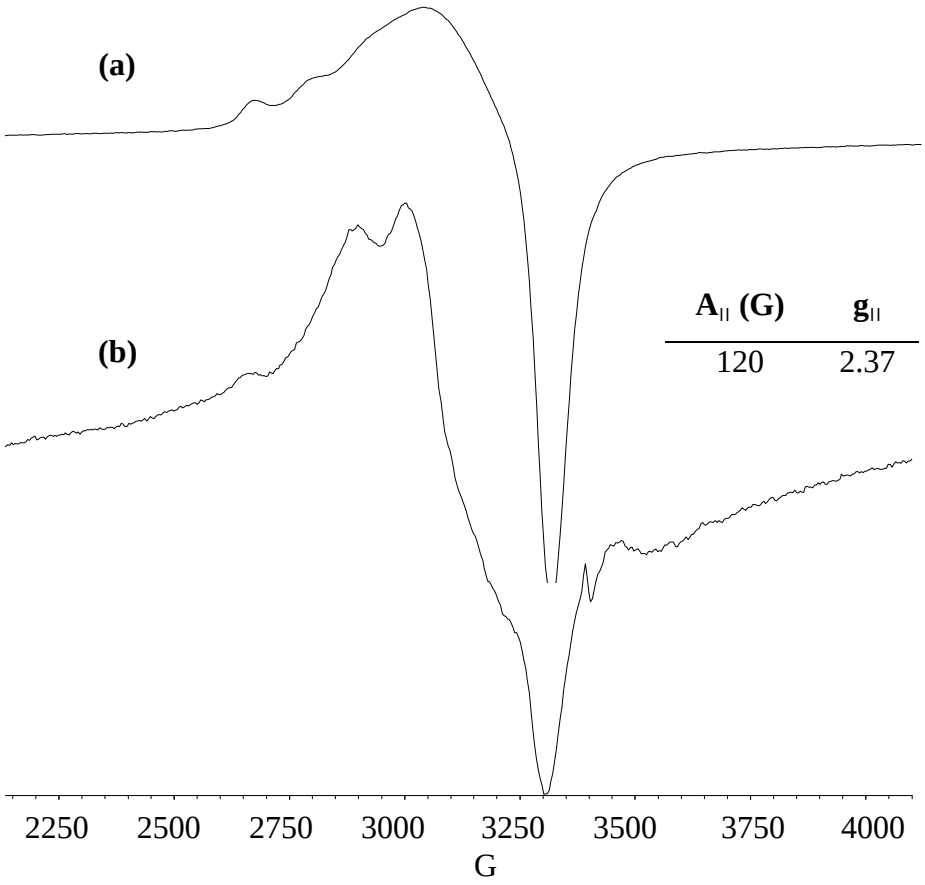

Figure 9.28: ESR spectra of calcined Cu-SAPO STA-7 (a) and Cu-SAPO STA-6 (b) and table of parameters for STA-7.

Measurement of the parallel hyperfine splitting constant for this sample was not attempted due to uncertainty in the exact positions of corresponding features. The sharp signal at approximately 3400G is characteristic of carbon radical species present in

pyrolised carbon such as charcoal.[77] It is possible that, as observed in the case of Cu/Ni-SAPO STA-6, some residual carbon may be present within the pores of this material.

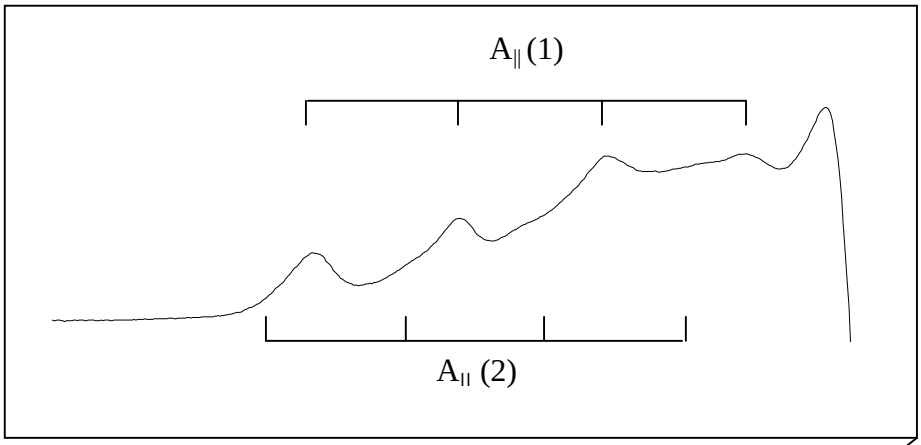

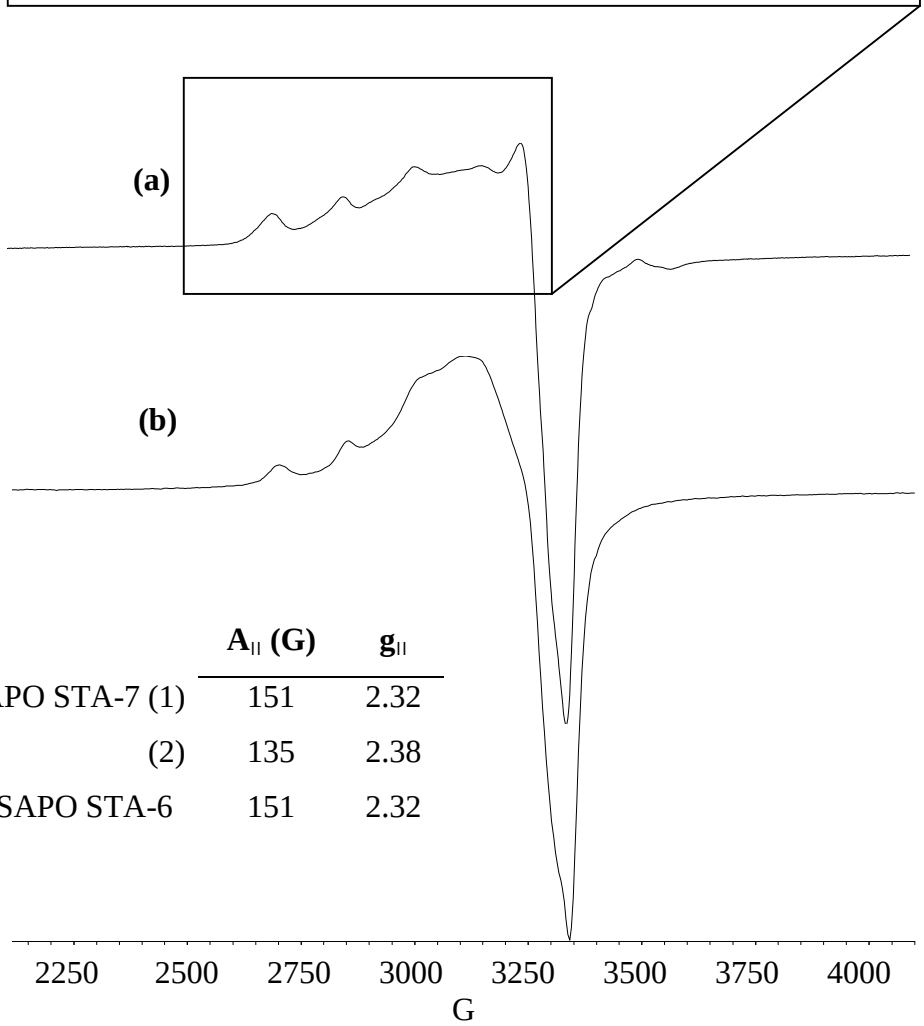

	$A_{\perp}$ (G)	$g_{\perp}$
Cu-SAPO STA-7 (1)	151	2.32
(2)	135	2.38
Cu-SAPO STA-6	151	2.32

Figure 9.29: ESR spectra of calcined and dehydrated Cu-SAPO STA-7(a) and Cu-SAPO STA-6 (b) with expanded view of the perpendicular region of the STA-7 spectrum. Table of associated parameters.

To permit a fairer comparison with crystallographic data, ESR spectra of calcined and dehydrated samples were collected (Figure 9.29). The spectrum of Cu-SAPO STA-7 exhibits improved separation of the parallel and perpendicular regions compared to other samples and contains four strong signals in the parallel region. Closer inspection of the spectrum reveals a second group of signals displaced to lower Gauss. ESR parameters compare favourably with those of other dehydrated Cu-containing phases (Table 9.9). Consideration of the possible locations of Cu^{2+} cations within the pores of this material as identified from powder crystallography suggests that sites Cu1 and Cu2 (Figure 9.27(a)) will posses similar symmetry since they are both within 8MR windows. Both of these positions refine with fractional occupancies of approximately 0.09. Site Cu3 occupies a different environment and refines to a much lower occupancy of 0.02. It is therefore suggested that sites Cu1 and Cu2 will possess similar, if not identical, ESR parameters and probably correspond to the most intense signal group (1) (Figure 9.29), while site Cu3 may be responsible for the weaker signal group (2). No evidence of other environments (e.g. Cu4) was observed.

The spectrum of Cu-SAPO STA-6 exhibits a marked change upon dehydration associated with the removal of coordinating water (and residual carbon species). Interestingly, however, only one environment can be identified in this spectrum despite the locating of two possible sites (with equal occupancies) in powder crystallography. ESR parameters for this signal are identical to those observed for sites Cu1 and Cu2 in STA-7 and it is suggested, therefore, that this signal is due to site Cu4 in SAPO STA-6 (i.e. that within the 8MR window). It is unlikely that sites Cu3 and Cu4 in SAPO STA-6 would possess identical ESR parameters and it is thought, therefore, that site Cu3 may in fact be occupied by residual water or template species rather than Cu^{2+} cations.

Nitrogen adsorption was conducted gravimetrically on a calcined sample of the Cu-SAPO STA-7 at -175^{o}C. As observed for the Cu-free (S)APO STA-7, the resulting isotherm (Figure 9.30) exhibits a typical type I profile. A maximum uptake of approximately 18.2% by mass is observed suggesting an internal pore volume of approximately 0.23cm^3/g. This value compares well with that of (S)APO STA-7 discussed earlier.

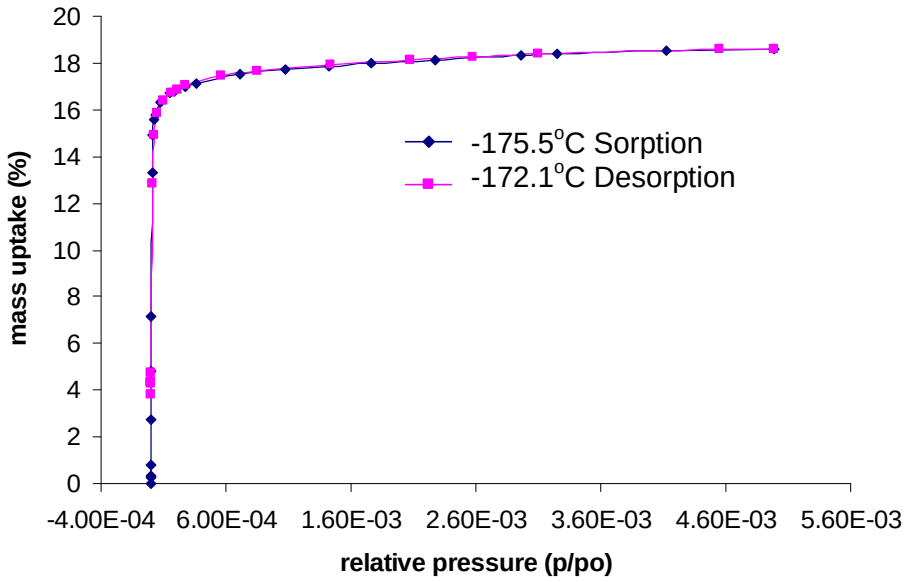

Figure 9.30: Nitrogen adsorption/desorption isotherm for calcined Cu-SAPO STA-7.

Summary

Strategies developed in the MgAPO regime for targeting the STA-6 and STA-7 structures appear to transfer far more readily to SAPO synthesis than to AlPO synthesis. In this manner, SAPO analogues of these topologies have been synthesised in the presence of Cu-cyclam and (for the first time) mixtures of Cu- and Ni-cyclam by selection of the appropriate co-base. Indeed this method appears to be particularly effective for the incorporation of Ni and/or Cu to the pores of these topologies.

Chapter 10: Non-metallated Cyclam in co-templating Studies of SAPO and Silicate Synthesis

10.1: Synthesis of SAPO STA-6 and STA-7

For comparison with studies of metallated cyclam, the non-metallated macrocycle was also employed as an SDA (in the presence of DP, TEAOH and DIP co-bases) in SAPO syntheses. In this regime, the non-metallated macrocycle behaves in an identical manner to its transition metal-coordinated form and directs the formation of STA-6 and STA-7 in the presence of DP and TEAOH, respectively. As in the case with Cu-cyclam, employing DIP as the co-base resulted in a mixture of both phases.

^{29}Si MAS NMR of this (non metallated) as-made SAPO STA-6 material (Figure 10.1(a)) shows one resonance at δ –93ppm. This may be attributed to $Si(Al)_4$ units and implies P substitution by Si as expected.[73] The ^{13}C MAS NMR spectrum (Figure 10.1(d)) exhibits several signals arranged in two groups centred on δ 18 and 43ppm. The equivalent spectrum of cyclam starting material (Figure 9.16(d)) exhibits a broad signal at δ 54.1ppm attributed to the eight CH_2 groups attached directly to the four nitrogens, and a less intense signal at δ 28.0ppm due to the central carbon of the $CH_2CH_2CH_2$ moiety. Comparison with the spectrum for STA-6 suggests that the macrocycle may be adopting several different configurations within the pores resulting in the observed splitting of the signals. Signals at δ 43.8 and 34.9ppm are therefore assigned to the CH_2 groups attached directly to nitrogen, and signals at δ 26.2, 19.6 and 11.5ppm are assigned to the central carbon of the $CH_2CH_2CH_2$ moiety. The ^{27}Al MAS NMR spectrum of this material (Figure 10.1(c)) exhibits a signal at δ 33.8ppm consistent with tetrahedral aluminium in framework materials, while a broad signal to lower field is indicative of five or six coordinate aluminium and suggests coordination by extraframework hydroxyl and/or water molecules. A signal at δ -29.1ppm in the ^{31}P MAS NMR spectrum (Figure 10.1(d)) is typical of tetrahedral phosphorus. However, the cause of additional resonances in this spectrum is unclear.

^{29}Si and ^{13}C MAS NMR spectra of SAPO STA-7 are discussed in the following section.

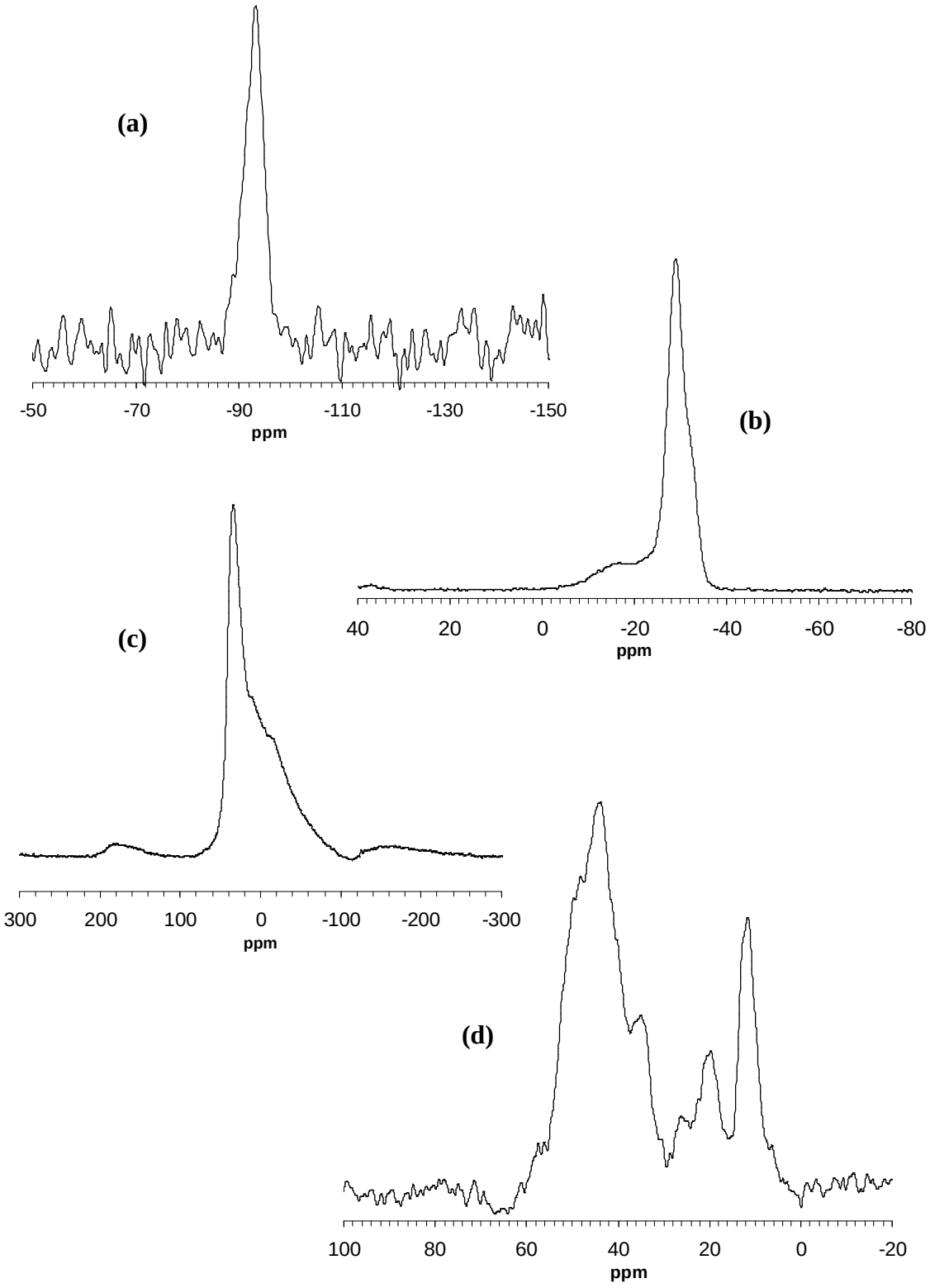

Figure 10.1: (a) ^{29}Si, (b) ^{31}P (c) ^{27}Al and (d) ^{13}C MAS NMR spectra of as-made SAPO STA-6.

To compare the levels of Cu loading achievable via templating by Cu-cyclam with that possible from ion-exchange, a calcined sample of non-metallated SAPO STA-7 was stirred at 70^{o}C in a 0.1 molar aqueous Cu (II) acetate solution. After two hours the solution was refreshed and the whole process was repeated several times. EDX analysis of the filtered, washed (water) and dried sample suggests an approximate unit cell composition of $Cu_{0.46}Al_{22.2}(Si_{7.4}P_{18.4})O_{96}$. Comparison with the approximate unit cell composition of as-made Cu-cyclam-containing SAPO STA-7 ($(CuL)_{2.09}(NC_8H_{20})_{2.09}Al_{22.9}(Si_{6.26}P_{18.78})O_{96}$) indicates that much greater Cu loading can be achieved via the Cu-cyclam templating route. By eliminating the ion exchange step, this latter approach is also far more convenient involving only synthesis and calcination.

10.2: Exploring the Si-Al-P Composition Field of SAPO STA-7

Due to its three-dimensional pore system, STA-7 holds greatest potential for catalytic application. It would therefore be interesting to increase Si substitution and possibly improve the stability and catalytic properties of this material. Employing cyclam (no metal) and TEAOH as SDAs, a series of syntheses of varying gel composition (with all other variables constant) were conducted to investigate whether Si substitution in the framework could be increased from previously observed values of approximately 13% of total T-sites. In this way, a transition from substituted SAPO to pure aluminosilicate or indeed pure silicate STA-7 might be observed.

Explicit in this proposal is the joining of AlPO, aluminosilicate and silicate syntheses across the compositional field, which in itself presents a major challenge due to the differences in gel conditions required in their respective syntheses. One major factor is pH; while AlPOs and SAPOs require near neutral conditions, aluminosilicates and silicates require strongly alkaline conditions primarily to promote the dissolution of the silica starting material. A possible means of circumventing this inherent problem is to employ fluoride as a mineralizer and improve the solubility of silicate ions at neutral pH. Otherwise, the utilisation of higher pH in the formation of silicates and aluminosilicates would dissolve the AlPO framework and obscure any link between the phase syntheses.

As discussed in Chapter 1, Si substitution can, theoretically, proceed via a number of different mechanisms. In reality, the SM2 mechanism is most common whereby only P is replaced by Si to produce isolated $Si(Al)_4$ units or larger aluminosilicate domains – as in SAPO-35.[78] A coupled substitution could either proceed via replacement of adjacent P and Al atoms (SM3), or, more likely, by a combined SM2/SM3 mechanism to produce $Si(Si)_4$ units and thus avoid unlikely P-O-Si bonds. This latter situation has been observed, for example, in SAPO-18 (AET).[79]

Hence, three synthetic strategies were adopted in these studies and are illustrated in Figure 10.2. These are:

(1) gradually replace P in the synthesis gel with Si to target SM2 (green route)

(2) gradually replace both Al and P in equal amounts by Si in the synthesis gel to target SM3 (blue route)

(3) gradually replace both Al and P in un-equal amounts by Si in the synthesis gel to target a combined SM2/SM3 mechanism (red route).

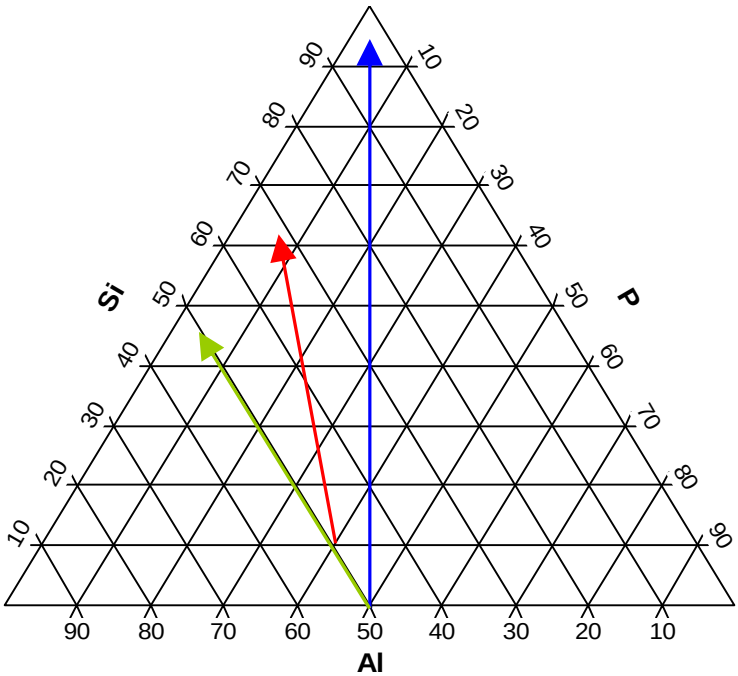

Figure 10.2 : Synthetic routes adopted in the exploration of the Si-Al-P composition field of SAPO STA-7.

(a)

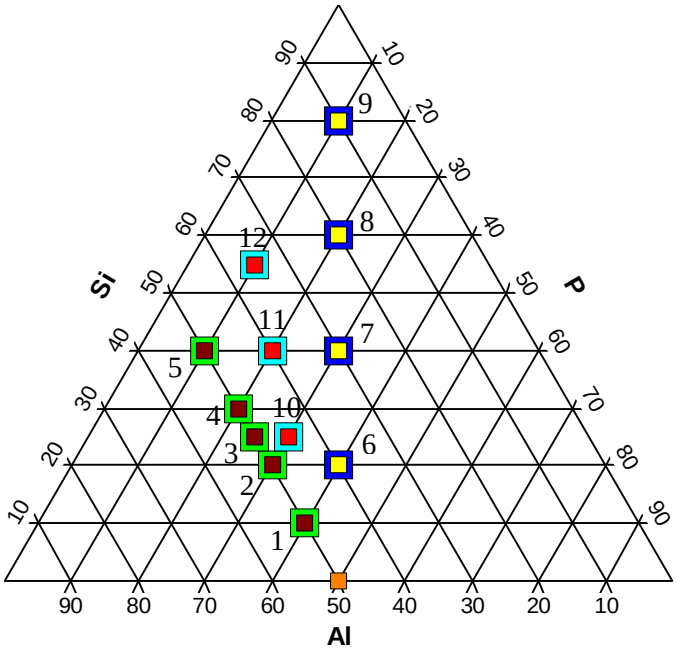

(b)

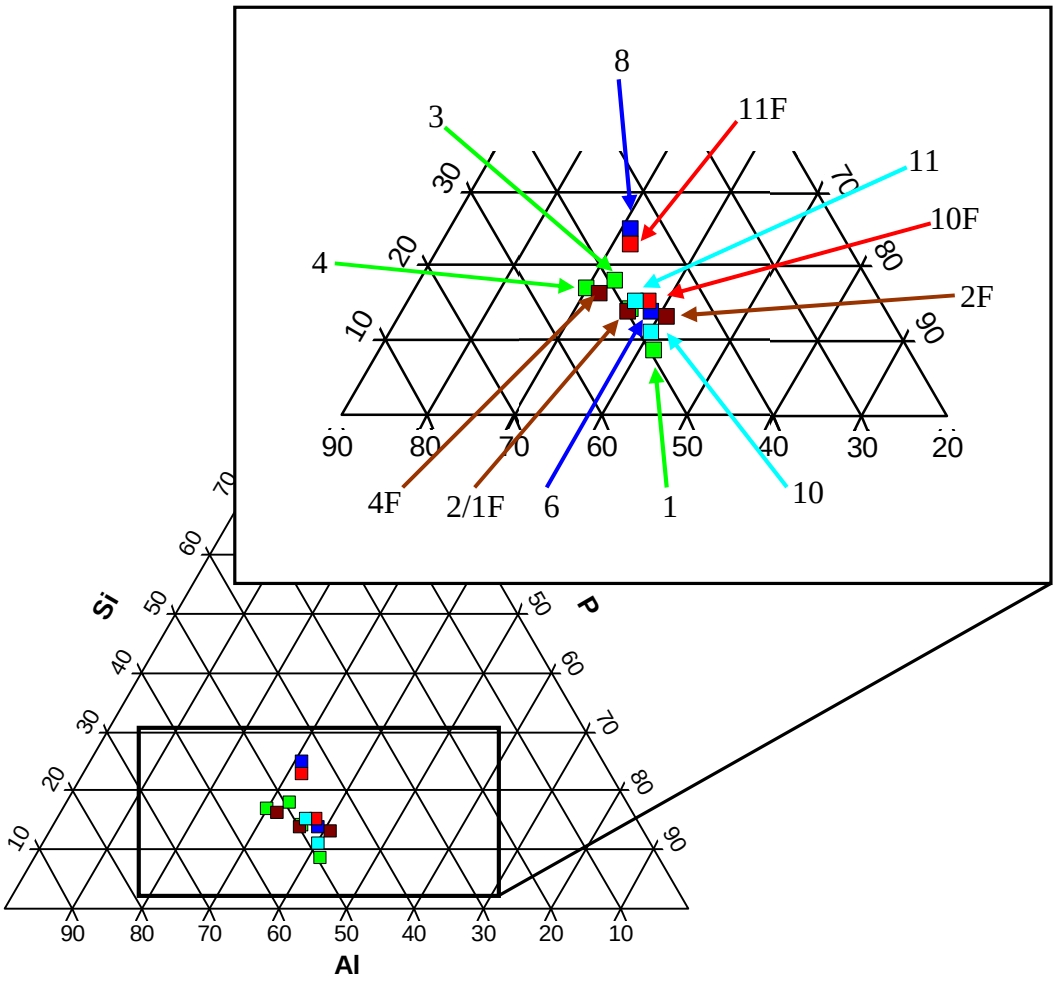

Figure 10.3: (a) SAPO gel compositions employed in these studies (with sample numbers as referenced in the text) and (b) Si/Al/P composition of resulting products (from ICP analysis, error of approximately 10% has been omitted for clarity)

Figure 10.3(a) illustrates gel compositions employed in these three approaches. Each was conducted in the presence and absence of fluoride (represented by small and large squares, respectively).

The first route extends from the previously prepared SAPO (10% Si) along the 50% Al contour towards pure aluminosilicate. These syntheses were initially conducted in the absence of fluoride as a direct comparison with the previous SAPO synthesis. XRD analysis (Figure 10.4) suggests that the desired phase has been achieved as far as gel composition 20% P, 30% Si. However, further reduction of the gel P content results in an amorphous phase. Elemental analysis (Table 10.1) of the crystalline products suggests that although synthesis 1 has resulted in a framework composition similar to that of the gel (Figure 10.3(b)), preparations 2-4 have converged to a framework composition of approximately 17% Si, 33% P, 50% Al. This composition lies a little below that of their gels and is consistent with Si substitution levels observed to date.

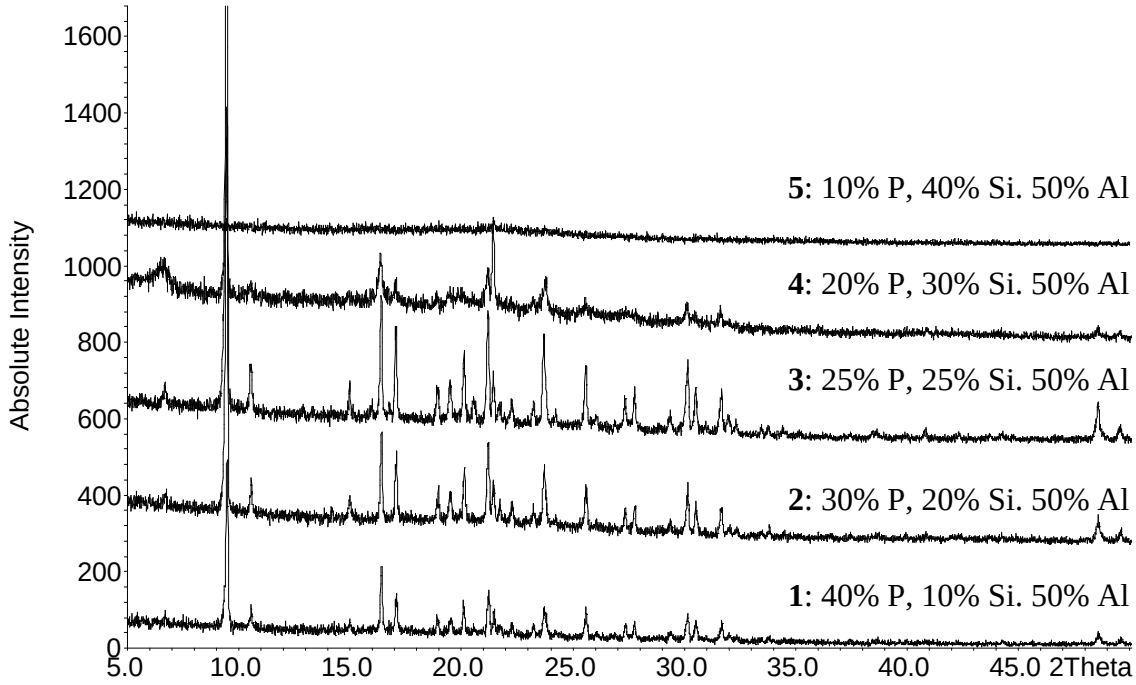

Figure 10.4: XRD patterns of as-made samples 1-5 with synthesis gel T-atom compositions.

Although repeating these preparations in the presence of 0.5 molar equivalent HF had no effect on syntheses 2 and 4 (Table 10.1), elemental analysis would appear to suggest that the presence of fluoride has raised the degree of substitution slightly in synthesis 1 from approximately 9% to 14% (of total T-sites). However, gels of composition 50% Al, 40% Si, 10% P remained amorphous.

A second approach leads from the pure AlPO towards pure silicate by maintaining a 1:1 ratio of Al:P and increasing the proportion of Si in the synthesis gel. Synthesis series 6-9 was conducted in the presence of fluoride as a direct extension of the pure AlPO syntheses discussed earlier. XRD analysis of products from this composition range (Figure 10.5) indicates a transition from phase pure (S)APO STA-7 (AlPO with trace Si), through a mixed-phase zone to a phase-pure secondary phase at gel composition 20% Al, 20% P, 60% Si. This secondary phase would appear to be the SAPO analogue of [F,cyclam]-AlPO-CHA but is not stable upon calcination. As observed in the previous series, reduction of P content to 10% results in an amorphous product.

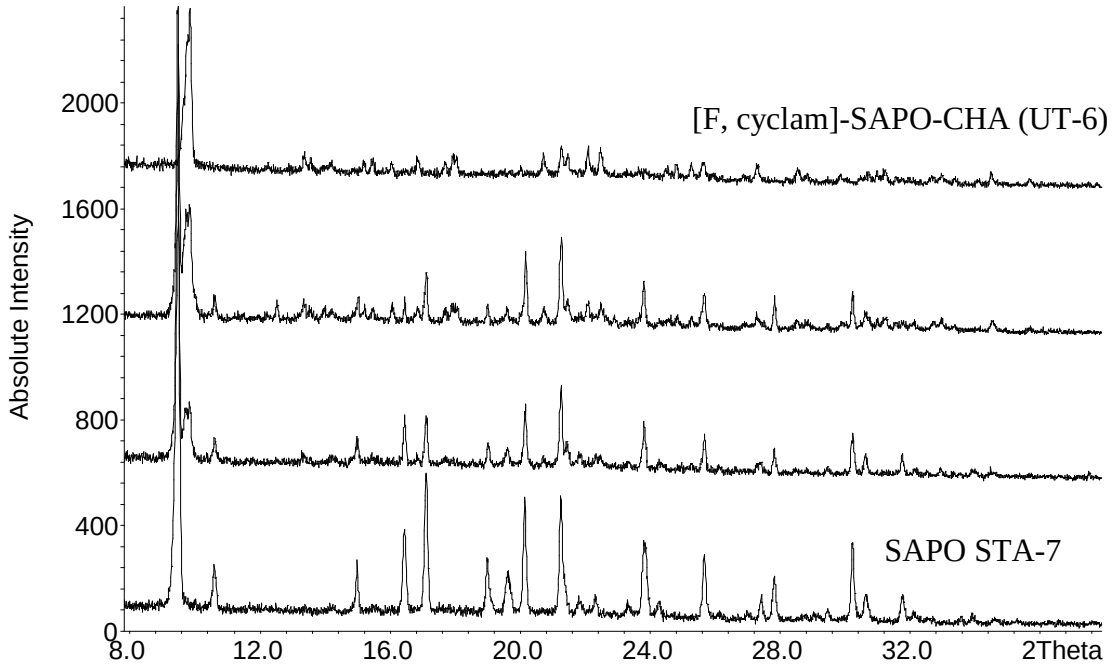

Figure 10.5: XRD patterns of products from synthesis series 6-9 and including phase pure SAPO STA-7 for comparison, illustrating a transformation from STA-7 to [F, cyclam]-SAPO-CHA (UT-6).

This series of preparations was also conducted in the absence of fluoride. As expected, [F-cyclam]-SAPO-CHA is not observed in these preparations, which yield (except for an anomalous result for synthesis 6) phase-pure SAPO STA-7. Initial elemental analysis of this series suggested a Si loading of up to 45% of total T-sites for synthesis 8. Examination of this product under the electron microscope revealed a significant quantity of amorphous material and subsequent re-sonication and cleaning of the sample reduced this maximum to 25%. Although a small quantity of amorphous material remains in this sample (Figure 10.8(a)), EDX analysis of selected clean crystals suggests a silicon loading of 23% of total T-sites (Table 10.1) in agreement with ICP results. This represents the highest silicon loading observed to date in this phase and may be due to the formation of silicate regions within the structure via a coupled SM2/SM3 process.

A third series of syntheses was conducted (syntheses 10-12) in an alternative approach that aimed to form silicate islands within the structure. Once more, gels with P content of 10% were unsuccessful, however syntheses of composition 30% P, 45% Al, 25% Si and 20% P, 40% Al, 40% Si yielded STA-7 both in the presence and absence of fluoride. ICP analysis of samples 10, 11 (no fluoride) and 10F suggests compositions similar to those obtained in syntheses 1-4 (Table 10.1) with silicon loading reaching a maximum of approximately 16%. As with syntheses 1-4, elemental analysis suggests that Si predominately substitutes for P via an SM2 mechanism, although a small proportion of Al substitution via an SM3-type mechanism might also occur. Indeed, assuming 100% occupancy of the α- and β-cages by the organic SDAs, a maximum charge of 6+ per unit cell is possible (2+ from each of two diprotonated cyclam rings, and 1+ from each of two TEA^+ cations). This would permit a maximum of six Si atoms per cell if SM2 were the sole mechanism in operation. Out of a total of 48 T-sites in the unit cell of STA-7, six Si atoms represents 12.5% and it is therefore not impossible that a small amount of SM3 is occurring.

Sample no.	Approximate inorganic composition	Sample no.	Approximate inorganic composition
1	$Al_{23.8}(Si_{4.21}P_{20.0})O_{96}$	6	$Al_{22.7}(Si_{6.62}P_{18.6})O_{96}$
2	$Al_{23.8}$ $(Si_{6.86}P_{17.4})O_{96}$	8	$Al_{21.1}(Si_{12.0}P_{14.9})O_{96}$
3	$Al_{23.7}(Si_{8.74}P_{15.6})O_{96}$	8 (EDX)	$Al_{19.3}(Si_{11.1}P_{17.4})O_{96}$
4	$Al_{25.0}(Si_{8.02}P_{15.0})O_{96}$	10	$Al_{23.5}(Si_{5.38}P_{19.4})O_{96}$
1F	$Al_{24.0}(Si_{6.70}P_{17.3})O_{96}$	11	$Al_{23.0}(Si_{7.7}P_{17.3})O_{96}$
2F	$Al_{22.0}(Si_{6.38}P_{19.6})O_{96}$	10F	$Al_{22.6}(Si_{7.39}P_{18.2})O_{96}$
4F	$Al_{24.9}(Si_{7.9}P_{15.2})O_{96}$	11F	$Al_{21.6}(Si_{11.0}P_{15.4})O_{96}$
		11F (EDX)	$Al_{21.4}(Si_{10.0}P_{16.5})O_{96}$

Table 10.1: Approximate unit cell compositions of as-made SAPO STA-7 materials (from ICP analysis except where stated otherwise), F denoted syntheses conducted in the presence of fluoride ions.

As a representative sample of this typical composition, and with sufficient quantity, product 10F was analysed by solid-state NMR spectroscopy. The ^{29}Si MAS NMR spectrum (Figure 10.6(a)) reveals a strong signal at δ -92.07ppm, in the region where signals from $Si(Al)_4$ and $Si(Al)_3Si$ units overlap, accompanied by perhaps four further signals at δ -96.2, -100.5, -106.3 and -110.6ppm. These additional signals are typical in spectra of silicate island-containing microporous SAPO materials[79] and can perhaps be attributed to $Si(Al)_3(Si)$, $Si(Al)_2(Si)_2$, $Si(Al)(Si)_3$ and $Si(Si)_4$ units, respectively. A signal at δ -110.6ppm is certainly characteristic of $Si(Si)_4$ units. Indeed, the spectrum bears a striking resemblance to that of silicate island-containing, and structurally similar, SAPO-18 (Figure 10.7). It is therefore thought that small silicate regions may have been formed for the first time within the STA-7 framework.

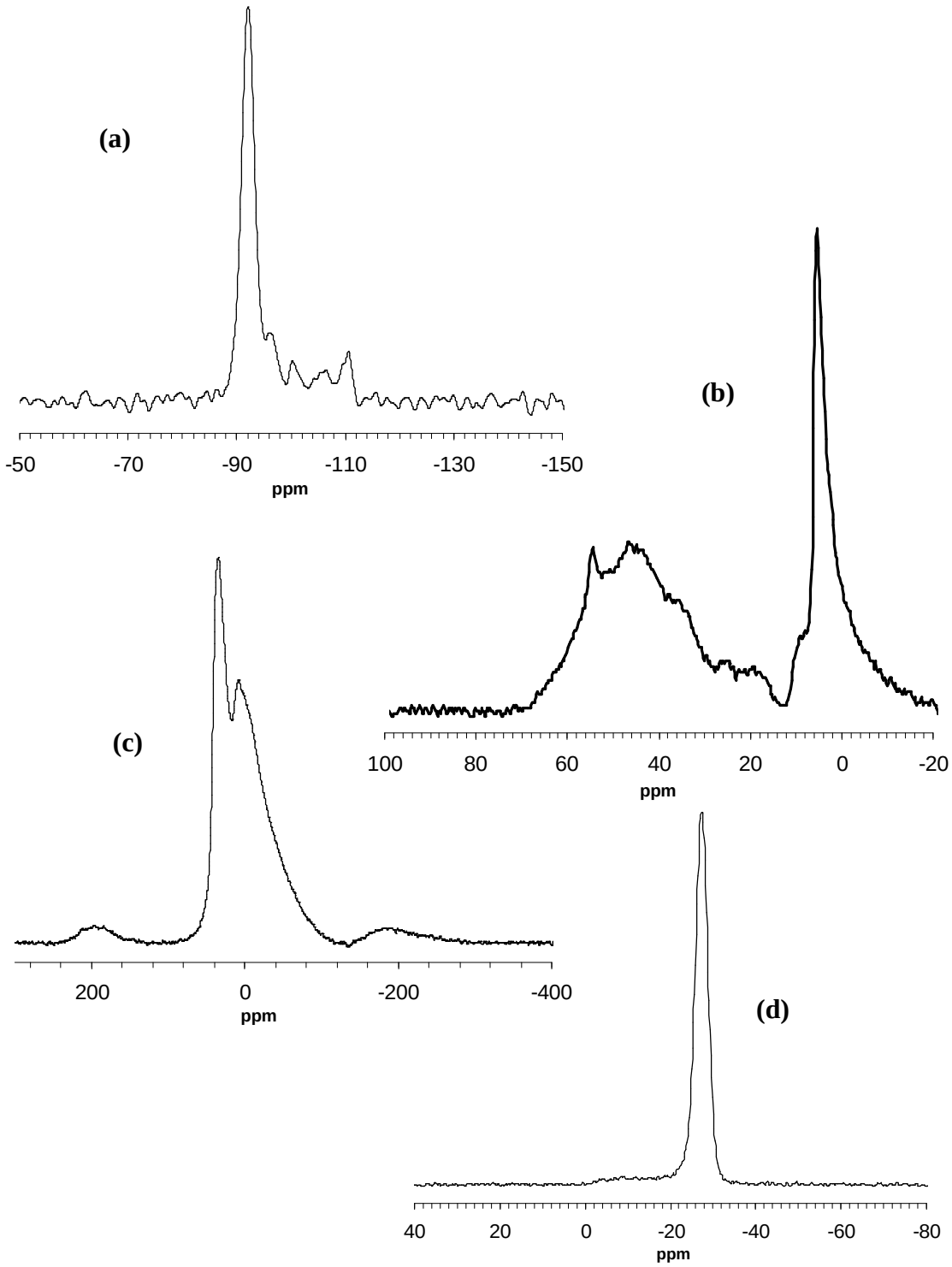

Figure 10.6: (a) ^{29}Si, (b) ^{13}C, (c) ^{27}Al and (d) ^{31}P MAS NMR spectra of as-made SAPO STA-7 (sample 10F).

The ^{31}P MAS NMR spectrum of sample 10F (Figure 10.6(d)) exhibits one signal at δ -27.5ppm characteristic of tetrahedral phosphorus. Similarly, a signal at δ 34.4ppm in the ^{27}Al MAS NMR spectrum (Figure 10.6(c)) is suggestive of tetrahedral aluminium in framework materials, while a further signal at δ 7.74ppm may be due to association of extraframework fluoride, hydroxyl groups and/or water molecules with aluminium sites resulting in five or six coordination.[73]

The ^{13}C MAS NMR spectrum (Figure 10.6(b)) of this sample is comparable to that of (S)APO STA-7 (Figure 9.16(c)). Sharp signals at δ 7.8ppm and 52.9ppm are attributed to CH_3 and CH_2 groups of TEA, respectively, while a broader signal at δ 45ppm together with signals at 26.2, 20.0 and 11.1ppm are consistent with the equivalent spectrum for cyclam in the cage of SAPO STA-6 (Figure 10.1(d)). The sharp profile of signals from TEA implies that the co-base may be relatively mobile within the β-cage.

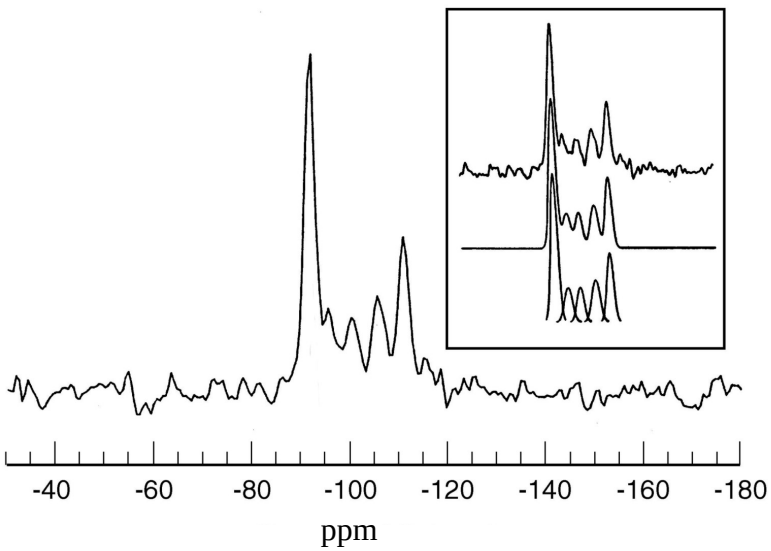

Figure 10.7: ^{29}Si MAS NMR spectrum of silicate island-containing SAPO-18, adapted from ref. 79. Deconvolution is illustrated in the inset.

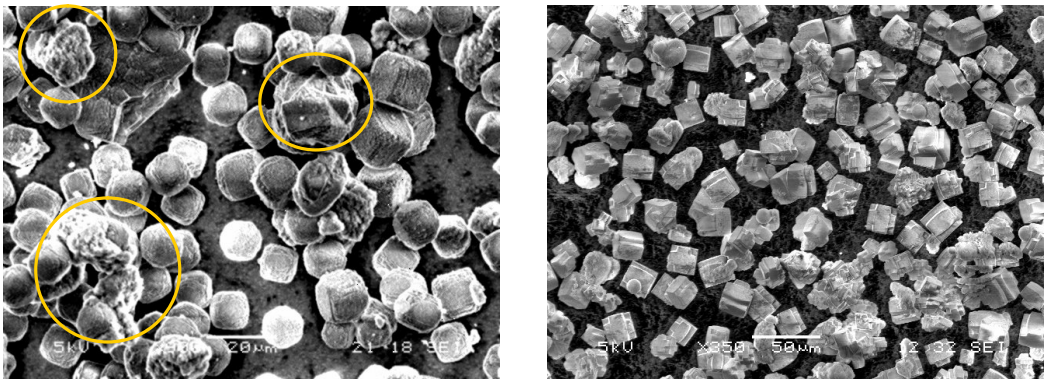

a **b**

Figure 10.8: SEM images of representative views of (a) samples 8 (after re-sonification, amorphous material circled) and (b) 11F.

As observed in synthesis 10, addition of fluoride to synthesis 11 would also appear to increase the level of silicon loading in the product phase. Indeed, silicon loading has been increased to a level comparable to that in product 8 (Table 10.1). However, unlike product 8, this sample appears far more crystalline and contains very little amorphous material (Figure 10.8(b)). EDX analysis of selected crystals suggests a composition in close agreement with ICP results, indicating that silicon loading of 21% has been achieved with substitution of both P and Al sites.

The introduction of fluoride to the synthesis gels studied in this work appears to affect the outcome of each series in a different manner. As discussed above, the addition of fluoride to syntheses 6-9 resulted in the formation of a secondary phase (probably SAPO UT-6), which becomes more favoured as the loading of silicon in synthesis gels increases. In syntheses 1-5, addition of fluoride appears to increase the rate at which a maximum silicon content is attained but would not appear to increase the level of this maximum beyond approximately 17% (Figure 10.9(a)). In contrast, the presence of fluoride in syntheses 10 and 11 would appear to increase the level of silicon loading beyond that observed in its absence (Figure 10.9(b)) and may have resulted in a silicon loading of approximately 21% (of total T-sites). This, along with the composition of sample 8 (synthesised in the absence of fluoride), represents the highest observed silicon content for this phase at present.

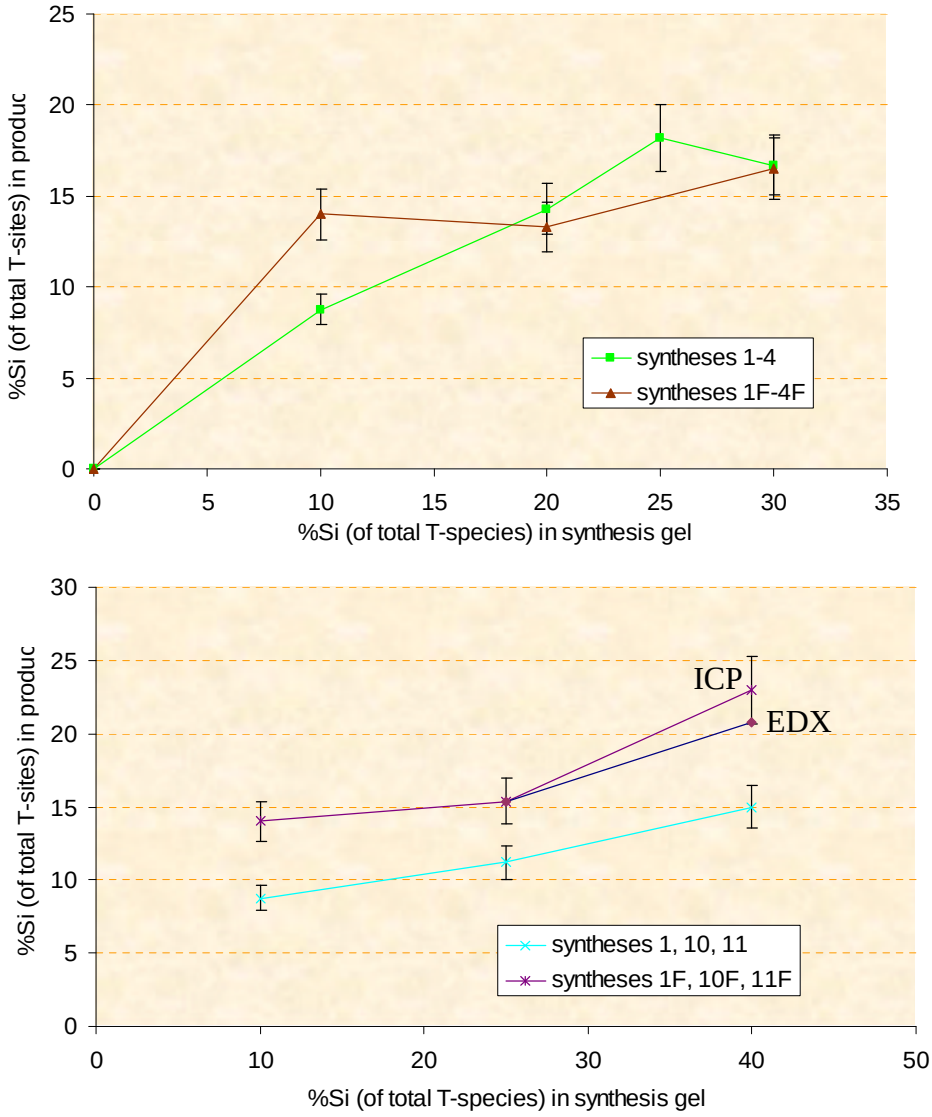

Figure 10.9: Comparison of the effect of adding fluoride to synthesis gels on the loading of Si in product materials.

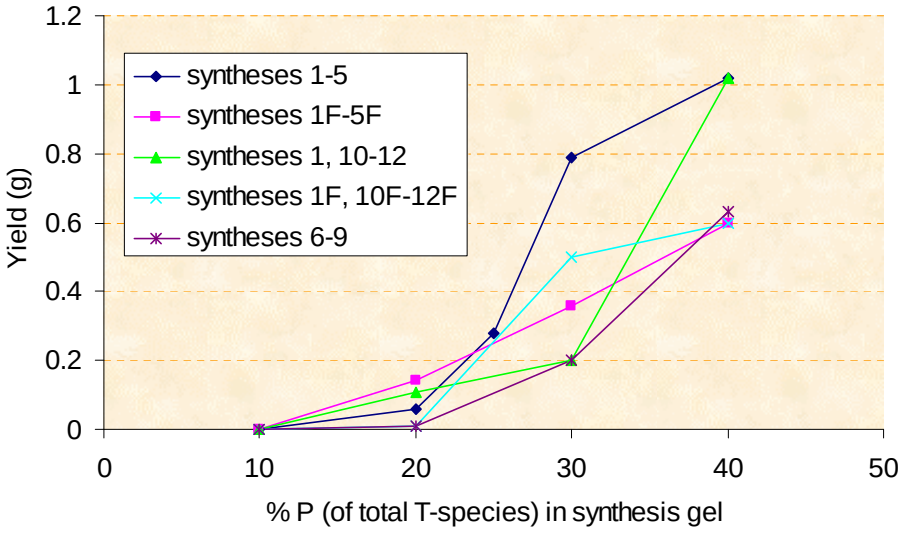

Figure 10.10: Plot of yield (g) vs. % P (of total T-species) in synthesis gels.

On traversing any of the three synthesis routes discussed above, there would appear to be a minimum tolerable value of P in the synthesis gel. Syntheses in which the gel P content was lowered to 10% (of T species) failed to crystallise, and in general, a decrease in product crystallinity and yield is observed on travelling along each of these synthesis routes (Figures 10.10 and 10.11). It is likely, therefore, that aluminosilicate and silicate analogues of STA-7 may be unattainable – at least under the conditions studied here.

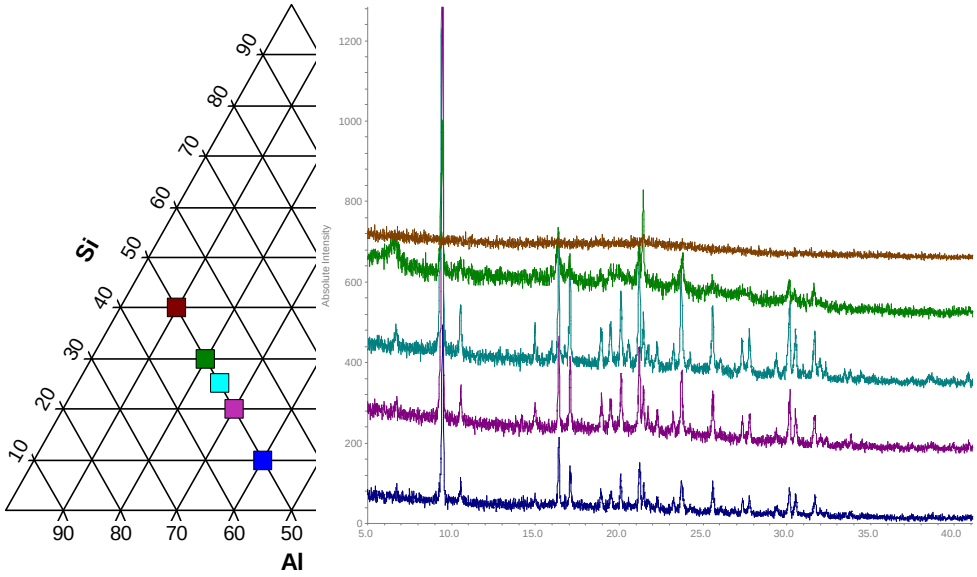

Figure 10.11: Comparison of product crystallinity across syntheses 1-5 illustrating a decrease in product crystallinity as gel P levels decrease. A minimum of between 10-20% P is tolerated in synthesising SAPO STA-7.

10.3: Cyclam in a Silicate Regime

By way of an extension to studies of the Si-Al-P composition field, it was decided to investigate the activity of cyclam with TEAOH and DP as SDAs in a silicate regime. Although crystallisation of gels containing only 10% P failed to crystallise, it was hoped that by varying other parameters, a crystalline product could be achieved.

Cyclam and TEAOH

Table 10.2 lists gel compositions and conditions employed in this study. The introduction of cyclam and TEAOH to a purely silicate gel at pH7 produced no product.

Increasing the pH through to 14 also had no effect. Fluoride was introduced to help aid dissolution of silica but this too had little effect both at neutral and alkaline conditions. Attempts to increase the rate of crystallisation by introducing a small equivalent of Ge were also unsuccessful, as were combined fluoride/Ge syntheses at pH7. However, a crystalline product *was* obtained by including both fluoride and Ge at alkaline conditions. Crystallisation time is also important with a full six days required for a product to form.

Si	H_2O	Cyclam	TEAOH	HF	GeO	pH	T(^oC)	Product
1	40	0.06	1.9	0.0	0.0	7-14	190	amorphous
			2.0	0.5	0.0	7-12		
			1.9	0.0	0.2	7, 12		
			1.7	0.5	0.2	7		
			3.1	0.5	0.2	12		ZSM-5 + Zeolite β

Table 10.2: Optimisation of cyclam/TEAOH-containing silicate synthesis. Species quantities given as molar equivalents.

Examination of the product by optical microscopy revealed two crystal morphologies: long rod-like crystals and cube-like, blocky crystals, suggesting a two-phase mixture had been formed. Indeed, this was confirmed by XRD analysis, which revealed that germanosilicate ZSM-5[80] (MFI) and zeolite β (BEA) had been synthesised.

It was assumed that the cyclam and TEAOH were acting as two independent templating species, resulting in a two-phase mixture. Therefore, in order to synthesis phase-pure samples, the proportions of cyclam and TEAOH introduced to the synthesis gel were varied. As illustrated in Figure 10.12, the presence of solely TEAOH directs the formation of germanosilicate β, as might be expected. By increasing the quantity of cyclam, and reducing the quantity of TEAOH, accordingly, a mixed phase product gives way to phase-pure germanosilicate MFI, suggesting that cyclam directs the formation of this phase. However, a preparation involving only cyclam failed to crystallise. Furthermore, CHN analysis of pure as-made materials suggests that only TEA^+ is present in both phases, and syntheses employing Cu-cyclam failed to produce any

purple-coloured products. In this germanosilicate regime and under these conditions, cyclam appears to behave in a very different manner to what has been observed previously. Considering the system in terms of SDA and co-base suggests a role reversal; TEAOH may be considered as the active SDA, and cyclam simply adjusts the synthesis pH and does not become incorporated into the crystallising product (cf. DP with cyclam in a MgAPO system). However, cyclam must, nevertheless, exert some kind of structure-directing effect in inhibiting the crystallisation of zeolite β and favouring the formation of ZSM-5.

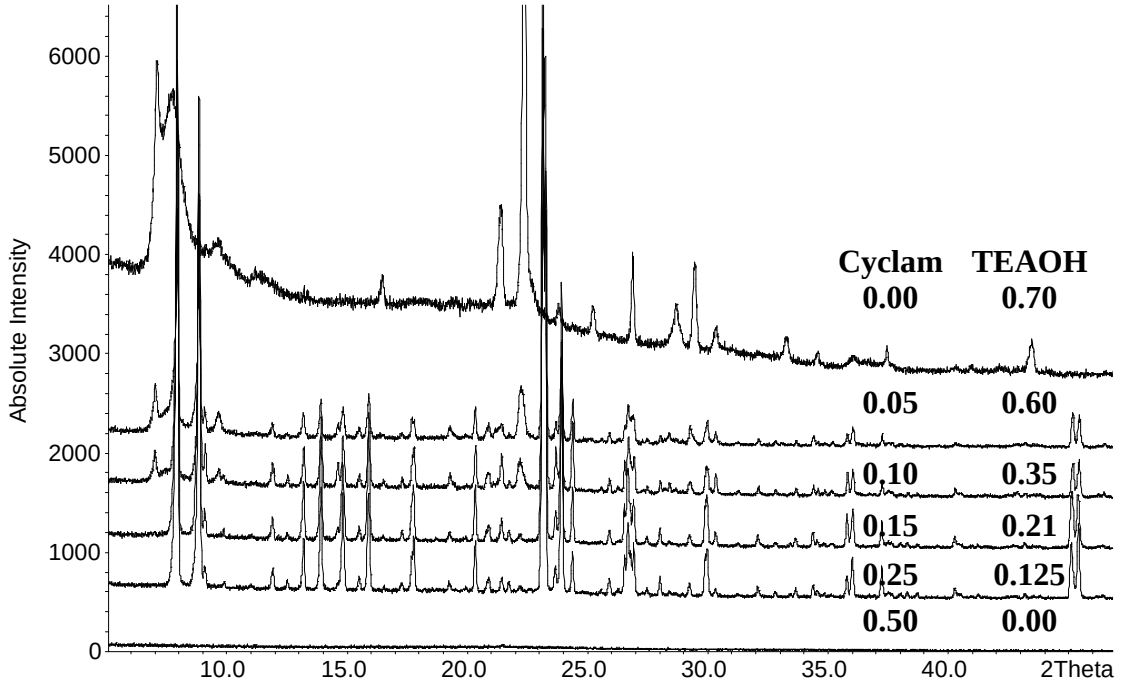

Figure 10.12: Variation of cyclam and TEAOH quantities in the synthesis gels yielded phase pure germanosilicate ZSM-5 and zeolite β (molar equivalents of cyclam and TEAOH are given on the right).

Although hampered by twinning (goodness of fit value = 22%), single crystal analysis of as-made germanosilicate MFI confirmed the topology as correct (Figure 10.13) and identified probable locations of the TEA^+ nitrogen atoms.

Germanosilicate MFI can be synthesised from gels containing from 0.07eq to at least 0.4eq Ge (i.e. Si/Ge = 14.2-2.5). Beyond Si/Ge = 14.2, no crystalline product is obtained under these conditions. Although Ge loading of the gel is tolerated at least as far as Si/Ge = 2.5, increasing Ge levels in framework T-sites would reduce the stability of the product and therefore minimal Ge loading is favoured.

(a)

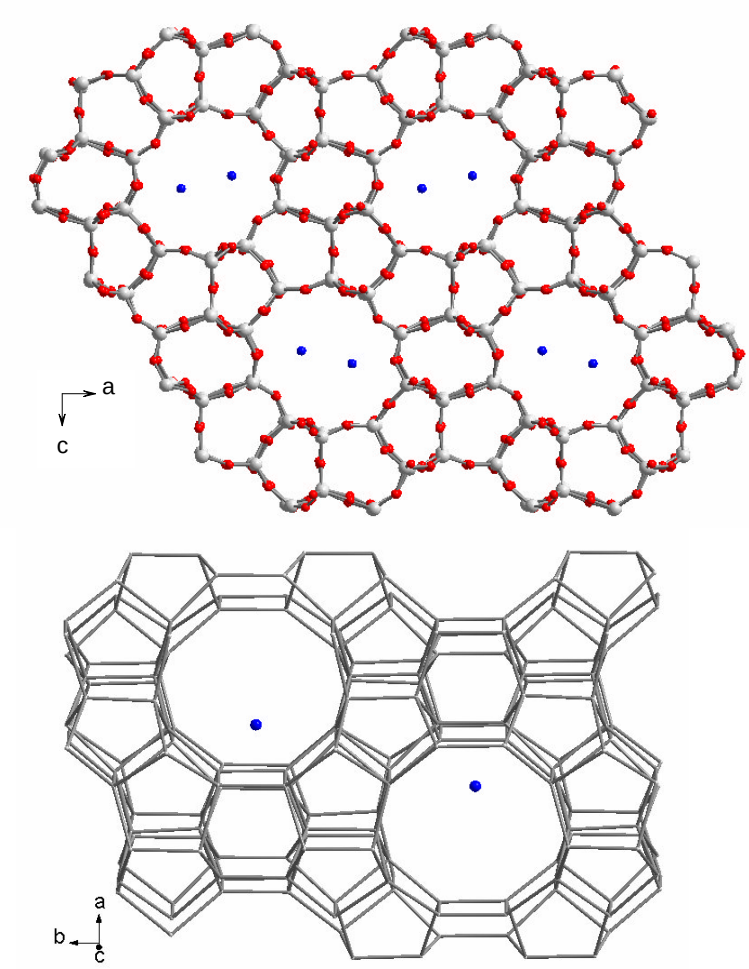

(b)

a (Å)	*b* (Å)	*c* (Å)	Space group
13.412(3)	19.944(5)	19.982(5)	$P2_12_12_1$

Figure 10.13: (a) Structure of germanosilicate MFI as solved from single crystal analysis, viewed along the b axis (grey = Si/Ge, red = O, blue = N); (b) side view of main channel showing locations of TEA^+ nitrogen atoms at channel intersections (oxygens removed); table of refined cell parameters.

The germanosilicate β formed above is an intergrowth of the A and B polymorphs[81] (estimated at 40:60 from the appearance of the XRD pattern[82]). A third polymorph (C) was synthesised by Corma *et al.*[83] as a germanosilicate in the presence of a selection of templating species, including TEAOH. Unlike polymorphs A and B, polymorph C contains D4R units, which are thought to be favoured/stabilised by Ge. In this way, it has been proposed, Ge will direct the formation of polymorph C regardless of the templating agent. However, under the conditions employed here, it would also seem possible to prepare the A/B intergrowth in the presence of Ge.

To test the apparent inhibition of β growth by cyclam, the macrocycle was introduced to similar gels in the presence of dibenzyldimethylamine (DBDMA) (Figure 10.14), which has been shown to direct the formation of β (as an A/B intergrowth) in the past.[84] Principal syntheses are listed in Table 10.3. At first, a test synthesis was conducted at similar conditions as before but in the presence of DBDMA only. Under such condition (i.e. alkaline pH, 190^{o}C etc.) no crystalline product was achieved. However, lowering the gel pH to 7 and working at 170^{o}C resulted in the formation of rod-like crystals. Interestingly, XRD analysis revealed that polymorph C had been formed even at such low Ge loading. As in the case with germanosilicate β A/B above, introducing cyclam to this system prevented the crystallisation of germanosilicate β C even when present at very low levels (Figure 10.15). However, no secondary phase was observed – indicative, perhaps, of a more specialised templating ability of DBDMA compared to TEAOH. Decreasing the level of Ge introduced to the synthesis gel also prevented product crystallisation.

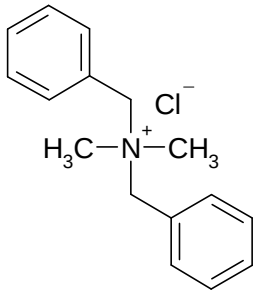

Figure 10.14: DBDMA employed as a zeolite β template.

Si	Ge	H_2O	HF	DBDMA	Cyclam	pH	T (^{o}C)	Product
1	0.2	40	0.5	1.42	0.00	10	190	-
				0.71	0.00	7	190	-
				0.71	0.00	7	170	(Ge,Si) β C
				0.53	0.06	7	170	-
				0.23	0.31	7	170	-
				0.00	0.62	7	170	-
	0.1			0.71	0.00	7	170	-

Table 10.3: Summary of germanosilicate syntheses employing DBDMA and cyclam. Species quantities given as molar equivalents.

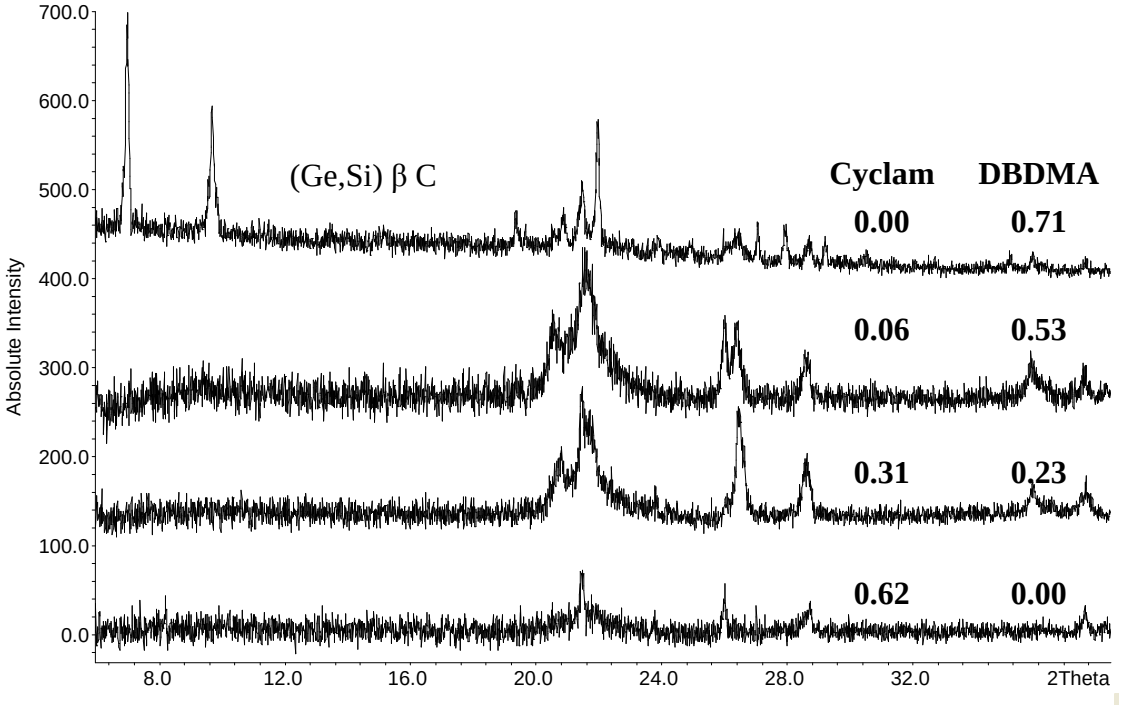

Figure 10.15: XRD patterns of as-made samples prepared in the presence of DBDMA and cyclam with molar equivalents listed on the right.

Cyclam and DP

Replacing TEAOH with DP in the above germanosilicate regime (second entry in Table 10.4) yielded a product of fine needle-like crystals. The XRD pattern of this product bears a close resemblance to that of the silicate ZSM-23 (MTT). Literature-reported[85] unit cell parameters for this phase were refined against experimental XRD data in $P12_11$ symmetry using the GSAS package (Figure 10.16 and Table 10.5) and confirmed that this is indeed the correct phase (although a small amount of impurity is present).

Si	H_2O	Cyclam	DP	HF	GeO	pH	T(^oC)	Product
1	40	0.00	2.5	0.5	0.2	10	190	(GeSi) MTT
		0.18	2.1					
		0.60	1.1					
		1.00	0.4					amorphous

Table 10.4: Summary of germanosilicate syntheses employing cyclam and DP

CHN analysis of this material revealed a C/N ratio of 3.5, suggesting that perhaps both cyclam and DP are present. However, preparations involving Cu- and Ni-cyclam failed to incorporate these complexes into the structure and yielded white MTT-like crystals. Indeed, the same phase is obtained with only DP present in the synthesis gel. On decreasing the proportion of DP present (and increasing the proportion of cyclam, accordingly), crystallinity is lost and no other phase is observed. It would therefore appear that DP is dominating the structure direction in this system, favouring the formation of a germanosilicate MTT material.

No crystalline product is observed in analogous syntheses employing HB with cyclam under these conditions and gel compositions.

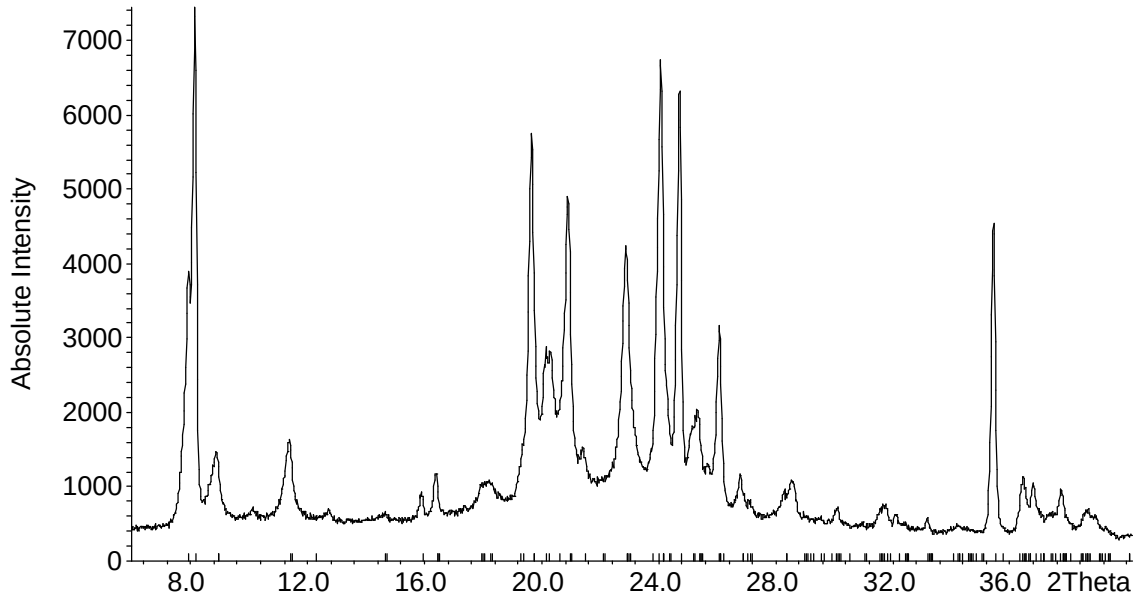

Figure 10.16: XRD pattern of as-made DP-containing germanosilicate MTT with reflection positions (marked above the 2θ axis) corresponding to refined unit cell.

	***a* (Å)**	***b* (Å)**	***c* (Å)**	***β* (°)**
ZSM-23	11.129	5.025	21.519	89.85
(Ge,Si) MTT	11.102(3)	5.049(1)	21.537(4)	89.81(3)

Table 10.5: Literature and refined unit cell parameters for ZSM-23 and as-made germanosilicate MTT.

10.4: Summary

In the SAPO regime, non-metallated cyclam would appear to act in a similar fashion to metallated cyclam in directing the formation of either STA-6 or STA-7 depending on the identity of the co-base present. This macrocycle, therefore, provides a convenient route to the synthesis of both metallated and non-metallated SAPO analogues of these phases.

Studies of the SAPO-cyclam-TEAOH system reveal a strong dependence on the gel composition when synthesising SAPO STA-7 with crystallinity lost as gel P content decreases. However, elemental analysis and preliminary NMR studies suggest that, by working at the extremes of the SAPO STA-7 crystallisation field (with or without fluoride present), Si loading can be forced beyond the theoretical level associated with SM2 substitution with the concomitant formation of aluminosilicate/silicate islands. It is possible that silicon loading of up to approximately 23% of total T-sites can be achieved at gel compositions 20%Al 20%P 60%Si and 40%Al 20%P 40%Si (with fluoride) with the latter gel yielding a product of superior crystallinity and purity. It would not appear to be possible to achieve pure silicate STA-7 under the conditions studied here. Instead, cyclam appears to inhibit the formation of zeolite β and favours crystallisation of the MFI topology, despite its absence in this crystalline product. In contrast, this macrocycle has no effect over DP under the same conditions.

Chapter 11: Further Studies into the Synthesis of AlPO-Related Phases Employing Metallocomplexes and co-Bases as Structure Directing Agents

To complement the studies involving cyclam discussed in previous chapters, a number of further metallocomplexes have also been employed as potential SDAs (in combination with co-bases) to expand the range of topologies into which transition metals can be introduced via the templating approach. Beginning with the azamacrocycle cyclen (1,4,7,10-Tetraazacyclododecane), and progressing to cyclam/cyclen derivatives, polyamine complexes and finally cobalticinium, this chapter discusses the results of these studies.

11.1: Cyclen as a Structure Directing Agent

As a comparison with cyclam, the azamacrocycle cyclen was selected to investigate any effect caused by decreasing the ring size. Table 11.1 summarises principal syntheses conducted in these studies.

Complexed metal	Co-base	Product (by XRD)
Cu	TEAOH	MgAPO-18 + MgAPO-5
	DIP	MgAPO-18 + MgAPO-5
	DP	MgAPO-18
	HB	MgAPO-18 + MgAPO-5
Cu + Ni	DP	MgAPO-18 + MgAPO-5
No metal	DP	MgAPO-18
		SAPO STA-6
		AlPO-11 + AlPO UT-6

Table 11.1: Summary of products obtained from cyclen in the presence of a selection of co-bases.

The deep blue Cu-cyclen complex was introduced to typical MgAPO gels in the presence of four different co-bases (DP, DIP, HB and TEAOH) to investigate any influence these combinations would have on the direction of crystallisation. In contrast to syntheses conducted in the presence of Cu-cyclam and different co-bases, Cu-cyclen favours the formation of deep blue-coloured MgAPO-18 (AEI) regardless of the co-base employed (Figure 11.1). This is in agreement with earlier reports[50] of the direction of CoAPO-18 formation by Ni-cyclen in the presence of DP and it would appear that the various co-bases exert very little structure-directing effect in this system. It should be noted, however, that TEA^+ cations are known to stabilise the AEI cage,[86] although CHN analysis of as-made samples suggests the presence of only the macrocycle. A red shift of the absorption band in the solid-state UV-Vis spectrum relative to that observed for Cu-cyclam is consistent with literature reports for the Cu-cyclen complex.[87] It is observed that products obtained in the presence of DIP, HB and TEAOH possess a small MgAPO-5 impurity. Although this phase was observed to possess no colour under the optical microscope, DP was selected as the co-base of choice for targeting MgAPO-18 in this fashion. Indeed, a MgAPO synthesis involving unmetallated cyclen and DP also yielded phase pure MgAPO-18.

These results encouraged the synthesis of a mixed Cu/Ni-cyclen-containing MgAPO-18 material by introducing equal quantities of the two complexes to a typical gel in the presence of DP. As in Cu-cyclen-containing samples, CHN analysis of the resulting material confirmed the presence of cyclen only (C/N = 2.1) and EDX analysis of the plate-like crystals indicated that both Ni and Cu are indeed present, and suggests an approximate unit cell composition of $(Ni\text{-}cyclen)_{1.01}(Cu\text{-}cyclen)_{2.55}(Mg_{5.33}Al_{19.18})P_{13.6}O_{96}$. XRD analysis revealed a small quantity of MgAPO-5 impurity. However, these easy-to-find hexagonal crystals showed negligible Cu and Ni content during EDX examination.

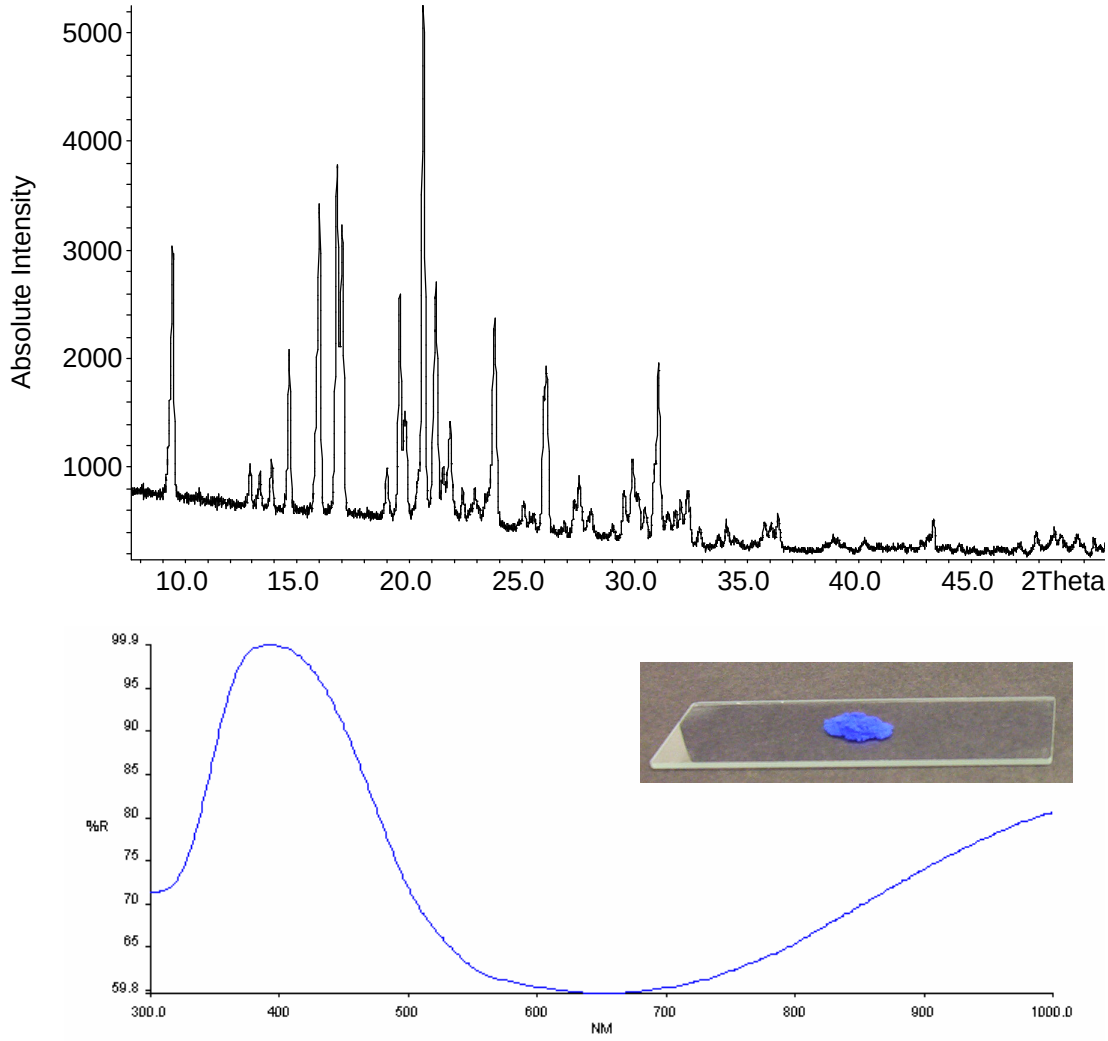

Figure 11.1: Typical XRD pattern (top) and photograph and solid-state UV-Vis spectrum (bottom) of as-made Cu-cyclen-containing MgAPO-18.

Rietveld refinement starting from literature atomic coordinates of AlPO-18 against XRD data of calcined and dehydrated Cu-MgAPO-18 (procedure as before, refined parameters listed in Appendix E(4)) confirmed the AEI topology and *C2/c* symmetry as being correct. Unit cell parameters refined as a = 13.532(2)Å, b = 12.678(3)Å, c = 18.435(4)Å, β = 89.70(3)^{o}. Fourier difference maps located possible Cu^{2+} positions either side of the D6R unit analogous to Cu4 in SAPO STA-7 (Figure 9.27). This position drifted slightly on refinement towards the 8MR window of the large cage with Cu-O distances of 2.06 and 1.93Å. It is believed that partial loss of crystallinity upon calcination hampered the satisfactory refinement of this material. In particular, thermal parameters for framework atoms refined slightly high while that of Cu refined negative.

The latter was therefore fixed at a reasonable value of 0.025. Final R_{wp} and R_p values of 11.1% and 19.6%, respectively, were obtained. The occupancy of the Cu location refined to 0.224, which, combined with its multiplicity of 8, suggests 1.79 Cu per unit cell. This is slightly below the estimated cell composition of (Cu-cyclen)$_{3.60}$(Mg$_{5.98}$Al$_{19.6}$)P$_{23.6}$O$_{96}$ (from EDX, CHN and TGA data combined).

Figure 11.2 illustrates the refined structure of calcined and dehydrated Cu-MgAPO-18. The AEI topology is most conveniently described as being built from layers of 4MR-connected D6R units, which connect (also via 4MRs) to produce pear-shaped cages (four per unit cell). In this way, the AlPO-18 structure may be regarded as a relative of STA-7 (SAV) and chabazite[88] (CHA). Figure 11.3 illustrates the different D6R connectivities in these three topologies, which may be compared in terms of their structural layers. In CHA, all D6R units tilt in the same direction and layers are simply translated along the *c*-axis giving an AAAA stacking sequence. In AEI, all D6R units tilt in the same direction within any given layer. A mirror plane, however, relates adjacent layers, so that the direction of tilt in one layer is opposite to that in the adjacent layer and an ABAB stacking sequence exists. The SAV topology may also be regarded as possessing an ABAB stacking sequence in which adjacent layers are related by a mirror plane. However, in this structure type, each layer is composed of two types of D6R chains, which are themselves related by a mirror plane. As a result, layers are composed of oppositely tilting chains. A hypothetical fourth member of this structural family would possess the same layer type as SAV (i.e. composed of alternately tilting chains of D6Rs) and be stacked in an AAAA sequence. As yet, this topology has not been observed experimentally.

Like STA-7, the AlPO-18 framework possesses a three-dimensionally connected pore system, connected via 8MRs. As a consequence, the rate of loss of organic species upon calcination is also very swift and is illustrated by the TGA thermogram in Figure 11.4.

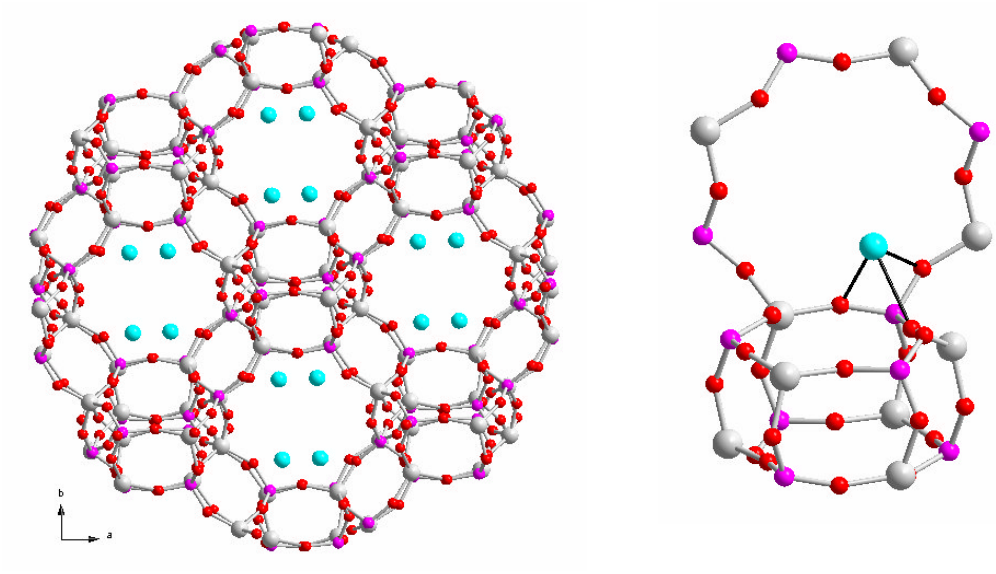

(a)

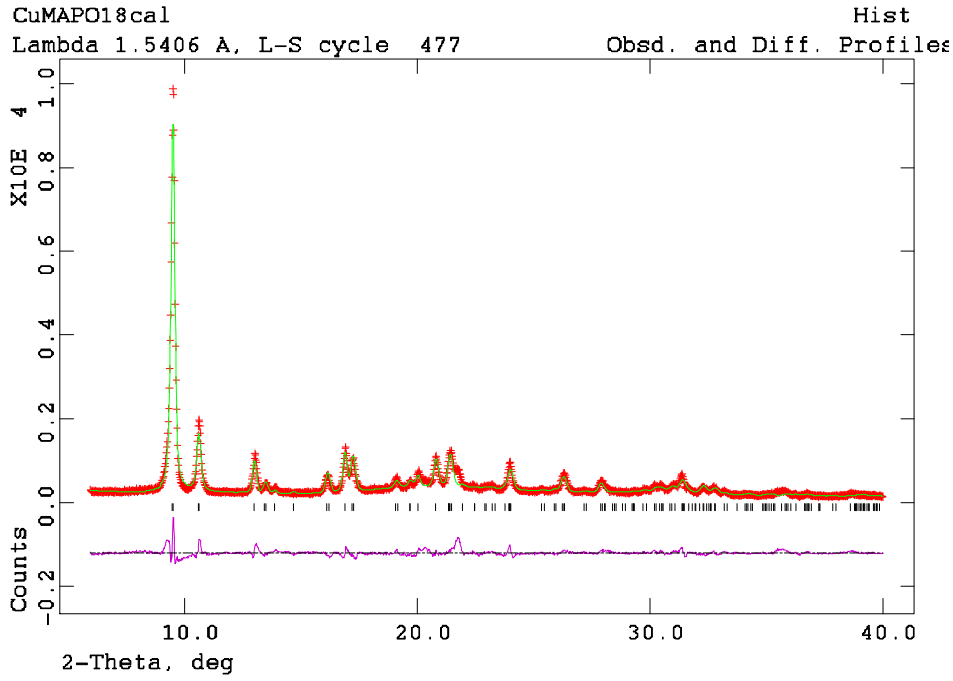

(b)

Figure 11.2: (a) Refined structure of calcined and dehydrated Cu-MgAPO-18 with detail of a possible Cu location shown on the right (purple = P, grey = Al/Mg, red = O, cyan = Cu), (b) Rietveld refinement plot (red = experimental data, green = model, purple = difference).

Unfortunately, attempts to target Cu and/or Ni-containing SAPO-18 resulted in amorphous products while the vividly coloured complexes remained in solution. Interestingly, however, a SAPO synthesis in the presence of non-metallated cyclen with DP resulted in the formation of SAPO STA-6, and a similar synthesis in the AlPO

regime resulted in a mixture of AlPO-11 and AlPO UT-6. For both of these samples, CHN analysis suggests only cyclen is present. Repeating the latter synthesis in the presence of Cu-cyclen, however, failed to introduce the complex to either AlPO-11 or UT-6, resulting instead in the formation of the dense phase berlinite (blue Cu-cyclen remained in solution).

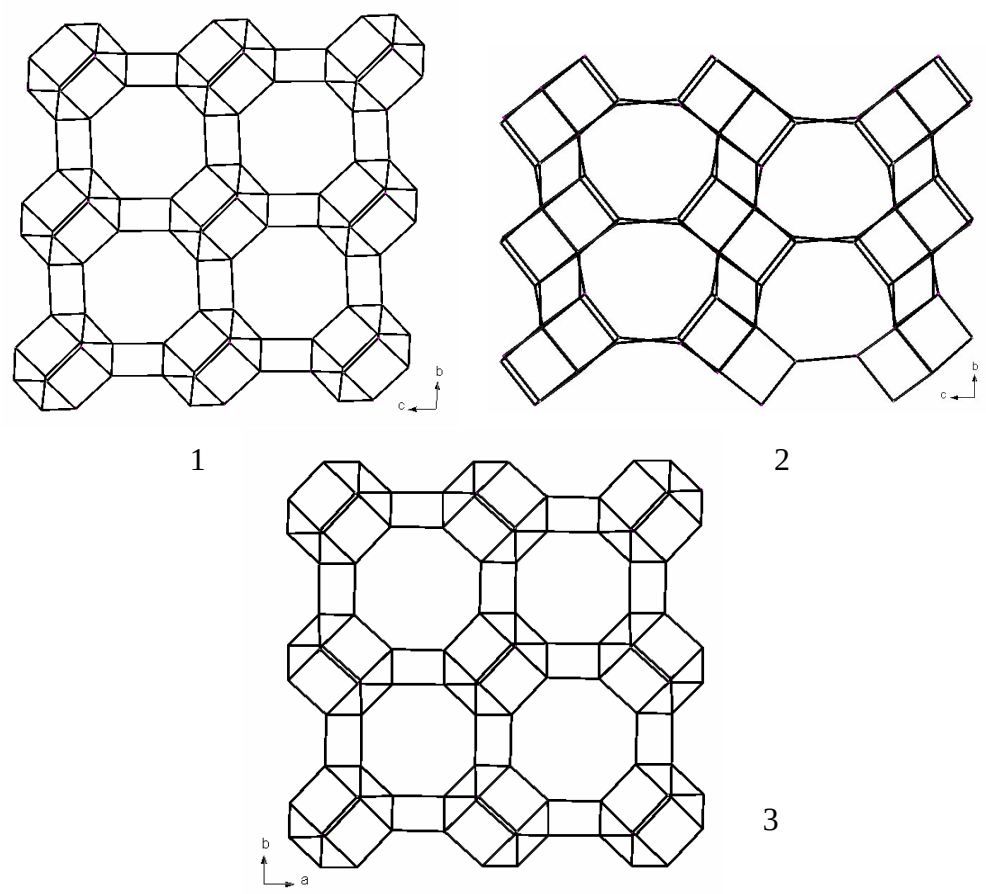

(a)

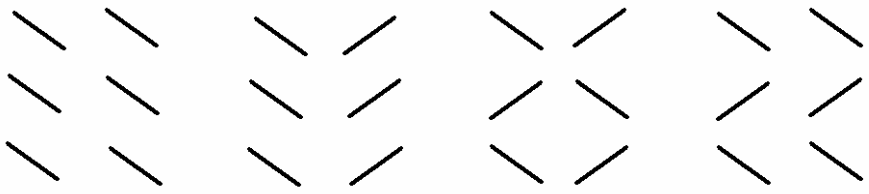

(b)

Figure 11.3: (a) Comparison of the CHA (1), AEI (2) and SAV (3) topologies (oxygen atoms removed for clarity), (b) two-dimensional schematic representation of the direction of tilt of D6R units within CHA (1), AEI(2), SAV(3) and a fourth hypothetical structure.

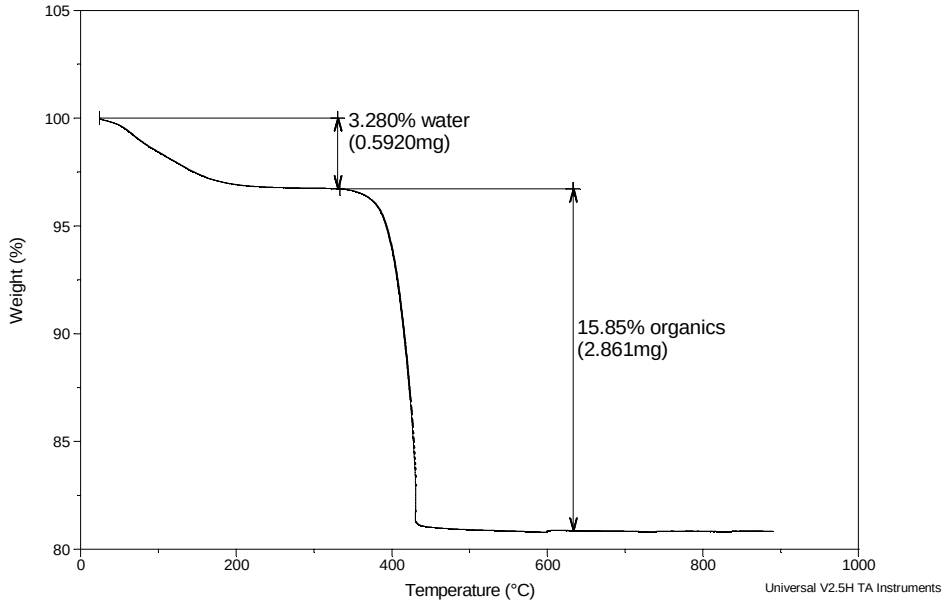

Figure 11.4: TGA thermogram of Cu-cyclen-containing MgAPO-18

Cyclen, as an SDA, would not appear therefore to be as flexible in application as its larger relative cyclam. In the MgAPO system Cu and Ni-cyclen complexes invariably direct the formation of the AEI topology, and any structure-directing ability possessed by the co-base would appear to be insignificant in their presence. In contrast, however, these complexes show no structure-directing ability in SAPO and AlPO systems. Moreover, the formation of crystalline SAPO and AlPO phases in the absence of transition metals suggests that the structure-directing ability of cyclen in these circumstances is far more susceptible to the geometric subtleties caused by complexation compared to cyclam. This may be due to differences in coordination geometry between the two macrocycles. As typified by ESR parameters values in the region of those observed above for Cu-cyclam-containing materials, this complex possesses a square planar CuN_4 arrangement[87] and probably two weakly coordinating axial water molecules, which are easily accommodated in the STA-6 and STA-7 cages. The metal cation therefore resides within the plane of the macrocycle ring and the overall size and shape of the SDA as a whole is not hugely altered, although it will be more rigid. ESR analysis (Figure 11.5) of as-made Cu-cyclen-containing MgAPO-18 suggests $A_{\|}$ and $g_{\|}$ values of 182G and 2.20, respectively (literature reported values: 184 and 2.19, respectively[87]). Compared to equivalent values of, for example, as made Cu-cyclam-containing STA-6 ($A_{\|}$ = 206G and $g_{\|}$ = 2.16), these values are consistent with a trend to higher $g_{\|}$ and lower $A_{\|}$ values as square-planar geometry becomes disfavoured.

It is probable, therefore, that the Cu-cyclen complex exhibits a square-pyramidal geometry within the pore of this material with five-coordination being completed by an apical water molecule. Indeed, Fourier difference maps produced during Rietveld refinement of as-made Cu-cyclen-containing MgAPO-18 (procedure as before) revealed an off-centre location for the Cu^{2+} cation in the AEI cage (Figure 11.5, atomic coordinates: 0.44(2), 0.11(2), 0.20(3)). It is probable, therefore, that the metal cation does reside outside the cyclen ring – a consequence of the shorter N-N distance. It is thought that this more dramatic change in the species' size, and any associated alteration in rigidity enforced upon it on complexation, precludes its incorporation into AlPO UT-6 and removes its ability to stabilise the SAPO STA-6 cage. In a MgAPO system, however, the square pyramidal complex stabilises the AEI cage as effectively as the nonmetallated macrocycle.

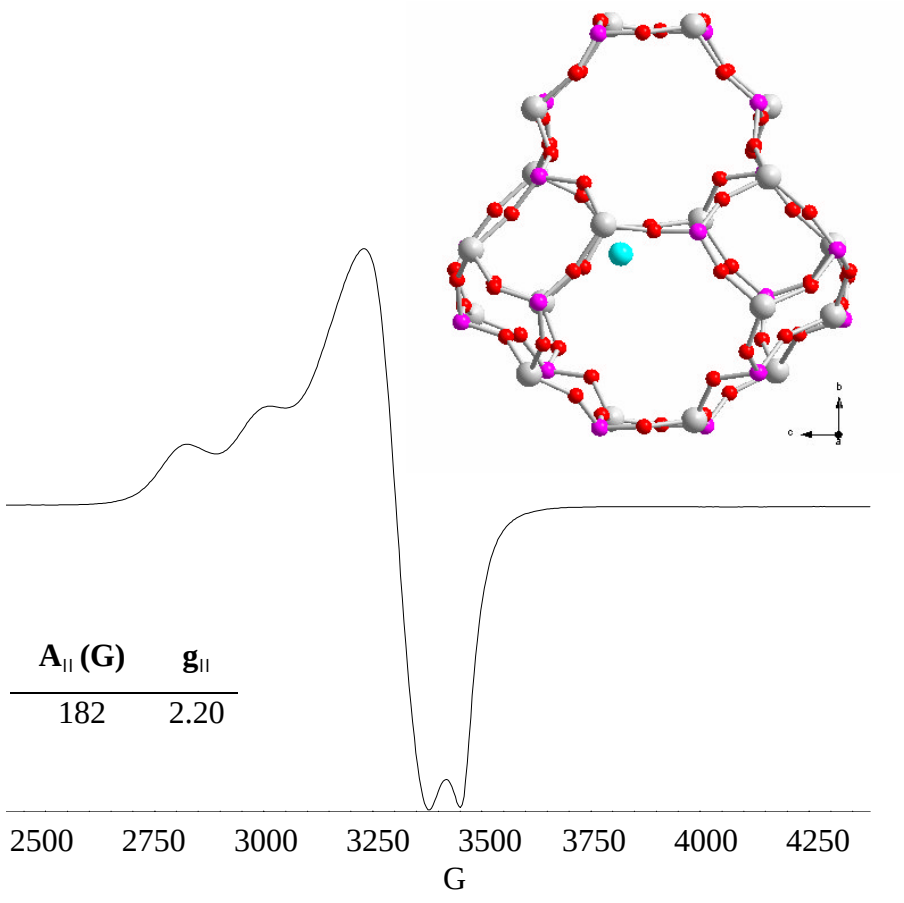

Figure 11.5: (a) Refined, off-centre Cu^{2+} location in as-made Cu-cyclen-containing MgAPO-18 (purple = P, grey = Al/Mg, red = O, cyan = Cu), (b) accompanying ESR spectrum.

In general, the cyclen/co-base structure-directing strategy is less widely applicable than analogous cyclam techniques. As a means of introducing transition metal cations to AlPO-related phases, it would appear to be limited to MgAPO-18 materials, under the conditions studied here.

11.2: Cyclam and Cyclen Derivatives as Structure Directing Agents

As an expansion of studies into cyclam and cyclen, the structure-directing ability of a selection of novel derivatives of these macrocycles was also probed. Figure 11.6 illustrates the six different ligands studied. These were synthesised by the research group of Prof. H. Handel at Université de Bretagne Occidentale and supplied to us by Dr Véronique Patinec. The ligands were used as supplied in their hydrochloride salt form.

Due to the limited supply of these materials, only a small selection of syntheses were possible (Table 11.2) and, once again, MgAPO gels were chosen as the test system due to their higher crystallisation rates. DP and TEAOH were selected as co-bases since they have exhibited strongly contrasting behaviour in previous syntheses.

Typically, products consisted of MgAPO-5 (AFI), MgAPO-34 (CHA) or mixtures of the two. The AFI topology is often considered as a default AlPO product since it can be synthesised in the presence of many different SDAs[72] and often appears as an unwanted impurity. Nevertheless, these ligands offer a possible means of introducing Cu and/or Ni to the pores of this material. The hexagonal AFI topology[89] possesses a one-dimensional pore system of straight 12MR channels, and it is easy to appreciate how these ligands can stabilise such channels thanks to their linear shape.

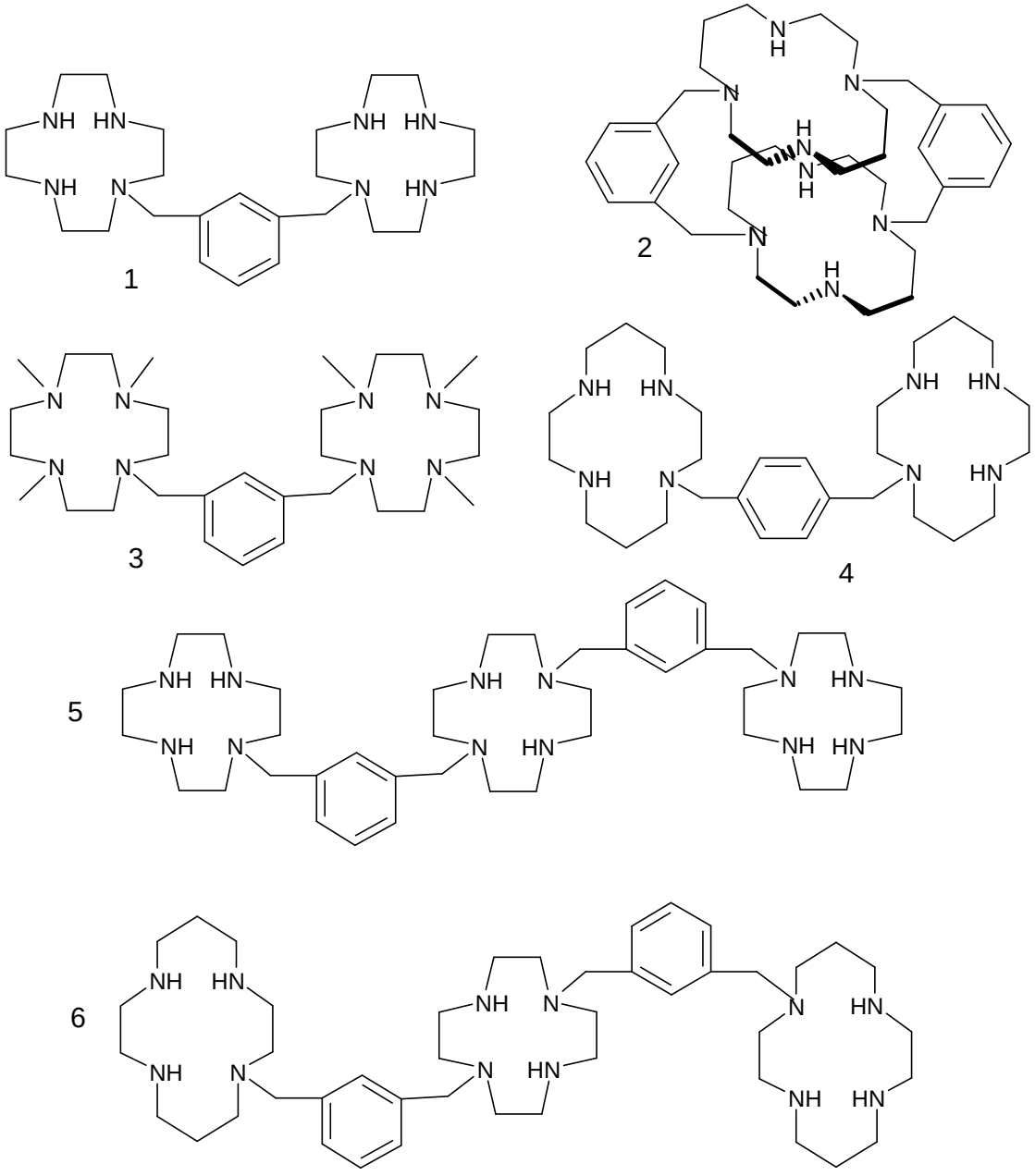

Figure 11.6: Cyclam and Cyclen derivatives studied as potential structure-directing agents. Their adopted working names are (1) bis-cyclen, (2) trimacrocycle, (3) methyl-bis-cyclen (4) bis-cyclam, (5) tris-cyclen and (6) tris(cyclamcyclencyclam)

Ligand	Complexed metal	Co-base	Product (by XRD) (sample number referred to in text and Table 11.3)
Bis-cyclen	Cu	TEAOH	MgAPO-5 (1a)
		DP	MgAPO-5 (1b)
		DIP	MgAPO-5 (1c)
Trimacrocycle	Cu + Ni 1:1	TEAOH	MgAPO CHA (2a)
		DP	MgAPO-5 (2b)
	Ni	DP	Amorphous (2c)
Methyl-bis-cyclen	No metal	DP	MgAPO-5 (3a)
	Cu	DP	Amorphous (3b)
Bis-cyclam	Cu + Ni 1:1	TEAOH	MgAPO-5 (4a)
		DP	MgAPO-5 (4b)
	Ni	TEAOH	MgAPO-5 + MgAPO CHA (4c)
Tris-cyclen	Cu	TEAOH	MgAPO-5 + MgAPO CHA (5a)
		DP	MgAPO-5 (5b)
Tris(cyclamcyclencyclam)	Cu + Ni 1:2	TEAOH	MgAPO CHA (6a)
		DP	MgAPO-5 (6b)

Table 11.2: Syntheses conducted in the presence of Cu- and Ni-containing cyclam and cyclen derivatives.

Most successful in terms of introducing Cu to the pores of MgAPO-5 was the bis-cyclen derivative. Complexed to Cu only, this species produced deep blue crystals of phase-pure MgAPO-5 regardless of the co-base present. The presence of Cu, as suggested by the vivid colour of the product, was later confirmed by EDX analysis (Table 11.3). The solid-state UV-Vis spectrum of these as-made materials (Figure 11.7) is very similar to that of Cu-cyclen-containing MgAPO-18 (Figure 11.1) with a broad band at 620nm suggesting that the complex is present intact. Although no change in product was observed on changing the identity of the co-base, CHN analysis indicates that while only the ligand is present in sample 1b, both ligand and TEA^+ cations are present in sample 1a (in a 1:1 ratio). This is confirmed by solid-state ^{13}C MAS NMR studies of sample 1a (Figure 11.8(a)), which shows a superimposition of signals from TEA (δ

6.6ppm CH_3, 52.3ppm CH_2 Figure 11.14(a)) and the ligand (δ 42ppm CH_2, 131.3ppm aromatic; Figure 11.8(b) * = spinning side bands (SSB)). It would also appear from the signal width that the TEA^+ species is more mobile in the pore of MgAPO-5 than the complex, as might be expected from its smaller size and therefore increased freedom of movement. Interestingly, the presence of Cu^{2+} did not quench the signal of the ligand as might have been expected (Cu-cyclam-containing SAPO STA-7 shows no signals corresponding to the macrocycle in its ^{13}C MAS NMR spectrum). It is possible that not all of the ligand in this sample is coordinating to copper. Indeed, CHN analysis suggests slightly more ligand is present than would be necessary to complex the quantity of copper suggested from EDX analysis. This would not appear to be the case for other preparations involving this ligand and it is thought that this behaviour, which, nevertheless, permitted the confirmation of the ligand's presence within the product phase, is anomalous and peculiar to this particular preparation only.

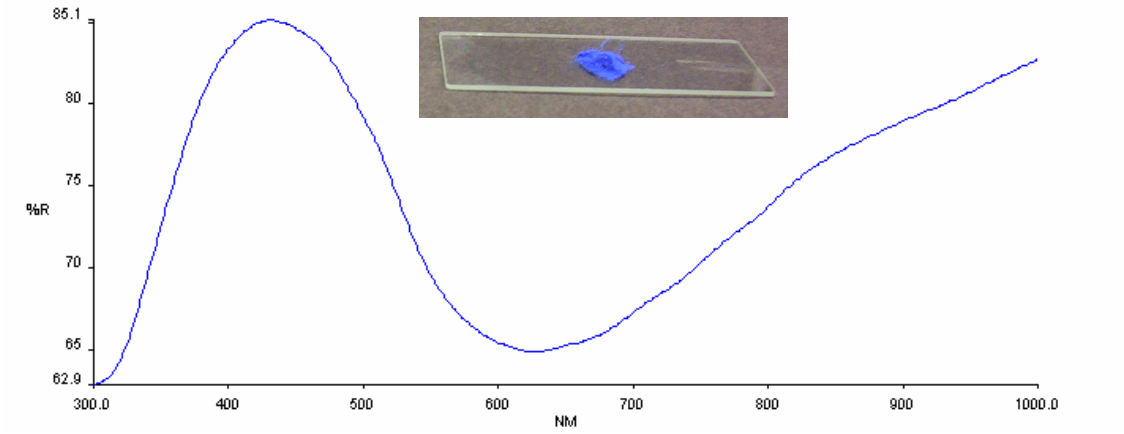

Figure 11.7: Solid-state UV-Vis spectrum and photograph of as-made Cu-bis-cyclen-containing MgAPO-5.

With a larger supply of the bis-cyclen ligand available, a MgAPO gel was also prepared in the presence of DIP. Deep blue crystals of MgAPO-5 were once again obtained and, as in the case of sample 1a, the co-base was found to be occluded in the product (ligand:DIP = 1:1). Elemental analysis (Table 11.3), however, suggests that the inclusion of TEA^+ and DIP species to the pore system does not reduce the level of

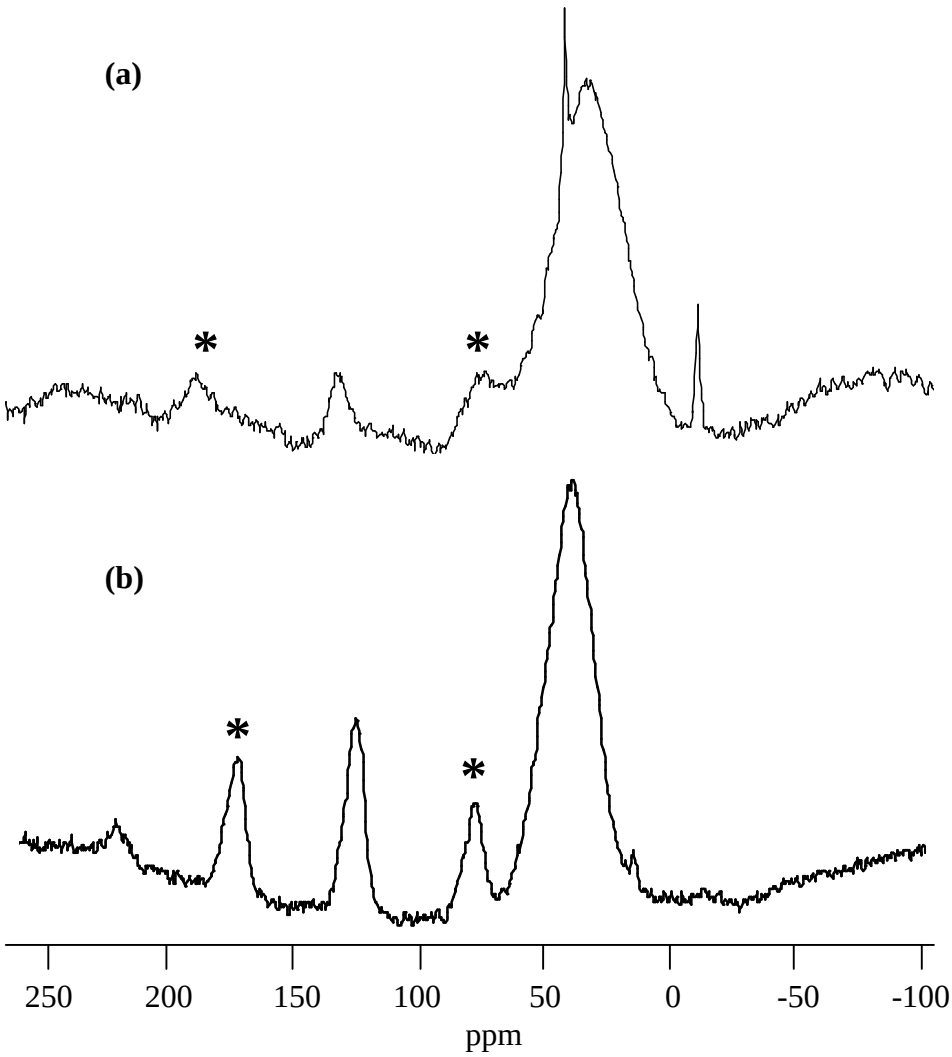

Figure 11.8: Solid state ^{13}C MAS NMR spectra of (a) as-made MgAPO-5 (1a), and (b) bis-cyclen starting material (= SSB).*

complex up-take with generally 0.5 complexes per unit cell in the three samples. It would appear, therefore, that no competition exists between the occluded co-bases and complex, with the two species perhaps occupying different sites within the channel system.

These materials are stable to calcination at 550^{o}C, 3^{o}C/min under oxygen, producing turquoise-coloured materials. Reitveld refinement of literature atomic coordinates for AlPO-5 against XRD data for calcined and dehydrated sample 1b was conducted as before and confirmed the structure and *P6cc* symmetry with final R_{wp} and R_p values of

13.07% and 7.70%, respectively (Figure 11.9 and Appendix E(5)). Preferred extra-framework Cu^{2+} locations were probed via Fourier difference maps. However, although a number of electron density peaks in the Fourier maps were at reasonable distances from framework oxygens and occupied plausible locations close to the channel walls, their input to the refinement as Cu had negligible effect on the R-values and they often refined with negative occupancies. EDX analysis (Table 11.3) suggests only one Cu per unit cell. If this is distributed over a number of different sites it might be very difficult to locate preferred locations for these materials from powder data.

The Cu complex of the bis-cyclen ligand was also employed with DP in a SAPO preparation in an attempt to synthesise SAPO-5. However, the importance of the framework composition became evident once more with the failure of this gel to crystallise.

Methylation of this ligand (Ligand 3) was found to have a detrimental effect on its structure-directing ability. Although the Cu complex would appear to be stable under hydrothermal conditions (the vivid blue colour was present in the liquid phase of the product mixture), it did not direct the crystallisation of a MgAPO gel in the presence of DP. However, direction of the synthesis of MgAPO-5 *was* achieved by this ligand in the absence of any transition metals, indicative of the subtleties involved in the templating process.

The tris-cyclen derivative (ligand 5) was less successful than its smaller relative. Although pale blue crystals of MgAPO-5 were obtained regardless of the co-base, these were in much lower yield and suffer from the presence of a brown impurity. The presence of TEAOH would also appear to favour the formation of MgAPO-34 (CHA). The brown impurity phase (probably responsible for an absorption band at 400nm in the solid-state UV-Vis spectrum, Figure 11.10) is thought to be MgAPO-5 with decomposed organic fragments occluded in the channel system and suggests that this complex may not be as robust under these conditions. Elemental analysis of a small quantity of blue MgAPO-5 crystals separated from the brown phase suggests that approximately 0.32 complexes are present per unit cell, giving a similar Cu loading (i.e. one per cell) to that observed for Cu-bis-cyclen.

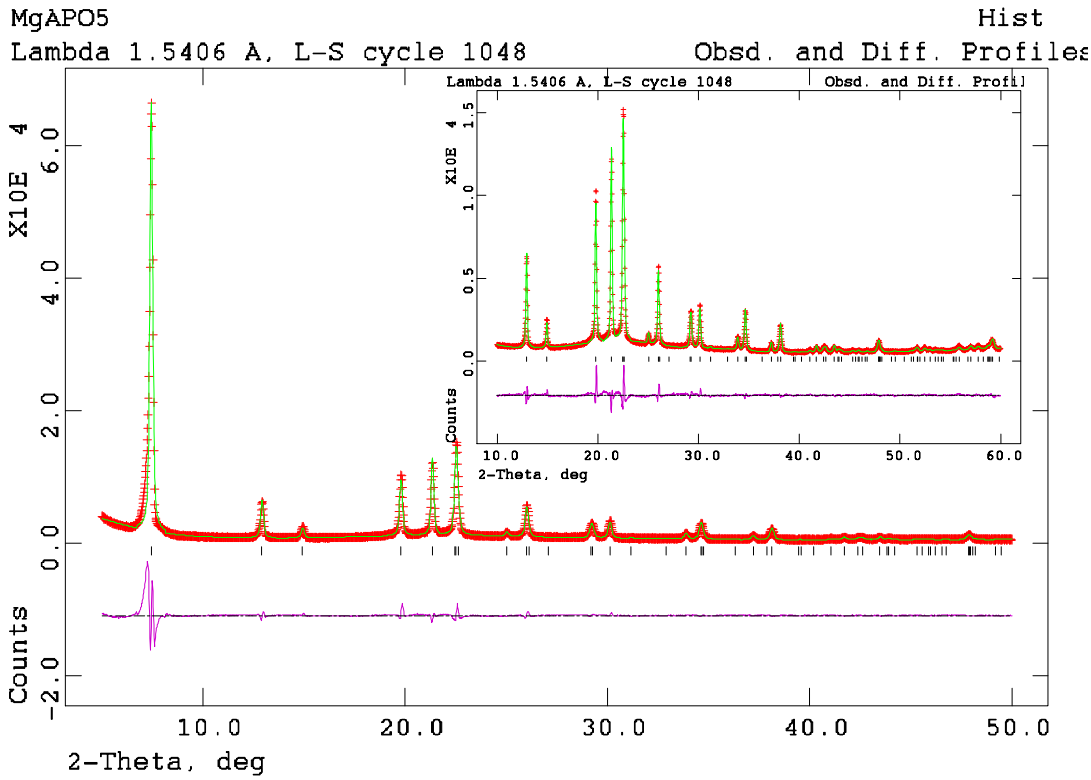

Figure 11.9: Reitveld refinement plot for calcined and dehydrated Cu-MgAPO-5 (red = experimental data, green = model, purple = difference plot). Inset: data region from 10 to 50°2θ.

Sample number	Material type	Approximate unit cell composition
1a	Cu-MgAPO-5	$(Cu_2L)_{0.31}L_{0.20}(NC_8H_{20})_{0.51}(Mg_{1.52}Al_{10.2})P_{12.3}O_{48}$
1b	Cu-MgAPO-5	$(Cu_2L)_{0.53}(Mg_{2.02}Al_{10.2})P_{11.8}O_{48}$
1c	Cu-MgAPO-5	$(Cu_2L)_{0.52}(NC_6H_{14})_{0.52}(Mg_{1.19}Al_{10.7})P_{12.02}O_{48}$
2b	Cu/Ni-MgAPO-5	$(Cu_{0.1}Ni_{0.09}L_{0.39})(Mg_{1.34}Al_{10.6})P_{11.9}O_{48}$
4a	Cu,Ni-MgAPO-5	$(Ni_{0.15}Cu_{0.19}L_{0.62})(NC_8H_{20})_{0.62}(Mg_{1.38}Al_{10.6})P_{12.1}O_{48}$
4b	Cu,Ni-MgAPO-5	$(Ni_{0.14}Cu_{0.12}L_{0.56})(Mg_{1.32}Al_{10.6})P_{12.0}O_{48}$
5b	Cu-MgAPO-5	$(Cu_3L)_{0.32}(Mg_{1.63}Al_{9.95})P_{12.4}O_{48}$
6b	Cu,Ni-MgAPO-5	$(Ni_2CuL)_{0.31}(Mg_{1.08}Al_{10.8})P_{12.1}O_{48}$

Table 11.3: Elemental analysis of phase-pure as-made Cu/Ni-containing MgAPO materials (from CHN, EDX and TGA analysis) L denotes the relevant ligand.

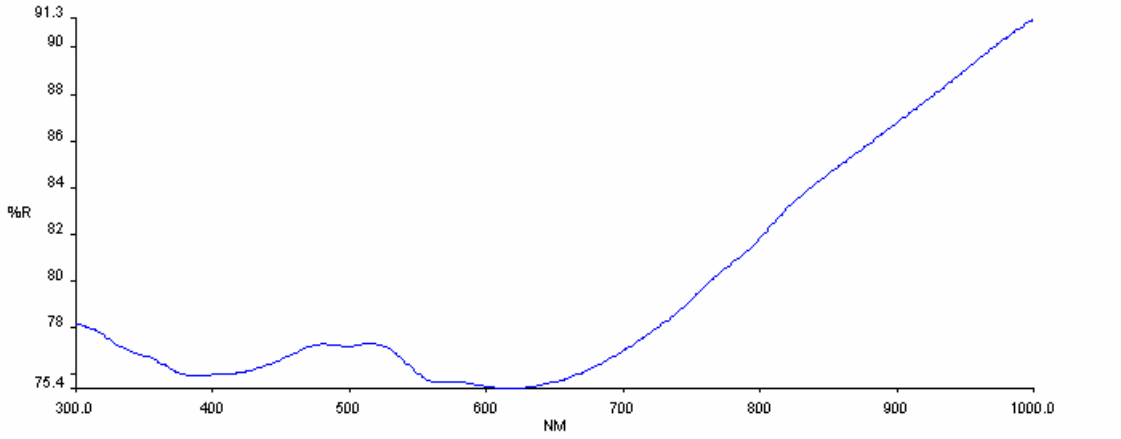

Figure 11.10: Solid-state UV-Vis spectrum of as-made Cu-tri-cyclen-containing MgAPO-5.

The bis-cyclam derivative (ligand 4) was investigated as a possible medium for the introduction of both Cu and Ni into the micropores of the product phase. As with the syntheses involving bis-cyclen, TEAOH would appear to be present in the product phase but does not affect the level of complex loading. CHN and TGA analysis suggests approximately 0.6 ligands per unit cell in both samples 4a and 4b. Solid state ^{13}C MAS NMR spectroscopy (Figure 11.11(a)) on as-made sample 4b confirms the presence of the ligand only (δ 10.4ppm and 20.2ppm CH_2-*C*H_2-CH_2, 46.4ppm *C*H_2-N, 132ppm aromatic, * = SSB) while that of product 4a (Figure 11.11(b)) exhibits signals from both the ligand (δ 20.2ppm CH_2-*C*H_2-CH_2, 45ppm *C*H_2-N, 130ppm aromatic, * = SSB) and TEA^+ (δ 6.8ppm CH_3, 52.6ppm CH_2). However, EDX analysis indicates only 0.1-0.2 Cu/Ni per unit cell (Table 11.3) suggesting that the complex has possibly demetallated. Indeed, these materials only possess a very pale salmon-beige colour. Nevertheless, solid-state UV-Vis spectroscopy reveals a weak band at 490nm consistent with a mixture of Cu and Ni cyclam (Figure 11.12) and it is possible that what little Cu/Ni remains is still coordinated by the ligand.

Syntheses involving Ligand 6 (tris(cyclamcyclencyclam)) are comparable to those with tris-cyclen and are indicative of the dominating effect of TEAOH in the presence of these larger complexes. Although complex-free MgAPO-34 is obtained from TEAOH-containing gels, DP permits the inclusion of the Cu/Ni complex of this ligand to the pores of MgAPO-5.

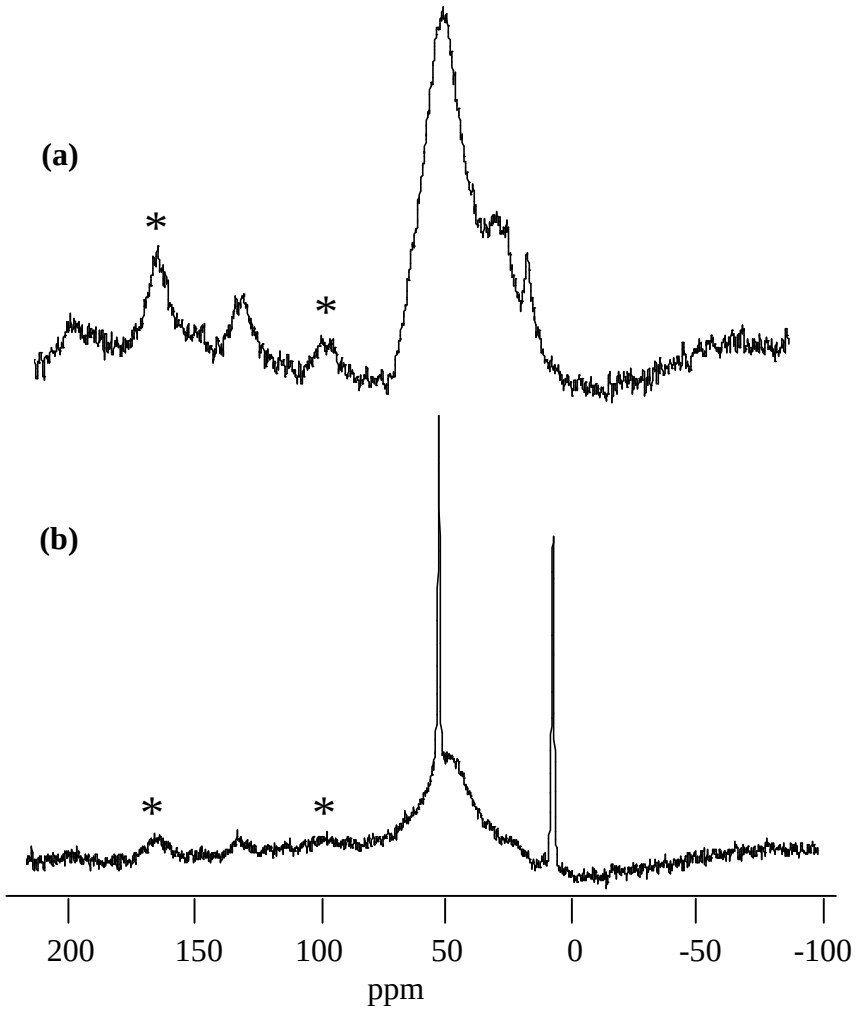

Figure 11.11: ^{13}C MAS NMR spectra of Cu/Ni-bis-cyclam-containing MgAPO-5 prepared in the presence of (a) DP and (b) TEAOH (= SSB).*

In the preparation of this complex, two molar equivalents of Ni were introduced to the ligand prior to the addition of one equivalent of Cu. Since the complexation constant (logK) for Ni (II) cyclam (22.2) is greater than that for Ni (II) cyclen (16.4),[90] it was hoped that Ni would be preferentially coordinated by the cyclam moiety of the ligand. The later-added Cu would then be coordinated by the cyclen moiety (logK 23.3, compared to 26.5 for Cu cyclam[91]). Elemental analysis (Table 11.3) of the MgAPO-5 product phase suggests approximately 0.3 complexes per unit cell (comparable to loading levels for tris-cyclen) with Cu and Ni present in a 1:2 ratio as intended. Although the solid-state UV-Vis spectrum of this sample (Figure 11.13) is a little ambiguous, it is possible that both octahedral (920, 560, 360nm) and square-planar (450nm) Ni^{2+} are present[70] (i.e. Ni-cyclam with and without two axial water molecules), while a weak shoulder at 600nm may be due to the Cu-cyclen moiety.

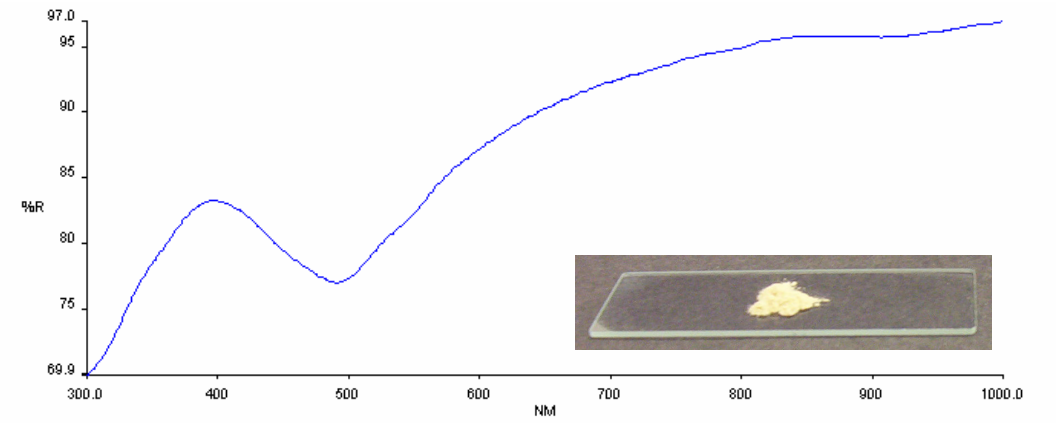

Figure 11.12: Solid-state UV-Vis spectrum and photograph of as-made Cu/Ni-bis-cyclam-containing MgAPO-5 (sample 4b).

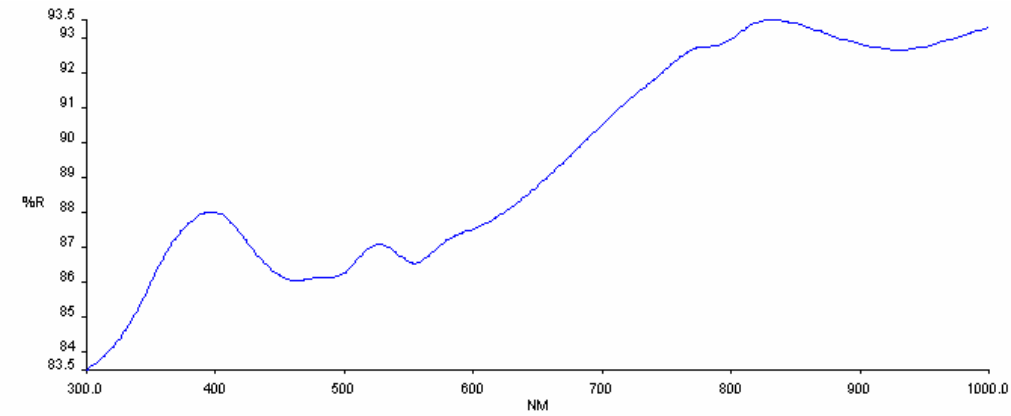

Figure 11.13: Solid-state UV-Vis spectrum of as-made Cu/Ni-tris(cyclamcyclencyclam)-containing MgAPO-5 (sample 6b).

The Cu/Ni complex of ligand 2 (trimacrocycle) was perhaps the least successful as an SDA for the introduction of Cu and Ni to the pores of microporous materials. Once again, TEAOH dominated structure direction by forming MgAPO-34 with the exclusion of the complex. CHN analysis confirms the presence of predominantly TEA^+ cations (C/N = 7), and the solid state ^{13}C MAS NMR spectrum exhibits two sharp signals due to the CH_3 (δ 6.9ppm) and CH_2 (δ 52.7ppm) groups of the co-base (Figure 11.14(a)).

CHN and ^{13}C MAS NMR analysis (Figure 11.14(b)) of product 2b (obtained when DP was employed as the co-base) indicate the presence of only the ligand. However, while approximately 0.4 ligands are present per unit cell (Table 11.3), EDX analysis suggests

only 0.2 cations and it is likely, therefore, that this complex has also partially demetallated.

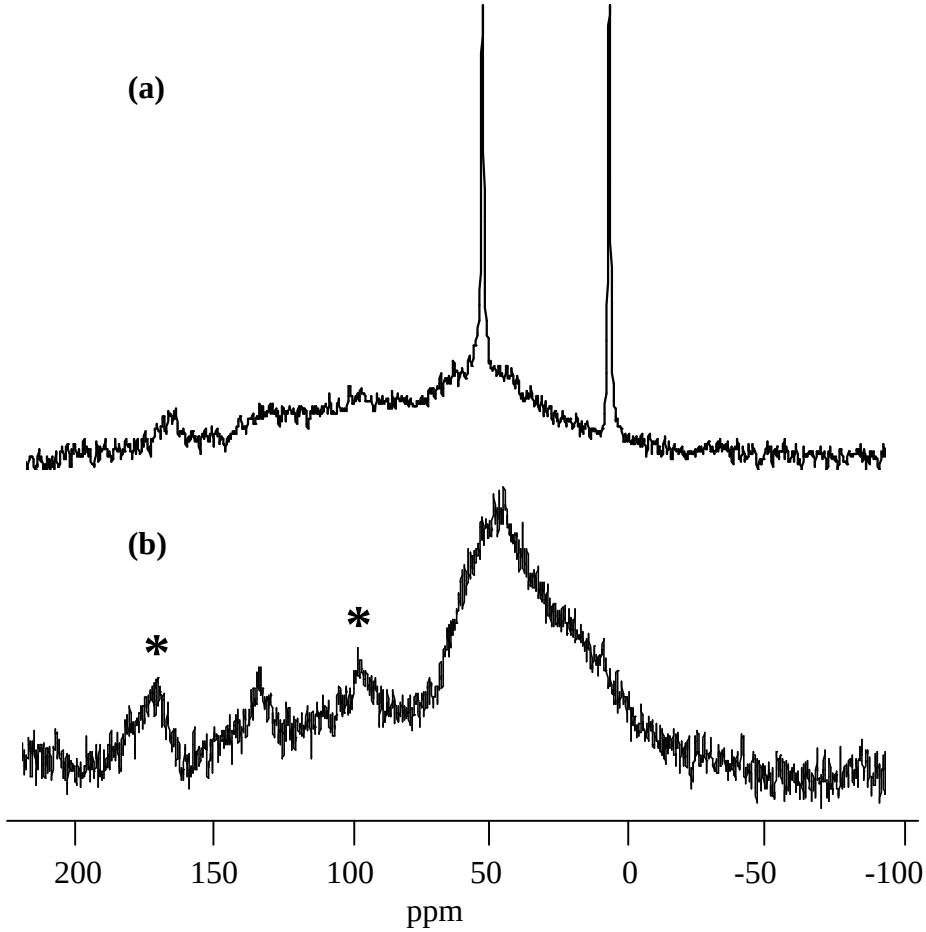

*Figure 11.14: ^{13}C MAS NMR spectra of (a) TEA^+-containing MgAPO-34 and (b) trimacrocycle-containing MgAPO-5 (δ 20ppm CH_2-CH_2-CH_2, 47ppm CH_2-N, 132ppm aromatic, * = SSB).*

These exploratory syntheses suggest that, while most of these ligands provide routes to the incorporation of Cu and Ni to the pores of MgAPO-5, there are a few subtleties involved – not least due to the co-base employed. Most notably, rather than acting as a co-template, TEAOH acts in competition with most of the larger complexes and results in the formation of MgAPO-34. With the smaller complexes of bis-cyclen and bis-cyclam, however, this effect is not observed and although TEA^+ cations are present in the product phase they do not appear to exclude the complex. As inferred from previous studies, DP would appear to be a far weaker SDA and permit the incorporation of most complexes to MgAPO-5. Demetallation and/or partial decomposition appear to be a

problem with complexes of bis-cyclam, macrotricycle and tris-cyclen under the conditions studied. Consequently, bis-cyclen and tris(cyclamcyclencyclam) are regarded as the most effective means of introducing Ni and/or Cu to the pores of MgAPO-5 with approximately one Cu^{2+} or [1/3Cu^{2+} 2/3Ni^{2+}] per unit cell achievable under these conditions.

11.3 Complexes of Polyamines as Structure Directing Agents

Ni complexes of linear polyamines have in the past proved successful in directing the formation of AFI, AEL, AWO and CHA topologies.[23,24,61] As a complementary study to syntheses involving cyclam and cyclen, a selection of polyamine complexes of Cu were examined as potential SDAs. Figure 11.15 illustrates the polyamines employed and Table 11.4 lists principal representative syntheses conducted as part of these studies. Once again DP and TEAOH were selected as co-bases due to their contrasting behaviour.

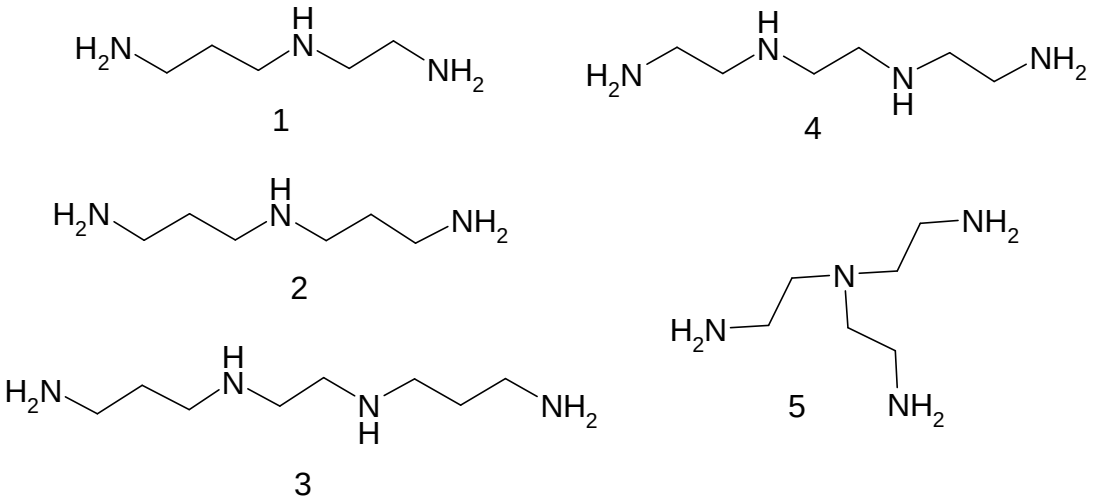

Figure 11.15: Polyamines employed as ligands in these studies (1) N-(2-aminoethyl)-1,3-propanediamine (2) dipropyltriamine (3) N,N'-bis(3-aminopropyl)ethylenediamine (4) triethylenetetramine (5) tris(2-aminoethyl)amine

Ligand	Co-base	Product (by XRD)
Triethylenetetramine	DP	SAPO-34
		AlPO UT-6
	TEAOH	SAPO-34
N,N'-bis	DP	SAPO-34
(3-aminopropyl)ethylenediamine	TEAOH	
N-(2-aminoethyl)-1,3-	DP	Amorphous
propanediamine	TEAOH	SAPO-34
Dipropyltriamine	DP	SAPO-34
	TEAOH	
Tris(2-aminoethyl)amine	DP	SAPO-34
	TEAOH	

Table 11.4: Principal syntheses conducted in the presence of polyamine Cu complexes.

Crystalline SAPO products obtained from these Cu complexes invariably possessed the CHA topology (SAPO-34). However, all products bar those obtained from Cu(triethylenetetramine) were grey in colour and it is therefore thought that, in these cases, the Cu complex decomposed during hydrothermal treatment. The products obtained from Cu(triethylenetetramine) were deep blue in colour suggesting that the complex had remained intact and become incorporated in the crystalline product. EDX analysis confirmed the presence of Cu, and CHN analysis indicates that both the complex and co-base are present in both samples in a 1:1 ratio. Approximate unit cell compositions are given in Table 11.5.

Co-base employed	Approximate unit cell composition
DP	$(CuL)_{0.2}(NC_6H_{14})_{0.2}Al_{17.5}(Si_{4.2}P_{14.3})O_{72}$
TEAOH	$(CuL)_{0.3}(NC_8H_{20})_{0.6}Al_{17.8}(Si_{3.4}P_{14.8})O_{72}$

Table 11.5: Approximate unit cell compositions of Cu(triethylenetetramine)-containing SAPO-34 (CHA) (L = ligand).

While the CHA topology might have been expected from syntheses conducted in the presence of TEAOH, it is interesting that the same phase is obtained in the presence of DP. The complex would appear to be able to fit inside the CHA cage and possibly exert some stabilising or structure-directing effect. It is interesting to note the similarity between this complex and that between Cu and cyclen, which directs the formation of MgAPO-18 (AEI). It is inviting to suggest that the removal of a $-CH_2CH_2-$ unit from cyclen results in the formation of the structurally-related CHA topology in the same way that increasing the ring circumference from cyclen to cyclam results in the formation of the other family member STA-7, although it will be remembered that Cu-cyclen-containing *SAPO* gels did not crystallise. Figure 11.16 illustrates ^{29}Si, ^{31}P and ^{27}Al MAS NMR spectra of Cu(triethylenetetramine)-containing SAPO-34. These are comparable to spectra discussed previously for SAPO materials, but are remarkable in that the presence of paramagnetic copper (II) has not quenched the signal.

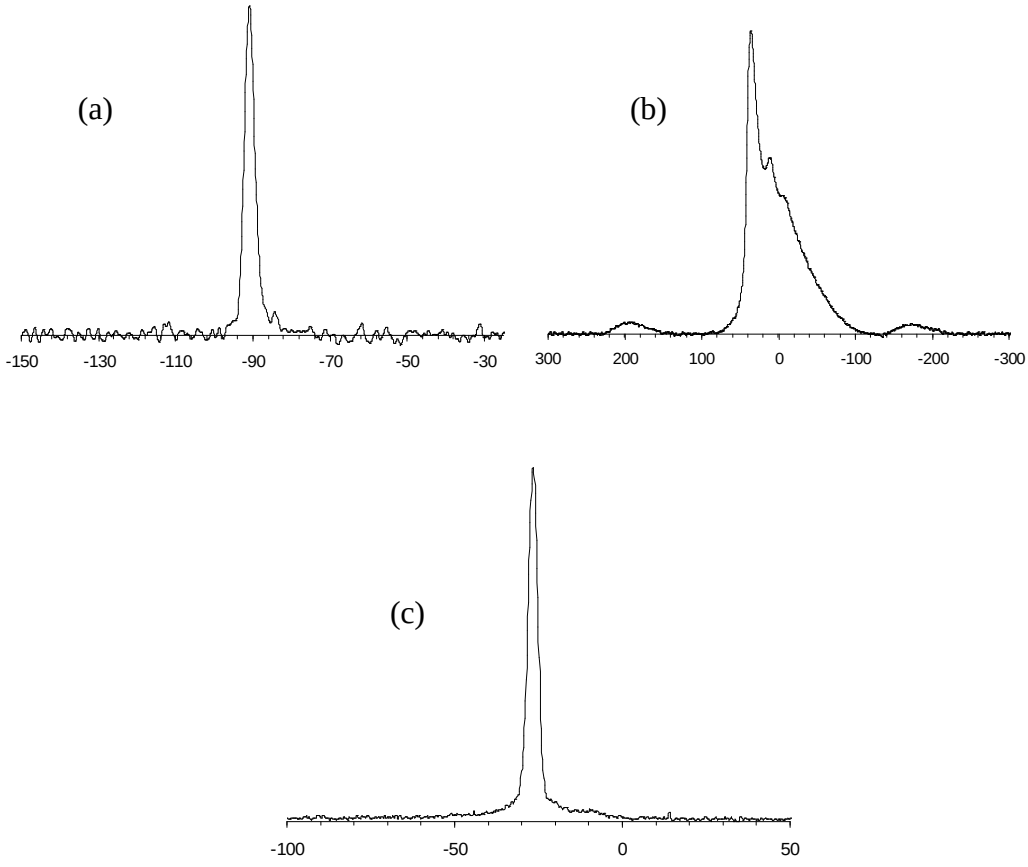

Figure 11.16: (a) ^{29}Si, (b) ^{27}Al and (c) ^{31}P MAS NMR spectra of Cu(triethylenetetramine)-containing SAPO-34.

Applying the Cu(triethylenetetramine) complex and DP to an AlPO synthesis resulted in the formation of the CHA variant UT-6 with the complex (only) occluded within the structure. A similar result in the presence of the Ni complex encouraged the synthesis of a mixed Cu/Ni-triethylenetetramine-containing AlPO UT-6. Figure 11.17 illustrates solid-state UV-Vis spectra of these three materials characterising the blue, yellow and blue-black colours of the Cu-, Ni- and Cu/Ni-containing samples, respectively.

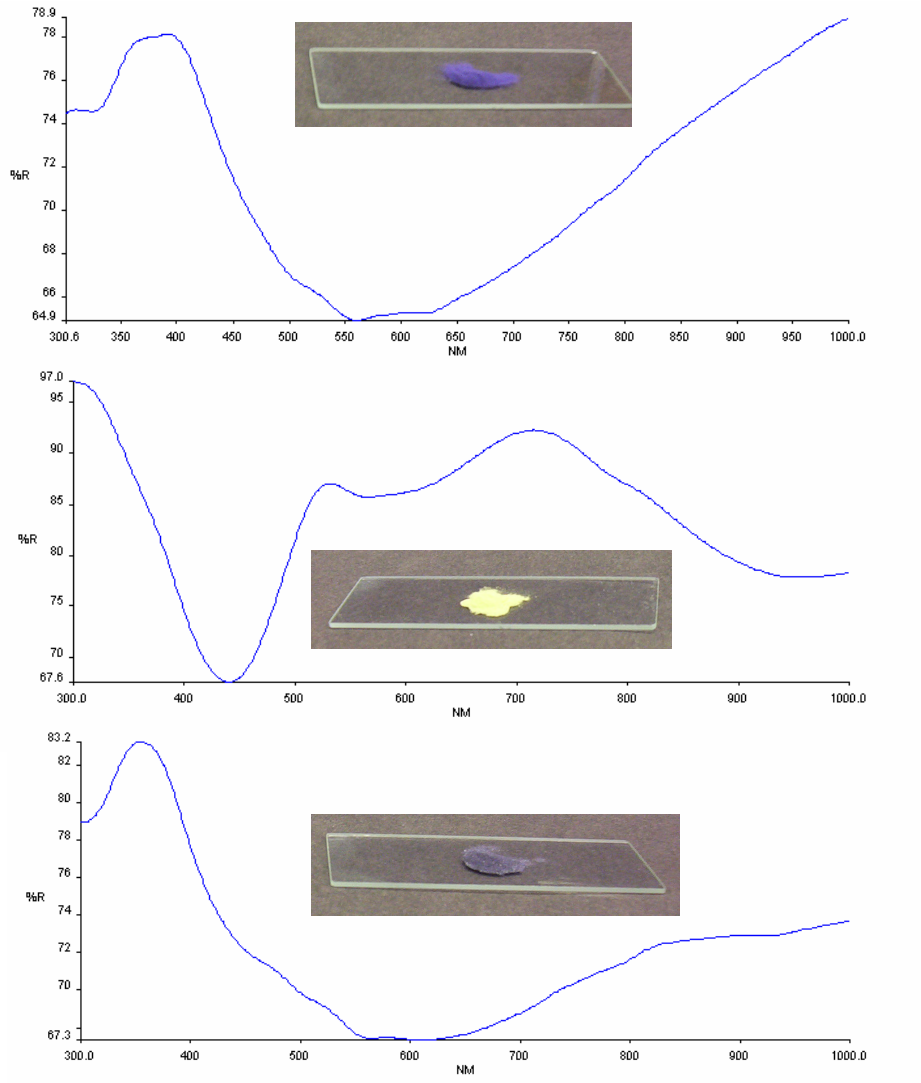

Figure 11.17: Solid-state UV-Vis spectra and photographs of as-made AlPO UT-6 containing (top) Cu- (middle) Ni- and (bottom) Cu/Ni-triethylenetetramine.

While the spectrum of the Cu-triethylenetetramine-containing sample is very similar to that of Cu-cyclen-containing MgAPO-18 and that of $[Cu(NH_3)_4(H_2O)_2]^{2+}$ (λ_{max} = 588nm[70]), the spectrum for Ni-triethylenetetramine-containing UT-6 suggests the

presence of both square-planar (λ_{max} = 430nm) and octahedral (λ_{max} = 600 and 960nm, a third band at 400nm is obscured by the square-planar band) Ni^{2+} and it is thought that the Ni complex may be interconverting between both geometries (six-coordination being achieved by two axial water molecules). The spectrum of the mixed Cu/Ni-triethylenetetramine-containing sample may be considered as a superposition of these two spectra. All three materials proved to be unstable upon calcination.

The structure of UT-6 (Figure 11.18) is similar to that of AlPO-34 (CHA) but each D6R unit contains one octahedral Al (as AlO_4F_2), which connects to that of another 6MR through two bridging fluoride ions. The importance of fluoride ions in the synthesis of this phase is demonstrated by the failure of a Cu(triethylenetetramine)-containing AlPO gel to crystallise in its absence.

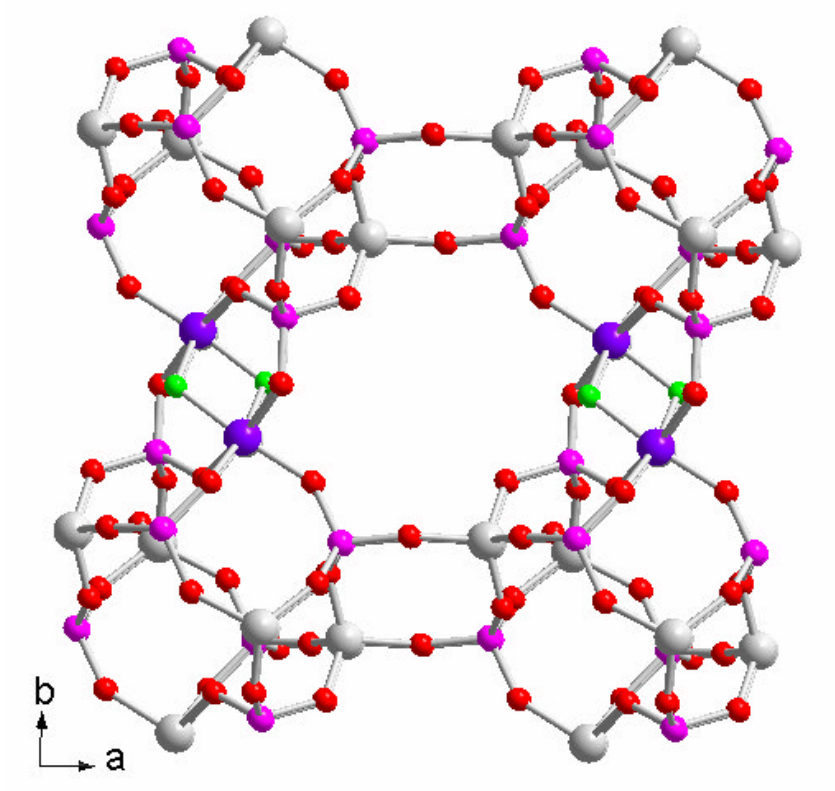

Figure 11.18: Structure of AlPO-UT-6 viewed along the c-axis. Octahedral Al are coloured deep purple for clarity (red = O, green = F, purple = P, grey = tetrahedral Al).

Cu and Ni complexes of diethylenetriamine (deta) were also employed as SDAs in AlPO syntheses in the presence of both DP and TEAOH (Table 11.6). The $Ni(deta)_2$

complex directed the formation of pink needle-like crystals of AlPO-5 (Figure 11.19) in the presence of DP as reported by Garcia *et al.*[24] Replacing DP with TEAOH had no effect on the outcome of the preparation. Elemental analysis of as-made materials confirms that only the complex is present, with an approximate unit cell composition of $(Ni(deta)_2)_{2.02}Al_{12.7}P_{11.3}O_{48}$. The solid-state UV-Vis spectrum of this material (Figure 11.20) is consistent with the octahedral Ni complex[24] with three bands at approximately 380, 550 and 920nm.

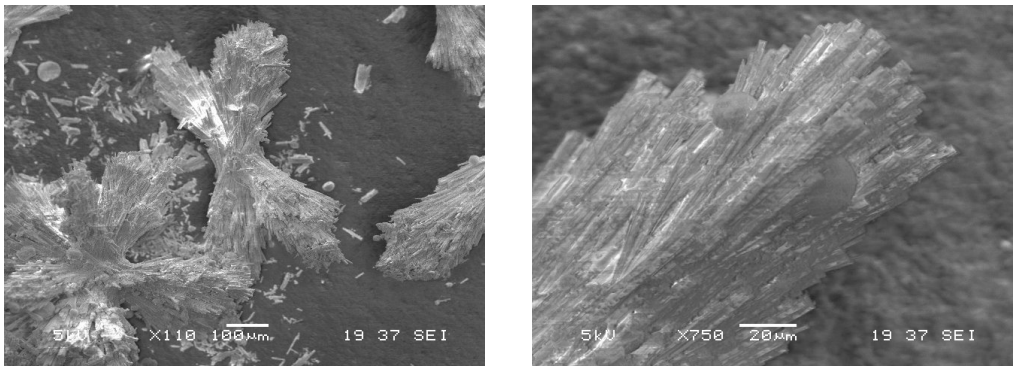

Figure 11.19: SEM images of as-made $Ni(deta)_2$-containing AlPO-5.

Extending this system to $Cu(deta)_2$ yielded blue crystals of $Cu(deta)_2$-containing AlPO-5 in the presence of TEAOH as expected. However, in the presence of DP, $Cu(deta)_2$-containing AlPO-11 (AEL) was produced. CHN analysis of both of these materials implies that the complex is present only in a small amount, suggesting co-base/complex ratios of 4 and 8 for the DP and TEAOH samples, respectively. This is reflected in EDX results, which suggest very low Cu loadings of around 0.1 Cu per unit cell. It is thought, therefore, that the complex has been entrained in the crystallising phase as a space filler rather than as an active template and it is possible that the respective co-bases have exerted a larger structure-directing influence in these examples. The bis-cyclen ligand discussed earlier, therefore, remains the most effective means of introducing Cu^{2+} cations to the channels of the AFI topology.

Complexed metal	Co-base	Product (by XRD)
Ni	DP	AlPO-5
	TEAOH	AlPO-5
Cu	DP	AlPO-11
	TEAOH	AlPO-5
Cu + Ni	DP	AlPO-5 + AlPO-11 + others
	TEAOH	AlPO-5 + AlPO-11 + others

Table 11.6: AlPO syntheses conducted in the presence of Cu- and Ni-deta complexes.

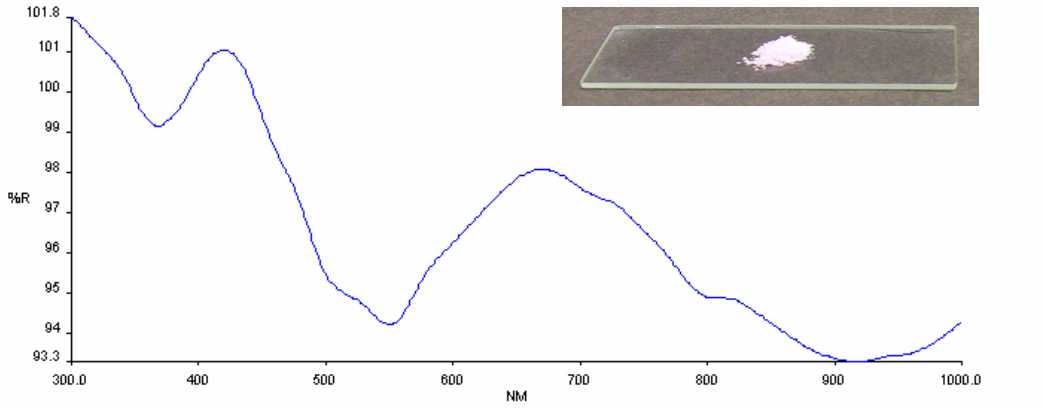

Figure 11.20: Solid-state UV-Vis spectrum and photograph of as-made Ni(deta)$_2$-containing AlPO-5.

Combining Cu and Ni deta complexes in AlPO syntheses to target a mixed metal AlPO resulted in mixtures of several phases. Examination of these product mixtures by optical microscopy revealed lilac-coloured needles and green-coloured blocky crystals among randomly shaped colourless crystals, and it is thought that each complex (and possibly the co-bases) act as competing SDAs to produce mixtures of different phases.

Summary

Unlike their closely related azamacrocycle counterparts, Cu complexes of linear polyamines do not benefit from the so-called macrocyclic effect – i.e. an added stability caused by the cyclic nature of the chelating ligand.[129] As a result, many of the

complexes of linear polyamines studied here would not appear to be stable to hydrothermal conditions. Notable exceptions are Cu(triethylenetetramine) and $Cu(deta)_2$, which afforded the synthesis of SAPO-34 (CHA), AlPO UT-6, AlPO-5 (AFI) and AlPO-11 (AEL). While combining Cu- and Ni-deta complexes resulted in the formation of mixed-phase products, a mixture of Cu- and Ni-triethylenetetramine complexes afforded Cu/Ni-containing AlPO UT-6. However, this latter material proved unstable upon calcination.

11.4 Cobalticinium as a Structure Directing Agent

Syntheses employing transition metal complexes as SDAs in this work have focussed on those of Cu and Ni. One reason for this is the reluctance of these metals to occupy tetrahedral framework positions, increasing the likelihood of them remaining complexed to the ligand involved. Indeed, test cases in which brown Co-cyclam was introduced to fluoride-containing AlPO gels resulted in demetallation of the complex and formation of blue CoAPO STA-7 (in the presence of TEAOH) and CoAPO-11 (in the presence of DP). The latter product also contained the inorganic-organic hybrid material CoAPO-cyclam-1. Co-cyclam would therefore not appear to be as stable under these conditions as the Cu and Ni analogues, and Co^{2+} preferentially substitutes into the AlPO framework. As discussed in Chapter 7, cobalticinium has in the past proved successful as an SDA in the synthesis of microporous materials. Therefore, the structure-directing ability of this species in the presence of different co-bases was investigated as a potential means of introducing Co to the pores of AlPO-related phases (Table 11.7).

Despite literature reports of cobalticinium directing the formation of AlPO-16 in the presence of tripropylamine,[27] this phase was not observed in AlPO syntheses conducted in this work, even in the presence of tripropylamine. Indeed AlPO gels failed to crystallise in the presence of this organometallic. It is possible that the use of the hexafluorophosphate salt as opposed to the hydroxide salt has some influence on this system. Much more successful were MgAPO syntheses, which yielded MgAPO-35 (LEV) regardless of co-base (Figure 11.20 and Table 11.8). Cobalticinium has been reported to direct the formation of a Levynite-like aluminosilicate (denoted ZSM-45) previously by Valyocsik.[92] However, to our knowledge, this is the first time the MgAPO analogue of this topology has been templated by cobalticinium. The bright yellow as-

made materials become indigo on calcination and retain their structural integrity (Figure 11.20). The solid-state UV-Vis spectrum of as-made MgAPO-35 compares favourably with that of cobalticinium-containing AlPO-5[28] and indicates that the template is present intact. Bands at 490 and 580nm in the spectrum of the calcined material are thought to be equivalent to those at 490 and 540nm in the spectrum of $[Co(H_2O)_6]^{2+}$,[70] suggesting the presence of hydrated Co^{2+} cations.

EDX and CHN analysis suggests a unit cell composition of $(Co(C_5H_5)_2)_{4.85}(Mg_{5.19}Al_{21.8})P_{26.9}O_{108}$, implying that approximately five of the six cages per unit cell of the LEV structure are occupied by cobalticinium species.

Organometallic	Co-base	Product (by XRD)
Cobalticinium	DP	MgAPO-35
		SAPO-11 + SAPO-5
		Ge,Si octadecacil
	TEAOH	MgAPO-35
	DIP	MgAPO-35
	HB	MgAPO-35
Permethylcobalticinium	DP	AlPO berlinite
	TEAOH	AlPO CHA
	DIP	AlPO berlinite

Table 11.7: Crystalline product synthesised in the presence of cobalticinium and permethylcobalticinium

	***a* = *b* (Å)**	***c* (Å)**	***γ* (°)**
Literature (LEV)	13.338	23.014	120
Co-MgAPO-35	13.281(4)	23.203(3)	120

Table 11.8: Comparison of literature unit cell parameters for the Levyne structure and refined parameters for as-made cobalticinium-containing MgAPO-35 (in R-3m symmetry).

While attempts to target SAPO-35 in this way resulted, at best, in mixtures of (white) SAPO-11 and SAPO-5, introduction of cobalticinium to a germanosilicate synthesis in the presence of DP (analogous to similar studies in the presence of cyclam) yielded bright yellow crystals of the clathrasil octadecasil.

Unfortunately, permethylcobalticinium has proved unsuccessful as an SDA. The orange-yellow colour associated with this species remained in the liquid phase of the synthesis mixtures studied, while any crystalline products are colourless. This implies that, although stable under hydrothermal conditions, permethylcobalticinium does not influence the crystallisation process of AlPO-related phases under the conditions studied here. Indeed, TEAOH would appear to act as a stronger templating agent by directing MgAPO-34 (CHA) synthesis (Table 11.7).

To remove the apparently competing TEAOH, dipropylamine and diisopropylamine were employed in its stead since, from studies with cyclam, these appear to be much weaker templating agents. However, the production of dense-phase berlinite indicates that neither of the species exerts any influence over crystallisation in this system.

A further MgAPO synthesis was conducted in the presence of Cu cyclam, TEAOH and 10% permethylcobalticinium to investigate whether the permethylcobalticinium would be entrained into the STA-7 structure that would be templated by the cyclam and TEAOH. However, although the desired phase was obtained, EDX analysis indicates that no Co is present, and it would appear that the organometallic species once again remained in the liquid phase.

Summary

These results indicate that while cobalticinium would not appear to direct the crystallisation of AlPO and SAPO gels under the conditions examined here, it acts as a very effective SDA for the formation of MgAPO-35. Variation of the co-base in this system would not appear to have any effect over the crystallisation process with structure direction being dominated by cobalticinium.

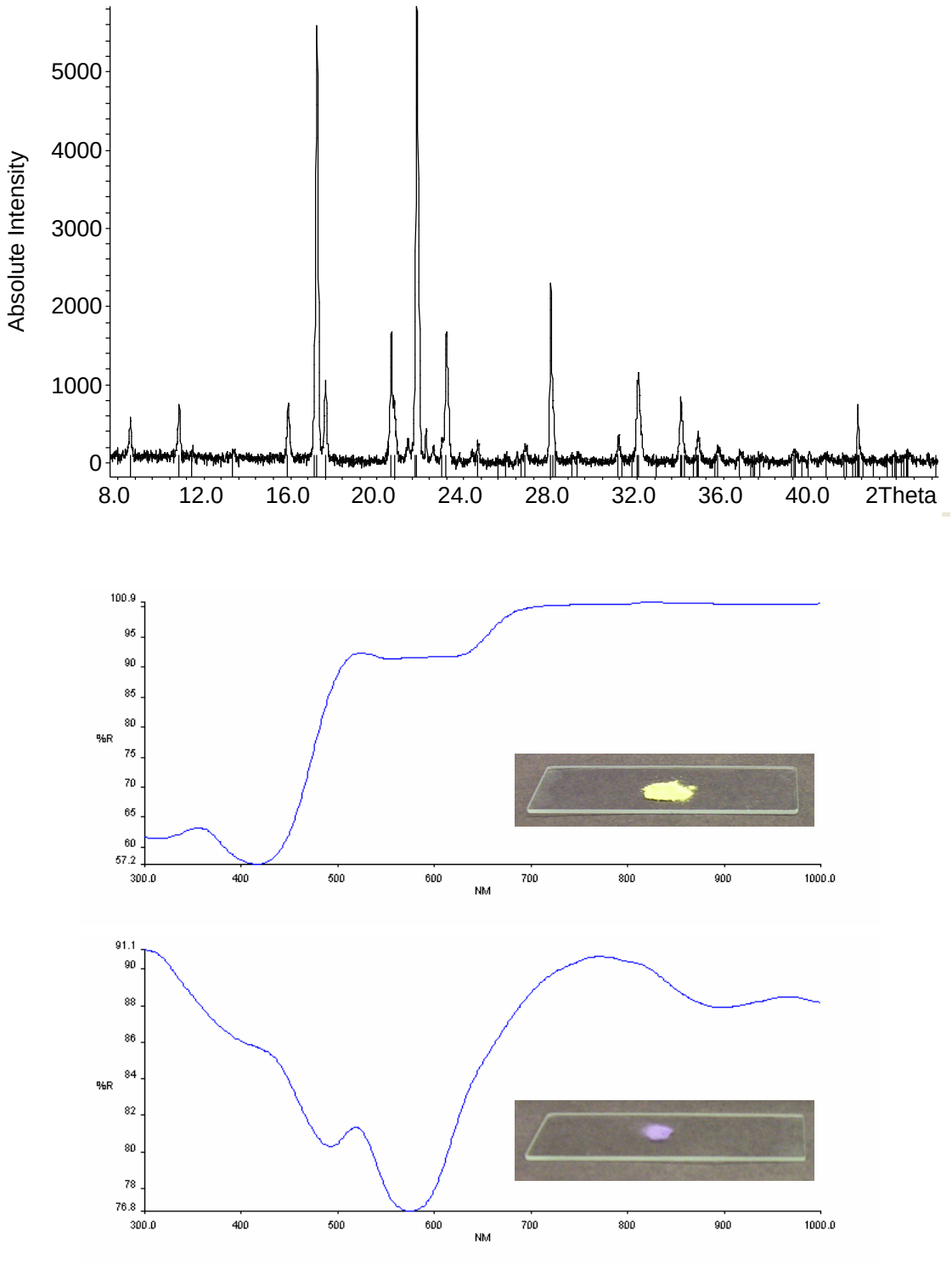

Figure 11.20: (Top) powder XRD pattern of as-made cobalticinium-containing MgAPO-35 with refined reflection positions marked above the 2θ axis, (middle) solid-state UV-Vis spectrum and photograph of as-made cobalticinium-containing MgAPO-35 and (bottom) solid-state UV-Vis spectrum and photograph of calcined Co-MgAPO-35.

Chapter 12: General Summary and Conclusions

A particular aim of syntheses conducted in this work was to expand the range of topologies available from AlPO-related gels employing the combined transition metal complex/co-base structure directing approach. Focussing particularly on complexes of Cu and Ni, a number of materials can now be targeted in this way and are summarised in Table 12.1.

During the course of these studies it became apparent that particular structure directing conditions are not always readily transferable from one system to another. As a result, many of the observed topologies could only be synthesised in one or two compositional regimes. This is most likely due to a combination of differences in interactions between the SDA and gel components and variations in T-atom geometries conspiring to favour or preclude particular phase synthesis. Notable examples are the inability of Cu-cyclen and cobalticinium to direct the formation of SAPO-18 and AlPO/SAPO-35, respectively.

The most widely transferable structure-directing system studied here is that involving complexes of cyclam. Simply by altering the co-base present Cu- and Cu/Ni-containing STA-6 and STA-7 can be obtained in most of the compositional regimes studied. In this respect, these SDA/co-base pairs behave most like true templating agents. Yet even here, targeting of AlPO analogues proved troublesome with the competitive formation of layered and dense phases.

The formation of AlPO-11 in the presence of Ni-cyclam (compared to STA-7 in the presence of Cu-cyclam), and the previous observation that phase-pure Ni-cyclam-containing SAPO STA-7 cannot be obtained[101] suggests a subtle effect due to the identity of the transition metal present. Indeed, in studies of complexes of linear polyamines, changing from $Ni(deta)_2$ to $Cu(deta)_2$ resulted in a phase change from AlPO-5 to AlPO-11. Furthermore, in the case of macrocyclic SDAs, the phase obtained from a transition metal-containing complex is not necessarily the same as that obtained from the non-metallated ligand – probably due to alterations in size, shape and flexibility of the SDA. Consequently, predicting a product is very difficult.

Topology	Composition	Metal	Complexing ligand	Co-base
SAS	MgAPO	Cu	Cyclam	DP
		Cu + Ni		
	SAPO	Cu		
		Cu + Ni		
	AlPO (post calcination)	Cu		
SAV	MgAPO	Cu	Cyclam	TEAOH or DIP
		Cu + Ni		TEAOH
	SAPO	Cu		
		Cu + Ni		
	AlPO (+ AlPO –5 impurity)	Cu		
AEL	AlPO	Ni	Cyclam	TEAOH or DIP or DP
		Cu	deta	DP
AEI	MgAPO	Cu	Cyclen	DP or DIP or HB
		Cu + Ni		DP
AFI	MgAPO	Cu	Bis-cyclen	DP or TEAOH or DIP
		Cu + Ni	Tris(cyclamcyclencyclam)	DP
	AlPO	Cu	deta	TEAOH
		Ni		DP or TEAOH
CHA	SAPO	Cu	Triethylenetetramine	DP or TEAOH
UT-6	AlPO	Cu	Triethylenetetramine	DP
		Ni		
		Cu + Ni		
LEV	MgAPO	Co	Cobalticinium	DP or DIP or TEAOH or HB

Table 12.1: Summary of topologies obtainable from transition metal complex/ co-base structure-directing approaches developed during this work.

As a technique for the introduction of transition metal cations or oxide particles to the pores of AlPO-related phases, directing the crystallisation by the addition of a transition metal complex is a viable option provided the target topology can be obtained in the desired composition. Post synthesis calcination revealed the superior stability of SAPO products and yielded stable, cation-containing materials with potential catalytic applications. Comparison with ion-exchange studies suggests higher Cu-loading levels are possible in SAPO STA-7 via the structure direction method. MgAPO and AlPO samples exhibited variable stabilities on calcination depending on the topology and calcination conditions. Nevertheless, transition metal cations have been introduced to the SAS, SAV, AFI, LEV and AEI topologies.

However, further to issues outlined above, this technique suffers from a number of inherent limitations. These are:

(1) *A complex's stability under hydrothermal conditions.* In some of the syntheses studied, the metallocomplex decomposed during synthesis and crystallisation proceeded with or without direction from the co-base. This was particularly the case in syntheses involving complexes of linear polyamines. In contrast, macrocyclic complexes possess the advantage of added stability.
(2) *A complex's inactivity as an SDA.* For example, permethylcobalticinium failed to direct crystallisation of any of the gels studied here despite being stable under hydrothermal conditions. Also, a particular complex's structure directing ability is heavily dependent on the gel composition.
(3) *T-site competition.* This may be coupled with the complex's stability (i.e. complexation constant) but is also due to geometric preference of the metal involved. This technique is most successful when applied to complexes of metals which disfavour tetrahedral geometry.

Nevertheless, this technique is successful in providing a route to the incorporation of Cu and Ni (and to an extent Co) in a variety of materials.

A further aspect of studies conducted in this work was the investigation of any effect caused by the addition of co-bases to the synthesis gels. During these studies, an appreciation of the influence certain co-bases can exert on the crystallisation of AlPO-

related phases was developed. These influences were found to be advantageous or disadvantageous depending on the system and circumstances.

In general, the co-bases studied would appear to act as passive pH moderators and not influence the phase obtained. In this manner, use of expensive SDAs was minimised. Any structure-directing ability exhibited by the co-base often resulted in the formation of separate competing phases rather than the co-templating of a single phase. In many cases, the co-base-directed phase formed with the exclusion of the metallocomplex (as in the case with some cyclam/cyclen derivatives and TEAOH), but in others the complex was entrained in this crystallising phase due to a coincidental ability of the complex to fit into its cage/channel system, with the result of low metal loadings. Consequently, these additives should be employed with care.

A notable exception to this generalisation is the behaviour of cyclam in the presence of different co-bases. Only in the case of cyclam and TEAOH/DIP is true co-templating observed due to the ability of these co-bases to stabilise the β-cage of STA-7.

General impressions obtained during the course of these studies suggest a scale of relative structure-directing 'strengths' for the co-bases employed. Based on the results of syntheses conducted in this work, the four co-bases studied may be ordered thus: TEAOH > DIP > HB ≥ DP. The identity of the resulting product will then depend on the structure-directing 'strength' of the metallocomplex *relative* to that of the co-base. However, it is also evident that these relative structure-directing 'strengths' are also influenced by gel composition. For example, Cu-cyclam would appear to possess a stronger structure-directing ability than DP, but an equal ability to TEAOH. In the MgAPO regime Cu-cyclam and DIP exhibit equal 'strengths' and favour STA-7 formation, while in SAPO gels DIP would appear to be weaker and allow the formation of STA-6 impurity.

Although many topologies *can* be targeted through appropriate combination of complex and co-base, each system behaves differently and should be considered in its own circumstances. Clearly there are many subtle effects operating in these systems and it is difficult to assign structure direction to the sole influence of the metallocomplex, co-base or gel composition. Instead, all of these components should be considered

collectively when dealing with the direction of zeotype crystallisation. The organic and metallocomplex species studied here may not be considered as true ‘templating’ agents in that they do not consistently yield the same, unique structure. However, as structure directing agents, they will favour the crystallisation of certain phases, provided the inorganic composition and all other synthesis parameters are conducive to the formation of these topologies.

References

1. M. Endregard, D. G. Nicholson, M. Stocker and B. Beagley, *J. Mater. Chem.*, 1995, **5**, 485
2. A. Lund, D. G. Nicholson, G. Lamble and B. Beagley, *J. Mater. Chem.*, 1994, **4**, 1723
3. N. Nunes, F. Costa, A. M. Fonseca, I. C. Neves, M. A. Carvalho and C. Ribeiro, *Mater. Sci. Forum Part 1 and 2*, 2006, **514-516**, 1246
4. C. Bowers and P. K. Dutta, *J. Catal.*, 1990, **122**, 271
5. C. Jin, W. Fan, Y. Jia, B. Fan, J. Ma and R. Li, *J. Molec. Catal. A*, 2006, **249**, 23
6. T. M. Salama, A. H. Ahmed, Z. M. El-Bahy, *Microporous Mesoporous Mater.*, 2006, **89**, 251
7. M. Salavati-Niasari, *J. Molec. Catal. A*, 2006, **245**, 192
8. K. Kervinen, P. C. Bruijnincx, A. M. Beale, J. G. Mesu, G. von Koten, R. J. M. K. Geddink and B. M. Weckhuysen, *J. Am. Chem. Soc.*, 2006, **128**, 3208
9. B. Zhan and Z. Li, *J. Chem. Soc., Chem. Commun.*, 1998, 349
10. S. P. Varkey, C. Ratnasamy and P. Ratnasamy, *J. Molec. Catal. A*, 1998, **135**, 295
11. Y. H. Xu, Z. Yu, F. Chen, S. H. Liu and X. Z. You, *J. Solid State Chem.*, 1999, **146**, 157
12. M. P. Attfield, S. J. Weigel, F. Toulelle and A. K. Cheetham, *J. Mater. Chem.*, 2000, **10**, 2109
13. B. Gomez-Lor, M. Iglesias, C. Cascales, E. Gutierrez-Puebla and M. A. Monge, *Chem. Mater.*, 2001, **13**, 1364
14. K. Morgan, G. Gainsford and N. Milestone, *J. Chem. Soc., Chem. Commun.*, 1995, 425
15. D. J. Williams, J. S. Kruger, A. F. McLeroy, A. P. Wilkinson and J. C. Hanson, *Chem. Mater.*, 1999, **11**, 2241.
16. Y. Wang, J. Yu, Z. Shi and R. Xu, *J. Solid State Chem.*, 2003, **170**, 176
17. G. Yang and A. C. Sevov, *Inorg. Chem.*, 2001, **40**, 2214
18. M. J. Gray, J. D. Jasper and A. P. Wilkinson, *Chem. Mater.*, 1997, **9**, 976
19. (a) Y. Wang, P. Chen, J. Li, J. Yu, J. Xu, Q. Pan and R. Xu, *Inorg. Chem.*, 2006, **45**, 4764 (b) S. M. Stalder and A. P Wilkinson, *Chem. Mater.*, 1997, **9**, 2168

20. K. Morgan, G. Gainsford and N. Milestone, *J. Chem. Soc., Chem. Commun.*, 1997, 61
21. D. A. Bruce, A. P. Wilkinson, M. G. White and J. A. Bertrand, *J. Chem. Soc., Chem. Commun.*, 1995, 2059
22. D. A. Bruce, A. P. Wilkinson, M. G. White and J. A. Bertrand, *J. Solid State Chem.*, 1996, **125**, 228
23. N. Rajic, A. Meden, P. Sarv and V. Kaucic, *Microporous Mesoporous Mater.*, 1998, **24**, 83
24. R. Garcia, I. J. Shannon, A. M. Z. Slawin, W. Zhou, P. A. Cox and P. A. Wright, *Microporous Mesoporous Mater.*, 2003, **58**, 91
25. J. R. DeBord, Y. Zhang, R. C. Haushalter, J. Zubieta and C. J. O'Connor, *J. Solid State Chem.*, 1996, **122**, 251
26. B. Lin and S. Liu, *Polyhedron*, 2000, **19**, 2521
27. L. Schreyeck, P. Caullet, J. C. Mougenel, J. Patarin and J. L. Paillaud, *Microporous Mater.*, 1997, **11,** 161
28. B. J. Balkus, A. G. Gabrielov and S. Shepelev, *Microporous Mater.*, 1995, **3**, 489
29. K. J. Balkus and S. Shepelev, *Microporous Mater.*, 1993, **1**, 383
30. P. Behrens C. Panz, V. Hufnagel, B. Linndlar, C. C. Freyhardt and G. van de Goor, *Solid State Ionics*, 1997, **101-103**, 229.
31. S. Kallus, J. Patarin and B. Marler, *Microporous Mater.*, 1996, **7**, 89
32. C. C. Freyhardt, M. Tsapatsis, R. F. Lobo, K. J. Balkus and M. E. Davis., *Nature*, 1996, **381**, 297
33. K. J. Balkus, M. Biscotto and A. G. Gabrielov, *Stud. Surf. Sci. Catal.*, 1997, **105**, 415
34. R. F. Lobo, M. Tsapatsis, C. C. Freyhardt, S. Khodabandeh, P. Wagner, C. Chen, K. J. Balkus, S. I. Zones and M. E. Davis, *J. Am. Chem. Soc.*, 1997, **119**, 8474
35. J. Martinez-Triguero, M. J. Diaz-Cabanas, M. A. Camblor, V. Fornes, Th. L. M. Maesen and A. Corma, *J. Catal.*, 1999, **182**, 463
36. K. J. Balkus, A. G. Gabrielov and S. I. Zones, *Stud. Surf. Sci. Catal.*, 1995, **97**, 519
37. T. A. Khan and J. A. Hriljac, *Inorg. Chim. Acta*, 1999, **294**, 179

38. T. Chatelain, J. Patarin, R. Farre, O. Petigny and P. Schulz, *Zeolites*, 1996, **17**, 328
39. T. Chatelain, J. Patarin, E. Fousson, M Soulard, J. L. Guth and P. Schulz, *Microporous Mater.*, 1995, **4**, 231
40. E. W. Valyocsik, U.S. Patent 5 670 131, 1997
41. F. Delprato, L. Delmotte, J. L. Guth and L. Huve, *Zeolites,* 1990, **10,** 546
42. F. Dougnier, J. Patarin, J. L. Guth and D. Anglerot, *Zeolites*, 1992, **12**, 160
43. J. L. Paillaud, P. Caullet, L. Schreyeck and B. Marler, *Microporous Mesoporous Mater.*, 2001, **42**, 177
44. L Schreyeck, J. Stumbe, P. Caullet, J. C. Mougenel and B. Marler, *Microporous Mesoporous Mater.*, 1998, **22**, 87
45. M. J. Maple, E. F. Philp, A. M. Z. Slawin, P. Lightfoot, P. A. Cox and P. A. Wright, *J. Mater. Chem.,* 2001, **11**, 98
46. D. S. Wragg, G. B. Hix and R. E. Morris, *J. Am. Chem. Soc.*, 1998, **120**, 6822
47. D. Wragg and R. E. Morris, *J. Mater. Chem.*, 2001, **11**, 513
48. P. S. Wheatley, C. L. Love, J. J. Morrison, I. J. Shannon and R. E. Morris, *J. Mater. Chem.,* 2002, **12,** 477
49. P. S. Wheatley and R. E. Morris, *J. Solid State Chem.,* 2002, **167**, 267
50. R. Garcia, T. D. Coombs, I. J. Shannon, P. A. Wright and P. A. Cox, *Top. Catal.*, 2003, **24,** 115
51. R. Garcia, E. F. Philp, A. M. Z. Slawin, P. A. Wright and P. A. Cox, *J. Mater. Chem.*, 2001, **11**, 1421
52. S. I. Zones, *Chem. Mater.*, 2002, **14**, 313
53. T. Wessels, L. B. McCusker, Ch. Baerlocher, P. Reinert and J. Patarin, *Microporous Mesoporous Mater.*, 1998, **23**, 67
54. A. Merrouche, J. Patarin, M. Soulard, H. Kessler and D. Anglerot, *Molecular Sieves – Synthesis of Microporous Materials*, M. Occelli Ed., New York, 1992, Vol 1, 384
55. L. Sierra, C. Derouche, H. Gies and J. L. Guth, *Microporous Mater.,* 1994, **3**, 29
56. P. Reinert, C. Schott-Darie and J. Patarin, *Microporous Mater.,* 1997, **9**, 107
57. L. Schreyeck, P. Caullet, J. C. Mougenel and B. Marler, *Proc. 12th Int. Zeolite Conf.,* 1999, 1731
58. C. S. Blackwell, R. W. Broach, M. G. Gatter, J. S. Holmgren, D. Yan, G. L. Lewis, B. I. Mezza, T. M. Mezza, M. A. Miller, J. G. Moscoso, R. L. Patton, L.

M. Rohde, M. W. Schoonover, W. Sinkler, B. Wilson and S. T. Wilson, *Angew. Chem. Int. Ed.*, 2003, **42**, 1737

59. V. Patinec, P. A. Wright, P. Lightfoot, R. A. Aitken and P. A. Cox, *J. Chem. Soc., Dalton Trans.*, 1999, 3909
60. P. A. Wright, M. J. Maple, A. M. Z. Slawin, V. Patinec, R. A. Aitken, A. Welch and P. A. Cox, *J. Chem. Soc., Dalton Trans.*, 2000, 1243
61. R. Garcia, *Synthesis and Characterisation of Aluminophosphate-Based Materials Prepared with Nickel Complexes as Structure Directing Agents*, PhD Thesis, University of St Andrews, 2003
62. STOE Win XPOW (version 1.04), STOE & Cie GmbH, Hilpertstrasse, D-64296, Darmstadt, 1999
63. A. C. Larson and R. B. von Dreele, Generalized Crystal Structure Analysis System, Los Almos National Laboratory, USA, 1988
64. SHELXTL 6.14, G M Sheldrick, Bruker AXS, Madison, 2004
65. P. J. Goodhew and F. J. Humphreys, *Electron Microscopy and Analysis*, 2nd Ed., Taylor and Francis, 1988
66. Y. Dong, G. A. Lawrance, L. F. Lindoy and P. Turner, *J. Chem. Soc. Dalton Trans.*, 2003, 1567
67. L. Fabbrizzi, L. Montagna and A. Poggi, *J. Chem. Soc., Dalton Trans.*, 1987, 2631
68. S. V. Rosokha, Y. D. Lampeka and I. M. Maloshtan, *J. Chem. Soc., Dalton Trans.*,1993, 631
69. Y. Dong, L. F. Lindoy, P. Turner and G Wei, *J. Chem. Soc., Dalton Trans.*, 2004, 1264
70. F. A. Cotton, G. Wolkinson, C. A. Murillo and M. Bochmann, *Advanced Inorganic Chemistry*, 6th Ed., John Wiley and Sons, 1999
71. S. Oliver, A. Kuperman, A. Lough and G. A. Ozin, *J. Mater. Chem.*, 1997, **7**, 807
72. B. M. Lok, T. R. Cannan and C. A. Messina, *Zeolites*, 1993, **3**, 282
73. C. S. Blackwell and R. L. Patton, *J. Phys. Chem.*, 1988, **92**, 3965
74. J. Dedecek, Z. Sobalik, Z. Tvaruzkova, D. Kaucky and B. Wichterlova, *J. Phys. Chem.*, 1995, **99**, 16327
75. S. A. Yashnik, Z. R. Ismagilov and V. F. Anufrienko, *Catalysis Today*, 2005, **110**, 310

76. M. Narayana and L. Kevan, *J. Phys. C: Solid State Phys.*, 1983, **16**, 361
77. Personal correspondence from Prof. J. C. Walton, St Andrews
78. H. J. Jung, C. H. Shin and S. B. Hong, *J. Phys. Chem. B*, 2005, **109**, 20847
79. J. S. Chen, P. A. Wright, J. M. Thomas, S. Natarajan, L. Marchese, S. M. Bradley, G. Sankar, C. R. A. Catlow, P. L. Gaiboyes. R. P. Townsens and C. M. Lok, *J. Phys. Chem.*, 1994, **98**, 10216
80. Z. Gabelica and J. L. Guth, *Angew. Chem. Int. Ed.*, 1989, **28**, 81
81. J. B. Higgins, R. B. LaPierre, J. L. Schlenker, A. C. Rohrman, J. D. Wood, G. T. Kerr and W. J. Rohrbaugh, *Zeolites*, 1988, **8**, 446
82. M. M. J. Treacy and J. B. Higgins, *Collection of Simulated XRD Powder Patterns for Zeolites*, 4rd Ed., International Zeolite Association, Elsevier, 2001
83. A. Corma, M. T. Navarro, F. Rey, J. Rius and S. Valencia, *Angew. Chem. Int. Ed.*, 2001, **40**, 2277
84. M. Arranz, J. Pere-Pariente, P. A. Wright, A. M. Z. Slawin, T. Basco, L. Gomez-Hotiguela and F. Cora, *Chem. Mater.*, 2005, **17**, 4374
85. B. Marler, C. Deroche, H. Gies, C. A. Fyfe, H. Grondey, G. T. Kokotailo, Y. Feng, S. Ernst, J. Weitkamp and D. E. Cox, *J. Appl. Cryst.*, 1993, **26**, 636
86. A. Simmen, L. B. McCusker, Ch. Baerlocher and W. M. Meier, *Zeolites*, 1991, **11**, 654
87. K. Miyoshi, H. Tanaka, E. Kimura, S. Tsuboyama, S. Murata, H. Shimizu and K. Ishizu, *Inorg. Chim. Acta.*, 1983, **78**, 23
88. L. S. Dent and J. V. Smith, *Nature*, 1958, **181**, 1794
89. J. M. Bennett, J. P. Cohen, E. M. Flanigen, J. J. Pluth and J. V. Smith, *ACS Sym. Ser.*, 1983, **218**, 109
90. V. J. Thom and R. D. Hancock, *J. Chem. Soc., Dalton Trans.*, 1985, 1877
91. V. J. Thom, G. D. Hosken and R. D. Hancock, *Inorg. Chem.*, 1985, **24**, 3378
92. E. W. Valyocsik, US Patent, 4 556 549, 1985

APPENDICES: Attached CD

Appendix A: Single Crystal Data for TNU-6

Appendix B: Refined Framework Atomic Coordinates, Bond Lengths and Angles for TNU-7, Ga-MAZ and Ga-MOR

- B(1): Na-TNU-7 (from synchrotron data)
- B(2): Na-Ga-MAZ (from synchrotron data)
- B(3): Na-Ga-MOR (from synchrotron data)
- B(4): Na-TNU-7 (from neutron data)

Appendix C: Theoretical Frameworks Related to the MFI and MEL Topologies

Appendix D1: Refined Atomic Parameters, Bond Lengths and Angles for As-made TNU-9 with Energy Minimised Template Locations

Appendix D2: Refined Cell and Atomic Parameters, Bond Lengths and Angles for As-made TNU-9 with Refined Template Locations

Appendix E: Refinement Data Discussed in Part 3

Refined Cell Parameters, Atomic Coordinates and Selected Bond Lengths and Angles for Calcined:

- E(1): Cu-MgAPO STA-6
- E(2): Cu-SAPO STA-6
- E(3): Cu-SAPO STA-7
- E(4): Cu-MgAPO-18
- E(5): Cu-MgAPO-5

Appendix A: Single Crystal Data for TNU-6

```
_chemical_formula_sum
 'Ga24 K24 O96 Si24'
_chemical_formula_weight          4821.84

loop_
 _atom_type_symbol
 _atom_type_description
 _atom_type_scat_dispersion_real
 _atom_type_scat_dispersion_imag
 _atom_type_scat_source
 'Ga'  'Ga'   0.2307   1.6083
 'International Tables Vol C Tables 4.2.6.8 and 6.1.1.4'
 'K'  'K'   0.2009   0.2494
 'International Tables Vol C Tables 4.2.6.8 and 6.1.1.4'
 'O'  'O'   0.0106   0.0060
 'International Tables Vol C Tables 4.2.6.8 and 6.1.1.4'
 'Si'  'Si'   0.0817   0.0704
 'International Tables Vol C Tables 4.2.6.8 and 6.1.1.4'

_symmetry_cell_setting            ?
_symmetry_space_group_name_H-M    ?

loop_
 _symmetry_equiv_pos_as_xyz
 'x, y, z'
 'x-y, x, z+1/2'
 '-y, x-y, z'
 '-x, -y, z+1/2'
 '-x+y, -x, z'
 'y, -x+y, z+1/2'

_cell_length_a                    18.1723(3)
_cell_length_b                    18.1723(3)
_cell_length_c                    8.5127(6)
_cell_angle_alpha                 90.00
_cell_angle_beta                  90.00
_cell_angle_gamma                 120.00
_cell_volume                      2434.54(18)
_cell_formula_units_Z             1
_cell_measurement_temperature     293(2)
_cell_measurement_reflns_used     ?
_cell_measurement_theta_min       ?
_cell_measurement_theta_max       ?

_exptl_crystal_description        ?
_exptl_crystal_colour             ?
_exptl_crystal_size_max           ?
_exptl_crystal_size_mid           ?
_exptl_crystal_size_min           ?
_exptl_crystal_density_meas       ?
_exptl_crystal_density_diffrn     3.289
```

```
_exptl_crystal_density_method     'not measured'
_exptl_crystal_F_000              2304
_exptl_absorpt_coefficient_mu     7.975
_exptl_absorpt_correction_type    ?
_exptl_absorpt_correction_T_min   ?
_exptl_absorpt_correction_T_max   ?
_exptl_absorpt_process_details    ?

_exptl_special_details

_diffrn_ambient_temperature       293(2)
_diffrn_radiation_wavelength      0.69110
_diffrn_radiation_type            ?
_diffrn_radiation_source          'fine-focus sealed tube'
_diffrn_radiation_monochromator   graphite
_diffrn_measurement_device_type   ?
_diffrn_measurement_method        ?
_diffrn_detector_area_resol_mean  ?
_diffrn_standards_number          ?
_diffrn_standards_interval_count  ?
_diffrn_standards_interval_time   ?
_diffrn_standards_decay_%         ?
_diffrn_reflns_number             28303
_diffrn_reflns_av_R_equivalents   0.0824
_diffrn_reflns_av_sigmaI/netI     0.0621
_diffrn_reflns_limit_h_min        -26
_diffrn_reflns_limit_h_max        26
_diffrn_reflns_limit_k_min        -26
_diffrn_reflns_limit_k_max        26
_diffrn_reflns_limit_l_min        -12
_diffrn_reflns_limit_l_max        12
_diffrn_reflns_theta_min          1.26
_diffrn_reflns_theta_max          31.13
_reflns_number_total              5434
_reflns_number_gt                 4976
_reflns_threshold_expression      >2sigma(I)

_computing_data_collection        ?
_computing_cell_refinement        ?
_computing_data_reduction         ?
_computing_structure_solution     ?
_computing_structure_refinement   'SHELXL-97 (Sheldrick, 1997)'
_computing_molecular_graphics     ?
_computing_publication_material   ?

_refine_special_details

_refine_ls_structure_factor_coef  Fsqd
_refine_ls_matrix_type            full
_refine_ls_weighting_scheme       calc
_refine_ls_weighting_details
 'calc w=1/[\s^2^(Fo^2^)+(0.1000P)^2^+0.0000P] where P=(Fo^2^+2Fc^2^)/3'
_atom_sites_solution_primary      direct
_atom_sites_solution_secondary    difmap
_atom_sites_solution_hydrogens    geom
```

```
_refine_ls_hydrogen_treatment     mixed
_refine_ls_extinction_method      none
_refine_ls_extinction_coef        ?
_refine_ls_abs_structure_details
 'Flack H D (1983), Acta Cryst. A39, 876-881'
_refine_ls_abs_structure_Flack    0.45(3)
_refine_ls_number_reflns          5434
_refine_ls_number_parameters      253
_refine_ls_number_restraints      1
_refine_ls_R_factor_all           0.1151
_refine_ls_R_factor_gt            0.1101
_refine_ls_wR_factor_ref          0.3018
_refine_ls_wR_factor_gt           0.2972
_refine_ls_goodness_of_fit_ref    1.964
_refine_ls_restrained_S_all       1.964
_refine_ls_shift/su_max           5.928
_refine_ls_shift/su_mean          0.069

loop_
 _atom_site_label
 _atom_site_type_symbol
 _atom_site_fract_x
 _atom_site_fract_y
 _atom_site_fract_z
 _atom_site_U_iso_or_equiv
 _atom_site_adp_type
 _atom_site_occupancy
 _atom_site_symmetry_multiplicity
 _atom_site_calc_flag
 _atom_site_refinement_flags
 _atom_site_disorder_assembly
 _atom_site_disorder_group
Ga1 Ga -0.17233(8) -0.67287(10) 0.38244(17) 0.0148(3) Uani 1 1 d . . .
Ga2 Ga -0.16633(9) -0.50486(9) 0.88263(18) 0.0202(4) Uani 1 1 d . . .
Ga3 Ga -0.00032(7) -0.33532(7) 0.5071(2) 0.0089(3) Uani 1 1 d . . .
Ga4 Ga -0.01231(7) -0.84381(7) 0.39658(15) 0.0043(3) Uani 1 1 d . . .
Si1 Si -0.16522(19) -0.5096(2) 0.4963(4) 0.0098(7) Uani 1 1 d . . .
Si2 Si -0.1755(2) -0.6751(3) -0.0044(5) 0.0166(8) Uani 1 1 d . . .
Si3 Si 0.01230(19) -0.15959(18) 0.5149(4) 0.0053(6) Uani 1 1 d . . .
Si4 Si 0.00079(16) -0.66877(16) 0.3986(5) 0.0083(7) Uani 1 1 d . . .
O1 O -0.1384(7) -0.5687(8) 0.3855(14) 0.040(3) Uani 1 1 d . . .
O2 O -0.2665(7) -0.5389(7) 0.4698(17) 0.039(3) Uani 1 1 d . . .
O3 O -0.1021(8) -0.4091(6) 0.4359(12) 0.031(3) Uani 1 1 d . . .
O4 O -0.1467(6) -0.5256(6) 0.6803(12) 0.024(2) Uani 1 1 d . . .
O5 O 0.0674(7) -0.5724(7) 0.4713(12) 0.023(2) Uani 1 1 d . . .
O6 O 0.0091(6) -0.6603(6) 0.2163(17) 0.033(3) Uani 1 1 d . . .
O7 O -0.0985(8) -0.7013(8) 0.4583(12) 0.025(2) Uani 1 1 d . . .
O8 O -0.0705(6) -0.6283(7) -0.0557(11) 0.020(2) Uani 1 1 d . . .
O9 O -0.2046(7) -0.6039(7) -0.0327(17) 0.040(3) Uani 1 1 d . . .
O10 O -0.2345(8) -0.7628(7) -0.1196(16) 0.043(3) Uani 1 1 d . . .
O11 O -0.1941(6) -0.7135(6) 0.1822(14) 0.028(2) Uani 1 1 d . . .
O12 O 0.0304(8) -0.7357(6) 0.4544(13) 0.028(3) Uani 1 1 d . . .
O13 O 0.0459(5) -0.1401(5) 0.6931(9) 0.0113(14) Uani 1 1 d . . .
O14 O 0.0595(5) -0.0697(5) 0.4076(9) 0.0102(14) Uani 1 1 d . . .
O15 O 0.0293(9) -0.2344(7) 0.4345(12) 0.029(3) Uani 1 1 d . . .
```

O16 O -0.0931(6) -0.1954(5) 0.5119(11) 0.0167(17) Uani 1 1 d . . .
K1 K 0.3333 -0.3333 0.1999(7) 0.0194(10) Uani 1 3 d S . .
K2 K 0.14722(17) -0.18414(16) 0.1986(3) 0.0145(5) Uani 1 1 d . . .
K3 K 0.0000 0.0000 0.1777(5) 0.0108(8) Uani 1 3 d S . .
K4 K -0.00202(17) -0.47707(19) 0.1954(4) 0.0203(6) Uani 1 1 d . . .
K5 K -0.13801(17) -0.33561(17) 0.1989(4) 0.0155(5) Uani 1 1 d . . .
K6 K -0.3333 -0.6667 0.2025(6) 0.0188(9) Uani 1 3 d S . .

loop_
 _atom_site_aniso_label
 _atom_site_aniso_U_11
 _atom_site_aniso_U_22
 _atom_site_aniso_U_33
 _atom_site_aniso_U_23
 _atom_site_aniso_U_13
 _atom_site_aniso_U_12
Ga1 0.0119(6) 0.0226(7) 0.0121(7) 0.0098(6) 0.0035(5) 0.0104(5)
Ga2 0.0182(7) 0.0138(6) 0.0118(8) 0.0045(6) -0.0084(6) -0.0046(5)
Ga3 0.0088(6) 0.0063(6) 0.0113(8) -0.0002(4) -0.0002(4) 0.0034(4)
Ga4 0.0000(5) 0.0018(4) 0.0059(6) 0.0029(4) 0.0031(4) -0.0036(3)
Si1 0.0064(14) 0.0088(14) 0.0107(17) 0.0064(11) -0.0033(10) 0.0010(12)
Si2 0.0075(14) 0.033(2) 0.0125(18) 0.0174(15) 0.0104(12) 0.0125(14)
Si3 0.0000(11) 0.0084(13) 0.0036(13) 0.0001(10) -0.0003(10) -0.0008(9)
Si4 0.0090(14) 0.0122(14) 0.0056(18) 0.0020(11) 0.0031(11) 0.0068(11)
O1 0.045(7) 0.043(7) 0.021(5) 0.001(5) -0.002(5) 0.015(6)
O2 0.012(5) 0.018(5) 0.085(10) 0.002(6) -0.015(5) 0.006(4)
O3 0.044(7) 0.002(4) 0.023(6) 0.014(3) 0.003(4) -0.006(4)
O4 0.017(4) 0.023(5) 0.025(5) -0.004(4) -0.001(4) 0.004(4)
O5 0.022(5) 0.031(5) 0.012(4) -0.008(4) 0.006(4) 0.011(4)
O6 0.016(5) 0.030(6) 0.018(6) 0.006(4) -0.001(4) -0.013(4)
O7 0.040(6) 0.035(6) 0.015(5) 0.011(4) 0.011(4) 0.029(5)
O8 0.012(4) 0.030(5) 0.015(5) -0.008(4) 0.003(3) 0.009(4)
O9 0.020(5) 0.017(5) 0.081(10) -0.001(6) 0.001(6) 0.009(4)
O10 0.047(7) 0.035(6) 0.045(7) 0.007(6) 0.034(6) 0.020(6)
O11 0.025(5) 0.023(5) 0.039(6) -0.002(5) -0.003(5) 0.015(4)
O12 0.043(7) 0.009(4) 0.028(6) -0.013(4) -0.024(5) 0.011(5)
O13 0.012(4) 0.013(3) 0.005(3) -0.002(3) 0.000(3) 0.003(3)
O14 0.015(4) 0.017(4) 0.000(3) -0.001(3) 0.002(3) 0.008(3)
O15 0.056(8) 0.021(5) 0.018(5) -0.002(4) 0.005(5) 0.026(5)
O16 0.017(4) 0.012(4) 0.013(4) 0.004(3) 0.005(3) 0.001(3)
K1 0.0113(12) 0.0113(12) 0.036(3) 0.000 0.000 0.0057(6)
K2 0.0176(11) 0.0132(10) 0.0126(11) -0.0026(10) -0.0060(11) 0.0076(9)
K3 0.0140(11) 0.0140(11) 0.0043(16) 0.000 0.000 0.0070(5)
K4 0.0149(12) 0.0281(14) 0.0144(13) 0.0032(12) 0.0012(10) 0.0082(10)
K5 0.0179(11) 0.0166(11) 0.0169(12) 0.0047(9) 0.0028(11) 0.0123(10)
K6 0.0140(12) 0.0140(12) 0.028(3) 0.000 0.000 0.0070(6)

_geom_special_details

loop_
 _geom_bond_atom_site_label_1
 _geom_bond_atom_site_label_2
 _geom_bond_distance
 _geom_bond_site_symmetry_2
 _geom_bond_publ_flag

Ga1 O1 1.672(12) . ?
Ga1 O2 1.753(11) 5_545 ?
Ga1 O7 1.782(11) . ?
Ga1 O11 1.821(11) . ?
Ga2 O10 1.673(12) 3_446 ?
Ga2 O9 1.729(12) 1_556 ?
Ga2 O5 1.803(10) 4_545 ?
Ga2 O4 1.836(10) . ?
Ga3 O15 1.746(11) . ?
Ga3 O3 1.762(11) . ?
Ga3 O6 1.786(15) 4_545 ?
Ga3 O8 1.797(10) 4_545 ?
Ga4 O16 1.755(9) 5_545 ?
Ga4 O12 1.783(10) . ?
Ga4 O14 1.790(8) 3_545 ?
Ga4 O13 1.811(8) 4_544 ?
Si1 O2 1.655(11) . ?
Si1 O4 1.658(11) . ?
Si1 O3 1.679(9) . ?
Si1 O1 1.676(13) . ?
Si2 O9 1.642(12) . ?
Si2 O11 1.700(12) . ?
Si2 O8 1.712(10) . ?
Si2 O10 1.715(14) . ?
Si3 O13 1.607(9) . ?
Si3 O14 1.684(9) . ?
Si3 O16 1.686(9) . ?
Si3 O15 1.683(10) . ?
Si4 O6 1.559(16) . ?
Si4 O12 1.628(11) . ?
Si4 O5 1.672(11) . ?
Si4 O7 1.673(11) . ?
K1 O2 2.808(13) 2_554 ?
K1 O2 2.808(13) 4_544 ?
K1 O2 2.808(13) 6_654 ?
K1 O9 3.048(13) 4_545 ?
K1 O9 3.048(13) 2 ?
K1 O9 3.048(13) 6_655 ?
K1 O4 3.067(9) 2_554 ?
K1 O4 3.067(9) 4_544 ?
K1 O4 3.067(9) 6_654 ?
K2 O16 2.699(8) 2_554 ?
K2 O10 2.715(11) 4_545 ?
K2 O7 2.731(11) 4_544 ?
K2 O12 3.260(13) 5_655 ?
K2 O6 3.263(11) 5_655 ?
K2 O3 3.365(13) 2_554 ?
K3 O14 2.824(8) 3 ?
K3 O14 2.824(8) 5 ?
K3 O13 3.052(7) 6_554 ?
K3 O13 3.052(7) 2_554 ?
K3 O13 3.052(7) 4_554 ?
K3 O14 3.070(8) 6_554 ?
K3 O14 3.070(8) 4_554 ?
K3 O14 3.070(8) 2_554 ?

K4 O5 2.631(10) 4_544 ?
K4 O4 2.682(10) 4_544 ?
K4 O8 2.714(11) 4_545 ?
K5 O11 2.671(10) 3_445 ?
K5 O12 2.701(10) 4_544 ?
K5 O13 2.739(8) 6_554 ?
K5 O5 3.216(12) 4_544 ?
K5 O7 3.375(12) 3_445 ?
K6 O9 2.848(14) 5_545 ?
K6 O9 2.848(14) 3_445 ?
K6 O2 3.037(13) 5_545 ?
K6 O2 3.037(13) 3_445 ?
K6 O11 3.051(9) 5_545 ?
K6 O11 3.051(9) 3_445 ?

loop_
 _geom_angle_atom_site_label_1
 _geom_angle_atom_site_label_2
 _geom_angle_atom_site_label_3
 _geom_angle
 _geom_angle_site_symmetry_1
 _geom_angle_site_symmetry_3
 _geom_angle_publ_flag
O1 Ga1 O2 112.6(6) . 5_545 ?
O1 Ga1 O7 114.6(6) . . ?
O2 Ga1 O7 111.0(5) 5_545 . ?
O1 Ga1 O11 110.8(5) . . ?
O2 Ga1 O11 101.3(6) 5_545 . ?
O7 Ga1 O11 105.3(5) . . ?
O10 Ga2 O9 113.5(5) 3_446 1_556 ?
O10 Ga2 O5 111.9(6) 3_446 4_545 ?
O9 Ga2 O5 111.2(5) 1_556 4_545 ?
O10 Ga2 O4 109.1(6) 3_446 . ?
O9 Ga2 O4 101.3(5) 1_556 . ?
O5 Ga2 O4 109.4(5) 4_545 . ?
O15 Ga3 O3 109.4(5) . . ?
O15 Ga3 O6 112.0(5) . 4_545 ?
O3 Ga3 O6 105.8(4) . 4_545 ?
O15 Ga3 O8 112.3(5) . 4_545 ?
O3 Ga3 O8 106.9(5) . 4_545 ?
O6 Ga3 O8 110.1(5) 4_545 4_545 ?
O16 Ga4 O12 108.4(5) 5_545 . ?
O16 Ga4 O14 115.0(4) 5_545 3_545 ?
O12 Ga4 O14 108.9(5) . 3_545 ?
O16 Ga4 O13 107.5(4) 5_545 4_544 ?
O12 Ga4 O13 111.6(4) . 4_544 ?
O14 Ga4 O13 105.4(4) 3_545 4_544 ?
O2 Si1 O4 111.3(6) . . ?
O2 Si1 O3 110.7(6) . . ?
O4 Si1 O3 113.1(5) . . ?
O2 Si1 O1 110.5(6) . . ?
O4 Si1 O1 105.7(6) . . ?
O3 Si1 O1 105.4(6) . . ?
O9 Si2 O11 112.5(6) . . ?
O9 Si2 O8 106.8(6) . . ?

O11 Si2 O8 112.7(5) . . ?
O9 Si2 O10 110.5(6) . . ?
O11 Si2 O10 104.4(6) . . ?
O8 Si2 O10 109.9(5) . . ?
O13 Si3 O14 110.2(4) . . ?
O13 Si3 O16 109.4(5) . . ?
O14 Si3 O16 107.2(4) . . ?
O13 Si3 O15 111.0(5) . . ?
O14 Si3 O15 110.6(5) . . ?
O16 Si3 O15 108.3(6) . . ?
O6 Si4 O12 108.2(6) . . ?
O6 Si4 O5 106.3(5) . . ?
O12 Si4 O5 109.8(5) . . ?
O6 Si4 O7 111.8(5) . . ?
O12 Si4 O7 110.4(6) . . ?
O5 Si4 O7 110.2(5) . . ?
Ga1 O1 Si1 132.4(7) . . ?
Si1 O2 Ga1 138.7(8) . 3_445 ?
Si1 O3 Ga3 127.5(7) . . ?
Si1 O4 Ga2 140.6(6) . . ?
Si4 O5 Ga2 125.3(6) . 4_544 ?
Si4 O6 Ga3 170.3(6) . 4_544 ?
Si4 O7 Ga1 128.5(6) . . ?
Si2 O8 Ga3 124.5(6) . 4_544 ?
Si2 O9 Ga2 139.5(8) . 1_554 ?
Ga2 O10 Si2 130.5(7) 5_544 . ?
Si2 O11 Ga1 138.6(6) . . ?
Si4 O12 Ga4 128.1(6) . . ?
Si3 O13 Ga4 143.8(5) . 4_545 ?
Si3 O14 Ga4 130.6(5) . 5_655 ?
Si3 O15 Ga3 128.3(7) . . ?
Si3 O16 Ga4 132.5(5) . 3_445 ?

Appendix B: Refined framework atomic coordinates, bond lengths and angles for TNU-7, Ga-MAZ and Ga-MOR

(1) Na-TNU-7 (from synchrotron data)

Atom	***x***	***y***	***z***	**U_{iso} (x 100)**
T(1)	-0.2500	0.16294(4)	-0.00396(3)	2.07(3)
T(2)	-0.2500	0.0747(5)	0.1037(5)	2.07(3)
T(3)	-0.2500	0.1607(4)	0.2119(3)	2.07(3)
T(4)	0.035(1)	0.1617(3)	-0.0893(2)	2.07(3)
T(5)	0.0472(1)	-0.0203(3)	0.1447(3)	2.07(3)
T(6)	0.043(1)	0.0577(3)	0.2489(5)	2.07(3)
T(7)	0.2500	0.1637(4)	0.3958(3)	2.07(3)
T(8)	0.2500	0.1675(4)	0.5187(3)	2.07(3)
T(9)	-0.047(1)	0.0524(3)	0.3633(2)	2.07(3)
T(10)	0.050(1)	-0.0513(3)	0.4516(2)	2.07(3)
O(1)	-0.2500	0.2500	0.012(1)	3.9(1)
O(2)	-0.2500	0.113(1)	0.0479(5)	3.9(1)
O(3)	-0.2500	0.130(1)	0.1523(4)	3.9(1)
O(4)	-0.2500	0.2500	0.203(1)	3.9(1)
O(5)	-0.078(1)	0.134(1)	-0.0376(4)	3.9(1)
O(6)	-0.064(1)	0.028(1)	0.1017(4)	3.9(1)
O(7)	-0.079(1)	0.1348(5)	0.2473(2)	3.9(1)
O(8)	-0.019(3)	0.2500	-0.105(1)	3.9(1)
O(9)	-0.015(2)	-0.006(1)	0.2064(4)	3.9(1)
O(10)	0.2500	0.156(1)	-0.074(1)	3.9(1)
O(11)	0.2500	-0.004(1)	0.137(1)	3.9(1)
O(12)	0.2500	0.084(1)	0.251(1)	3.9(1)
O(13)	-0.004(2)	0.1108(4)	-0.1413(4)	3.9(1)
O(14)	-0.001(2)	0.018(1)	0.3051(3)	3.9(1)
O(15)	0.2500	0.2500	0.377(1)	3.9(1)
O(16)	0.2500	0.2500	0.545(1)	3.9(1)
O(17)	0.2500	0.159(1)	0.4571(3)	3.9(1)

Continued on next page

O(18)	0.071(1)	0.127(1)	0.372(1)	3.9(1)
O(19)	0.075(1)	0.1253(5)	0.5387(5)	3.9(1)
O(20)	0.014(1)	-0.021(1)	0.3928(3)	3.9(1)
O(21)	0.0000	0.0000	0.5000	3.9(1)
O(22)	-0.2500	0.069(1)	0.374(1)	3.9(1)
O(23)	-0.2500	0.089(1)	0.538(1)	3.9(1)

Bond length (Å)

T(1)-O(1)	1.63(1)	T(5)-O(6)	1.63(1)	T(9)-O(14)	1.66(1)	Na(C)-O(19)	3.09(2)
T(1)-O(2)	1.61(1)	T(5)-O(9)	1.67(1)	T(9)-O(18)	1.61(1)	Na(C)-O(23)	3.06(2)
T(1)-O(5)	1.65(1)	T(5)-O(11)	1.63(1)	T(9)-O(20)	1.58(1)	Na(D)-O(9)	2.11(2)
		T(5)-O(13)	1.66(1)	T(9)-O(22)	1.61(1)	Na(D)-O(13)	3.17(2)
T(2)-O(2)	1.61(1)					Na(D)-O(14)	3.05(2)
T(2)-O(3)	1.61(1)	T(6)-O(7)	1.67(1)	T(10)-O(19)	1.65(1)	Na(E)-O(8)	2.34(2)
T(2)-O(6)	1.65(1)	T(6)-O(9)	1.65(1)	T(10)-O(20)	1.63(1)	Na(E)-O(13)	2.30(3)
		T(6)-O(12)	1.64(1)	T(10)-O(21)	1.60(1)	Na(F)-O(1)	2.22(3)
T(3)-O(3)	1.65(1)	T(6)-O(14)	1.66(1)	T(10)-O(23)	1.67(1)	Na(F)-O(2)	2.89(3)
T(3)-O(4)	1.63(1)					Na(F)-O(3)	2.52(3)
T(3)-O(7)	1.66(1)	T(7)-O(15)	1.63(1)	Na(A)-O(2)	2.98(1)	Na(F)-O(4)	2.71(2)
		T(7)-O(17)	1.59(1)	Na(A)-O(5)	2.69(1)		
T(4)-O(5)	1.67(1)	T(7)-O(18)	1.63(1)	Na(A)-O(6)	2.72(1)	Na(A)-Na(A)	3.786(1)
T(4)-O(8)	1.70(1)			Na(B)-O(7)	2.73(2)	Na(E)-Na(E)	2.2(1)
T(4)-O(10)	1.68(1)	T(8)-O(16)	1.63(1)	Na(B)-O(15)	2.40(3)	Na(B)-Na(B)	2.71(1)
T(4)-O(13)	1.66(1)	T(8)-O(17)	1.61(1)	Na(B)-O(18)	2.88(2)	Na(C)-Na(C)	1.01(1)
		T(8)-O(19)	1.61(5)				

O-T-O bond angles (^{o})

O(1)-T(1)-O(2)	111(1)	O(6)-T(5)-O(9)	116(1)	O(16)-T(8)-O(17)	117(1)
O(1)-T(1)-O(5)	117(1)	O(6)-T(5)-O(11)	104(1)	O(16)-T(8)-O(19)	110(1)
O(2)-T(1)-O(5)	103(1)	O(6)-T(5)-O(13)	116(1)	O(17)-T(8)-O(19)	106(1)
O(5)-T(1)-O(5)	103(2)	O(9)-T(5)-O(11)	113(2)	O(19)-T(8)-O(19)	108(1)

Continued on next page

O(2)-T(2)-O(3)	118(1)	O(9)-T(5)-O(13)	100(1)	O(14)-T(9)-O(18)	108(1)
O(2)-T(2)-O(6)	100(1)	O(11)-T(5)-O(13)	109(1)	O(14)-T(9)-O(20)	98(1)
O(3)-T(2)-O(6)	111(1)	O(7)-T(6)-O(9)	114(1)	O(14)-T(9)-O(22)	113(1)
O(6)-T(2)-O(6)	119(1)	O(7)-T(6)-O(12)	106(1)	O(18)-T(9)-O(20)	119(1)
O(3)-T(3)-O(4)	100(1)	O(7)-T(6)-O(14)	107(1)	O(18)-T(9)-O(22)	112(1)
O(3)-T(3)-O(7)	115(1)	O(9)-T(6)-O(12)	104(1)	O(20)-T(9)-O(22)	108(1)
O(4)-T(3)-O(7)	110(1)	O(9)-T(6)-O(14)	104(1)	O(19)-T(10)-O(20)	108(1)
O(7)-T(3)-O(7)	105(1)	O(12)-T(6)-O(14)	106(1)	O(19)-T(10)-O(21)	101(1)
O(5)-T(4)-O(8)	111(1)	O(15)-T(7)-O(17)	109(1)	O(19)-T(10)-O(23)	101(1)
O(5)-T(4)-O(10)	107(1)	O(15)-T(7)-O(18)	106(1)	O(20)-T(10)-O(21)	119(1)
O(5)-T(4)-O(13)	113(1)	O(17)-T(7)-O(18)	112(1)	O(20)-T(10)-O(23)	117(1)
O(8)-T(4)-O(10)	110(1)	O(18)-T(7)-O(18)	112(1)	O(21)-T(10)-O(23)	109(1)
O(8)-T(4)-O(13)	105(1)				
O(10)-T(4)-O(13)	111(1)				

(2) Na-Ga-MAZ (from synchrotron data)

Atom	***x***	***y***	***z***	**U_{iso} (x100)**
T(1)	0.4865(2)	0.1537(2)	0.25	3.4(1)
T(2)	0.0937(2)	0.3553(2)	0.0451(3)	3.4(1)
O(1)	0.7468(2)	1.4936(4)	0.25	6.7(3)
O(2)	0.5799(3)	1.130(1)	0.25	6.7(3)
O(3)	0.093(1)	0.377(1)	0.25	6.7(3)
O(4)	0.1005(3)	0.4332(3)	0.923(1)	6.7(3)
O(5)	0.159(1)	0.318(1)	1.006(1)	6.7(3)
O(6)	0.2771(2)	0	0	6.7(3)

Bond length (Å)		**O-T-O bond angles (^{o})**	
T(1)-O(1)	1.651(3)	O(1)-T(1)-O(2)	103.2(4)
T(1)-O(2)	1.638(3)	O(1)-T(1)-O(4)	111.6(3)
T(1)-O(4)	1.649(3)	O(2)-T(1)-O(4)	111.6(3)

Continued on next page

		O(4)-T(1)-O(4)	107(1)
T(2)-O(3)	1.618(3)		
T(2)-O(4)	1.642(4)	O(3)-T(2)-O(4)	111.5(4)
T(2)-O(5)	1.660(4)	O(3)-T(2)-O(5)	111(1)
T(2)-O(6)	1.572(3)	O(3)-T(2)-O(6)	105.5(4)
		O(4)-T(2)-O(5)	120(1)
Na(A)-O(4)	2.73(1)	O(4)-T(2)-O(6)	99(1)
Na(D)-O(5)	2.34(1)	O(5)-T(2)-O(6)	108.6(4)
Na(A)-Na(A)	3.8427(1)		

(3) Na-Ga-MOR (from synchrotron data)

Atom	***x***	***y***	***z***	**U_{iso} (x100)**
T(1)	0.20113(1)	0.4281(2)	0.54193(4)	2.32(4)
T(2)	0.1934(2)	0.1904(2)	0.5427(5)	2.32(4)
T(3)	0.0861(1)	0.3846(2)	0.25	2.32(4)
T(4)	0.0849(2)	0.2261(1)	0.25	2.32(4)
O(1)	0.1289(4)	0.4134(4)	0.426(1)	4.4(1)
O(2)	0.1170(3)	0.195(1)	0.429(1)	4.4(1)
O(3)	0.2661(3)	0.3827(3)	0.478(1)	4.4(1)
O(4)	0.0939(5)	0.3051(3)	0.25	4.4(1)
O(5)	0.1721(5)	0.199(1)	0.75	4.4(1)
O(6)	0.181(1)	0.415(1)	0.75	4.4(1)
O(7)	0.232(1)	0.5	0.5	4.4(1)
O(8)	0.25	0.25	0.5	4.4(1)
O(9)	0	0.407(1)	0.25	4.4(1)
O(10)	0	0.200(1)	0.25	4.4(1)

Bond length (Å)				O-T-O bond angles (^{o})	
T(1)-O(1)	1.59(1)	Na(B_{mor})-O(1)	2.97(1)	O(1)-T(1)-O(3)	109.5(4)
T(1)-O(3)	1.56(1)	Na(B_{mor})-O(9)	2.65(1)	O(1)-T(1)-O(6)	108(1)
T(1)-O(6)	1.622(4)	Na(C)-O(2)	2.52(1)	O(1)-T(1)-O(7)	111(1)
T(1)-O(7)	1.595(4)	Na(C)-O(10)	2.72(2)	O(3)-T(1)-O(6)	112(1)
		Na(D)-O(3)	2.72(2)	O(3)-T(1)-O(7)	103(1)
T(2)-O(2)	1.62(1)	Na(D)-O(7)	2.65(2)		
T(2)-O(3)	1.66(1)	Na(B_{mor})-Na(B_{mor})	3.746(1)	O(2)-T(2)-O(3)	112(1)
T(2)-O(5)	1.609(4)	Na(C)-Na(C)	2.1(1)	O(2)-T(2)-O(5)	107.3(4)
T(2)-O(8)	1.613(4)	Na(D)-Na(D)	3.94(2)	O(2)-T(2)-O(8)	112.8(4)
				O(3)-T(2)-O(5)	107(1)
T(3)-O(1)	1.636(4)			O(3)-T(2)-O(8)	112.0(3)
T(3)-O(4)	1.62(1)			O(5)-T(2)-O(8)	105(1)
T(3)-O(9)	1.62(1)			O(1)-T(3)-O(1)	108(1)
				O(1)-T(3)-O(4)	108.3(4)
T(4)-O(2)	1.291(4)			O(1)-T(3)-O(9)	110.5(4)
T(4)-O(4)	1.61(1)			O(4)-T(3)-O(9)	112(1)
T(4)-O(10)	1.62(1)			O(2)-T(4)-O(2)	115(1)
				O(2)-T(4)-O(4)	110.9(4)
				O(2)-T(4)-O(10)	102.6(4)
				O(4)-T(4)-O(10)	115(1)

(4) Na-TNU-7 (from neutron data)

Atom	*x*	*y*	*z*	U_{iso} (x 100)
T(1)	-0.2500	0.1638(3)	-0.0053(4)	2.2(1)
T(2)	-0.2500	0.069(1)	0.1043(5)	2.2(1)
T(3)	-0.2500	0.159(1)	0.2080(5)	2.2(1)
T(4)	0.037(1)	0.1661(5)	-0.0828(4)	2.2(1)
T(5)	0.036(1)	-0.0201(5)	0.1481(4)	2.2(1)
T(6)	0.040(1)	0.062(1)	0.2519(4)	2.2(1)

Continued on next page

T(7)	0.2500	0.163(1)	0.3969(5)	2.2(1)
T(8)	0.2500	0.164(1)	0.5178(4)	2.2(1)
T(9)	-0.041(1)	0.0514(5)	0.3619(4)	2.2(1)
T(10)	0.046(1)	-0.0513(5)	0.4539(3)	2.2(1)
O(1)	-0.2500	0.2500	0.011(1)	1.9(1)
O(2)	-0.2500	0.109(1)	0.0433(4)	1.9(1)
O(3)	-0.2500	0.129(1)	0.1495(4)	1.9(1)
O(4)	-0.2500	0.2500	0.209(1)	1.9(1)
O(5)	-0.079(1)	0.1375(4)	-0.0381(4)	1.9(1)
O(6)	-0.069(1)	0.0176(4)	0.100(4)	1.9(1)
O(7)	-0.082(1)	0.1339(5)	0.2405(3)	1.9(1)
O(8)	0.007(2)	0.2500	-0.0961(5)	1.9(1)
O(9)	-0.017(1)	-0.0011(4)	0.2056(3)	1.9(1)
O(10)	0.2500	0.157(1)	-0.0761(5)	1.9(1)
O(11)	0.2500	-0.011(1)	0.1295(5)	1.9(1)
O(12)	0.2500	0.075(1)	0.247(4)	1.9(1)
O(13)	-0.0137(1)	0.1110(5)	-0.1338(4)	1.9(1)
O(14)	-0.024(1)	0.0253(5)	0.3041(3)	1.9(1)
O(15)	0.2500	0.2500	0.377(1)	1.9(1)
O(16)	0.2500	0.2500	0.538(1)	1.9(1)
O(17)	0.2500	0.158(1)	0.4542(4)	1.9(1)
O(18)	0.078(1)	0.1234(4)	0.3661(3)	1.9(1)
O(19)	0.075(1)	0.1234(5)	0.5343(4)	1.9(1)
O(20)	0.019(1)	-0.0172(5)	0.3985(4)	1.9(1)
O(21)	0.0000	0.0000	0.5000	1.9(1)
O(22)	-0.2500	0.080(1)	0.3749(4)	1.9(1)
O(23)	-0.2500	0.088(1)	0.532(1)	1.9(1)

Bond length (Å)

T(1)-O(1)	1.56(1)	T(5)-O(6)	1.63(1)	T(9)-O(14)	1.57(1)	Na(C)-O(23)	2.95(1)
T(1)-O(2)	1.64(1)	T(5)-O(9)	1.58(1)	T(9)-O(18)	1.59(1)	Na(D)-O(9)	2.68(4)
T(1)-O(5)	1.64(1)	T(5)-O(11)	1.70(1)	T(9)-O(20)	1.63(1)		

Continued on next page

		T(5)-O(13)	1.70(1)	T(9)-O(22)	1.70(1)	Na(D)-O(14)	2.33(4)
T(2)-O(2)	1.74(1)					Na(E)-O(8)	2.25(2)
T(2)-O(3)	1.60(1)	T(6)-O(7)	1.63(1)	T(10)-O(19)	1.63(1)	Na(E)-O(13)	2.78(3)
T(2)-O(6)	1.66(1)	T(6)-O(9)	1.71(1)	T(10)-O(20)	1.58(1)	Na(F)-O(1)	2.3(4)
		T(6)-O(12)	1.61(1)	T(10)-O(21)	1.55(1)	Na(F)-O(1)	2.16(2)
T(3)-O(3)	1.61(1)	T(6)-O(14)	1.58(1)	T(10)-O(23)	1.72(1)	Na(F)-O(2)	2.88(1)
T(3)-O(4)	1.64(1)					Na(F)-O(3)	2.60(1)
T(3)-O(7)	1.60(1)	T(7)-O(15)	1.65(1)	Na(A)-O(2)	2.96(1)	Na(F)-O(4)	2.60(2)
		T(7)-O(17)	1.48(1)	Na(A)-O(5)	2.74(1)		
T(4)-O(5)	1.54(1)	T(7)-O(18)	1.69(1)	Na(A)-O(6)	2.66(1)	Na(A)-Na(A)	3.791(1)
T(4)-O(8)	1.57(1)			Na(B)-O(4)	2.86(3)	Na(B)-Na(B)	4.1(1)
T(4)-O(10)	1.63(1)	T(8)-O(16)	1.63(1)	Na(B)-O(7)	2.53(2)	Na(C)-Na(C)	0.5(2)
T(4)-O(13)	1.70(1)	T(8)-O(17)	1.65(1)	Na(B)-O(15)	2.93(3)	Na(E)-Na(E)	0.8(1)
		T(8)-O(19)	1.58(1)	Na(B)-O(18)	3.12(2)		

O-T-O bond angles (^{o})

O(1)-T(1)-O(2)	114(1)	O(6)-T(5)-O(9)	119(1)	O(16)-T(8)-O(17)	113(1)
O(1)-T(1)-O(5)	117(1)	O(6)-T(5)-O(11)	102(1)	O(16)-T(8)-O(19)	111(1)
O(2)-T(1)-O(5)	101(1)	O(6)-T(5)-O(13)	101(1)	O(17)-T(8)-O(19)	104(1)
O(5)-T(1)-O(5)	105(1)	O(9)-T(5)-O(11)	119(2)	O(19)-T(8)-O(19)	114(1)
O(2)-T(2)-O(3)	112(1)	O(9)-T(5)-O(13)	113(1)	O(14)-T(9)-O(18)	105(1)
O(2)-T(2)-O(6)	100(1)	O(11)-T(5)-O(13)	99(1)	O(14)-T(9)-O(20)	108(1)
O(3)-T(2)-O(6)	116(1)	O(7)-T(6)-O(9)	105(1)	O(14)-T(9)-O(22)	111(1)
O(6)-T(2)-O(6)	111(1)	O(7)-T(6)-O(12)	116(1)	O(18)-T(9)-O(20)	115(1)
O(3)-T(3)-O(4)	111(1)	O(7)-T(6)-O(14)	108(1)	O(18)-T(9)-O(22)	105(1)
O(3)-T(3)-O(7)	113(1)	O(9)-T(6)-O(12)	107(1)	O(20)-T(9)-O(22)	112(1)
O(4)-T(3)-O(7)	106(1)	O(9)-T(6)-O(14)	104(1)	O(19)-T(10)-O(20)	114(1)
O(7)-T(3)-O(7)	106(1)	O(12)-T(6)-O(14)	116(1)	O(19)-T(10)-O(21)	102(1)
O(5)-T(4)-O(8)	114(1)	O(15)-T(7)-O(17)	112(1)	O(19)-T(10)-O(23)	99(1)
O(5)-T(4)-O(10)	117(1)	O(15)-T(7)-O(18)	105(1)	O(20)-T(10)-O(21)	116(1)
O(5)-T(4)-O(13)	105(1)	O(17)-T(7)-O(18)	116(1)	O(20)-T(10)-O(23)	117(1)
O(8)-T(4)-O(10)	105(1)	O(18)-T(7)-O(18)	101(1)	O(21)-T(10)-O(23)	106(1)

Continued on next page

O(8)-T(4)-O(13)	112(1)
O(10)-T(4)-O(13)	105(1)

Appendix C: Theoretical Frameworks related to the MFI and MEL topologies.

Prompted by the apparent similarities between TNU-9 and the MFI topology indicated from HRTEM images, initial attempts to solve the structure of TNU-9 adopted a model building approach. In these studies, structural units if the MFI topology were rearranged to investigate whether the observed unit cell could be obtained while maintaining the characteristic MFI pore projection. Before any theoretical structure models could be built, however, an understanding of the MFI topology and its relative MEL was necessary.

MFI

The MFI topology may be regarded as being built from 5^8-cages (Figure B.1) (i.e. cages bound by eight 5MRs). For the purposes of describing the structures detailed below, these cages can be regarded as possessing 'equatorial' and 'axial' ends as defined in Figure B.1. As a point of reference, units and chains are described with the leftmost cage oriented with its 'equatorial' end to the left.

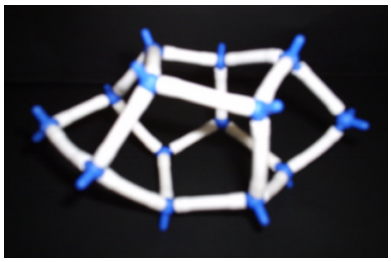

Figure B.1: 5^8-cage, from which all structures discussed below are constructed, with 'axial' and 'equatorial' ends to right and left, respectively.

5^8-cages can be fused together in two ways: (1) 'up and back' (denoted UB) (Figure B.2(a)) and (2) 'down and front' (denoted DF) (Figure B.2(b)) - equivalent to (1) rotated 180^o about its long axis.

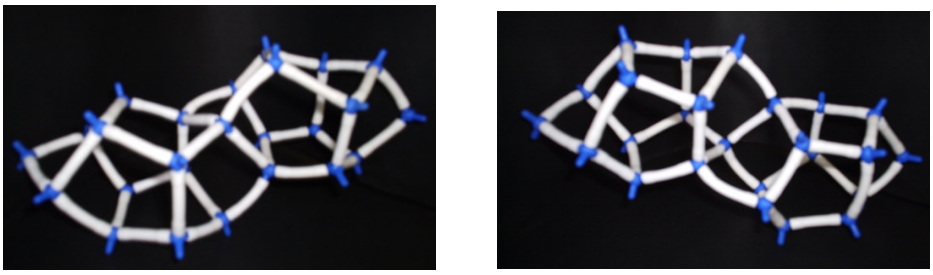

(a) (b)

Figure B.2: (a) 'Up and back' and (b) 'down and front' arrangements of 5^8-cages.

A further two possibilities are the mirror images of (1) and (2): 'up and front' (UF) (Figure B.3(a)) and 'down and back' (DB) (Figure B.3(b)).

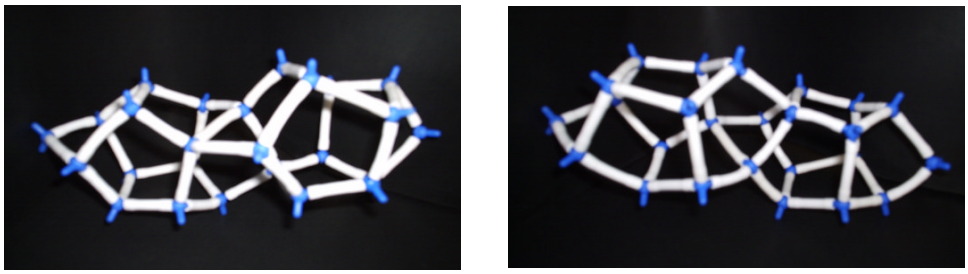

(a) (b)

Figure B.3: (a) 'Up and front' and (b) 'down and back' arrangements of 5^8-cages.

In these ways, chains of 5^8-cages can be constructed. These chains can link to form layers from which an entire framework can be built. MFI is composed of layers that are constructed from two different types of chain (related by a mirror plane): UB, DF, UB, DF…… and DB, UF, DB, UF….. These chains have a sinusoidal character and link across a mirror plane at their closest points to form 10MR openings (Figure B.4). Additional, or 'filler', T-atoms, which do not belong to a 5^8-cage, are introduced to complete the chain connectivity (black atoms in Figure B.4). The resulting layers are stacked in an ABAB fashion where B is created by rotating A by 180^o about the axis perpendicular to the plane of the layer and displacing it by one cage length to the left (Figure B.5). Hence, a centre of inversion relates adjacent planes. The resulting MFI topology possesses a two-dimensional pore system in which straight 10MR channels (Figure B.6) perpendicularly intersect sinusoidal channels (Figure B.7).

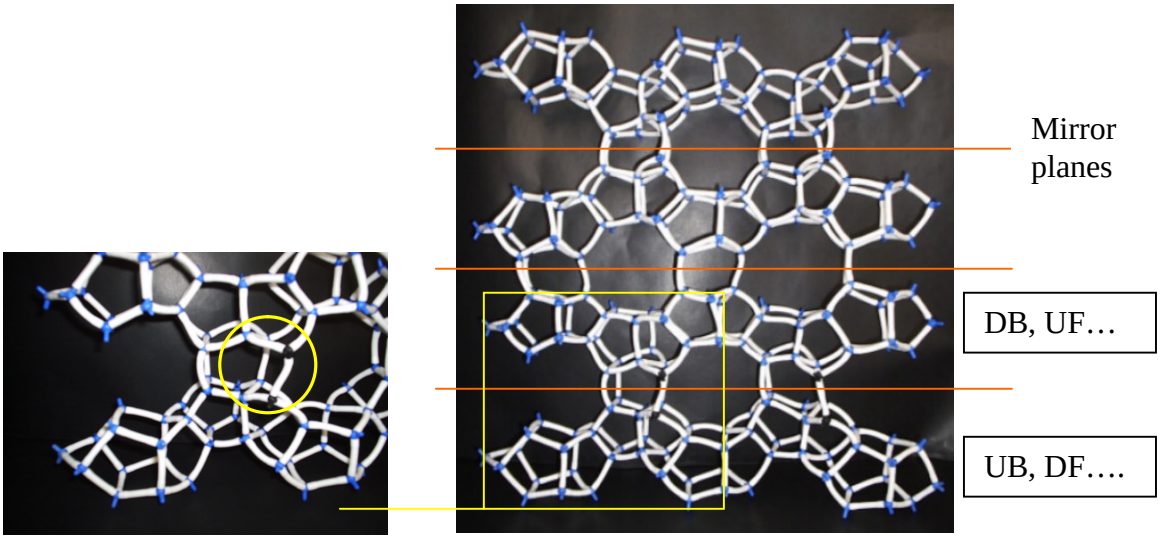

Figure B.4: Structural layer from which the MFI topology is constructed with chain types and mirror planes indicated. Detail of the chain connectivity is shown on the left with 'filler atom' (black) circled.

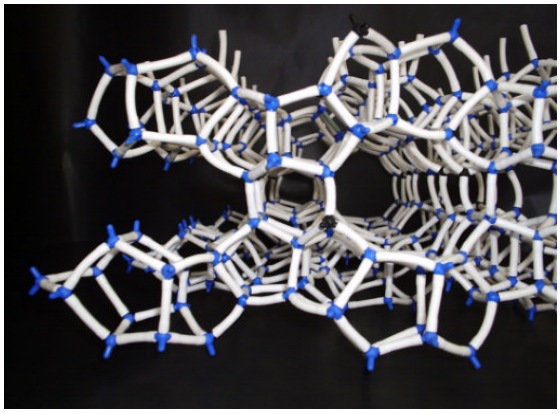

Figure B.5: Edge-on projection of two connected layers in the construction of the MFI topology.

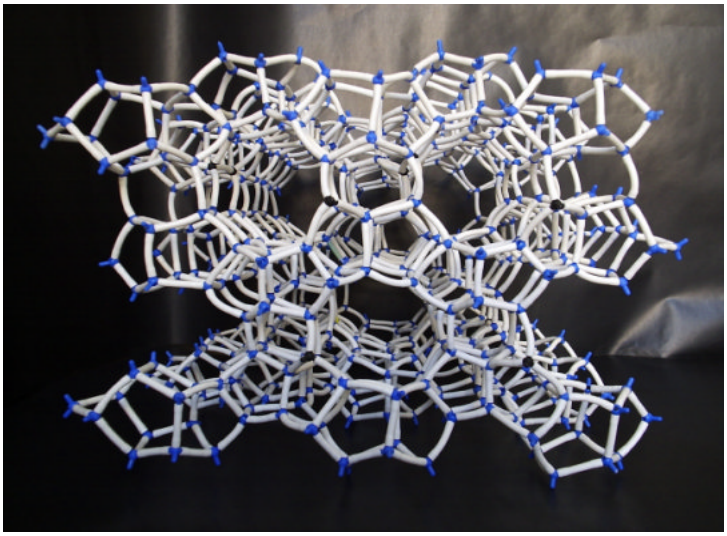

Figure B.6: MFI topology viewed edge-on to the structural layers (along the b-axis) illustrating the straight 10MR channels.

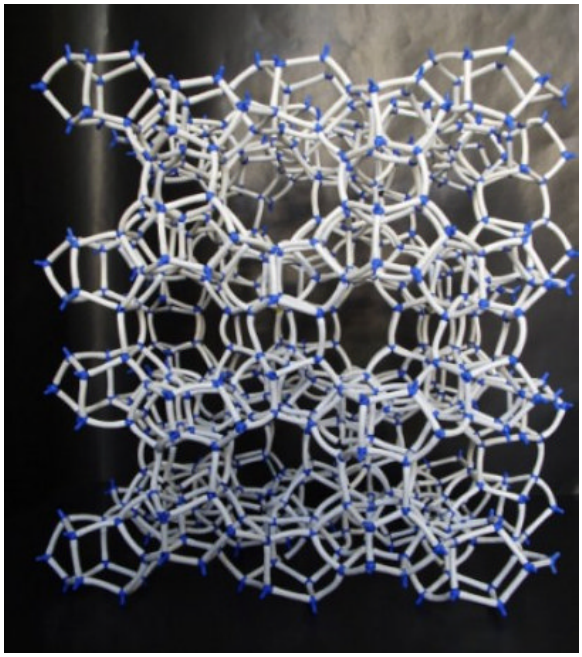

Figure B.7: MFI topology viewed along the path of the sinusoidal channels.

MEL

The MEL topology is constructed from the same layer-type as MFI, but with a mirror plane relating adjacent layers (Figure B.8). In this manner, the sinusoidal channels are 'straightened' and projections along the *a*- and *b*-axes become identical.

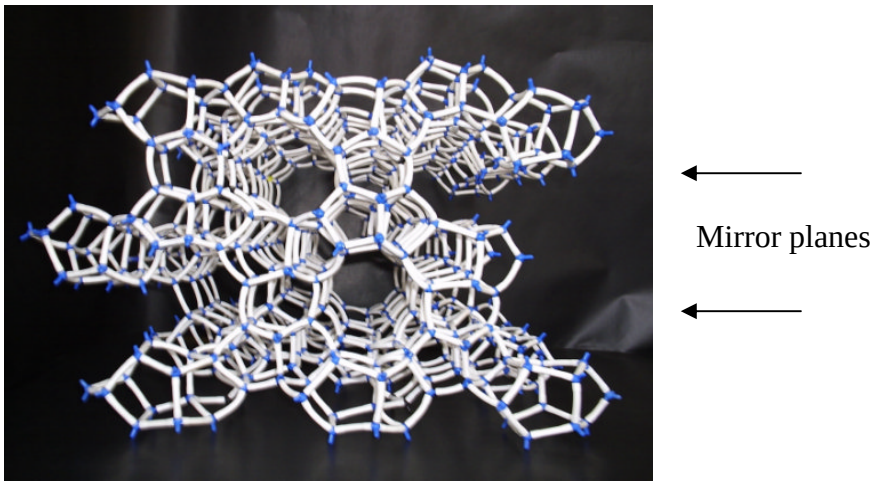

Figure B.8: MEL topology viewed along the a/b-axes illustrating the relationship between adjacent structural layers (horizontal).

It became evident that further variations of the layer-layer relationship would not generate a plausible framework and therefore the search for a possible model for TNU-9 began by re-visiting the chain-building step.

Model 1

Since the observed unit cell for TNU-9 is monoclinic, a chain was constructed with each additional 5^8-cage in a 'down' position – i.e. DF, DB, DF, DB…..(Figure B.9).

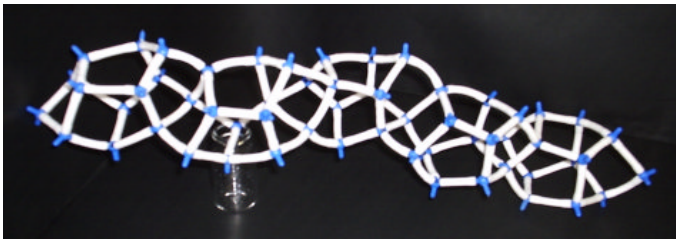

Figure B.9: DF, DB, DF, DB…chain.

Layers were constructed by attaching such a chain to its mirror image across a mirror plane (Figure B.10) (with ‘filler T-atoms included).

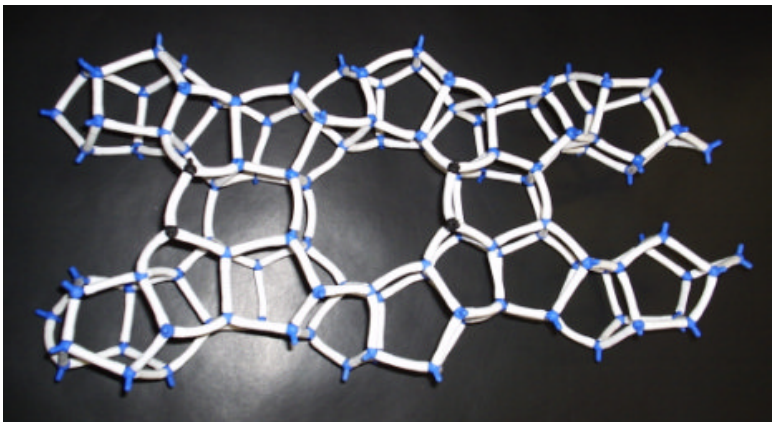

Figure B.10: Construction of a structural layer by the connection of two mirror-related chains. (additional atoms shown black).

Stacking these resulting layers directly on top of each other generated a monoclinic structure with straight 8MR pores running between the layers (Figure B.11) and an MFI-like projection (with straight 10MR channels) along the cell diagonal (Figure B.12). However, the estimated unit cell parameters were a = 14.8Å b = 21.9Å c = 13.9Å β = 140^{o}, with Cm symmetry (TNU-9: a = 28.2219Å, b = 20.0123Å, c = 19.4926Å, β = 92.33^{o}). As a test case, estimated atomic coordinates for Model 1 (measured manually from photographs of the model unit cell) were energy-minimised by Dr Paul Cox at the University of Portsmouth (under constant pressure simulations and in P1 symmetry), and the resulting atomic parameters were used to generate the theoretical powder XRD pattern, is illustrated in Figure B.13.

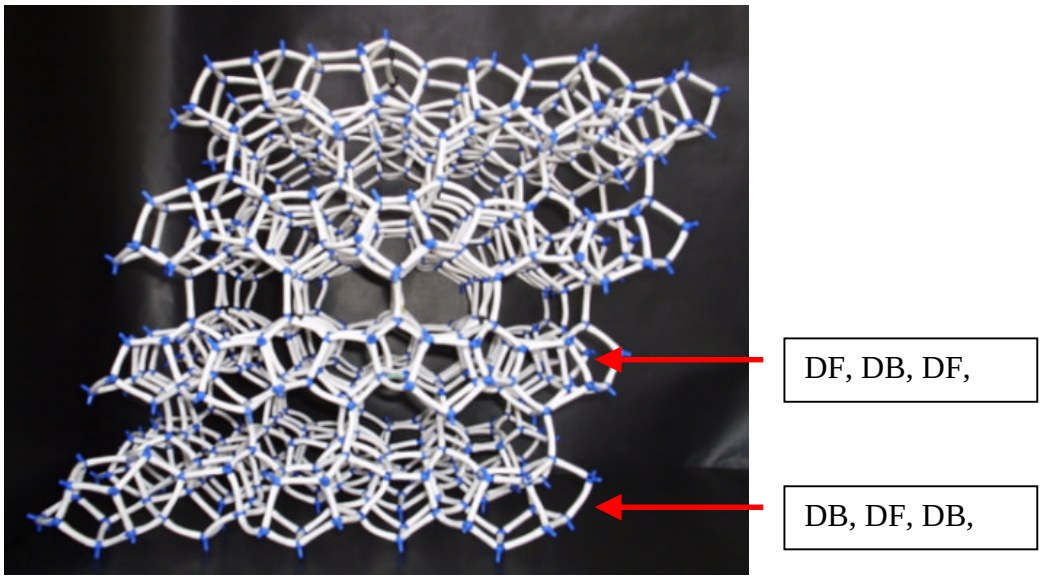

Figure B.11: Model 1 viewed along the b-axis (edge-on to structural layers) illustrating the straight inter-layer 8MR channels.

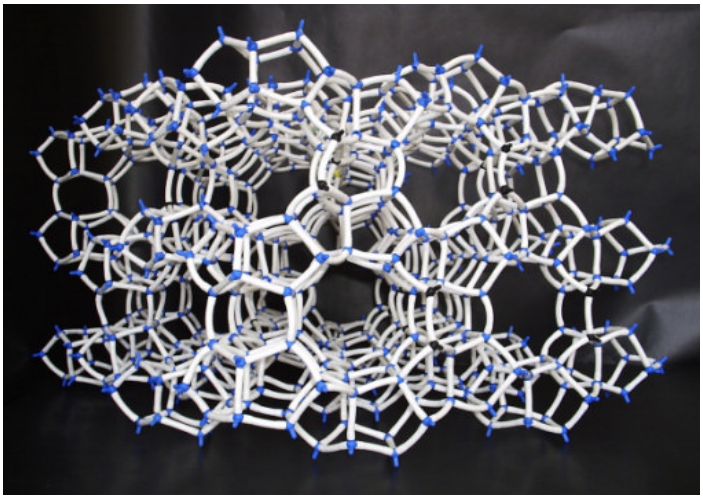

Figure B.12: View of Model 1 along [101] revealing an MFI-like projection with straight 10MR channels.

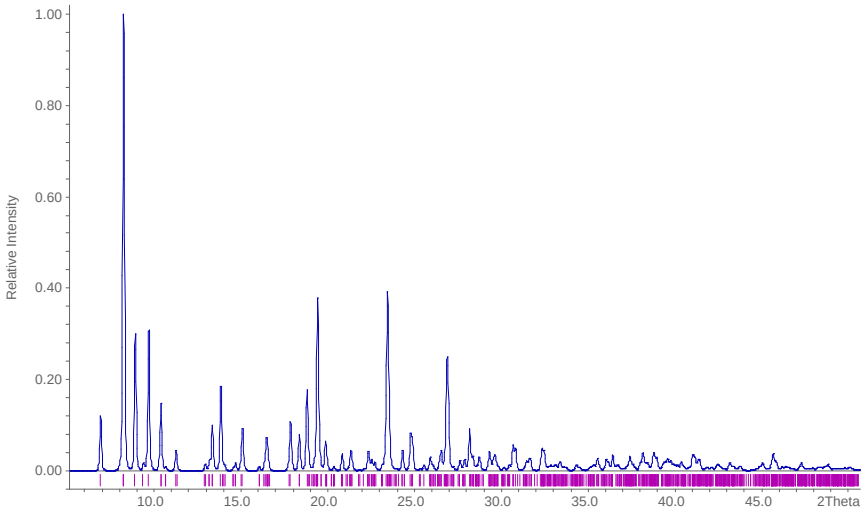

Figure B.13: Theoretical XRD pattern for the energy-minimised framework of Model 1. Energy-minimised cell parameters: a = 13.9651Å, b = 19.8588Å, c = 13.5249Å, α = 90.255°, β = 137.495°, γ = 89.775°.

Model 2

Model 2 was generated from Model 1 by rotating every second layer by 180° about the axis perpendicular to its plane. While the result was to increase the cell dimensions to values more comparable to those desired (*a* = 21.9Å *b* = 14.5Å *c* = 20.23Å), orthorhombic symmetry ($Cmc2_1$) was restored and the MFI-like projection was lost due to the creation of a sinusoidal 10MR pore system (Figure B.14).

Model 3

Model 3 was generated in an attempt to double the repeat between stacked layers in Model 1 and therefore enlarge the unit cell while maintaining monoclinic symmetry. Model 1 was split into *horizontal* layers (i.e. those planes containing 8MRs and parallel to the 10MR channels) and every second layer was flipped 180° about the axis perpendicular to the long axis of its constituent chains. In this manner, mirror planes no longer related adjacent chains in the re-assembled *vertical* layers. Yet although the 8MR channels are lost (consistent with HRTEM images), a doubling between vertical layers was not created.

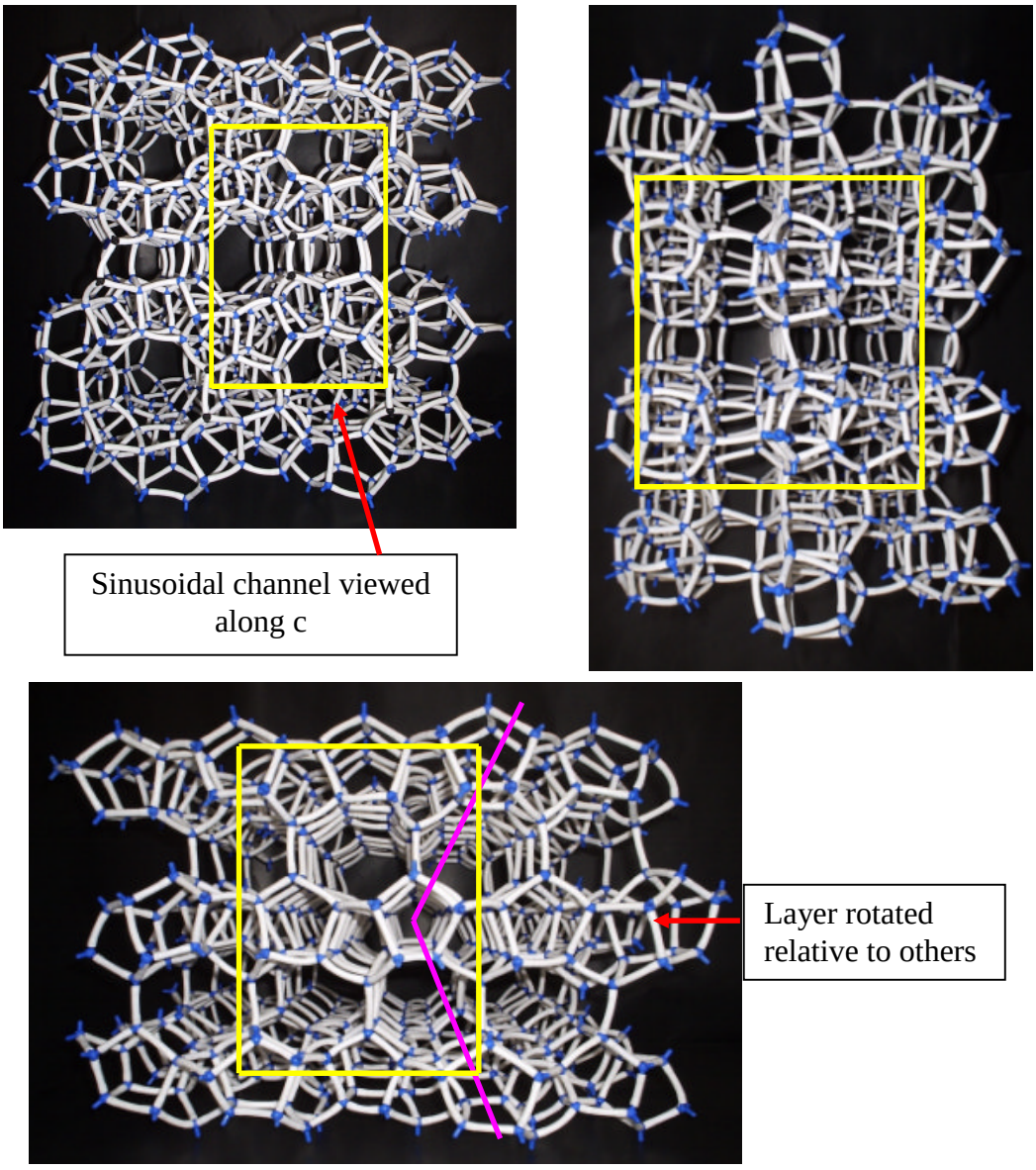

Figure B.14: Model 2 viewed along the c-axis (top left), b-axis (top right) and a-axis (bottom). Unit cell is indicated in yellow and sinusoidal path of the 10MR-channels is indicated by the pink line.

Model 4

This model (Figure B.15) was also generated by altering Model 1. Firstly, Model 1 was split into horizontal layers as in the building of Model 3 above. Every second layer was

flipped 180^{o} about the axis *parallel* to the long axis of its constituent chains. In order to re-connect the horizontal layers and generate an MFI-like projection with straight 10MR channels, the flipped layers were rotated by approximately 45^{o} about the axis perpendicular to their plane. As a consequence, the original (vertical) layer type is lost and the structure must be regarded as being composed of these horizontal layers, whereby every second layer is identical but displaced slightly along the axis parallel to the 10MR channels (Figure B.16). The resulting triclinic unit cell, however, was estimated to be a = 13.98Å, b = 22.50Å, c = 10.50Å, α = 105^{o}, β = 105^{o}, γ = 90^{o}.

Model 5

Similar treatment to that described above can also be given to Model 3.

Further Possibilities

The models described above are generated from the same original chain-type – i.e. DF, DB, DF, DB….. and its mirror-related equivalent. Many other chain-types are also possible, including, for example, UB, DB, UF, DF…. and UB, DB, UF, DB, UB….., all of which may generate an MFI-like projection and 10MR channels. However, variations in the chain composition in this way would act to enlarge the unit cell in the direction parallel to the long axis of the chains and not perpendicular to the plane of the layers as required.

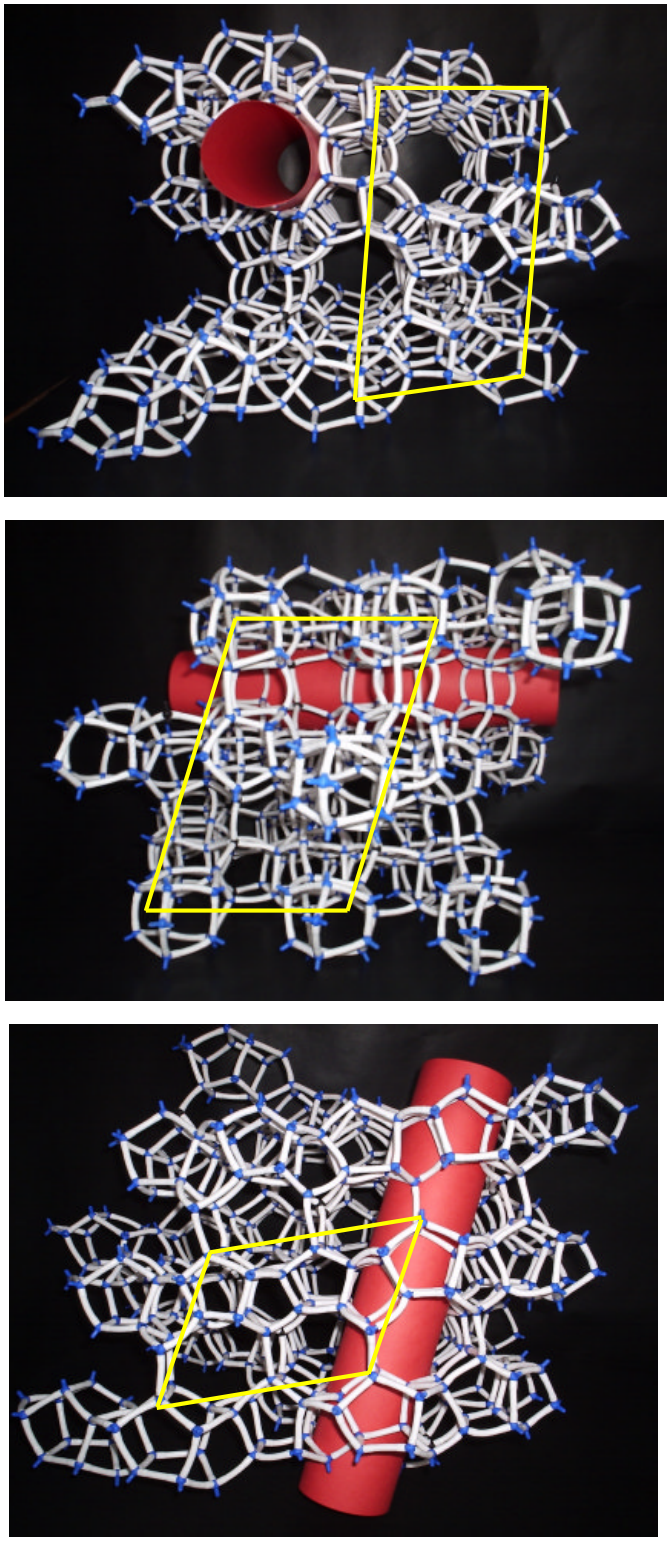

Figure B.15: Projections of Model 4 along the c-axis (top), a-axis (middle) and b-axis (bottom). Unit cell indicated in yellow and one 10MR channel is highlighted in red tube.

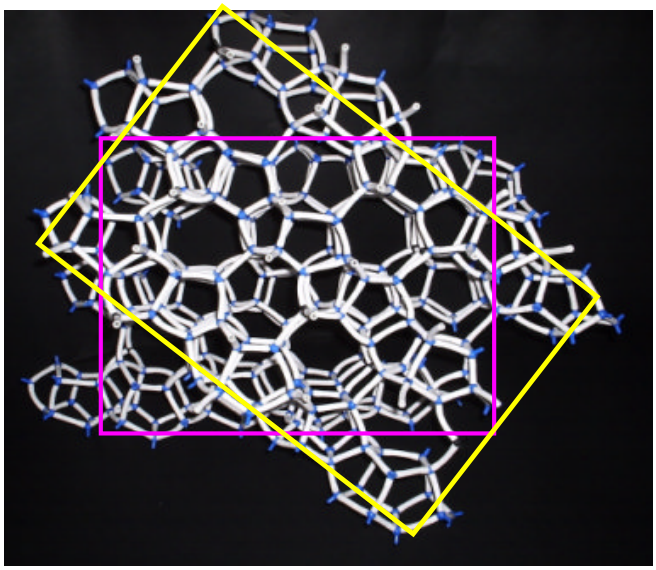

Figure B.16: Model 4 viewed along the b-axis with relationship of adjacent layers indicated in yellow and pink.

Appendix D1: Refined Atomic Parameters, Bond Lengths and Angles for As-made TNU-9 with Energy Minimised Template Locations

Atom	*x*	*y*	*z*	frac	Uiso	Mult
Si1	0.1017(4)	0.1881(7)	0.7077(6)	1	0.0183(11)	8
Si2	0.0033(4)	0.3105(7)	0.1449(6)	1	0.0183(11)	8
Si3	0.1528(4)	0.1861(7)	0.1679(6)	1	0.0183(11)	8
Si4	0.0900(5)	0.1201(7)	0.9296(6)	1	0.0183(11)	8
Si5	0.1059(4)	0.3092(7)	0.0853(6)	1	0.0183(11)	8
Si6	0.0048(5)	0.0769(5)	0.1467(7)	1	0.0183(11)	8
Si7	0.1041(5)	0.4253(5)	0.7112(7)	1	0.0183(11)	8
Si8	0.1511(4)	0.4243(5)	0.1716(7)	1	0.0183(11)	8
Si9	0.1020(5)	0.0774(5)	0.0850(7)	1	0.0183(11)	8
Si10	0.2524(4)	0.3799(7)	0.2277(7)	1	0.0183(11)	8
Si11	0.1465(5)	0.0770(5)	0.8033(7)	1	0.0183(11)	8
Si12	0.1665(4)	0.3830(7)	0.4393(6)	1	0.0183(11)	8
Si13	0.1009(5)	0.3796(7)	0.3055(6)	1	0.0183(11)	8
Si14	0.2372(5)	0.0746(5)	0.6154(7)	1	0.0183(11)	8
Si15	0.0002(5)	0.4222(5)	0.2571(7)	1	0.0183(11)	8
Si16	1.0010(4)	0.1902(7)	0.2531(6)	1	0.0183(11)	8
Si17	0.2368(4)	0.3107(7)	0.6214(7)	1	0.0183(11)	8
Si18	0.1419(4)	0.3093(6)	0.7995(6)	1	0.0183(11)	8
Si19	0.1643(4)	0.2225(7)	0.4346(6)	1	0.0183(11)	8
Si20	0.1028(4)	0.2191(7)	0.3042(6)	1	0.0183(11)	8
Si21	0.1674(5)	0.4249(5)	0.5865(7)	1	0.0183(11)	8
Si22	0.0857(5)	0.2787(7)	0.9314(6)	1	0.0183(11)	8
Si23	0.1658(4)	0.1888(7)	0.5840(7)	1	0.0183(11)	8
Si24	0.2529(4)	0.2199(7)	0.2233(7)	1	0.0183(11)	8
O1	0.0404(6)	0.0897(11)	0.9036(11)	1	0.0169(19)	8
O2	0.0850(8)	0.1993(6)	0.9320(12)	1	0.0169(19)	8
O3	0.1282(7)	0.0975(12)	0.8769(8)	1	0.0169(19)	8
O4	0.1045(7)	0.0932(12)	0.0048(6)	1	0.0169(19)	8
O5	0.1225(6)	0.1889(13)	0.6330(7)	1	0.0169(19)	8
O6	0.1217(9)	0.2510(9)	0.7507(12)	1	0.0169(19)	8
O7	0.1191(8)	0.1204(9)	0.7450(11)	1	0.0169(19)	8
O8	0.0449(4)	0.1928(13)	0.7016(9)	1	0.0169(19)	8
O9	0.0508(5)	0.0978(12)	0.1081(11)	1	0.0169(19)	8
O10	0.1094(11)	0	0.0996(16)	1	0.0169(19)	4
O11	0.1417(6)	0.1173(8)	0.1289(11)	1	0.0169(19)	8
O12	0.2015(5)	0.0923(12)	0.8055(12)	1	0.0169(19)	8
O13	0.1365(11)	0	0.7899(17)	1	0.0169(19)	4
O14	0.1199(7)	0.3039(12)	0.8735(8)	1	0.0169(19)	8
O15	0.1060(7)	0.3055(11)	0.0038(6)	1	0.0169(19)	8
O16	0.0347(5)	0.3088(11)	0.9175(8)	1	0.0169(19)	8
O17	0.2092(4)	0.1926(11)	0.1772(10)	1	0.0169(19)	8
O18	0.3016(4)	0.1948(12)	0.1935(11)	1	0.0169(19)	8
O19	0.2484(8)	0.1901(12)	0.2985(6)	1	0.0169(19)	8
O20	0.2531(8)	0.3000(6)	0.2255(12)	1	0.0169(19)	8
O21	0.0523(4)	0.3104(14)	0.1076(10)	1	0.0169(19)	8
O22	0.9994(9)	0.2474(10)	0.1951(10)	1	0.0169(19)	8
O23	-0.0014(9)	0.3773(9)	0.1890(10)	1	0.0169(19)	8
O24	0.1324(8)	0.2459(9)	0.1201(11)	1	0.0169(19)	8
O25	0.1302(7)	0.1868(11)	0.2421(8)	1	0.0169(19)	8

O26	0.1303(8)	0.3775(8)	0.1113(10)	1	0.0169(19)	8
O27	0.0071(12)	0	0.1668(15)	1	0.0169(19)	4
O28	1.0005(8)	0.1197(8)	0.2150(9)	1	0.0169(19)	8
O29	0.1274(7)	0.4109(14)	0.6397(9)	1	0.0169(19)	8
O30	0.0484(4)	0.4115(14)	0.7053(11)	1	0.0169(19)	8
O31	0.1287(8)	0.3807(8)	0.7693(10)	1	0.0169(19)	8
O32	0.1160(12)	0.5	0.7328(17)	1	0.0169(19)	4
O33	0.1243(8)	0.4124(11)	0.2408(8)	1	0.0169(19)	8
O34	0.1455(10)	0.5	0.1478(14)	1	0.0169(19)	4
O35	0.2061(5)	0.4074(12)	0.1867(11)	1	0.0169(19)	8
O36	0.2507(9)	0.4051(12)	0.3060(7)	1	0.0169(19)	8
O37	0.1690(8)	0.3025(6)	0.4415(12)	1	0.0169(19)	8
O38	0.2171(5)	0.4138(11)	0.4269(11)	1	0.0169(19)	8
O39	0.1485(6)	0.4111(12)	0.5098(6)	1	0.0169(19)	8
O40	0.1284(7)	0.4003(10)	0.3767(8)	1	0.0169(19)	8
O41	0.0463(5)	0.4033(12)	0.3047(10)	1	0.0169(19)	8
O42	0.1040(8)	0.2994(6)	0.2966(11)	1	0.0169(19)	8
O43	0.1932(7)	0.1190(8)	0.5888(12)	1	0.0169(19)	8
O44	0.2195(9)	0	0.6103(17)	1	0.0169(19)	4
O45	0.0031(12)	0.5	0.2362(16)	1	0.0169(19)	4
O46	0.0486(4)	0.1950(12)	0.3012(10)	1	0.0169(19)	8
O47	0.2126(6)	0.3810(8)	0.6063(12)	1	0.0169(19)	8
O48	0.2844(5)	0.3063(12)	0.5799(10)	1	0.0169(19)	8
O49	0.2006(7)	0.2505(9)	0.6029(13)	1	0.0169(19)	8
O50	0.1460(6)	0.1949(12)	0.5059(6)	1	0.0169(19)	8
O51	0.1271(6)	0.1984(10)	0.3759(7)	1	0.0169(19)	8
O52	0.1843(11)	0.5	0.5940(18)	1	0.0169(19)	4

1N1	0.4924	0.1431	0.5019	0.25	0.024(10)	8
1C1	0.4522	0.1892	0.4815	0.25	0.024(10)	8
1H1C1	0.4221	0.1823	0.5155	0.25	0.024(10)	8
1H2C1	0.4379	0.1806	0.4286	0.25	0.024(10)	8
1C2	0.4705	0.2610	0.4915	0.25	0.024(10)	8
1H1C2	0.4825	0.2816	0.4425	0.25	0.024(10)	8
1H2C2	0.4427	0.2950	0.5094	0.25	0.024(10)	8
1C3	0.5121	0.2550	0.5437	0.25	0.024(10)	8
1H1C3	0.5059	0.2848	0.5899	0.25	0.024(10)	8
1H2C3	0.5450	0.2744	0.5218	0.25	0.024(10)	8
1C4	0.5170	0.1800	0.5601	0.25	0.024(10)	8
1H1C4	0.5545	0.1651	0.5686	0.25	0.024(10)	8
1H2C4	0.4996	0.1700	0.6090	0.25	0.024(10)	8
1C5	0.4739	0.0747	0.5226	0.25	0.024(10)	8
1H1C5	0.4500	0.0818	0.5655	0.25	0.024(10)	8
1H2C5	0.4498	0.0549	0.4811	0.25	0.024(10)	8
1C6	0.5092	0.0181	0.5455	0.25	0.024(10)	8
1H1C6	0.5404	0.0409	0.5727	0.25	0.024(10)	8
1H2C6	0.4927	-0.0117	0.5858	0.25	0.024(10)	8
1C7	0.5272	-0.0303	0.4897	0.25	0.024(10)	8
1H1C7	0.5393	-0.0008	0.4459	0.25	0.024(10)	8
1H2C7	0.5600	-0.0544	0.5102	0.25	0.024(10)	8
1C8	0.4925	-0.0853	0.4612	0.25	0.024(10)	8
1H1C8	0.4992	-0.0900	0.4060	0.25	0.024(10)	8
1H2C8	0.4558	-0.0654	0.4610	0.25	0.024(10)	8
1C9	0.4842	-0.1505	0.5674	0.25	0.024(10)	8
1H1C9	0.4509	-0.1231	0.5750	0.25	0.024(10)	8
1H2C9	0.4810	-0.1997	0.5926	0.25	0.024(10)	8

1H3C9	0.5129	-0.1235	0.5955	0.25	0.024(10)	8
1C10	0.4576	-0.1999	0.4571	0.25	0.024(10)	8
1H1C10	0.4558	-0.1911	0.4009	0.25	0.024(10)	8
1H2C10	0.4212	-0.1916	0.4745	0.25	0.024(10)	8
1C11	0.4743	-0.2719	0.4706	0.25	0.024(10)	8
1H1C11	0.4641	-0.3062	0.4282	0.25	0.024(10)	8
1H2C11	0.4582	-0.2921	0.5170	0.25	0.024(10)	8
1C12	0.5281	-0.2665	0.4822	0.25	0.024(10)	8
1H1C12	0.5470	-0.2935	0.4423	0.25	0.024(10)	8
1H2C12	0.5394	-0.2894	0.5319	0.25	0.024(10)	8
1C13	0.5394	-0.1912	0.4819	0.25	0.024(10)	8
1H1C13	0.5676	-0.1783	0.5209	0.25	0.024(10)	8
1H2C13	0.5539	-0.1781	0.4316	0.25	0.024(10)	8
1C14	0.5246	0.1351	0.4432	0.25	0.024(10)	8
1H1C14	0.5068	0.1054	0.4021	0.25	0.024(10)	8
1H2C14	0.5352	0.1832	0.4204	0.25	0.024(10)	8
1H3C14	0.5577	0.1088	0.4590	0.25	0.024(10)	8
2N1	0.5729	0.5093	0.4091	0.25	0.024(10)	8
2C1	0.6098	0.5425	0.4561	0.25	0.024(10)	8
2H1C1	0.6028	0.5361	0.5112	0.25	0.024(10)	8
2H2C2	0.6110	0.5971	0.4483	0.25	0.024(10)	8
2C2	0.6583	0.5116	0.4421	0.25	0.024(10)	8
2H1C2	0.6680	0.4739	0.4818	0.25	0.024(10)	8
2H2C2	0.6872	0.5489	0.4429	0.25	0.024(10)	8
2C3	0.6512	0.4779	0.3724	0.25	0.024(10)	8
2H1C3	0.6761	0.4362	0.3650	0.25	0.024(10)	8
2H2C3	0.6560	0.5141	0.3304	0.25	0.024(10)	8
2C4	0.5995	0.4549	0.3739	0.25	0.024(10)	8
2H1C4	0.5847	0.4427	0.3218	0.25	0.024(10)	8
2H2C4	0.5984	0.4076	0.4032	0.25	0.024(10)	8
2C5	0.5326	0.4797	0.4485	0.25	0.024(10)	8
2H1C5	0.5094	0.4501	0.4127	0.25	0.024(10)	8
2H2C5	0.5474	0.4421	0.4853	0.25	0.024(10)	8
2C6	0.5006	0.5277	0.4891	0.25	0.024(10)	8
2H1C6	0.5224	0.5581	0.5258	0.25	0.024(10)	8
2H2C6	0.4825	0.5636	0.4539	0.25	0.024(10)	8
2C7	0.4631	0.4889	0.5282	0.25	0.024(10)	8
2H1C7	0.4412	0.4594	0.4909	0.25	0.024(10)	8
2H2C7	0.4818	0.4518	0.5615	0.25	0.024(10)	8
2C8	0.4306	0.5328	0.5725	0.25	0.024(10)	8
2H1C8	0.4155	0.5735	0.5397	0.25	0.024(10)	8
2H2C8	0.4532	0.5592	0.6117	0.25	0.024(10)	8
2C9	0.4107	0.4426	0.6536	0.25	0.024(10)	8
2H1C9	0.3829	0.4189	0.6837	0.25	0.024(10)	8
2H2C9	0.4274	0.4023	0.6243	0.25	0.024(10)	8
2H3C9	0.4380	0.4619	0.6910	0.25	0.024(10)	8
2N2	0.3906	0.4969	0.6074	0.25	0.024(10)	8
2C10	0.3541	0.4698	0.5557	0.25	0.024(10)	8
2H1C10	0.3541	0.4147	0.5543	0.25	0.024(10)	8
2H2C10	0.3607	0.4851	0.5023	0.25	0.024(10)	8
2C11	0.3051	0.4957	0.5745	0.25	0.024(10)	8
2H1C11	0.2770	0.4577	0.5673	0.25	0.024(10)	8
2H2C11	0.2946	0.5388	0.5416	0.25	0.024(10)	8
2C12	0.3119	0.5180	0.6489	0.25	0.024(10)	8
2H1C12	0.3082	0.4753	0.6844	0.25	0.024(10)	8

2H2C12	0.2862	0.5565	0.6635	0.25	0.024(10)	8
2C13	0.363	0.544	0.6505	0.25	0.024(10)	8
2H1C13	0.3624	0.5943	0.6280	0.25	0.024(10)	8
2H2C13	0.3780	0.5501	0.7036	0.25	0.024(10)	8
2C14	0.5533	0.5575	0.3557	0.25	0.024(10)	8
2H1C14	0.5366	0.6015	0.3792	0.25	0.024(10)	8
2H2C14	0.5812	0.5771	0.3228	0.25	0.024(10)	8
2H3C14	0.5261	0.5340	0.3210	0.25	0.024(10)	8
3N1	0.2967	0.9941	0.0523	0.25	0.024(10)	8
3C1	0.2963	0.9339	0.0985	0.25	0.024(10)	8
3H1C1	0.3325	0.9216	0.1181	0.25	0.024(10)	8
3H1C2	0.2829	0.8879	0.0728	0.25	0.024(10)	8
3C2	0.2668	0.9526	0.16	0.25	0.024(10)	8
3H1C2	0.2757	0.9227	0.2063	0.25	0.024(10)	8
3H2C2	0.2285	0.9458	0.1476	0.25	0.024(10)	8
3C3	0.2788	1.026	0.1703	0.25	0.024(10)	8
3H1C3	0.3134	1.0312	0.1983	0.25	0.024(10)	8
3H2C3	0.2522	1.0529	0.2001	0.25	0.024(10)	8
3C4	0.2813	1.0515	0.0966	0.25	0.024(10)	8
3H1C4	0.2451	1.0686	0.0817	0.25	0.024(10)	8
3H2C4	0.3043	1.0961	0.0937	0.25	0.024(10)	8
3C5	0.3452	1.0055	0.0226	0.25	0.024(10)	8
3H1C5	0.3533	0.9625	-0.0107	0.25	0.024(10)	8
3H2C5	0.3425	1.0477	-0.0142	0.25	0.024(10)	8
3C6	0.3897	1.0201	0.0705	0.25	0.024(10)	8
3H1C6	0.4039	1.0699	0.0582	0.25	0.024(10)	8
3H2C6	0.3793	1.0249	0.1243	0.25	0.024(10)	8
3C7	0.43	0.9678	0.0683	0.25	0.024(10)	8
3H1C7	0.4137	0.9191	0.0782	0.25	0.024(10)	8
3H2C7	0.4549	0.9753	0.1128	0.25	0.024(10)	8
3C8	0.458	0.9633	0.0009	0.25	0.024(10)	8
3H1C8	0.4345	0.9807	-0.0423	0.25	0.024(10)	8
3H2C8	0.4625	0.9096	-0.0108	0.25	0.024(10)	8
3C9	0.502	1.0689	0.0173	0.25	0.024(10)	8
3H1C9	0.4913	1.0719	0.0708	0.25	0.024(10)	8
3H2C9	0.4751	1.0958	-0.0152	0.25	0.024(10)	8
3H3C9	0.5358	1.0965	0.0150	0.25	0.024(10)	8
3C10	0.5449	0.9637	0.0385	0.25	0.024(10)	8
3H1C10	0.5393	0.9090	0.0387	0.25	0.024(10)	8
3H2C10	0.5464	0.9792	0.0931	0.25	0.024(10)	8
3C11	0.5915	0.979	0.0027	0.25	0.024(10)	8
3H1C11	0.6163	0.9363	0.0044	0.25	0.024(10)	8
3H2C11	0.6103	1.0213	0.0280	0.25	0.024(10)	8
3C12	0.5777	0.999	-0.0709	0.25	0.024(10)	8
3H1C12	0.5940	0.9664	-0.1092	0.25	0.024(10)	8
3H2C12	0.5889	1.0508	-0.0815	0.25	0.024(10)	8
3C13	0.5236	0.9932	-0.0736	0.25	0.024(10)	8
3H1C13	0.5063	1.0296	-0.1085	0.25	0.024(10)	8
3H2C13	0.5152	0.9438	-0.0946	0.25	0.024(10)	8
3C14	0.2614	0.9842	-0.007	0.25	0.024(10)	8
3H1C14	0.2594	1.0282	-0.0414	0.25	0.024(10)	8
3H2C14	0.2706	0.9408	-0.0392	0.25	0.024(10)	8
3H3C14	0.2250	0.9752	0.0104	0.25	0.024(10)	8
3N2	0.5061	0.9975	-0.0029	0.25	0.024(10)	8

4N1	0.2405	0.5805	0.9807	0.25	0.024(10)	8
4C1	0.1987	0.6247	0.9915	0.25	0.024(10)	8
4H1C1	0.1834	0.6153	1.0419	0.25	0.024(10)	8
4H2C1	0.1692	0.6153	0.9538	0.25	0.024(10)	8
4C2	0.2167	0.697	0.9915	0.25	0.024(10)	8
4H1C2	0.1931	0.7325	1.0167	0.25	0.024(10)	8
4H2C2	0.2212	0.7153	0.9386	0.25	0.024(10)	8
4C3	0.2644	0.6904	1.0298	0.25	0.024(10)	8
4H1C3	0.2597	0.6902	1.0859	0.25	0.024(10)	8
4H2C3	0.2889	0.7316	1.0186	0.25	0.024(10)	8
4C4	0.2822	0.6223	1.0061	0.25	0.024(10)	8
4H1C4	0.3073	0.6313	0.9651	0.25	0.024(10)	8
4H2C4	0.3030	0.5984	1.0485	0.25	0.024(10)	8
4C5	0.2355	0.5162	1.0213	0.25	0.024(10)	8
4H1C5	0.2314	0.5292	1.0759	0.25	0.024(10)	8
4H2C5	0.2014	0.4914	1.0067	0.25	0.024(10)	8
4C6	0.2758	0.4636	1.0216	0.25	0.024(10)	8
4H1C6	0.3105	0.4892	1.0240	0.25	0.024(10)	8
4H2C6	0.2757	0.4364	1.0705	0.25	0.024(10)	8
4C7	0.2755	0.4132	0.9619	0.25	0.024(10)	8
4H1C7	0.2759	0.4402	0.9128	0.25	0.024(10)	8
4H2C7	0.3101	0.3889	0.9644	0.25	0.024(10)	8
4C8	0.2376	0.3575	0.9544	0.25	0.024(10)	8
4H1C8	0.2018	0.3798	0.9586	0.25	0.024(10)	8
4H2C8	0.2384	0.3443	0.9004	0.25	0.024(10)	8
4C9	0.2312	0.3100	1.0674	0.25	0.024(10)	8
4H1C9	0.1986	0.3402	1.0703	0.25	0.024(10)	8
4H2C9	0.2259	0.2647	1.0969	0.25	0.024(10)	8
4H3C9	0.2609	0.3368	1.0935	0.25	0.024(10)	8
4N2	0.2416	0.2932	0.9959	0.25	0.024(10)	8
4C10	0.2068	0.2411	0.9695	0.25	0.024(10)	8
4H1C10	0.1969	0.2475	0.9150	0.25	0.024(10)	8
4H2C10	0.1735	0.2401	0.9966	0.25	0.024(10)	8
4C11	0.2303	0.1732	0.9775	0.25	0.024(10)	8
4H1C11	0.2145	0.1349	0.9428	0.25	0.024(10)	8
4H2C11	0.2269	0.1561	1.0307	0.25	0.024(10)	8
4C12	0.2812	0.1896	0.9627	0.25	0.024(10)	8
4H1C12	0.2855	0.1921	0.9067	0.25	0.024(10)	8
4H2C12	0.3063	0.1518	0.9835	0.25	0.024(10)	8
4C13	0.2891	0.2587	0.9944	0.25	0.024(10)	8
4H1C13	0.3061	0.2522	1.0463	0.25	0.024(10)	8
4H2C13	0.3154	0.2865	0.9659	0.25	0.024(10)	8
4C14	0.2434	0.5654	0.9053	0.25	0.024(10)	8
4H1C14	0.2158	0.5295	0.8870	0.25	0.024(10)	8
4H2C14	0.2388	0.6105	0.8734	0.25	0.024(10)	8
4H3C14	0.2784	0.5448	0.8926	0.25	0.024(10)	8
Ow1	0.4516(19)	0.5	0.3930(31)	1	0.025	4
Ow2	0.1648(19)	0	0.2677(33)	1	0.025	4

Selected Bond Lengths

Atom 1	Atom 2	Bond distance Å
Si1	O5	1.593(8)
Si1	O6	1.604(8)
Si1	O7	1.609(8)

Si1	O8	1.607(8)
Si2	O16	1.587(8)
Si2	O21	1.592(8)
Si2	O22	1.609(8)
Si2	O23	1.602(8)
Si3	O11	1.603(8)
Si3	O17	1.603(8)
Si3	O24	1.610(8)
Si3	O25	1.607(8)
Si4	O1	1.590(8)
Si4	O2	1.599(8)
Si4	O3	1.590(8)
Si4	O4	1.598(8)
Si5	O15	1.589(8)
Si5	O21	1.596(8)
Si5	O24	1.610(8)
Si5	O26	1.608(8)
Si6	O1	1.597(8)
Si6	O9	1.588(8)
Si6	O27	1.596(8)
Si6	O28	1.592(8)
Si7	O29	1.595(8)
Si7	O30	1.597(8)
Si7	O31	1.579(8)
Si7	O32	1.591(8)
Si8	O26	1.596(8)
Si8	O33	1.592(8)
Si8	O34	1.598(8)
Si8	O35	1.606(8)
Si9	O4	1.598(8)
Si9	O9	1.589(8)
Si9	O10	1.593(8)
Si9	O11	1.596(8)
Si10	O12	1.582(8)
Si10	O20	1.608(8)
Si10	O35	1.601(8)
Si10	O36	1.610(8)
Si11	O3	1.600(8)
Si11	O7	1.604(8)
Si11	O12	1.583(8)
Si11	O13	1.593(8)
Si12	O37	1.620(8)
Si12	O38	1.587(8)
Si12	O39	1.590(8)
Si12	O40	1.627(8)
Si13	O33	1.593(8)
Si13	O40	1.613(8)
Si13	O41	1.617(8)
Si13	O42	1.624(8)
Si14	O36	1.606(8)
Si14	O38	1.580(8)
Si14	O43	1.599(8)
Si14	O44	1.583(8)
Si15	O23	1.604(8)
Si15	O30	1.601(8)
Si15	O41	1.611(8)

Si15	O45	1.619(8)
Si16	O8	1.604(8)
Si16	O22	1.610(8)
Si16	O28	1.599(8)
Si16	O46	1.607(8)
Si17	O19	1.597(8)
Si17	O47	1.591(8)
Si17	O48	1.603(8)
Si17	O49	1.614(8)
Si18	O6	1.600(8)
Si18	O14	1.598(8)
Si18	O18	1.600(8)
Si18	O31	1.589(8)
Si19	O37	1.618(8)
Si19	O48	1.599(8)
Si19	O50	1.603(8)
Si19	O51	1.593(8)
Si20	O25	1.602(8)
Si20	O42	1.622(8)
Si20	O46	1.606(8)
Si20	O51	1.585(8)
Si21	O29	1.591(8)
Si21	O39	1.589(8)
Si21	O47	1.587(8)
Si21	O52	1.589(8)
Si22	O2	1.598(8)
Si22	O14	1.600(8)
Si22	O15	1.593(8)
Si22	O16	1.576(8)
Si23	O5	1.587(8)
Si23	O43	1.602(8)
Si23	O49	1.616(8)
Si23	O50	1.603(8)
Si24	O17	1.592(8)
Si24	O18	1.597(8)
Si24	O19	1.594(8)
Si24	O20	1.609(8)

Selected O-T-O Angles

O5	Si1	O6	109.4(10)
O5	Si1	O7	107.6(10)
O5	Si1	O8	109.9(9)
O6	Si1	O7	109.8(10)
O6	Si1	O8	108.6(10)
O7	Si1	O8	111.6(10)
O16	Si2	O21	103.0(9)
O16	Si2	O22	112.6(10)
O16	Si2	O23	111.0(10)
O21	Si2	O22	111.3(10)
O21	Si2	O23	109.9(10)
O22	Si2	O23	109.0(10)
O11	Si3	O17	107.3(9)
O11	Si3	O24	108.2(10)
O11	Si3	O25	110.8(10)
O17	Si3	O24	109.5(10)

O17	Si3	O25	109.4(9)
O24	Si3	O25	111.5(10)
O1	Si4	O2	108.3(10)
O1	Si4	O3	107.4(10)
O1	Si4	O4	110.4(10)
O2	Si4	O3	111.6(10)
O2	Si4	O4	109.2(10)
O3	Si4	O4	110.0(9)
O15	Si5	O21	108.5(9)
O15	Si5	O24	111.2(10)
O15	Si5	O26	109.5(9)
O21	Si5	O24	109.0(10)
O21	Si5	O26	107.5(10)
O24	Si5	O26	111.0(10)
O1	Si6	O9	108.5(10)
O1	Si6	O27	109.1(10)
O1	Si6	O28	109.7(10)
O9	Si6	O27	110.4(11)
O9	Si6	O28	110.3(10)
O27	Si6	O28	108.8(8)
O29	Si7	O30	110.5(9)
O29	Si7	O31	109.7(10)
O29	Si7	O32	108.2(11)
O30	Si7	O31	110.7(10)
O30	Si7	O32	112.2(11)
O31	Si7	O32	105.4(9)
O26	Si8	O33	111.2(10)
O26	Si8	O34	108.6(9)
O26	Si8	O35	109.3(10)
O33	Si8	O34	110.1(11)
O33	Si8	O35	107.9(10)
O34	Si8	O35	109.7(9)
O4	Si9	O9	107.8(10)
O4	Si9	O10	111.0(11)
O4	Si9	O11	111.3(10)
O9	Si9	O10	108.4(10)
O9	Si9	O11	110.2(10)
O10	Si9	O11	108.2(8)
O12	Si10	O20	109.3(10)
O12	Si10	O35	110.1(9)
O12	Si10	O36	109.7(10)
O20	Si10	O35	110.0(10)
O20	Si10	O36	109.9(10)
O35	Si10	O36	107.7(10)
O3	Si11	O7	109.2(10)
O3	Si11	O12	106.5(9)
O3	Si11	O13	109.5(11)
O7	Si11	O12	110.8(10)
O7	Si11	O13	109.6(9)
O12	Si11	O13	111.2(11)
O37	Si12	O38	110.9(10)
O37	Si12	O39	110.3(10)
O37	Si12	O40	105.0(9)
O38	Si12	O39	108.6(10)
O38	Si12	O40	111.9(10)
O39	Si12	O40	110.1(9)

O33	Si13	O40	111.9(10)
O33	Si13	O41	107.5(10)
O33	Si13	O42	107.5(10)
O40	Si13	O41	110.8(9)
O40	Si13	O42	108.8(10)
O41	Si13	O42	110.3(10)
O36	Si14	O38	108.4(10)
O36	Si14	O43	107.2(10)
O36	Si14	O44	110.8(11)
O38	Si14	O43	112.9(10)
O38	Si14	O44	111.8(11)
O43	Si14	O44	105.6(9)
O23	Si15	O30	108.1(10)
O23	Si15	O41	109.5(10)
O23	Si15	O45	109.7(10)
O30	Si15	O41	113.2(9)
O30	Si15	O45	107.5(10)
O41	Si15	O45	108.8(10)
O8	Si16	O22	111.3(10)
O8	Si16	O28	107.1(10)
O8	Si16	O46	110.7(9)
O22	Si16	O28	108.0(10)
O22	Si16	O46	111.3(10)
O28	Si16	O46	108.2(10)
O19	Si17	O47	106.3(10)
O19	Si17	O48	107.7(9)
O19	Si17	O49	110.2(10)
O47	Si17	O48	108.6(9)
O47	Si17	O49	111.2(10)
O48	Si17	O49	112.5(10)
O6	Si18	O14	110.0(10)
O6	Si18	O18	109.9(10)
O6	Si18	O31	111.7(10)
O14	Si18	O18	110.4(9)
O14	Si18	O31	107.5(10)
O18	Si18	O31	107.2(10)
O37	Si19	O48	107.7(10)
O37	Si19	O50	107.5(10)
O37	Si19	O51	114.2(10)
O48	Si19	O50	111.1(10)
O48	Si19	O51	109.8(10)
O50	Si19	O51	106.6(9)
O25	Si20	O42	108.8(10)
O25	Si20	O46	110.1(10)
O25	Si20	O51	110.7(10)
O42	Si20	O46	108.7(10)
O42	Si20	O51	109.3(10)
O46	Si20	O51	109.2(9)
O29	Si21	O39	111.3(9)
O29	Si21	O47	109.4(10)
O29	Si21	O52	109.2(11)
O39	Si21	O47	111.4(10)
O39	Si21	O52	109.8(11)
O47	Si21	O52	105.6(9)
O2	Si22	O14	109.3(10)
O2	Si22	O15	109.6(10)

O2	Si22	O16	111.8(10)
O14	Si22	O15	108.2(9)
O14	Si22	O16	109.6(10)
O15	Si22	O16	108.2(9)
O5	Si23	O43	110.6(10)
O5	Si23	O49	109.9(10)
O5	Si23	O50	108.9(9)
O43	Si23	O49	111.8(10)
O43	Si23	O50	105.7(9)
O49	Si23	O50	109.9(10)
O17	Si24	O18	110.2(9)
O17	Si24	O19	107.2(9)
O17	Si24	O20	111.2(10)
O18	Si24	O19	108.7(10)
O18	Si24	O20	108.9(10)
O19	Si24	O20	110.6(10)

Appendix D2: Refined Cell and Atomic Parameters, Bond Lengths and Angles for As-made TNU-9 with Refined Template Locations

a = 23.239(1) *b* = 20.0792(5) *c* = 19.4540(6) β = 92.593(2) volume = 11019.4(6)Å^3

atom	x	y	z	occupancy	U_{iso}, Å^2	Multiplicity
Si1	0.1012(7)	0.1880(10)	0.7071(9)	1	0.0130(17)	8
Si2	0.0039(7)	0.3105(11)	0.1464(10)	1	0.0130(17)	8
Si3	0.1529(7)	0.1852(10)	0.1684(10)	1	0.0130(17)	8
Si4	0.0897(7)	0.1176(11)	0.9306(10)	1	0.0130(17)	8
Si5	0.1062(6)	0.3091(10)	0.0855(9)	1	0.0130(17)	8
Si6	0.0049(7)	0.0770(7)	0.1476(11)	1	0.0130(17)	8
Si7	0.1043(7)	0.4274(9)	0.7122(11)	1	0.0130(17)	8
Si8	0.1512(7)	0.4237(8)	0.1724(10)	1	0.0130(17)	8
Si9	0.1014(7)	0.0776(7)	0.0871(10)	1	0.0130(17)	8
Si10	0.2532(7)	0.3797(11)	0.2287(10)	1	0.0130(17)	8
Si11	0.1463(7)	0.0766(7)	0.8041(11)	1	0.0130(17)	8
Si12	0.1661(7)	0.3815(11)	0.4396(10)	1	0.0130(17)	8
Si13	0.1010(7)	0.3772(10)	0.3059(10)	1	0.0130(17)	8
Si14	0.2370(7)	0.0745(8)	0.6148(11)	1	0.0130(17)	8
Si15	0.0006(7)	0.4235(8)	0.2557(12)	1	0.0130(17)	8
Si16	1.0017(7)	0.1893(10)	0.2546(10)	1	0.0130(17)	8
Si17	0.2375(7)	0.3113(11)	0.6219(10)	1	0.0130(17)	8
Si18	0.1420(6)	0.3091(10)	0.7988(9)	1	0.0130(17)	8
Si19	0.1640(7)	0.2210(10)	0.4341(10)	1	0.0130(17)	8
Si20	0.1031(7)	0.2168(10)	0.3047(10)	1	0.0130(17)	8
Si21	0.1681(8)	0.4252(8)	0.5874(11)	1	0.0130(17)	8
Si22	0.0857(7)	0.2771(10)	0.9313(10)	1	0.0130(17)	8
Si23	0.1662(7)	0.1892(11)	0.5838(10)	1	0.0130(17)	8
Si24	0.2524(7)	0.2198(11)	0.2242(10)	1	0.0130(17)	8
O1	0.0402(9)	0.0869(17)	0.9038(17)	1	0.0135(30)	8
O2	0.0850(12)	0.1972(10)	0.9326(19)	1	0.0135(30)	8
O3	0.1283(11)	0.0949(19)	0.8783(13)	1	0.0135(30)	8
O4	0.1035(11)	0.0911(19)	0.0064(10)	1	0.0135(30)	8

O5	0.1225(9)	0.1883(20)	0.6327(12)	1	0.0135(30)	8
O6	0.1220(13)	0.2511(15)	0.7490(18)	1	0.0135(30)	8
O7	0.1184(13)	0.1211(14)	0.7466(17)	1	0.0135(30)	8
O8	0.0446(6)	0.1941(20)	0.7005(14)	1	0.0135(30)	8
O9	0.0508(8)	0.1013(16)	0.1102(18)	1	0.0135(30)	8
O10	0.1063(17)	0	0.1043(24)	1	0.0135(30)	4
O11	0.1426(9)	0.1159(12)	0.1294(16)	1	0.0135(30)	8
O12	0.2013(7)	0.0920(18)	0.8058(18)	1	0.0135(30)	8
O13	0.1367(17)	0	0.7887(25)	1	0.0135(30)	4
O14	0.1203(11)	0.3013(19)	0.8731(12)	1	0.0135(30)	8
O15	0.1051(10)	0.3049(18)	0.0039(9)	1	0.0135(30)	8
O16	0.0346(8)	0.3068(18)	0.9160(13)	1	0.0135(30)	8
O17	0.2091(7)	0.1929(18)	0.1769(15)	1	0.0135(30)	8
O18	0.3013(6)	0.1932(19)	0.1958(17)	1	0.0135(30)	8
O19	0.2457(12)	0.1901(18)	0.2990(10)	1	0.0135(30)	8
O20	0.2533(12)	0.2998(10)	0.2265(19)	1	0.0135(30)	8
O21	0.0527(7)	0.3120(21)	0.1086(16)	1	0.0135(30)	8
O22	1.0014(14)	0.2477(15)	0.1977(16)	1	0.0135(30)	8
O23	-0.0027(13)	0.3783(14)	0.1879(15)	1	0.0135(30)	8
O24	0.1321(13)	0.2449(14)	0.1205(18)	1	0.0135(30)	8
O25	0.1305(11)	0.1846(16)	0.2426(12)	1	0.0135(30)	8
O26	0.1312(12)	0.3774(13)	0.1110(15)	1	0.0135(30)	8
O27	0.0100(17)	0	0.1671(23)	1	0.0135(30)	4
O28	0.9988(13)	0.1189(12)	0.2161(14)	1	0.0135(30)	8
O29	0.1280(11)	0.4129(22)	0.6409(13)	1	0.0135(30)	8
O30	0.0483(7)	0.4171(23)	0.7061(17)	1	0.0135(30)	8
O31	0.1270(12)	0.3806(11)	0.7703(15)	1	0.0135(30)	8
O32	0.1192(19)	0.5	0.7369(26)	1	0.0135(30)	4
O33	0.1249(12)	0.4094(17)	0.2414(13)	1	0.0135(30)	8
O34	0.1450(16)	0.5	0.1500(22)	1	0.0135(30)	4
O35	0.2062(7)	0.4072(19)	0.1885(17)	1	0.0135(30)	8
O36	0.2521(13)	0.4056(19)	0.3066(11)	1	0.0135(30)	8
O37	0.1683(12)	0.3010(10)	0.4401(19)	1	0.0135(30)	8
O38	0.2166(8)	0.4131(18)	0.4262(17)	1	0.0135(30)	8
O39	0.1495(10)	0.4095(19)	0.5108(10)	1	0.0135(30)	8
O40	0.1275(11)	0.3989(15)	0.3777(13)	1	0.0135(30)	8
O41	0.0466(7)	0.4023(19)	0.3028(16)	1	0.0135(30)	8
O42	0.1042(13)	0.2970(9)	0.2987(18)	1	0.0135(30)	8
O43	0.1933(10)	0.1192(13)	0.5873(19)	1	0.0135(30)	8
O44	0.2190(14)	0	0.6082(27)	1	0.0135(30)	4
O45	0.0061(19)	0.5	0.2323(25)	1	0.0135(30)	4
O46	0.0493(7)	0.1913(19)	0.3026(15)	1	0.0135(30)	8
O47	0.2135(9)	0.3820(12)	0.6085(19)	1	0.0135(30)	8
O48	0.2845(8)	0.3084(18)	0.5787(16)	1	0.0135(30)	8
O49	0.2010(12)	0.2510(14)	0.6037(21)	1	0.0135(30)	8
O50	0.1457(10)	0.1948(18)	0.5060(9)	1	0.0135(30)	8
O51	0.1277(10)	0.1944(16)	0.3758(11)	1	0.0135(30)	8
O52	0.1857(17)	0.5	0.5928(28)	1	0.0135(30)	4
1N1	0.505(9)	0.121(4)	0.491(14)	0.25	0.0147	8
1C1	0.481(13)	0.170(9)	0.445(17)	0.25	0.0147	8
1C2	0.491(21)	0.240(6)	0.475(24)	0.25	0.0147	8
1C3	0.510(19)	0.228(10)	0.550(23)	0.25	0.0147	8
1C4	0.507(13)	0.151(12)	0.560(14)	0.25	0.0147	8
1C5	0.481(9)	0.056(6)	0.488(19)	0.25	0.0147	8
1C6	0.507(13)	0.0000	0.527(15)	0.5	0.0147	4

1C7	0.514(13)	-0.064(5)	0.485(20)	0.25	0.0147	8
1C8	0.480(8)	-0.120(5)	0.501(19)	0.25	0.0147	8
1C9	0.510(12)	-0.200(14)	0.584(11)	0.25	0.0147	8
1N2	0.497(7)	-0.187(5)	0.511(11)	0.25	0.0147	8
1C10	0.460(8)	-0.236(6)	0.490(16)	0.25	0.0147	8
1C11	0.485(11)	-0.303(5)	0.479(16)	0.25	0.0147	8
1C12	0.538(11)	-0.285(9)	0.475(17)	0.25	0.0147	8
1C13	0.539(9)	-0.207(9)	0.473(16)	0.25	0.0147	8
1C14	0.554(9)	0.112(13)	0.470(18)	0.25	0.0147	8
2N1	0.576(4)	0.5000	0.486(6)	0.5	0.0147	4
2C1	0.625(5)	0.5000	0.516(7)	0.5	0.0147	4
2C2	0.658(5)	0.503(21)	0.454(12)	0.25	0.0147	8
2C3	0.626(9)	0.485(17)	0.390(8)	0.25	0.0147	8
2C4	0.578(7)	0.466(8)	0.419(8)	0.25	0.0147	8
2C5	0.542(6)	0.471(7)	0.532(12)	0.25	0.0147	8
2C6	0.501(7)	0.518(9)	0.548(15)	0.25	0.0147	8
2C7	0.464(6)	0.487(17)	0.594(13)	0.25	0.0147	8
2C8	0.417(6)	0.527(13)	0.591(13)	0.25	0.0147	8
2C9	0.389(9)	0.423(12)	0.635(16)	0.25	0.0147	8
2N2	0.380(4)	0.495(14)	0.628(6)	0.25	0.0147	8
2C10	0.333(5)	0.504(25)	0.593(7)	0.25	0.0147	8
2C11	0.296(4)	0.499(32)	0.650(11)	0.25	0.0147	8
2C12	0.325(8)	0.508(23)	0.719(8)	0.25	0.0147	8
2C13	0.376(7)	0.523(15)	0.698(8)	0.25	0.0147	8
2C14	0.563(5)	0.5698(23)	0.471(9)	0.25	0.0147	8
3N1	0.2967	0.9941	0.0523	0.25	0.0147	8
3C1	0.2963	0.9339	0.0985	0.25	0.0147	8
3C2	0.2668	0.9526	0.1600	0.25	0.0147	8
3C3	0.2788	1.0260	0.1703	0.25	0.0147	8
3C4	0.2813	1.0515	0.0966	0.25	0.0147	8
3C5	0.3452	1.0055	0.0226	0.25	0.0147	8
3C6	0.3897	1.0201	0.0705	0.25	0.0147	8
3C7	0.4300	0.9678	0.0683	0.25	0.0147	8
3C8	0.4580	0.9633	0.0009	0.25	0.0147	8
3C9	0.5020	1.0689	0.0173	0.25	0.0147	8
3N2	0.5061	0.9975	-0.0029	0.25	0.0147	8
3C10	0.5449	0.9637	0.0385	0.25	0.0147	8
3C11	0.5915	0.979	0.0027	0.25	0.0147	8
3C12	0.5777	0.999	-0.0709	0.25	0.0147	8
3C13	0.5236	0.9932	-0.0736	0.25	0.0147	8
3C14	0.2614	0.9842	-0.007	0.25	0.0147	8
4N1	0.2405	0.5805	0.9807	0.25	0.0147	8
4C1	0.1987	0.6247	0.9915	0.25	0.0147	8
4C2	0.2167	0.6970	0.9915	0.25	0.0147	8
4C3	0.2644	0.6904	1.0298	0.25	0.0147	8
4C4	0.2822	0.6223	1.0061	0.25	0.0147	8
4C5	0.2355	0.5162	1.0213	0.25	0.0147	8
4C6	0.2758	0.4636	1.0216	0.25	0.0147	8
4C7	0.2755	0.4132	0.9619	0.25	0.0147	8
4C8	0.2376	0.3575	0.9544	0.25	0.0147	8
4C9	0.2312	0.31	1.0674	0.25	0.0147	8
4N2	0.2416	0.2932	0.9959	0.25	0.0147	8
4C10	0.2068	0.2411	0.9695	0.25	0.0147	8

4C11	0.2303	0.1732	0.9775	0.25	0.0147	8
4C12	0.2812	0.1896	0.9627	0.25	0.0147	8
4C13	0.2891	0.2587	0.9944	0.25	0.0147	8
4C14	0.2434	0.5654	0.9053	0.25	0.0147	8
Na1	0.456(4)	0.5	0.392(7)	0.5	0.025	4

Selected bond lengths

Si1	O5	1.592(13)
Si1	O6	1.605(13)
Si1	O7	1.611(12)
Si1	O8	1.604(12)
Si2	O16	1.593(13)
Si2	O21	1.592(13)
Si2	O22	1.611(12)
Si2	O23	1.598(13)
Si3	O11	1.604(13)
Si3	O17	1.595(12)
Si3	O24	1.615(13)
Si3	O25	1.601(12)
Si4	O1	1.593(12)
Si4	O2	1.604(12)
Si4	O3	1.592(13)
Si4	O4	1.599(13)
Si5	O15	1.589(12)
Si5	O21	1.596(12)
Si5	O24	1.616(12)
Si5	O26	1.611(13)
Si6	O1	1.596(12)
Si6	O9	1.591(13)
Si6	O27	1.598(12)
Si6	O28	1.591(13)
Si7	O29	1.593(13)
Si7	O30	1.596(12)
Si7	O31	1.583(13)
Si7	O32	1.587(13)
Si8	O26	1.596(12)
Si8	O33	1.589(12)
Si8	O34	1.600(12)
Si8	O35	1.605(12)
Si9	O4	1.596(12)
Si9	O9	1.591(13)
Si9	O10	1.598(12)
Si9	O11	1.594(13)
Si10	O12	1.582(13)
Si10	O20	1.605(12)
Si10	O35	1.607(13)
Si10	O36	1.604(13)
Si11	O3	1.595(13)
Si11	O7	1.609(13)
Si11	O12	1.584(12)
Si11	O13	1.588(12)
Si12	O37	1.617(12)
Si12	O38	1.592(13)

Si12	O39	1.586(13)
Si12	O40	1.627(13)
Si13	O33	1.588(13)
Si13	O40	1.614(13)
Si13	O41	1.616(13)
Si13	O42	1.619(13)
Si14	O36	1.598(13)
Si14	O38	1.585(13)
Si14	O43	1.599(13)
Si14	O44	1.583(12)
Si15	O23	1.601(13)
Si15	O30	1.601(13)
Si15	O41	1.612(13)
Si15	O45	1.611(12)
Si16	O8	1.606(13)
Si16	O22	1.614(12)
Si16	O28	1.600(13)
Si16	O46	1.602(12)
Si17	O19	1.591(13)
Si17	O47	1.589(13)
Si17	O48	1.604(13)
Si17	O49	1.617(12)
Si18	O6	1.601(12)
Si18	O14	1.603(12)
Si18	O18	1.602(12)
Si18	O31	1.589(13)
Si19	O37	1.615(12)
Si19	O48	1.600(13)
Si19	O50	1.601(13)
Si19	O51	1.587(12)
Si20	O25	1.602(13)
Si20	O42	1.615(12)
Si20	O46	1.603(13)
Si20	O51	1.584(13)
Si21	O29	1.591(13)
Si21	O39	1.589(13)
Si21	O47	1.587(13)
Si21	O52	1.585(13)
Si22	O2	1.606(12)
Si22	O14	1.604(13)
Si22	O15	1.593(13)
Si22	O16	1.577(13)
Si23	O5	1.591(12)
Si23	O43	1.600(13)
Si23	O49	1.620(12)
Si23	O50	1.601(13)
Si24	O17	1.593(13)
Si24	O18	1.600(13)
Si24	O19	1.591(13)
Si24	O20	1.607(12)

1N1	1C1	1.480(26)
1N1	1C4	1.472(26)
1N1	1C5	1.454(26)
1N1	1C	1.470(27)

1C1	1C2	1.555(27)
1C2	1C3	1.551(27)
1C3	1C4	1.558(28)
1C5	1C6	1.527(28)
1C6	1C7	1.535(28)
1C7	1C8	1.513(28)
1C10	1C11	1.553(27)
1C11	1C12	1.551(27)
1C12	1C13	1.564(28)
1N2	1C8	1.441(26)
1N2	1C9	1.475(27)
1N2	1C10	1.489(26)
1N2	1C13	1.473(26)

2N1	2C1	1.478(26)
2N1	2C4	1.481(26)
2N1	2C5	1.462(26)
2N1	2C	1.474(26)
2C1	2C2	1.555(27)
2C2	2C3	1.550(27)
2C3	2C4	1.554(28)
2C5	2C6	1.539(28)
2C6	2C7	1.538(28)
2C7	2C8	1.542(28)
2N2	2C8	1.453(26)
2N2	2C10	1.477(26)
2N2	2C13	1.479(26)
2N2	2C9	1.465(26)
2C10	2C11	1.552(28)
2C11	2C12	1.552(27)
2C12	2C13	1.549(28)

Selected Bond Angles

O5	Si1	O6	108.4(15)
O5	Si1	O7	108.6(15)
O5	Si1	O8	110.1(13)
O6	Si1	O7	108.7(15)
O6	Si1	O8	108.7(15)
O7	Si1	O8	112.3(15)
O16	Si2	O21	103.0(13)
O16	Si2	O22	112.9(15)
O16	Si2	O23	109.5(15)
O21	Si2	O22	111.3(16)
O21	Si2	O23	109.9(16)
O22	Si2	O23	110.1(15)
O11	Si3	O17	106.9(14)
O11	Si3	O24	108.5(15)
O11	Si3	O25	110.5(15)
O17	Si3	O24	108.8(15)
O17	Si3	O25	109.9(15)
O24	Si3	O25	112.1(15)
O1	Si4	O2	108.8(15)
O1	Si4	O3	107.3(15)

O1	Si4	O4	110.3(15)
O2	Si4	O3	111.1(16)
O2	Si4	O4	109.0(16)
O3	Si4	O4	110.3(14)
O15	Si5	O21	107.9(14)
O15	Si5	O24	111.5(15)
O15	Si5	O26	109.9(14)
O21	Si5	O24	109.1(15)
O21	Si5	O26	106.8(15)
O24	Si5	O26	111.5(15)
O1	Si6	O9	108.6(15)
O1	Si6	O27	109.3(16)
O1	Si6	O28	110.2(15)
O9	Si6	O27	109.8(16)
O9	Si6	O28	110.0(15)
O27	Si6	O28	108.9(13)
O29	Si7	O30	111.5(14)
O29	Si7	O31	109.9(16)
O29	Si7	O32	108.4(16)
O30	Si7	O31	110.1(15)
O30	Si7	O32	113.0(17)
O31	Si7	O32	103.6(13)
O26	Si8	O33	111.3(15)
O26	Si8	O34	108.9(14)
O26	Si8	O35	109.4(15)
O33	Si8	O34	110.7(17)
O33	Si8	O35	106.4(15)
O34	Si8	O35	110.0(13)
O4	Si9	O9	107.5(15)
O4	Si9	O10	111.4(16)
O4	Si9	O11	111.5(15)
O9	Si9	O10	107.7(16)
O9	Si9	O11	110.7(15)
O10	Si9	O11	108.0(13)
O12	Si10	O20	110.1(16)
O12	Si10	O35	109.9(15)
O12	Si10	O36	109.6(15)
O20	Si10	O35	109.6(16)
O20	Si10	O36	110.4(16)
O35	Si10	O36	107.3(15)
O3	Si11	O7	109.6(15)
O3	Si11	O12	106.7(14)
O3	Si11	O13	109.6(17)
O7	Si11	O12	110.8(15)
O7	Si11	O13	109.4(15)
O12	Si11	O13	110.7(17)
O37	Si12	O38	111.4(16)
O37	Si12	O39	111.3(16)
O37	Si12	O40	104.1(14)
O38	Si12	O39	107.8(15)
O38	Si12	O40	111.6(16)
O39	Si12	O40	110.8(14)
O33	Si13	O40	112.1(16)
O33	Si13	O41	106.3(15)
O33	Si13	O42	108.0(15)
O40	Si13	O41	110.5(14)

O40	Si13	O42	108.6(15)
O41	Si13	O42	111.4(16)
O36	Si14	O38	108.2(15)
O36	Si14	O43	107.0(15)
O36	Si14	O44	111.2(17)
O38	Si14	O43	112.8(16)
O38	Si14	O44	112.3(17)
O43	Si14	O44	105.3(14)
O23	Si15	O30	108.5(15)
O23	Si15	O41	109.5(15)
O23	Si15	O45	108.1(15)
O30	Si15	O41	113.9(14)
O30	Si15	O45	107.8(16)
O41	Si15	O45	109.1(16)
O8	Si16	O22	110.5(15)
O8	Si16	O28	106.4(15)
O8	Si16	O46	111.3(14)
O22	Si16	O28	108.8(15)
O22	Si16	O46	111.0(15)
O28	Si16	O46	108.6(15)
O19	Si17	O47	106.3(15)
O19	Si17	O48	106.7(14)
O19	Si17	O49	111.0(15)
O47	Si17	O48	107.6(14)
O47	Si17	O49	111.8(15)
O48	Si17	O49	113.0(15)
O6	Si18	O14	109.6(15)
O6	Si18	O18	110.0(15)
O6	Si18	O31	111.4(15)
O14	Si18	O18	111.0(15)
O14	Si18	O31	107.3(15)
O18	Si18	O31	107.4(15)
O37	Si19	O48	108.2(15)
O37	Si19	O50	106.8(15)
O37	Si19	O51	115.4(16)
O48	Si19	O50	110.4(15)
O48	Si19	O51	109.1(15)
O50	Si19	O51	106.9(13)
O25	Si20	O42	109.6(15)
O25	Si20	O46	110.0(15)
O25	Si20	O51	109.6(15)
O42	Si20	O46	109.8(15)
O42	Si20	O51	109.7(15)
O46	Si20	O51	108.1(14)
O29	Si21	O39	111.6(14)
O29	Si21	O47	109.6(15)
O29	Si21	O52	109.4(17)
O39	Si21	O47	111.4(15)
O39	Si21	O52	109.9(17)
O47	Si21	O52	104.7(14)
O2	Si22	O14	108.8(16)
O2	Si22	O15	109.8(15)
O2	Si22	O16	111.7(16)
O14	Si22	O15	108.9(14)
O14	Si22	O16	109.5(15)
O15	Si22	O16	108.1(14)

O5	Si23	O43	110.3(16)
O5	Si23	O49	110.2(15)
O5	Si23	O50	108.0(13)
O43	Si23	O49	112.3(15)
O43	Si23	O50	104.7(14)
O49	Si23	O50	111.2(15)
O17	Si24	O18	109.8(14)
O17	Si24	O19	106.3(14)
O17	Si24	O20	111.5(16)
O18	Si24	O19	109.4(15)
O18	Si24	O20	109.3(15)
O19	Si24	O20	110.6(15)
Si4	O1	Si6	156.4(23)
Si4	O2	Si22	174.1(24)
Si4	O3	Si11	154.1(24)
Si4	O4	Si9	160.9(22)
Si1	O5	Si23	151.4(22)
Si1	O6	Si18	173.4(27)
Si1	O7	Si11	157.2(25)
Si1	O8	Si16	141.7(20)
Si6	O9	Si9	142.9(24)
Si9	O10	Si9	154.2(32)
Si3	O11	Si9	140.9(20)
Si10	O12	Si11	151.3(23)
Si11	O13	Si11	151.2(31)
Si18	O14	Si22	159.3(24)
Si5	O15	Si22	153.5(22)
Si2	O16	Si22	138.5(19)
Si3	O17	Si24	145.8(21)
Si18	O18	Si24	149.5(22)
Si17	O19	Si24	148.0(22)
Si10	O20	Si24	178.9(24)
Si2	O21	Si5	168.4(24)
Si2	O22	Si16	174.4(25)
Si2	O23	Si15	153.6(25)
Si3	O24	Si5	169.0(26)
Si3	O25	Si20	154.4(23)
Si5	O26	Si8	149.4(23)
Si6	O27	Si6	151.0(30)
Si6	O28	Si16	148.7(23)
Si7	O29	Si21	151.7(28)
Si7	O30	Si15	145.9(24)
Si7	O31	Si18	151.4(24)
Si7	O32	Si7	133.6(29)
Si8	O33	Si13	166.4(24)
Si8	O34	Si8	146.5(29)
Si8	O35	Si10	159.4(24)
Si10	O36	Si14	167.1(24)
Si12	O37	Si19	172.3(22)
Si12	O38	Si14	155.9(23)
Si12	O39	Si21	142.2(20)
Si12	O40	Si13	148.4(20)
Si13	O41	Si15	147.6(22)
Si13	O42	Si20	169.7(23)
Si14	O43	Si23	150.2(23)
Si14	O44	Si14	141.7(29)

Si15	O45	Si15	144.7(32)
Si16	O46	Si20	142.5(20)
Si17	O47	Si21	149.7(23)
Si17	O48	Si19	151.1(22)
Si17	O49	Si23	177.7(27)
Si19	O50	Si23	137.0(19)
Si19	O51	Si20	140.6(20)
Si21	O52	Si21	143.0(31)
1C1	1N1	1C4	106.1(34)
1C1	1N1	1C5	111(4)
1C1	1N1	1C	108(4)
1C4	1N1	1C	108(4)
1C4	1N1	1C5	107(25)
1C5	1N1	1C	109(4)
1C8	1N2	1C9	111(4)
1C8	1N2	1C10	111(4)
1C8	1N2	1C13	117(4)
1C9	1N2	1C10	107(4)
1C9	1N2	1C13	106(4)
1C10	1N2	1C13	104.7(33)
1N1	1C1	1C2	108(4)
1C1	1C2	1C3	104.9(26)
1C2	1C3	1C4	105.1(30)
1N1	1C4	1C3	107(4)
1N1	1C5	1C6	115(4)
1C5	1C6	1C7	114(26)
1C6	1C7	1C8	114(4)
1C7	1C8	1N2	111(16)
1C11	1C10	1N2	107(4)
1C10	1C11	1C12	104.6(24)
1C11	1C12	1C13	104.6(31)
1C12	1C13	1N2	105(4)
2C1	2N1	2C4	106.1(33)
2C1	2N1	2C5	113(4)
2C1	2N1	2C	107(4)
2C4	2N1	2C5	114(4)
2C4	2N1	2C	107(4)
2C5	2N1	2C	110(4)
2N1	2C1	2C2	106(4)
2C1	2C2	2C3	105.9(26)
2C2	2C3	2C4	104.3(30)
2N1	2C4	2C3	106(4)
2N1	2C5	2C6	113(4)
2C5	2C6	2C7	114(4)
2C6	2C7	2C8	112(4)
2C7	2C8	2N2	113(4)
2C8	2N2	2C10	112(4)
2C8	2N2	2C13	112(4)
2C8	2N2	2C9	111(4)
2C10	2N2	2C9	108(4)
2C10	2N2	2C13	109(15)
2C13	2N2	2C9	108(4)
2N2	2C10	2C11	106(4)

7C10	7C11	7C12	105.8(26)
7C11	7C12	7C13	104.4(30)
7N2	7C13	7C12	106(4)

Appendix E: Refinement Data Discussed in Part 3

(1) Refined cell parameters, atomic coordinates and selected bond lengths and angles for calcined Cu-MgAPO STA-6

***a* (Å)**	***b* (Å)**	***c* (Å)**	**Volume (Å^3)**
14.322(1)	14.322(1)	10.200(1)	2092.0(4)

Atom	***x***	***y***	***z***	***Occupancy***	**U_{iso} (x100)**
Al(1)	0.260(2)	0.111(2)	0.000	1	2.0(1)
Al(2)	0.395(1)	-0.105(1)	-0.250	1	2.0(1)
P(1)	0.267(2)	-0.114(2)	0.000	1	2.0(1)
P(2)	0.610(1)	-0.110(1)	-0.250	1	2.0(1)
O(1)	0.234(2)	-0.024(3)	0.000	1	2.4(2)
O(2)	0.337(2)	-0.145(3)	-0.103(2)	1	2.4(2)
O(3)	0.505(2)	-0.127(1)	-0.205(2)	1	2.4(2)
O(4)	0.179(3)	-0.167(3)	0.000	1	2.4(2)
O(5)	0.689(2)	-0.145(2)	-0.143(2)	1	2.4(2)
Cu(1)	0.38(2)	0.87(2)	0.000	0.03(1)	2.0(3)

Bond length (Å)			
Al(1)-O(1)	1.96(4)	P(1)-O(1)	1.37(4)
Al(1)-O(4)	1.65(3)	P(1)-O(2)	1.53(3)
Al(1)-O(5)	1.70(3)	P(1)-O(4)	1.48(5)
Al(2)-O(2)	1.81(2)	P(2)-O(3)	1.59(4)
Al(2)-O(3)	1.67(4)	P(2)-O(5)	1.65(3)
Cu(1)-O(2)	1.25(2)		

O-T-O bond angles (°)			
O(1)-Al(1)-O(4)	115(2)	O(1)-P(1)-O(2)	120(2)
O(1)-Al(1)-O(5)	111(2)	O(1)-P(1)-O(4)	101(3)
O(4)-Al(1)-O(5)	100(2)	O(2)-P(1)-O(2)	90(2)
O(5)-Al(1)-O(5)	118(3)	O(2)-P(1)-O(4)	114(2)
O(2)-Al(2)-O(2)	113(3)	O(3)-P(2)-O(3)	111(2)
O(2)-Al(2)-O(3)	98(1)	O(3)-P(2)-O(5)	114(1)
O(3)-Al(2)-O(3)	115(2)	O(5)-P(2)-O(5)	91(3)

(2) Refined cell parameters, atomic coordinates and selected bond lengths and angles for calcined Cu-SAPO STA-6

***a* (Å)**	***b* (Å)**	***c* (Å)**	**Volume (Å^3)**
14.316(1)	14.316(1)	10.267(1)	2104.2(3)

Atom	***x***	***y***	***z***	***Occupancy***	U_{iso} **(x100)**
Al(1)	0.266(1)	0.107(1)	0.000	1	1.6(2)
Al(2)	0.392(1)	-0.108(1)	-0.250	1	1.6(2)
P(1)	0.263(1)	-0.115(1)	0.000	0.75	1.6(2)
P(2)	0.609(1)	-0.110(1)	-0.250	0.75	1.6(2)
Si(1)	0.263(1)	-0.115(1)	0.000	0.25	1.6(2)
Si(2)	0.609(1)	-0.110(1)	-0.250	0.25	1.6(2)
O(1)	0.241(1)	-0.011(1)	0.000	1	2.9(3)
O(2)	0.323(1)	-0.138(1)	-0.119(1)	1	2.9(3)
O(3)	0.508(1)	-0.126(1)	-0.209(1)	1	2.9(3)
O(4)	0.166(1)	-0.161(1)	0.000	1	2.9(3)
O(5)	0.675(1)	-0.138(1)	-0.138(1)	1	2.9(3)
Cu(1)	0.574(4)	0.52(1)	0.47(1)	0.047(2)	5.1(3)
Cu(2)	0.25(2)	0.25(2)	0.250	0.037(5)	5.1(3)

Bond length (Å)			
Al(1)-O(1)	1.72(1)	P/Si(1)-O(1)	1.53(1)
Al(1)-O(4)	1.73(1)	P/Si(1)-O(2)	1.53(1)
Al(1)-O(5)	1.71(1)	P/Si(1)-O(4)	1.54(1)
Al(2)-O(2)	1.73(1)	P/Si(2)-O(3)	1.53(1)
Al(2)-O(3)	1.73(1)	P/Si(2)-O(5)	1.54(1)
Cu(1)-O(1)	2.4(1)	Cu(2)-O(2)	2.3(4)
Cu(1)-O(4)	2.4(1)	Cu(2)-O(5)	2.3(4)

O-T-O bond angles (^{o})			
O(1)-Al(1)-O(4)	107(1)	O(1)-P/Si(1)-O(2)	109(1)
O(1)-Al(1)-O(5)	111(1)	O(1)-P/Si(1)-O(4)	103(1)
O(4)-Al(1)-O(5)	108(1)	O(2)-P/Si(1)-O(2)	107(1)
O(5)-Al(1)-O(5)	112(1)	O(2)-P/Si(1)-O(4)	114(1)
O(2)-Al(2)-O(2)	108(1)	O(3)-P/Si(2)-O(3)	112(1)
O(2)-Al(2)-O(3)	109.0(4)	O(3)-P/Si(2)-O(5)	109.3(4)
O(3)-Al(2)-O(3)	110(1)	O(5)-P/Si(2)-O(5)	103(1)

(3) Refined cell parameters, atomic coordinates and selected bond lengths and angles for calcined Cu-SAPO STA-7

***a* (Å)**	***b* (Å)**	***c* (Å)**	**Volume (Å^3)**
18.648(5)	18.648(5)	9.405(1)	3270.4(2)

Atom	***x***	***y***	***z***	***Occupancy***	**U_{iso} (x100)**
Al(1)	0.935(1)	0.337(1)	0.419(2)	1	0.8(1)
Al(2)	0.826(1)	0.545(1)	0.344(2)	1	0.8(1)
Al(3)	1.055(1)	0.567(1)	0.171(3)	1	0.8(1)
P(1)	0.833(1)	0.436(1)	0.597(2)	0.75	0.8(1)
P(2)	0.953(1)	0.661(1)	0.344(2)	0.75	0.8(1)
P(3)	0.934(1)	0.447(1)	0.171(2)	0.75	0.8(1)
Si(1)	0.833(1)	0.436(1)	0.597(2)	0.25	0.8(1)
Si(2)	0.953(1)	0.661(1)	0.344(2)	0.25	0.8(1)
Si(3)	0.934(1)	0.447(1)	0.171(2)	0.25	0.8(1)
O(1)	0.865(1)	0.369(1)	0.521(4)	1	1.8(2)
O(2)	0.940(2)	0.378(1)	0.257(3)	1	1.8(2)
O(3)	0.922(1)	0.248(1)	0.391(3)	1	1.8(2)
O(4)	0.841(2)	0.502(1)	0.508(2)	1	1.8(2)
O(5)	0.863(1)	0.441(2)	0.747(2)	1	1.8(2)
O(6)	0.862(2)	0.486(1)	0.216(3)	1	1.8(2)
O(7)	0.880(1)	0.621(1)	0.345(3)	1	1.8(2)
O(8)	0.738(1)	0.566(1)	0.329(3)	1	1.8(2)
O(9)	1.002(2)	0.645(1)	0.208(3)	1	1.8(2)
O(10)	0.986(1)	0.641(1)	0.494(3)	1	1.8(2)
O(11)	1.005(1)	0.490(1)	0.198(2)	1	1.8(2)
O(12)	0.923(2)	0.426(2)	0.012(2)	1	1.8(2)
Cu(1)	0.686(3)	0.26(1)	0.44(1)	0.09(1)	3.6(3)
Cu(2)	0.22(1)	0.184(4)	0.66(1)	0.09(1)	3.6(3)
Cu(3)	0.25(4)	0.01(1)	0.25(3)	0.03(1)	3.6(3)

Bond length (Å)					
Al(1)-O(1)	1.72(2)	P/Si(1)-O(1)	1.56(2)	Cu(1)-O(1)	2.2(2)
Al(1)-O(2)	1.72(2)	P/Si(1)-O(3)	1.53(2)	Cu(1)-O(3)	2.1(2)
Al(1)-O(3)	1.70(2)	P/Si(1)-O(4)	1.49(2)		
Al(1)-O(10)	1.73(2)	P/Si(1)-O(5)	1.52(2)	Cu(2)-O(7)	2.3(1)
				Cu(2)-O(8)	2.2(1)
Al(2)-O(4)	1.78(2)	P/Si(2)-O(7)	1.55(2)		
Al(2)-O(6)	1.76(2)	P/Si(2)-O(8)	1.48(2)	Cu(3)-O(3)	2.1(3)
Al(2)-O(7)	1.74(2)	P/Si(2)-O(9)	1.60(2)	Cu(3)-O(5)	2.6(1)
Al(2)-O(8)	1.70(2)	P/Si(2)-O(10)	1.58(2)		
Al(3)-O(5)	1.72(2)	P/Si(3)-O(2)	1.52(2)		
Al(3)-O(9)	1.79(2)	P/Si(3)-O(6)	1.58(2)		
Al(3)-O(11)	1.74(2)	P/Si(3)-O(11)	1.58(2)		
Al(3)-O(12)	1.77(2)	P/Si(3)-O(12)	1.56(2)		

O-T-O bond angles (^{o})					
O(1)-Al(1)-O(2)	112(2)	O(5)-Al(3)-O(9)	119(2)	O(7)-P/Si(2)-O(8)	105(2)
O(1)-Al(1)-O(3)	109(2)	O(5)-Al(3)-O(11)	110(2)	O(7)-P/Si(2)-O(9)	114(2)
O(1)-Al(1)-O(10)	107(2)	O(5)-Al(3)-O(12)	104(2)	O(7)-P/Si(2)-O(10)	103(2)
O(2)-Al(1)-O(3)	108(1)	O(9)-Al(3)-O(11)	110(2)	O(8)-P/Si(2)-O(9)	104(2)
O(2)-Al(1)-O(10)	105(1)	O(9)-Al(3)-O(12)	105(2)	O(8)-P/Si(2)-O(10)	114(2)
O(3)-Al(1)-O(10)	115(2)	O(11)-Al(3)-O(12)	109(2)	O(9)-P/Si(2)-O(10)	116(2)
O(4)-Al(2)-O(6)	105(2)	O(1)-P/Si(1)-O(3)	107(2)	O(2)-P/Si(3)-O(6)	108(2)
O(4)-Al(2)-O(7)	106(1)	O(1)-P/Si(1)-O(4)	111(2)	O(2)-P/Si(3)-O(11)	105(2)
O(4)-Al(2)-O(8)	109(2)	O(1)-P/Si(1)-O(5)	109(2)	O(2)-P/Si(3)-O(12)	108(2)
O(6)-Al(2)-O(7)	107(1)	O(3)-P/Si(1)-O(4)	106(2)	O(6)-P/Si(3)-O(11)	116(2)
O(6)-Al(2)-O(8)	117(1)	O(3)-P/Si(1)-O(5)	108(2)	O(6)-P/Si(3)-O(12)	106(2)
O(7)-Al(2)-O(8)	112(1)	O(4)-P/Si(1)-O(5)	116(2)	O(11)-P/Si(3)-O(12)	113(2)

(4) Refined cell parameters, atomic coordinates and selected bond lengths and angles for calcined Cu-MgAPO-18

***a* (Å)**	***b* (Å)**	***c* (Å)**	***β* (°)**	**Volume (Å^3)**
13.533(2)	12.678(3)	18.435(5)	87.70(3)	3163(1)

Atom	***x***	***y***	***z***	***Occupancy***	**U_{iso} (x100)**
Al(1)	0.116(1)	0.050(1)	0.167(1)	1	6.4(3)
Al(2)	0.122(1)	-0.218(1)	0.943(1)	1	6.4(3)
Al(3)	-0.224(1)	-0.092(1)	0.049(1)	1	6.4(3)
P(1)	0.223(1)	-0.097(1)	0.055(1)	1	6.4(3)
P(2)	-0.113(1)	-0.233(1)	0.929(1)	1	6.4(3)
P(3)	-0.116(1)	0.026(1)	0.159(1)	1	6.4(3)
O(1)	-0.166(2)	-0.072(2)	0.131(1)	1	7.2(1)
O(2)	-0.144(2)	-0.164(3)	-0.007(1)	1	7.2(1)
O(3)	-0.002(1)	-0.251(2)	0.932(2)	1	7.2(1)
O(4)	0.138(2)	-0.169(3)	0.030(1)	1	7.2(1)
O(5)	0.195(2)	-0.033(2)	0.121(1)	1	7.2(1)
O(6)	-0.005(1)	0.017(2)	0.144(2)	1	7.2(1)
O(7)	-0.157(2)	0.124(2)	0.121(1)	1	7.2(1)
O(8)	-0.333(2)	-0.161(2)	0.064(2)	1	7.2(1)
O(9)	0.134(2)	0.037(2)	0.260(1)	1	7.2(1)
O(10)	0.189(2)	-0.332(2)	0.927(2)	1	7.2(1)
O(11)	-0.140(2)	-0.180(1)	0.858(1)	1	7.2(1)
O(12)	-0.253(2)	0.027(2)	1.008(1)	1	7.2(1)
Cu(1)	0.43(1)	0.84(1)	0.508(3)	0.22(2)	2.5(2)

Bond length (Å)					
Al(1)-O(5)	1.73(1)	Al(3)-O(1)	1.73(1)	P(2)-O(2)	1.53(1)
Al(1)-O(6)	1.75(1)	Al(3)-O(2)	1.74(1)	P(2)-O(3)	1.52(1)
Al(1)-O(9)	1.74(1)	Al(3)-O(8)	1.74(1)	P(2)-O(8)	1.53(1)
Al(1)-O(11)	1.74(1)	Al(3)-O(12)	1.72(1)	P(2)-O(11)	1.53(1)
Al(2)-O(3)	1.74(1)	P(1)-O(4)	1.54(1)	P(3)-O(1)	1.51(1)
Al(2)-O(4)	1.74(1)	P(1)-O(5)	1.51(1)	P(3)-O(6)	1.53(1)
Al(2)-O(7)	1.74(1)	P(1)-O(10)	1.53(1)	P(3)-O(7)	1.53(1)
Al(2)-O(10)	1.73(1)	P(1)-O(12)	1.52(1)	P(3)-O(9)	1.53(1)
		Cu(1)-O(3)	2.1(1)	Cu(1)-O(8)	1.9(1)

O-T-O bond angles (^{o})					
O(5)-Al(1)-O(6)	108(1)	O(1)-Al(3)-O(2)	108(1)	O(2)-P(2)-O(3)	110(1)
O(5)-Al(1)-O(9)	110(1)	O(1)-Al(3)-O(8)	109(1)	O(2)-P(2)-O(8)	108(1)
O(5)-Al(1)-O(11)	109(1)	O(1)-Al(3)-O(12)	110(1)	O(2)-P(2)-O(11)	110(1)
O(6)-Al(1)-O(9)	111(1)	O(2)-Al(3)-O(8)	111(1)	O(3)-P(2)-O(8)	110(1)
O(6)-Al(1)-O(11)	109(1)	O(2)-Al(3)-O(12)	110(1)	O(3)-P(2)-O(11)	109(1)
O(9)-Al(1)-O(11)	109(1)	O(8)-Al(3)-O(12)	109(1)	O(8)-P(2)-O(11)	109(1)
O(3)-Al(2)-O(4)	109(1)	O(4)-P(1)-O(5)	112(1)	O(1)-P(3)-O(6)	108(1)
O(3)-Al(2)-O(7)	110(1)	O(4)-P(1)-O(10)	107(1)	O(1)-P(3)-O(7)	110(1)
O(3)-Al(2)-O(10)	107(1)	O(4)-P(1)-O(12)	108(1)	O(1)-P(3)-O(9)	110(1)
O(4)-Al(2)-O(7)	110(1)	O(5)-P(1)-O(10)	109(1)	O(6)-P(3)-O(7)	109(1)
O(4)-Al(2)-O(10)	112(1)	O(5)-P(1)-O(12)	111(1)	O(6)-P(3)-O(9)	110(1)
O(7)-Al(2)-O(10)	108(1)	O(10)-P(1)-O(12)	109(1)	O(7)-P(3)-O(9)	109(1)

(5) Refined cell parameters, atomic coordinates and selected bond lengths and angles for calcined Cu-MgAPO-5

***a* (Å)**	***b* (Å)**	***c* (Å)**	***β* (°)**	**Volume (Å^3)**
13.687(1)	13.687(1)	8.3145(5)	120	1348.9(1)

Atom	***x***	***y***	***z***	***Occupancy***	**U_{iso} (x100)**
Al(1)	0.329(2)	0.458(1)	0.093(1)	1	4.8(2)
P(1)	0.118(2)	0.450(1)	0.218(2)	1	4.8(2)
O(1)	0.194(2)	0.418(1)	0.138(3)	1	8.1(4)
O(2)	-0.004(2)	0.357(1)	0.176(3)	1	8.1(4)
O(3)	0.122(2)	0.459(2)	0.392(2)	1	8.1(4)
O(4)	0.158(2)	0.570(2)	0.162(4)	1	8.1(4)

Bond length (Å)			
Al(1)-O(1)	1.69(2)	P(1)-O(1)	1.48(2)
Al(1)-O(2)	1.69(2)	P(1)-O(2)	1.56(2)
Al(1)-O(3)	1.68(2)	P(1)-O(3)	1.45(2)
Al(1)-O(4)	1.72(3)	P(1)-O(4)	1.51(2)

O-T-O bond angles (°)			
O(1)-Al(1)-O(2)	108(1)	O(1)-P(1)-O(2)	106(2)
O(1)-Al(1)-O(3)	110(1)	O(1)-P(1)-O(3)	118(2)
O(1)-Al(1)-O(4)	109(1)	O(1)-P(1)-O(4)	104(2)
O(2)-Al(1)-O(3)	111(1)	O(2)-P(1)-O(3)	106(2)
O(2)-Al(1)-O(4)	109(1)	O(2)-P(1)-O(4)	119(2)
O(3)-Al(1)-O(4)	109(1)	O(3)-P(1)-O(4)	104(2)